TRIBOLOGY SERIES, 29
EDITOR: D. DOWSON

FRICTION SURFACE PHENOMENA

GEORGE P. SHPENKOV

ELSEVIER

FRICTION
SURFACE PHENOMENA

TRIBOLOGY SERIES

Editor

D. Dowson (Gt. Britain)

Advisory Board

W.J. Bartz (Germany)
R. Bassani (Italy)
B. Briscoe (Gt. Britain)
H. Czichos (Germany)
K. Friedrich (Germany)
N. Gane (Australia)
W.A. Glaeser (U.S.A.)
H.E. Hintermann (Switzerland)
K.C. Ludema (U.S.A.)
T. Sakurai (Japan)
W.O. Winer (U.S.A.)

Vol. 6 Friction and Wear of Polymers (Bartenev and Lavrentev)
Vol. 7 Microscopic Aspects of Adhesion and Lubrication (Georges, Editor)
Vol. 8 Industrial Tribology – The Practical Aspects of Friction, Lubrication and Wear (Jones and Scott, Editors)
Vol. 9 Mechanics and Chemistry in Lubrication (Dorinson and Ludema)
Vol. 10 Microstructure and Wear of Materials (Zum Gahr)
Vol. 11 Fluid Film Lubrication – Osborne Reynolds Centenary (Dowson et al., Editors)
Vol. 12 Interface Dynamics (Dowson et al., Editors)
Vol. 13 Tribology of Miniature Systems (Rymuza)
Vol. 14 Tribological Design of Machine Elements (Dowson et al., Editors)
Vol. 15 Encyclopedia of Tribology (Kajdas et al.)
Vol. 16 Tribology of Plastic Materials (Yamaguchi)
Vol. 17 Mechanics of Coatings (Dowson et al., Editors)
Vol. 18 Vehicle Tribology (Dowson et al., Editors)
Vol. 19 Rheology and Elastohydrodynamic Lubrication (Jacobson)
Vol. 20 Materials for Tribology (Glaeser)
Vol. 21 Wear Particles: From the Cradle to the Grave (Dowson et al., Editors)
Vol. 22 Hydrostatic Lubrication (Bassani and Piccigallo)
Vol. 23 Lubricants and Special Fluids (Stepina and Vesely)
Vol. 24 Engineering Tribology (Stachowiak and Batchelor)
Vol. 25 Thin Films in Tribology (Dowson et al., Editors)
Vol. 26 Engine Tribology (Taylor, Editor)
Vol. 27 Dissipative Processes in Tribology (Dowson et al., Editors)
Vol. 28 Coatings Tribology – Properties, Techniques and Applications in Surface Engineering (Holmberg and Matthews)
Vol. 29 Friction Surface Phenomena (Shpenkov)

TRIBOLOGY SERIES, 29
EDITOR: D. DOWSON

FRICTION SURFACE PHENOMENA

George P. Shpenkov
University of Silesia
Sosnowiec, Poland

ELSEVIER
Amsterdam • Lausanne • New York • Oxford • Shannon • Tokyo 1995

ELSEVIER SCIENCE B.V.
Sara Burgerhartstraat 25
P.O. Box 211, 1000 AE Amsterdam, The Netherlands

ISBN 0 444 81684 4

This book is printed on acid-free paper

Printed in The Netherlands

PREFACE

The constantly growing interest in tribology, the science of friction, lubrication and wear, and particularly in the investigation of surface phenomena in the friction zone can be attributed to the recent remarkable increase in number of various friction pairs and to much stricter requirements for performance of machines, instruments and apparatuses where they are found.

Analysis of the current state and development trends in tribology shows that a qualitatively new stage in the investigation of friction has begun. The characteristic feature of this stage is closer study of physicochemical processes of contact. This has resulted in the detection of a series of new friction phenomena prompting revision of the traditional methods of wear prevention.

Making use of favorable friction phenomena (selective transfer, tribo-polymerization, abnormally low friction in a vacuum, viscous flow of metals as result of hydrogen absorption at high temperature, etc.) plus wide introduction of new methods for combating harmful phenomena (e.g. hydrogen wear of metals, seizing etc.) could offer considerable potential economic benefits. This has been confirmed by further investigations on the physicochemistry of friction conducted after the first publication an author's book on this subject in 1978. Support gained, enabled the production of new lubricating materials, using selective transfer during sliding, and also theoretical study of this phenomenon.

What does "selective transfer" and "hydrogen wear" of metals mean? Since the subject of the book is closely related to these phenomena, appropriate definition of both are necessary.

The term "***selective transfer***" (**ST**) is an adopted abbreviation for decreased wear and the coefficient of friction, which is a result of non-oxidized thin copper film formation induced by sliding. Conversely, the term "***hydrogen wear***" (**HW**) is an adopted abbreviation for increased wear of metals, a result of hydrogen absorption induced by sliding.

Fundamental investigations of the ST mechanism are not as advanced as the traditional sections of friction theory. Selective transfer is the most pronounced manifestation of mechanochemistry and physicochemistry of the boundary friction process. The widely differing opinions on this subject indicate the complexity of

the problem and are also the reason why it is not fully described in scientific literature.

Progress in investigations on contact interactions of solids under friction, for example the study of new phenomena such as ST and HW, is only possible if based on advances in the physics of solids surfaces, contact phenomena and mechanics of damage, mechanochemistry, electrochemistry, materials technology, etc.. This book represents an attempt to fulfil this demand. In physics the most vital problem is the study of structural, electrophysical and physicochemical properties of real surfaces of solids subjected to mechanical and various physicochemical effects, including friction (i.e. the study of the surface) modified in various friction conditions. In chemistry most important is the investigation of adsorption and chemisorption of lubricants and the lubricant effect mechanism.

A deep understanding of friction and wear processes requires first, investigation of the influence of the numerous effects accompanying the friction process, i.e. mechanical, electrical, hydroacoustic, physicochemical and other effects, their influence on physicochemical properties, structure of working surfaces etc.

In the book as well as results of studies concerned with certain aspects of phenomena appearing in the process of influencing contacting surfaces, and with detecting the relations between the observed characteristics and behavior of investigated materials in the process of mechanical treatment and friction (with particular reference to selective transfer and hydrogen wear) are presented. The principle followed here is to combine varied experimental facts, physical concepts and investigation methods, which at first sight appear to be unrelated, and using this approach to determine general rules.

Particular attention is paid to the quality of surface preparation and to surface properties, and to interaction between lubricants and the surfaces of real metals. A lubricant, in the broad sense, is taken to mean a third body (interlayer), differing in properties and composition, lying between the contacting surfaces. The lubricant, apart from its main function of reducing friction and wear, also promotes the formation of optimum roughness for the given pairs and conditions, influences the nature of submicrostructural changes and phase composition of working surfaces, separates and at the same time modifies the friction surfaces etc.

Summarized in this book are results of investigations on certain surface phenomena observed during mechanical treatment and friction, mainly of metals used in friction assemblies, working under ST and subjected to hydrogen absorption. The nature of interaction in the systems "metal–boundary lubricant medium–metal" is studied. Theoretical concepts are formulated on the ST and HW mechanisms, one causing abnormally low the coefficient of friction and wear (ST), and the other catastrophic damage to surface layers under friction (HW). Some physical methods of friction investigation not yet published in the literature are briefly discussed, and application examples are given. Noteworthy are the

methods of contact potential difference (CPD) and Mössbauer spectroscopy through conversion electrons and also discussion of new results, obtained with their help. In tribology and surface physics, the Mössbauer electron spectroscopy method is of particular importance due to its high sensitivity. This is a nondestructive selective method for the investigation of structure, phase composition, dynamics of the crystal lattice etc. of surface layers (which are most informative at a depth of 10 – 100 nm).

The first chapter presents interrelated fundamental characteristics of a solid and its surface, such as surface energy and surface tension, and the phenomena of contact interaction of solids' surfaces with each other, and with other phases in static. A brief description is given of the main aspects of a molecular-mechanical theory of friction, including analysis of the assumption of shear resistance positive gradient. Mechanical (deformation) properties of a double electrical layer are considered, and a mechanical model of a double electrical layer (DEL) is given and verified. Certain properties of solids, including friction coefficient, are determined by the value of surface tension, which in its turn varies with adsorption of surfactants contained in the lubricant. Also presented is the mechanism of adsorptive plasticization of surfaces, which has a great influence on the friction process during lubrication with surfactants.

The chapter also gives the reader a general understanding of fundamental surface phenomena which provide the background of their dynamic interaction in mechanical treatment and under friction.

The second chapter deals with the laws governing influence of mechanical effects on the surface. This is illustrated by hand polishing of surfaces with abrasive cloths of various grain sizes. Another highly sensitive recorded parameter is the electron work function (EWF). The experimentally obtained CPD dependence on quality of mechanical treatment of solids, which proved to be universal for the investigated materials, is discussed. An analysis is given of CPD kinetics after ceasing mechanical action in the friction process with adsorption of lubricant molecules. Results presented in this chapter also make it possible to distinguish a group of seven metals possessing a combination of properties, such that under defined friction conditions the ST of each may be predicted. Investigations were carried out on standard constructional metals and alloys under natural conditions (in air).

The fundamentals of the ST-theory under friction are given in the third chapter, and the most characteristic physicochemical processes in ST are considered. The relation between metals' resistance to wear during ST and the electron work function, influence of abrasive particles on the ST effect and other problems are analyzed. From this the electrochemical mechanism of the phenomenon may be determined. The fourth chapter is devoted to an analysis of the simultaneous effects of high pressure and shift deformation, taking place in the zones of actual surface

contact under friction, on structural changes of the contacting surfaces and ambient conditions. The phenomenon of air ionization with perturbation of the boundary friction regime, is described. On the basis of latest results, one more possible mechanism of the "servo vitae" layer formation during ST is discussed. According to N.S. Enikolopyan et al, (Scientific Discovery. Diploma No 288, 1984) high pressures together with shift deformation, which are the necessary main components of the friction process, impart immense chemical and physical energy to the material, and in particular, promote solid monomers' polymerization at abnormally high reaction velocities. According to the author, this offers great potential for utilization in tribology and tribotechnology, but this would need the cooperation of a wide group of tribologists to gain further knowledge of its internal mechanism. The main characteristics of the given phenomenon are given in this chapter, paying special attention to the frequency of processes occurring in the surface layers of friction bodies.

The great possibilities of the Mössbauer electron spectroscopy method, widely used in physics for solving tribology problems are shown in the fifth chapter. Particular tribology problems described here are then solved by this method. These were the following; explaining the polishing mechanism and structure of modified surfaces, the phase composition of surface layers of friction metals, polishing effect, investigation of surface layers anisotropy resulting from specific treatment, etc.

The sixth chapter is devoted to the influence of external electromotive force (EMF) sources on contact resistance and friction pairs' wear, in which ST in the de-energized regime is possible. ST display, electrocapillary and electroplastic effect in current-conducting pairs, and also lubricant influence, are considered. Results of studies allowed certain recommendations to be made aimed at increasing reliability and longevity of lubricated sliding electrical contacts.

The mechanism of hydrogen absorption and hydrogen wear under friction is dealt with in the final, seventh chapter. The calculation of temperature distribution along the normal to the surface into the depth of a sample under friction, is presented. The phenomenon of metal passage to the viscous flow state under hydrogen saturation in the friction process, at temperatures much lower than melting temperatures, is also described. Propositions for HW prevention and the use of ST for this purpose are given.

Current aspects of certain important practical tribology problems discussed in the book are stressed in the conclusion together with considerations of friction process control.

Thus, the reader is offered a review of new ideas and methods in tribology to be used in tribotechnology.

This book is a revised and supplemented version of the author's monograph "Physicochemistry of Friction" (University Publishers, Minsk, 1991). It is intended

for scientific, engineering and technical workers but may also be of value to graduates and students dealing with tribology and tribotechnology. It is hoped that the problems solved by various physical considerations and methods will prove of interest to physicists. The book could also be useful for chemists specializing in lubrication.

Those who have not yet needed to deal with the problems of tribology may begin to learn how complicated, interesting and diverse is the world of friction, and what knowledge it demands. In this way, the author hopes it may attract attention to the problems of tribology among those physicists and chemists who have not yet made their choice in science.

While apologizing for the inadequacies of this book, the author would be grateful for all comments.

It is my pleasure to express sincere thanks to Professor Douglas Godfrey for his friendly and valuable comments related to the translation of the seventh chapter. I also wish to thank Professor Nikolai Myshkin and his assistants for their correction of the entire English text. Many thanks to my son, Maxim, who has assisted me at all stages in the preparation of this manuscript.

George P. Shpenkov

Sosnowiec, 1994

This Page Intentionally Left Blank

CONTENTS

This Page Intentionally Left Blank

Chapter 1

INTERACTION OF SOLIDS

1.1. Surface Energy and Surface Tension

The interaction of solids in friction proceeds on their surfaces. Any surface can be considered as an imperfection of a three-dimensional crystal structure. The break of the lattice periodicity causes a change in the coordination number of the surface atoms, and rehybridization of their bonds. As a result, the atomic arrangement and spacing alter. Here, $Z_v > Z_s$ is usually the case, where Z_v is the coordination number in the crystal volume and Z_s is the same on the surface.

Generally, equilibrium chemical bonds on the surface and in the adjacent region differ from those in the bulk. A disrupted surface structure and an ordered structure in the bulk have no sharp boundary, therefore, a certain transition layer can exist. Two-dimensional structures appear on the crystal surface with atomic spacing different from those in the bulk. The difference in molecular interactions is responsible for an excess of the energy at the interface, which is the surface energy. Thus, molecules at the phase interface, unlike molecules in the bulk, are subjected to the forces, the resultant of which is directed into the solid. Naturally, a part of the substance located at the interface has some specific features, distinct from those of the substance in the bulk. Besides, on the surface and in the near-surface layers phase transitions occur. This fact specifies a number of phenomena, referred to as surface phenomena, like catalysis, adsorption, capillary forces, electronic and molecular processes on the semiconductor surface, the Rehbinder effect, adhesion, etc. The special properties of the surface have the greatest influence upon the behavior of semiconductor devices with sizes commensurable with the thickness of the surface layer.

When considering the effect of mechanical treatment and the interaction of solids in friction from a physicochemical standpoint, the energy parameters should be considered which characterize a solid and its surface, primarily, the surface energy and the surface tension.

Surface energy. The surface energy depends on the nature and structure of a solid and has a definite value corresponding to the surface thermodynamic equilibrium and its saturated vapor [1].

The surface energy distribution is anisotropic. Thus, theoretical calculation of

the model of a 360-atomic lattice for Ca, Ag, Al, Pb, Cu, and Ni has revealed that, in all the above-listed metals, planes (111) have the minimum surface energy σ and planes (110) have the maximum.

The problem of theoretical prediction of the surface energy is more intricate than to predict the atomic bond energy. Discontinuity of the metal lattice leads to a modulation of the volume density of conductivity electrons. Near the boundary, at distances of an order of the atomic size, the density falls from the bulk value to zero. A task of the metal surface theory is to adequately identify the character of the electron density fall. In the solid state theory, this problem is solved with the theory of heterogeneous electron systems (the self-consistent theory of normal state of heterogeneous "electron gas"), specifically, with the density functional method (DFM) [2].

The DFM is also employed in calculating other characteristics of the metal surface, in particular, the electron work function (EWF) Φ and the surface energy σ. In most cases, the calculations are based on the simplest "gel" model, when the metal lattice is replaced by a homogeneous positive background.

The calculations make it clear a double electric layer (DEL) forms near the background boundary with the size of an order of an atom. Since the electron density $n(x)$ does not fall abruptly to zero at the boundary, the "electron gas" extends outward, thereby reducing the kinetic energy of the electrons and increasing the potential energy that restricts further diffusion of the electron density.

On the basis of the DFM and the minimum energy principle of the normal state, for relatively simple models of a solid, a considerable advance has been made in explaining numerous experimental data on the surface energy and the EWF as well as in solving many other problems of the surface physics [2].

Alongside with the development of theoretical predictions, many empirical or semiempirical equations are suggested to relate the surface energy to some physical constants of metals [3]. Thus, for example, a method of crystal cracking in a certain crystallographic direction is used for measuring σ . The equation relating the surface energy to mechanical characteristics of the metal, such as the Young modulus E, appears as

$$\sigma=(6F^2L^2)/(E\omega^2 t_1^3),$$

where F is the force required for propagation of a crack;

L is the length of the crack opening;

ω is the specimen width, and

$2t_1$ is the thickness of the specimens.

A number of studies proposes a simple calculation, yielding approximate values which, however, satisfactorily represent correlations in σ for various metals. As an illustration of a fairly acceptable empirical formula relating σ to the basic

characteristic of a solid, namely, EWF, we may present the equation derived by S.N. Zadumkin for planes (h,k,l) may be presented:

$$\sigma_{hkl}=k_1\Phi_{hkl}(n/V_{sp})^{5/6},$$

where $k_1=1.15$ for $Z_v=8$ and $k_1=1.08$ for $Z_v=12$; n is the number of valence electrons; and V_{sp} is the specific molar volume.

Surface tension. A general thermodynamic approach to equilibrium of a surface layer with two neighboring volume phases gives the following expression for the total surface layer energy

$$U^{(s)} = TS^{(s)} + \gamma s + \sum_i \mu_i n_i^{(s)}, \tag{1.1}$$

where $T=\partial U/\partial S$ is the layer temperature (the intensity factor);

$S^{(s)}$ is the layer entropy (the capacitance factor);

s is the phase interface area;

$\gamma = (\partial U / \partial s)_{S,n_i,\ldots}$ is the intensity factor similar to pressure in the volume phase $\partial U/\partial V=-P$, which is called the layer surface tension (the dimensions of γ are J/m^2 or N/m);

$\mu_i=\partial U/\partial n_i$ is the chemical potential of the component i in the layer (the intensity factor); and

$n_i^{(s)}$ is the excess of the components i in the surface layer.

The surface tension γ enters into expressions for the excess free surface energy of the layer $\sigma^{(s)}$ defined in accordance with equation (1.1) as

$$\sigma^{(s)} = U^{(s)} - TS^{(s)} = \gamma s + \sum_i \mu_i n_i^{(s)}. \tag{1.2}$$

The surface tension is governed by the nature of contacting phases. In surfactant adsorption the Rehbinder effect manifests itself in a variety of forms [4.5]. They include a reduction of the surface potential causing metal softening; origination and subsequent propagation of cracks resulting in the fracture of solids; dramatic fall of the interfacial energy inducing a spontaneous dispersion accompanied by generation of particles of colloidal sizes. The effects stem for the most part from a decrease in the free surface energy of a solid at the boundary with the medium.

In adsorption of surfactants (specifically, of diphilic molecules), the surface tension of the liquid phase diminishes appreciably. Because the surface tension and the free surface energy for a "single-component" liquid are numerically equal, any reduction of the surface tension entails an equivalent reduction of the free surface energy. It ensues from Gibbs' fundamental equation (1.2) for the interfacial layer that the interfacial surface tension γ is defined as the free surface energy

$\sigma^{(s)}$ of a unit surface area at constant temperature and composition of the layer:

$$\gamma = (\partial\sigma^{(s)} / \partial s)_{T, n_i^{(s)}, \ldots}.$$

For solids, such identity does not hold true and the relation between the two quantities is as follows: $\gamma=\sigma+s(\partial\sigma/\partial s)_T$, where s is the surface area.

The difference between the surface energy σ and the surface tension γ is that the first is the work needed for the unit surface area formation and the second is the work required for increasing the available surface by the same magnitude. For liquids, it is as a rule, $\partial\sigma/\partial s=0$, since a uniform density of the liquid film establishes in the surface layer nearly instantaneously, following the film deformation (no matter how much mercury may spread, its physical characteristics remain unchanged). When the solid surface is under tension, the average atomic spacing in the surface layer varies and, accordingly, the conditions of atomic interaction alter (with a tensile-stressed solid metal, the surface area properties also change simultaneously) [3].

The surface layer may be considered in the first approximation as surface phases of variable composition, with the properties being functions of the distance from the interface.

Generally, the "surface phase" has the following thermodynamics. A change in the total internal energy of the system ΔU due to the increment Δs of a new "surface phase" from the side of one of the two bordering phases is $\Delta U=U^s-U_1$, where U^s is the total internal energy of the new "surface phase" and U_1 is the total internal energy of the part of volume V. In conformity with equation (1.1), the expression for ΔU has the form:

$$\Delta U=T(S^s-S_1)+(N^s-N_1)+\gamma\Delta s,$$

where N^s is the particle number in the surface phase and N_1 is the particle number in the part of volume V. A surface identification of the total internal energy of the system is

$$U_s=\Delta U/(\Delta s)=T(S^s-S_1)/(\Delta s)+\mu(N^s-N_1)/(\Delta s)+\gamma=TS_s^*+\mu\Gamma+\gamma.$$

Here, $S_s^*=(S^s-S_1)/(\Delta s)$ is the surface densification of entropy and

$\Gamma=(N^s-N_1)/(\Delta s)$ is the surface densification of the substance, or adsorption. The surface densification of the free energy of the system (the specific free surface energy) is defined as

$$\sigma_s=U_s-TS_s^*=\mu\Gamma+\gamma. \qquad (1.3)$$

From (1.3) follows $\sigma_s\neq\gamma$. Then, as the "surface phase" is generated, the work is spent not only on creating the surface but also on varying the substance density

in the surface layer.

Hence the reduction of the surface tension cannot be treated as a fall of the free surface energy. Thus, for plane (111) of NaCl crystals, $\sigma_s \approx 0.187$ N/m, whereas $\gamma_s \approx 0.562$ N/m.

The surface tension γ is one of the most important characteristics. Many properties of solids are dependent on the surface tension, among them adsorption wettability, adhesion, electron emission (photo-, thermal, exoelectron, and other types), mechanical properties (hardness, creep, friction coefficient, and others), electrochemical phenomena, etc. Thus, the surfactant adsorption causes a change in the surface tension. For example, argon adsorption on the clean surface of a glass rod results in its elongation, equivalent to heating by 523 K.

Solids have heterogeneous surfaces characterized by the presence of areas with different energy and, therefore, with different surface tension (a composition heterogeneity, different crystallographic orientations of individual crystals and crystal lattice imperfections). Adsorption molecules tend to cluster in active centers. In this connection, studies of adsorption have revealed a strong influence of the pretreatment and the state of the surface on the adsorption on metals.

Adsorption of surface-active organic and inorganic ions is also influenced by the metal nature. Ions, highly surface-active on one metal, are low-active or inactive at all on another. For example, hydroxyl ions, which are surface-inactive on mercury even at large pH of solution, are well-adsorbed on iron. Naphthalene molecules, representing two condensed benzene rings, have a flat arrangement on iron, nickel and lead surfaces and a vertical arrangement on a copper surface. Decylamine molecules adsorb on lead, copper, and nickel by hydrocarbon tails of molecules, and an NH_2 group is directed into the solution. The decylamine molecules are oriented to the iron surface by an NH_2 group. Nonetheless, the mechanism of different orientations of decylamine molecules on metals with identical chemical characteristics (like iron and nickel) has not been fully understood [6].

The surface tension of solids depends on the electric potential jump at the interface. It exists at the solid-liquid interface, if both phases are somewhat conducting. Any change in the interfacial electric potential is accompanied by alteration in the character of phenomena occurring on the solid surface [7]. So, changes in the potential of a gold electrode in aqueous solutions cause its elongation and changes in the potential of a high-porous carbon electrode electrode results in its deformation [9].

Studies in correlation of the surface tension γ and the potential φ [7] allowed to ascertain of the fundamental difference between γ and the reversible surface generation work σ for a solid electrode, which was first noticed by Gibbs.

According to the Lippmann equation

$$\partial\sigma/\partial\varphi=-q \tag{1.4}$$

where q is the surface density of the electrode charge. It is apparent from equation (1.4), that σ varies monotonously with the potential. The relative surface θ, the surface change density q, and the potential φ are correlated by the equation

$$\partial\gamma/\partial\varphi=-q-\partial q/\partial\theta, \tag{1.5}$$

where θ is the ratio of the solid surface area after deformation and before [7].

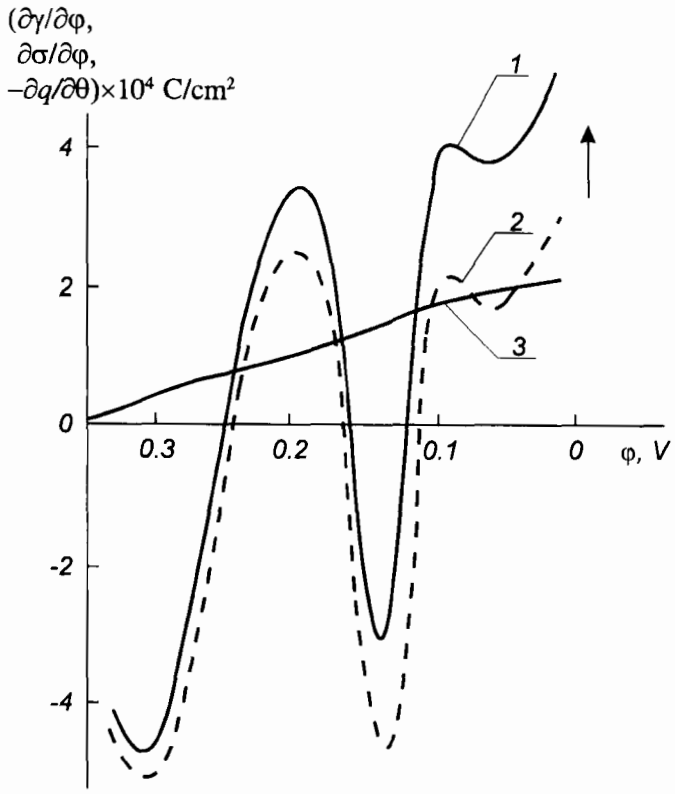

Fig. 1.1. Difference between the surface tension γ and the reversible unit surface area generation work σ of a solid electrode at the level of derivatives of these quantities with respect to the potential φ for platinum in 1 n. H_2SO_4 [7]: 1) $\partial\gamma/\partial\varphi$; 2) $\partial q/\partial\theta$; 3) $\partial\sigma/\partial\varphi$.

Subtracting equation (1.4) from equation (1.5) gives the change in the charge density as a result of elastic deformation of the electrode at the constant potential

$$\partial\gamma/\partial\varphi-\partial\sigma/\partial\varphi=-\partial q/\partial\theta.$$

Experimental results [7] (Fig. 1.1) show that $\partial q/\partial\theta$ in equation (1.5) dominates over q and determines mainly the dependence of γ as function, of φ.

It is already mentioned above, that some mechanical properties of solids are specified by the surface tension. In particular, Bowden, Bockris and other scientists investigated the friction coefficient f between two metals, immersed into an electrolyte, as a function of the specimen potentials. In that case, a maximum f was found near zero charge potential. The dependence of the friction coefficient (and the metal hardness) on the potential, as demonstrated by P.A. Rehbinder et al., has a shape of the electrocapillary curve. The metal hardness and friction coefficient diminish as the electrode potential shifts to the positive or negative relative to the zero charge potential of the metal and organic substances are adsorbed at the electrode-solution interface (for more details see Sect. 6.5).

1.2. Double Electric Layer at the Phase Interface

Inequality between the electrochemical potentials of contacting phases gives rise to a potential jump that manifests itself in the double electric layer (DEL) generation accompanied by a decrease in the free energy of a system.

Several studies treated the electron distribution and the DEL formation on pure surfaces of metal crystals for the ideal case of ultra-high vacuum.

The metal surface generation affects the distribution of mobile electrons in the metal, stipulating the effects of electron emission and electron density levelling. The electrons are forced to escape from the surface, since otherwise their density distribution gradient would cause the kinetic energy on the surface to increase to infinity. The electron escape from the surface rises the surface positive charge and the outside negative charge, i.e. the DEL forms that increases the metal EWF (Fig. 1.2).

The initial potential of the metal electron prior to the emission is

$$\varphi_o(z)=0 \text{ for } z<z_B, \text{ and}$$

$$\varphi_o(z)=\varphi_{o1}=(W_F+\Phi)-(4\pi e^2\rho_o)/\beta^2 \text{ for } z>z_B,$$

where z is the distance to the DEL boundary;

z_B is the DEL width on the surface;

W_F is the kinetic energy of the electron at the Fermi Level;

Φ is the metal EWF;

β is the constant; and ρ_o is the electron density of the metal.

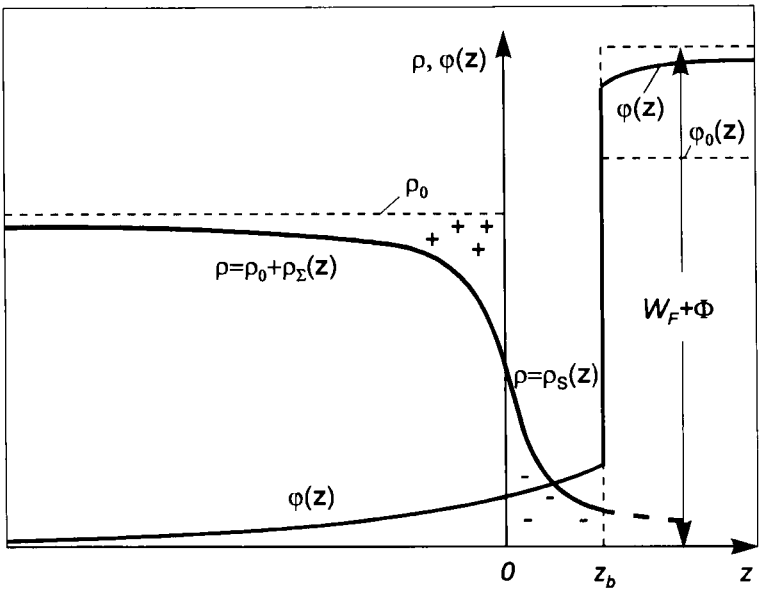

Fig. 1.2. Distribution of the electron density and the potential normal to the metal surface [10].

The width z_B is a function of W_F, Φ and the wave number k_F of the electron at the Fermi level:

$$z_B k_F = \frac{3}{4}\left(\frac{\pi}{2} + \left(\frac{\Phi}{W_F} - 1\right)\arcsin\sqrt{\frac{W_F}{W_F + \Phi}} - \sqrt{\frac{\Phi}{W_F}}\right). \tag{1.6}$$

For monovalent metals $k_F = 1.92/r_s$, where r_s is the sphere radius per one atom of the metal volume. From expression (1.6) it follows that for nickel, Φ=4.5 eV, W_F=7.0 eV, r_s=0.140 nm, and z_B=0.029 nm, and for platinum, Φ=5.0 eV, W_F=5.0 eV, r_s=0.158 nm, and z_B=0.035 nm.

The potential $\varphi_{\rho_s}(z)$ of the electron inside the DEL with the charge density $-e\rho_s(z)$, where $\rho_s(z)$ is the excess electron density arising from the emission, for $z<0$ is equal to

$$\varphi_{\rho_s}(z) = (2\pi e^2 / \beta^2 \rho_0)\exp(-\beta z); \tag{1.7}$$

and for $z>0$, to

$$\varphi_{\rho_s}(z) = (-2\pi e^2 / \beta^2 \rho_0)\exp(-\beta z) + 4\pi e^2 / \beta^2 \rho_0. \tag{1.8}$$

Expressions (1.7) and (1.8) are obtained by integrating the Poisson equation $d^2\varphi_{\rho_s} / dz^2 = -(4\pi e^2) / \rho_s(z)$ with the boundary conditions:

$\varphi_{\rho_s}(z) = 0$ at z=-∞, $d\varphi_{\rho_s}(z)/dz = 0$ at z=±∞ and $\varphi_{\rho_s}(z)$ is continuous at z=0.

The sum of the potentials $\varphi_o(z)$ and $\varphi_{\rho_s}(z)$ given the net potential (see Fig.1.2).

The electron density smoothing effect is accounted for by the corollary of the electronic metal theory, according to which the lower the electron energy the smoother is the confining surface [10] (Fig.1.3). The DEL, resulting from smoothing the electron distribution over the surface, decreases the work function by a value dependent on the original surface structure. The emission depends, in its turn, on the original structure just slightly and produces the DEL that increases the EWF.

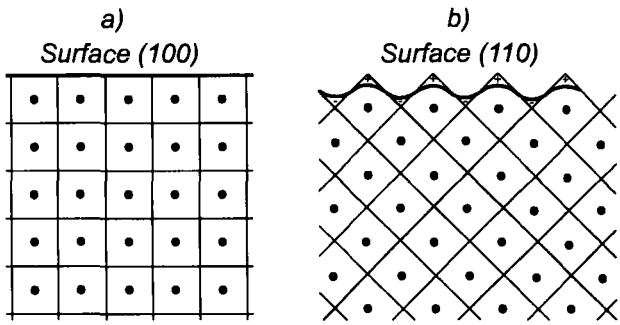

Fig. 1.3. Electron density smoothing and net DEL (a simple cubic lattice): a) no smoothing on plane (100); b) noticeable smoothing on plane (110) [10].

In friction of solids, the surfaces of like or unlike materials contact either directly or through a lubricant that may be of any nature. In this case, the interfacial potential jumps, induced by various factors, are influenced by tribochemical and triboelectric phenomena that complicate the study of processes occurring in the contact zone.

In this connection, we treat the contact potential difference (CPD) and the DEL formation in statics for heterogeneous phases participating in friction.

Metal$_1$–metal$_2$ contact. Metals have electronic-conductivity. An electrochemical potential of metal electrons may be expressed by μ_e=-W_F+kTlnC$_e$, where W_F is the Fermi level (energy); C_e is the thermodynamic concentration of valence electrons (C_e is a dimensionless quantity indicating how the concentration of given particles relates to their maximal possible concentration). For metals, $C_e \approx 1$ because the number of valence electrons in metals is great and $\mu_e \approx -W_F$.

At room temperature, like at T=0 K, the metal electron gas remains mostly degenerate such that the energy is almost independent of the temperature, the

electrochemical potential of the degenerate electron gas coincides identically with the Fermi boundary energy (W_F).

An equilibrium height of the barrier of the two metals is

$$-\Delta W = -\Delta A = kT \ln(C_e^1 / C_e^2),$$

where -ΔA is the total thermodynamic work.

Since $C_e^1 \approx C_e^2 \approx 1$, the equilibrium potential barrier approaches zero.

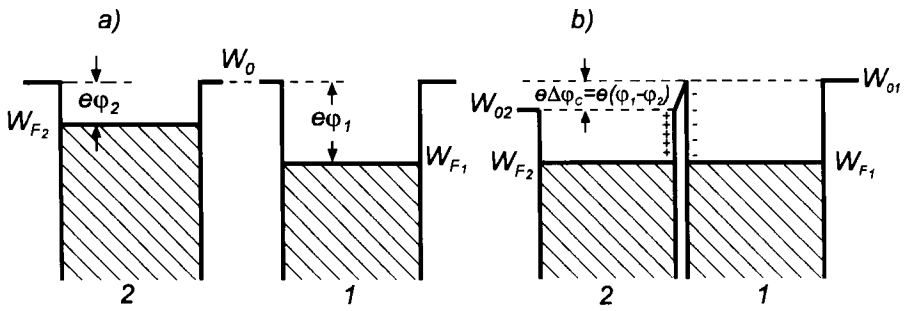

Fig. 1.4. Energy configuration of the metal$_1$–metal$_2$ contact: a) prior to their contact; b) after equilibrium is reached.

Electrons transit from the metal with a smaller work function (Fig.1.4), equal to $\varphi_2 = (W_0 - W_{F_2})/e$, where W_0 is the energy of the electron (with zero velocity) outside the metal, to the metal with a large EWF equal to $\varphi_1 = (W_0 - W_{F_1})/e$, and, correspondingly, these with a lower Fermi energy will persist until the Fermi levels in both metals coincide, forming at contact a common system. In the narrow boundary layer, a potential jump, equal to the difference between the Fermi levels ($W_{F_1} - W_{F_2}$), originates, which inhibits further electron transition from metal$_2$ to metal$_1$.

The contact does not alter the metal work functions, therefore at equilibrium, when $W_{F_1} = W_{F_2} = W_F$, the energy levels W_{01} and W_{02} differ by $e(\varphi_1 - \varphi_2)$. Thus, the equilibrium gives rise to the CPD $\Delta\varphi_c$, compensating the interfacial potential barrier

$$\Delta\varphi_c = \varphi_1 - \varphi_2. \tag{1.9}$$

The contact between two metals must be rectifying. Its voltage-current characteristic (for $U<\Delta\varphi_c$) is defined by the equation

$$I = I_s(e^{eU/kT} - 1), \tag{1.10}$$

where I is the net current across the contact in both directions; I_s is the saturation current; and U is the external potential difference.

In normal conditions, however, a two-metal contact is not rectifying. This is due to the fact that, in contact, the DEL is thin (the effective thickness of the spatial charge layer in metals d_{eff} is not larger than 10^{-7} cm) and, therefore, transparent to the tunnel effect. Expression (1.10) is satisfied if the thickness of a gap between the volume charge layers of the two metals is increased. In practice this is achieved by an electron-depleted dielectric layer that is very thin in the contact, yet thick enough to arrest the tunnel effect.

A capacitance of the potential barrier in the contact per unit area may be expressed in the form $C_c=\Delta\sigma/(\Delta\varphi_c)=\varepsilon\varepsilon_o/d_{eff}$, if it is assumed that the DEL forms a plane capacitor. Then, the surface density of the excess charge is $\Delta\sigma=\varepsilon\varepsilon_o\Delta\varphi_c/d_{eff}$. Assuming $\varepsilon=1$and $\Delta\varphi_c=1$ V, we have $\Delta\sigma=8.85\times10^{-3}$ C/m^2, which corresponds to the surface density of the excess electrons $\Delta n\approx5.5\times10^{16}$ m^{-2}, whereas, in a monatomic metal layer 5 nm, thick they number about 5×10^{18} m^{-2}.

For metal interaction through the outer contact surfaces, the presence of surface barriers dependent on the state of the boundary surfaces should be considered. In that case the CPD is somewhat different from determined from equation (1.9) [11].

Metal–semiconductor contact. The contact phenomena occurring at the metal–semiconductor boundary have been analyzed thoroughly in many studies (e.g. [12]), therefore, only specific examples of the phenomenon will be considered.

Assume we have an *n*-type semiconductor with the electron work function much larger than that of metal $\Phi_s>>\Phi_m$, the volume concentration of the majority of charge carriers being rather small. The electron transition from the metal to the semiconductor proceeds until the electrochemical potentials of electrons in the bulk μ_e and on the surface μ_{es} of the semiconductor equalize, thereby creating a field that inhibits further electron transition from the metal to the semiconductor. Thus, at equilibrium we have $\mu_e=\mu_{es}$ or

$$-W_c^0 + e\varphi + kT\ln C_e = -W_c^0 + e\varphi_s + kT\ln C_{es}$$

where W_c^0 is the total potential energy of the *n*-type electron minus the potential energy in the electrostatic field;

φ and φ_s are the electrostatic potentials of electrons in the bulk and on the contacting surface of the semiconductor;

$e\varphi$ and $e\varphi_s$ are the potential energies of electrons in the electrostatic field in the bulk and on the surface; and

C_e and C_{es} are the thermodynamic electron concentrations in the bulk and on the surface of the semiconductor. The contact potential jump in the spatial charge layer of the semiconductor is

$$\Delta\varphi_s = (kT/e)\ln(C_{es}/C_e). \qquad (1.11)$$

For $C_e\approx10^{-3}$ to 10^{-4} and $C_{es}=1$, from expression (1.11) we obtain $\Delta\varphi_s\approx0.18$ V.

Hence, at the CPD larger than this, the semiconductor surface acquires metallic properties. As in the case of a metal-to-metal contact, the initial barrier at the boundary is balanced by the CPD virtually to the full and it is close to zero, whereas the entire potential barrier is located in the spatial charge layer of the semiconductor.

The effective thickness L of the spatial charge layer in contact, i.e. the depth to which the field penetrates in the semiconductor, is

$$L = \sqrt{2\varepsilon \Delta\Phi / (e^2 n)},$$

where ε is the absolute permittivity of the medium and n is the concentration of charge carriers in the semiconductor. Value L increases together with the work function difference $\Delta\Phi$ between the metal and semiconductor, as the concentration of charge carriers in the semiconductor reduces.

This case relates to the formation of n-n^+ junction of the so-called antibarrier layer with a reduced electric resistance (Fig.1.5,a).

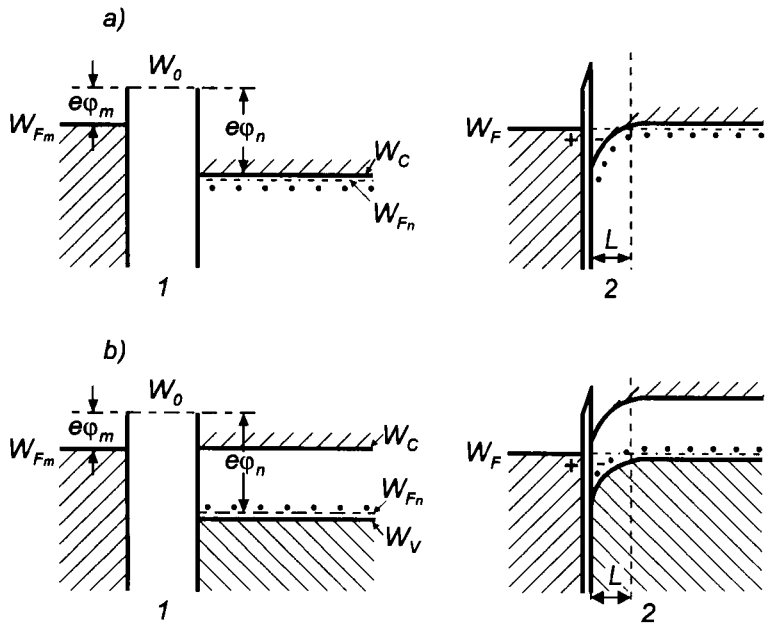

Fig. 1.5. Formation of antibarrier (a) and inversion (barrier) (b) layers:
1) metal and semiconductor before contact;
2) metal-semiconductor junction after equilibrium is reached;
W_{Fm} and W_{Fs} are the Fermi levels of the metal and semiconductor, respectively; W_c is the conduction band bottom energy; and W_v is the valence band top energy.

When the *p*-type semiconductor is in contact with the metal, given that $\varphi_s >> \varphi_m$, the contact potential jump in the spatial charge layer of the semiconductor is

$$\Delta\varphi_s = \frac{\Delta W_g}{e} + \frac{kT}{e} \ln C_h, \tag{1.12}$$

where ΔW_g is the forbidden band width (equal to 1.5 eV for copper oxide (I) Cu_2O) and C_h is the thermodynamic hole concentration ($C_h \approx 10^{-3}$).

Relation (1.12) follows from equation (1.11), if the concentration of the minority of charge carriers (electrons) in a *p*-type semiconductor that pass from the metal to the semiconductor, is expressed in the terms of concentration of the majority of carriers (holes).

For Cu_2O, $\Delta\varphi_s$=1.3 V. Thus, with the contact potential difference greater than 1.3 V and corresponding in the sign to the semiconductor saturation with minority carriers, an inversion, or the so-called barrier, layer (a *p-n*-junction) emerges (Fig.1.5,b) on the semiconductor surface.

If the work function difference between the semiconductor and the metal is insignificant, i. e. insufficient for the concentration C_{es} to increase to unity, the potential barrier in the contact zone assumes an intricate form and consists of electrostatic and initial barriers arranged in series.

Thus, in conformity with the above statements, knowing the EWF of the contacting materials and the conductivity type of the semiconductor, one would think it possible to predict which contact, ohmic or cutoff-type are produced. In reality, however, this rule often fails, primarily because of the screening effect of surface states that contribute to the EWF of both surfaces.

Metal–electrolyte contact; structure of the double electric layer. A distinctive feature of a metal-electrolyte contact as against the metal-semiconductor contact is a huge DEL capacitance, corresponding to the spacing between capacitor plates equal to about 10^{-8} cm, if the double layer is likened to the capacitor. Here arises a field of strength of the order of 10^8 V/cm, which is two orders of magnitude higher than that for the maximal field originating in solids. It is due to the following [13]. Negative electrolyte ions are attracted to the metal surface with a positive potential. However, the electrons of negatively charged ions cannot get into the metal either on their own or due to the tunnel effect, because, electrically, they are several electronvolts lower than the Fermi level in the metal (Fig.1.6).

The carrier concentration in the electrolyte at the Fermi level is negligible. Elevating the energy of negative ions up to the Fermi level of the metal necessitates a field of the order of 10^8 V/cm, achieved when concentration of charged ions in the electrolyte increases.

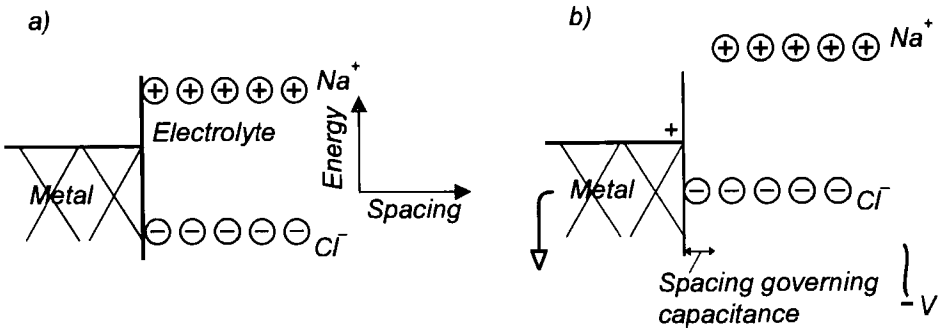

Fig. 1.6. Metal-to-electrolyte contact energy configuration [13]:
a) no bias voltage; b) negative voltage is applied to the electrolyte.

In most cases, a source of energy needed for electrons to pass from the electrolyte to the metal is produced by chemical reactions starting before the electrons of negative ions are brought to the Fermi level. For example, O_2 formation in water electrolysis is accompanied by energy release sufficient for converting an electron of the ion OH^- to one of the states close to the Fermi level of a metal.

As Colraush (1872) first noted, the electrode-solution interface may be represented as a large capacitor with the "plate" spacing equal to the ion radius. Such representation likens the interface to the DEL or, as it is often called, to the "plane capacitor", the theory developed by Helmholtz. Figure 1.7 gives the charge distribution and the potential variation in the DEL according to Helmholtz. The DEL potential jump $\varphi_{s\text{-}m}=\Delta\varphi$ is calculated from the formula $\Delta\varphi=4\pi\rho d/\varepsilon$, where ρ is the charge density of the plates; d is the effective ion radius; and ε is the permittivity of the medium filling the space between the plates.

The DEL theory was subsequently developed by Gouy, Chapman, Stern, Graham and others. These studies founded of the classic DEL theory, i.e. the Helmholtz-Gouy-Chapman-Stern theory, that suggested an explanation of the experimental results obtained in investigation of electrokinetic and electrocapillary phenomena. Through determining more accurately the DEL potential depth, interpretation was made of the existence of kinetic potential, the phenomenon of specific adsorption, the effect of ion concentration and types on the DEL structure, and some other features of the DEL behavior. Though the classic theory is valid only for very dilute solutions it is the only one available at present. The model suggested by Helmholtz failed to explain the dependence of the DEL capacitance and interfacial tension on the solution concentration and temperature. The Gouy-Chapman model, while ignoring the proper ion sizes, took into account the attraction and repulsion of ions by and from a charged electrode surface and their

thermal motion. This produced obtaining results, correct only qualitatively; a quantitative calculation, however, produced results substantially different from the experimental data.

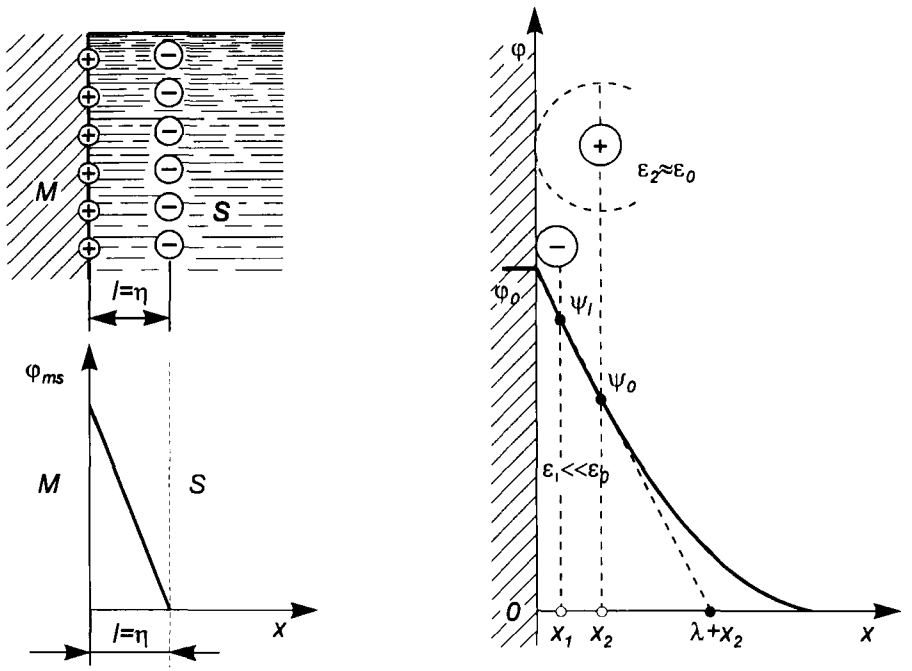

Fig. 1.7. Diagram of the DEL structure and variation in the potential φ_{ms} following Helmholtz.

Fig. 1.8. The DEL structure at the electrode–solution interface [15]: x_1, Helmholtz inner plane; x_2, Helmholtz outer plane; λ , effective thickness of the diffuse layer

The Stern model combined the essential points of the preceding models, offering a one-sided explanation of experimental facts, and included the proper ion sizes and the forces of nonelectrostatic ion interaction with metals. Modern DEL theories are based on Stern's double layer model [15]. The double electric layer (Fig. 1.8) consists of the Helmholtz dense part, referred to as a Helmholtz outer plane, with the thickness of the order of the mean radius of hydrated electrolyte ions ($x_2 \cong 0.3$–0.4 nm) and of the diffuse part with the volume charge density decreasing away from the metal surface. The effective thickness of the diffuse layer [15] is

$$\lambda = \sqrt{\varepsilon_0 \varepsilon_2 RT / 2cF^2}\ \sec h(\psi_0 F_\Phi / 2RT),$$

where ε_2 is the dielectric constant of the diffuse layer, approximately equal to that in the solution bulk ($\varepsilon_2 \approx \varepsilon_s$);

c is the molar ion concentration;

F_Φ is the Faraday number; and

ψ_o is the potential of the Helmholtz outer plane.

In the Helmholtz part, ions are confined both by electrostatic forces (electric centers of such ions reach only the Helmholtz outer plane) and by non-Coulomb forces, viz. by forces of specific adsorption. The relevant plane of localization of the electric centers of specifically adsorbed ions ($x=x_1$) is named the Helmholtz inner plane, i.e. ions enter the dense layer. In connection with this, the number of ions in the dense part depends on the electrolyte nature. The dielectric constant of the dense layer is considerably smaller than that in the solution ($\varepsilon_1 << \varepsilon_s$). Should the solution contain specifically adsorbable ions, their number in the Helmholtz layer is not be equivalent to the metal surface charge but rather exceed it by a certain magnitude. Given this, a surface recharge occurs. For example, the surface recharge is the case in the DEL of a positively charged metal (Fig.1.9), if the solution contains surface-active anions. Thus, we have two DEL models (see Fig.1.8 and 1.9).

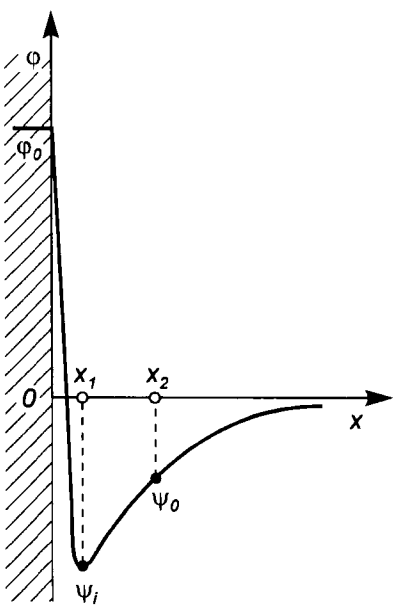

By the law of electroneutrality, the metal surface charges q_m must be balanced out by the charge of ions attracted to the metal surface q_s that is equal to the sum of charge densities in the Helmholtz q_H and diffuse q_d layers, i.e. by the net charge of the Helmholtz inner and outer planes:

$$q_s = q_H + q_d = - q_m \qquad (1.13)$$

The Helmholtz inner plane charge is $q_H = z_i F_\Phi A_i$, where z_1 is the charge of a specifically absorbed ion with allowance for the sign; A_i is the surface concentration of there ions; and q_m and A_i (and, therefore, q_H as well) are determined experimentally; q_d can also be obtained from the above formula.

Fig. 1.9. Potential distribution in DEL in conditions of surface recharge with specifically adsorbed ions [15].

Similarly, the DEL capacitance may be expressed as consisting of two capacitors connected in series, viz. of the capacitors of dense C_H and diffuse C_d layers: $1/C = 1/C_H + 1/C_d$.

The general equation of Stern's theory for 1,1-valence electrolyte (the expanded equation (1.13)) has the form

$$\frac{\varepsilon}{4\pi r_i}(\varphi_{s-m} - \xi) = F_\Phi \Gamma_{\max}((1+\frac{1}{c}\exp\frac{W_- - F_\Phi \xi}{RT})^{-1} - (1+\frac{1}{c}\exp\frac{W_+ - F_\Phi \xi}{RT})^{-1}) +$$

$$+\sqrt{\frac{\varepsilon RTc}{2\pi}}(\exp\frac{F_\Phi \xi}{2RT} - \exp\frac{-F_\Phi \xi}{2RT}),$$

where ε is the dielectric constant;

r_i is the ionic radius;

φ_{s-m} is the potential jump between the solution and the metal;

ξ is the electrokinetic potential (the potential of the Helmholtz inner plane);

F_Φ is the Faraday constant;

Γ_{max} is the maximal number of ions able to adsorb on the unit surface area,

c is the electrolyte concentration;

W_- and W_+ are the adsorption energies of the electrolyte anions and cations; and

R is the universal gas constant.

The DEL theory makes it possible to obtain the dependence of the potential of the outer Helmholtz plane ψ_0 on the diffuse layer charge q_d and the electrolyte concentration c for the diffuse layer [15]:

$$\psi_0 = \frac{2RT}{F}\ln((1+\frac{q_d^2}{4A^2c})^{1/2} - \frac{q_d}{2Ac^{1/2}}),$$

where $A=(2\varepsilon_0\varepsilon_2 RT)^{1/2}$.

This equation allows to find the diffuse layer capacitance C_d:

$$C_d = \frac{F}{2RT}\sqrt{4A^2c + q_d^2}\,.$$

The above-given DEL model, however, is far from perfection. It insufficiently accounts for: discontinuity and heterogeneity of the layer structure along the normal to the interface; the effect of phases, forming the plates, on the DEL thickness, i.e. on the particle interaction; variations in the composition of the interfacial DEL as the equilibrium potential changes, etc.

Stern's theory of DEL structure, despite the noted and other demerits (it disregards a partial charge transfer in specific adsorption of ions, is applicable

only to some metals in the presence of organic compounds, it neglects deformation of the ion sheath, etc.), explains validly the electrokinetic and electrocapillary phenomena, as well as the structure and basic properties of DEL.

Metal–surfactant contact; nonpolar molecules. The DEL is formed on the metal surface in adsorption of surfactants as well. The DEL structure is governed in this case both by the structure and the electric state of the surface and by a surfactant nature. The adsorption for elementary substances is described by the Langmuir isotherm equation

$$\theta=\Gamma/\Gamma_{\infty}=\beta c/(1+\beta c),$$

where θ is the extent to which the surface is filled with the adsorbate;

Γ is the adsorption extent (the surface excess);

Γ_{∞} is the monolayer capacitance;

β is the adsorption equilibrium constant (adsorption index); and

c is the solution concentration.

The adsorption index may be determined from the relation $\beta=g\exp(A/RT)$. Here, g is the entropy multiplier and A is the total work of adsorption (adsorption heat).

Within the experimental error, most of the adsorption data may be described by the simple Langmuir equation. The interaction between adsorbed molecules at large saturation, especially for large organic surfactant molecules when their interaction facilitates subsequent adsorption, is taken into account by A.N. Frumkin by introducing the so-called attraction factor γ_1:

$$\beta_c=[\theta/(1-\theta)]exp(-2\gamma_1\theta).$$

It is clear from this equation that, at rather small the saturations θ , the Frumkin isotherm transforms to that of Langmuir.

In surfactant adsorption, the DEL is achieved both within adsorbed dipole molecules (Fig.1.10) and at the metal–solution interface.

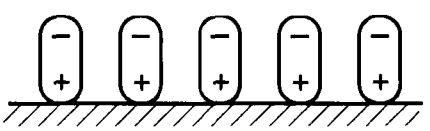

Fig. 1.10. Diagram of the adsorption layer with identical orientation of polar molecules.

Concentration of charge carriers (electrons) in metals is high, therefore, the metals can be classified as nonpolar adsorbents. However, investigations have revealed that, in adsorption of nonpolar hydrocarbon molecules on metals, large

dipole moments with positive external charges are induced therein. Thus, in many cases metals exhibit properties of a polar adsorbent, which is indicative of the existence of a force field near the solid surface [16].

Studies reveal that, as the surface potential changes, the molecules of organic substances are adsorbed only in the neighborhood of the zero-charge potential, when the field strength of the metal-solution DEL is low. The potential jump will be specified by the number of adsorbed molecules (the saturation θ), their dipole moment, and the orientation.

1.3. Mechanical Model of Double Electric Layer

In some engineering applications involving mechanical, hydroacoustic, and other effects in interfaces, the DEL experiences significant deformations. However, DEL deformation properties have been studied poorly. Only some authors [17] briefly report the influence of deformability of various types of ion sheaths on the signal magnitude in measuring the differential capacitance.

All foregoing DEL models assume that the plane, passing through the centers of electrostatically adsorbed ions (the Helmholtz plane), is at a well-defined distance from the metal surface, equal to the effective ion radius. Assuming an ion as a rigid nondeformable sphere carrying a charge is not quite right. Therefore, the available theories of double layer structure ignore vibratory processes registered in DEL under hydroacoustic, mechanical or electric effects. At the same time, a new approach has been advanced in interpreting the results of periodic deformations of the electrode or of its potential changes, viz. the "estunce" method [7], but it has not gained wide recognition.

A mechanical model of the DEL [18,19], resting on the Helmholtz concept expresses the electrostatically absorbed ion as a charged nucleus surrounded by a deformable shell (Fig.1.11). In a static state, when the electrode potential does not

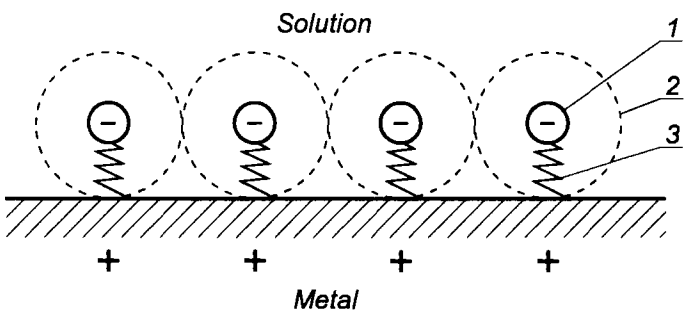

Fig. 1.11. Mechanical model of DEL: 1) charged ion nucleus; 2) elastic sheath; 3) resilient simulation.

change or its mechanical excitation occur, the ion is in equilibrium that is characterized by a certain deformation of the shell (or resilient simulation).

Consideration will be given to the processes proceeding in the DEL with a stepwise variation in the electrode charge.

Since the electrostatic adsorption force is related directly to the electrode charge, a Δq in the latter will cause a corresponding alteration in the attraction force of the ion sheath by Δf_{el}. The balance between the electrostatic adsorption forces and the elastic force of the sheath will lead to additional deformation of the ion by Δd. For small deformations, it may be assumed that the elastic force increment of the ion sheath Δf_{elast} is proportional to the first power of Δd:

$$\Delta f_{elast}=-k_c\Delta d, \tag{1.14}$$

where k_c is the elasticity coefficient of the ion sheath of DEL. To find the increment in the electrostatic adsorption force Δf_{el} we assume the DEL as a plane capacitor. The plane capacitor energy is $W_{el}= q^2/2C$, where q is the charge of one of the capacitor plates and C is the capacitance. Now we calculate the work needed to separate the capacitor plates by Δd:

$$A = F\Delta d = \frac{\partial W_{el}}{\partial d}\Delta d = -\frac{q^2}{2C^2}\frac{\Delta C}{\Delta d}\Delta d.$$

Hence follows the force of electrostatic attraction between the plates (the pondermotive force):

$$f_{el} = -F = \frac{q^2}{2C^2}\frac{\Delta C}{\Delta d}.$$

The increment of the electrostatic adsorption force Δf_{el}, resulting from the change of the electrode charge by Δq, is defined as:

$$\Delta f_{el} = \frac{q}{C^2}\frac{\Delta C}{\Delta d}\Delta q, \tag{1.15}$$

where C is the differential capacitance of the DEL, i.e. the capacitance at a specified electrode potential φ_m.

This force, deforms the ion sheath of the DEL until the increment of the elastic force Δf_{elast} counterbalances Δf_{el}. Consequently, the new equilibrium state will be characterized by mutual compensation of these forces: $\Delta f_{elast}= \Delta f_{el}$. .

Substituting the forces (1.14) and (1.15) into the above equality yields

$$-k_c\Delta d = -\frac{q}{C^2}\frac{\Delta C}{\Delta d}\Delta q,$$

whence
$$\frac{\Delta d}{\Delta q} = \frac{q}{k_c C^2}\frac{\Delta C}{\Delta d}. \tag{1.16}$$

Next we consider the case when the ion sheath is exposed from the side of the liquid or electrode to a mechanical force Δf_{mech} directed normally to the interface. This force, deforms the ion sheath by $\Delta d=\Delta f_{mech}/k_c$. With the surface charge unchanged, the electrode potential alters by

$$\Delta\varphi = -\frac{q}{C^2}\frac{\Delta C}{\Delta d}\Delta d = -\frac{q}{k_c C^2}\frac{\Delta C}{\Delta d}\Delta f_{mech},$$

whence
$$\frac{\Delta\varphi}{\Delta f_{mech}} = -\frac{q}{k_c C^2}\frac{\Delta C}{\Delta d}. \tag{1.17}$$

If a periodic force with the amplitude $\Delta f'_{mech}$ is applied to DEL, the electrode potential varies periodically with a frequency equal to excitation. Since frequency characteristics of the electrode–electrolyte system are unknown, it does not seem possible to compute the potential amplitude $\Delta\varphi$. Therefore, expression (1.17) for the sheath periodic excitation has the form

$$\frac{\Delta\varphi'}{\Delta f'_{mech}} = \xi_1 - \frac{q}{k_c C^2}\frac{\Delta C}{\Delta d}, \tag{1.18}$$

where $\Delta\varphi'$ and $\Delta f'_{mech}$ are the peak values of variations of the electrode potential and inducing force; ξ_1 is the coefficient determining frequency characteristics of the system.

Similar reasoning is also appropriate when the electrode charge varies by the harmonic law with an amplitude $\Delta q'$. Then relation (1.16) for the peak values of Δd and Δq appears as

$$\frac{\Delta d'}{\Delta q'} = \xi_2 \frac{q}{k_c C^2}\frac{\Delta C}{\Delta d}. \tag{1.19}$$

With equal frequencies of electric and mechanical actions and with small amplitudes of variations, the frequency coefficients ξ_1 and ξ_2 can be equalized, and then, based on equations (1.18) and (1.19), we can write

$$\left|\frac{\partial d'}{\partial q'}\right| = \left|\frac{\partial \varphi_,}{\partial f'_{mech}}\right|, \tag{1.20}$$

i.e. the potential-dependence for the amplitude of deformation variations of the DEL ion sheath with variations of the charge density of the solid electrode q' is described by the same curve as the electrode potential variations under periodic deformation. These expressions are valid for the cases when the metal–electrolyte interface can be presented as a plane capacitor. Best suited to such idealization are boundary layers formed on chemically pure noble metals, where any reactions are precluded. For technical metals, such a view is not quite correct because, apart from the physical adsorption, a specific adsorption may occur on the metal surface, namely, chemisorption, and electrochemical reactions.

Using the proposed model of DEL subjected to elastic strain, it is possible to explain some experimental data from a different standpoint [7]. According to it, the deformation of the ion sheath by mechanical vibrations of the electrode is neglected, the signal is believed to result from a change in the area of a wettable electrode surface. Based on these assumptions, an equation was derived that coupled the dependencies of variation amplitudes of the surface tension γ with variations of the charge density of the solid electrode q (the so-called direct effect) and of the potential φ with variations of the relative area of the solid electrode s (the inverse effect, known as an "elastic charging") on the mean electrode potential φ_m:

$$\frac{\partial \gamma}{\partial q} = \frac{\partial \varphi}{\partial s} \tag{1.21}$$

However, the equality of the direct and inverse effects is also apparent from equation (1.20) that treats other processes at the interface. To validate equation (1.20) and, thereby, the assumption of a significant role of the ion sheath deformation, an experiment was conducted, using a setup designed by the authors of [18] (Fig.1.12,a).

Electrochemical cell 9, fabricated from a nonreactive material (PTFE), is pressed against a massive base of shielded chamber 2. To the chamber base, electromagnet 12 is attached, producing via membrane 11 sound vibrations on the cell bottom with a frequency twice as high as that of audio-signal generator 10, driving the electromagnet. Two electrodes (operating 8 and auxiliary 1) are fixed in holder 3. While acting on the wettable surface of the electrode, a hydroacoustic wave periodically deforms the DEL ion sheath. Once amplified selectively in 4, a variable component of the potential is detected in 5 and delivered to the input Y of XY - recorder 6. A sweep voltage from a potentiostat, connected to the cell, is sent to input X. A time constant of the potentiostat must be much in excess of the voltage oscillation period on the DEL. This corresponds to the measuring mode at a constant surface charge (Q=const). Oscillograph 7 is incorporated in the circuit for controlling the amplifier tuning to a double frequency of the generator.

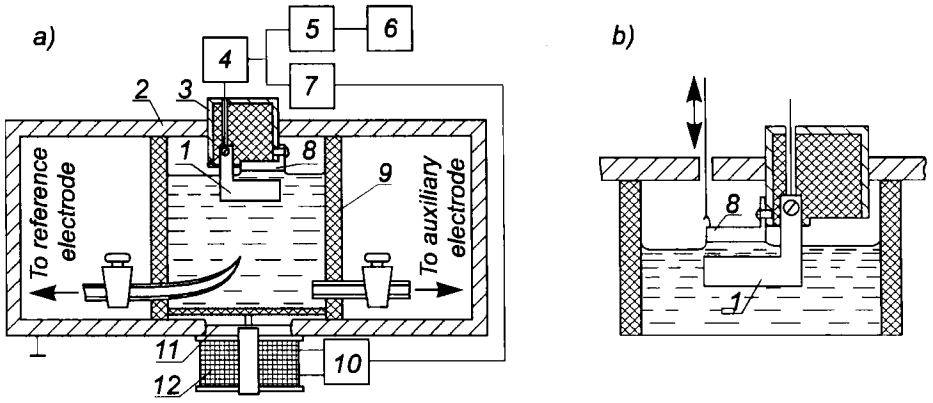

Fig. 1.12. Block diagram of the design for recording the deformation of the adsorption layer under hydroacoustic and mechanical action on the DEL:
a) general view; b) the way the electrodes are secured when the specimen is mechanically excited;
1) auxiliary electrode; 2) shielded chamber; 3) holder; 4) selective amplifier; 5) amplitude detector; 6) XY-recorder; 7) oscillograph;
8) operating electrode; 9) electrochemical cell; 10) audio-signal generator;
11) membrane; 12) electromagnet.

The cell design allows also to investigate of the ion sheath deformation under mechanical vibrations of the operating electrode (Fig.1.12,b). With the aid of a flexible tie (a capron thread), the electrode is linked to the membrane of the second electromagnet (not shown in the figure), mounted on top of the chamber.

The design (see Fig.1.12,b) resembles that reported in [7] and, in the opinion of the author of that book, must record the "elastic charging". With the design in Fig.1.12,a , the "elastic charging" is totally excluded (the electrode is not deformed and the area of the wettable surface does not change).

From similarity of the deformation curves (Fig.1.13), one displaying the deformation of the adsorption layer and the other, the "elastic charging", it may be inferred that the latter is either entirely absent or affects minimally the signal magnitude in these experiments. The experimental conditions are as follows: ν=120 Hz; the working surface area of the electrode is 5×15 mm^2; the thickness is 5 mm; φ_m is taken relative to the standard hydrogen electrode; the sweep is 20 mV/s. When passing through the minimum within of 0.1–0.2 V, the phase of the measured signal changes by π, which is attributable to an electrode surface recharge. The same phase change occurs in the reverse sweeping at the minimum point, where the potential is equal to -0.02 V. The electrode potential $1.5<\varphi_m<-0.05$ V is typified by an abrupt rise of the signal. Apparently gas bubbles appearing on the electrode cause deformation.

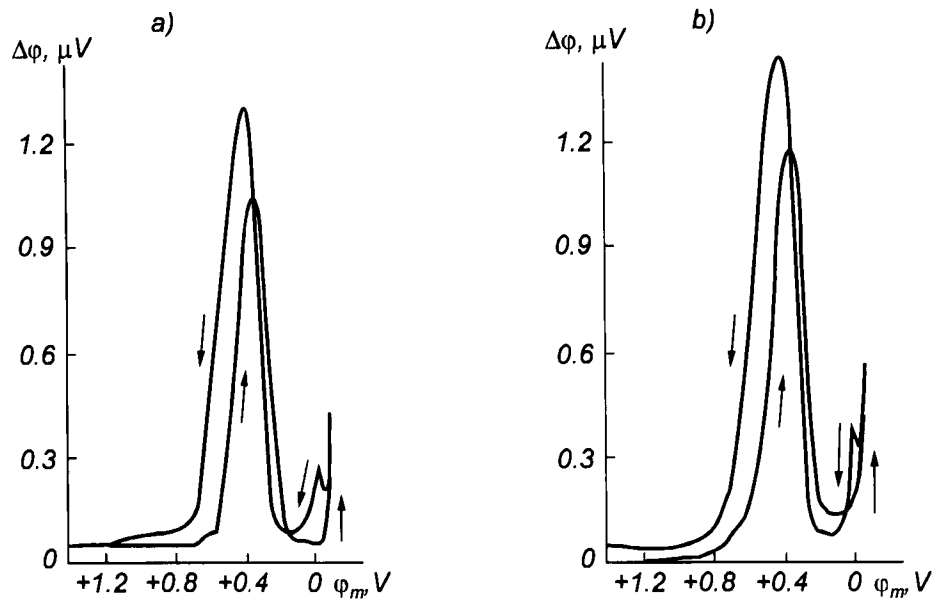

Fig. 1.13. The amplitude of potential variation $\Delta\varphi$ for a periodically excited adsorption layer versus the mean electrode potential φ_m under hydroacoustic pressure (a) with an amplitude of 20 Pa and under mechanical excitation of the specimen (b) with an amplitude at the end reaching 0.1 mm: Q=const for platinum in 1 n-H_2SO_4.

Thus, the examined mechanical model of the DEL interprets the direct and inverse effects (equation (1.21)) in the context of ion deformation of a double layer.

1.4. Friction; Positive Gradient Rule

Fundamentals of friction, lubrication, and wear have not been investigated adequately. The main reason is an inadequate application of the basic results of natural sciences. Apart from mechanics of elastic and plastic media, advances in metallurgy, solid state physics, physics and chemistry of surface, etc., are implied. Another important reason is that many theoretical studies treat pathological phenomena, i.e. those occurring in transient processes or when normal flow modes are disturbed.

The friction force is not conservative, its value is governed by the tangential stresses, arising in the relative motion of bodies. The nature of the stresses is conditioned eventually by a molecular interaction in the boundary layer with the

thickness of the order of a few nanometers, experiencing continuous shear. Nevertheless, the friction coefficient is defined as a numerical ratio of the dynamometer indications for two orthogonal forces, which exactly fit into a mathematical form for a great number of semiempirical theories of friction.

By the state of contacting surface, friction of ideally clean (juvenile) surfaces as well as the hydrodynamic and boundary lubrication are distinguished. The first two types are not dominate in engineering. The boundary lubrication is of great practical interest when contact surfaces are separated by very thin adsorption layers.

The contact surface is wavy and rough, therefore, a contact occurs only on separate spots which in combination make up the real contact area S_r. It is not larger than 0.01 to 0.10% of the nominal area S_n. The spots of contact are 3 to 50 μm in diameter and group on of the wave crests in zones named a contour area S_c ($S_c \approx 0.5–0.15 S_n$). The distance between the contact spots does not exceed the basic length corresponding to the given surface roughness, according to [GOST] (The USSR State Standard) [20]. The apparent contact area constitutes the nominal S_n contact surface. The spots of contact have a structure sketched in Fig. 1.14. If two conducting materials are in contact, the

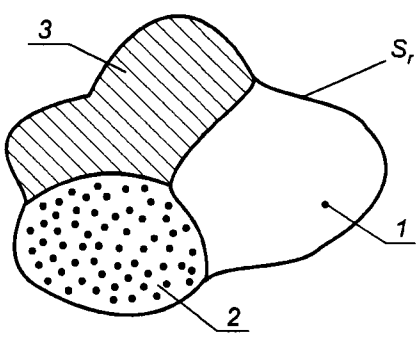

Fig. 1.14. Structure of the real contact area S_r: 1, 2) spots of metal and quasi-metal contact; 3) spots of nonconducting surface (coated with an insulating film of oxide etc.).

electric current flows only through areas 1 and 2 of the real contact surface S_r. At these points, there is a metal or quasi-metal contact characterized by electron conductivity. The quasi-metal contact is effected through monomolecular films, on contact spots due to the tunnel effect and to the formation of metal bridges. The rest of the surface is coated with insulating films (oxides, sulfides, etc.) and does not conduct electric current (spot 3).

According to Amontons , the friction coefficient is

$$f_\sigma = T/N, \quad \text{or} \quad f_\sigma = \tau/\sigma_r ,$$

where f_σ is the friction coefficient by normal stress;

T and N are the tangential and normal forces, respectively;

τ is the tangential stress when shearing the junctions; and

σ_r is the normal stress on the spots of contact.

Amontons has also formulated the relation of the friction force T and the real contact area S_r:

$$T = S_r\tau.$$

Under some simplifying assumptions, the generalized friction law is written [20] as:

$$_t = \begin{cases} f_\sigma\sigma_n, & 0 \le N \le kS_n / f_\sigma^*, \\ f_\sigma\sigma_n^* = const, & N > kS_n / f_\sigma^*. \end{cases} \tag{1.22}$$

Here, k is the shear strength (the shear constant) of a less resistant metal;

f_σ and f_σ^* are the coefficients of semidry and dry friction, respectively;

τ_k and σ_n are the average tangential and normal stresses on the nominal contact area S_n; and

$\sigma_n^* = k / f_\sigma^*$.

In the molecular-mechanical theory, the external friction is a deformation of thin surface layers, accompanied by breaks of adhesion bonds between the films that cover the bodies, i.e. the friction coefficient is defined as the sum of two components, adhesion and deformation: $f = f_{adh} + f_{def}$.

The binomial equation for friction force was first suggested by Coulomb and thereafter by many scientists, including B.V. Deryagin. Following Deryagin,

$$F_{fr} = f(N+N_0),$$

where f is the friction coefficient;

N is the total load; and

N_0 is the equivalent action of attraction forces when the tangential component of molecular attraction is neglected.

B.V. Deryagin attributed the latter condition to the fact that attraction forces have a broad range of action and reduce with distance more gradually, whereas isopotential surfaces for these forces should be less steep and smoother [21]. Therefore, tangential components of these forces can be regarded equal to zero, considering only normal components and assuming their resultant to be constant and unchangeable with the shear. This circumstance presumably was a basis for further recognition of the idea of a friction composed of two components.

According to Kragelskii [22], the coefficient of dry friction in a contact of a rigid rough surface, simulated by segments of equal radii, and an elastic half-space is defined by the trinomial relation

$$f = (\tau_0 / P_r) + \beta + k'\alpha_H\sqrt{h_1 / R}, \tag{1.23}$$

where τ_0 and β are the friction parameters in the equation $\tau_n=\tau_0+\beta P_r$ that characterize the shear strength of the molecular bond;

τ_n are the tangential stresses due to molecular interactions in the real contact;

τ_0 is the shearstrength of the adhesion bond without compression;

β is the adhesion bond piezocoefficient increasing together with normal stress;

P_r is the real pressure;

k' is the coefficient characterizing the shape and distribution of roughness, k'~0.4;

$\alpha_H=2.2\alpha$ is the hysteresis factor;

α is the hysteresis losses in volume deformation;

h_1/R is the relative penetration of unit roughness;

h_1 is the penetration depth; and

R is the curvature radius of a unit roughness.

The molecular component of the friction coefficient f_m is thus defined by the equation $\tau_n=f_m P_r$. The quantities τ_0 and β depend on the operating conditions of a friction pair. With the account of the third body at the interface between two solids (adsorption layers of lubricant, water, and gas molecules) and origination of a viscous flow alongside with volume deformation, the following expression is derived for τ_0 and β [22]:

$$_0 = A(T)C_1 \exp(\beta_1/(kT)),$$

$$\beta = A(T)C_1 \exp(\beta_1/(kT))\gamma/(kT).$$

Here, $A(T)$ is a function of temperature; C_1 = dv/dz is the rate of shear; $\beta_1$and γ are the constants at invariable temperature; and k is the Boltzmann constant.

Methods to calculate the molecular (adhesion) component are unavailable so far. However, a possibility of its experimental determination is suggested [23]. As far as the deformation component is concerned, the coefficient of external static friction can be predicted only in some cases.

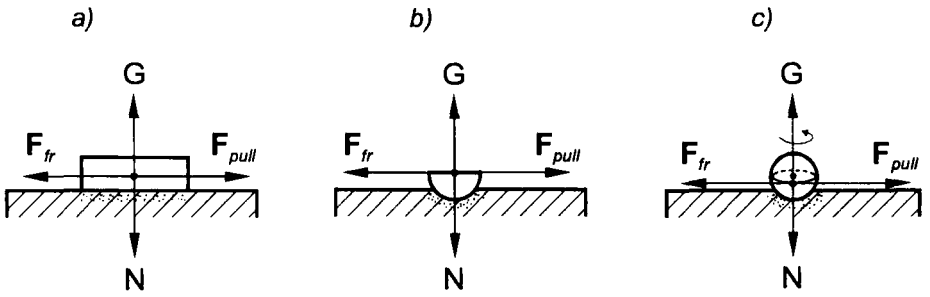

Fig. 1.15. Schemes of identifying the friction force.

The existing experimental schemes to identify the friction force are not radically different in their mechanical sense (Fig.1.15). The first scheme (a) is classic, it establishes the equality of forces ($\mathbf{N} \perp \mathbf{F}_{fr}$) via the friction coefficient. The second (b) formed a basis for establishing the deformation and adhesion components of the friction force. The third (c) is devised to determine the adhesion component of the external friction coefficient [23] and to verify the assumption of additivity of the deformation and adhesion components.

Taking into account the dependence of σ and the penetration depth of the unit roughness h_1 on the load, the solid surface microtopography and physico-mechanical properties of a less rigid material in the friction pair, I.V. Kragelskii and N.M. Mikhin obtained the following equation for the friction coefficient in the expanded form:

$$f = k_1 \left(\frac{Rb^{1/\nu}}{h_{\max}} \right)^{\nu/(2\nu+1)} \frac{\tau_0}{P_c^{2\nu+1}} \left(\frac{1-\mu^2}{E} \right)^{2\nu/(2\nu+1)} + \beta + k_2 \alpha \left(\frac{h_{\max}}{Rb^{1/\nu}} \right)^{\nu/(2\nu+1)} \left(\frac{P_c}{E} \right)^{1/(2\nu+1)}, \quad (1.24)$$

where b and ν are characteristics of the height distribution of roughness;

k_1 and k_2 are the coefficients obtained as functions of ν;

h_{max} is the maximum height of asperity;

P_c is the contour pressure;

μ is the viscosity; and

E is the elastic modules of material.

Expressions (1.22) to (1.24) neglect the effect of sliding velocity and temperature on mechanical properties of solids and assume the bearing and physical contact areas coinciding. Also, no account is taken of "wearlessness" and of hydrogen wear, i.e. properties of contacting bodies and films originating on friction surfaces are assumed unchangeable by friction. Thus, relations (1.22) to (1.24) are valid only for static friction or steady-state sliding friction.

The existing theories ignore the extremely sophisticated set of physicochemical processes involved in friction. A complete description of the friction process requires consideration of the characteristic parameters: roughness, mechanical properties as a function of temperature; components of a combined contact, when a dry film exists on some of points and a liquid film, in the others; mechanical properties variation in time (rheological processes); and mechanochemical processes in the frictional contact.

The account of the physicochemical and mechanochemical phenomena determining the friction process is most intricate.

In order to describe any wear mechanism regardless of its nature, the following equation for wear rate I_h [24] is derived proceeding from the formulated concept of the specific wear i_h: $I_h=i_h\alpha^*P_n/P_r$, where i_h is the removed material with thickness Δh^* based on real contact unit area over the sliding path equal to the mean diameter of the contact spot d ($i_h=\Delta V^*/(dS_r)=\Delta h^*/d$ because $\Delta V^*=S_r\,\Delta h^*$); α^* is the nominal to friction area ratio; and P_n is the nominal pressure.

The general analytic expression of the a steady-state wear rate in the case of friction fatigue has the form

$$I = (a/n)\sqrt{h_1/R}(P_n/P_r),$$

where I is the wear rate;

a is the coefficient dependent on the shape of asperity and on the height distribution (generally, a=0.15 to 0.20);

n is the number of cycles until failure;

h_1/R is the deformation zone depth (relative penetration);

P_n is the nominal pressure (it usually varies between 1 and 20 MP_a);

P_r is the real pressure on the contact (for elastic contact, it is close to the elastic modules divided into 10 to 50 as a function of roughness, it approaches hardness for plastic contact).

The ratio P_n/P_r is of the order of 10^{-2} to 10^{-3}. The ratio h_1/R, responsible for the wear type, cannot exceed 0.3 (above which microshearing starts), and for elastic contact it ranges from 10^{-3} to 10^{-4}. Accordingly, if $(h_1/R)^{1/2}$ is not larger than 10^{-2}, i.e. its contribution to the wear rate is insignificant.

The greatest effect on the wear rate I is produced by the cycle number n, varying from 10^2 to 10^{10}. It is expressed by the following relation referred to as the fatigue curve:

$$n = (\sigma_0/\sigma)^t \quad \text{or}$$

$$n = (\varepsilon_0/\varepsilon)^t, \tag{1.25}$$

where σ_0 and ε_0 are, correspondingly, the failure stress and strain under single loading that are obtained by extrapolating the fatigue curve;

σ is the active amplitude stress;

ε is the active strain; and

t is the parameter defining the resistance of a material to repeated loading.

The cycle number n can be increased by changing the index t. It has been established experimentally that, depending on the physicochemical processes, this index can range from 4 or 5 to 10 or 15. The n can be increased by decreasing the friction coefficient. This necessitates a reduction of two nondimensional relations, viz. τ/σ_s, the rheological resistance in the third body to the yield stress of the base, and h_1/R, the relative penetration depth.

Friction is characterized by the type of contact, in which plastic deformation, determined by the relative penetration death h_1/R, is dominant.

The limiting relative penetration depth (Fig. 1.16), corresponding to transition from external to internal friction, i.e. to such a mode when asperities on one surface scrape up the material of the countersurface, is defined by the inequality

$$h_1 / R \le 0.5(1 - 2\tau / \sigma_s), \tag{1.26}$$

where τ is the shear strength of adhesion bond and

σ_s is the yield stress of the strained half-space.

It is seen from inequality (1.26) that, even with a nonzero penetration, friction stops completely, if the ratio τ / σ_s exceeds half of the yield stress.

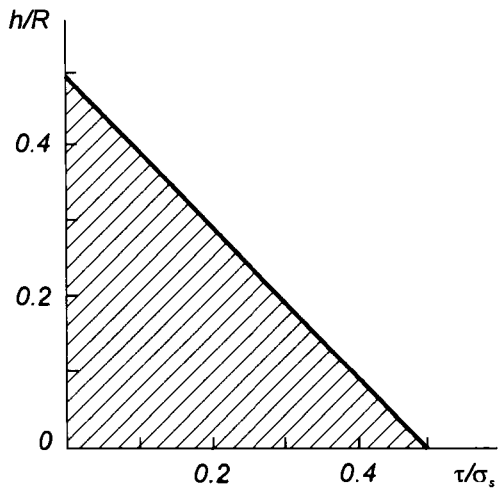

Fig. 1.16. External friction zone (hatched) versus penetration depth and adhesion bond strength [25].

Hence it may be deduced that no material, homogeneous over the depth, must be used, because $\tau=0.5\sigma_s$ for any material.

Apparently, the external traction needs a less strong material film on the solid surface. The fact implies a more rigorously formulated [22] concept of the external friction threshold defining the limit of external friction and transition to internal friction. This concept is known as the positive gradient rule (a positive degradation of mechanical properties in depth), expressed quantitatively by the ratios τ / σ_s and h_1/R.

Following this rule, any reduction in friction and wear needs a maximum possible localization of deformation in the thin surface layer. A localized positive gradient of the shear strength can be produced by lubricating layers, adsorptional softening or merely by a local temperature rise at fairly high sliding speeds.

The optimal thickness of the film is determined by the minimum friction coefficient f, i.e., it is dependent on all the parameters in expressions (1.22) – (1.24).

The positive gradient rule should be satisfied to achieve boundary lubrication.

1.5. Adsorptional Softening of Surfaces

The plastic flow of a crystal is a change in shape, caused by origination and movement of dislocations in the sliding plane, and their emergence on the crystal surface (discharging). The adsorptional softening decreases the yield stress (under constant-rate tension) or increases the creep rate (at constant load).

The adsorptional softening of the surface layer by the action of surfactants has a substantial effect on friction, improves the surface run-in, enlarges the real contact area, and thereby reduces specific pressure and friction force. Therefore, let us consider in brief the basic point of this phenomenon theory, first studied by P.A. Rehbinder in 1928.

Properties of surface layers are characterized by the following thermodynamic parameters: free and total energies, chemical potential, and entropy. Besides, the mechanism of adsorptional reduction of strength is dictated by the nature of molecular forces (physical or molecular adsorption) active in the surfaces layers.

According to modern views, the strength reduction in complete absence of volume diffusion and corrosion is associated with easier dislocation emergence on the surface of the deformed crystal as a result of reduced surface energy of the solid in the surfactant. Here, the work A_m and the probability P of shearing and cracking by virtue of weak spots (sections with an increased defect density) in the solid surface layers are determined by the interfacial energy σ_{12} (equal to A_m per unit area) [26]:

$$A_m = \sigma_{12} S_m; \quad P = C \exp(-A_m / (kT);$$

were $C = \exp(\beta NV_m / (kT); \quad S_m = \delta_m{}^2; \quad V_m = \delta_m{}^3;$

δ is the defect spacing or the size of structural inhomogeneity of ultra-microblocks (of the order of a colloidal particle size about 10^{-6} cm);

N is the stress;

β is the factor ($\beta>0$ for tensile stress and $\beta<0$ for compressive stress).

It should be emphasized that the effect is generally possible only when the external load and the surfactant medium act on the body simultaneously, i.e. when the surface is in a stressed state. Unless cracks appear in the material, it retrieves its strength and deformation properties after the surfactant medium has been removed.

The surfactant adsorption affects the interaction of dislocations with the surface

by diminishing the surface-energy barrier that inhibits dislocations on the surface causing crystal softening with an insignificant decrease of interfacial tension (by a few hundredths of joule per square meter). With a several fold decrease of σ_{12}, of brittleness goes up. The work of producing free unit surface area of the crack under the conditions of quasi-brittle fracture σ is related to the tensile stress N by Griffith's equation $N = \lambda\sqrt{E\sigma / l}$, where λ is the factor of an order of unity; E is the Young modulus; $2l$ is the crack length; and σ can also be understood as the irreversible dissipation energy in a thin layer of plastic deformation near the crack surfaces per free surface unit area, since its value is 10^2 to 10^3 times as large as the predicted surface energy σ_{12}.

The surfactant adsorption is most active on surface defects, which are failure nuclei having excessive free energy, stimulating their development. Migration of surfactant molecules to microcrack pores, or to spots of high concentration of stresses, lowers the stress level, thereby increasing dramatically the probability of this defect, that is, microcracks may transform into failure cracks. Experiments and results show that Griffith's theory does not apply to the adsorption effect [27].

The variety of manifestations of the Rehbinder effect is in the fact that the strength adsorption decrease of depends on the interfacial energy, reduction it depends on the specimen prehistory, in its turn, namely on the treatment; on the relationship between surface and volume defects; on the physicochemical features of the interaction of surfactant molecules with the solid surface; on the types and sizes of interacting molecules; and on the types of interacting atoms, specifically, on the structure of their electron shells, on the difference between crystallochemical radii, and on the mixing entropy. Surfactants dissolved in nonpolar solvents of relatively low concentrations are the strongest, when a saturated monomolecular layer forms on the solid surface. The adsorption effect of surfactants depends on the surface deformation conditions and on special features of mechanical action exerted on it (on the rate, periodicity, etc.) [4, 5].

We consider a theoretical model suggested by G.P. Cherepanov [25] that includes adsorption of both ambient liquid and gas. According to this model, a stretched adsorption layer film (for example, a wetting liquid) is sufficient for a noticeable loosening and breaking of the surface bonds (brittle failure) of a solid.

The above model consider a solid as a set of material points with a preset potential of coupled interactions which allows all possible stable structures to be found (reasoning from the condition of the minimum net potential of the system). With a finite number of particles, a stable periodic structure will be confined spatially by a surface layer of particles packed more loosely and, correspondingly, having bonds stretched tangentially rather than into the body.

The limiting tension force of a single bond in the surface layer F_{max} rises tentatively like for an ideal lattice, equal to about

$$F_{\max} \approx 0.1Ea_0^2$$

where E is the Young modulus and

a_0 is the atomic spacing.

Hence, the limiting tension of the layer per unit length (along the surface) at the surface layer thickness a_0 is

$$\gamma_n = F_{\max} / a_0 \approx 0.1Ea_0 \tag{1.27}$$

Essentially, equation (1.27) estimates the liquid surface tension, since the liquid surface is always in a limiting state because of yield. In solids the equilibrium tension of the surface bond F is appreciably less than F_{max} and reaches this value only in ruptures on the surface layer. The nature of the surrounding medium has a pronounced effect on the magnitude of the surface bond tension F, either softening the surface layer or making it brittle.

Let us examine a liquid-filled up cavity of the surface crack positioned perpendicularly to the tension direction (Fig.1.17). Under external loads,

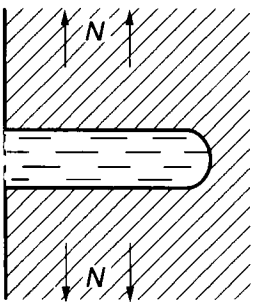

Fig. 1.17. Schematic of the crack cavity, filled up with liquid, emerging on the surface normally to the stretching direction [27].

rupture cracks emerge in the adsorption liquid layer, their sources being microscopic cavities resulting from thermal vibrations of molecules. These cracks is last very little, of an order of relaxation time, their incidence (or an average time between the ruptures τ) is defined by the activation energy of the fluctuation process W_0, liquid tensile stress σ_f, and temperature T:

$$\tau = \tau_0 e^{\frac{W_0 - V\sigma_f}{RT}}, \tag{1.28}$$

where $\tau_o \approx 10^{-12}$ sec;

V is the activation volume;

$\sigma_f = k_s \Delta S/S$;

k_s is the elastic constant of the adsorption layer, similar to the liquid body elasticity modulus; and

$\Delta S/S$ is the relative change of the layer-to-solid contact area.

Equation (1.28) suggests a unified explanation of delayed failure and the effect

of loading rate. At follows from calculations [27], that tensile stress of the liquid in the crack is much greater than the adsorption film tension. Therefore, in accordance with equation (1.28), liquid ruptures will occur frequently (the value of W_0-$V\sigma_f$ is small) and, in case the liquid wets the solid, the edges of the crack that reach the solid surface will diverge, forming a wedge with the angle π-2α (Fig.1.18); and the *AB* bond is stretched. The breaking condition for the *AB* bond, as evident from Fig.1.18, is

$$a_0\gamma \cos\alpha > F_{max} - F, \tag{1.29}$$

where α is the wetting angle.

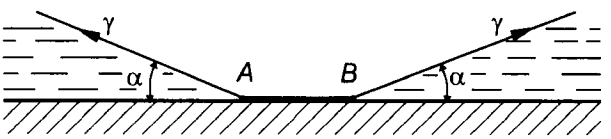

Fig. 1.18. Wedge formation with the angle π-2α on the crack opening edge near the surface (liquid wets solid) [27].

The bond may break, when the liquid surface tension is fairly large and α small. The microcavity, gets filled with liquid molecules, the effect of tensile stresses becomes still greater, therefore τ diminishes and the cavity transforms into a crack through of successive bond breaks by the athermic mechanism. Without wetting, a sharp crack of the liquid rupture closes immediately on reaching the solid surface, because α is larger than π/2. Following this theoretical model, softening occurs when condition (1.29) is not satisfied [27]. Here, a mere loosening of the atomic bonds in the solid is the case, i.e. there is an adsorption reduction in the strength of the spots, where surfactant molecules have penetrated.

It is clear from the above that, for the Rehbinder effect to manifest itself, normal stresses must necessarily be tensile and adsorbed molecules must wet the solid metal well enough. A direct relation between the wetting character and the adsorption reduction of the strength is validated readily by experiment [28]. So, mercury with dissolved zinc (4%) wets aluminum and its alloys far better than pure mercury; accordingly, the aluminium strength decreases in this case in half the time.

A reduction of the surface energy barrier by virtue of the physical adsorption decreases the total stress due to dislocation emergence on the surface. A greater plastic shearing occurs (that is, a greater number of dislocations emerges) per time unit at a fixed external stress.

Chapter 2

SURFACE STATE; ENERGY CHARACTERISTIC

2.1. Measuring of Electron Work Function for Surface State Evaluation

Physical and chemical properties of metals are determined by their nature, they are characterized, in particular, by the electron work function (EWF) and ionizing potential of a metal, its electronegativity, the standard electrode potential, generated in a solution and related to the electrochemical corrosion and other parameters.

The electron work function is one of the fundamental characteristics in the electron theory of metals and semiconductors. Changes of EWF yield important information about many processes occurring on solid surfaces and in the interphase surface layers. The electron work function depends on the surface state, it is sensitive to structural changes and, accordingly, to the quality and the method of surface machining, presence of oxides, adsorption gas layers, lubricant molecules, etc. (physical interpretation of such changes differ in every particular case) stimulating research on of this characteristic behavior which is very important, primarily, for the development of vacuum and semiconductor electronics.

The electron work function $e\varphi$ is defined as an average energy which is necessary for electron to escape from the solid to the distance x from the surface where classic mirror image force potential equal to $-e^2/(4x)$ is negligible. The distance is of the order of 10^{-4} cm. The work of escaping from the metal takes place in a thin surface layer where electrons are subjected to forces tending to attract them into a metal. The thickness of the surface layer is of the order of some interatomic distances.

In accordance with the zone theory of solids the electronic energy in a crystal is negative. In order to escape from the crystal the electron must, therefore, receive an additional energy sufficient to overcome some energy barrier at the solid–vacuum interface. This additional energy can be the true energy $\chi=W_{vac}-W_c$, where W_{vac} is the free electronic energy in vacuum, W_c is the energy of the bottom of the conduction band, and thermodynamic EWF $\Phi=\chi+W_c-W_F= W_{vac}-W_F$, where W_F is the Fermi energy (Fig. 2.1). If not specified otherwise, EWF is understood as a thermodynamic work function because the Fermi energy governs the properties of solids especially semiconductors (e.g., the dependence on concentration and the nature of impurities, temperature, etc.).

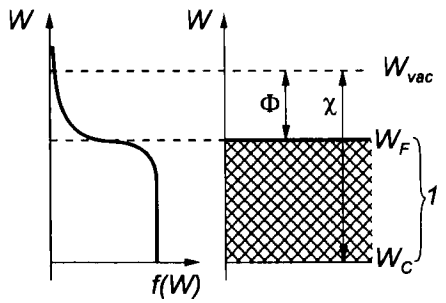

Fig. 2.1. Energy diagram of the metal–vacuum interface: left is a plot of the Fermi-Dirack distribution function; 1) the electron-filled part of the allowed electronic energy zone.

The work function is anisotropic and depends on the surface structure. Hence are the differences in the work functions of crystal facets, with different Miller indices and their heterogeneity over the polycrystalline surface, because different crystal faces appear on the surface. The work function depends on foreign metal atoms or adsorbed oxygen films which may be on the surface, humidity, etc., on characteristics of adsorbed particles, the extent of surface filling, the lattice geometry, etc. In view of the above, EWF for standard solid surfaces may be expressed by

$$e\varphi=-e\varphi'+W_{vac}-W_F, \tag{2.1}$$

where φ' is the surface potential determined by the interface structure and depending on impurities, different types of surface defects, etc.

In fact, the surface potential φ' is the main contributor to the EWF $e\varphi$. Since it is impossible to discriminate experimentally between the thermodynamic EWF Φ from $e\varphi'$ while measuring changes in $e\varphi'$, it should be remembered that the changes are mainly caused by surface potential variations.

The adsorption-induced potential leap on the surface is caused by the fact that, in a general case, adsorption gives rise to an additional average dipole moment of a unit surface area. Therefore, by introducing an additional potential leap, adsorption effects in the surface layer can be treated phenomenologically. The adsorption-induced potential leap in rough approximation is expressed by Langmuir's formula

$$\Delta\varphi'=n_sP/(\varepsilon\varepsilon_o),$$

where P is the constant or induced dipole moment of the adsorbed molecule or ion normal to the surface ($P>0$, when the positive dipole tip is directed from the surface, and $P<0$, when it is directed to the surface);

n_s is the dipole concentration per unit surface area;

ε_o is the electrical constant; ε is the medium permittivity.

The outer coating of the double layer can be charged positively or negatively (e.g., adsorption of caesium or oxygen molecules on tungsten, respectively). One can see (Fig. 2.1) that the EWF change $e\Delta\varphi$ is equal to $e\Delta\varphi'$ and has the opposite sign. If the pre-adsorption level is assumed zero $e\Delta\varphi'$ will be equal to the surface potential.

Having measured the surface potential (assuming P independent of the filling), it is possible to calculate the dipole moment P:

$$e\Delta\varphi'=P\theta n_{max}/(\varepsilon\varepsilon_0),$$

where θ is a fraction of the total number of adsorption centers n_{max}, occupied by dipoles.

The contact potential difference (CPD) method is widely used for measuring EWF. It is assumed that there is no close contact between metals, i.e. they are separated by a small vacuum clearance, and $\Phi_1<\Phi_2$. Then metals can exchange electrons only though thermal emission, since, when $T\neq0$, according to the Fermi-Dirack distribution (see Fig. 2.1) there are always electrons with the energy $W>W_F$, $W\geq\Phi$ inclusive. According to Richardson-Dashman's equation the thermal electron emission current is $j=A_0T^2e^{-\Phi/kT}$, where $A_0=4\pi k^2me/h^3$ (m and e are the electron mass and the charge; h is Plank's constant), different current ($j_1>j_2$ as $\Phi_1<\Phi_2$) flows from the metals. The region of the first metal adjacent to the contact will be charged positively and that of the second metal, negatively, the so-called external CPD $\Delta\varphi_c=U_c$ appears. After thermodynamic equilibrium has been established, CPD is determined from currents equality $j_{10}=j_{20}$ in terms of the thermodynamic EWF difference $\Phi_2-\Phi_1$:

$$A_0T^2e^{-\Phi_1/kT}=A_0T^2e^{(-\Phi_2+e\Delta\varphi_c)/kT},$$

where

$$\Delta\varphi_c=(1/e)(\Phi_2-\Phi_1) \tag{2.2}$$

The contact field penetration limited by Debye's screening stretch

$$L_d=\sqrt{\varepsilon\varepsilon_0kT/(n_0e^2)},$$

will determine the maximum vacuum clearance d between the metals. So, $d\approx1$cm at $\Phi_2-\Phi_1\approx1$ eV.

Relation (2.2) can also be obtained from the analysis of electron redistribution in two metals which are not in a vacuum, by using the free electron model. In this case two metals in directl contact at particular sites or measuring circuit leads are considered. The equilibrium state is established by the electron tunnelling through the potential barrier. The presence of external CPD means that an electric

field exists between the contacting metal surfaces and the outer space and the surfaces are electrically charged.

The EWF is measured by the CPD method, for studying electron-donor and electron-acceptor properties and the mechanism of action of oil additives [29], and for gauging the adsorptional behavior of oils [30] and fuels [31], when determining the hydrogen saturation of metals and alloys [32, 33] and investigating surface properties of semiconductors, boundary layers on metal surfaces [34], tribophysical and tribochemical processes [35–37]. It is an experimental method used to investigate catalysis, the contact potential difference very useful for studying the surface–medium interaction kinetics [38], for measuring the charge in the surface phase [39], etc. The most convenient method used to determine the contact potential difference is the dynamic capasitor technique [40] based on measurements of external (compensating) voltage U_c at the moment when current disappears in the dynamic capasitor circuit formed by the test electrode and a standard (gold or platinum) electrode.

The block diagram of the experimental design is shown in Fig. 2.2. The compensation voltage U_c generated in phase detector 5 is supplied to standard electrode 2 through high-ohm resistor 3 and registered by voltmeter 6. The specimen is fixed and during measurements it is has the "ground" potential adding some advantages to such configuration.

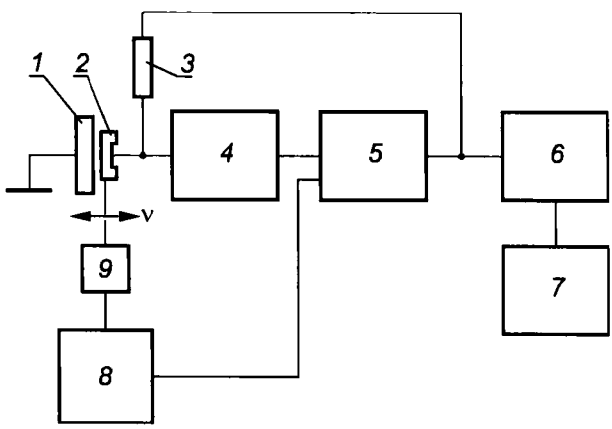

Fig. 2.2. Block diagram of the CPD measuring circuit: 4) amplifier; 7) recording potentiometer; 8) modulator; 9) electromechanical vibrator (other symbol are given in the text).

The circuit has the following characteristics: measurement range ±2 V; input resistance of 2.5×10^9 Ohm; compensation circuit time constant of <1sec; error within ±5 mV. It is equal to the residual non-compensated variable signal at the amplifying arm output [42].

The measurement error in a general case is determined by a net parasitic signal appeared together with a useful signal in the dynamic capasitor, due to the structural characteristics depending on the distance between the "plates" of the dynamic capasitor, vibration frequency, and input resistance.

The voltage U_c measured by the dynamic condenser method may be equal to the contact potential difference $\Delta\varphi_c$ (see (2.2)) only in the case of atomically pure surfaces. For real surfaces U_c is determined by the charge space distribution in the surface phase [11]. A variable of field in the dynamic capasitor can affect the surface charge redistribution which is especially important for semiconductors and dielectrics. However, this fact insignificantly impairs the method's usefulness, it is not the value U_c but the changes accompanying different surface processes which matter most.

It follows from the analysis of the dynamic capasitar method features that when there is a dielectric layer on the metal surface with thickness l, dielectric permittivity ε with a plane bound charge has density σ, then

$$U_c = -(\sigma l / (\varepsilon_0 \varepsilon) + \Delta\varphi_k)$$

(which agrees with the expression (2.1.)). If a dipole layer of polar molecules having thickness r is sorbed on the face of the surface dielectric, the dipole layer contribution to U_c determined by the dipole moment of this layer $\Delta U_{c.d.} = -\sigma r / \varepsilon_0$ only. For metals free of surface dielectric, it can be assumed $U_c \cong \Delta\varphi_c$ [11] (see (2.2)).

A characteristic feature of the dynamic capacitor method used to determine CPD is simplicity of measurements. Like the popular exoelectron emission (EEE) technique, the CPD method, while simpler, is slightly sensitive to the type of a surface defect, it is only its indicator [43]. Therefore, CPD is a generalized characteristic reflecting relaxation processes in the excited surface [44–52].

This chapter deals with the results obtained by the author together with V.G. Kuznetsov (sect. 2.2–2.5) and A.L. Zharin (sect. 2.5, 2.7) [41, 44–52].

2.2. Correlation of Work Function and Metal Surface Treatment

During surface treatment (cutting, grinding, mechanical or electrolytic polishing, etc.) thin surface layers change their structure and properties, therefore in all cases surface properties reflect the nature of the surface origin. Mechanical, physicochemical properties, and, consequently, many operating characteristics of parts relating to their durability and reliability (dynamic and impact strength, wear and corrosion resistance, etc.) depend on the quality of surface machining. Indeed, as it is shown by previous experience, the causes of essential changes in the operating characteristics of materials contacting in friction are connected with

structural features of interphase surface layers.

Some modern physical methods are used to investigate surface properties and the quality of machining. They are diffraction (radiography, electron and neutron diffractometry, resonance structural (e.g., Mössbauer) spectroscopy, ferromagnetic resonance, metallography, microhardness measurements, etc., but they all do not allow to understand completely the surface interaction peculiarities. To control surface properties and, eventually, to produce specific conditions of the surface behavior, it is necessary to know the physical and chemical parameters characterizing solids, such as EWF.

The most common machining is grinding and polishing with bonded abrasives. It is found that the structure of metal surface and the deformed layer thickness after such machining change substantially, depending on the machining mode (speed, temperature, etc.), abrasive dispersity, original metal properties. Machining, including grinding and polishing, inevitably involves plastic deformation. In each particular case, machining produces a peculiar complicated stress pattern, definite roughness and microrelief and, potential areas where future destruction sites will result from interaction with the medium, differently hardened sites appear. Polishing changes the surface properties most heavily.

All processes involved in changing the surface layer structure should considerably affect the EWF as the most structure-sensitive physical parameter of metals, this fact was used by many researchers. For example, the influence of the machining type (grinding and polishing) on EWF [53, 54], intensity of EEE [54, 55], is intrinsically connected with EWF because exoelectron emission characterizes local EWF changes and its cause has been studied. However, application and evaluation of reported measurements of EWF or CPD are difficult because only fragments of the measured quantities different for the same metals are cited without specifying the exact measurement time after machining is finished, the class of roughness, etc. Hence, there is an unreasonable (at the first glance) scatter, lack of coincidence, and discrepancy in experimental results [53–55]. According to some sources, the electron work function of a polished metal surface is stronger than that of ground surfaces and EEE intensity is less. According to other reports, the EEE intensity is a EWF inverse function as it is stronger on polished surfaces than on ground surfaces.

A detailed study of the influence of alloy and metal surface machining quality (roughness) on EWF [44, 49] was carried out on a specially designed apparatus [41] (Fig. 2.2). The design could be used to determine EWF by Kelvin measuring CPD [40] with the useful signal automatic compensation CPD with gold as a reference standard practically immediately (about 1 or 2 sec) after machining, and to study CPD kinetics at the normal atmospheric pressure and room temperature, thus it was possible to take account of the influence of the ambient medium on interphase processes upon standard metal surfaces. Calibration was carried out by periodic CPD measurements between the standard electrode and the control

plate made from gold. During measurements with the standard electrode potential charged within 10 mV, the specific error did not exceed ±5 mV. To maintain identical conditions and to exclude the influence of variations in the ambient parameters on the specimen during measurements, the apparatus was placed in a sealed acrylic box. In all cases the integral quantity was measured, or the area-averaged CPD (the averaging area was 20 mm^2, i.e. the reference electrode area).

The following materials (ISO) were selected for tests: Cu-ETP copper, CuZn39Pb2 and CuZn37 brasses, bronzes (CuBe2Ni, CuSi3Mn1, CuSn6, CuAl9Mn2), 3/VII steel which were rough machined by various files, ground with various coarse grain sized abrasives (GOST 3647-71, The USSR State Standard), and polished to roughness class 12 by fine emery paper and felt. These materials were chosen because copper alloys in contact with steel are able to initiate selective transfer in a reducing medium [25]. In order to clarify some of the relations obtained in the studies, experiments were carried out with zinc (a component of brass) and aluminium. The specimens were washed (if necessary) in alcohol, petroleum ether, B-70 aviation petrol, or toluene.

TABLE 2.1

Surface roughness class (GOST 2789-73)

Class	Category	R_a, μm
6	a	2.5 - 2.0
	b	2.0 - 1.6
	c	1.6 - 1.25
7	a	1.25 - 1.00
	b	1.00 - 0.80
	c	0.80 - 0.63
8	a	0.63 - 0.50
	b	0.50 - 0.40
	c	0.40 - 0.32
9	a	0.32 - 0.25
	b	0.25 - 0.20
	c	0.20 - 0.16
10	a	0.160 - 0.125
	b	0.125 - 0.100
	c	0.100 - 0.080
11	a	0.080 - 0.063
	b	0.063 - 0.050
	c	0.050 - 0.040
12	a	0.040 - 0.032
	b	0.032 - 0.025
	c	0.025 - 0.020

The surface roughness was measured according to GOST 2789-73 by a recording roughness indicator determining arithmetic mean surface profile deviation R_a in micrometers, Table 2.1).

Surface roughness of metals with different mechanical properties after treatment by abrasive cloths of the same grain size are different (Table 2.2).

The contact potential difference of the materials after grinding with abrasive cloths of different grain sizes with the same abrasive material (14A, GOST 6456-75) and after polishing shows that different surface roughness results in different CPD values. It appeared that CPD as a function of roughness $U_c=f(R_a)$ immediately after abrasive grinding had a strictly definite form, common for all studied materials, characterized by two distinctive CPD maximal (EWF minima, see formula (2.2)).

One of the maxima (Fig. 2.3) occurs at roughness 9, the other at roughness 11c to 12a. Washing of the surface with organic solvents to remove wear products and abrasive particles did not change the double-crest shape of the curve but only

TABLE 2.2

R_a values after abrasive polishing

Grain size of abrasives, μm	R_a, μm	
	CuZn37	Cu-ETP
40 - 28	0.075	0.11
63 - 50	0.25	0.38
100 - 80	0.53	1.0
160 - 125	1.78	2.41

altered its relative position caused by a common (at all Ra) decrease or increase of absolute CPD values with different solvent types.

The following important peculiarity is that at roughness 12 and higher the surfaces had the maximum EWF. This finding agrees with [53, 54] and explains the experimental data of [55].

The third peculiarity is that these two groups of metals differ in the ratio of the two CPD maxima. So, unlike other materials in the experiment, copper had the second CPD maximum U_{2max} (roughness 11c–12a) less than the first U_{1max} (roughness 9). Naturally, such differences in copper after grinding from the other metals may be attributed to their different nature. It is apparent a definite relation exists between this feature and the ability of copper to ST. This problem will be discussed in detail a little later. As for copper alloys, the difference in ratios between the maxima can be attributed not only to the nature of the main component but also to the nature and the smear of alloying agents (see the curves for CuZn37 brass, copper and zinc, Fig. 2.3).

It is also found that further changes in CPD, after grinding is stopped and the metals are aged in air (kinetics), depend on both the type of a material and the machining (roughness). However, the distinctive double-crest shape of the CPD versus the R_a curve remains unchanged. Ageing in the air decreases CPD (increases EWF), the higher fineness the larger decrease, i.e., $\Delta U_c=U_{co}-U_{cl}$ in absolute value increases as the roughness parameter R_a decreases. This can be seen, for example, from comparison of the curves $U_c=f(R_a)$ for CuZn37 brass obtained immediately (U_{co}, the solid line) and 15–17 h (U_{cl}, the dashed line) after machining is stopped.

The obtained dependence of U_c on the roughness parameter R_a can not be fully attributed to the difference in the surface profile parameters because measurements of the roughness in the range of class 6 to 12 should not affect practically the EWF value. The total surface area is nearly independent of roughness [56, 57]. Only the distance between the reference electrode and median line of the roughness profile of the electrode (the line the *M*1, *M*2, Fig. 2.4), which is the line having the nominal profile shape, changes. Roughness parameter R_p (the distance between the peak line and the median line) changes maximum by 10 μm.

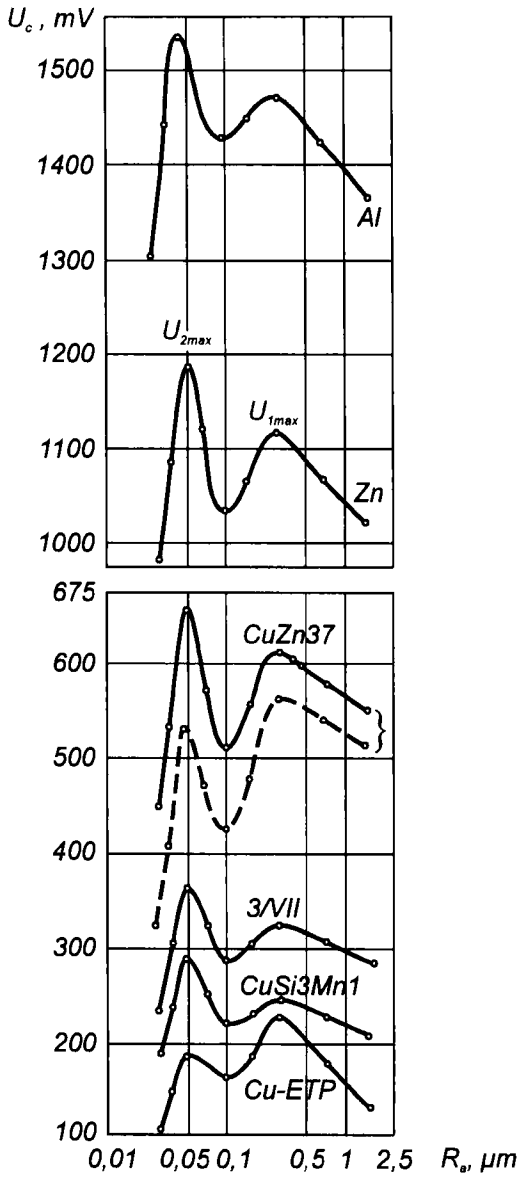

Fig. 2.3. CPD of aluminium and zinc (a), Cu-ETP copper, CuSi3Mn1 bronze, 3/VII steel and CuZn37 brass (b) as a function of roughness (arithmetic mean surface profile deviation R_a) obtained immediately (the solid line) after grinding with emery paper of various grain size and washing with toluene, after 15-17 h (the dash line).

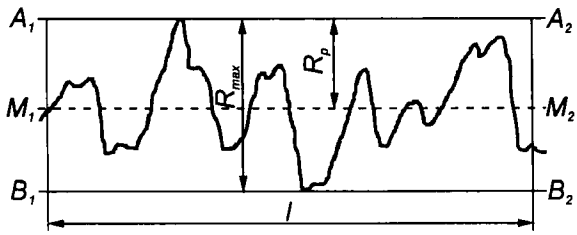

Fig. 2.4. Surface roughness parameters [20]: *l*) base length; A_1-A_2) line of profile asperities; B_1-B_2) line of valleys; R_p) the tallest peak; R_{max}) maximum height of roughness.

Though the largest error of the CPD meter operating as a vibration capacitor [42] is connected with the distance between the "plates" of the dynamic capacitor, variations of the CPD caused by this 10 μm change in the distance is within the systematic measurements error for this instrument.

Surface machining produces extensive very fine microcuts left by abrasive particles. They result in the formation of a greatly distorted layer (it will be called the *A* zone) (Fig. 2.5). The zone *A* includes the relief layer R_z and the layer R_{cr} underlying it and saturated with cracks. Moreover, such machining causes a complicated plastic deformation of the surface layer which results a zone with extensive residual deformation (zone *B*, or a zone with increased dislocation density R_d) under the layer R_{cr}. The maximum stress appears at the boundary between zones *A* and *B*, the minimum at the boundary between the zone *B* and the original intact metal. The two zones make up a mechanically deformed layer, its thickness can be calculated from the formula $R=k_0D$, where *D* is the grain size; k_0 is the coefficient different for unlike materials. The thickness of the first layer (zone *A*) is 0.1 of the total thickness of the deformed layer.

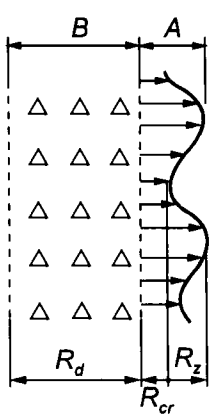

Fig. 2.5. Simplified diagram of the surface layer structure.

Abrasive machining with different particles size results mainly in different thickness of the entire mechanically deformed layer and surface profile projections; changes in the surface structure (pulverization of grains, formation of secondary structures and Beilby's layer); in the different depth of the boundaries between zones A and B characterized by maximum stresses and maximum dislocation density and, consequently, different density of surface defects.

Physicochemical properties of the machined surface depend, to a great extent, on the above factors as shown experimentally. Therefore, in order to explain the obtained U_c versus R_a (see Fig. 2.3) and CPD kinetics after machining, the influence of microgeometry should be considered in connection with the surface physical state for a given roughness.

In order to explain the features of relations between CPD and the surface machining quality, the theory of fatigue failure of materials [58–61], and the concepts on influence of the number, nature, and dynamics of defects contained in the surface metal layer on EWF are used.

As a result of coarse machining to roughness 6–7 the surface layer would acquire a great number of different defects which are active centers with lower EWF [36, 54, 62]. This is responsible for a relatively high EWF and a substantial increase of the EEE intensity caused by a decrease of Φ [36, 63].

A further increase of CPD (decrease of EWF) between roughness 6–7 (R_a=1.25 to 2.00 μm) and smaller R_a may be explained by a greater misalignment and pulverization of metal blocks and grains and, as a result, intensive formation of defects and new surfaces take place. It is accompanied by an increase of the density of surface dislocations largely associated with changes of EWF which increases the number of active centers with a smaller EWF [36, 64]. The EWF change $\Delta\Phi$ due to the surface dislocations and submicrorelief (surface steps and ribs at atomic size) averages to $\Delta\Phi \cong 0.1...0.3$ eV, whereas the vacancies change of Φ by about 0.04 eV [65]. The Φ of EWF depends on the defect concentration N_d direct proportion the logarithm of concentration $\Phi=\Phi_d+0.5RT\ln N_d$, where Φ_d is the partial work function of the defective atoms depending on the molar volume of the metal.

The dislocation density in a metal can not grow infinitely. There are many reports, that the maximum possible density is $N_{max}=(0.5–1.0)\times10^{12}$ cm^{-2} [66]. At N_{max} interactions between dislocations become more intensive, internal stresses in dislocation pileups increase, dislocations stop, in their turn and arrest dislocations and accompanying point defects under the metal surface. As a result, the number of active centers with low EWF ceases to increase upon saturation.

The maximum CPD (the minimum EWF) with roughness 9 (R_a=0.29 μm) characterizes the maximum of juvenile surfaces, residual stresses in the crystal lattice, changes in the surface submicrorelief during formation of displacement lines associated with the changes in the dislocation density. The difference between the maximum and minimum EWF of metals machined from roughness 6 to 9 is partially proportional to the deformation potential [67] equal to the distortion of the Fermi energy by deformation. On the basis of the nonlinear theory of dislocations the formula was derived and the order of magnitude of the local deformation potential $\Delta\varphi_n^d$, induced by the action of one flat pileup of n-coplanar dislocations was calculated. For points M of the fine layer adjacent to the surface

of a plastically deformed metal it is $\Delta\varphi_n^{\,d}(M) \approx -0.0165n$ V, where n is the number of dislocations in one pileup. When n=10

$$\Delta\varphi_n^{\,d}(M) \approx -0.16\,\text{V}.$$

Numerous experiments have revealed that EEE centers coincide with the sites of dislocations emerging on the surface, i.e. the sites where displacement lines come out to the surface, the EEE characterizes the EWF which causes local changes (decrease). In a fine surface layer near the dislocation pileup local deformation-induced changes of the chemical electron potential are compensated by equivalent changes in the external electron energy of the double surface layer formed by the free electron cloud over the metal surface and by positive atomic ions of the crystal lattice matrix, as a result, the Fermi level is smoothed but the electron work function is changed.

A subsequent CPD decrease (Φ increase) with roughness 9 to 10c–11a seems to be caused by the fact that, after a certain critical dislocation density (corresponding to V_{max} in Fig. 2.3) is reached, further fine machining of the surface with fine grain emery paper initiates intensive submicrocracks formation in particular near-surface microvolumes. It agrees with the main statements of the theory of fatigue failure of metals [27, 58, 59]. The outflow of vacancies formed when dislocations pile up away from submicroscopic cracks reduces the number of surface active centers with lower EWF.

The growth of submicrocracks favors loosening of the surface layer and appearance of fatigue microcracks (irreversible damages), i.e. as the number of machining cycles increases, microcracks and local plastic flow in particular microvolumes continue to grow. In this case the density of vacancies with no time to scatter [58, 59] substantially increases which seem to be the cause of abrupt subsequent CPD leap (EWF drop) roughness 11.

Initial failure of metal microvolumes and transition of the surface to a highly dispersed crystalline state is characterized by appearance of the second CPD maximum U_{2max} (EWF minimum) at roughness 11c–12a. It seems likely that the mechanism of failure of the crystalline surface is not so common for copper than for other metals (see Fig. 2.3.). This can be seen from the CPD maxima ratios at roughness 11c-12a and 9: for copper $U_{2max}/U_{1max}<1$, for the other metals $U_{2max}/U_{1max}>1$. It is most likely that the formation of a soft surface layer is more common for copper.

A very fine abrasion, or polishing, starts after that, the theory of which is not complete yet, as there is no clear explanation of the polishing mechanism. According to some researchers [68] the formation of debris in the process of polishing is excluded, only the removal of material at the molecular level (molecular type of wear) occurs. It was G.T. Beilby who noticed the analogy between polishing and liquid vaporization [68]. The liquid surface always remains

smooth as long as there is enough heat for liquid evaporation by individual molecules. At intensive heat transfer bubbles appear and the surface becomes rough. The same pattern is observed in friction: the optimum mode leads to molecular wear; higher load results in abrasive wear and formation of large particles. In polishing plastic deformation changes so drastically that crystals are completely crushed and mixed up. In this case *X*-ray photograph of the surface reveals transformation of metals into a nearly amorphous state.

In the case of polishing (roughness 12) the CPD is minimum (the EWF is maximum). The *X*-ray and electron diffractometric studies of polished surfaces show that their fine surface layers (so-called Beilby layers) with the thickness from 10^{-3} μm to several micrometers contain of many randomly located, very fine crystals with the size of several elementary cells [16]. It means that the surface is in a highly dispersed crystalline state.

The crushed, ultradispersed (0.1–0.01 μm particles size) surface structure has high strength if particles are densely packed or "glued" by very thin defect free interlayers. Polishing or finishing is known to remove defects resulting increase of the volume strength by the order of magnitude 2 or 3 [69]. The minimum CPD (maximum EWF) observed on surfaces machined to roughness 12c and up (see Fig. 2.3) may probably be attributed to the minimum dislocation density in the finest surface layer with the optimum submicrorelief. It cannot be also excluded that stronger secondary structures and dislocation-free structures are produced by polishing [70].

The state of surface layers after machining within roughness 9c and 11c (between grinding and polishing) is reflected in the CPD versus the roughness curve by the deep CPD minimum.

Different friction pairs, including sliding electrical contacts, at initial roughness 8–10 manifest the minimum wear intensity and contact resistance at U_{1max} (see Fig. 2.3).

The fact that the relation $U_c=f(R_a)$, is universal for many materials with various microstructure suggests the existence of a common mechanism controlling the movement and formation of dislocations, origination and growth of cracks. It is supported by many studies on fatigue failure of metals [27] which show that the growth rate of fatigue cracks is independent on the microstructural characteristics of materials.

2.3. Kinetics of Electron Work Function of Machined Metal Surfaces

The hypothesis of the nature of the double-crest CPD versus the surface machining quality curve as a roughness function suggested in the previous section (Fig. 2.3) required thorough verification and validation. Naturally, the CPD kinetics were investigated first of all [44], i.e. the kinetics of the surface energy

state thermodynamic equilibrium evaluation in the ambient medium after machining is stopped, which is an important problem. For this $U_c=f(t)$ was measured in the air immediately after treatment, without washing.

The experimental results (Fig. 2.6) are presented for the same materials as in Fig. 2.3 ground with the emery paper 14A (GOST 6456-75). The curves $U_c=f(t)$ are recorded for five machining modes (curve 1, roughness 6–7; curve 2, roughness 9; curves 3, roughness 10c–11a; curve 4, roughness 11c–12a; curve 5, roughness 12c) by a recording potentiometer [41].

It was noted before, the double-crest shape of the CPD versus R_a curve remains after ageing specimens in the air for any time duration, however the EWF behavior in many cases was different and depended on both the nature of the material and the quality of machining (see Fig. 2.6). Thus, the CPD of aluminium after machining to roughness 6–7 (curve 1) and 9 (curve 2) and the CPD of copper after machining to roughness 9 showed an abrupt decrease during the initial 2 or 3 minutes, followed by a smooth decrease. For copper after machining to roughness 6–7 and for other materials (brass, steel, bronze, zinc) in both cases (curves 1 and 2) the initial abrupt drops of CPD changed subsequently to a slow growth up to a certain maximum after which CPD decreased again reaching a value corresponding to the surface state environment equilibrium, the maximum being different for different kinds of machining. It is apparent that EWF is practically independent of the oxide thickness, but depends on premachining of specimens under the same ageing conditions. The estimation of SiO_2 charge of silicon by Kelvin's method in [71] showed that premachining only yielded CPD values different in time.

The CPD kinetics at roughness 10c–11a (curve 3) substantially differ from other cases. Such machining (see Fig. 2.3) yields the minimum CPD (maximum EWF) in the curve $U_c=f(R_a)$. Roughness 10c–11a is intermediate between grinding and polishing. As it was mentioned earlier, the minimum CPD is connected with the saturation of submicroscopic cracks owing to transformation of submicrocracks into fatigue cracks which cause substantial growth of the number of vacancies, with no time to disperse.

A substantial drop of U_c (increase of Φ) during first minutes after machining is stopped is observed in all cases of the roughest machining. After polishing to roughness 11c–12a (curve 4) and 12c (curve 5) the CPD kinetics of all metals are qualitatively the same, they are characterized by a rapid fall, followed by a slow decrease.

Since grinding can contaminate the surface with abrasive which penetrate into the surface layer and, besides, chemical interaction of the abrasives with the glued base and the metal cannot be excluded, similar experiments of surface machining were carried out using abrasives of various grain sizes and a different abrasive material (K3, GOST 100054-75), of the same grain size and type but from a different manufacturer and, also, with files of different cut. Though the absolute

CPD was different at the same surface roughness (depending on the abrasive used), a relative shift of the CPD for various roughness surfaces (see Fig. 2.3) and the CPD behavior after machining to the same roughness (see Fig. 2.6), were preserved.

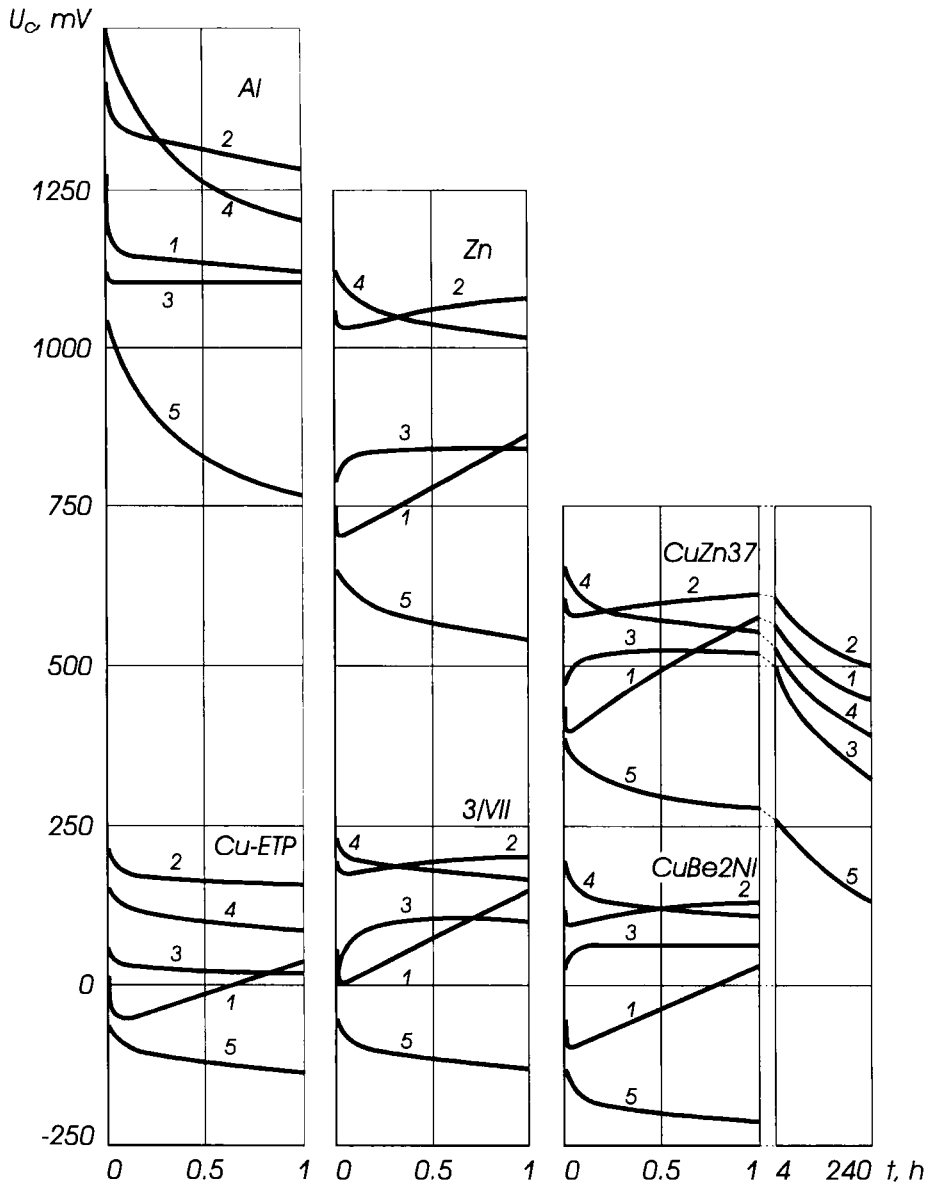

Fig. 2.6. The CPD kinetics of metals and alloys immediately after grinding with the emery paper of different grain sizes.

The CPD shape versus the roughness curve after removing (for example, by washing in toluene) abrasives and debris remained the same, differences in CPD caused by different types of abrasives disappeared. It cannot be denied that abrasion leads inevitably to contamination of metal surfaces which cannot be removed by any organic solvents. It is due to penetration of abrasive particles into the metal, the low-energy secondary ion mass spectrometry of copper surface [72] showed that abrasives Al_2O_3 and SiC produce a substantial aluminium and silicon contamination of the surface. The best surface finish is achieved by chemical pickling in HCl. However, changes in Φ observed in measuring the area integral EWF caused by penetration of a different material are insignificant, because they are within the error of the method and introduce an insignificant steady component which does not change the EWF kinetics of the main material. The use of organic solvents greatly changes the CPD kinetics of the fresh air-aged surface affecting the interaction of absorbed solvent molecules with the metal.

After machining of metals and alloys, apart from adsorption of oxygen and other active substances from the atmosphere which gives rise to adsorption and oxide layers, some other processes are induced by disturbed equilibrium of the surface and underlying layers which have different relaxation times. These processes should be taken into account in the interpretation of the CPD kinetics (see Fig. 2.6). For example, rapid relaxation which manifests itself in a more or less abrupt drop of CPD during the first several minutes for all materials without exception after various types of machining, excluding the roughness 10c–11a (curve 3), cannot be explained only by surface oxidation in the air. Oxidation of steel alone should immediately increase the CPD since EWF for iron oxide (II) FeO formed in contact of the juvenile steel surface with the atmospheric oxygen [36, 73] is less than that of iron and amounts to 3.85 eV against 4.77 eV. Rapid relaxation can be attributed to another mechanism dominating on surfaces of all the materials without exception during the first minutes of machining.

When machining metals with abrasives local heating occur where surfaces are in direct contact, dislocations of macro- and microdefects in the metal surface layer develop, adsorption and chemisorption interactions of the friction surface with the environment result from continuous removal and damage of the oxide layer. For this reason, initially an abrupt decrease of EWF and, as a consequence, EEE of the metal surface during machining occurs which is stimulated by temperature and strong oxidation [36, 63]. An abrupt EWF increase during the first minutes after machining can probably be attributed to the fact that, apart from oxidation and moisture condensation in cooling, the effect of EEE attenuation charges the outer oxide surface negatively in this case. Such charge results from capture of a rapidly subsiding electron flow, tunnelled by adsorbed oxygen atoms from active centers of chemically inhomogeneous deformed metal surfaces. In this process an additional barrier inhibiting further electron escape and thereby increasing EWF appears on the surface. Thus, the oxide surface charge screens

off the surface, the initial oxidation kinetics and the oxide structure determine the initial EWF kinetics which may be inferred from EEE. Attenuation of EEE is very complicated (Fig. 2.7) [63].

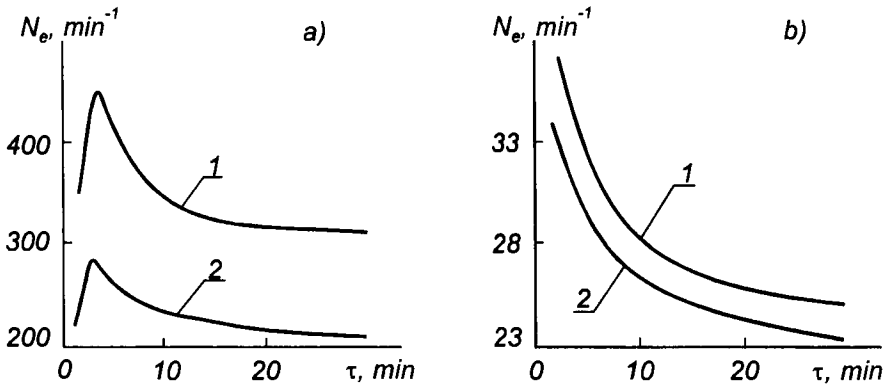

Fig. 2.7. Exoelectron emission N_e from the surfaces of steel C25e (a) and aluminium (b) specimens after reversive (1) and unilateral (2) dry friction.

One can see from Fig. 2.7 that in some metals during the first minutes after machining a slightly delayed increase in EEE is observed [61] which is followed by a slow decrease to the background level. Such electronic emission should correlate with the EWF behavior (see Fig. 2.6). However, this correlation cannot be found, since [63] reports no data on the roughness of surfaces for which EEE was measured, machining conditions were different in the cases shown in Figs. 2.6 and 2.7.

It is known that the coarser the surface machining, the more rapidly macro- and microdefects develop, the diffusion, adsorption, and chemisorption is more probable, and the more intensive is EEE (Fig. 2.7, curve 1). Therefore, after coarse machining electrons more readily escape and initial increase in EWF is observed, it is especially clearly visible after grinding (see curves 1 and 2, Fig. 2.6).

A different shape of the curve for machined aluminium and steel surfaces (curves 1 and 2, Fig. 2.6,a, e) and for copper (curve 2, Fig. 2.6,d) can be attributed to oxygen chemisorption and the effects of oxygen compounds on EWF. So, whereas EWF for aluminium is 4.23 eV, for aluminium oxide Al_2O_3 it is 4.7 eV, i.e., oxidation of the aluminium surface in the air is accompanied by an increase in Φ. As in the case with aluminium, copper oxidation should lead to a decrease in CPD since EWF for copper is 4.40 eV and EWF for copper oxide (I) Cu_2O and copper oxide (II) CuO measured by different authors, are 4.90–5.15 eV and 4.35–5.34 eV, respectively [74]. It is also proven by CPD kinetics after grinding to roughness 9 (curve 2, Fig. 2.6,d), that steel as well as copper oxidation after surface grinding results in a higher CPD because EWF for iron

oxide (II) FeO unlike aluminium is smaller than for iron. Therefore, the initial EWF relaxation for steel is less than that for aluminium: a combination of both these processes (oxidation and electron tunnelling) has the opposite tendency in steel.

It is known [73] that the following iron oxides can be found on steel in the direction from the surface: Fe_2O_3, Fe_3O_4, $FeO+Fe_3O_4$, FeO. Then, the inflection of curves 1 and 2 which occurs after 3–4 h (not shown in Fig. 2.6 and outlined just slightly on curve 2) may be explained by further oxidation of steel with the formation of iron oxide (II, III) Fe_3O_4 and iron oxide (III) Fe_2O_3. Unlike iron oxide (II) FeO, these oxides are not iron-soluble and have no great effect on steel properties. Besides, the oxide film contains an intermediate product of oxidation, such as iron hydrate $Fe(OH)_3$.

The studies [36, 63] carried out to investigate the effect of friction on oxidation of the working metal surfaces by measuring EEE, EWF, and thickness of the oxide layer, showed that after moisture condensation on steel surfaces, oxidation reduces EWF. This agrees with the well known concept [75]. Adsorption of water molecules is accompanied by binding to the metal through the oxygen atom which gives its electron away to the metal. The surface is charged positively decreasing EWF. When gas corrosion is developed metal electrons are transferred to oxygen. The double electric layer formed in this case on the surface has the opposite polarity of "the plates". The additional barrier for electron escape (a negative charge of the outer plate of the double electric layer) which appears in this case, increases EWF. Thus, different electron transfer directions in chemical adsorption of moisture molecules and oxygen atoms seem to cause further inflection of the EWF curves for steel when ageing in the air is extended, they have the same shape as those shown in Fig. 2.6,b for brass. Experimental results discussed in the 2.6 support the assumption that under longtime exposure to the air structural transformations starts in growing oxides.

Explanation that oxidation alone additionally changes the CPD kinetic curves for different metals is sufficient only for metals machined with roughness 9 (curves 2, Fig. 2.6) because after that (see 2.2) dislocations and accompanying pinpoint defects are arrested under the surface.

In other cases the surface oxidation is accompanied with side effects depending mainly on the number and dynamics of defects in the metal surface layer after machining, in particular, differing mobility of defects when they emerge on the surface [62].

Therefore, attention should be paid to the pronounced difference between the CPD kinetics under the surface at roughness 6–7 (curve 1) and the kinetics after machining to roughness 9 (curve 2) which is manifested, first, by a greater initial relaxation of CPD (more abrupt EWF increase) after coarse machining (curve 1); second, by a further CPD steep rise (decrease of Φ) for all, excluding aluminium, materials machined to roughness 6–7. As it was stated in 2.2, during such

machining the density of structural damages (vacancies and dislocations) is below the critical density, and they are not fixed. In this case, dislocations and point defects accompanying them can relatively freely reach the surface, as a result the number of active centres with reduced EWF grows together with CPD grows. For aluminium the direction of the oxidation effect is opposite to that for defects emerging on the surface, it is more essential and dominates in this processes which is shown by curve 1 for Al (see Fig. 2.6). In this case, EWF gradually increases at a slower rate in comparison with curve 2. For copper, the situation is similar to aluminium when both factors act in opposite directions, however, defects which come to the surface, change the copper potential more substantially towards lesser EWF: the slopes of curves 1 and 2 have different signs. Thus, the hypothesis used to explain the CPD kinetics proposed by the authors [62] when analyzing the shape of the EEE curves, is consistent with the experimental data shown in Fig. 2.6 and can be used for their correct interpretation.

For all copper alloys the CPD kinetics after surface grinding (curves 1 and 2, Fig. 2.6) as the reflection of structural transformations on the surface is similar to that for 3/VII steel. This fact can be attributed to the presence of other chemically active elements besides copper. This is confirmed by comparison of CuZn37 CPD kinetics (see Fig. 2.6,c) with zinc CPD kinetics (see Fig. 2.6,b).

The CPD kinetics shown by curves 3 (machining to roughness 10c–11a) and curves 1 is determined, apart from oxidation, by the surface dynamics of a metal surface. So, after the critical dislocation density has been reached (the kinetics, in this case, is demonstrated by curve 2), further mechanical action results in the formation of submicrocracks, i.e., in relaxation and reduction of critical dislocation density which leads to a considerable increase of the absolute EWF value (see positions of curves 2 and 3 in Fig. 2.6). Further outflow of vacancies formed on the metal surface into the submicrocracks reduces the number of active centers on the surface [62], increasing EWF and, occasionally, decreasing EEE [76] (see the shapes of curves 2 and 3, Fig. 2.6). Therefore, in the first minutes after machining the CPD kinetics shown by the initial portion of curve 3 is characterized by the absence of initial drop of CPD (or by its low value for both aluminium and copper). Moreover, during the first minutes after machining to roughness 10c–11f, CPD increases more rapidly than in the case indicated by curve 2. It is caused by the fact that the effect of electron tunnelling which should have resulted in CPD drop, decreases, the role of vacancies coming out to the metal surface and forming active centers with reduced EWF, and stronger CPD, grows.

The difference in CPD kinetics for copper (curves 2 and 3, Fig. 2.6,d) from the kinetics for other metals can be attributed to the fact that the mobility of point defects in copper is lower than, for instance, in aluminium [61], or zinc. Therefore, CPD kinetics for copper in both the cases is similar and is determined mainly by oxidation. This fact (low mobility of vacancies) was one of the main factors which favored selective transfer in friction of copper, since the main structural criterion

of ST occurrence in the contact zone is a high surface density of point defects (vacancies) at a low dislocation density [25, 77, 78].

Polished surfaces characterized by different physical behavior (capability to dissolve, photoelectric properties, hardness, etc.), which should influence CPD, are of particular interest.

The shape of the CPD kinetic curves following polishing (curves 4 and 5, Fig. 2.6) is the same for all materials, therefore, the kinetics slightly depend on the types of material and seem to result from an increased chemical resistance as compared with the surface after grinding, polished surfaces are characterized by a greater adsorption potential [16].

A valuation of the EWF kinetics within the framework of the theory of wear failure of metals ([58, 59] and others) and in terms of the concept explaining the EEE processes [36, 54, 62–65, 79] explains the nature of the double-crest shape of the CPD dependence on the surface machining (see Fig. 2.3).

2.4. Correlation of Work Function and Quality of Machining Different Metals

Expansion of the range of materials in investigation has revealed a very interesting feature, vis. the height of the second CPD maximum U_{2max} (corresponding to roughness 12) in the equation $U_c=f(Ra)$ (see Fig. 2.3) is less than U_{1max} (roughness 9) not only for copper. This finding was reported in [44] (2.2) when the ST mode was implemented for copper. Meanwhile, copper is not the only metal which is selectively transferred from one surface to the other and is deposited in the form of a finest "servovitae" film that produces the minimum friction coefficient and wear. Selective transfer in friction was also observed for gold and silver in glycerine [25], as well as in sliding electrical contacts from gold [80, 81]. Then, a natural question is: if there are any other metals similar to copper, silver, and gold which show in friction some specific behavior and can produce ST. Moreover, common properties of selective transfer exhibited by copper, silver and gold should apparently be manifested in the relationship between EWF and the machining quality of these metals.

A thorough study (Fig. 2.3) for a large class of the most common pure polycrystalline metals of the 4th period and, also, of some elements within the groups of the Periodic System, gave the following results. According to U_{1max} and U_{2max} all the materials can be divided into two groups. Group 1 contains seven metals for which $U_{2max}<U_{1max}$ (V, Cr, Co, Ni, Cu, Ag, Au); the second group contains elements for which $U_{2max}>U_{1max}$ (Fe, Zn, Cd, Al, Ti, Sn, Ta, Mo, W and others). As an example, results for some metals of the two groups are presented in Fig. 2.8. Common properties within the selected groups are displayed also in the CPD kinetics after surface machining (Fig. 2.6, curves 2 and 3, and Fig. 2.9).

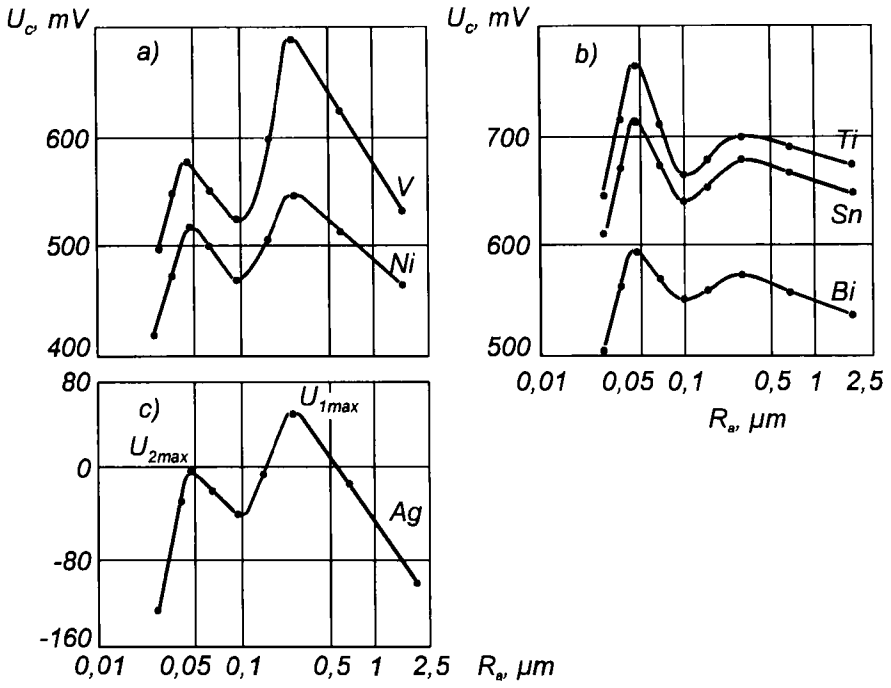

Fig. 2.8. CPD of vanadium and nickel (a), titanium, tin, bismuth (b), and silver (c) versus roughness immediately after surface abrasive machining and washing in toluene

The 1st group of metals has similar CPD kinetics both up to roughness 9 (curve 2) and roughness 10c–11a (curve 3). The CPD kinetics of the 2nd group of metals differ considerably from the 1st group of metals. It is known [67] and validated by direct measurements that EWF is substantially less near dislocations and at the largest defect pile-ups. Vacancies formed in deformation, diffuse to the surface where they transfer their energy to electrons, thereby decreasing EWF [79]. Diffusion of vacancies to the surface from the bulk of a specimen continues for some time after deformation. This fact can explain the initial increase of EEE after machining of some metals. With this in view, the different shapes of curves 2 and 3 (Fig. 2.6) for copper was explained in 2.3 by lower mobility of defects (vacancies) outcoming to the surface, in comparison with other metals. Therefore, the CPD kinetics for copper at roughness 9 and 10c–11a is controlled mainly by oxidation and is characterized by initially fast, then slow decrease in U_c (increase of EWF).

The experimental results allow to assume that the low mobility of defects (vacancies) coming to the surface is also inherent to the other six elements selected from the 1st group [44].

Common properties of the seven transition metals, V, Cr, Co, Ni, Cu, Ag, Au, exhibited under mechanical action on other surfaces, is not occasional and is certainly caused by similar atomic structures of materials, namely, the distribution of electron charge densities conditioned by central attracting forces to the positively charged nuclei, mutual repulsion, magnetic interactions, and correlated movements of electrons. Besides, the commonness is determined by internal electron properties, such as their dualism being particles and waves, spin characteristics, space distribution of α- and β-spin densities, and some other more intricate factors [82]. To find the interrelation between numerous properties of chemical elements and their internal structures is a very difficult problem. Nevertheless, using the available data, we will try to find a common factor for the group of seven transition metals.

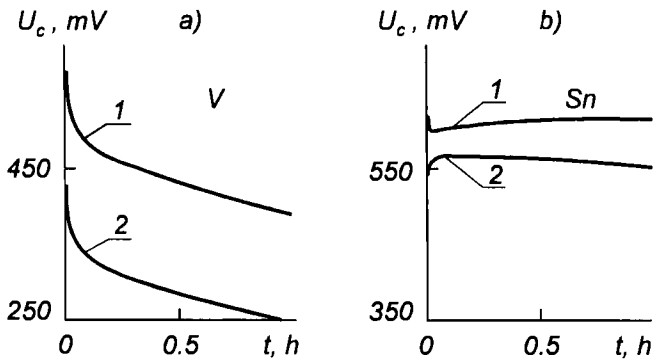

Fig. 2.9. CPD kinetics of vanadium (a) and tin (b) immediately after machining to roughness 9 (1) and 10c–11a (2), without washing their surfaces.

Accurate calculation of the electron interaction energy should take into account the correlation effect in the electron motion in the atom, or the effect of irregular forces with their instantaneous potentials and instantaneous movements of each surrounding electron. The correlation energy is associated with a certain exo-effect which additionally stabilizes the atom. The correlation energy rapidly increases with the number of electrons in the atomic shell, with the growing nuclear charge at a constant number of electrons. There are dynamic and non-dynamic correlations depending on the disturbing interelectron interaction of functions 2*s* and 2*p*, because of the geometrical proximity of electron clouds of the same basic quantum number. The correlation energy depends on the multiplicity and orbital angular moment of the electron term, it decreases as the total spin grows, etc. [82].

Let us consider the correlation energies for 3d-elements of the 4th period of the Periodic System. Figure 2.10 is a plot of correlation energy variations for $d_n \rightarrow d_{n+1}$ processes, in particular, $Mn3d^54s^2 \rightarrow Mn^+3d^64s^0 + e^-$. Here one 4s-electron

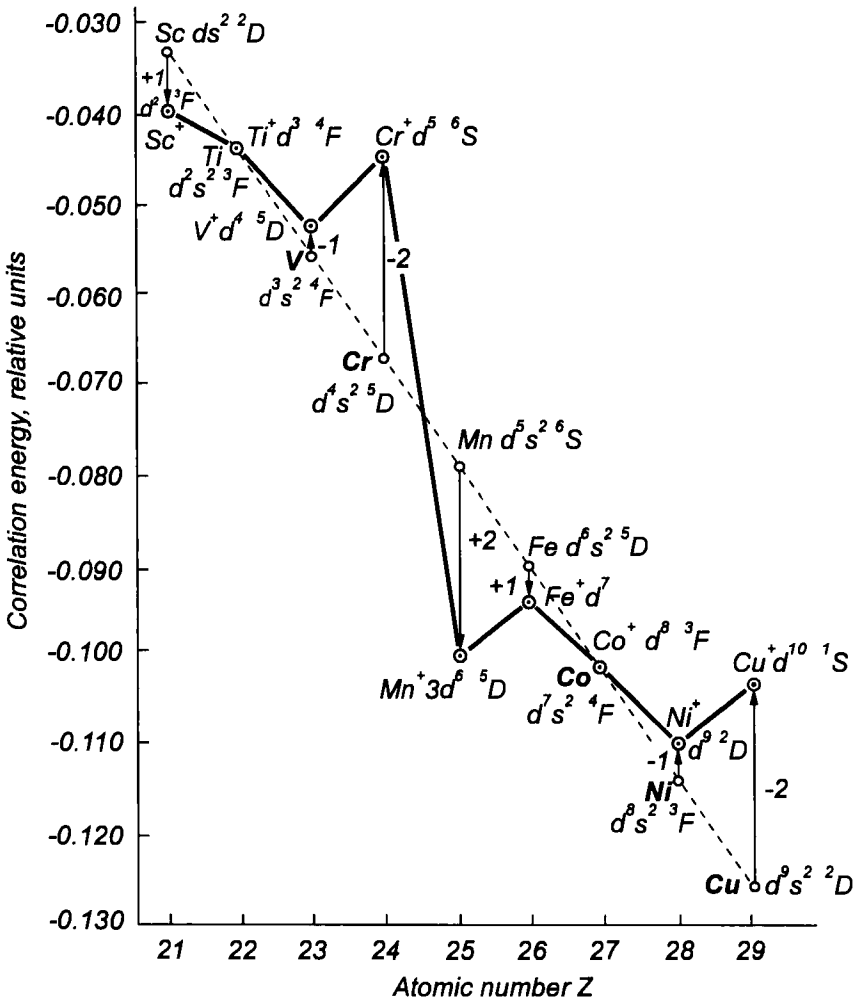

Fig. 2.10. Correlation energy variation for $d^n \rightarrow d^{n+1}$ processes [82].

is taken away from the neutral atom and simultaneously another 4s-electron passes to 3d-state. The dash straight line passes through the points of titanium and cobalt for which the angular moment variations are zero. The total difference between large negative Cr^+d^5 and large positive Mn^+d^6 deviations reaches 1.5 eV (0.055 at. unit), the metals of the group having negative deviations (see Fig. 2.10) are V^+d^4 (-1), Cr^+d^5 (-2), Ni^+d^5 (-1) and Cu^+d^{10} (-2). Irregular forces responsible for correlation of electron movements are very important for determination of typical individual features of chemical elements, they influence the chemical behavior of the element [82]. It is illustrated by an example of ionization potentials

of neutral and normal atoms of 3d-elements (Fig. 2.11). The upper smooth curve characterizes the configuration $d^{n+1}s$ ((n+1)=5 for chromium and 10 for copper), the lower curve corresponds to points of the curve at n= 0, 1, 5, 6, 10. The energies of vanadium, cobalt, and nickel atoms occupy an intermediate position preparing the transition to the line $d^{n+1}s$. The transition of one of 4s-electrons to 3d-level for Crd^4s^2 and Cud^9s^2 is exothermal in the normal state, therefore, deviations in electron configuration formulas in a series of atomic positions, clearly seen for Crd^5s and $Cud^{10}s$, are natural and the corresponding state is the normal ground state of neutral atoms. Endoeffects for vanadium and nickel atoms are very small, especially for nickel.

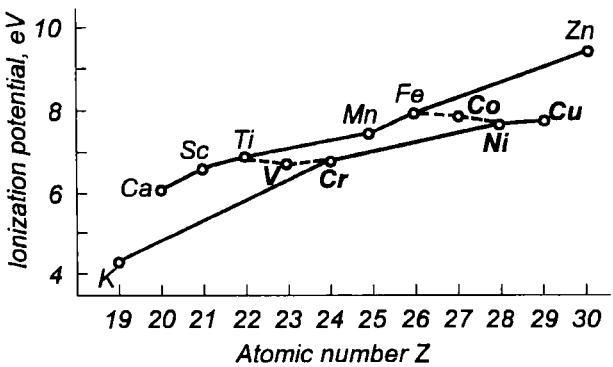

Fig. 2.11. Ionization potentials of the atoms of 3d-elements [82].

The separation energy of 3d-electrons is higher than that of 4s-electrons. As Z increases from scandium to zinc, the work function of 3d-electrons increases by 9.2 eV against 2.8 eV for 4s-electrons. In the case of separation of s-electrons from the configurations Md^ns^2 the excited states of M^+ cations, except for chromium and copper, are observed only for vanadium, cobalt, and nickel. Then, spontaneous exotransition of excited states $*V^+$, $*Co^+$, $*Ni^+$ to stable states V^+, Co^+, Ni^+:

$$d^3s^2 \rightarrow *V^+d^3s^1 \rightarrow V^+d^4s^0;$$
$$Cod^7s^2 \rightarrow *Co^+d^7s^1 \rightarrow Co^+d^8s^0;$$
$$Nid^8s^2 \rightarrow *Ni^+d^8s^1 \rightarrow Ni^+d^9s^0,$$

reduces the work of ionization separation of s-electrons from vanadium, cobalt, and nickel atoms, it corresponds to anomalous positions of ionization potential points in Fig. 2.11, i.e., the substitution of *d* for *s* in charged atoms M^+ is exothermic only for vanadium, cobalt, and nickel, whereas for chromium and copper such transition is exothermic even in the normal state. It is quite probable

that the decrease in the ionization potential of s-electrons is responsible for a considerably larger CPD drop (EWF decrease) ΔU_c in our group of seven metals in comparison with the others between of roughnes 6–7 and 9 which was reflected by a relatively steeper right maximum U_{1max} in the curve $U_c=f(R_a)$ (see Fig. 2.8). As was noted earlier, mechanical excitation of the surface machined to roughness 9 yields the critical dislocations density, hence, the minimum EWF (maximum CPD). Meanwhile, a smaller work of separation of s-electrons from V, Cr, Co, Ni, Cu atoms by spontaneous exotransition from excited d-state to the stable state reduces additionally the potential barrier for electron escape which is reflected in a steeper right CPD maximum U_{1max}.

Submicrocracks and resulting relaxation of dislocations accompanying fresh vacancies reduce the density of defects and substantially decrease U_c down to a deep minimum (Figs. 2.3 and 2.8). Transformation of submicrocracks into fatigue cracks stimulates a substantial [58] increase in the number of vacancies with no time to scatter, therefore, the tendency is towards decreasing EWF (increasing U_c). The probability of fatigue cracks caused by microplastic deformation is higher [83], if the defect packing energy is lower. It is relatively high for copper, amounting to about 6×10^{-2} J/m^2 against 5×10^{-3} J/m^2 for CuZn37 copper alloy. Therefore, the surface fatigue failure during machining is less typical for copper since formation of dislocation pile-ups and fatigue cracks is inhibited, whereas the formation of a soft surface layer is a common feature. In the meantime, the mobility of vacancies diffusing to the surface from the specimen for copper and the other six metals of this group is lower than, for example, for aluminium [64], zinc, and other metals. Accordingly, a further increase of CPD in Cr, Co, Ni, Cu, Ag, Au at roughness 11c–12a is not so sharp: the left maximum of CPD U_{2max} is less than U_{1max} (Fig. 2.8).

In the deformed near-surface metal layer after grinding the diffusion coefficient is nearly 10 to 10^2 times higher than that in the electropolished specimen [84]. The thinnest deformed surface layer has the highest diffusion permeability. Defects from surface machining are responsible for diffusion intensification, a large density of defects induces substantial structural metastability. Stability of structural disturbances in the surface layer after machining vary for metals having different dislocation structures. Stability of the defective structure (the hardened state) was studied with the diffusion permeability [85] as a measure. After grinding iron and nickel their blocks and the density of dislocations in the surface layers were practically the same. Subsequent annealing at 0.5 T_{ml} for 5h showed that the size of iron blocks compared with nickel were almost 3 times larger (1.4×10^{-4} cm for iron and 5.2×10^{-5} cm for nickel), and the dislocation density was smaller by about an order of magnitude (1.5×10^8 cm^{-2} against 1.1×10^9 cm^{-2}). Thus, due to different mobility of vacancies coming out to the surface, the hardened areas in α-iron (and, also, in molybdenum) are less stable than those in nickel and copper [85].

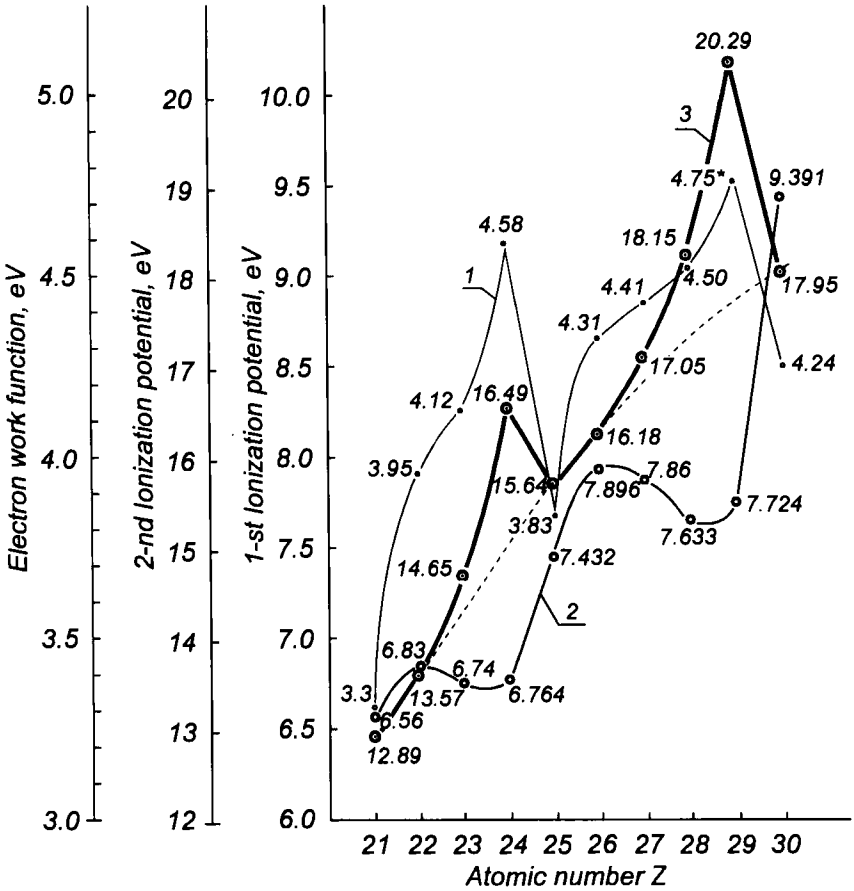

Fig. 2.12. Electron work function (1) of chemical elements (polycrystals) [74], the first (2) and second (3) ionization potentials of 3d-atoms [87]:
* the value borrowed from [88].

The reasons of slower diffusion may be different. One of them seems to be associated with the formation of oxide films on the surface which reduce the diffusion permeability. According to thermodynamics, at low oxygen pressure metals must oxidize spontaneously (at 300K this pressure is approximately 1.3×10^{-4} Pa) [86]. The chemisorbed oxygen layer is metastable in respect to the oxide and the interaction mechanism of the surface oxide with the thermodynamically stable volume oxide is different for many metals because of different chemisorption heat, probability of oxygen adhesion, and capability of the chemisorbed layer to rearrange with the formation of oxide phase. Measurements of EWF reported in many studies [86] showed that metals of the nickel group (copper among them) and the aluminium group (iron among them) had different EWF kinetics in interaction with oxygen. The peculiarity of the nickel group metals

is the low activation energy during oxygen penetration into the crystalline lattice.

Because of EWF considerable scatter, the recommended vales [74] are taken for plotting $\Phi=f(z)$, the relation obtained which correlates with the 2-nd ionization potential (curves 1 and 3 in Fig. 2.12). As a rule, nearly all elements of the 1st transition period form 2^+ oxidation compounds (excepting scandium for which it is 3^+). Copper is the only element in this group which has a relatively stable oxidation state of 1^+, the most stable compounds are formed by copper at oxidation of 2^+ [89]. Figure 2.13 shows the oxidation potentials of the elements for the process M(solid)$\rightarrow M^{2+}+2e$ (in acid solution) [89]. Comparison of Figs. 2.12 and 2.13 shows that oxidation potentials decrease exactly with the increase of ionization potentials and correlate well with the first ionization potential.

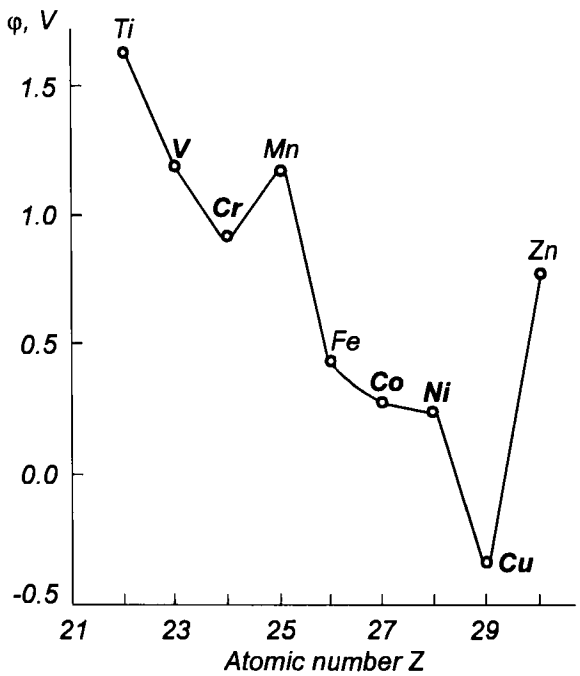

Fig. 2.13. Oxidation potentials (in acid solution) M(solid) $\rightarrow M^{2+}+2e$ for elements of the 1-st transition period [89].

The list of common properties of the group of seven metals can be continued but the data reported are quite sufficient to find that the EWF behavior in mechanical action (Figs. 2.3, 2.6, 2.8, 2.9) was not casual. Therefore, it may be assumed that due to common properties the ST mode can be implemented in friction not only on copper, silver, gold but also on vanadium, chromium, cobalt, and nickel since the structural criterion (a considerable density of point defects (vacancies) at low dislocation density in the surface film) is found for all metals

of the group. Other requirements associated with the electrochemical mechanism of selective transfer (it will be discussed later) can apparently be proper selection of materials and lubricants for friction pairs according to physical and chemical parameters.

It should be noted that, all seven metals of this group possess, a high plasticity and considerable corrosion resistance. It has been known for a long time that pure chromium has a very low friction coefficient. Iron alloys containing about 20% of chromium and about 10% of nickel have the highest wear resistance.

So, no wear was found for 15/13 steel that worked in pair with copper in glycerine at 50 °C and 4.7 MPa [90] for 310 h and a very weak ST of copper (which could not be observed visually) was detected by spectral analysis. Atomic copper deposition (ST) in the electrolytic chromium–bronze pair [91] was also studied. In particular, in friction in AMG-10 lubricant, though mechanical parameters of friction indicate that the mode is close to ST (the friction coefficient and wear are very small), there is no copper transfer to both surfaces (a copper film is only formed on the bronze surface). Probably, in this case as well as in the previous case [90], the friction mode, the counterbody and the lubricant nature are more favorable for ST of copper than for ST of chromium. It cannot be excluded that in other modes of operation conditions can be created for stable ST of chromium predominantly.

Intensive search for new materials operating in ST mode is due to the acute need to increase wear resistance and life of electrical contacts and to reduce consumption of noble metals. Therefore, it seems reasonable to continue and extend the studies and practical use in electrical contacts other transition metals from the group, namely, vanadium, chromium, cobalt, nickel, and copper.

2.5. Influence of Semiconductor Surface Treatment on Electron Work Function

Improvement of semiconductor surface preparation technology in production of integrated circuit determines the quality of instruments because the efficiency of subsequent production operations – epitaxy, diffusion, oxidation, etc. – will depend on the semiconductor cleanness, the nature of adsorption films, etc. Surface control in production is carried out mainly by destructive testing on the so-called satellite plates. Nondestructive methods are also known which are based on measurements of electrophysical parameters of semiconductor surfaces since the parameters essentially depend on the presence of alien atoms and structural surface damages. In particular, a method is suggested which is based on the light probe scanning of a semiconductor plate and measurements of emission flux [92]. The method is based on the increase of emission activity of defective surface sites during photoexcitation as they have excessive energy and are characterized by a

smaller EWF. EEE parameters closely related to EWF are measured [93] which are highly sensitive to minute changes in processing conditions as well as evaluation of subsequent treatment of semiconductors. In particular, measurements of thermally stimulated EEE are very useful for determination of the damaged layer depth and the number of defects in the heated material. Though the depth of the directly emitting layer in EEE is 10–100 nm, the EEE parameters depend on the depth of the damaged layer (8–11 μm) [94], since EEE appears sensitive to the structure and the physical state of deeper surface underlying layers. The enumerated measurement methods [92, 93] are time consuming, require stimulations (for instance, photoexcitation), and can be used only in vacuum; therefore, they have low efficiency and are only suitable for laboratory conditions.

The dynamic capacitor method used for measurement of EWF [41] when checking the finish of semiconductor plates is very informative [48]. Plates (40 mm in diameter) of KEF-20 silicon chip crystals were investigated. The plates were oriented in crystallographic plane (111) after surface conditioning necessary for subsequent integrated circuit production: 1) cutting; 2) polishing with ASM 3/2 paste to remove at least 25 μm; 3) polishing with ASM 1/0 paste to remove 10 μm; 4) chemical and mechanical polishing (CMP) by aerosol with different amounts of removed material (1–2, 5–8, 10–13, 15–18, 20–25, 30 μm); 5) washing. The back side of the plates was polished using the same pastes. It was assumed that after removal of 10 μm to 13 μm layer by chemical and mechanical polishing, the mechanically damaged layer resulted fran the first three operations was completely removed.

The dependence of the KEF-20 silicon CPD on the material removed by chemical and mechanical polishing and washing in the composition used in the process (it will be called *A*) is shown in Fig. 2.14. The listed CPD values are the arithmetic mean of five or six integral measurements on different sites of the plate relative to the 5 mm diameter reference gold electrode. The CPD increases (EWF decreases) at initial increase of the layer thickness removed by CMP up to 5–8 μm. This can probably be attributed to the fact that (according to 2.2) the rough layer R_z and the underlying layer R_{cr} are removed (Fig. 2.5). During this process the subsequent zone with large residual stresses (B-zone of higher dislocation density, R_d) appears.

Abrupt decrease of CPD (increase of EWF) follows after additional CMP removal of the defective layer. The minimum and constant CPD when removed layer increases from 15 to 18 μm and more, indicate complete removal of the mechanically damaged layer. As one can see from Fig. 2.14 where 1, 2 and 3 designate plates with the same layer of 10 to 13 μm removed by CMP, such removal is critical and insufficient for guaranteed elimination of the defective layer. For validation plates 1, 2, and 3 were additionally scanned by the reference gold

1.2 mm diameter electrode, in order to check uniformity of EWF over the plate area with resolution of 0.6 mm.

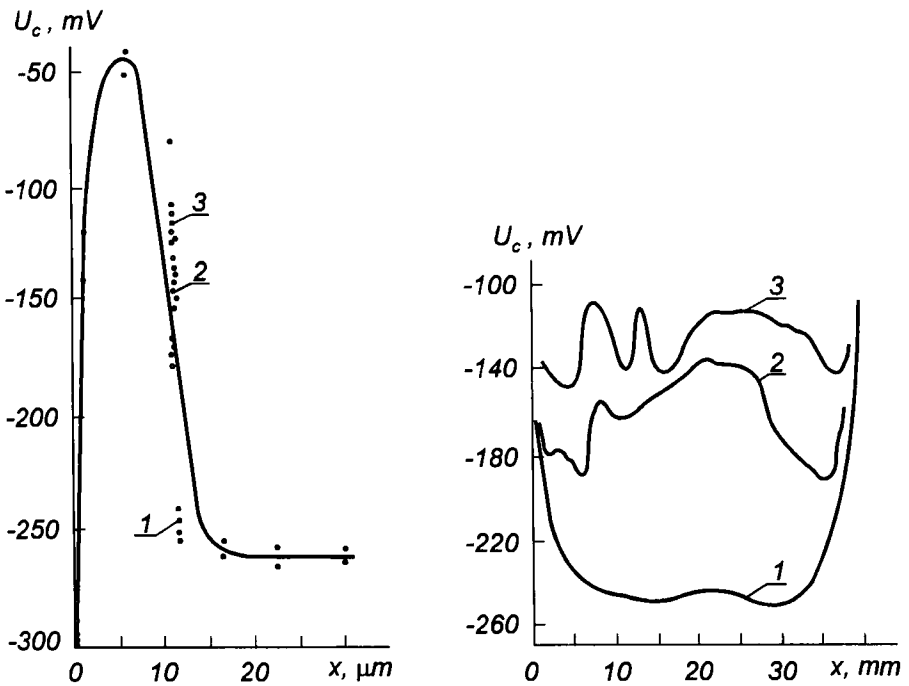

Fig. 2.14. Dependence of CPD of the plate of KEF-2 (111) silicon on the amount of material removed by chemical and mechanical polishing and washing.

Fig. 2.15. Scanning of three plates of KEF-20 silicon along the diameter, with layer 10 to 13 μm removed by chemical and mechanical polishing and followed by washing.

Indeed (Fig. 2.15), for plates 1 for which a 10–13 μm layer seems to be sufficient for complete removal of the damaged layer, EWF is not only maximum, it is constant also over the larger part of the area, excepting edges. Apparently, because of specific growing conditions of chip the peripheral defect density is higher than in the body. It may result from irregular crystal growth rates in the body and over the periphery when it is removed from the melt, nonuniform distribution of impurities, etc.

Plates 2 and 3 differ from plates 1 not only in a larger absolute CPD but, also, in a wide scatter and variations of CPD over the area. Considerable differences in CPD for plates with the same, (10–13) μm layer removed cannot be found immediately by traditional microscopic testing after pickling the plate in a

chromium agent. Only after subsequent epitaxial buildup and pickling in the same agent these differences were exposed, i.e., they affected the epitaxial layer quality. As it can be expected, plates with a larger Φ value have a smaller defect density (U_c=-220 to -260 mV and ρ=(2.2 to 1.4)$\times 10^3$ cm^{-2}, U_c=-70 to -120 mV and ρ=(11.0 to 6.2)$\times 10^3$ cm^{-2}).

The CPD value is also very sensitive to the quality of washing of semiconductor plates which affects the quality of finished products. Chemical treatment affects the characteristics of surface states and the charge localized on the surface and results in the variations of the surface potential φ_s. It appears that successive substitution of the surface washing route of compositions *B* and *C* for *A* to improve the production process, results each time in the formation of such surface potential at which EWF value becomes larger (U_{cA}=-200 mV, U_{cB}=-260 mV, U_{cC}=-440 mV). .

The quality of chemical treatment of silicon plates used in integrated microelectronics was thoroughly investigated by CPD measurement. In this procedure the distribution of $U_c(x)$, where x is the coordinate along the arbitrarily chosen line over the silicon plate surface, was recorded automatically. The diameter of the standard platinum electrode was 0.5 mm. Comparison of the distributions $U_c(x)$ was carried out for an area-averaged value of U_c and dispersion σ^2 characterizing the CPD spread over the plate. For a thorough analysis of CPD distributions, the mode, median, scale, and variation coefficients were computed and a histogram was plotted. Analogous measurements [95] were carried out by measuring the capacitor photoelectromotive force which appears between the silicon plate and the semiconductor metal electrode located at a distance of 50 μm while illuminating the test sites of the surface by a laser beam (λ=0.63 μm, the light spot diameter is 0.5 mm). However, physical interpretation of the changes in the capacitor photoelectromotive force induced by chemical treatment, is difficult because of the nonlinear relation of the photoelectromotive force (U_{ph}) with φ_s and the dependence of U_{ph} on the parameters of recombination and adhesion centers.

Quality control of semiconductor material treatment by measuring CPD during which the test surface does not contact the measuring device and is not, therefore, "injured" or contaminated, is widely used in improving semiconductor production.

2.6. Kinetics of Contact Potential Difference in Adsorption of Lubricants

The influence of lubricant on physical, chemical and, eventually, mechanical properties can be clearly traced by investigating CPD of metallic surfaces after lubricant adsorption. This example is also important, because studies of CPD kinetics, if there is no electrochemical corrosion, give key to the information about

the nature of adsorption: first, whether the surface layer is formed due to physical adsorption or chemical interaction; second, the reaction directions and rates, the charge sign of double coating electric layer, the catalytic activity of juvenile and oxidized metal surfaces.

As an example, we will consider the results of the studies of the effect of TsIATIM-201 and TsIATIM-221 lubricants (greases, GOST) on the surface states of steel and copper alloys. These and some other materials (lubricants and alloys) are taken as objects because they are used in sliding electrical contacts and in the majority of friction assemblies operating in ST mode. Before applying the lubricant, the specimens were prepared in an ordinary way: polished with emery paper to the required roughness and washed in B-70 gasoline (GOST). Excessive lubricant was carefully removed by an ashless filter.

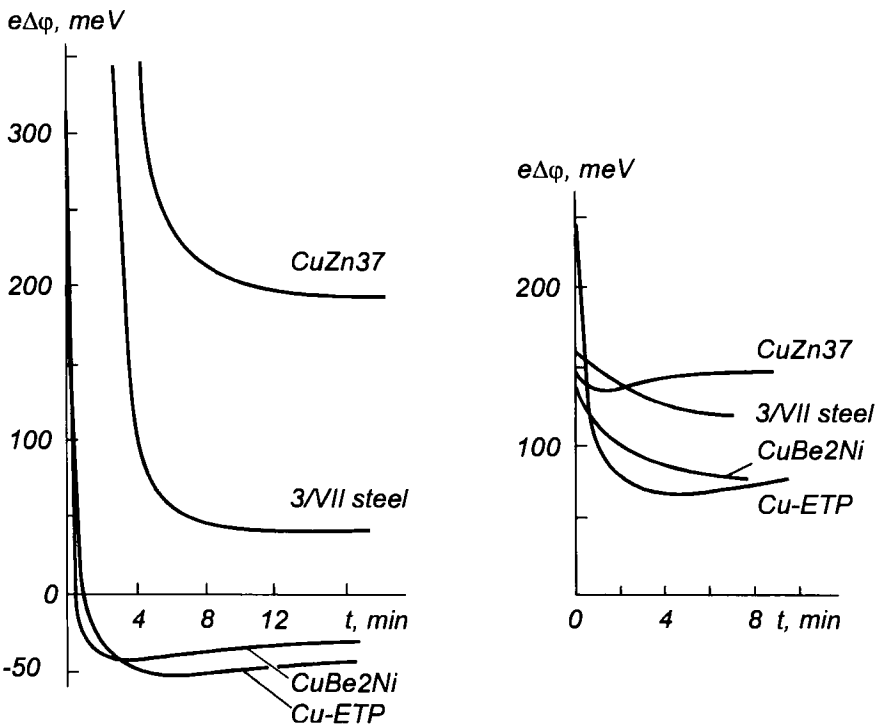

Fig. 2.16. EWF kinetics of Cu-ETP copper, CuBe2Ni bronze, 3/VII steel, and CuZn37 brass in adsorption of TsIATIM-201 grease17–20 h after machining to roughness 7 and washing:$\Delta\varphi$ is the difference between the measured instantaneous φ and the reference φ_0 by the moment of lubrication.

Fig. 2.17. The same as in Fig. 2.16: using TsIATIM-221 grease.

The EWF values (eφ) of steel and brass approximately 8 min after application of TsIATIM-201 grease to their machined surfaces exposure to atmosphere for about 20 h (Fig. 2.16), increase compared with the initial values: eφ of brass increases by about 200 meV, that of 3ΛVII steel by 40 meV. On the contrary, eφ of copper and bronze, having reached the steady state after 3 or 4 min, decreases by 30 and 40 meV. Similar kinetics are observed when using MVP oil (GOST). Meanwhile, TsIATIM-221 (and OKB-122-7 grease, GOST) increases eφ of all four metals (Fig. 2.17). However, in most cases an abrupt discontinuous increase of eφ can be observed just after lubrication, the increase being remarkably high with TsIATIM-201 and OKB-122-7.

The curves (Figs. 2.16 and 2.17) reflect the kinetics of lubricant molecular adsorption on oxidized metallic surfaces. The kinetics are determined by the state of surface layers which develop after machining, washing, and exposure to the air. So, Δφ kinetics for CuBe2Ni bronze treated as in the previous case, without lubrication, in air showed the following behavior. Initially, the EWF increases; after 17 h it passes through the maximum ($e\Delta\varphi \approx 65$ meV), and decreases subsequently (see Fig. 2.18). Naturally, this behavior results not only from the oxide

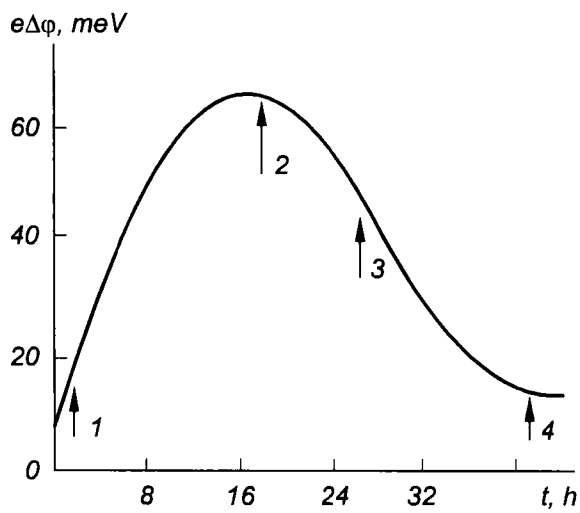

Fig. 2.18. eΔφ kinetics of CuBe2Ni bronze surface machined to roughness 7c and washed: $e\varphi_0$ is the EWF value at the initial moment, immediately after surface polishing.

film growth but, also, from time variation of the film behavior shown experimentally.(Fig. 2.19).

On applying TsIATIM-221 to bronze surface at different time after exposure to the air (marked by arrows in Fig. 2.18), the initial portion of the kinetic curve

changes abruptly, compare curves 1, 2 with curves 3, 4 (Fig. 2.19). Whereas at the initial time (a short-term exposure to the air) the jump of $e\varphi$ is positive, after more than 18 h (after $e\Delta\varphi$ passes the maximum) the lubricant adsorption at the initial time reduces $e\varphi$ (curves 3, 4 in Fig. 2.19).

The same behavior is also observed for copper lubricated with TsIATIM-221 and can, probably, be attributed to the dynamics of oxide film growth on machined and washed bronze surface, as well as to the change in its type of conductivity. Consequently, depending on the state of surface layers, lubricants initially behave as surfactants, sometimes they produce cathode, sometimes anode effect. Subsequently, the intensified chemisorption results in the formation of compounds abruptly changing the surface layer phase composition. It is illustrated by almost the same shift of $e\varphi$ for CuBe2Ni bronze (approximately after 8 min) to the positive region (Fig. 2.19, curves 1–4).

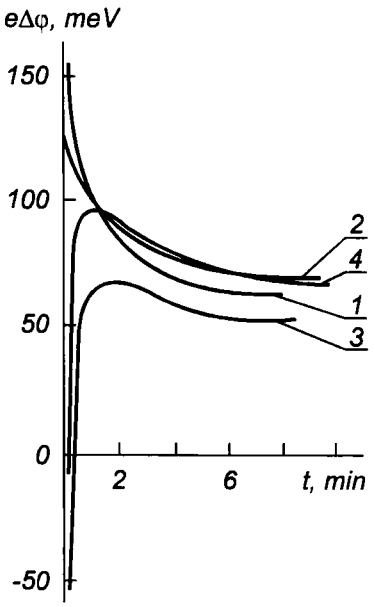

Fig. 2.19. $e\Delta\varphi$ kinetics of CuBe2Ni bronze surface machined to roughness 7c and washed after exposure to air for 1-3 h (1), 17 h (2), 26 h (3), and 41 h (4) followed by TsIATIM-221 application:
$\Delta\varphi$ is the difference between the measured instantaneous φ and the reference φ_{o1}, φ_{o2}, φ_{o3}, or φ_{o4} steady-state to the moment of lubrication.

Thus, application of lubricants to machined alloy surfaces washed in gasoline affects the kinetics of $e\varphi$. Under standard friction conditions juvenile metal surfaces interact almost instantaneously with the lubricant. Therefore, it is important to know how this particular metal surface will interact. The standard situation of juvenile surface appearance can often be encountered in friction units operating under high loads and severe conditions (high speed and temperature) when the absorption boundary layer is partly destroyed (especially, during the run-in) and close metal-to-metal contact occurs. Under such conditions, antiwear, antifriction, and other similar additives begin to work effectively, chemically interacting with the juvenile surface and modifying it. The standard situation can be simulated by applying lubricant immediately after grinding the surface.

A fresh juvenile surface is extremely reactive; such surface is a kind of catalyst which increases the reaction rate. In a certain approximation, a juvenile iron surface

can be compared with appropriately reduced iron–pyrophorus iron, which actively absorbs oxygen and heats up to 973–1073 K [96]. Some data confirm the high reactivity of juvenile 3/VII steel (Fig. 2.20). TsIATIM-221 grease based on PES-S-1 polyethylsiloxane liquid (without antioxidants) and low-viscosity MVP petroleum oil in steady operation (after approx. 10–12 min and especially during the first two minutes) decreases $e\varphi$ of 3/VII steel, CuZn37 brass and CuBe2Ni bronze, but increases it for Cu-ETP copper.

A considerable decrease of the $e\varphi$ of copper alloys after application of a thin lubricant layer can be due to quick oxidation of the lubricant, since copper alloys containing chemically active alloying elements are strong catalysts. Oxidation is accompanied by the formation of active groups with a relatively high polarity which act as combined anode-effect surfactants, decreasing the $e\varphi$ of metals. If the metal surface has positively or negatively charged sites, such surfactants are adsorbed and form chemisorptive compounds, primarily, at positively charged electron acceptor sites. In this case, a positive layer of surface dipoles appears on metal decreasing the $e\varphi$.

Anode-action inhibitors change abruptly the metal surface layer phase composition in which the products of interaction of the metal and oxygen of active groups [97], prevail. Anode-acting oil-soluble surfactants protect very effectively ferrous and nonferrous metals because chemisorptive compounds which they form, are insoluble in the oil.

At the same time, the decrease of the $e\varphi$ in surfactant adsorption is also conditioned by the effect of adsorption-related decrease in hardness and strength of solids [28], which is based on decrease of the free surface energy when unsaturated bonds of the metal surface crystal lattice are compensated by surfactant molecules. Electron exchange and formation of adsorbate-adsorbent bonds weaken the interatomic bonds of the metal crystal lattice and decrease the work required to form new surfaces.

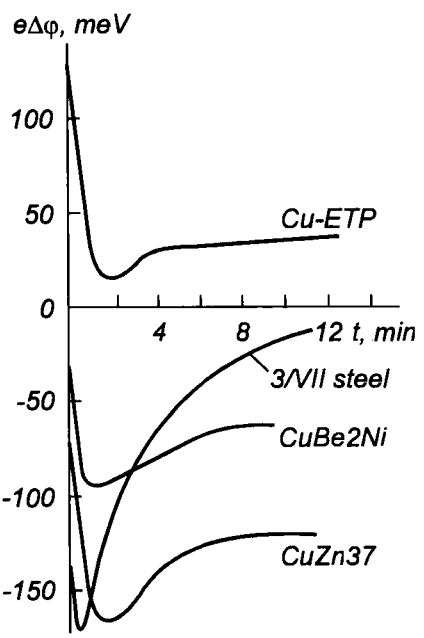

Fig. 2.20. Kinetics of $e\Delta\varphi$ for Cu-ETP copper, CuBe2Ni bronze, 3/VII steel, CuZn37 brass, immediately after the polishing (without washing) followed directly by application of TsIATIM-221 grease: $\Delta\varphi$ is the difference between φ values at the same time instances, with and without lubrication.

The capillary effect of strength reduction induced by the surface tension dependence on the polarizing potential supports the adsorption action of organic surfactants [28]. Adsorption must be inevitably accompanied by the surface tension reduction. These two processes are inseparable, therefore, presence of any medium on the solid surface relieves the surface layer, i.e., decreases the bond tension as compared with vacuum. There is a direct relation between the surface energy (surface tension) σ and φ (see 1.1). The following semi-empirical formula suggested by V.V. Demchenko and N.E. Khomutov, which relates to σ and φ, can be cited:

$$\sigma=\varphi Z/(1.885R^2\times10^{-10})\ \text{J/cm}^2, \tag{2.3}$$

where Z is the number of free electrons per atom;

R is the atom radius, 10^{-10} m.

It is apparent from Eq. (2.3) that adsorption decreases the surface tension on the interface, with decrease in φ. In this case, the adsorption layer facilitates the formation of surface defects or microcracks as nuclei of plastic displacement and ductile rupture, thus, favouring deformation in the very fine surface layer. In the long run, the Rehbinder effect has a favourable effect on stimulation of the initial stage of ST and creates conditions to satisfy the positive gradient rule.

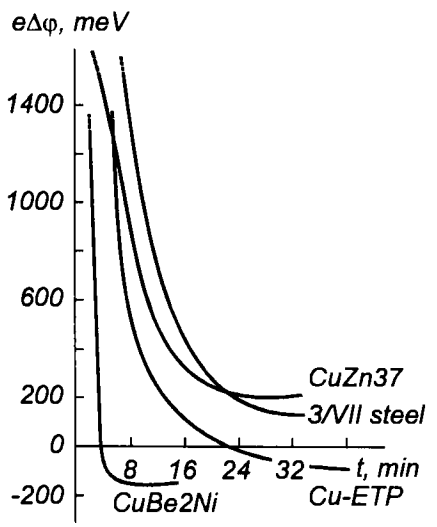

Fig. 2.21. The eΔφ kinetics of as-treated (without washing) Cu-ETP copper, CuBe2Ni bronze, 3/VII steel, CuZn37 brass, after application of TsIATIM-201 directly after treatment: Δφ is the same as in Fig. 2.20.

Grease TsIATIM-201 is more oxidation-protective as it contains, apart from MVP petroleum distillate oil, anti-oxidant diphenylamine (0.3%), a cathode-action surfactant which inhibits self-oxidation and transforms hydrocarbon radicals and peroxides induced by self-oxidation into stable molecules. Upon application of TsIATIM-201 to polished steel and copper alloy surfaces, a sharp increase of $e\varphi$ is observed up to values exceeding the measurement range of the apparatus [41] (in excess of 2 eV, Fig. 2.21). Grease OKB-122-7 has the same effect.

Aromatic diphenylamine $(C_6H_5)_2NH$ includes groups which give a net positive electron effect. The diphenylamine dipole moment in benzene at 293 K is 0.95 D. On adsorption, this additive forms a chemisorptive phase, first of all, at negatively charged metal sites. Electron affinity to metal surfaces appears lower than that to surfactants, so metal electrons pass over to the electron shell of the surfactant molecule. Electron density on the metal surface increases and the electronegative layer which increases EWF, is formed (Fig. 2.22) [97].

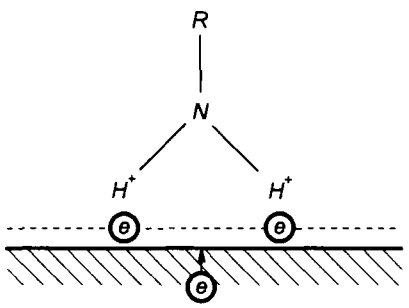

Fig. 2.22. Adsorption interaction diagram.

The bond energy of an inhibitor of the metal corrosion are determined by electron density of inhibitor atoms, i.e., by that quantity of electrons which are involved in the coordination bond with metal. The corrosion inhibitors which well protect ferrous metals, should enhance selective corrosion of non-ferrous metals, copper alloys in particular. It is connected with the formation of chemisorptive compounds soluble in oil between cathode-action surfactants and alloying chemically active elements of copper alloys.

Comparison of $\Delta\varphi$ kinetics of copper and bronze with $\Delta\varphi$ kinetics of steel (Fig. 2.21) shows that active chemisorption on copper alloy surfaces results in the change of $\Delta\varphi$ the sign. For beryllium bronze the inversion of the sign of $\Delta\varphi$ occurs after 3–4 min, for M1 copper – after 20 min.

Under developing electrochemical corrosion, it is impossible to infer adsorption or chemisorption character of surfactant-metal bond and, especially, to judge about possible polarization of metal surface [97] from the $\Delta\varphi$ value. However, according to the net effect on the alloys studied, OKB-122-7 and TsIATIM-201 can be identified as cathode-action lubricants increasing EWF of as-treated metal surfaces. They behave, in general, as combined cathode-action surfactants, serving as electron acceptors for metals.

The above examples show how strongly the change in $e\varphi$ after lubrication of metal surfaces depends on the lubricant composition and the metal nature, and how important the effect of the surface conditions on $e\varphi$ is. The changes of $e\varphi$ obtained for metals and alloys characterize the net electron effect of lubricant in which the most important role is played by surfactants.

Physical and chemical properties of oil change in operation of machines and mechanisms, both, as a result of oxidation and chemical transformations under high temperature and pressure at the spots of actual contacts of surfaces. Interacting with the molecules of oil, oxygen destroys them and new products are formed. The oxidation reaction rate (neglecting the effect of catalysts such as copper, lead, and their alloys, iron, etc.) depends on temperature, chemical composition, and concentration of reactants. Interacting with metal surfaces, some additives and products of their decomposition modify the friction surfaces chemically. These additives differ from the classic diphyl structure of surfactants; they have relatively active chemical groups which include atoms of chlorine, sulphur, phosphorus, and nitrogen (for instance, trichloromethilphosphonates $CCl_3PO(OR)_2$ and others).

All changes of the surface behaviour due to adsorption and chemical modifications have a direct effect on EWF. It is just natural since any surface interactions are of electrical nature.

To meet numerous requirements to oils, additives representing a large group of organic compounds with different functions, are introduced. The action of lubricants and additives and their effectiveness cannot be predicted in each particular case, therefore, they are chosen experimentally. As a series of studies have revealed, investigation of CPD kinetics of metals and alloys in the case of adsorption of lubricants and their components (surfactants and other substances) is also promising for the selection of lubricants.

2.7. Electron Work Function Variations of Solids in Sliding and the Method of Selecting Materials

Many studies were carried out to investigate the properties of contacting solid before and after sliding. The parameters under study are characteristics of the metal surface state, e.g., roughness, microstructure, hardness, dislocation density, EWF, etc. In these studies it takes a long time to remove the specimen from the sliding assembly and to fix it on a measuring device, a substantial part of information involved in sliding and characterizing the dynamics of this process, is lost.

In sliding, the surface layers of coupled pairs are formed in dynamics and change depending on operation mode, nature of contact materials, and lubricant properties. Elastic and plastic deformation and dispersion accompanied by physicochemical phenomena and continuous absorption and energy release take

place during the friction. Changes in the surface layer are almost uncontrollable, thus, monitoring of surface layer behaviour is also of special interest for predicting the wear resistance. The method of continuous registration of CPD averaged over the sliding track surface area [98] has been successfully used to solve the problem. We will consider the results of the first experiments carried out with this method (obtained by the author in cooperation with A.L. Zharin).

The difference in contact potential drop with friction and without friction is illustrated with the help of a 3/VII steel (disk)–CuSn6 (pins) pair at sliding speed of 2.2 m/sec and load of 0.25 MPa (TsIATIM-201 lubricant, see Fig. 2.23). At the moment the friction machine (AE-5) is switched on (1), the CPD magnitude drops abruptly (by approx. 50–100 mV); during sliding it acquires a steady value, and when switched off (2), CPD rises again. As long as the sliding pair continues to operate, the CPD discontinuity slightly diminishes.

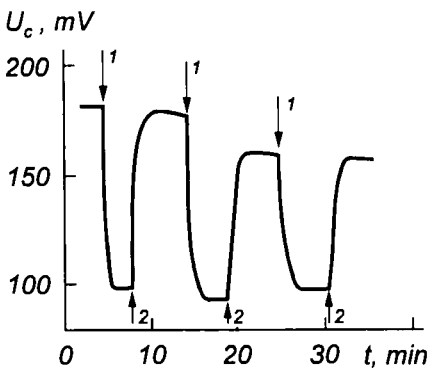

Fig. 2.23. CPD of disk made of 3/VII steel in sliding with CuSn6 bronze pins and without sliding.

Operation with a continuously replenished lubricant (Fig. 2.24) prevents the effect of lubricant contamination with debris on CPD. However, in sliding of both a steel–bronze pair (Fig. 2.23) and a bronze–bronze pair (Fig. 2.24) immediately after switching on (3), the CPD drops abruptly, then starts to increase gradually. The CPD of a clean disk is marked 1 in Fig. 2.24; a steady-state CPD following oil application to the disk before sliding starts is marked 2. The behaviour of the CPD–time curve after switching on the sliding assembly is associated with the running-in accompanied by the formation of boundary layers. After 4.5 or 5 hours of operation, the CPD of the sliding track reaches its maximum and remains at this level for about 1.5 h. It corresponds to the steady-state friction confirmed by the measurements of the friction torque (it is accompanied by insignificant selective copper transfer), then the CPD starts to decrease.

The running-in process of the assembly from copper alloys CuAl8Fe3–CuSn6, with glycerine as a lubricant, is accompanied by a slow increase of the sliding track CPD and lasts for a relatively long time (about 5 h); under steady-state operation conditions (for 1.5 h) CPD reaches its maximum; this operation is characterized by the minimum friction coefficient and, probably, by the minimum wear. The process of deformation of the boundary layer is characterized by a slow decrease of CPD. This fact was thoroughly investigated and the studies revealed periodicity in CPD variations, especially clearly manifested in dry sliding (see 4.5).

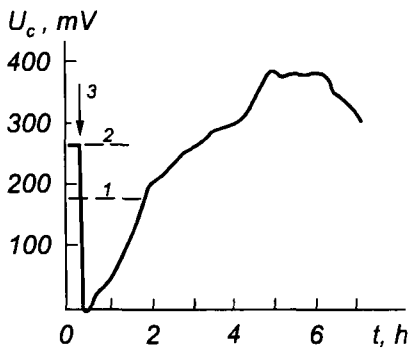

Fig. 2.24. Kinetics of sliding track CPD of a bronze disk made of CuAl8Fe3 in sliding with CuSn6 bronze pins: P=1 MPa; v = 2.2 m/sec; lubricant is glycerine (one drop per 6 sec).

Changes of the materials and lubrication modes affect the CPD kinetics (Fig. 2.25). Lubrication with a an interval one drop per 12 sec. (the experiments were carried out on an updated AE-5 type friction machine having a drop oilier (curve a), shows many discontinuities of CPD towards the positive region; sometimes the device went off scale because of galling and ionization (the latter will be discussed in Chapter 4) caused by permanent random ruptures of the boundary layer which resulted in direct contact at particular points. When the frequency of fresh supplies of oil increased (one drop per 6 sec), the situation changed drastically (curve b).

As the running-in period and the load increased, CPD gradually diminished and stabilized. In steady-state sliding CPD was independent of the load. Under these conditions a thin layer of copper transfer was observed on the surface clearly at the acute angle. The CPD value of 3/VII steel was less than that when lubrication was applied before sliding.

A continuous record of the sliding track CPD can be used to select tribological materials. The conventional methods cannot fully characterize the operation of a

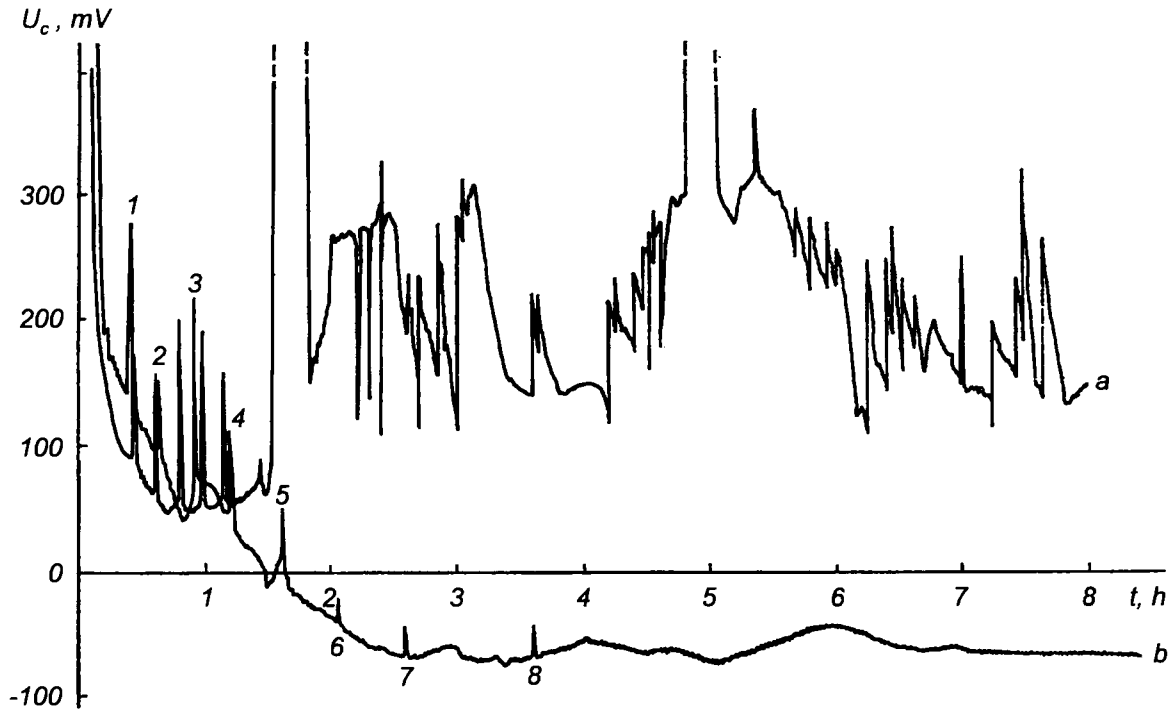

Fig. 2.25. The CPD kinetics of 3/VII steel surface in slidinig with Cu-ETP copper, in two glycerine lubrication modes and under periodic loading:
1) P=3; 2) 5; 3) 7; 4) 9; 5) 11; 6) 13; 7) 15; 8) 17 MPa.

pair and, therefore, cannot guarantee the correct choice of materials and lubricants. For instance, the method of selection which consists in measuring CPD of specimens and comparing it with the reference standard, using different lubricants under static conditions, and then selecting materials with higher CPD [35], provides only indirect and insufficient information.

Our results provide better selection of materials and lubricants. The method consists in measuring the area-averaged CPD of the track in sliding and coupling materials with stable CPD.

Continuous control of CPD on the sliding surface gives the most adequate information on the physicochemical character of performance of sliding pair, apart from measurements of friction and wear. Also, a stable steady-state sliding track CPD obtained during the test, characterizes the optimum operation and favourable combinations of pairs.

Chapter 3

PHYSICAL CHEMISTRY OF CONTACT INTERACTION AT SELECTIVE TRANSFER

3.1. Selective Transfer

The selective transfer was first discovered in bronze–steel sliding pairs with an alcohol-glycerine mixtures as a lubricant [99]. It includes evolution of copper from bronze, its accumulation on the surface, and partial transfer of copper to steel forming a thin soft layer of copper on both bronze and steel. The layer almost fully localized deformation and ensures minimum friction, high wear resistance and long service life of friction assemblies [25].

Practical use of selective transfer (ST) in wear prevention encountered great difficulties because of inadequate investigation of diverse and complicated processes.

The selective transfer is a unique phenomenon of active self-adaptation which is exhibited in friction of solids and minimizes losses in this interaction. ST has much in common with friction of animal and human joints [100].

Selective transfer manifests itself in the boundary conditions. The concept of boundary layer was first introduced by Hardy [16]. The influence of the field of a substrate coated with a thin layer of adsorbed material results in replication of the crystalline structure of the substrate in several monomolecular layers (about 1 μm thick). It is this very thin layer affected by the solid surface that is usually called the boundary layer. Interaction of the primary monolayer with the solid surface depends on the adsorption character and is either physical or chemical. The interaction inside multimolecular layers is physical in most cases.

Boundary lubrication exists when a very thin layer of the third phase (a "lubricant" of any nature and origin) separating the solid surfaces is within the boundaries of their influence [16]. In this connection ST can, on the one hand, be naturally identified as boundary lubrication on the other hand, ST may be considered a special friction mode because it is based on spontaneous formation of "*servovite*" layers* (which does not follow from the above definition of boundary lubrication).

---

* A "*servovite*" layer is a protective metal layer where a vacancy-dislocation deformation mechanism is realized in friction. The layer is affected by surfactants. "Servovite" is derived from the Latin words "*servo vitae*" which mean "to save life".

The "servovite" layer is formed on contacting solid surfaces from certain component of the friction pair (particularly copper) or component of the lubricant. With this in view ST can be defined as follows: it is a form of contact interaction which produces a very plastic oxide-free layer of metal (copper, gold, nickel, etc.) spontaneously in the gap on surfaces of friction bodies.

ST localizes deformation in the thin surface layer of copper transferred to steel or formed on copper alloy to the maximum extent.

It is very difficult to assess the capability of a friction pair to operate under ST condition. In order to select an optimum pair for this operation it is necessary to try combinations of alloys and to carry out wear tests in various lubricants which is extremely time consuming. Therefore, development of methods to predict properties of friction pairs from various alloys under ST conditions is an urgent problem, the key to which, in our opinion, is to establish relations between wear resistance and the crucial processes in the friction zone.

3.2. Physical Nature of Metal Seizure

Material can be transferred due to abnormal friction accompanied by seizure. Let us find similarities and differences between the seizure and ST.

Seizure (cold welding) of metal surfaces is a most dangerous type of damage which causes failure of friction unit as a whole. The majority of studies of the seizure dealt with the processes occurring on the contact surfaces of metals under their plastic deformation [101, 102]. Attempts have also been made to study the seizure mechanism in friction thoroughly [103]. However, theoretical studies in this field are few and the problem cannot be considered solved.

Seizure of any solid (metals, glass, polymers, etc.) is determined by direct contact between substantial sites of surfaces free from oxide and other films because of plastic or viscous deformation of the layers underlying the surface [104]. Seizure is a result of molecular (atomic) interactions. The rearrangement of the surface layers of solid in contact, as well as slower secondary processes of diffusion and recrystallization, proceed spontaneously and require much less energy than strain resulting in contact spot formation . If two approaching metal plates (e.g. copper) were free from oxide and other films, seizure would immediately occur in the places of their contact, i.e. a strong metal bond would form. The energy necessary for forming a transition layer from one lattice orientation (in grains of the 1-st plate) to the other one (in grains of the 2-nd plate) is compensated with excess by changes in the free surface energy of the metal in contact sites [104].

The free surface energy F of the metal in the air is 10^{-4} J/cm^2. When contact appears surface energy in the new interface falls abruptly approximately down to (2 to 3)$\times 10^{-6}$ J/cm^2 in the sites of slight disorientation of contacting grains, and

to (1 to 2)$\times 10^{-5}$ J/cm^2 in the sites of greater disorientation. Consequently, the reduction of free surface energy ($-\Delta F$) as a result of contact is of the order of magnitude of 10^{-4} J/cm^2 [104]. The total energy loss q_1, i.e. heat release in contact surface formation, will be of the order of magnitude of $\Delta F/n_1$ per atom of metal, where n_1 is the number of atoms on 1 cm^2 of the surface. Assuming $n_1 \approx 10^{15}$, $q_1 \approx 10^{-19}$ J/atom is obtained. Hence, the heat effect of metal contact formation is appreciable and exceeds the metal melting point of approximately 10^{-20} J/atom by an order of magnitude. It is difficult to assess the energy necessary for formation of a transition layer between differently orientated grains in contact by direct calculations. In Likhtman's opinion [104], this energy corresponds to the heat effect of polymorphic transformation and never exceeds it. Heat of polymorphic transformation is normally an order of magnitude less than the melting, consequently, the loss of surface energy accompanying the metal contact formation is quite enough to maintain it.

The analysis of seizure process of heterogeneous metals is burdened with differences in structures and parameters of crystal lattices, different solid state solubilities and atomic sizes. Some researchers have investigated the influence of mutual solubility of metals on their tribological properties, however actually no general relation between friction, adhesion, transfer, welding and mutual solubility of metals was found.

An excessive plastic deformation which expands the real contact area, is necessary to induce seizure of pure metals. Also, the decisive role in forming a strong bond is played by quantum processes of electron interactions [105]. In this case, the adhesion energy is a function of free surface energy which, in turn, depends on the origin of crystallographic lattice disorientation and the energy of atomic bonds [106]. The larger the negative free energy of forming bonding between two substances, the larger is (all other factors being equal) the permissible disorientation angle of crystal lattices of these substances relative to the interface and the quicker they seize, the more rapidly the free interphase energy is relaxed.

When two different metals form a contact surface and adhesion arises between them, the interphase surface system should be considered rough. In this case the atomic interface of the two metals constitutes a quasisurface. When metal lattice types and parameters are not identical, the bonding force of the inner interface will depend not only on the bond energy between metal atoms, but also on the bond direction relative to the main lattice and number of neighbors. In this connection, materials with strong covalent bonds which require mainly bonds of definite length and angles with six neighbors will not produce adhesion, since it is almost impossible to achieve a precise crystallographic coincidence of the lattices relative to the inner interface. Not much adhesion is observed also in the case when two monocrystals of germanium come into contact when they are oriented in the direction approximately parallel to plane (110).

This agrees with the known facts that it is impossible to press powders of most of materials with covalent bonds at temperatures corresponding to insignificant diffusion of atoms. However, metal bonds with eight or more neighbors are most likely to withstand considerable departures from the equilibrium, i.e. larger disorientation angles of lattices of materials in contact [106].

3.3. Seizure Mechanism in Selective Transfer; Electrochemical Mechanism of Transfer

While common seizure causes metal failure at a certain depth from the friction surface and eventual failure of parts, seizure in ST is a useful process.

Let us briefly consider the basic features of seizure in ST for a bronze–steel friction pair lubricated by glycerine.

1. In friction glycerine reduces copper oxide to copper, i.e. it conditions oxidation-free friction between bronze and steel.

2. Owing to the electrochemical effect of glycerine [107], the copper alloy surface is exposed to selective dissolution. It should be noted that, compared with doping components of copper alloys (zinc, tin, iron, aluminium, etc.), copper has the lowest solubility, and fine spotted porous copper layer is formed on bronze.

3. Some hardened and strained sites of the copper film on bronze disperse under load and glycerine effect, since they possess a relatively high elastic energy density and, consequently, a higher solubility. So, in the gap between the friction pair a fine dispersed copper appears which produces a colloid solution with glycerine, and the surfaces become aligned.

Forces causing further transfer of copper from the colloidal solution to steel will be considered below. The main processes which determine transfer of copper to steel are triboelectrical in addition to being electrochemical. The reduction reactions are accelerated by tribochemical processes, which, at the same time, favor polymerization of decaying glycerine molecules.

In steady-state friction a copper film is formed on contacting surfaces, which, as was shown by L.M. Rybakova and L.I. Kuksenova, have a low dislocation density (of an order of 10^9 cm^{-2}), a high density of vacancy-type defects (of an order of 10^{21} cm^{-3}) and an oxide interface with the base material. A low shear strength of the film is presumably a result of the vacancy-dislocation mechanism responsible for origination of surface layers in ST.

In prolonged tests a boundary layer of complex structure is formed in the contact (see Fig. 3.1). Adsorbed molecules 4 bonded by polymerized molecules 3 are sandwiched between plastic copper film 5, formed on bronze 6, and copper film formed on steel 1, it is apparently one of the causes of low friction coefficients.

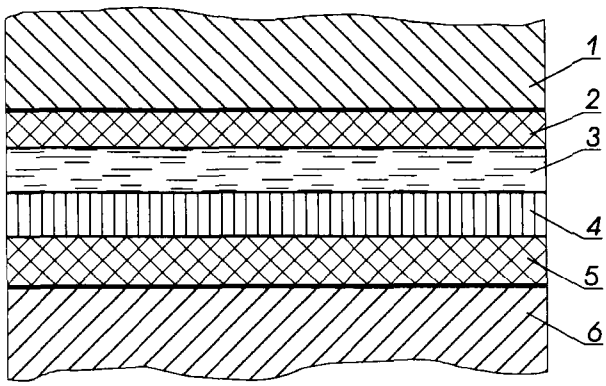

Fig. 3.1. Boundary layer structure in ST.

Let us consider an elementary section of the copper alloy–steel sliding pair. In the places of actual contact between the surfaces a potential jump occurs equal to the difference in Fermi levels of the two metals before the contact a CPD is formed between their free surfaces. If the specific load and velocity of relative displacement between the steel and copper alloy juvenile surfaces are small, thermoelectromotive force (thermo-EMF) in the contact can be neglected.

In Volta series metals (alloys) are arranged according to CPD so that every preceding metal (alloy) of the series, when in contact with the subsequent one, acquires a positive potential: (+) Al, Zn, Sn, Cd, Pb, Bi, brass, Hg, Fe, steel, Cu, Ag, Au, Te, Pt, Pd (-).

One can see from the series that brass has a lower EWF than iron or steel. They, in turn, have a lower EWF than copper, it is confirmed by the results of Chapter 2. If some alloys are arranged in the order in which EWF decreases, the following series results: copper Cu-ETP; bronzes CuSn6, CuBe2, CuSi3Mn1, CuAl9Mn2, CuAl10Fe3; steel 3/VII; steel C45e; CuSn4Pb4Zn3; brasses CuZn37, CuZn39Pb2. Hence, bronze CuSn4Pb4Zn3 has a lower EWF than steel 3/VII (roughly by 200 meV). That means that in contact spots steel has negative potential, whereas brass and bronze CuSn4Pb4Zn3 have positive. But in places, where there are no contact bridges redox reactions occur owing to the electrochemical action of lubricant. Since a copper alloy consists of elements more active chemically than copper itself, the elements will be selectively dissolved and removed by the lubricant from the friction zone.

The copper alloy surface can be presented as a set of galvanic microcells, each having copper as the positive pole, the anode are dissolving alloying components or the negative pole. For example, bronze CuSn4Pb4Zn3 is composed of tin, zinc, lead, and about 90% of copper. Their standard electrolytic potentials are -0.136; -0.7628 ; -0.126; 0.337 V, respectively [14]. As a result, copper is released on the

copper alloy. This, in turn, changes CPD. Steel has a more positive potential than copper.

Potential jumps at the bronze–electrolyte (φ_{be}) and steel–electrolyte (φ_{se}) interface in the aggregate do not equal the absolute value of CPD U_{bs}. The actual contact area does not exceed, at best, 0.01 of the visible friction area, therefore the contact pair is a system of short-circuited galvanic microcells (Fig. 3.2), with the EMF $E=\varphi_{be}-\varphi_{se}-U_{bs}$.

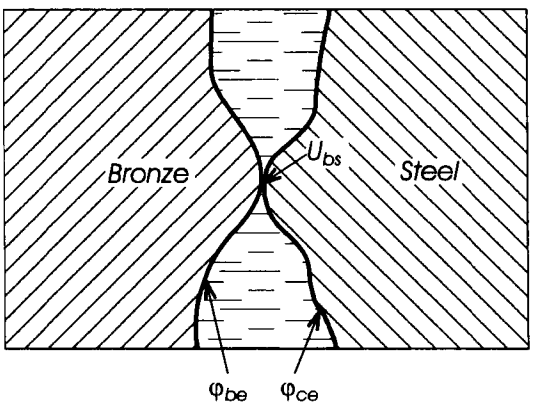

Fig. 3.2. Diagram of potentials originating in the liquid–dielectric system pair.

Electric current flows in the short-circuited galvanic cell. Electrons move from the negative electrode to the positive and ions start flowing in the liquid. Copper ions begin to deposit on cathode sites of the contacting steel surface bonding with it due to Coulomb and adhesive interaction, favouring reduction of the potential difference across the electrodes. Chemical oxidation and reduction on the electrodes results eventually in decreasing electromotive force (EMF) of short-circuited galvanic cells as the solution concentration near the electrode surfaces changes.

Such self-controlled process continues until a copper film forms on the electrodes. As a result, the EMF of the galvanic microcells become zero because $\varphi_{be}=\varphi_{se}=\varphi_{ce}$, U_{cc}, where φ_{ce} is the potential jump in the copper–electrolyte interface. The anodic dissolution decelerates and ceases.

So, seizure in ST differs from common seizure, which causes intensive damage of the surface, assuring in a very fine deformed (consequently, softer than the base material) underlying copper layer. Seizure is largely determined by electrochemical processes occurring in the interface [108].

The ST can be observed under certain conditions. When glycerine is used as lubricant it is restricted by a sliding speed of up to 6 m/sec and a temperature of 313 to 333 K at a load of 40 MPa [25]. This is quite clear, because the ST, like any other effect, can appear only within a certain range of boundary conditions.

In the case of high sliding speed, temperature and pressure, different phenomena will dominate.

The ST (atomic seizure) is most pronounced in copper and copper alloys with a high content of copper (90% and more). Why? It is common knowledge that all metals occupy a certain place in the series of activity (or voltage):

(-) Li, K, Ba, Ca, Na, Mg, Al, Mn, Zn, Cr, Fe, Co, Ni, Sn, Pb, **H**, Cu, Sb, Bi, Ag, Pt, Au (+).

The position of metals is determined sequentially by the loss of their valent electrons with transition into the ionic state [14]. Every preceding metal in this series is more active than the following and forces the latter from its salt solution.

The copper alloys studied in ST are arranged in the order of decreasing wear resistance's:

Cu-ETP, CuSn6, CuSn4Pb4Zn3, CuAl10Fe3, brasses (CuZn).

The standard electrode potentials of alloying elements (Sn, Zn, Pb, Al, Fe, Mn, etc.) of the copper alloys listed above appear negative since they are positioned to the left of hydrogen in the activity series, i.e. these metals tend to oxidize. Copper is positioned to the right of hydrogen in the activity series, i.e. it has a more positive potential and, consequently, reduction takes place on it. It is clear that brass possesses the minimum wear resistance and copper the maximum. Due to a higher chemical activity of zinc (ε^0_{Zn}= -0.7628 V, ε^0_{Cu} =+0.3370 V), making up at least 30% of the alloy the brass surface in ST dissolves and a rather thick porous, rapidly worn copper layer is formed on the brass surface.

CuSn6 and other tin bronzes have a higher wear resistance in ST as compared with CuAl10Fe3, since aluminium, iron, and manganese are chemically more active than tin and lead.

In the initial stage, when no copper film has yet appear on steel as a result of ST, thermoelectric currents, play an important role especially at high sliding speed. The currents intensify oxidation of friction surfaces and can reduce or increase their wear resistance.

The ST electrochemical mechanism is fully manifested in the properties of friction couples containing copper in corrosive media. Tests of thrust sealing rings [109] from cemented carbide VK6 (GOST) alloy installed in yokes from 15/13 stainless steel with copper inclusions and immersed in 5% sulfuric acid solution did not reveal any wear because copper film appears on the friction surfaces. When 15/13 steel containing copper (0.24%) is exposed to sulfuric acid, copper atoms lose electrons and dissolve ($Cu \rightarrow Cu^{++} + 2e$). If Cu^{++} ions are discharged in cathode sites and get reduced by the EMF of microgalvanic pairs and thermo-EMF (especially strong at real contact where flash temperature is high).

Hence, ST is determined by electrochemical processes taking place in the contact zone. Selective dissolution stimulates formation of a "servovite" layer on the surface reducing the friction coefficient to that of a liquid, substantially increasing the wear resistance of the pair.

For a more detailed study of the ST mechanism non-metal monocrystals can be used, semiconductors in particular. Properties of semiconductor crystals vary within a wide range depending on the types and content of impurities. This feature of semiconductors has been used for studying ST. To investigate microtransfer we can use sufficiently perfect monocrystals oriented in various crystallographic directions, with different types of conductivity (n- or p-type), and various concentrations of carriers can be used. This allows to determine the most general trends in the processes, excepting the grain boundary effect, etc.

In the case of ST between metal–semiconductor monocrystal, metal particles must appear on the monocrystal surface in friction. Diffusion of the metal would substantially alter the semiconductor properties. Depending on changes in the properties (for example, conduction type and value, concentration of carriers) or the optical absorption spectrum one can speak about particular elements presence, their concentration, etc. To implement the technique it is important to select materials according to their mechanical and physical properties to achieve ST in particular media.

Experimental procedure. Cu-ETP copper, CuZn32 brass, *p*- and *n*-type GDG 5.0/1.0 and GES 27/1.5 germanium (GOST) were used in a sliding pair. Mooth's microhardness of germanium is 6.25 which is very close to that of low-carbon steel Fe360A, the *HB* is 540 N/mm^2. Germanium specimens were oriented in plane (111), then ground, polished and etched. Brass was polished. Metallographic studies clearly show the pattern of etching (triangles) corresponding to orientation crystals in plane (111) on the germanium surface. The tests were carried out on a reciprocating friction machine. The machine made 32 double strokes (cycles) per minute. Pure glycerine served as a lubricant. After testing on the friction machine, the surfaces were washed in carbon tetrachloride, and photographed. The specimens were subjected to homogenizing annealing in vacuum at a temperature of 1083 K for 15 to 20 min. Then, electrical conductance was measured, conductivity type was determined and concentration of charge carriers in the specimens was calculated.

The initial stage of the copper transfer was studied. Therefore, the tests were carried out at minimum load (P=4 kPa), low sliding speed (V=12.3 cm/sec) and small number of working cycles (n=14,000).

The actual contact area in this case was minimal because after etching the whole crystal surface is pitted. Therefore, the specific pressure at the actual contact points of specimens was far in excess of the rated.

The experiments have revealed that selective transfer occurs in germanium–

copper, germanium–brass pairs in glycerine. When studying the germanium surface after sliding with brass in glycerine fine copper grains of a typical reddish color can be seen on etched surfaces. Copper transfer occurred only at the actual contact spots, no transfer could be observed elsewhere on the surface. Nor was copper transferred to the surface of the specimen which was in glycerine but had no contact with the copper alloy.

Copper particles localize (when examined directly after sliding) along the edges of etched pits, at various deformations of germanium crystal lattices, irregularly over the contact surface and without continuous films. When sliding with brass is prolonged, copper particles spread along the entire friction track filling the etched pits.

Surfaces of the same specimens, aged for a month in a sealed box, were photographed. It was noticed that the minute particles of copper previously scattered over the whole surface clustered in huge aggregations, i.e. copper particles coalesced (merged) by diffusion on surface defects, mainly along the boundaries of etched pits. A similar phenomenon of diffusion coalescence of metal grains on a non-metal substrate (on NaCl crystals) was observed in [110] and studied with electronic microscopy.

Coalescence of particles on surface defects is resulted from diffusion and conditioned by the fact that many defects of various nature on the surface of a germanium specimen are electrically charged centres. As a consequence, copper particles transferred by friction to the germanium surface also become electrically charged.

Analysis of surface sites where germanium actually contacts with the copper alloy shows that copper transfer does occur. The size of separate transferred particles is 0.5–1.5 μm, i.e. it is of the order of magnitude of colloidal particles after selective dissolution of the copper alloy. It is one of the essential differences between ST and dry friction when large blocks seize.

In order to determine the types and quantity of atoms transferred to germanium, specific resistance was measured and the conductivity type of specimens was established. Therefore, germanium specimens were washed in alcohol, carbon tetrachloride, and distilled water immediately after sliding and dried. Then they were exposed to the homogenizing annealing in vacuum at 810 °C for 15 to 20 min [111]. Such annealing made copper extremely soluble in germanium and uniformly distributed throughout the specimen. After the homogenizing annealing and rapid hardening, specific resistance of the germanium specimen was measured and changes of the conductivity type were determined from the thermo-EMF sign. Changes in the concentration of charge carriers were calculated using the known mobility of acceptors in germanium.

Germanium specimens of n-type ($N_n \cong 1.7 \times 10^{14}$ cm^{-3}) and p-type ($N_p \cong 6.2 \times 10^{14}$ cm^{-3}) were tested. After homogenizing annealing of all the specimens p-type conduction was changed to n-type conduction (thermal conversion)

(see Table 3.1.). This suggests that copper atoms are most likely to diffuse [111]. Conductivity of the specimens increased substantially and was within 0.7 to 0.9 $Ohm^{-1}\times cm^{-1}$.

TABLE 3.1

Variations of germanium properties

Specimen No	Conductivity type		Specific resistance, Ohmxcm		$\Delta p=N_a-N_d$, cm^{-3}
	Before annealing	After annealing	Before annealing	After annealing	
1	n	p	19.4	1.22	2.56×10^{15}
2	n	p	20.5	1.40	2.23×10^{15}
3	n	p	21.3	1.13	2.76×10^{15}
4	p	p	5.0	0.20	1.56×10^{16}

Changes in the electrically active (acceptor) copper concentration differs not more than two times from the total amount of diffusing copper atoms located in interstitial sites of germanium crystals behaving as donors. It is impossible to study these atoms by direct methods. The tests described above can measure the amount of copper transferred under minimum friction and to determine if selectively dissolved components of the copper alloy (aluminium, iron, manganese, etc.) are transferred to the crystal surface, for this it is necessary to study the temperature dependence of conduction or concentration of charge carriers.

The results suggest that in ST of copper alloy germanium and steel seizure does occur. Further parallel study and comparative investigation of the mechanism of this phenomenon will reveal its most general relations.

3.4. Boundary Layer Properties in Selective Transfer

The surface passivation in ST accompanied by formation of a plastic copper film on both copper alloy and steel is determined to a greater extent by electrochemical processes of selective dissolution of the copper alloy and transfer of dispersed copper particles to the steel surface. A favorable combination of materials of contact pairs (bronze–steel) and lubricant (glycerine, oils with surfactant additives) results in spontaneous origination of intermediate (boundary) layers on the contact surfaces which produce the minimum friction.

The processes occurring in water solutions are well described in electrochemistry. The processes in nonwater solutions (organic and nonorganic liquids and lubricants) have been studied poorly. In the case of selective etching of copper alloys in various lubricants it makes sense to speak about the activity of alloying

components only for a certain specific medium. However, a variety of research methods [112–114], allow to obtain sufficient information on the ST mechanism and properties of the boundary layers.

When a metal is immersed in a liquid with a sufficiently high dielectric constant with molecules having considerable dipole moments (for example, glycerine has ε=50 F/m), polar molecules orientated themselves near metal cations on the surface and favor their dissolution. Equilibrium expressed by the equality of chemical potentials of the substances in the two phases is achieved gradually. A similar process takes place when two dissimilar metals are immersed in a solution. In the latter case galvano-EMF appears. When friction assemblies operate in the ST mode polar surfactant or glycerine molecules are adsorbed on the surfaces by their active groups (hydroxyl (OH) or carboxyl (COOH), etc.) forming a double electric layer. As a result of chemical interaction of lubricant molecules with metals redox processes take place also causing the galvano EMF.

Measurements of the galvano EMF of certain metal electrodes from construction materials relative to the standard silver chloride electrode in glycerine show the values of the galvano EMF in statics up to 1,000 mV and more. In friction it is of great importance.

Sliding surfaces in a lubricant can be modelled as a system of two electrodes separated by a lubricant layer, abundant microelements acting on either electrode (Fig. 3.3), i.e. is a multielectrode system. This model is quite realistic since the sliding surfaces are actually polycrystalline with a definite roughness grains deformed in actual contact, various states and properties of boundary layers.

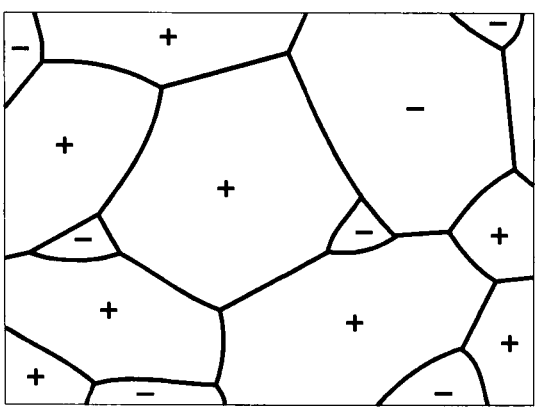

Fig. 3.3. Microelectrodes on metal surface.

An equivalent electric circuit of the boundary layer can be modelled as a pair of diodes connected in series or parallel. Electrochemical reactions are redox processes since they are accompanied by attachment and loss of electrons. If a

galvano-EMF arises between the electrodes, the equivalent circuit of the galvanic cell (the boundary layer) is a system of two capacitors connected in series, which is consistent with the suggested equivalent circuit (Fig. 3.4). The structure of the boundary layer determined by these capacitors is such that the influence of solid phases results in the formation of barrier layers.

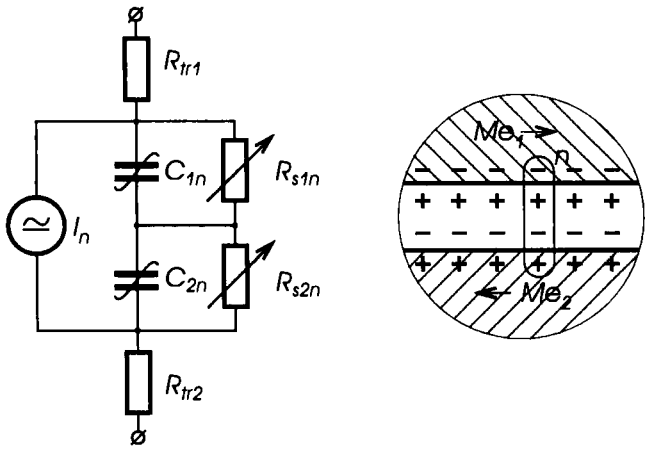

Fig. 3.4. Equivalent circuit diagram (a) of n-th "microcell" $metal_1$–lubricant–$metal_2$ (b) boundary layer.

In Fig. 3.4. C_{1n} and C_{2n} are DEL capacitors of two n-th microsites of sliding surfaces contacting via lubricant consisting of a barrier and diffusion capacitors; R_{s1n} and R_{s2n} are DEL resistors of these microsites with leaks shunting them, conduction anisotropy dependent on the polarity of applied voltage (variation of R_{sn} is connected, first, with anisotropy of electrical properties of molecules forming the DEL, second, with variation of the actual contact area in sliding); R_{tr1} and R_{tr2} - are series-connected electrical resistors from the materials of contacting pairs and leads; I_n is the current of the n-th galvanic cell.

The barrier component of the metal–semiconductor contact capacitance is determined by the formation of zones with n- and p-type conductivity on the metal surface which is due to the presence of oxide and other boundary films. Since many metals are coated with films having semiconductor properties, the chemical reactions take place on semiconductor surfaces.

In order to find the integral value of the galvano-EMF E it is necessary to sum up all E_n, where n is the number of "electrode" pairs of opposite microsites of metal polycrystalline surfaces.

Measurements of galvano-EMF E, the barrier effect (rectified voltage U), boundary layer resistance R and friction force F allow to study the main electrophysical properties of boundary layers in ST. The studies were conducted

on a friction machine AE-5, the sliding pairs were kept in the oil bath. The AE-5 machine is designed for testing materials in pure sliding three cylindrical specimens rubbing against a rotating disk. The design of the machine permits to vary the speed, load, temperature, lubricant for different sliding pairs within a wide range.

Specimens of 3/VII steel (a disk) and CuSn4Pb4Zn3 bronze (a pin) were tested. Glycerine, AMG-10 hydraulic fluid (GOST), and MS-20 oil (GOST) were used as lubricants. Immediately prior to the experiment the specimens were ground by fine-grain emery paper. Running water was used for cooling.

The steady-state ST between the contacting surfaces, with traces of copper and smooth surface forms the boundary layer durable even after substantial load increase (this is indicated by a nonzero resistance R (Fig. 3.5)). Rectification effect in the range of loads under study ($U \neq 0$) implies that the boundary layer formed by polar lubricant molecules (glycerine, in this case) adsorbed on the surfaces, are arranged in a properly oriented way. Compensation of solid-phase fields by adsorbed molecules reduces the interaction of sliding pairs to dispersion interaction of inactive groups of molecules (hydrocarbon tailings). In this case the friction coefficient f is minimum (about 0.01).

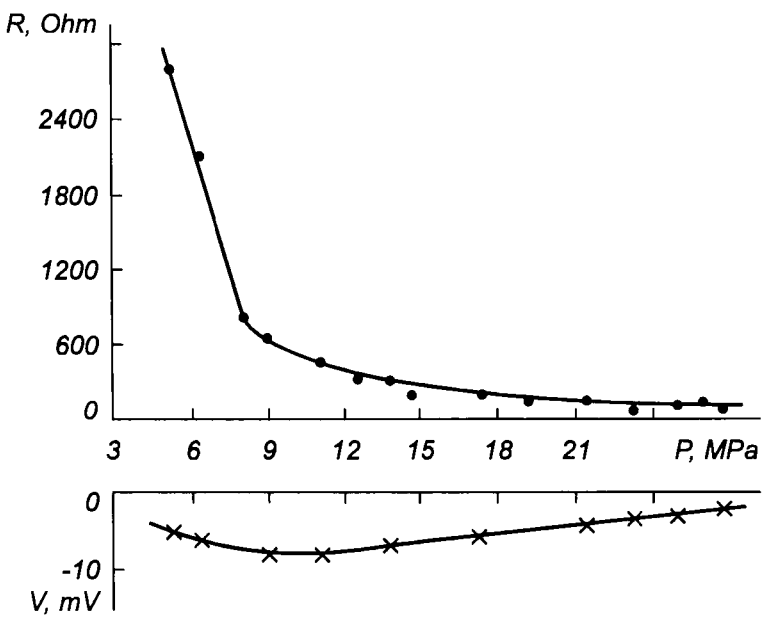

Fig. 3.5. Plot of R (a) and U (b) versus specific load P at sliding speed V=1.6 m/sec: steady-state ST; glycerine as lubricant.

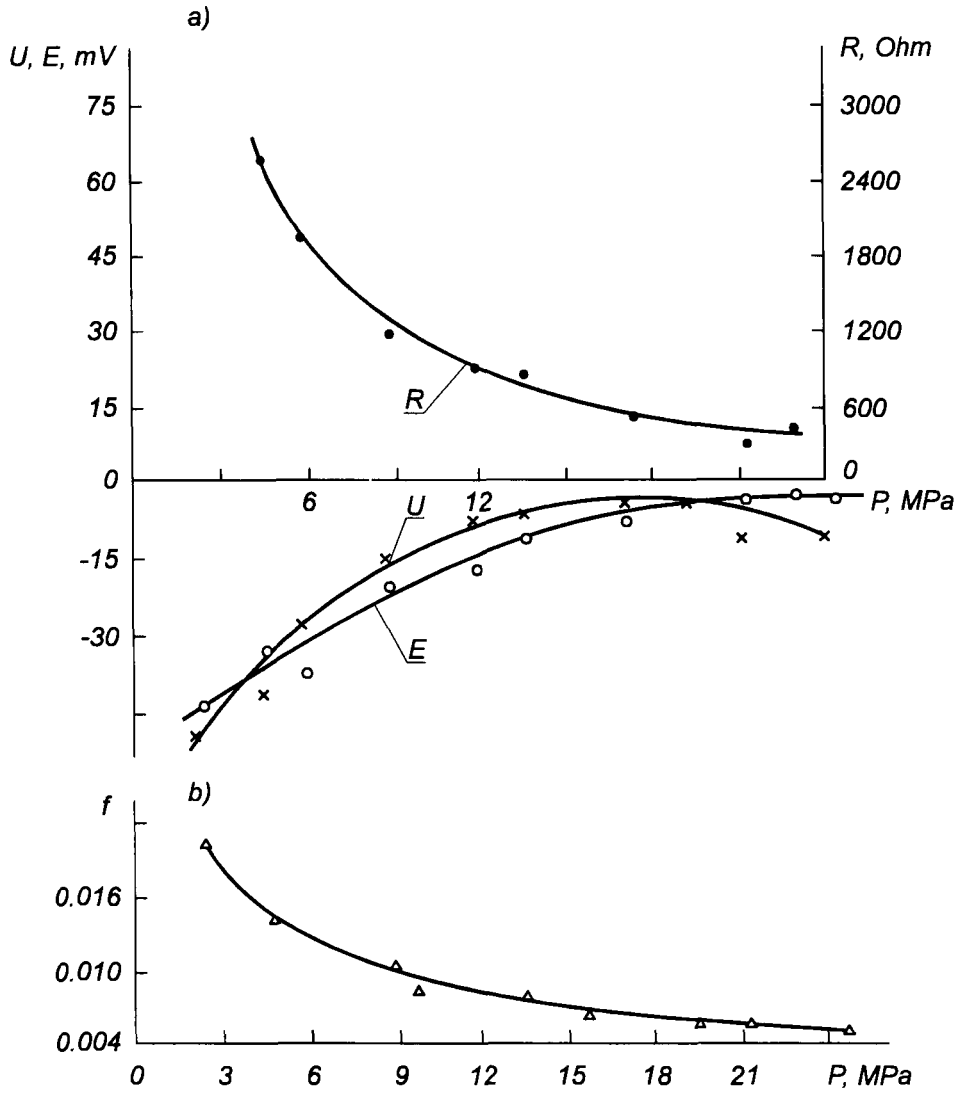

Fig. 3.6. Plot of R, E, U (a) and f (b) versus specific load P at sliding speed V=1.6 m/sec: running-in; glycerine as lubricant.

Analysis of the equivalent circuit (see Fig. 3.4) shows that, once an actual contact of juvenile surfaces is achieved in sliding, R_{s1n} and R_{s2n} tend to zero, galvano-EMF being zero too. Then the main contributor to the integral EMF is the thermo-EMF. A considerable resistance of the boundary layer, galvano-EMF and rectification effect within a wide load range (see Fig. 3.5) suggest that

deformation in the steady-state ST is effected through the lubricant boundary layer molecules chemically adsorbed on the surface.

As was shown by measurements of galvano-EMF in glycerine, the potential of 3/VII steel relative to CuSn4Pb4Zn3 bronze is positive (250 mV). The galvano EMF sign for the same pairs in glycerine is retained also in running-in (Fig. 3.6), i.e. intensive copper alloy oxidation occurs. Bronze Bp.SnZnPb and other leaded bronzes corrode with abnormal intensity in organic solvents, because lead forms highly soluble complexes with organic acids (this is the origin of the lead plate corrosion test). As a result of sliding the alloying components of CuSn4Pb4Zn3 (tin, zinc, lead), as chemically more active than copper, saponify the copper alloy surface during sliding. Copper also leaves the surface (disperses) from highly deformed sites (it has a higher elastic energy and is therefore chemically more active).

Just as in any galvanic cell in our *steel+|glycerine|-CuSn4Pb4Zn3* "cell", ion flow takes place. Ions leaving the copper alloy move towards the steel surface and discharge there (e.g. copper ions, according to equation $Cu^{++}+2e \rightarrow Cu$), arrested by Coulomb attraction forces and adhesion. Chemically more active alloying elements from the bronze surface also oxidize on the steel surface owing to the formation of microgalvanic pairs. A very fine copper layer (a "servovite" film) appears on the CuSn4Pb4Zn3 and 3/VII steel alloy surfaces, i.e. an equilibrium is attained gradually which can be only disturbed by changes of the mode and friction conditions.

If the static galvano-EMF of the CuSn4Pb4Zn3 sliding pair in glycerine 3/VII steel is about 200 mV, increasing load gradually decreases the EMF to several millivolts. The sign of the EMF depends on the activity of material in the organic lubricant, the structure and properties of sliding surfaces, engagement factor for the direct and inverse pairs (materials of the disk and pins are interchanged in the inverse pair).

Dissolution of CuSn4Pb4Zn3 alloy (acceleration of ST) is fostered by the loss of accumulated excess electrons through a chain of external devices. If the specimens are isolated, ST slows down.

It should be noted that initially, after the load is incremented, the friction force grows, U, E decrease, the resistance R even approaches zero (especially at high loads), i.e. sometimes a direct contact between juvenile surfaces takes place. All parameters stabilize to values typical of the given load gradually as the running-in proceeds.

Tests of the inverse pair are interesting (the lower specimen is a disk of CuSn4Pb4Zn3, the upper ones are from 3/VII steel (Fig. 3.7)). However, in this case too, the upper specimens have a negative EMF, consequently the EMF sign in friction is determined not only by the chemical activity of all the members of a given alloy in the lubricant, but also by the friction mode. The upper specimens (6 mm diameter), being permanently in contact with the lower specimen, are subjected to deformation to a greater extent and, in addition, are hotter. Oxidation

processes on the upper specimens diminish quite rapidly (the negative potential value decreases rapidly).

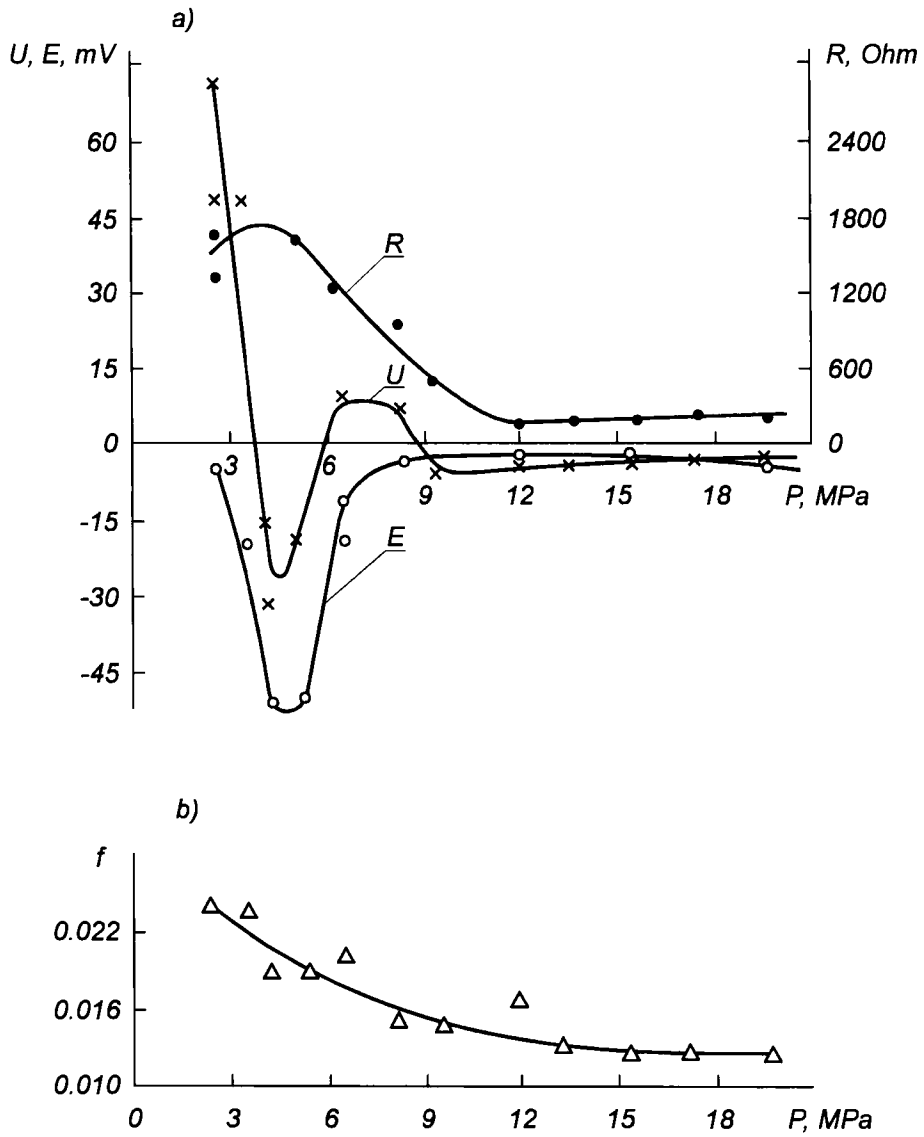

Fig. 3.7. Plot of R, E, U (a) and f (b) versus specific load for an inverse pair: sliding speed V=1.6 m/sec; glycerine as lubricant.

When the test was completed the surfaces of 3/VII steel specimens were covered with a very fine smooth copper film. In this case resistance of the boundary layer partly determined by its thickness, does not depend on the load. A considerable

increase of temperature (in the test the temperature of the specimens varied from 40 to 45 °C) reduces the load capacity and breaks the oil film.

The boundary layer parameters U, E and R were investigated as a function of the rotation speed at a constant relatively low load (P=0.3 MPa) upon ground specimens in the oil batch with the same lubricant (glycerine).

The EMF sign of copper alloy specimens (CuSn4Pb4Zn3) was negative for some time, while that of steel (3/VII) was positive. Later, however, the lubricant was "saturated" with corrosion products and the EMF sign changed to the opposite (Fig. 3.8). At the beginning concentrations of copper ions and ions of alloying elements in the lubricant were lower than necessary to achieve the equilibrium, the copper alloy would release ions and would be negatively charged. As concentration of copper alloy ions in glycerine increases the equilibrium state is lost. Ions of copper and other elements lose their hydrate shell and discharge onto the metal, the copper alloy becomes positively charged. After that no selective transfer is observed. A low friction coefficient in the test is determined by a strongly concentrated copper suspension in the lubricant which forms a quasiliquid layer near the contacting surfaces which is deformed without breaking.

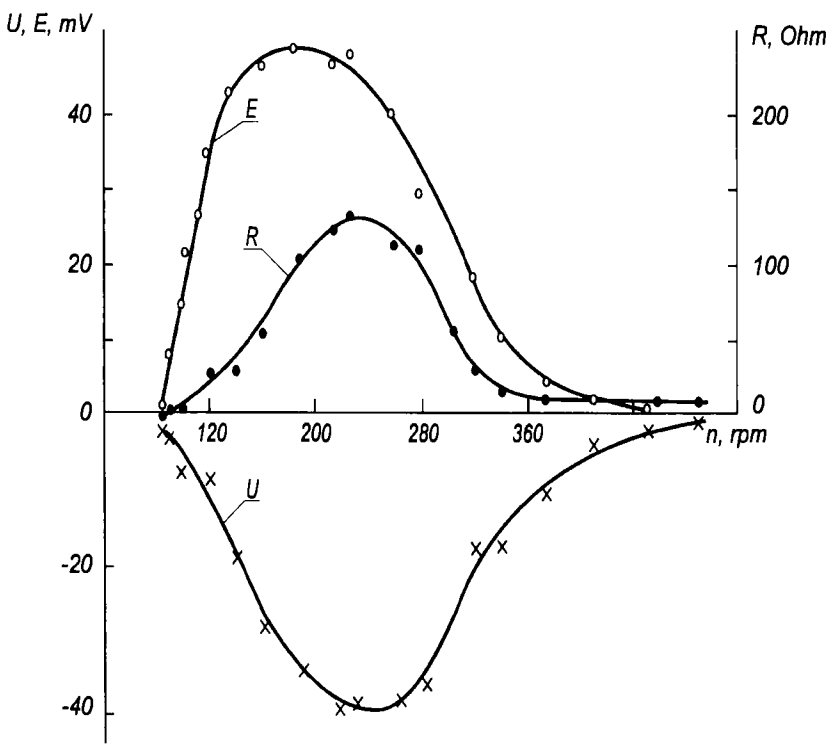

Fig. 3.8. Plot of U, E, and R of the boundary layer versus the speed of rotation, for a pair operating in the glycerine bath.

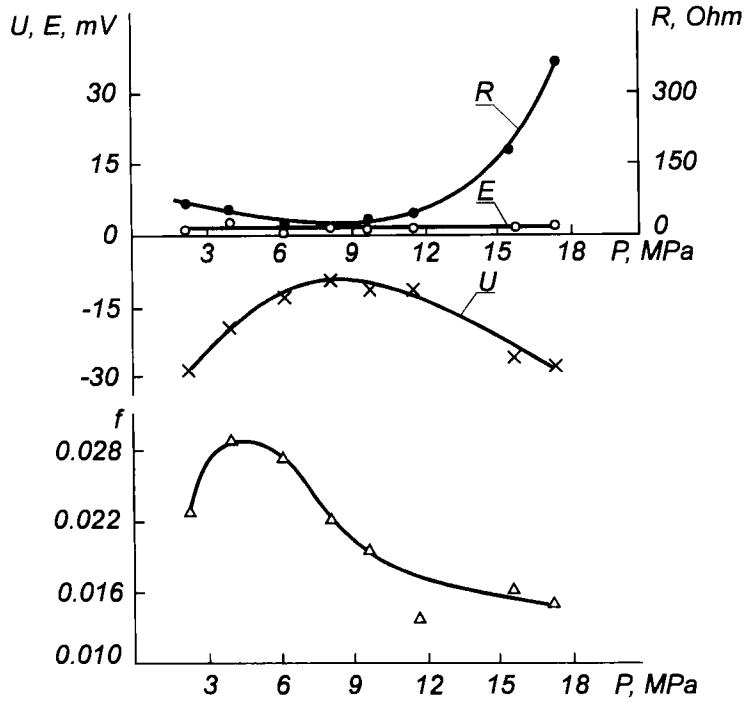

Fig. 3.9. Plot of R, E, U (a) and f (b) versus specific load; sliding speed V=1.6 m/sec; AMG-10 as lubricant, one drop per sec.

The rectification effect takes place both in the case of a considerable inherent EMF of the pair but also when it is absent or small (comparable with thermo-EMF). So, a direct pair of the same materials was tested in AMG-10 lubricant (Fig. 3.9). The inherent EMF appeared to be positive and to vary from 0.75 to 1.5 mV. Meanwhile, the rectified voltage is relatively high and ST is most pronounced and shorter than with glycerine as a lubricant.

The test of one pair of materials at certain sliding speeds supports the opinion that, in ST, electro- and tribochemical processes take place which characterize the phenomenon. The electric field induced by contacting solid phase surfaces and by lubricant molecules promotes transfer of dispersing copper ions from one surface to the other, i.e. it determines to some extent, the atomic seizure forming a "servovite" film on the steel surface. In steady-state sliding the value of rectified current (voltage) depends on many factors, on the composition and properties of the lubricant, in the first place, as well as on the nature of sliding surfaces.

Presence of DEL with electrical barrier action within a wide range of loads suggests that, in ST with glycerine or other oils with surfactant additives, orientation of lubricant molecules occurs.

Reduction of the friction coefficient with increase of load in ST can be attributed to both the thinning of the lubricant layer to a bimolecular value and formation of a passivating copper film fully receiving deformation in friction together with lubricant molecules.

The "orientation" effect disappears as the relative sliding speed of sliding pairs increases, resistance of the boundary layer falls down to zero, EMF (generally consisting of galvano- and thermo-EMF) also falls to the smallest possible values, which can probably be attributed to the absence of conductivity asymmetry caused by arrangement of lubricant molecules tangential to the direction of motion at high sliding velocity [16].

3.5. Relation Between Wear Resistance of Metals in Selective Transfer with Galvano-EMF in Statics

A necessary condition for initiation of ST is the occurrence of electrochemical process in the steel–lubricant–copper alloy system which can be simulated as a galvanic cell. As a result of selective dissolution of the copper alloy surface in a reducing medium the copper concentration on the surface increases, due to ST a "servovite" copper film is formed on the mated steel surface. Properties of the "servovite" film determines the wear resistance of the sliding pair. Dissolution of the copper alloy, for example in glycerine or alcohol-glycerine mixtures, is similar to the ST of metal alloys in water solutions of acids.

In order to ensure the optimum ST the "servovite" film must cover a certain part of the contacting surface, have a certain concentration of alloying components and their oxides, and be softened by the lubricant. All these parameters and properties depend on the conditions of dissolution of the copper alloy, its phase composition, and structure.

With the system steel–lubricant–copper alloy presented as a galvanic cell it is possible to reveal some trends in the formation of the "servovite" film in stationary conditions. The properties and the rate of alloy dissolution and properties of the resulting copper film can be inferred from the galvano-EMF and the potential-versus-time curves [115].

For this the potentials of copper alloys were measured relative to a thin layer platinum electrode (ETPL-01M) and galvano-EMF "cells" *steel-|glycerine|+ copper alloy*. Glycerine was chosen as the lubricant since it is best tested in ST conditions. Measurements were taken by the well-known technique [116] using a high input resistance voltmeter. Cylindrical electrodes with insulated waterline were used. The cell EMF variations in time were measured until the steady-state was achieved. Average EMF values of for a series of specimens of each alloy are given in Table 3.2. The alloys are arranged in the order of decreasing wear resistance when rubbing against C45e steel in glycerine (ST mode).

It is apparent from the table that the EMF of *steel C45e-|glycerine|+ copper alloy* "cells" are also arranged in accordance with the place the of copper alloy in the wear resistance series.

TABLE 3.2

Average EMF of copper alloys in glycerine relative to the various materials, mV

Sample	Platinum	Steel			
		C45e	3/VII	TC80	Fe360A
CuBe2	-185	+410	+360	+300	+325
CuSn6	-170	+400	+265	+200	+310
CuCr1	-160	+375	+230	+250	+320
CuSn10Ni1P1	-145	+350	+210	+225	+300
Cu-ETP	-125	+320	+260	+250	+250
CuSn4Pb4Zn3	-625	-225	-250	-200	-135
CuAl10Fe3	-225	+200	+125	+210	+235
CuZn39Pb2	-192	-50	-220	-210	-50

Such consistency of EMF and wear resistance suggests that the galvano-EMF occurring in the friction zone has a pronounced effect on ST which is especially large in the initial stage. For example, potentials of bronzes, except CuSn4Pb4Zn3, are shifted to the positive area, i.e. bronzes in glycerine are capable of passivation. The most wear-resistant bronzes have the highest potentials too. Brass acquires a negative potential relative to steels which corresponds to its intensive dezincification and formation of a thick layer of copper on steel which wears out rapidly enough in friction because of its porosity.

In order to ensure stability of ST, the resulting copper film must have passivating properties which are determined, in addition to the above mentioned factors, by the presence of oxides of alloying components. Thus, the high negative potential of bronze CuSn4Pb4Zn3 relative to steels and platinum can be attributed to a high chemical activity (EMF of the *lead-|glycerine|+steel C45e* "cell" is 125 mV). Alloys CuSn4Pb4Zn3 have better antifriction properties as compared to CuAl10Fe3 and brasses which is attributable to formation of complexes with lead (metal soaps in interaction of alloying components with glycerine and products of its oxidation) and, evidently, to a low surface dissolution rate.

The passivating action of the "servovite" film may be revealed when analyzing the potential versus time curves (see Fig. 3.10,a) which show that Cu-ETP, CuAl10Fe3, CuSn10Ni1P1, CuCr1 in glycerine are passivated, and CuZn39Pb2, CuBe2, CuSn4Pb4Zn3, CuSn6, are dissolved. Potentials of the former alloys shift gradually to the positive area, while the latter ones to the negative area. How should we then explain the low wear resistance of CuAl10Fe3 in ST?

Second electrodes (steel and platinum in our case) are known to effect significantly electrochemical processes. Relative to steel C45e, potentials of Cu-ETP, CuSn10Ni1P1, CuCr1, CuSn6, CuBe2 (see curves 1 through 5, Fig. 3.10,b) move towards the positive side with time (a passivation process goes on). The resulting copper film is thin and dense, while in the case of CuAl10Fe3 (curve 8) dissolution occurs and a thick, porous film is formed which is easily worn away. CuSn4Pb4Zn3 (curve 12) has negative potential relative to steel and also dissolves, therefore its wear resistance in glycerine is also low. In the case of brass CuZn39Pb2 (curve 6) zinc dissolves actively forming a thick and loose layer of copper which slows down the reaction as demonstrated by the potential shifting to the positive side. Brass has the lowest wear resistance of all the alloys. This can be explained both by the fact that the copper layer is loose and relatively reduces oxides of alloying components, thus substantially impairing mechanical properties of the "servovite" film.

The experiments show that: galvano-EMF in ST determines wear resistance, higher wear resistance corresponds to more positive potentials of copper alloys in lubricant; wear resistance depends on the passivating action of the copper film. Presence of beryllium, phosphorus, chromium, nickel in bronzes improves passivation of the copper alloy and increases wear resistance (CuBe2, CuSn6, CuCr1, CuSn10Ni1P1); doping of a copper alloy with light metals reduces wear resistance of the alloy due to their active selective dissolution. In ST when a thick porous copper film appears, and due to the consequent increase in concentration of light metal oxides, the copper film would hardly dissolve in glycerine (CuAl10Fe3, brasses).

3.6. Role of EMF in Selective Transfer at Low Sliding Speed

In unsteady sliding and under high loads a direct contact of mated sliding surfaces can frequently be observed. Investigation of ST in such sliding conditions is of considerable interest.

The ST behavior was investigated [117] in glycerine at low sliding speed (0.08 m/sec) within a wide range of load (4 to 90 MPa); EMF and conductance were measured. Knowledge of the conductance can provide information on the lubricant layer thickness and the direct metal contact existence. EMF was recorded by a galvanometric photoamplifier, the friction zone conductance was measured with an amperemeter-voltmeter. Steel TC80–copper alloy (CuSn4Pb4Zn3, CuAl10Fe3, CuSn10Ni1P1, CuSn6) sliding pairs were investigated. Specimens were aligned on a friction machine cleaned and degreased by conventional procedures. The sliding pair (shaft–brush) was continuously lubricated with glycerine, the shaft being partly immersed in the lubricant bath (see Fig. 3.11,a).

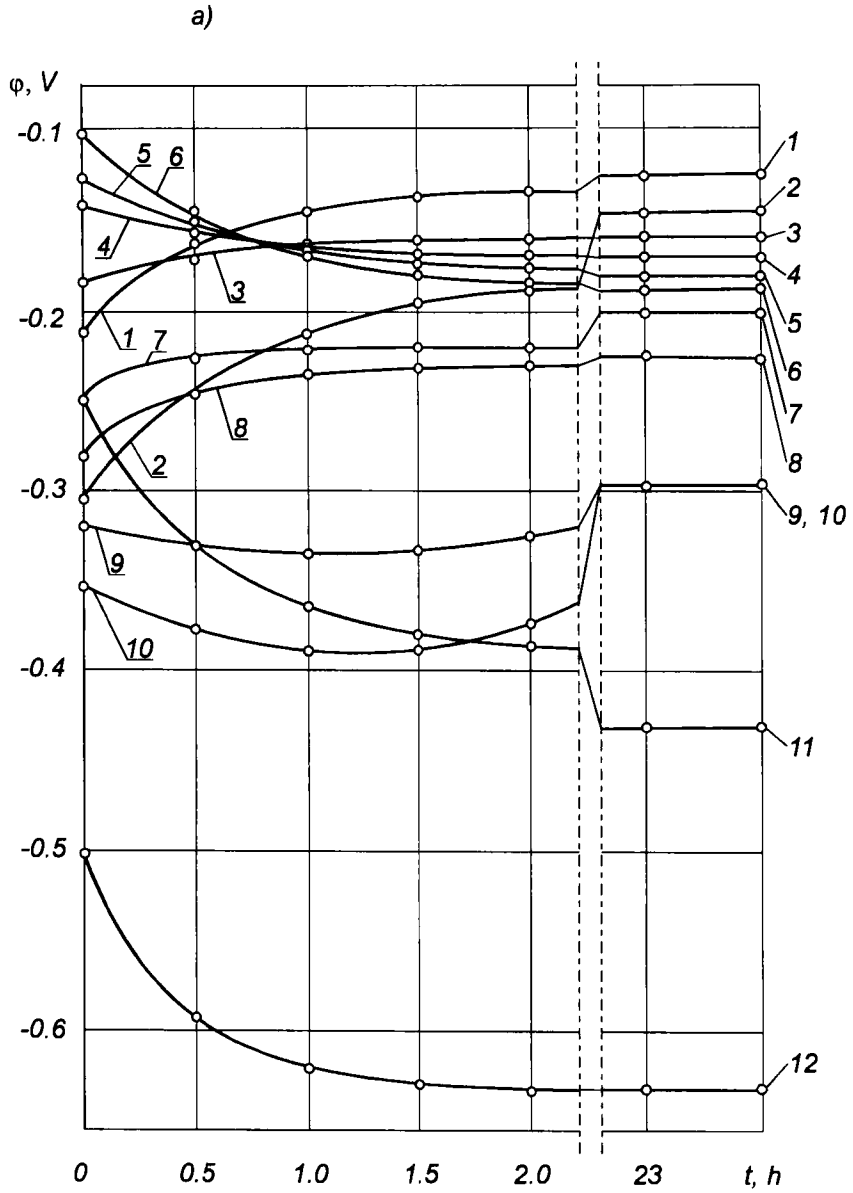

Fig. 3.10. Potential versus time for alloys in glycerine relative to platinum electrode (a) and steel C45e (b);
alloys: 1) Cu-ETP, 2) CuSn10Ni1P1, 3) CuCr1,
4) CuSn6, 5) CuBe2, 6) CuZn39Pb2, 7) steel TC80, 8) CuAl10Fe3,
9) steel 3/VII, 10) steel C45e, 11) steel Fe360A, 12) CuSn4Pb4Zn3.

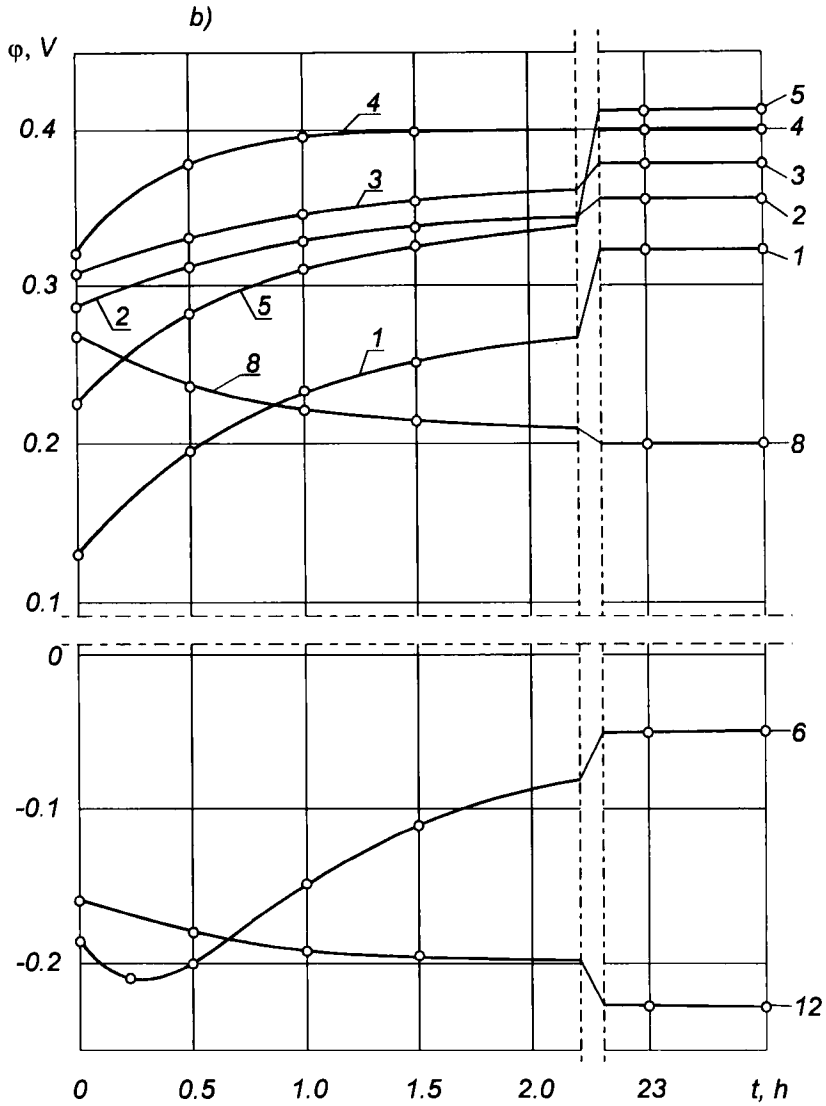

After 10 to 15 min under load 4 to 10 MPa copper was observed in some places of the contact. With time sliding tracks were covered with a fine uniform mirror layer of copper. EMF of the tested pairs varied from 35 to 120 15 μV, the values of contact resistance ranged from 0.07 to 0.10 Ohm (see Fig. 3.11,b). Such values of inherent EMF as well as the sliding pair resistance can be a proof that a direct contact of the sliding surfaces takes place. Besides, absence of rectification, i.e. the intermetal contact, is shown, voltage-current characteristics (VCC) as variations of the current from zero to the maximum in the reverse direction without altering the VCC slope when passing zero.

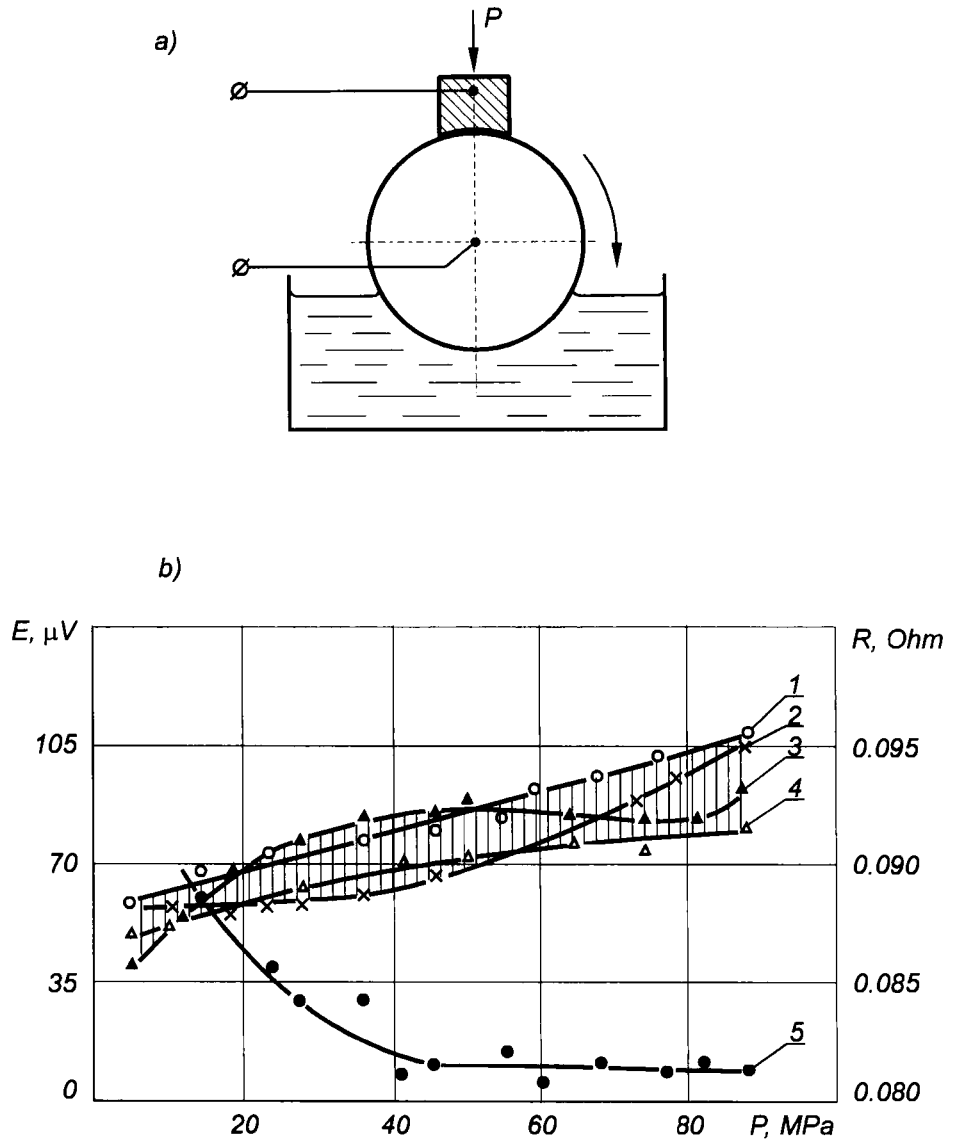

Fig. 3.11. Sliding assembly diagram (a) and plot of EMF E (b) of pairs steel TC80–copper alloys (CuSn6, CuSn10Ni1P1, CuSn4Pb4Zn3, CuAl10Fe3) (curves 1–4, respectively) and contact resistance R of TC80–CuSn4Pb4Zn3 pair (curve 5) versus specific load.

The measured small values of EMF and contact resistance suggest that the major contribution of galvano-EMF to the registered integral EMF is small, it is caused by the source with a lower internal resistance, i.e. the values of thermo-EMF of the sliding couples show an insignificant growth as the specific load increases.

No direct relation has been found between the EMF and the load. The EMF is influenced by the temperature. Due to the low contact resistance, thermocurrents in the friction zone can reach appreciable values.

The experimental results confirm the appearance ST at low sliding speed and under high pressure. The lubricant is surface-active and can reach any place of actual contact. Under high pressure plastic deformation of specimens reaches appreciable values, the area of actual contact increases, respectively. Inhibiting penetration of the lubricant into contact zones and therefore direct interaction of the metal surfaces is decisive. Such properties of the sliding contact is also favored by the sliding assembly design [117].

Under such sliding conditions pressure build up in the contact and cause plastic flow of the material and local phase and structural changes in the surface layer. Plastic deformation induces heat release in the contact zones. Depending on the process intensity and heat dissipation conditions, the temperature on the sliding surfaces may vary, sometimes being very high.

The newly very active sites or the surface free from oxides and adsorbed films, in the contact zone, are coated with the lubricant. As this occurs, the interaction process between the excited surface sites and the lubricant become much more active since fluctuating residual stresses in these sites and the lubricant electrochemical action are directed towards the same sites on the surfaces. The local microgalvanic couples formed by such conditions on the sliding surfaces generate electric current. As these couples operate, metal ions from more active component of this galvanic pair pass into solution, i.e. intensive selective anode dissolution of the alloy is observed and a copper-enriched layer is formed on the surface.

The active sites of the fine surface layer with the loose copper-enriched structure contact with steel repeatedly with certain frequency. Due to favorably oriented thermocurrents and to the high temperature making copper ions highly mobile, copper transfer to the steel surface by electrical diffusion becomes more probable. The electrical transfer mechanism consists in migration of ions under the electrical field effect [118] reaching a considerable value owing to the high-density current passage through the area of actual contact.

3.7. Changes of Metal Electrode Potentials in Lubricants Favouring Selective Transfer

Some publications treat the negative influence of electrochemical reactions within the entire combination of processes involved in sliding, i.e. corrosive failure is considered together with the molecular-mechanical wear. Particularly, behavior of steel was studied in acid solutions, neutral media of various concentrations [119, 120]. It was shown that the electrode potential could serve as the most

general characteristic to assess the influence of electrochemical processes on the state of sliding surfaces.

Studies of metal electrode potentials were carried out in statics and in rubbing with a solid dielectric in glycerine. Sliding [120] was effected between stationary specimen 2 (8 mm diameter) from CuSn4Pb4Zn3 and CuSn6 bronzes, steel C45e, CuZn39Pb2and CuZn37 brasses, Cu-ETP copper and rotating disk 1 (43 mm diameter) from porcelain or another solid dielectric (see Fig. 3.12).

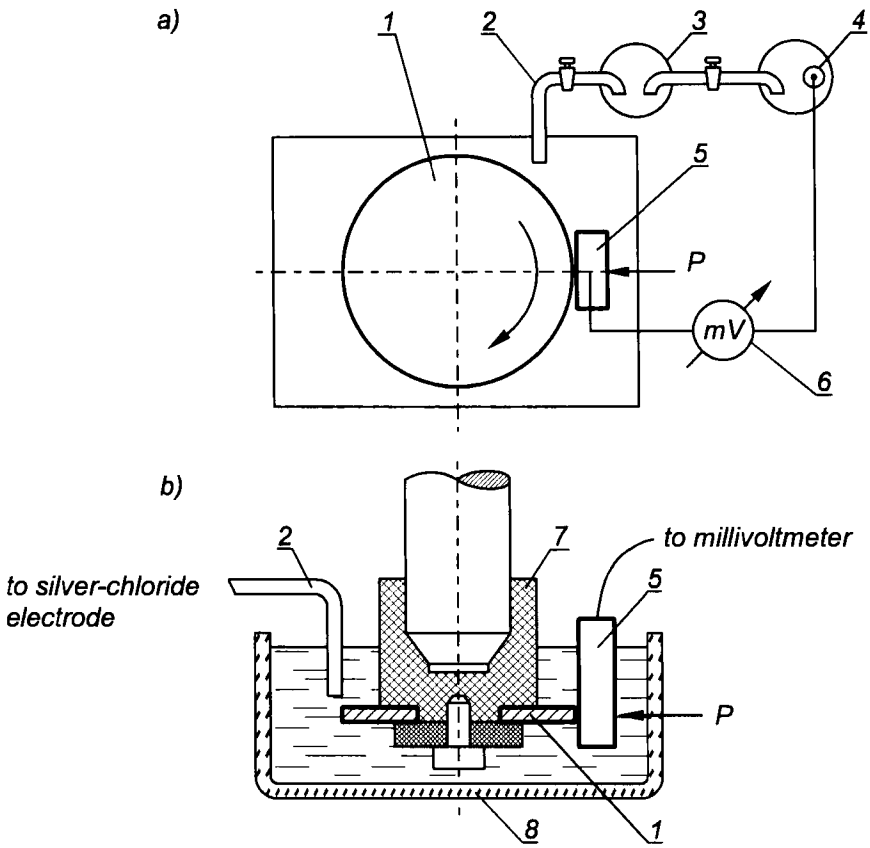

Fig. 3.12. Sliding unit diagram (a) and block diagram for measuring electrode potential in sliding (b): 1) porcelain disk; 2) electrolytic switch (10% agar-agar solution in 1 n. KCl); 3) intermediate vessel; 4) EVL-1M3 silver-chloride electrode; 5) specimen; 6) high-resistance millivoltmeter; 7) fabric-based laminate holder; 8) lubricant bath.

The specimen was covered with polyethylene film except the place of contact with the disk. Sliding parameters: pressure P=0.8 to 1 MPa; sliding speed – V=0.22 m/sec. Prior to the test the specimens were polished bright and aligned

to mate sliding surfaces. The electrode potential was measured with high-resistance millivoltmeter 6. Silver-chloride electrode 4 served for reference [121]. Since the specific load and speed of relative displacement between the surfaces were low, various thermoelectrical effects can be neglected.

For 2 to 3 h after immersion of the specimens into glycerine a relatively rapid potential drop is observed (Fig. 3.13). Subsequently, its certain steady value is reached. For CuZn39Pb2 and CuZn37 (curves 2 and 1) in 4 h kinetics of the electrode potential passes through the minimum growing after that to a steady-state value. Such electrode potential properties of brasses can probably be explained by a slowdown of anodic dissolution of more active components due to the saturation of surfaces with copper and formation of oxide films protecting the surface from the lubricant action.

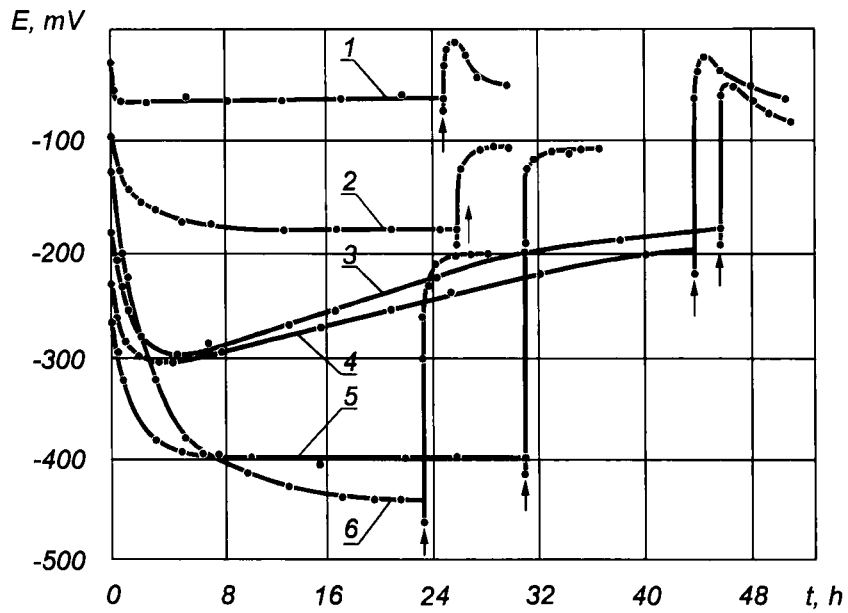

Fig. 3.13. Variations of specimens potential in glycerine versus time: 1) CuZn37; 2) CuZn39Pb2; 3) Cu-ETP; 4) steel C45e; 5) CuSn4Pb4Zn3; 6) CuSn6.

Steel C45e has the most negative steady-state potential in statics, while copper has the most positive one (see Table 3.3). The influence of the solvent types on the electrode potential is quite comparable with the influence of the metal itself [14], therefore the arrangement of alloys in the decreasing (increasing) order of their potentials, shown in Table 3.3, may be different for other lubricants.

Apart from anodic dissolution of particular surface portions due to the lubricant electrochemical effect, thermodynamic processes are caused by water in the

TABLE 3.3

Steady-state potential in glycerine, mV

Specimen	In static	In sliding
Steel C45e	-440	-200
CuSn4Pb4Zn3	-400	-110
CuZn37	-200	-58
CuZn39Pb2	-182	-75
CuSn6	-175	-100
Cu-ETP	-55	-46

lubricant. Water and organic substance (glycerine) "compete" on the surface [122]. Consequently, the boundary layer contains water molecules. All electrodes located in the electrochemical series between hydrogen and oxygen electrodes are thermodynamically unstable in contact with air and water. In this case oxygen should be reduced and transformed into water with simultaneous oxidation of appropriate metals. For example, copper changes to the state of divalent ions in the solution with simultaneous oxygen reduction.

A characteristic feature of electrode processes in organic media is their irreversibility. But the irreversible system cannot provide quite a definite potential, its value can be found only experimentally. Evidently, the potential variations are too caused by the work of microcells, which are formed in liquid dielectrics [107].

The start of sliding (Fig. 3.13) marked by an arrow instantly shifts the specimen potentials towards the negative side from the steady-state values. This shift can be explained by a partial removal of oxide films from the surface leading to more pronounced anodic process. Subsequently, after several hours the potential shifts to the positive, i.e. all the alloys are passivated in sliding.

The high chemical activity of doping elements contained in the copper alloy on the fresh (juvenile) surface formed in sliding promotes intensive dissolution of the alloy and formation of a passivating copper layer on its surface. This is specifically remarkable for brasses when their potentials approach that of copper.

3.8. Wear Resistance of Metals in Selective Transfer and Work Function

The experimental relation between wear resistance of metals in ST and their EWF is an additional argument for the ST electrochemical mechanism.

The EMF of a working galvanic cell is made up by the difference between absolute potential leaps of electrodes (i.e. points in metals and solution) $\varphi_{m1/s}$ and $\varphi_{m2/s}$ plus the contact potential between two electrodes $\Delta\varphi_{m1/m2}$:

$$E=\Delta\varphi_{m1/m2}+(\varphi_{m1/s}-\varphi_{m2/s}). \tag{3.1}$$

The contact potential is expressed in terms of the EWF of the respective metals: and Φ_{m1} and Φ_{m2}, because $\Delta\varphi_{m1/m2}=(\Phi_{m1}-\Phi_{m2})/e$.

According to (3.1) galvano-EMF is directly related to EWF Φ; therefore it is reasonable to assume that wear resistance is related to Φ.

The practical significance of the finding of such relationships is important since it allows to implement simple techniques for predicting wear resistance of various sliding pairs in ST. Usually, in order to assess the ability of a pair of materials to induce ST in a particular medium and to achieve a high wear resistance, long comprehensive tests are performed on various kinds of friction machines, including four-ball lubricant tester (GOST 9490-75), full-scale and bench methods of assessment [123], based on the evaluation of friction coefficients, antiwear and antiscore properties, wear spot size.

Attempts to relate wear resistance of metals to physical properties of surfaces, particularly to their surface energy , have been made before [124, 125]. The practical difficulty that excluded the use of this relation in practice is the absence of a simple and reliable method of finding the surface energy of metals at room temperature. Semiempirical expressions used to determine the surface energy σ also failed to find application in solving this problem.

Attempts have been made to find relation between wear resistance of metals and EWF measured by the CPD technique [126], a technique has been advanced to determine antifriction properties of materials [35]. It consists in measuring the CPD of each specimen of the sliding couple and the reference standard in various lubrication media. It is suggested to choose materials with a high CPD in a given lubrication medium for sliding pairs. Prior to applying a lubricant the surface of the test specimen was ground to roughness 7–8, then it was washed with gasoline, ethyl alcohol and wiped with activated carbon powder.

However, this surface pre-treatment is invalid since it changes considerably the surface potential and, respectively, the surface EWF (see Chapter 2) and distorts the real picture of lubricant interaction with juvenile portions of sliding surfaces even more than without washing and drying. The measuring technique is inadequate as a whole. In addition, there is no explanation of the fact why wear resistance in glycerine is different for various copper alloys.

In similar studies [127] CPD was measured in air but using an installation [41] which had some advantages (see Chapter 2). Another technique was used for preparing surfaces of metals before CPD measurements, namely, glycerine was applied to the specimen surfaces immediately after grinding (in order to avoid or reduce considerably the effect of adsorption and oxide films) with abrasive to roughness 9. As shown in 2.2, such treatment is characterized by the maximum number of local changes in EWF Φ caused by a certain critical density of dislocations on the surface; it features a weaker kinetics (see 2.3).

Table 3.4 shows the results of CPD measurements with gold as a reference

standard immediately after applying a thin layer of glycerine onto the machined surface. The copper alloys are arranged in the decreasing order of wear resistance in a test for sliding with steel C45e in glycerine.

TABLE 3.4

Range of wear resistance of alloys and CPD relative to Au, steel C45e, copper Cu-ETP; meV

Specimen	V_{alloy}/Au	V_{alloy}/steel C45e	V_{alloy}/Cu-ETP
CuBe2	+90	+220	-10
CuSn6	+110	+200	-30
Cu-ETP	+80	+230	
CuAl10Fe3	+220	+90	-140
Steel C45e	+310		-230
CuZn37	+520	-210	-440

As shown in 3.5, this wear resistance series of copper alloys working in pair with steel in glycerine correlates with the series of their galvano-EMF in statics. It is also seen that high wear resistance in ST is not typical for all copper alloys.

As seen from the data, Bronzes CuBe2 and CuSn6 have a larger EWF compared with steel. A clear alignment period can be observed for these bronzes [25] in sliding with steel in glycerine. The sliding surfaces of bronzes and the mated steel are covered with a thin copper layer over the entire test after alignment. Wear resistance of these bronzes (like that of steel) is very high. It is noteworthy that the larger Φ of the copper alloy relative to steel, the higher its wear resistance. Copper Cu-ETP occupies the 3rd, not the 1st line in the wear resistance series because it ranks far below bronzes CuBe2 and CuSn6 in mechanical properties (hardness, strength).

As the EWF difference between the copper alloy and steel decreases, the copper alloy wear resistance also falls. Bronze CuAl10Fe3 has a much lower wear resistance in sliding with steel in glycerine as compared, for instance, with bronze CuSn6. Bronze CuAl10Fe3 leads to [25] a larger copper transfer to the steel surface, however, there is no inverse transfer of copper. A thick copper layer adheres to the steel surface, then peals off the steel specimen.

Brass CuZn37 has a still lower wear resistance, the EWF difference between it and steel being negative.

Thus, wear resistance of copper alloys–steel sliding pairs in glycerine (ST) is determined to a great extent by the EWF difference between these materials which is another evidence that the ST mechanism is predominantly electromechanical.

3.9. Influence of Hydrogen on Selective Transfer

When the operation mode of the bronze–steel pair is disturbed, a harder material (steel) is transferred to a softer (bronze) [25] Hydrogen is assumed to be responsible for this abnormal process [128]. It is assumed that as a temperature of 348 to 353 K is reached, the sliding surface is apparently hydrogenated since a brittle failure of the steel surface layer and the resultant transfer of the debris to the mated bronze are observed.

Absorption of hydrogen by metals is known [129] to be accompanied by reduction of failure and fatigue strength, by appearance of microcracks and other defects in the metal which impair its mechanical properties. The criterion of hydrogenation is the reduction of metal plasticity and increasing brittleness. The effect of hydrogen on mechanical properties starts to manifest itself even when its content is $(1...2)\times10^{-5}$ m^3/kg. (Carbon steel C45e contains approximately 3×10^{-5} m^3/kg which proportionally decreases metal plasticity and failure resistance. At a hydrogen content $(8...10)\times10^{-5}$ m^3/kg the steel failure becomes brittle, i.e. fracture of the specimen replaces ductile failure [130].

Pickling, degreasing, electroplating, welding, heat treatment, etc., favor generation of diffusion-capable hydrogen, parts become hydrogenated to some extent [129, 130].

The initial stage of the ST is the electrochemical process of copper alloy dissolution by a surfactant-containing lubricant. The process rate dictated by the nature and the concentration of surfactant in the lubricant, pH of the medium, friction mode. Due to mechanochemical phenomena, reactions impossible under normal conditions, can occur in the friction zone [131].

Let us consider the effect of hydrogen on ST for the case of glycerine. From the point of view of electrochemistry, the *steel*-$|C_3H_5(OH)_3|$+ *bronze* system is a galvanic cell, characterized by the difference of potentials between the free ends. For some bronzes (in glycerine) with steel it occasionally exceeds 400 mV (see Table 3.2). In the galvanic cell a flow of ions occurs with hydrogen ions reduced on steel just as they are on the cathode.

Glycerine is a triatomic alcohol containing hydrogen both in OH and C_3H_5 groups. It actively absorbs moisture and dissolves in water in any proportions. Glycerine, however, is a weak acid which dissolves many metal oxides forming alcoholates [132]. Acidity of the medium is characterized by pH, therefore its variations in operation are of interest. The original acidity of commercial glycerine is pH=6. This means that glycerine contains hydrogen ions making it an acidic medium. After repeated application of glycerine in the AE-5 frictional machine in which the CuSn4Pb4Zn3–CuSn6 sliding pair was tested, pH of glycerine appeared as high as 7.1, i.e. the medium turned from acidic to neutral. This fact suggests that in ST, when sliding couples actually work without wear, the lubricant appreciably changes its properties. The absorption isotherm revealed [133] that

the surface tension of waste glycerine compared to the fresh in the air interface decreases by 6×10^{-7} J/cm^2, viscosity goes down too. It is an indication of destructive mechanochemical processes in glycerine accompanied by the formation of high molecular acid salts and low molecular products which is confirmed by chemical analysis and mass spectrometry.

After prolonged use the lubricant cannot support and excite ST. This fact can be explained as follows. The chemical properties of glycerine are determined by the presence and interplay of three hydroxyl groups (OH). Glycerine acidity is higher than that of monatomic alcohol, it is therefore capable to form water-soluble alcoholates (glycerinates) not only with alkali metals but also with metal oxides. An example of such compound is the combination of ZnO with $C_3H_5(OH)_3$.

Pure metals should probably react with hydrogen release. Experimental data suggest that the loss of initial properties of glycerine can probably be attributed to the fact that after realization of ST conditions appear for irreversible chemical reactions. As a result of forming wear products glycerine loses its chemically active lubricating properties i.e. equilibrium is set between the metal and its ions in the solution increasing water concentration in glycerine and decreasing viscosity appreciably impairing its lubricating behavior.

In this case hydrogen evolution on steel as a cathode due to its small overvoltage [14] can probably be induced by a partial dissociation of water and electrochemical processes accompanying sliding. At normal temperature in the contact zone these processes do not result in a considerable increase of hydrogen content. In the initial stage of ST when contacting metal surfaces are coated with oxide films, glycerine dissolves them preparing these surfaces for more complicated electrochemical processes underlying the ST [25, 108].

All metals with a potential more negative than that of the hydrogen electrode in contact with water or water solutions, are thermodynamically unstable. In this case metal oxidation takes place with simultaneous water decomposition and hydrogen release. Almost all the doping components in the copper alloy are placed before hydrogen in the electrochemical series, i.e. it is quite natural for them to be oxidized first. Copper is placed after, hydrogen in the electrochemical series should not go into the solution, i.e. it should not be transferred to steel. A reverse phenomenon is observed in practice.

Both copper and glycerine easily form complex compounds. In sliding such compounds are formed with copper ions dispersed from the copper film as a result of repeated deformation of the surface layer. The complex compounds improve the friction coefficient of the couple, promote catalysis of the processes involved in oxygen transfer. Consequently, ST always involves hydrogen generated in the electrochemical processes. Its effect on ST depends on temperature variations in sliding.

Temperature increase in the sliding zone leads higher glycerine and water dissociation constants, the rate of anodic dissolution of the alloy and generation

of hydrogen. Higher hydrogen concentrations facilitate its intensive penetration into steel. This process is induced by deformations inevitable in sliding. Hydrogen penetrates into the steel lattice and deforms it. Combining in molecules, it creates high stress (up to 1.3 MPa [129, 130]) in the surface layer defects exceeding even the ultimate strength of the metal itself. Thus, conditions are created for strengthening the metal surface layer and lessening its plasticity which disturb the positive gradient of mechanical properties through the depth [22] and stimulate destruction of the surface layer of the stronger material (steel).

Tests were conducted to find the ultimate seizure load for specimens which had not been subjected to special hydrogenation, and specimens electrolytically hydrogenated for 1 to 6 h following a conventional method [129] (Fig. 3.14).

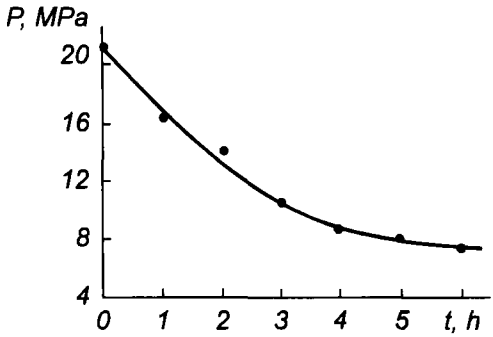

Fig. 3.14. Ultimate seizure load of steel 3/VII versus hydrogenation time.

Specimens of steel 3/VII and bronze CuSn10Ni1P1 were tested in AE-5 friction machine. Lubricant SU (industrial 50 oil, GOST) was used, which does not excite ST, i.e. no additional hydrogen was expected in the sliding zone under normal operating conditions (T=303 to 313 K) during the test. It appeared that hydrogenated specimens tended to seize at loads approximately 2 to 2.5 times lower than nonhydrogenated ones. In this case the absorbed hydrogen was sufficient to exhibit hydrogenic embrittlement.

3.10. Initiation of Selective Transfer by Powders

The ST is based on mechanochemical processes which consist in developing such conditions in the sliding zone when kinematic pairs self-recover and regenerate the worn layer similarly to the movable joints of living organisms [99].

What inhibits "wearlessness" in ST? The first tests of ST have shown that it is restricted (up to 6 m/sec), by temperatures (313 to 333 K) and loads (to 40 MPa). However many sliding units in ST are practically unprotected against natural air-borne abrasives (mainly quartz particles) which contaminate lubricants,

fuel, etc. The particles in the sliding zone, penetrate between the mated surfaces and microcut them. This is accompanied by activation of dispersion and selective dissolution of copper alloy which naturally increases wear. Penetrating, abrasive particles also promote oxidation.

In ST a very thin "servovite" copper film gradually appears on steel only in the actual contact spots between mated surfaces to separate them.

It was found [131] that deformation would stimulate many chemical reactions. Therefore, a conclusion may follow that the mechanical effect can be used to modify chemical behavior. It appears that achievement and acceleration of many chemical reactions involve continuously the reactants (direct participants in the reaction or catalysts) in very fine surface deformations of high intensity.

Thus, it can be assumed that during the initial ST abrasive particles tear the bronze surface, scratch the steel and accelerate anodic dissolution of doping components in the copper alloy stimulating the formation of "servovite" layers on mated surfaces.

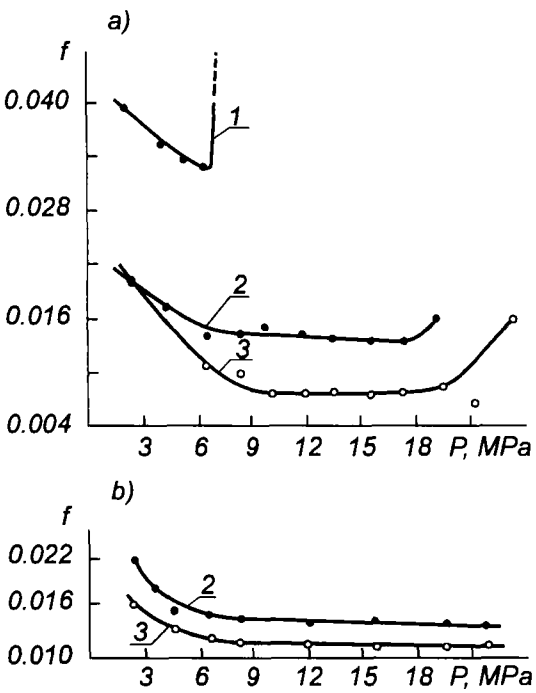

Fig. 3.15. Friction coefficient as a function of load for CuSn4Pb4Zn3–steel 3/VII pair with AMG-10 lubricant (a) and glycerine (b): 1) for abrasives with grain size of up to 5 μm; 2) without abrasive; 3) for abrasives with grain size of up to 3 μm.

In most cases large abrasive particles increase wear of the harder mated member (for example, steel) penetrating into the softer material (for example, bronze) [134]. Particles of about 100 to 200 μm produce microcuts evidenced by microchips in the debris, investigation of their effect on ST is irrelevant.

The author has investigated the relation between the size of abrasive grains 7 μm and less in diameter introduced into the lubricant between sliding surfaces and friction coefficient of various sliding couples both with and without ST, under various loads [135]. The effect of microabrasive particles (1–3 μm) was also investigated when they activate ST, without producing catastrophic wear. This choice was not occasional. The size of mechanical impurities (debris) in AS-6 oil (GOST) is 0.8–3.0 μm after use [136], as it is much more capable to separate surfaces than fresh oil. Fine particles and debris in the lubricant improve wear resistance of sliding pairs [137].

The tests were performed in a AE-5 friction machine. Abrasives of variable grain sizes were introduced into silicon carbide lubricant and 9.2 Mohs' scratch hardness was used. The case of severe contamination of sliding surfaces with natural abrasive was thus simulated. Air-borne abrasives were introduced in concentrations below 2% of the lubricant weight.

Abrasives with grains up to 5 μm (curve 1 in Fig. 3.15) in the lubricant result in a sharp increase of the friction coefficient and heating of the surfaces causing seizure under fairly low loads.

The favorable effect of microabrasive grains up to 3 μm in size are clearly manifested. These particles both accelerate the mating process and noticeably reduce friction forces in the contact (curve 3 in Fig. 3.15). Experimental results on a minimum friction coefficient, optimum, and ultimate loads with glycerine and AMG-10 (ST) and SU oil (no ST), as a lubricant, for surfaces run-in by microabrasives with 3 μm grains, and harnesses of the materials in the test are given in Table 3.5.

One of the most important factors which inhibits the optimum sliding mode under normal conditions is the chaotical microrelief of surfaces produced by cutting and forming. Abrasives with grains up to 3 μm in size accelerate the running-in of the actual contact area, and ultimately the limiting sliding load (curves 2 and 3). Interaction of abrasive particles during the initial phase of sliding facilitates formation of microrelief with surface roughness, uniform in size and shape. The abrasive particles, smoothing out imperfections in the initial period, enhance catalytic processes, promote the development of optimum conditions for ST.

The action of coarse abrasives in lubricant has much in common with the action of colloidal metal particles [138] favouring rapid transition to steady operating friction.

Thus, introduction of a definite amount of abrasive powder into the lubricant accelerates the run-in of surfaces in ST. It can thus be recommended to add

TABLE 3.5

Tribotechnical parameters of copper alloys sliding against the steel 3/VII and their hardness

Specimen	Minimum friction coefficient			Load, MPa						HB, $\times 10^{-3}$
				optimum			ultimate			
	glycerine	AMG-10	SU	glycerine	AMG-10	SU	glycerine	AMG-10	SU	N/mm^2
Cu-ETP	0.014	0.009	0.017	8–27	8–20	2–14	35	24	19	0.44
CuCr1	0.014	0.005	0.015	10–25	14–22	2–19	35	23	20	0.5–0.7
CuSn10Ni1P1	0.010	0.010	0.016	8–25	12–21	2–8	35	22	14	
CuSn4Pb4Zn3	0.012	0.008	0.018	10–25	3–21	6–10	35	22	14	0.6
CuBe2	0.013	0.012	0.016	10–25	12–22	2–15	35	25	15	0.6-0.8
CuSn6	0.015	0.019	0.020	12–15	6–16	2–18	20	20	19	1.76
CuAl8Fe3	0.019	0.010	0.038	8–10	6–18	6–11	20	19	12	1.6-2.0
CuAl10Fe3	0.018	0.008	0.028	5–10	6–16	6–10	15	19	14	1.25–1.70
CuAl10Ni5Fe4	0.013	0.005	0.028	10	4–30	2–12	15	34	13	1.35–1.55
CuBe2 (Hard)	0.030	0.022	0.022	8–9	2.5	2–4	13	4	8	3.5–4.0

abrasive particles, up to 3 μm in size, to commercial lubricants in running-in and mating of sliding assemblies with steel–copper alloy contacting pairs. The preliminary experiments conducted on an IS-4A test bench to speed up the mating of RGS-150-59 reduction gear couple in the conventional lubricant medium (cylinder oil 52, GOST) with a maximum 2% content of abrasive powder (silicon carbide) with grain size of up to 3 μm confirmed the results obtained by the author in the test on a AE-5 friction machine. It was found that the abrasive considerably shortened the time of forming a contact spot of gear wheels. When running the reduction gear in the conventional lubricant, the efficiency after 33 h was 0.713, while in the lubricant with abrasive powder the same result was observed after 2.5 h [139].

The idea of using microabrasives with grains of up to 3 μm as an oil additive gained further development. Investigations in this direction according to T.L. Marinich have proven that the use of superfine abrasive (0.1–3.0 μm) of piezoactive quartz-containing and quartz-forming mineral raw materials (low-ore copper and nickel rocks, red-stripe ferruginous quartzite, tungsten-bearing ore, etc.) is especially promising. It has not yet been found finally why superfine powders of these materials used as additives not only to oils but also to fuels have such favorable effect. It may be attributed to natural excitation and activation of tribochemical reactions in the presence of quartz particles owing to piezoeffect and availability of additive compounds of many chemical elements from the Periodic Table. It seems likely that particles of piezoquartz up to 3 μm in size in resonance vibrations, have such minimum energy (frequency) which is sufficient for stimulating excitation of energy levels of molecules. Piezoquartz particles accumulate heat and stress energy under mechanical excitation by discrete portions, dissipate it maintaining the quantum vibratory character of activation and inhibition of tribochemical reactions in friction. In most cases no abrasive effect of fuels and oils containing superfine powders of minerals is observed, practically there is no wear of counterbodies, the friction coefficient and fuel consumption are reduced.

3.11. Generalized Schematic Description of Selective Transfer

The dynamic multilayer structure of the 3-rd intermediate phase produced in ST and acting as a lubricant on the "servovite" layer of the plastic metal film which is quasiliquid in friction, almost fully undertakes the mechanical load. The minimum friction coefficient is partly a result of weak van der Waals interactions between nonpolar parts of the lubricant components, products of their destruction, including tribosurfactants and intermediate reaction products in the friction zone.

The ST stems largely from triboelectrochemical corrosion, i.e. it can be

explained convincingly from electrochemical positions. In particular, the established relation between the wear resistance of metals in ST and galvano-EMF, realization of ST in corrosion-active media such as sulfuric acid and caustic soda, and other results described above support this explanation (3.3 to 3.5, 3.7).

In all the cases ST can be observed in lubricants or their decomposition products which are, although to a different extent, active corrosion media. The action of a corrosion medium on a metal surface is, first of all, connected with the inhomogeneous structure of the metal alloy surface, i.e. with nonuniform chemical and electrochemical behavior of separate sites of the surface [140]. A metal surface roughness contacts, for example, with foreign metals, different in the nature of structural components, grain boundaries, presence of heterogeneous atoms in the alloy or various imperfections (dislocations), etc. Even the surface of the alloy like a homogeneous solid solution is electrochemically heterogeneous (at the atomic level). Therefore, the model of friction surfaces in lubricant is presented as a system of two electrodes separated by a lubricant layer with numerous microcells affecting both (see Fig. 3.3, 3.4), i.e. this is a multielectrode system (see 3.4).

More negative or less passivated and, consequently, less stable phases dissolve predominantly in multiphase heterogeneous alloys. The selective corrosion, accumulation on the surface of a more corrosion-resistant phase in the given environment takes place. In homogeneous solid solutions cathodic processes localize predominantly on atoms of the doping component which is positive or more stable in the given conditions, while anodic ones do that on atoms of the electrically negative, less stable element. It is reported [140] that atoms of various elements of alloys of the solid solution type (or intermetal compounds) never lose completely their identity.

Examples of electrochemical dissolution of anodic atoms from alloys are full selective dissolution of aluminium from nickel–aluminium alloy during its treatment with alkali and transformation of the alloy into spongy nickel with a highly developed surface; selective dissolution of copper from gold–copper alloy [141] with the formation of a gold-enriched layer about 7–8 μm thick on the alloy surface; selective anodic dissolution of zinc or copper in α-brasses depending on the applied potential [141]; enrichment of the iron-chromium solid solution surface with atoms of chromium in the area of passive state potential. All these examples confirm the assumption [140] that atoms of various metals do not change appreciably their electrochemical properties when a solid solution is formed.

Taking into consideration the above , we can, with more confidence, distinguish the main feature which makes ST different from the other friction phenomena and outline its mechanism. A complex of irreversible processes resulting in a kind of chemical surface modification with a structure which cannot be destroyed under thermodynamic equilibrium is the basic ST principle. These processes take place

at boundary lubrication on the background of plasto-elastic deformation which is one of the major stimulators of all reactions (it lowers their threshold).

It is known that dependence of material durability (the life time of interatomic bond τ under load) on the stress σ and temperature T is expressed by the following equation [142]:

$$\tau=\tau_o exp[(U_o-\gamma\sigma)/kT], \tag{3.2}$$

where τ_o, U_o and γ are parameters characterizing the strength of a solid body, τ_o on the average, for all materials regardless of their chemical composition, types of bonding forces, and structure is of the order of 10^{-13} sec; U_o is the initial energy barrier (bond destruction energy), different for various materials; its value is close to that of interatomic bond disintegration energy in solids, the value insensitive to structural changes. The coefficient γ depends considerably on structural changes such as heat treatment, impurities, orientation and plasticization (for polymers), crystallographic orientation and dislocation density. This general equation of durability is valid for a great number of various materials within a wide range of service lives, stresses, and temperatures.

Such form of the expression when durability exponentially depends on temperature and temperature is in the denominator of the exponent index provides much information [142]. The point is that the same functional dependence of kinetic parameters on temperature is also observed for a large number of other phenomena (for example, diffusion, evaporation, exhalation of chemical reactions, etc.) brought about by random thermal atomic motion and, consequently, by irregular distribution of heat energy between them.

Obviously, it will be quite right to use such kind of Boltzmann relation for ST based on a set of kinetic effects. Then U_o is the activation energy of the corresponding process. If it is a chemical reaction in ST, U_o is excessive energy, as compared to the average molecular energy at a given temperature molecules should possess in order to react chemically i.e. it depends on the energy of active centres. The most important role is assigned to γ , the only structure-sensitive coefficient in this fundamental equation. Let us write the equation for the friction coefficient f in a form similar to (3.2):

$$f=f_o exp[(U_o-\gamma\sigma)/kT] \tag{3.3}$$

The experiment shows that equation (3.3) gives a true qualitative description of the friction coefficient within a certain range of loads. Studies of alcohol dehydrogenation on copper subjected to various treatments

$$R{-}CH_2{-}OH \xrightarrow{Cu} R{-}CH{=}O+H_2$$

have proven (in accordance with Taylor's theory of active centres [143]) that if treatment induces various discontinuities in the crystal lattice, the resultant surface

a)

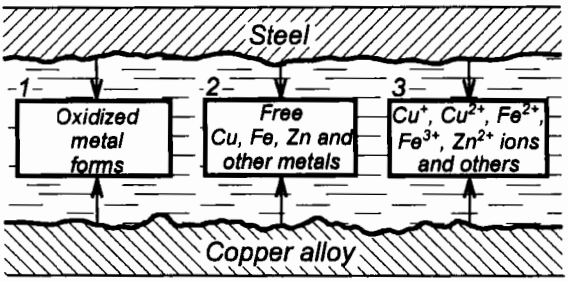

Surface dispersion (1st- stage)

b)

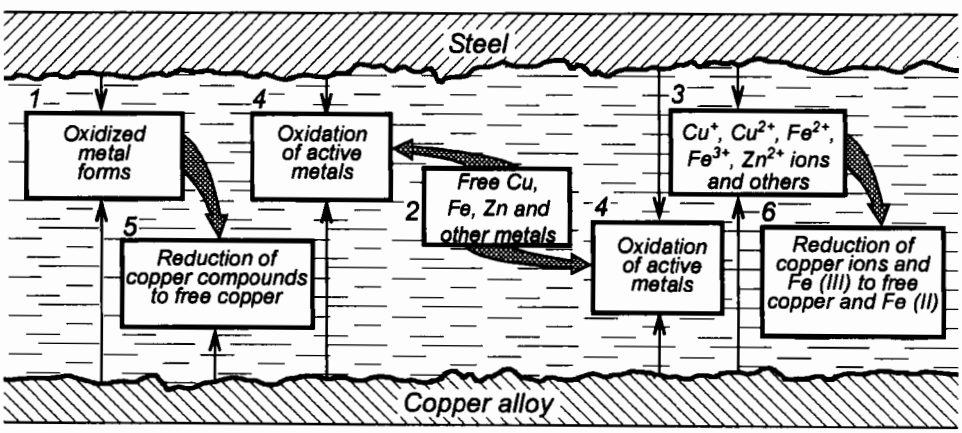

Redox processes (2-nd stage)

c)

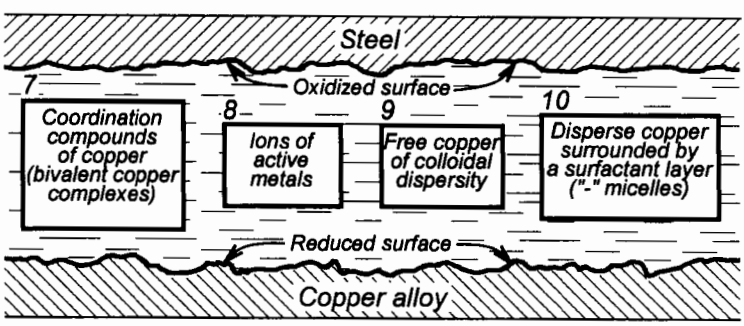

Steady-state friction (3-rd stage)

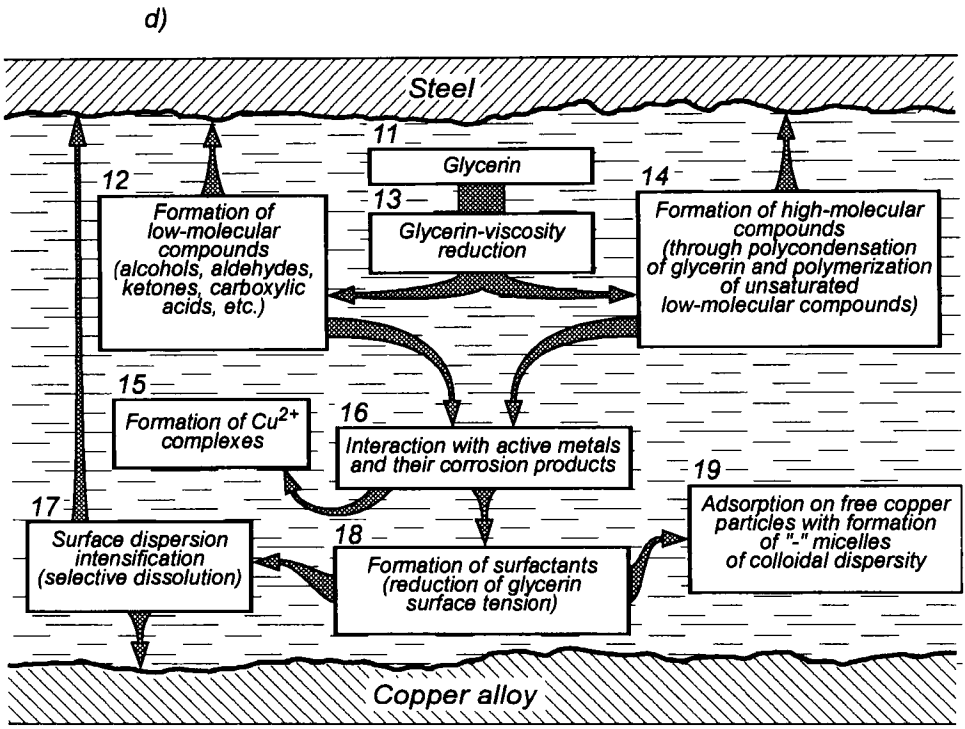

Tribochemical transformations of the lubricant (4-th stage, during 1–3 stages)

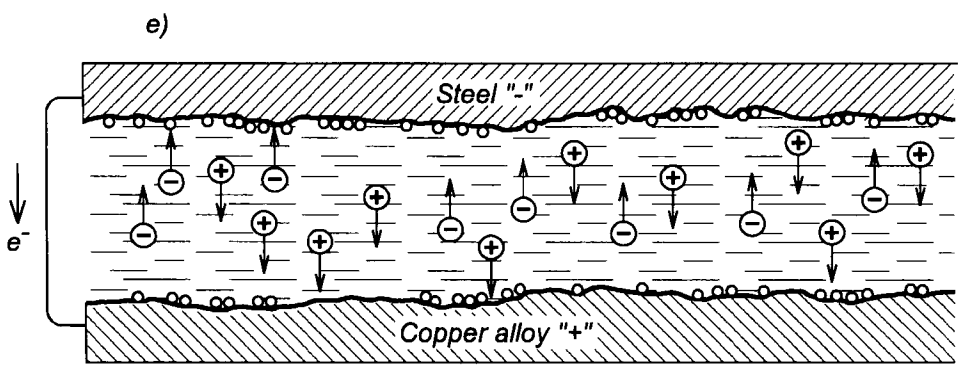

Formation of a "servovite" layer (5-th stage)

Fig. 3.16. A simplified diagram of physicochemical processes in boundary friction of copper alloy against steel in glycerine (ST mode) which induce the formation of a copper film.

will be catalytically active. Fig. 3.15 shows the friction coefficient f versus load P obtained [135] for the CuSn4Pb4Zn3–steel 3/VII sliding pair with glycerine lubricant (curve 2) and glycerine containing silicon carbide abrasive microparticles (curve 3) (see 3.10). A small size of abrasive grains (up to 3 μm) ensure such dispersivity of the microcell system providing particle size below the thickness of the lubricant boundary layer and it don't cause substantial abrasive wear. Activating catalytic and other processes on the surfaces, SiC particles promote the development of friction mode at a given load, reducing thereby the energy barrier U_o. The mating is accelerated considerably, the friction energy losses diminishes. The friction coefficient has the minimum possible value for the given conditions, much lower than that observed even in conventional ST (see curves 2 and 3).

For the first time ST was observed in sliding of steel–copper alloy couples in glycerine [25]. Therefore this three-phase steel–glycerine–copper alloy system which has been studied most thoroughly is a classic example. Fig. 3.16 shows a simplified diagram [144] of chemophysical processes in such a system. Initially surface dispersion occurs due to plasto-elastic deformations , friction, temperature increase, triboelectrochemical corrosion and Rehbinder effect (see Fig. 3.16,a). Large pressure gradients at actual contacts and high shear rate promote the smoothing out of some roughness (microrelief formation) raising temperature near the contacts. After that the solution (lubricant) becomes saturated with initial debris, such as metal oxide particles (1), metals (copper, iron, zinc, and other components of steel and copper alloy) (2), univalent and bivalent copper ions (Cu^{+}, Cu^{2+}), iron ions (Fe^{2+}, Fe^{3+}), zinc ions (Zn^{2+}), etc. (3).

At the same time, chemical transformation of glycerine is activated in the friction zone, including formation of complex bivalent copper compounds (15) (see Fig. 3.16,d). Simultaneously, redox reactions (4–6) take place (see Fig. 3.16,b), copper compounds (5) and copper ions (6) are reduced to free copper. The reductants are active metals such as iron, zinc, tin, lead, etc., as well as glycerine transformation products, for example, aldehydes or carboxylic acids. Fig. 3.17 shows the mass spectrum of the products of tribochemical transformation of glycerine used as lubricant for bronze–steel pairs [145]. Analysis of this spectrum and the results obtained by chemical and chemophysical methods have revealed a wide spectrum of alcohols, acids, aldehydes, and other surfactant products of glycerine transformation playing a main role in the process of corrosion and dispersion of surface layers. Thus, the lubricant layer is saturated with surfactants which are products of tribochemical reactions.

The formation of complexes in sliding is described in [146–149]. It is shown that in sliding of copper on steel in solutions of some salicylalanilines bivalent copper salicylalanilinates are produced. The latter were separated from solution and also found on the sliding surfaces [147]. The initial stage of the chemical reaction of complex formation is attributed to sorption of ligand molecules on

short-living active centres of chemisorption occurring on the newly formed metal surfaces in sliding. This is followed by reorientation of adsorbed molecules, transfer of an electron from the metal atom to the ligand and formation of the Me–O valence bond. Nondivided nitrogen pairs form the Me–N donor-acceptor bond with the metal. Later on, the weakened bond of the copper atom breaks away from the parent metal lattice resulting in detachment of the complex and its transfer into the solution.

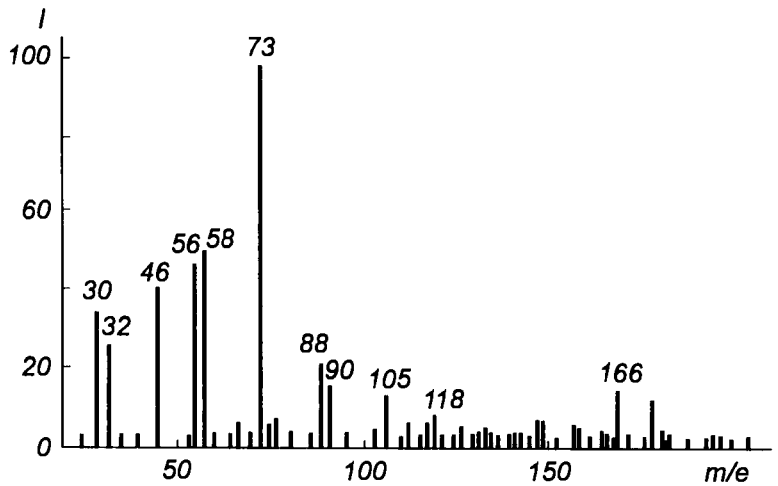

Fig. 3.17. Mass spectrum of glycerine transformation products during sliding [145].

In steady-state conditions (see Fig. 3.16,c) the lubricant is a disperse system saturated mainly with ions of copper and other active metals (8), free copper of colloidal size (9), negatively-charged micelles, dispersive copper surrounded by a layer of anion-active surfactants (10), complex compounds of bivalent copper (7).

Formation of the copper "servovite" layer on friction surfaces occurs in the following way. Under the effect of the field in the electrochemical $metal_1$–lubricant–$metal_2$ system, owing to formation of EMF, ordered motion of "+" copper ions and "-" micelles towards the surfaces takes place (see Fig. 3.16,e), where they are discharged and collapse, respectively, forming free copper. Besides, a crystal layer of copper complex may form on the surfaces. Copper alloys sliding against steel under boundary lubrication with petroleum-based oils with 8-oxyquinolinate additive produces a crystal multimolecular layer of coordination compounds (copper 8-oxyquinolinate) of a maximum thickness of 100 nm on both copper and steel [148, 149]. Since the process of formation and decay of the complex compound in sliding obviously takes place in any tribochemical reactions, it is reasonable to attribute the formation of the "servovite" layer to disintegration and formation of coordination compounds too [149].

The strict division into five stages shown in Fig. 3.16 is certainly conventional as all the processes proceed with different speed simultaneously, gradually dying out at different rates after dynamic equilibrium is reached.

The triboelectrochemical reaction is accompanied by the production and adsorption of atomic hydrogen on the fresh copper film inhibiting the oxidation process. Absence of oxide films has a beneficial effect on the movement of dislocations, i.e. it facilitates plastic deformation of copper in sliding. A high mobility of dislocations is also achieved by the action of tribosurfactants.

The factors alongside with the effect of lubricant and polymerization products prevent direct contact of copper surfaces considerably reduce the friction coefficient and wear.

3.12. Other Processes Responsible for Selective Transfer of Copper

The cases of copper deposition which researchers often encounter and even have to control are quite frequent in chemistry. To a certain extent, they also show up in friction if the same or similar conditions are developed, i.e. a definite combination of metals and suitable properties of the lubricant.

Copper ion deposition on steel is explained, in particular, by contact substitution of iron for copper in solutions of its simple salts [14]. If sufficient metallic iron is in contact with the copper salt solution, iron dissolution and copper deposition will continue until the activity ratio of their ions satisfies the equation

$$a_{Cu^{2+}}/a_{Fe^{2+}}=10^{-26} \tag{3.4}$$

(it is obtained by making electrode potentials of particular reactions equal and by substituting standard potentials [14] for the equilibrium state). Thus, with ferroion activity equal to unity, copper activity is only 10^{-26}, i.e. the solution is almost completely free from bivalent copper ions.

It was shown in the previous sections that atomic rearrangements in the surface layers of copper alloys were caused by difference of chemical activities of atoms in the solid solution relative to the environment.

However, saturation of solid solution surfaces with certain atoms is known also to be caused by difference in surface energy of the components and variations of elastic energy when atoms emerge on the surface [150]. The latter case plays an especially important role in the process of dynamic contact of metals and alloys and dominates if the surface energies of the components are close to each other. Upward diffusion of particular atoms in solid solutions in the field of elastic stresses caused by surface relaxation in thermodynamic equilibrium, was observed on specimens at rest even after treatment at room temperature [151]. Therefore it would be natural to suggest that friction, activating the process, will saturate the surface quicker and will finally produce a fine copper film.

Based on the study of rearrangement of atoms near the surface of small particles in the Cu–Ni system forming a continuous range of solid solutions, an equation was obtained [150, formula (60)] which describes the distribution of components in the field of stresses. The finding suggests that the surface is saturated with atoms of large size. Indeed, copper atoms saturate the surface of solid solution particles, covering actually the entire surface layer of copper as the average atomic size increases.

It is reported in some publications that saturation of surface layers of both small particles and large Cu–Ni specimens with copper depends on the surface state.

Redistribution of the components in the alloy surface layer always accompanies the friction process, it changes as the stressed state of the surface, the surface defects and, correspondingly the elements diffusion rate vary [152]. This fact is confirmed in [153,154].

3.13. Development of the Concept of Selective Transfer

The ST discovered by D.N. Garkunov and I.V. Kragelsky, is termed the effect of "wearlessness" which results from a dramatic reduction of wear rate and energy losses for ST and resembles the process to wear-free friction in living organisms [99].

Subsequent investigation of ST stimulated expansion of the range of its application and, at the same time resulted in ambiguous interpretation of the phenomenon, misinterpreting ST as a term and, in some cases, even the phenomenon was rejected. In this connection, it became necessary to specify the range of ST manifestation and the main characteristics of the phenomenon, to indicate the most effective means of its implementation, and prospects of application.

For such analysis we cite the original definition of ST registered in the Goscomizobreteniy (State Committee for Inventions) as discovery No 41 [99]: *"It has been found that in friction of copper alloys on steel under conditions of boundary lubrication excluding oxidation of copper, a phenomenon of selective transfer of copper from the solid solution of copper alloy to steel and its reverse transfer from steel to copper alloy occurs accompanied by the reduction of friction coefficient to its liquid state and resulting in appreciable reduction of wear of the friction pair".*

As one can see, the copper alloy–steel pair for which this phenomenon was found first is mentioned in the definition. It also states that the growth of the copper film thickness on the contacting surfaces is caused by copper particles released by the copper alloy. Conditions in which this phenomenon can occur are also described in general terms, no information is given about its mechanism. Indeed, this definition is unable to specify all the directions how the effect of

"wearlessness" may develop, it only explains the novelty. At the same time the description [99] contains the essence of the phenomenon. In the analysis of its practical significance it is noted that "*for the first time a process of self-recovery and regeneration of the worn layer which takes place in moving joints of living organisms has been effected in kinematic couples*". Thus, it is the basic idea of the discovery realized in a particular case of the copper alloy–steel pair. It indicates a wide range of manifestations and ways to investigate the ST mechanism, not restricting it by this particular case.

It was also reported in the description [99] that, based on the discovery, a finish antifriction abrasiveless treatment had been developed which consisted in application of thin layers of copper-based alloys on friction surfaces containing no copper ; subsequently ST is realized in these layers in certain lubricants (1958). The "metal-plating lubricant" concept was introduced, composition of this lubricant (1962) and some processes of producing friction parts, methods of increasing their durability were suggested.

Analysis of the discovery description and everything achieved subsequently shows that the relevant ideas and methods have fruitful and gained further development.

Recognition of the mechanism of copper ion ST from the solid solution of copper alloy and inverse transfer of copper ions from steel back to copper alloy expanded its application in different pairs without the copper alloy. The main feature of the phenomenon was preserved, such as the formation of a very fine nonoxide film much softer than the substrate on the friction surfaces (the "servovite" film) with thickness from several atomic layers to 1–2 μm with simultaneous reduction of the friction coefficient to values typical of liquid friction.

We outline the points most important in modelling ST for the service conditions of friction assemblies, their design, and modes of operation.

1. In order to realize ST a source of plastic metal particles and conditions for their generation are necessary in the friction zone. They can be produced by dissolution of the counterbody solid alloy, transported by the lubricant as a result of selective dissolution of copper-containing pipelines or other structural components (such is the case in refrigerator compressors), released from composite materials (where particles of a metal and/or its salts are fillers) as a result of diffusion into the friction-activated surface under strain.

There are many ways to saturate the friction zone with plastic metal particles. In internal combustion engines and compressors (cylinders and pistons made of cast iron or aluminium alloys) copper-containing inserts are used; friction brassing and bronzing of friction surfaces is effected; self-lubricating metal-ceramic (for example aluminium-based) counterpairs saturated with particles and other solid additions are made, etc. Introduction of particles of plastic metals (it turned out later it is better to introduce their salts) directly into the lubricant, and then, together with it, into the friction zone, has received wide application.

2. For realization of ST, in addition to plastic metals, conditions are necessary for a stable process of spontaneous formation of the so-called "servovite" layer nonoxidizable in friction. These conditions are achieved by a correct choice of lubricant and additives, specific for particular friction assembly depending on the contact geometry, sliding speed, load, temperature and materials.

3. Investigation of the ST mechanism has revealed that noble metals (silver and gold) widely used in electric contacts can also be selectively transferred and deposited on friction surfaces. It is also shown (see 2.4) that ST should apparently be manifested by vanadium, chromium, nickel, and cobalt. Ability of other chemical elements to selective transfer cannot be ruled out which is supported by experimental results at "Mechanobr" (St. Petersburgh) on application of particles of natural minerals.

In solving the problem of ST realization in researchers gradually took the way of creating lubrication compounds including both particles of plastic metals or their salts and a variety of additives which, in combination with the base lubricant, could cause excitation and self-regulation of the process, activate redox reactions when a friction assembly is started and produce their steady-state conditions, resulting metal deposition and adhesion to surfaces to form the "servovite" film, etc. Such lubrication materials are called metal-plating lubricants as it was suggested by one of the authors of [99] together with V.G. Shymanovsky.

Before the discovery of the "wearlessness" effect the metal-plating (deposition of metals) in friction was an unwanted effect since such homogeneous pairs as copper–copper, bronze–bronze, brass–brass fail. Processes occurring in the contact zone in metal-plating and subsequent operation of the friction assembly were excluded even in favorable cases of application. It should be noted that solid additives insoluble in oils (most frequently graphite and molybdenum disulfide) have long been used to improve the operational properties of lubricants, but their operation mechanism differs from that of ST. Soft metal powders, such as lead, zinc, copper, etc., were also added to lubricants, but only as sealing agents to fill gaps between mated parts (for example, in threaded connections) or as weighting additions (lead filings). Lubrication composites with metal powders were used exclusively in threaded, current-conducting, and other specific units. Such lubricant cannot produce the "wearlessness" effect and the metal-plating layer they formed is liable to oxidation.

In metal-plating the mechanical principle of operation of dispersed metal particles is manifested. The particles weakly adhere to the surface filling its irregularities and reducing its roughness. The action of metal-plating lubricants (MPL) is based on adhesion when dispersed particles of metals strongly adhere to the surface ensuring ST. When MPL is used, the metal-plating layer changes in friction, it is enriched with copper and no oxidation occurs. The layer structure also changes, a vacancy-dislocation mechanism of surface microdeformation is realized in it which forms a basis for ST [99].

Lubrication materials of a new type (MPL) basically different from the previously known lubricants with metal powders were developed as the functioning mechanism of metal-plating layers became better understood and by the possibility to realize most effectively ST both without changing the design and materials of a friction assembly and redesigning it. When ST is realized, MPL modify the contacting surfaces and the protective metal film is formed, subjected in the process of plastoelastic deformation to action of chemically active elements of the lubrication material, tribodestruction products are thereafter transformed into the "servovite" film. It should be noted that the most promising MPL are those containing metal salts (for example, copper salts) or other chemical compounds with metals.

In view of a qualitatively new approach to lubricants which produce the "wearlessness" effect, it is necessary to define MPL. According to D.N. Garkunov, metal-plating lubricants contain 0.1–10 mass % of the additives: powders of metals, alloys and their oxides, salts and complex compounds of metals, organometallic compounds. Application of MPL produces the "wearlessness" which is characterized by formation of a thin, hard-oxidized self-reducing protective metal film of lubricant additives on friction surfaces of operating parts. The film thickness may vary from several atomic layers to 1–2 μm.

When MPL is used to induce ST, modification consists in a partial change of the structure and phase composition of counterbody surfaces where the film was formed. Little attention was paid to this fact, only deposition of the metal plastic layer on surfaces was noted. It is due to the fact that the main changes of the surface layer under friction at boundary lubrication take place at a depth of 0.1–0.3 μm, but it is difficult to detect them by conventional methods including roentgenography. The problem of studying such layers to observe the surface modification by friction with MPL was successfully solved by Mössbauer spectroscopy on conversion electrons developed at the Byelorussian State University (see 5.6). The studies conducted by N.S. Yenikolopov's team on the effect of high pressure and shear strain (HP and SS) on material properties (see 4.4) are also noteworthy. An extraordinary high diffusion mobility of atoms and reactivity of materials of couples contacting under HP and SS were found with resulting modification of surfaces up to formation of new compounds and equilibrium solid solutions.

Thus, better understanding of the ST mechanism has expanded the domain of "wearlessness" manifestation. At the same time, misunderstanding of the principle of operation and use of MPL, their development by researchers of diverse specialization were often misleading as to what phenomenon responsible for the effect actually. In this connection we will emphasis the main features of the phenomenon which, although beyond the scope of conditions mentioned in the discovery formula [99], at the same time support the idea about self-organization in "wearless" friction pairs.

First, in all cases under consideration a surface build-up takes place accompanied by modification of the surface which finally improves its strength in the widest sense of the notion.

Second, all the surface build-up and modification in ST take place with a microlayer present in the friction zone, including particles of plastic metals or their chemical compounds in the binder and surfactants. The interlayer experiences HP and SS from the surfaces contacting in friction exceeding the yield strength of introduced plastic metals at the actual contact spots.

Finally, the main characteristic of the ST, i.e. formation of the "servovite" film on the friction surfaces, is preserved, the principal idea of realization and use of self-organized "wearlessness" in friction of solid bodies gains further development.

Such interpretation of the "wearlessness" allows to assess better its prospects (as the author did together with G.I. Bortnik). We will consider some of them.

For example, the method is promising to restore worn friction surfaces by introducing periodically MPL into to the zone of friction in non-stop operation without disassembling the unit and to extend its life. In this case plastic metal particles from lubricant are introduced deeply into the surface at its irregularities and diffuse rapidly, the defects are "cured", surface irregularities, cracks, micropores are filled (wear compensation). It is the surface layer modification with a partial change of its phase composition (it is supported by NGR spectroscopy of the surface) and an increase of the mass, (the layer build-up) that occurs. It enables to recondition friction surfaces at subsequent use of conventional lubricants.

We will consider a well-known surface strengthening method or surface plastic deformation (SPD). For realization of SPD rolling or sliding friction of the tool is made on the surface subjected to machining, tool vibrations, impact of tool on the machined surface, as well as combination of machining with plastic deformation. The SPD has some drawbacks: optimum deformation of the surface layer cannot be attained both in respect to the depth and the density of the crystal lattice defects, the process is often accompanied by microcracks. Chemical coating (for example, nickel) on the surface prior to SPD never improves the quality of the surface to be machined. Poor adhesion of coats, most of which cannot withstand high contact loads due to the formation of cracks, impairs the surface plasticity parameters, etc.

Use of special technological MPL capable of realizing the "wearlessness" appreciably enhances SPD effectiveness, improves the surface quality. High plasticity of metal particles relative to steel introduced during machining and stabilizing the microstructure, chemical activity of the medium required to induce ST, facilitate plastic deformation of the surface layer, increase its plasticity. Particles of plastic metals fill microcracks and other surface defects which are potential sources of subsequent failure in operation. Stimulated by pressure and shear, they diffuse towards the grain boundaries and phase interfaces to the surface

layer body. Plastic metal particles in surface microirregularities form an intermediate layer on the surface with special properties which performs one more very important function: it protects the friction surfaces from penetration of hydrogen.

In the process of friction, especially at heavy loads and high temperatures, conditions are created for further modification of surfaces subjected to plastic deformation. Triboalloying by metal particles introduced at SPD results from diffusion of doping elements on macro- and microdefects of the surface layer and high chemical activity of all the excited structural elements in the contact zone.

The "wearlessness" can also be used in machining, drawing and rolling, finishing, friction alloying, etc. The effect is attractive in manufacturing friction assemblies.

During assembly the friction parts are usually covered with a lubricant layer in which they will work. Thus, after assembly conditions are created for subsequent "healing" of surface macro- and microdefects, inevitable after finishing, which are the weak points of the surface, concentrators of stresses, sources of fatigue microcracks leading to wear and failure. A considerable run-in wear during test runs cannot be excluded. Special technological MPL on the friction surfaces cushions the work of the assembly in the initial period which is usually characterized by an increased shear resistance. The surface shear is reduced (low static friction moment) without scoring and seizure. Migration of dispersed metal particles introduced into the lubricant, their spontaneous distribution in the friction process over the entire working surface of the part improves heat removal and reduces the unwanted load effect in the initial period of operation.

Presence of additives including dispersed metal particles in the layer of a grease leads in the initial operation to structural adaptation and modification of both mated surfaces as a result of tribomechanochemical transformations. The surface roughness promotes favorable distribution of solid-phase microparticles. Part of microparticles fills defects of the surface, healing it. Discreteness of the contact ensures rapid interaction of solid-phase microelements with defects of the mated surfaces since microparticles in the structural defects damp vibrations inhibiting microdefects at the points of contact. Thus, simultaneously with the surface modification and strengthening a fine soft layer is formed on it.

The underlayer is strengthened due to the healing of defects, it is characterized by uniform distribution of dislocations. The barrier to dislocations is formed due to surface modification and partly due to the dispersed metal phase. This barrier enhances the strengthening effect. A strong base is created with a thin layer of modified surface spots and a soft external layer where deformations are localized in the process of dynamic interaction. At the same time, the surface microrelief required by the operating conditions is formed.

All these changes take place simultaneously on both contacting surfaces which ensure their equal strength and lead to equalization of electrochemical potentials,

setting the thermodynamic equilibrium. Subsequent depletion of active medium (metallized soft material), its replacement by a working lubricant (liquid or grease) takes place gradually in the operation without disturbing the contact equilibrium.

Hence, realization of the studied phenomenon in its new interpretation based on deep understanding and wide field of application starting from ST in its original form [99] supports the idea of self-organized formation of "wearless" friction pairs, similar to the friction pairs in living nature, it allows to achieve possible control over the friction process, and, in fact, to develop of a new technology or tribotechnology.

So, friction which has long been considered an unwanted effect (only this aspect of the phenomenon is usually considered) gradually becomes a creative factor.

3.14. An Example of the Selective Transfer Application; A New Multifunctional Additive

The realization of an operating mode when experiencing self-regeneration of wear, i.e. ST mode, is a tribological way of saving energy, fuel, lubricants and rubbing materials. This mode occurs in different conditions, particularly as a result of adding powder copper particles to lubricants.

The perspective of the usage of colloidal dispersion (ultradispersed) copper instead of powder copper for metal-plating lubricants, is analyzed here [155, 156].

The role of particle size. The subject of the influence of copper particles dispersity on metal-plating lubricants has not arisen earlier. Powder metals and their oxides are usually the basic of metal-plating lubricants. They are well-known in industry. They improve the maintenance properties of greases and liquid lubricants, decrease friction and wear, increase contact electroconductivity, etc. The size of the copper particles normally used, is up to 10 μm or more. It was also suggested that powdered copper be added to cutting oils [157, 158], but this idea did not have a practical application.

A lubricant medium in the steady state, ST mode is the dispersal system. This lubricant, as is known from preceding sections, is saturated essentially with copper ions, pure copper of colloidal dispersity, etc. (see Fig. 3.16). Research in the physicochemistry of ultradispersed systems shows that the reduction of the size of particles to 10–100 nm allows us to obtain materials with unique properties. It also suggests that the amount of copper induced in the metal-plating lubricant would be reduced to a greater extent than in smaller particles. The facts listed above give a hope that investigations of metal-plating plastic and liquid lubricants with ultradispersed copper particles can give interesting practical results.

Colloidal particles usage. The different chemical compounds of colloidal particles usage to improve the lubricant and fuel properties is well known. Some examples are listed below.

1. The lubricant for bearing, particularly for the gas bearings of a gyroscope with a colloidal form of a metal oxide hydrate, is indicated in [159]. The metal here was chosen from Cr, Mn, Fe and Co.

2. Ferromagnetic metal particles (Co, Fe, Ni or their alloys) of a colloidal dispersion are the basis for magnetic fluids [160].

3. Colloidal form particles were previously used as antismoke additives for an internal-combustion engine fuel, e.g., the method of "Fuel combustion by burning with colloidal dispersion of fine particles of divalent metal-iron oxide cpd" is indicated in [161]. In the combustion of fuels, a fuel, e.g., gasoline, kerosene, etc., is burned together with fine particles of an Fe cpd of formula MxnFe2O3 (where M is a divalent metal, e.g., Co, Ni, Sn, V, Ti, Fe, Cr, Mn, Cu, Zn, Ba, Ca, Mg, etc., and n is a number above 0).

Ultradispersed copper-containing additives. The analysis of the usage of colloidal systems in machinery, and an understanding of the ST mechanism principal basis has led us to suppose that not only copper powders but the colloidal dispersion copper (and a copper oxide) particles can give the maximum benefit when used as multifunctional additives for a technological medium: liquid lubricants or greases, internal-combustion engine (ICE) fuels, cutting fluids, and hydraulic liquids. The first short-time factory tests have proved this.

Ultradispersed copper and copper oxide (CuO) have been obtained by the chemical sedimentation from solutions. Then ultradispersed fine particles are coated with surfactant.

The size of both the ultradispersed copper particles and their oxides has been studied using the transmission electron microscopy method. The samples has been done by the replica method. A roentgenography method was used for phase composition determination. According to the obtained results, the dispersion particles of a copper oxide-contain additives look like the needles. They have crystalline structure of copper oxide. Their thickness is about 10 nm and length is up to 40 nm. But an additive with pure copper-contain ultradispersion particles consists of metal copper particles resembling a sphere. Their diameter is not more than 25 nm.

The experiments revealed that the additives for metal-plating lubricants, which contain ultradispersion metals or oxides, can be obtained not only as a type of solution but also as pastes and dry powders. They are easily dispersable in oils, fuel and water with a forming of stable colloid solutions.

In most cases a tendency to improve the maintenance characteristics of the ICE by use the additives was found. While using the ultradispersed CuO additive in motor oils, redox reactions take place. Copper oxide reduces to free copper.

Transfer and adhesion of their particles to the sliding surfaces occurs, particularly to the surface defects and irregularities, etc. (see 3.13).

The small size of the particles accelerates the surface modification, self-reducing and formation of a fine copper film. The wear of the ICE decreases (see Fig. 3.18) as well as fuel and lubricant expenditure. The pressure degree is enhanced and engine revolution at fix fuel expense increases also.

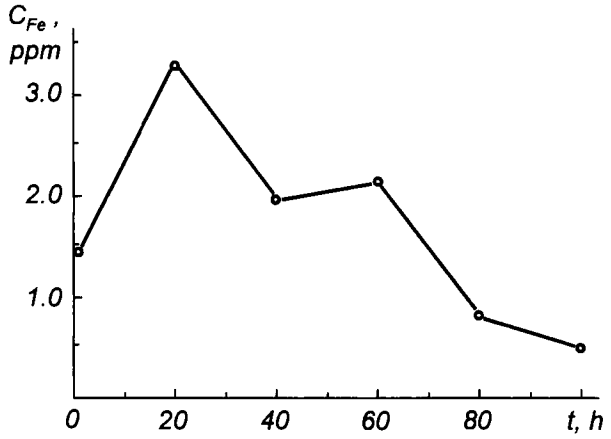

Fig. 3.18. Changes of iron concentration C_{Fe} (received by ferromagnetic method) in Superol Falco CD 15W/40 motor oil with the ultradispersed CuO additive vs. operating time of the SW 680/207 engine obtained in the engine-test chamber at the "PZL-MIELEC" plant (Poland).

The additive is characterized by a high effectivity of the action. Just a little quantity of the additive is enough, in the operating medium, to note an essential improvement of its maintenance properties. Only 0.005–0.010% of the additive is needed in the liquid lubricant. The concentration of the additive in greases is 0.05–0.10%.

The additive has also antismoke features, because copper oxide is quite an active oxidizer. When warmed together with different organic substances a copper oxide oxidizes, converting the carbon oxide into carbon dioxide and hydrogen into water. Therewith, the copper oxide is reduced into metal copper. Copper particles may also act in combustion on the ionic mechanism as with other metals of the Periodical System First Group which have a low ionization potential. An intensive ionization of the additive copper particles in the flame occurs. Both reasons partially elucidate the fact that like the additive in an ICE fuel, the additive lowers the concentration of harmful components in exhaust gas. Concentrations of CO, NOx, CH are decreased by up to 10%, especially on risen revolutions. Moreover, the additive in fuel produces the same positive effects as is seen in its

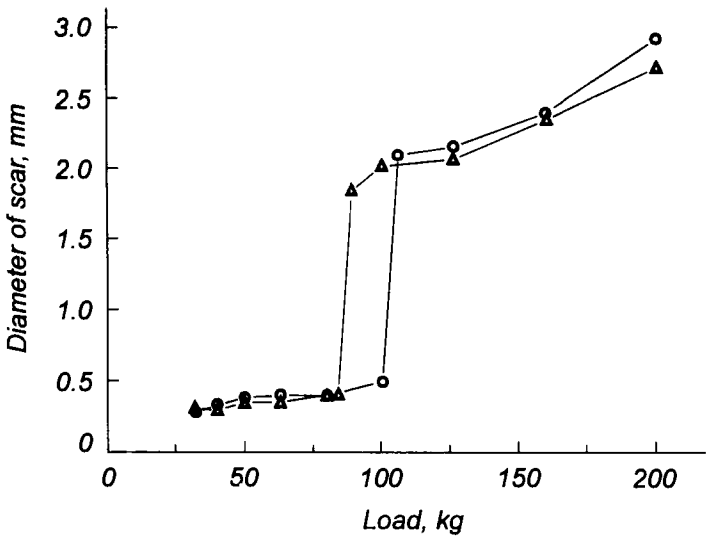

Fig. 3.19. Dependence of diameter of scar on load obtained with a four-ball lubricant tester (PN-76/C-04147) for Super Falco CD 15W/40 mineral oil. Operating conditions: 145 rpm; 60 s test time (instead of 10 s according to PN); environmental temperature; steel 1/XVII balls;
Δ) reference oil; o) reference oil + 0.007% ultradispersed CuO.

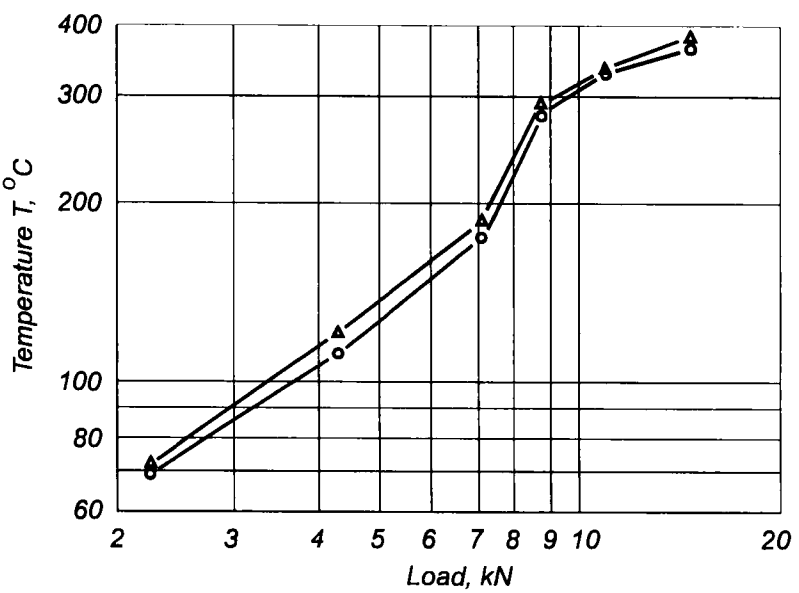

Fig. 3.20. Temperature changes in oil film vs. load obtained with Almen-Falex tribometer for Superol Falco CD 15W/40 mineral oil;
Δ) reference oil; o) reference oil + 0.006% ultradispersed CuO.

adding to motor oil. For example, the soot and smoke decrease, by 15% was found at low revolutions in SW 680/207 ICE of a truck which had a run of 100,000 km before the test with the additive.

Another results obtained on this engine after 100 hour tests at maximum power and torsional moment with the CuO additive in mineral motor oil Superol CD 15W/40 (ZN-88/MPChil/NF-185) are listed below.

- Fuel consumption is decreased by 2–5.8%.
- Mechanical efficiency is increased by 1.8–3%.
- Compression in a combustion chamber is increased by 4–5.7%.
- Motor oil consumption is decreased to 22%.
- The fuel combustion temperature is decreased to 10–15 °C.

The wear of the engine is essentially decreased (Fig. 3.18). Antiseizure and antiwear properties of the mineral oil are also better by about 10% with the additive. The examination was carried out with a four-ball lubricant tester (Fig. 3.19).

The temperature in the oil film insignificantly decreased. It was found during tests with tribometer Almen-Falex (IP 241T) (Fig. 3.20).

The positive results were also obtained during a testing of the additive influence on gear oils. The additive was added into Transol SP-100 gear oil (PN-90/C-96056) and the antiwear capacities of the resultant oils were evaluated by the Almen-Falex tribometer (Fig. 3.21). As can be seen from Fig. 3.21, the CuO ultradispersed particles exhibit good antiwear capacities. Moreover, the temperature in the oil film was decreased to 10 °C (Fig. 3.22,a).

Tests of the additive in hydraulic fluids give the next example of its application effectivity. Note, that the temperature in thin oil films in all above cases is decreased by the addition of CuO ultradispersed particles (Figs. 3.20, 3.22,a,b).

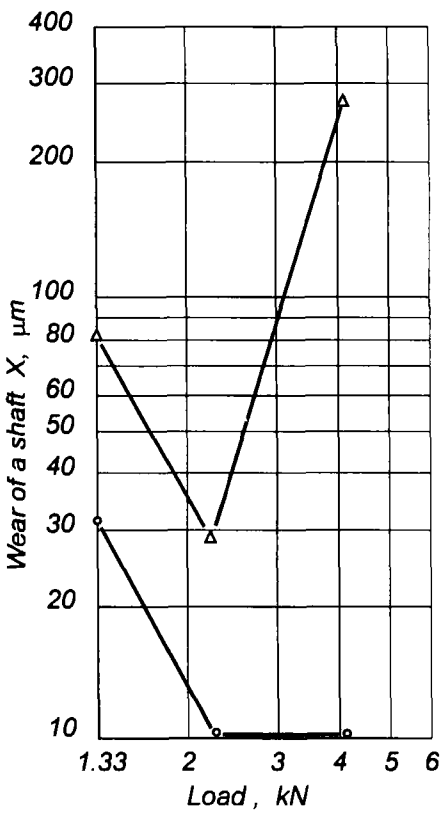

Fig. 3.21. Wear of a shaft vs. load at Almen-Falex tribometer for Transol SP-10 gear oil; ∆) reference oil; o) reference oil + 0.006% ultradispersed CuO.

The additive can be added also into a cutting oil. It was tested first in a broaching machine. The results have been; an increase in tool life by approximately 4 times, and at the same time the surface quality on the specimens also been improved. Furthermore, the surface on the specimens has been tested in scanning electron microscope and found no trace of copper in the surface. Therefore no reason to believe that using CuO ultradispersed particles will cause any problems with corrosion in non rubbing metals.

There are another data and evidence which suggest the success of using the additive in cooling liquids for all kinds of cutting processes.

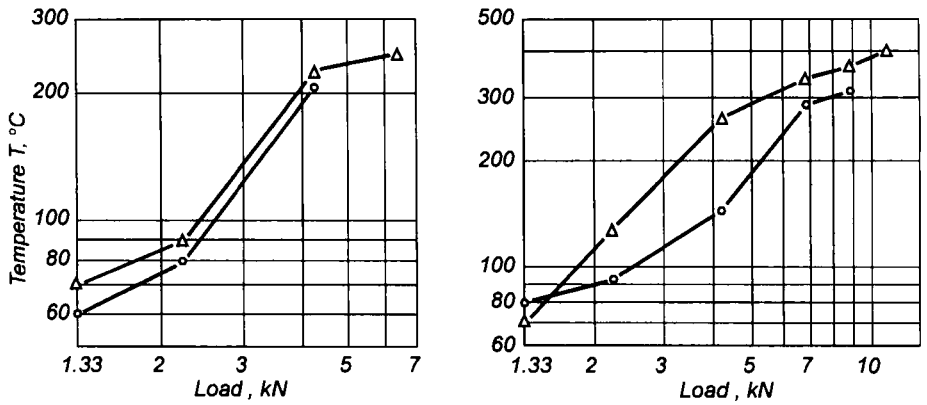

Fig. 3.22. Temperature changes in the Transol SP-10 gear oil (PN-90/C-96056) (a) and the Hydrol 40 hydraulic oil (PN-91/C-96057/04) (b) films versus load at Almen-Falex tribometer;
a) Δ – reference oil; o – reference oil + 0.006% ultradispersed CuO;
b) Δ – reference oil; o – reference oil + 0.018% ultradispersed CuO.

Concluding remarks. The quantitative transition from rough- to ultradispersion of copper particles leads to considerable qualitative changes of maintenance properties of metal-plating (copper-contain) lubricants. Thus, we can talk about a new generation of effective multifunctional additives on the basis of copper and its oxide of colloidal dispersion. It is beginning to take the place of additives with copper powders. Although the results presented here are partial, nevertheless they give hope for a further development of the research.

Chapter 4

THE ROLE OF HIGH PRESSURE AND SHEAR STRAIN IN FRICTION

4.1. Local Excitation Level

Experiments have revealed that high pressure is the necessary condition to produce the fine "servovite" film of a plastic metal on the working surfaces of counterbodies in boundary lubrication. In this case, the level of mechanical excitation and activation of physicochemical processes in the contact zone is high. Excitation of material particles is intensive in the real contact through collisions and elastoplastic deformation of counterbodies. The results are heat release, shearing stress, and broken chemical bonds, which produce micro- and macrocracks, local destruction of microvolumes, electron and photon emission, increased density of surface defects acting as chemically active centers. The lubricant and its degradation products in the excitation zone stimulate chemical reactions in deformed regions of the contact zone. The enhanced chemical activity of dislocations serves to evaluate quantitatively the dislocation density by etching crystals.

Thus, it is found that a copper film (in the case of ST) emerges only in the real contact and at high loads, i.e. the film is formed mainly in the running-in process, i.e. in cutting away and deformation of profile microasperities. He copper film is also known to appear in friction of pure copper against steel or in friction of steel or iron against steel if copper and polymer particles are present in the lubricant. This suggests that selective triboelectrochemical corrosion is the only one of the variety processes responsible for single-phase metallic films formation on mated surfaces. For instance, one such process can be material transfer when electric current is passed [80].

We will consider another mechanism resulting in the metal-particle transfer accompanied by surface modification. This mechanism can occur in friction together with the processes mentioned above, it is basically different from the ordinary seizure or the smearing of particles of one metal over another.

The cause of material microscopic transfer leading to the plastic metal film formation on friction surfaces consists in "plasma" generation in the microcontact zone, i.e. the zone of direct contact of microasperities. There are good grounds for the conclusion.

Like impacts in friction, statistically distributed roughness on mated solid surfaces are subjected to elastic and strong local plastic deformations which result in structural disordering and generation of dislocations. Energy produced in the contact lacks time to dissipate between interactions; therefore, a large amount of excessive free energy in the submicroscopic deformation should be taken into consideration. Here the contact experiences a strong excitation, resulting in the loosening and decaying structure.

Structural elements of the lattice of the mated solid acquire high energy [131, 162] characterized by thermodynamic instability. The reverse transition to the low-energy state is accompanied by release of large energy. The new metastable structures are characterized by strong excitation of the lattice; therefore, they cannot be described by the concept of macroscopic state.

When the crystal lattice detached elements mix up with medium components in highly dissociated and excited states, free electrons, etc. and produce the so-called submicroscopic "plasma" [162]. Thus, owing to high energy concentration, a momentary "plasma" state (10^{-7}–10^{-8} sec) appears in microcontact, accompanied by electron emission, transformation of the substance, activation of chemical reactions, and other processes (Fig. 4.1).

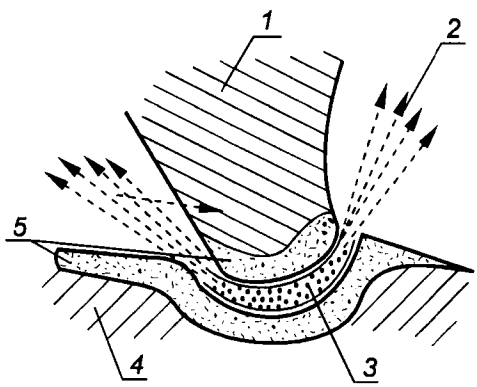

Fig. 4.1. Emission effects in the deformation zone [162]: 1) tool; 2) atoms, electrons, photons; 3) "plasma"; 4) workpiece; 5) hard shell (frozen structure self-recovered after termination of dynamic action).

Thus, this model applies to localized of direct dynamic interactions surface irregularities, evidenced by the following experimental results.

First, local temperature in contacts can rise up to 1073–1273 °C and higher due to the conversion of friction energy to heat in the region about 10^{-2} cm existing for 10^{-5} to 10^{-3} sec [163–165]. In the microcontact even for a shorter interval, the temperature is considerably higher. Thus, calculations based on emission measurements when crystals split [166], have shown that in the region about

3 nm size where a crack moves at a speed 1 km/sec, the temperature peak can be as high as several thousand Kelvin (for quartz its value is about 4700 K). The phenomenon of intensive local heating as a result of conversion of plastic deformation work into heat is described in detail in [166–170]. The local temperature rise in sliding friction can be approximated by the following expression [163, 171]:

$$\Delta T = fPv\left(4rI\left(\chi_1 + \chi_2\right)\right)^{-1},$$

where f is the friction coefficient;

P is the pressure on the contact surface;

v is the sliding speed;

r is the contact region radius;

I is the mechanical equivalent of heat;

χ_1 and χ_2 are thermal conductivities of the bodies subjected to friction.

Second, if the proposed model is true, the short-life local "microplasma" states, which represent a mixture of ions, electrons, and excited atoms according to [162], should bring about ionization of the ambient atmosphere. This ionization should exist along with EEE from the surface for a longer time than the lifetime of plasma. This effect has been found in sliding friction of metals.

4.2. Gas Ionization in Sliding of Metals

Contact interaction of solids in friction produces the three main groups of effects that occur on boundary surfaces, namely, mechanical (elastoplastic deformation, abrasion), electrophysical (adhesion, emission, generation of electrostatic charges, EMF etc.), and chemical phenomena. The extent of these factors influence upon wear and their interrelation depend on the friction conditions. For example, in the places of temporary or permanent contacts of metals with inadequate lubrication, mechanical excitation becomes so significant that it triggers off intensive chemical reactions in the contact zone, sometimes accompanied by photoemission or electron emission. Absorbed heat is the energy source of electrons.

When one member of the pair is from a dielectric material, gas ionization is observed during bond-breaking [172]. The ionization is generated by electrons that previously belonged to the solid and were emitted as a result of the adhesive contact loss or solid body crushing, attrition of the solid surface, and other processes related to dispersion [173]. In normal conditions, low-energy electrons (particularly, exoelectrons) cannot induce avalanche and initiate electric discharge into the atmosphere, because the ionization energy of atmospheric molecules exceeds 15 eV. Generally, exoelectron emission is the thermo- or photostimulated

emission or results of a chemical reaction [36, 174].

Emission of fast electrons with the energy about 10^3–10^5 eV is due to the loss adhesive contacts of polymer with glass, brass, and other materials or to the spalling of ion crystals in deep vacuum [173]. Conductive materials (silicon, bismuth, antimony) spalled in high vacuum does not cause emission of fast electrons because conductivity leakage of surface charges inhibit a high potential difference in appearing cracks. Emission of fast electrons at atmospheric pressure leads to generation of gas discharge processes.

EEE on metals is observed when surfaces are cleaned with a steel brush in oxygen, with abrasive powder in the air, in plastic deformation of metals, in friction and in other processes [36, 174]. It is found that the mean kinetic energy of exoelectrons escaping from the metal surface is not very high, it is within the range 0.1–0.6 eV. However, the kinetic energy of exoelectrons emitted from metal was measured after deformation stopped, it is apparent that correction for friction dynamics should be made [36]. Thus, the maximum exoelectron energy measured during machining of metals is 8 eV [175].

In sliding, even a thin lubricant boundary layer screens off electronic emission [36], making it impossible to measure dynamic EEE. Furthermore, to stimulate EEE from a friction surface, illumination quanta are additionally required with their energies depending on types of metals.

If a short-life highly excited state is generated in the places of collisions between asperities in friction, it is natural that near a microcontact should be ionized, positive ions in the atmosphere appear in the gas together with electrons and negative ions. A single break of the friction contact within the collision interval (microcontact) is the duration of interaction of asperities and about 10^8 atoms can escape from the surface layer. Meanwhile, the energy supplied to the microcontact (about 10^{-10} J) is sufficient to ionize the material [176]. It is apparent that to detect ionization experimentally, dynamic measurements should be made (the time interval between the ionization onset and detection should be reduced to the minimum).

In order to detect ionization in friction an experiment was conducted which consisted in continuous EWF dynamic capacitance measurements directly in friction. The CPD capacitance measurements are known to be based on the CPD sign equal to the EWF difference between the test specimen and the reference electrode (e.g., of gold), changes to the opposite are due to ionization of the gas gap in the dynamic capacitor [177]. Thus, by continuously measuring CPD and determining its sign along the friction path in the course of friction, it is possible to detect ionization without ambiguity.

The experiment was performed by the author together with A.L. Zharin using a special apparatus [98] (Fig. 4.2). Measurements were taken at the frequency of the dynamic capacitor formed by vibrating reference electrode 11 and the sliding path on specimen 10 or at the frequency of mechanical beats of rotating specimen

10 (disk) with automatic phase compensation of the measured CPD.

Fig. 4.3 shows typical time dependence of CPD for a steel surface (disk) upon which a CuSn6 pin slides. Digit 1 indicates the CPD value for a bare disk. At time 2, a thin layer of the TsIATIM-201 lithium-soap grease is applied

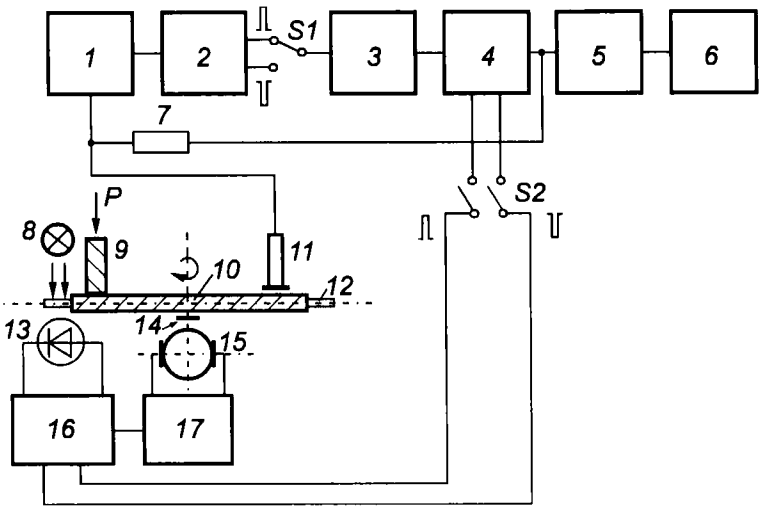

Fig. 4.2. Block diagram of the apparatus designed for dynamic measurement of CPD: 1) electrometer pre-amplifier; 2) phase rotator; 3) selective amplifier; 4) synchronous detector-integrator; 5) millivoltmeter; 6) recording potentiometer; 7) resistor (I G0hm); 8) lamp; 9) static specimen; 10) rotating electrode; 11) reference electrode; 12) light beam chopper; 13) photodiode; 14) current collector; S1, S2 switches; 15) electric motor; 16) reference signal generator; 17) electronic stabilizer of electric motor rpm.

to the disk and at that moment sharp peaks of the CPD characteristic to the positive domain and then to the negative domain are observed. These peaks are associated with the changes in the surface energy due to adsorption of lubricant and initial formation of the boundary layer. At time 3, the upper specimen of the friction couple (the pin) is brought into contact with the disk. As a result, the disk potential decreases abruptly owing to the disturbance of the adsorption (boundary) layer formed on the disk surface. Subsequently, the friction process stabilizes and the CPD value constantly rises. Repeated redeformation of the friction surface leads to the EWF reduction. Decrease of the thickness of the lubricant boundary layer exposes some points to direct contact (in the pin this is indicated by a slight broadening of the curve, time 4). As the lubricant runs thinner, the curve behavior suddenly changes: high peaks (up to several volts) into the positive domain appear due to the generation of strong local plastic deformations, galling, and local heating

of the contacting points. At time 5, the TsIATIM-201 grease is added again, and the curve shape returns to the previous, the friction process running similarly to that observed in moment 3.

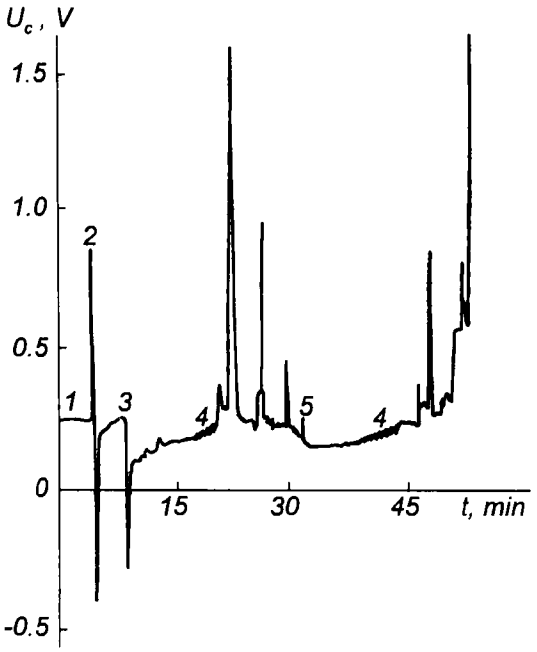

Fig. 4.3. Sliding path time dependence of CPD: P = 0.7 MPa; v = 2.2 m/sec.

Substantial changes in the compensation potential (leading in some cases to the off-scaling at 6 V) observed in the boundary lubrication (definition of friction modes according to Akhmatov [16]) can be attributed to ionization of the gap in the dynamic capacitor. As mentioned above, ionization changes the CPD sign to the opposite when the capacitance measurement is used. This changes by π the phase of the variable signal from the dynamic capacitor formed by the sliding path of the rotating specimen and the reference electrode. As a result, automatic compensation is lost.

To confirm the ionization emergence in transition from the boundary to limiting ("semidry") lubrication, the friction mode was changed by increasing the specific load up to 1.1 MPa. This resulted in earlier disturbance of the boundary lubrication, since the lubricant was not replenished during sliding (Fig. 4.4). In the case, the compensation potential (section 1) corresponds to positive CPD values of the sliding path whose EWF is lower than that of the reference electrode (gold). Depletion of the thin initial lubricant layer results in a gradual increase of the number of direct metal events heightening the excited state. In the microzone

emission of electrons, photons and ions of various energies occurs which ionize the gas layer over the sliding surface. Initially, the compensation potential rises slowly, then abruptly which results in decompensation (the overshooting). A change of the reference signal phase by π at time *a* by switch S2 (see Fig. 4.2) restores the phase ratio between the main and reference signals, the auto-compensation mode continues, however, the compensation sign changes to the opposite (see Fig. 4.4, section 2).

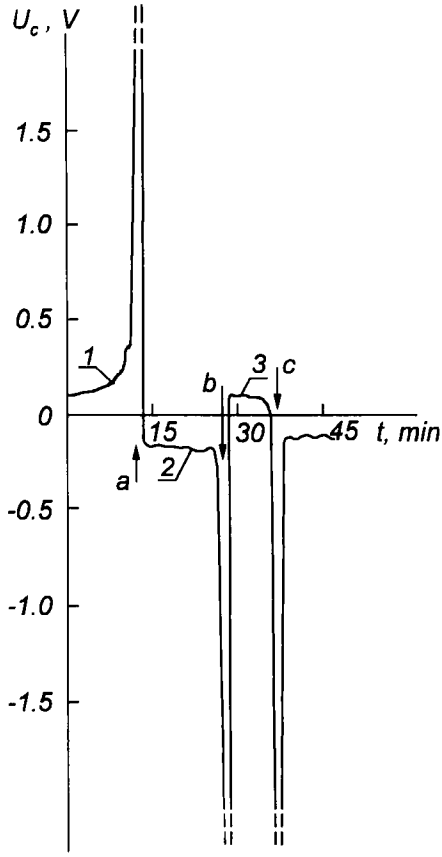

Fig. 4.4. Sliding path CPD time dependence: P=1.1 MPa.

Section 2 corresponds to the limiting boundary friction. At time *b* lubricant is added, the limiting boundary friction is replaced by the boundary friction, the number of direct metal contact decreases abruptly. In this case, friction proceeds through the boundary lubricant layer which relieves deformation. Direct contact practically stops and ionization disappears. The compensation potential falls drastically and decompensation of the apparatus takes place. To restore autocompensation, the phase main signal from the phase-rotator is changed by switch S1. As a result, compensation occurs in the positive domain (section 3) which corresponds to the boundary lubrication (as in section 1).

Lubricant depletion reinterrupts the boundary lubrication (time c), decompensates and overshoots readings this time into the negative domain since phases of the reference signals in sections 1 and 2 differ by π. Further recovery of autocompensation is achieved by changing the phase ratio between the main and the reference signals by switches S1 and S2 (see Fig. 4.2).

To prove ionization of the gas gap simultaneously with measuring CPD, as shown in Fig. 4.2, ionization current passing through the capacitor gap between the sliding path of the rotating disk and the surface of the stationary electrode (placed near the reference electrode with the same gap) was measured. For this, an integrating picoamperemeter (IPA-type) was used, its operation is based on a "pulsed-charging" method of measuring small currents [178, 179].

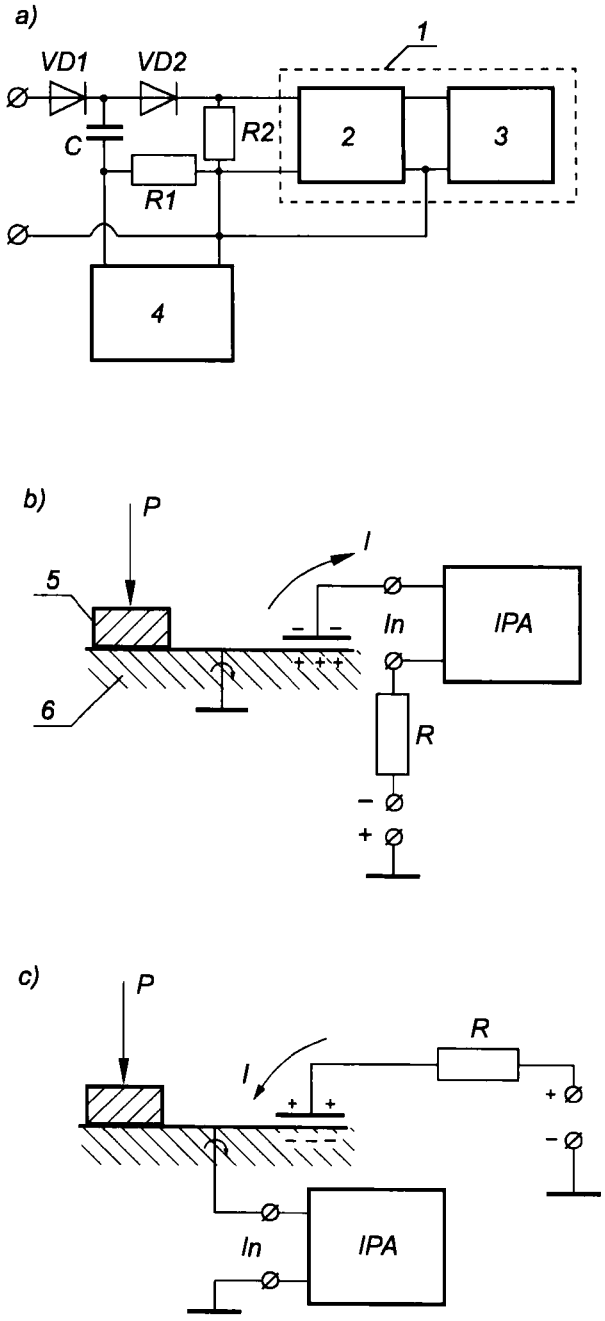

Fig. 4.5. Electrical block diagram of integrating picoamperemeter (IPA-type) (a) and circuit for direct measurements of ionization current (b, c).

The measuring device (Fig. 4.5) operates from an independent power source it is characterized by a high sensitivity, noise immunity, and accuracy. The IPA amperemeter (see Fig. 4.5,a) contains input diode VD1, standard integrating capacitor C, blocking diode VD2, resistors R1 and R2, tunable clock pulse generator 4, and current-pulse integrator 1 consisting of pulsed amplifier 2 connected in series with current-pulse integrator 3. The diodes are connected so that the p–n junction can be only biased by the measured current and the polarity of the generator pulses, so that they bias the p–n junction of the VD1 diode inversely and that of the VD2 diode directly.

The operation principle of this measuring device is the following. The generator pulse charges the standard capacitor to its amplitude. In the time interval between pulses, the standard capacitor is discharged by the current passing through the input diode, the capacitor, and resistor R1. At the times when pulses appear at the generator output (on resistor R1), the capacitor is charged completely through the blocking diode VD2 and resistor R2. The charge by the current through resistor R2 is registered by a current-pulse integrator. The charge at the capacitor is equal to the charge transmitted by the current during the time equal to the generator pulse repetition period. Therefore, by changing the generator pulse frequency, it is easy to measure the input current in a wide range from the integrated charge and integration time (the generator frequency).

High sensitivity to small currents is achieved because capacitor C discharged by the prolonged passage of the measured current, is recharged for a considerably shorter time and forms a high amplitude current pulse at resistor R2. Therefore the input resistance of device 1 can be low ohmic and a pulsed amplifier can be used for amplifying the signal. The current gain of the device is

$$k^* \approx T/\tau_c ,$$

where T is the pulse frequency of the generator;

τ_c is the recharge time of capacitor C.

It shows how many times the amplitude of the capacitor recharging current pulses are higher than the measured current (it can be 10^6–10^8). The gain k^* can be adjusted within a wide range by varying the frequency (the pulse repetition period) of the clock pulse generator. Diode VD1 serves to prevent the capacitor recharge current through the input current circuit.

If the CPD between the reference gold electrode and the sliding surface (see Fig. 4.2) is $V_{CPD} \approx 1$ V and the capacitance of the dynamic capacitor is $C_D = 10^{-12}$ F, then the charge at the capacitor is $Q = 10^{-12}$ C. A change of the capacitance by $\Delta C_D = 10^{-13}$ F at 50 Hz results in the bias current

$$I_b = \Delta Q/\Delta t = 5 \times 10^{-12} \text{ A}.$$

The emission current was estimated by A.L. Zharin from the formula $I_e \geq AV/R_H$, where A is the conversion factor of the dynamic capacitor (for the

capacitor value $C_0 \approx 10^{-13}$ F and modulation frequency ν=14 Hz, $A \approx 10^{-3}$); R_H is the input resistance of the CPD meter (R_H=1 GOhm). For the potential difference between the capacitor plates V_{CPD}=1.5 V (see Fig. 4.3), $I_e \geq 1.5 \times 10^{-12}$ A, i.e. the emission current is of the same order of magnitude as the bias current. Thus, ionization of the gas gap of the dynamic capacitor C_D (see Figs. 4.3 and 4.4) should induce the same ionization current but with the phase opposite to that of the bias current.

At the beginning of the experiment (see Fig. 4.5,b), the potential of the sliding path of lower specimen (disk) 6 is positive (the upper specimen 5 is the pin). The capacitor area in terms of the reference electrode area is 2.5 cm^2. The field strength in the capacitor (i.e. the decelerating field for electrons and negative ions emitted from the sliding path) E is 2000 V/cm. Without friction, the picoamperemeter reads zero. Friction was accompanied by the current generated by positive charges whose density was not stable and depended on the loading regime, speed, lubricant type, etc. Within the limits of the previous friction modes, the current (see Figs. 4.3 and 4.4) was $(1–5)\times10^{-12}$ A. It is likely that positive ions can be attributed, first, to triboplasma after transition from the limiting to the boundary and the dry friction, and, second, to tribochemical reactions and surface ionization due to the desorption of atoms and ions from the surface heated in friction.

Changes in the electric field direction of the capacitor (see Fig. 4.5,c) result in a 10- to 10^2 – fold increase in the current amplitude (for the same friction conditions). In this case the main contributors to the current through the "excited friction surface-collecting electrode (anode) circuit" are negative ions and electrodes.

The mean free path length of electrons is defined by the expression

$$\lambda_e = 5.64\left(\sqrt{2}n\pi d^2\right)^{-1},$$

where n is the number of molecules or atoms per 1 cm^3;

d is the "effective" atomic diameter (cm) [180].

Under normal conditions in air (T=0 °C, P=1013 GPa), $\lambda_e = 5.4\times10^{-5}$ cm. The friction surface produces a low energy electrons which cannot ionize the air. Obviously, the accelerating field strength is not sufficient to cause impact ionization. In the field with E=2000 V/cm, electrons acquire the energy $W = E\lambda_e \cong 0.1$ eV within the free path length. In this case, the free electron lifetime is very short ($t = 6.3\times10^{-7}$ sec) because of a high probability of adhesion to 0_2 and H_20 molecules. As a result, the anode plate of the capacitor attracts negative ions, mainly O_2^- [36, 180, 181], creating the current.

Thus, the experiment has revealed that the limiting, boundary, and juvenile friction modes of metals, cause generation of positive ions in the contact zone near friction surfaces accompanied by a considerably more intensive emission of

negative ions and electrons. Generation of both negative and positive ions has been confirmed by the studies of V.D. Evdokimov [182]. In contrast to exoelectrons, concentration of ions can be measured without using auxiliary illumination.

Thus, the fact of air ionization above the sliding path of two metals in boundary lubrication is experimentally validated and this supports Tissen's deformation model in the run-in. This regularity in sliding can be a basis for developing new methods of testing materials and for automatic control of friction modes including boundary lubrication [98]; testing of lubricants self-lubricating materials; studies of friction processes, etc.

4.3. The Possible Mechanism of the "Servovite" Layers Formation

Microtransfer is a consequence of triboplasma development in particular friction modes. As a result of the triboplasma condensation during its lifetime, all its components appear on the surfaces of contacting pairs. Transfer and deposition of metal particles from the plasma to mated surfaces are independent of melting and boiling points or metal hardness. It is possible that ST of copper particles is induced partly by the triboplasma emergent at local points during the running-in copper alloy–steel pairs in the interactions between microasperities, i.e. due to submicroplasmatic deposition on the contacting surfaces, mainly copper, because the copper strength and melting point are much lower than those of steel, therefore atoms and ions of copper dominate in plasma. Besides, triboplasma stimulates suspension of the components (ions, atoms, and particles of colloidal size) in the lubricant. Because of electrical fields, the suspension fails in direct contact spots stimulating adhesion of copper atoms or ions to friction surface.

Many experimental results can be explained by the microplasma in the friction zone. For example, the fact that in such pairs as glass–steel [183, 184], pig-iron–steel, steel–steel, metal–plastic [185] with a lubricant containing Cu particles and ions, ST occurs only at intimate contact of the surfaces and at sufficiently high specific loads. In acid evolution electrolytes, containing copper ions, copper transfer on the friction surface is independent of the nature of the paired materials. In a plastic–metal pair, copper is transferred both to the metal and to the plastic (fluoroplastic-4). However, the main condition of ST is the presence of water soluble acids (pH<7) and, copper ions in the lubricant. So, the pair 15/13–9b/13 steels, which tends to score in boundary friction, operates normally in ST [185].

ST was also observed in silicate glass–steel pairs in distilled water or petroleum emulsion [183, 184] because glass contains Cu^{++} and Cu^{+} ions produced by oxidizing the melt doped with Cu_20 powder (about 1.5%). Diffusion carries the copper ions to the glass surface which interact with the steel surface and lubricant and partly deposit onto the steel.

Air ionization near the friction surface when the boundary lubrication fails is the main experimental evidence of a highly excited state of the matter in the contact zone (triboplasma) in friction of steel–bronze pairs.

This transfer model is also supported by the fact that fine abrasives (grain size less than 3 μm) accelerate ST [135] since they enhance the chemical activity in the gap and increases the number of local areas of triboplasma evolution.

Besides, study of electric contacts revealed that ST resembled the bridge transfer or the erosion in sliding contacts when electric current is passed (see Chapter 6). Experiments on a modified AE-5 friction machine with grease applied once to the contact zone showed that electric current provides the formation of copper film. How fast the copper film appears and its thickness depend on the current density..

Experimentally bridges were found on the electrodes from various metals and alloys which consisted mainly of the anode material. In copper alloy–steel pairs thermocurrent of substantial density passes through the sites of direct contact of mated surfaces in the direction of copper transfer to steel. Break in the electric circuit between the contact pair and external parts of the device eliminates bridge erosion in bronze–steel pairs. Therefore, the formation of the "servovite" layer on steel should slow down. Experiments show suppression or even complete absence of transfer (no "servovite" film appears) after insulation of the contact pair.

Thus, the behavior of elementary metal transfer processes in wearless friction (ST) may be explained partly by triboplasma evolution and its transfer.

The analysis of the cases when ST occurs, allows to formulate prerequisites.

1. Lubricant (or its decomposition products) should electrochemically affect friction members and to reduce copper.

2. Copper should be present in the contact zone in any form and state (one or both members pairs are from copper, deliberate copper inclusions into the members, copper atoms or ions in the lubricant, copper pipelines in lubricating system, etc.).

3. Local temperature increase in contact which induces release of energy – appearance of the highly excited matter (triboplasma) stimulating selective dissolution of heterogeneous alloys and their dispersion in the lubricant.

4. Presence of inhomogeneous electric fields in the contact due to electrization, appearance of thermal or galvanic EMF or electric current passage.

Copper is not the only metal in friction pairs which is selectively transferred from one surface to another in a very thin "servovite" film yielding the least friction coefficient and wear. Selective transfer is also observed in sliding electric contacts made of gold [80, 81]. Because of the same properties found in mechanical action on surfaces of seven metals (Cu, Ag, Au, V, Cr, Co, Ni) (see 2.4) it may be suggested that ST is inherent to other elements mentioned, not only Cu, Ag, and Au.

4.4. Phenomena at the Interface Under High Pressure and Shear Strain

In terms of mechanics, friction can be expressed as a continuous sequence of simultaneous pressure and shear on the contact surfaces.

Under normal loads of tens of megapascals, which are common in many heavy loaded friction assemblies, plastic strain, shear, and cramping of microasperities. In this case, since the ratio of the actual contact surface area to the nominal one S_{act}/S_{nom} is less than 0.01, on the microcontacts with diameters in the contact plane of about 3 to 50 μm [20], pressure is developed amounting up to several thousands of megapascals. As a result, the actual pressure in plastic contacts of asperities approaches the material hardness. Under an ordinary average normal load of P=20 MPa and $S_{nom}/S_{act}=10^2$ the normal contact stress σ is $\sigma \geq 10^2 P = 2$ GPa that corresponds to HB hardness of some alloyed steels (the deformed copper hardness is 1.2 GPa). So, high pressure (especially during the run-in) accompanied by shear in friction induce some mechanochemical effects, many of them unachievable in other conditions.

Mechanical effects on chemical reactions have been known for a long time. It is described, in particular, by the relation which shows how the chemical potential varies under excessive external pressure ΔP [67]:

$$\mu = \mu_0 + RT \ln \bar{a}\,, \tag{4.1}$$

where μ_0 is the chemical potential of the substance in normal conditions;

$\bar{a} = a \exp((\Delta PV)/(kT))$ is the mechanochemical activity;

a is the thermodynamic activity (concentration of mechanically activated atoms);

V is the molar volume of the substance.

It follows from equation (4.1) that the mechanochemical activity is determined by the chemical potential which is a function of ΔP.

Mechanochemistry deals with mechanical effects on electrochemical reactions [67] and high-molecular compounds [186, 187], kinetics and nature of mechanochemical reactions in solid inorganic materials and metals [188, 189] etc. Let us consider some experimental studies of the combined action of high pressure (HP) and shear deformation (SD) on a solid in friction. It is this combined action that produces some unexpected results [190]. The first who discovered relation between high pressure and chemical transformations was Bridgeman (1937). More recently it was found that apart from traditional parameters that influence chemical reactions (pressure, temperature, reactant concentration), the shear stress is a substantial factor changing the reactivity by orders of magnitude [191, 192].

Such abnormal reactivity of substances in plastic flow is caused by the deformation of electronic shells, breakage of chemical bonds [193, 194] it manifests itself both in alternating directions of chemical reactions and in shifting the equilibrium towards products with smaller volumes [195]. This process is

accompanied by intensive crystal degradation, changes in macromolecular conformity of polymers [196], and intensive mixing at the atomic level [197, 198] as a result of which the mass transfer rate becomes abnormally high.

Degradation of molecular and metal crystals is caused both by the action of high pressure alone and by the combined action of HP and SD. A minimum size of various crystals, split by high pressure in combination with shear revealed by X-ray diffraction, is 5–10 nm (the threshold of the method sensitivity). The crystal size determined by various methods [199, 200] has the same order of 2–3 nm.

The fact of mixing under HP and SD at the molecular level is shown convincingly in the electron paramagnetic resonance (EPR) study of the behavior of spin-labelled macromolecules and a stable radical (2,2,6,6-tetramethylpyperidin-1-oxyl) introduced into a low-molecular crystal matrix (triethylendiamin) [196]. Selection of the objects excluded the influence of transformations on the experimental results at HP and SD. Spectra of the specimen containing the stable iminoxylic radical in concentration 10^{17} spin/cm^3 after grinding in a mortar with triethylendiamin (curve 1) and after the action of HP and SD (curve 2) are presented in Fig. 4.6. It shows that HP and SD increase the distance between the radicals due to substantial attenuation of the dipole or exchange interaction as the main contributor to the line broadening, and hyperfine splitting. Thus, under HP and SD the volume distribution of radicals is more uniform which is indicative of mixing at the molecular level.

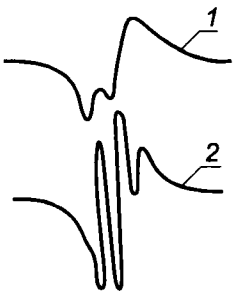

Fig. 4.6. EPR-spectrum of specimens after grinding in a mortar (1) and HP and SD action (2) [196].

Many questions in studies of HP and SD have not been answered as yet. So, the mechanism of a substantial increase of the mass-transfer rate is not clear enough. Meanwhile, experimental results demonstrate new feasibilities of the HP and SD for effective excitation of many solid phase reactions. The HP and SD leads to monomer polarization [197, 201], crystallization of amorphous alloys [199], appearance of metall complexes [148, 149] and solid solutions of unlike metals [198, 200], evolution of high-conductance of metal-polymer compositions [202, 203] etc.

Investigation of organic polymerization at HP and SD is of special interest to tribology. Since 1958 [204], when amorphous high-molecular products were found for the first time in friction of the platinum group of metals, extensive studies have been carried out, first to eliminate evolution of polymers impairing electric contacts, second, to induce tribopolymers and to maintain continuous generation of the polymer film destroyed and removed in friction since polymers decrease markedly the wear.

Apart from the HP and SD conditions, the nature of produced polymers

depends on the nature of the hydrocarbons in the lubricant base and additives. In particular, solid amorphous materials are produced mainly in the presence of unsaturated and aromatic hydrocarbons [201]. It has been found that in friction under severe loading conditions the benzene ring breaks and it transforms into an aliphatic hydrocarbon from which a polymer results subsequently. A model experiment [193] using an apparatus of Bridgeman's anvil type [205] showed that under HP and SD mononuclear aromatic compounds react actively, break the aromatic ring and form products incorporating polyenic chains. In this case, the pressure corresponding to initial transformation of aromatic compounds depends on the shear stress τ of the indifferent matrix incorporating an aromatic compound. The lower the stress, the higher τ. Results of studies of the influence of additives on the reactivity of aromatic cycles [193] suggest the radical mechanism of transformation of aromatic compounds under HP and SD. The same conclusion was made when studying a possibility to suppress polarization in friction by introducing some organometallic and iodine-containing compounds able to terminate chain reaction into organic media (lubricants) [146]. According to other data, the polarization mechanism can be either radical or ionic, depending on pressure under shear [206]. This conclusion was made in the study of polarization of unsaturated stable iminoxylic radicals under HP and SD. Polarization of these radicals under common conditions is impossible due to steric hindrances.

Formation of metal complexes improving the tribological properties of pairs under HP and SD is also essential for tribology. The formation of metal complexes in the porphyrin–metal system under HP and SD was studied and the activation energy of complex formation in the tetraphenylporphyrin (TPPn) – copper acetate (TPPn–$CuAc_2$) system was evaluated [195]. It appeared five times lower than the activation energy under common reaction conditions. Porphyrins are chosen as an object because the porphyrin ring is an active ligand in complex formation of different metals [207]. Metal complexes of porphyrins are usually produced at increased temperatures. At room temperature the metal complexes were obtained from a mixture of powder porphyrins and metal salts or pure metals at high pressure (P=1000–6000 MPa) and shear deformation [195]. It was found that the metal complex production was independent of the porphyrin structure (porphyrins were different in structure and stability) and slightly depended on a complex-forming metal. It indicates that HP and SD influence primarily the structure of the electronic cloud of organic molecules. It explains the absence of substantial differences in the reactivities of particular porphyrins.

The complex-formation effect depends on the nature of counterions in the metal salt. The best results were obtained with metal acetates, in particular, with copper acetate and TPPn the yield was 100% [195]:

$Cu(OCOCH_3)_2$	$Cu(NO_3)_2$	$CuCl_2$	$CuSO_4$	Cu_2O	CuO	Cu
100	79	64	45	45	5	5

Isolated atomic metal particles or cations are important for the redox reaction in the metal complex formation. In the case of copper oxide (I) the resulting atomic copper is attributed in [195] to the oxide decomposition as $Cu_2O \rightarrow Cu+CuO$, it explains a relatively high (45%) metallocomplex yield in the presence of copper oxide (I) in the initial mixture against copper oxide (II) and metallic copper (5%). Reaction of copper complex formation with TPPn is assumed as $TPPn-H_2+Cu \rightarrow H_2+Cu-TPPn$.

Isolated metal cations not combined with the counterion under HP and SD result from the salt crystal lattice plane shift and exposure of juvenile surfaces with noncompensated bonds. The complex-formation scheme (bivalent metal salt hydrates are used) without solvents can be assumed the following:

$$MeX_2(H_2O)_m+H_2Pn \rightarrow MePn(H_2O)_n+2HX(H_2O)_r+(m-n-2r)H_2O.$$

The activation energy of this process, as of other types of chemical interactions under HP and SD, is much lower than that in conventional reaction. For example, the energy barrier for the reaction initiation in the TPPn–Cu system under HP and SD evaluated from the temperature dependence of the reaction yield appeared five times lower [195].

Formation and decompensation of complex compounds are observed in suitable media at friction [146–148]. Presence of metal complexes on contacting surfaces decreases the friction coefficient and wear. Addition of 8-oxychinolin into the petroleum lubricant favors formation of bivalent copper complexes (bivalent copper 8-oxychinolinate) in copper alloy–steel pairs which improves the antifrictional behavior of lubricants. A copper complex is formed on the contacting surfaces as a multimolecular crystalline layer less than 100 nm thick. In the case of nickel an amorphous coordinated compound is formed [148]. A probable complex-formation mechanism (for bivalent copper salicylalanilinates) is suggested in boundary friction of copper–CuSn6 bronze pair in solution of some salicylalanilinates (1% alcohol solution was used) [146].

The tests were carried out on an end-face friction machine at pressure 5 MPa and sliding velocity of 0.3 m/sec; roughness of the contacting surfaces was of class 6 ($R_a \approx 2$ μm). After 20 min of testing the yield of the metal complex with a plane square structure was 20–30% of the theoretical limit. According to [146] such a complex is not formed under ordinary conditions by boiling alcohol solutions in the presence of copper powder. It is high pressure in combination with shear deformation that causes chemical interaction of the ligand with the metal. The suggested scheme of complex formation is presented in Fig. 4.7. Pressure and shear deformations in the metal contact produce juvenile surfaces with unsaturated chemical bonds which are highly active and consequently, short-lived centers of chemosorbtion of ligand molecules (see Fig. 4.7,a). Reorientation

of the molecules (see Fig. 4.7,b) is accompanied by electron transition from the metal atom to the ligand, hydrogen results in forming the Me–O valence bond and the donor-acceptor Me–N bond formed simultaneously. Break of the weakest (Cu_{lat}–Cu_{com}) bond by shear causes separation of the complex and its transition into the lubricant (dissolution).

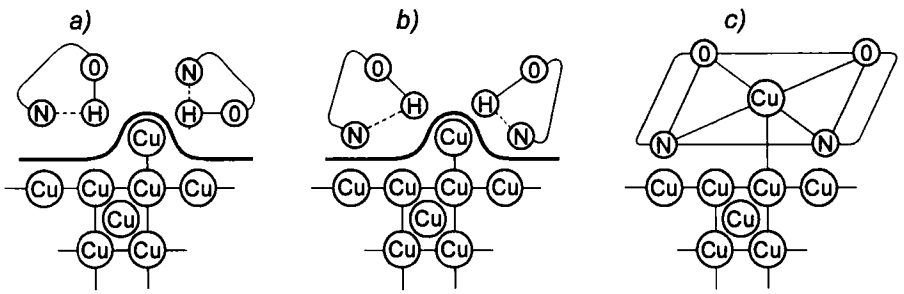

Fig. 4.7. Evolution of bivalent copper salicylalanilinates: a) adsorbtion; b) orientation; c) complex formation [146].

Introduction of particular isomeric aromatic Shiff's bases into the copper-containing plastic lubricant based on the "Lita" lubricant (GOST) is favorable for complex formation and improves substantially the characteristics of a metal-doped lubricant [208]. In this case, it was found that characteristics of the stereochemical molecular structure of additives had a substantial influence on their ability to participate in the complex-forming reactions. For instance, compounds containing OH^- and O_2^- groups in meta- and orthopositions are preferable for a complex formation over pair-substituted sites, in other words, that is the structure of the complex-forming molecules is more important than their elementary compositions in particular conditions.

One of solid antifriction additives usually introduced into lubricating materials is graphite. Added to a grease, it improves the antiwearing, antiscoring, and other characteristics of the lubricant, moreover such lubricating compositions decrease friction and wear at very high load and temperature. The working mechanism of antifriction dopes (graphite, in particular) are studied insufficiently [209]. Low friction coefficients of graphite-containing lubricants are explained only by their scale structure. Therefore laboratory studies of iron and carbon behavior under HP and SD with Bridgeman's anvils [210] are of great scientific and practical significance.

The studies were carried out at pressure from 1 to 6 GPa at room temperature. Fine-grained carbonyl iron (Fe) or ferrocene $(C_5H_5)_2Fe$ (Fer) and graphite (G) were used in the experiments. Mössbauer spectroscopy of specimens (60:40 Fe–G mixture) after HP and SD has shown that iron particles reduce in size presumably up to the atomic state and react with graphite producing Fe_3C and a complex of

atomic zero-valent iron with graphite (Fe^0–G), where atomic iron is located in the graphite interlayer. It has also been found that α-Fe microclusters of various sizes are formed inside graphite.

In 50:50 G-Fe specimens Fe^0–G complexes (due to destruction of about 30% of Fer molecules) appear after HP and SD where iron atoms (about one fifth) are located in the interlayer regions and atomic Fe+G complexes with iron atoms are located on the graphite surface. It is found that the reaction of Fe–G complex formation can occur not as a result of Fe decomposition to the atomic state but because of substitution of graphite for cyclopentadyenil ferrocen under HP and SD.

The results suggest that plastic flow may lead under high pressure to complex formation reactions with other complexons also.

Studies of the HP and SD effect on metals are highly noteworthy since the metals make the majority of friction assemblies in which high pressure on contact cause plastic deformation.

Characteristics of diffusion in metals and alloys under HP and SD were reported in some publications [198–200 etc.]. They revealed the mixing of materials at the atomic level, producing solid solutions and intermediate phases.

Mixing of polymers or molecular crystals at the molecular level releates to the overcoming of week Van der Waals forces; such mixing under HP and SD at the atomic level involves breaks of bonds with energies and diffusion activities of several orders larger than those typical for the liquid metal state.

Plastic flow enhances mass transfer despite counteraction of the hydrostatic pressure which inhibits diffusion [211, 212]. Plastic deformation at high pressure accelerates interaction between metals so much that material, with similar phase composition can be obtained from a roughly dispersed mixture without any heating.

A higher diffusion coefficient with simultaneously reduced activation energy under HP and SD suggests that greater diffusive activity can be attributed to the development of a branched boundary network (where surface and boundary diffusion is characterized by a lower activation energy) rather than to changes in the diffusion characteristics of a material since omnidirectional compression load can only increase the activation energy of diffusion through the lattice [212].

Under HP and SD the grain pulverization (increase in the grain boundary length, pulverization of the grain substructure involving emergence of an additional boundary network, network of cracks, loosening and other similar structural defects) should increase the diffusive activity. It is suggested that under such conditions the material near the boundaries is presumably in the state of dynamic amorphism maintained by plastic deformation.

Monolithic specimens 8 mm in diameter and 1–2 mm thick were obtained from a set of alternating copper and zinc plates, each 0.10 mm thick, under pressure 1.5 GPa and shear deformation of various extent $\mathscr{E}$ (by turning Bridgemen's anvil

male die with a specified revolution number n) [200]. X-ray diffraction and metallographic analyses of these specimens determined their phase composition and grain sizes. The plastic shear deformation was found from the relation $\mathfrak{F}=2\pi rnh^{-1}$, where $r\geq 13$ mm is the distance from the rotation axis; h is the thickness of the plastic deformation zone. The male die speed was 8 deg/sec, temperature variations did not exceed $\Delta T=15$ K.

First, as $\mathfrak{F}$ rises, the specimens become strongly pulverized. The interlayers with thickness of less than 20 μm for zinc extend in the shear direction. The intermediate ε-phase grows on the Cu–Zn contact in every direction and through the specimen bulk. The sequence of phase transformations in samples under HP and SD differs from that in the reaction diffusion without plastic deformation when the γ-phase appears first and other phases are not formed at all, if the temperature is below 523 K.

At $\mathfrak{F}=80$ growth of the ε-phase reaches the maximum and stops. Then a combination of Cu–ε–Cu interlayers prevails in the samples (the zinc concentration decreases to 23%) and deformation distributes uniformly over the phases. As a result, the most favorable conditions for further growth of the γ-phase with greater $\mathfrak{F}$ are created. The γ-phase interlayers are very small, close in size to 50 nm areas, as coherent scattering of Roentgen rays show in this phase.

Solid zinc and copper solutions are formed in the combination of Cu–γ–Cu phases prevailing in the specimens with $\mathfrak{F}>200$ and already at $\mathfrak{F}\approx 300$ the base of the specimens is made up by γ- and α-phases, their amount depend on the deformation extent (Fig. 4.8).

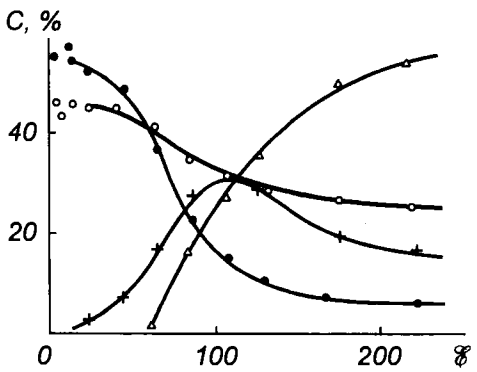

Fig. 4.8. Phase shares in specimens versus deformation extent [193]: •) zinc; o) copper; +) ε-phase; ∆) γ-phase.

Mechanical mixture of unlike metals under HP and SD is a thermodynamically unstable system, therefore other phases appear upon their contacts. A deformed state is nonequilibrium. The diffusion coefficient in the surface layer (in particular, in grinding, milling, sandblasting, or water-borne san polishing) exceeds that in

the electropolished specimen by a factor of $10–10^3$ [84, 213], i.e. the interface diffusion coefficients increase by several orders of magnitude. In this case the diffusion acceleration is due to the structural dispersing in deformation, appearance of a large number of surface defects, their high density causes a highly metastable deformed metal structure.

It is assumed [200] that the phase evolution is determined by the resistance to plastic deformation. Thus, the ε-phase appears first (microhardnesses of copper, zinc, and ε-phase are 1.2; 0.6; 1.1 GPa, respectively); then the γ-phase follows. The latter appears in conditions needed for its plastic deformation (H=4.7 GPa) which is achieved after forming a dispersed phase mixture with the least soft component (zinc).

Thus, large plastic deformation, degradation, accelerated diffusion, and phase transitions are realized under HP and SD. Since the same effects are also observed in superplasticity, it is suggested that the atomic mechanisms of these phenomena are similar [200]. In particular, the above mentioned increase in the diffusive mobility of atoms near the boundaries is attributed to the growing vacancy concentrations due to the superplasticity mechanism [214], because they are evaluated in these cases close to the value of the volume effect in melting. The diffusion coefficients along the grain boundaries are close in the order of magnitude to the liquid state near the melting point and equal to 10^{-10} m^2/sec [200].

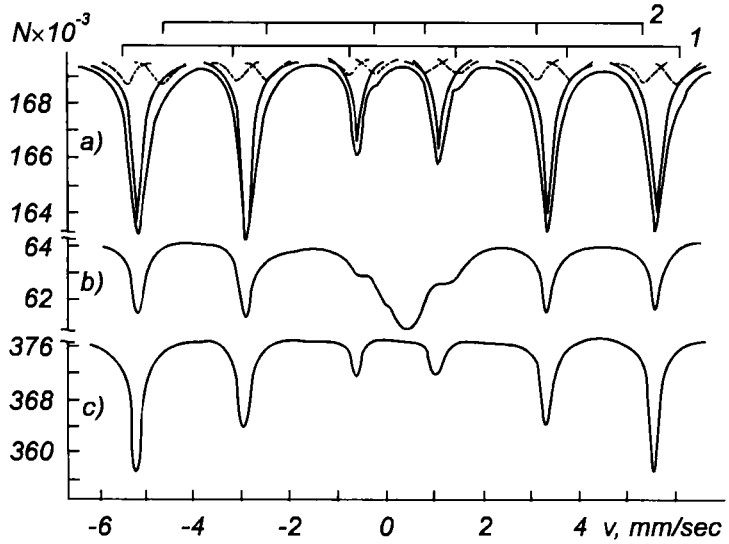

Fig. 4.9. Mössbauer spectra of specimens subjected to HP and SD [198]: a) 50:50 iron–nickel mixture (solid line refers to iron spectrum; dashed lines refer to solid solution or FeNi compound, their positions are shown by vertical dashes (sextets 1 and 2)); b) 50:50 iron–copper mixture (position of an additional line corresponding to solid solution); c) metallic iron.

Let us consider the formation of solid solutions in Fe–Ni, Fe–Cu systems under HP and SD [198]. Specimens from a mixture of powders with 50:50 Fe–Cu composition and 50:50 and 70:30 mass % Fe–Ni composition with grain sizes of 50 to 120 nm, were tested in the Bridgeman anvil type apparatus at P=4 and 8 GPa under SD. The structure and phase composition of the specimens were analyzed by Mössbauer spectroscopy. In nuclear gamma-resonance (NGR) spectra of ^{57}Fe nuclei Fe–Cu (Fig. 4.9,b) and Fe–Ni (Fig. 4.9,a) mixtures under HP and SD, lines were observed which, in comparison with the lines of the nonchanged spectrum of pure iron (Fig. 4.9,c) show evolution of binary phases in powder mixtures. A single broad line in the spectrum of Fe–Cu mixture (see Fig. 4.9,b) is typical of the spectra of aged solutions of iron in pure copper where iron atoms are partly clustered. The doublet line with a lower intensity and splitting of 0.6 mm/sec corresponds to the initial stages of aging of solid solutions when iron atoms form pairs. The total amount of iron introduced into the copper matrix was estimated about 10–15%.

In the spectrum of Fe–Ni mixture (see Fig. 4.9,a) two sets of low intensity lines were found by graphic subtraction of the metallic iron lines of corresponding intensity from the common spectrum of the mixture. Thus it was possible to reveal evolution of the disordered volume-centered cubic solid FeNi solution with 10% Ni content and the ordered NiFe compound in the mixture subjected to HP and SD [198].

While in the previous case [200] the growth of atomic diffusive mobility was attributed to the growing vacancy concentrations near the boundaries of grains and mixture particles, in this case very large effective diffusion coefficients are explained mainly by production of substantial number of dislocations, their clusters considerably enhance mass transfer. Plastic shear at high pressure lowers the diffusion activation barriers, initiates the ascending (along the defects) and drifting (together with the defects) diffusion of the mixture components. Besides, diffusion increases several orders at the boundaries between differently oriented grains and within a single grain, along the boundaries between mosaic blocks [213]. The number of these boundaries is infinite in powder mixtures.

Before [198, 200] formation of binary phases under HP and SD from dispersed mixtures was mentioned. However, under HP and SD binary crystal phases can also be produced when the initial system is an amorphous alloy [199]. A considerable mobility of atoms in the components cannot be due to the dynamics of the dislocation structure at all. The vacancy mechanism is likely to be the basic in the mixing at the atomic level. For crystal materials the interaction of dislocations by applied loads produces excessive vacancies and these vacancies are responsible for increased diffusive activity [212].

Structural changes in amorphous alloys at increased diffusion of atoms caused by HP and SD are determined by the fact that they are more favorable as regards energy in particular conditions. X-ray diffraction and NGR studies show that the

plastic flow is a vital factor at high pressure [199]. High pressure alone produces no changes in amorphous specimens, such as amorphous Fe–B alloys with boron content 15 at % (15B) and 17 at % (17B) subjected to pressure 8 GPa at room temperature.

HP and SD cause partial crystallization, characterized by the release of α-Fe (as in the thermal crystallization) and metastable Fe_3B alloy phases. It is due to a substantial increase in the intensity of metallic iron lines in the NGR spectra, appearance of two systems of additional lines and lower peaks in the crystallization heat generation curves (since the amorphous volume of alloys decreases after treatment) obtained from the differential thermal analysis (DTA) (Fig. 4.10). In 17B alloy both these phases crystallize simultaneously at temperatures about 700 K and in 15B alloy α-Fe crystallizes at temperatures about 685 K, Fe_3B at temperatures about 723 K.

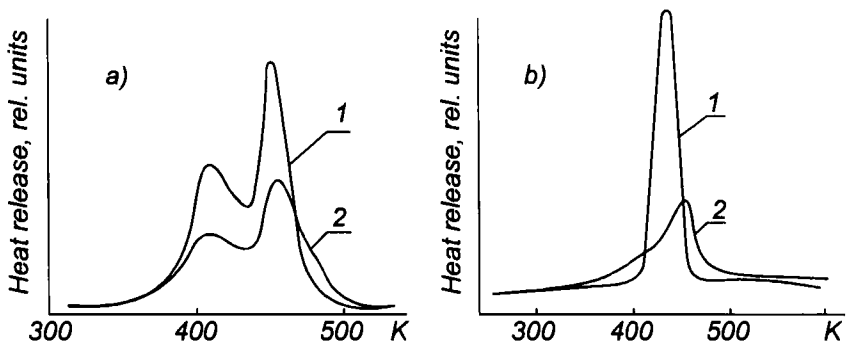

Fig. 4.10. The DTA data for the Fe–B (15 at % B) (a) and Fe–B (17 at % B) (b) alloys: 1) initial amorphous alloy; 2) after HP and SD treatment; heating rate is 10 °C/min [199].

Analysis of NGR spectra and electron-microscopic studies of HP and SD treated 17B alloy reveal the presence (apart from the initial solid amorphous solution) of three crystal phases (against two in the thermal crystallization), volume-centered cubic α-Fe, tetragonal and orthorhombical Fe_3B of two modifications. Characteristic dimensions of the phases are 2–3 nm. It is suggested [199] that differences in the crystal structure of Fe_3B after HP and SD and after heating are caused by the difference in volumes of elementary cells: a crystal structure of a smaller specific volume is energetically more favorable at high pressure.

4.5. Periodicity of Processes in Surface Layers During Friction

Surface processes during friction of metals and alloys in any media involve nucleation, propagation, and coalescence of dislocations, or their structural

dynamics in surface layers. External friction followed by plastic deformation is accompanied by variations of the dislocation structure.

Investigation of the dislocation structure is vital for experimental physics and chemistry of friction, lubrication, and wear. It provides a deeper insight into the nature of friction surface interactions.

Discovery of the periodicity of electrophysical and strength properties of surfaces in friction as a basis of the mechanism of the theory of fatigue failure of the surface layer (delamination wear) is one of the most important achievements of experimental physics of friction. The main reasons which led to the discovery of this phenomenon are, first of all, unceasing research aimed at finding the relations of wear at the microscopic level. These relations allow to find means how to reduce significantly friction and wear.

For the first time, serious attention has been given to the periodicity of surface behavior (the periodicity of defect accumulation with subsequent failure of a thin surface layer) when studying cyclic micro- [215] and macrostresses [216] in the surface layer in friction. Later on, the periodicity of microhardness [217], wear [218], friction coefficient [219], electric resistance [220], dislocation density from the broadening of X-ray diffraction lines [217, 221] etc., were found. Attention is mainly given to the few-cycle fatigue exhibited in the region of relatively high stresses which direct the supplied energy to the generation of microcracks during the first loading cycles.

Few-cycle fatigue is manifested by experimental curves of relative changes of electric resistance $\Delta R/R$ and diffraction line (220) width $\Delta B/B$ of α-Fe of specimens from steel C45e in dry sliding over a cylindrical surface of 1/XVII bearing steel at contact pressure of 1.3 GPa (Fig. 4.11).

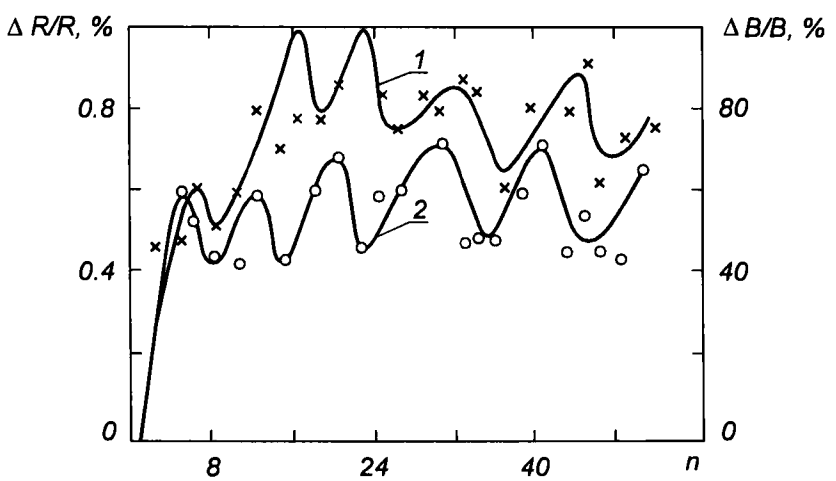

Fig. 4.11. Relative broadening of diffraction line (220) of α-Fe (1) and relative change of electric resistance (2) versus cylinder runs (specimen thickness is 0.2 mm) [220].

Accumulation of plastic deformation in friction [222] is characterized by a periodical curve explained by accumulation of defects in the crystal lattice [220], in accordance with Kragelsky's theory of friction fatigue [22, 225]. Increased defect density under repeated action on the specimen persists until a certain critical value when macroscopic surface defects (microcracks) appear. Later on, this process as the shape of curves 1 and 2 (see Fig. 4.11) shows it.

In 1973, started by N. Suh [223, 224] the theory of the delamination wear appeared which explained numerous friction relations observed experimentally. According to this theory, in the case of repeated slidin of one metal surface on the other defect accumulation in crystal lattice due to dynamic interaction of surface asperities takes place not directly on the external surface of the metal in friction but at some depth. Further accumulation and coalescence of defects under the surface leads to cracks and voids parallel to the surface. When the size of cracks becomes critical, the surface metal layer is sheared off in the form of a scale.

Dynamics of the process is not yet understood completely. However, though the theory of delamination wear is based on microscopic concepts, its macroscopic manifestations should be expected. For example, it may be suggested that the scaly debris separate from the sliding surface simultaneously rather than spontaneously. It follows that all the points on the sliding surface are exposed to approximately equal stresses produced by the second specimen of the pair. Besides, additional synchronization of wear scale separation may be due to increased tangential load on the nonseparated layer when asperities of one surface get into valleys on the other surface formed after separation of wear scales [56].

After removal of the scales the exposed underlying layers which have been walls of the former subsurface voids and cracks would experience to the same stresses from the counterbody. Thus, periodical processes should take place which are caused by accumulation of subsurface defects in the crystal lattice of exposed layers followed by their destruction.

This can occur in the region of the pure or so-called, multicycle fatigue at stress amplitudes below some critical value. Initial period a predominant subsurface layer flow is observed. This peculiarity in the surface behavior can be explained by the fact that surface grains and grains in the bulk of the metal are not equipotent as regards possible development of plastic deformation. Plastic deformation in surface grains is facilitated by the following factors: possible dislocation emergence on the free surface; lower stress exciting the action of Frank-Reed's sources since dislocation sources in the surface grains are mainly shaped as loops fixed at one end; preceding vacancy emergence on the surface that inhibits barrier evolution, as a result, slowing dislocation coalescence [226]. Multicyclic fatigue is divided into three periods [58]: incubation period involving a predominant plastic flow of a thin surface layer with thickness of an order of the size of one or several grains increasing its strength (due to the emergence of

separate dislocations on the surface, dipole formation, and development of a cellular structure); reversible damage (nucleation and development of submicroscopic cracks); irreversible damage (growth of microcracks into macrocrack).

If the model holds true, physical parameters of the metal surface, primarily surface energy and the electron work function connected with it, should show periodical variations. Indeed, the periodicity of variations of the surface EWF directly in sliding was found [52] experimentally [98] using a circuit with dynamic capacitor [50]. Some parameters of the apparatus: a reference gold electrode with a diameter of 1 mm was placed at a distance about 0.5 mm above the sliding path; the sliding path width depends on the diameter of specimens (pins) and is equal to 7 mm, i.e. it records EWF directly during sliding. In all the experiments below the angular rotational velocity of the disk was 0.43 sec^{-1} or equivalent to the relative sliding speed of 0.09 m/sec. The measurement error, together with EWF drift of the reference specimen, did not exceed 5 meV.

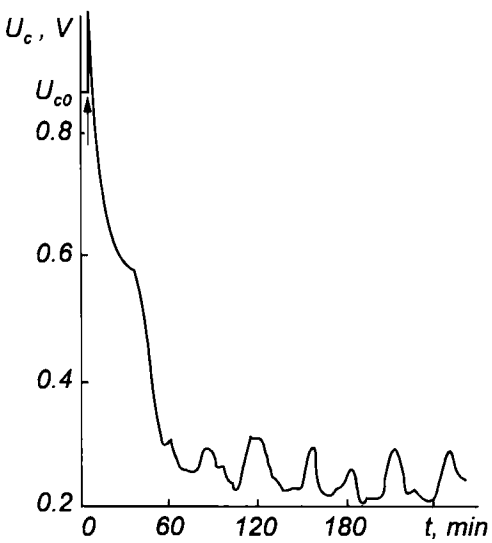

Fig. 4.12. Kinetics of external CPD in dry sliding between the surface of specimens (CuZn37 brass disk and CuSn6 bronze pins) and reference golden electrode; the arrow marks sliding start: load P = 0.05 MPa.

Kinetics of the contact potential difference (CPD) typical for many materials is presented in Fig. 4.12 [52]. Before sliding starts, the initial CPD is recorded for a brass disk. At the initial time CPD decreases from the initial to the steady value abruptly. This is the stage of destruction of oxide and absorbtion films, exposure of juvenile surfaces, and the running-in of sliding surfaces. This stage

lasts about 1 h (the stage of structural adaptation of the friction surfaces), a microrelief, optimal for particular conditions, is formed, friction-induced structural defects nucleate on the surface and in subsurface layers. Thus, from the shape of the CPD–time curve one can find the duration of the running-in period.

In steady-state operation changes in EWF of a surface in friction are periodical with an amplitude of up to 100 meV. The measurement error did not exceeds 5 meV, thus it can be inferred that these periodical variations are induced by the nature of physicochemical processes taking place on the surface rather than by a systematic error of the method.

The amplitude and duration of periodical EWF variations depend substantially on the conditions of friction. In Fig. 4.13 such periodical variations are shown at various normal loads. In Fig. 4.14 the EWF amplitude and oscillation period are plotted versus the normal load. Every point in Fig. 4.14 is a result of averaging over 10–15 oscillations. It can be seen that the variation amplitudes of EWF show a greater dispersion than the periodicity. It can possibly be due to a high sensitivity of the surface EWF to slightest changes in external conditions.

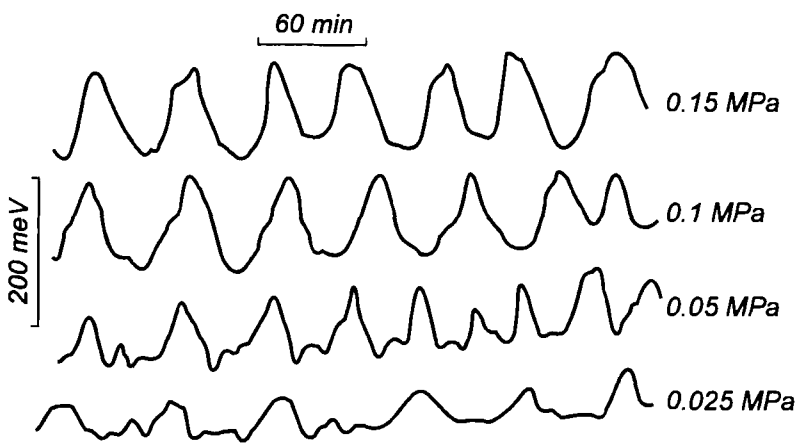

Fig. 4.13. Periodical EWF variations of CuZn37 brass surface in dry sliding on CuSn6 bronze and different normal pressures.

Periodical EWF variations for a particular sliding mode (see Fig. 4.14) take place during 10^3–10^4 disk rotation cycles (pins are fixed). Because of the contact roughness and simultaneous action of three upper specimens (pins) on the friction surface, the number of action cycles N is over an order higher. Since $N \geq 10^4$ to 10^5, in accordance to the criteria of [227], the multicyclic friction fatigue of the surfaces occurs in this case.

Initially, as the normal load rises, the EWF variation amplitude increases and the period decreases (see Fig. 4.14). Then, beginning with the load about

0.075 MPa, these parameters remain practically unchanged. Two factors control the rate of delamination wear [228, 229]: the void nucleation rate in the subsurface and the propagation velocity of subsurface cracks. As the load rises, both these processes intensify, exciting more all structural surface elements, naturally reducing the EWF (increasing the CPD). Therefore, the period of crystal lattice defect accumulation in the subsurface layers is shorter, followed by rapid development of cracks parallel to the surface, and eventually by stronger wear.

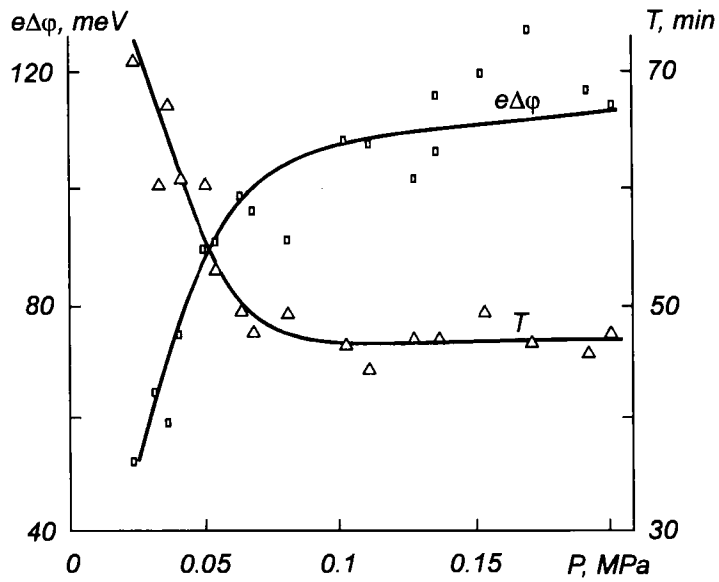

Fig. 4.14. Amplitude and duration of EWF variations between the CuZn37 brass surface and reference gold electrode versus normal load during sliding.

Further investigation of the EWF periodicity was carried out by A.L. Zharin, who used conventional and alternative methods. We will briefly discuss his results. Concurrent investigation of the specimens by conventional methods (optical and scanning electron microscopy, microhardness measurement, X-ray spectral analysis) requires to stop the friction machine, remove and prepare specimens. It is possible because the surface "remembers" the EWF variation periodicity phase long time after sliding (Fig. 4.15).

As it should be expected, the surface has the largest number of macroscopic defects in specimens with the maximum CPD and the smallest number of defects with the minimum CPD. Intensive development of cracks parallel to the surface corresponds to the middle ascending portions of the CPD curve. In such conditions (dry sliding) the cracks were about 40 μm deep. Microhardness HV is maximum on the surface and smoothly varies over the sample depth d; it is approximated

mainly by a smooth power function of the form $HV=ad^b$, where a, and b are the parameters of the curve having a break (double distribution) on its descending portion when average EWF values are achieved, i.e. in the specimens with subsurface cracks. The curve break is caused by the cracks and hardening in the surface layer underlying the cracks, producing the microhardness distribution similar to that of the external surface layer. The minimum hardening corresponds to the minimum EWF.

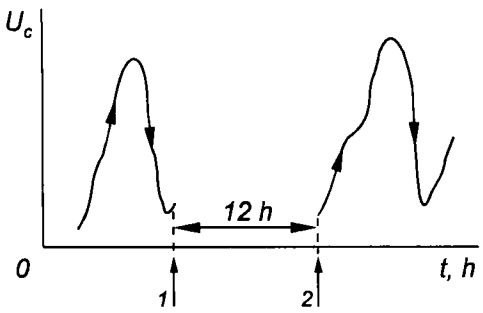

Fig. 4.15. Effect of storing ("memorizing") of CPD variation periodicity phase after interruption (1) and resumption (2) of friction.

Thus, an approximate picture of local surface layer failure can be in accordance with the results and the theory of fatigue failure. During of the EWF variation period, as the number of friction cycles increases, dislocations nucleate in the deformed subsurface layer, then submicrocracks appear and grow, making the material loose. Then microcracks appear, loosen it more and local plastic flow follows. The final stage is characterized by the growth of cracks parallel to the surface which produce pores and brittle local failure of the material by flaking.

This wear mechanism is confirmed by the results of studies of some materials and, in particular, by the absence of EWF periodicity on the friction surface of Cu-ETP copper (Fig. 4.16,a). In copper the surface wear exceeds the fatigue wear due to the defect packing high energy (about 6×10^{-2} j/m^2 against 5×10^{-3} J/m^2 for CuZn37 brass and other copper alloys), defects cluster, cracks nucleate slower in the surface layer.

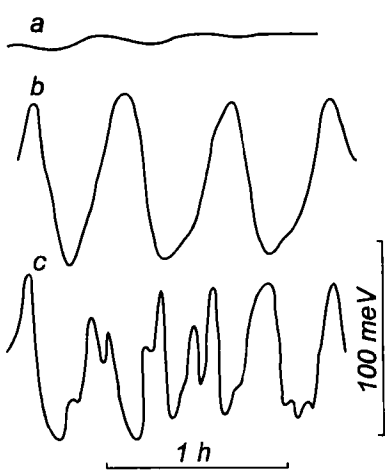

Strict periodicity of EWF variation is only typical for single phase solid solutions (for example, for CuZn37 brass, see Fig. 4.16,b). From the shape of the CPD kinetic curve materials with disordered periodicity of EWF variations were grouped and a more complex spectrum of EWF variations was found (see Fig. 4.16,c). This group includes multiphase solid solutions and dispersion-hardened

Fig. 4.16. The CPD kinetics of Cu-ETP copper (a), CuZn37 brass (b), CuAl8Fe3 bronze (c) during sliding.

alloys. Multiphase composition, dispersed solid inclusions, and secondary structures create a large number of centers where defects stop and accumulate, as a result, various mechanisms of fatigue crack nucleation are involved.

The results of EWF measurements are not sufficient to calculate the dislocation concentration, they provide only indirect information on their behavior. The dynamics of dislocations behavior can be exposed directly by recording variations of the ferromagnetic resonance (FMR) line width in ferromagnetics subjected to plastic deformation.

Broadening of the FMR line in a ferromagnetic subjected to plastic deformation is caused mainly by the presence of the linear defects-dislocations [230, 231]. For the first time, the increase of the FMR curve width ΔH has been found experimentally in nickel because its magnetization of saturation j_s is substantially smaller than that of other ferromagnetics. The relation between this parameter and ΔH has the form [231, 232]:

$$\Delta H \sim \lambda^2 j_S^{-3} , \tag{4.2}$$

where λ is the magnetostriction constant.

Plastic deformation of iron produces ΔH of about two orders of magnitude less than that of nickel. This properties is responsible for a wide use of nickel in such experiments.

The relation between the FMR line broadening, ΔH, and the dislocation concentration ρ is the following [230]:

$$\Delta H \approx \omega_0 a^2 \rho , \tag{4.3}$$

where ω_0 is the FMR frequency;

a is the lattice constant.

Relation (4.3) is valid if the FMR frequency is not too close to the minimum frequency of Waker's variations (natural, so-called, magnetostatic irregular variations) and characteristic dimensions R of dislocations (it is assumed that the distance between dislocations is of the order of R) are large enough to satisfy the condition

$$R >> a\sqrt{k\theta_c / (\mu_b M_0)} .$$

Here θ_c is the exchange constant with the order of magnitude of the Curie temperature;

k is the Boltzmann constant;

μ_b is the Bohr magneton;

M_0 is the magnetic moment of unit volume.

As a rule, the dislocation density is calculated in terms of FMR line broadening in plastically deformed nickel from the expression [231]:

$$\Delta H = 10^{-8} \rho \tag{4.4}$$

The average frequency of collisions of spin waves with **k**=0 with dislocations has its maximum at

$$R \approx a\sqrt{k\theta_c / (\mu_b M_0)}.$$

The dislocation density ρ in ferromagnetic is of the order of R^{-2}. Then, if M_0 has the order of 10^{-1} T, $\theta_c \cong 10^3$ K and $a \cong 10^{-8}$ cm, ρ is equal to

$$(\mu_b M_0 / k\theta_c) a^{-2} \approx 10^{12} \text{ cm}^{-2}.$$

Such concentrations can occur in plastic deformation and friction, they contribute substantially to ΔH. The dependence of ΔH on the deformation level of polycrystalline nickel may be an example (Fig. 4.17) [233]. Nickel of 99.99% purity with the initial gain size of about 240 μm was annealed before rolling at 973 K in 0.26 mPa vacuum for 4 h. At room temperature the maximum resonance line broadening exceeding 6×10^4 A/m corresponds to deformation ε=80%.

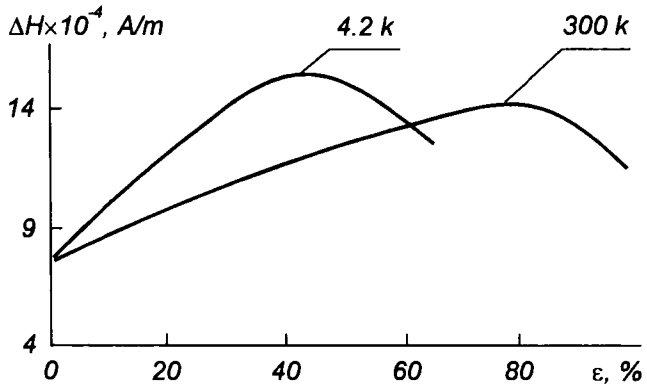

Fig. 4.17. FMR line broadening ΔH as function of polycrystalline nickel deformation rate [233].

Accumulation of plastic deformation in the metal surface layer in friction is characterized by a pronounced periodicity that is illustrated by Figs. 4.12 to 4.16 as well as by 4.18; in the last figure the nickel dislocation density ρ (curves 1 and 2) in the surface volume about 1 μm thick measured with the use of FMR [230] is plotted versus the friction test time with TsIATIM-201 (curve 1) and TsIATIM-201+3% of fluoroplastic (ftorplast-3) greases (curves 2 and 3) [234]. The results confirm that the properties of the surface layer varies periodically during friction.

Now, the observed periodicity will be explained in terms of the conventional concepts of dynamics of linear defects in plastic deformation [235].

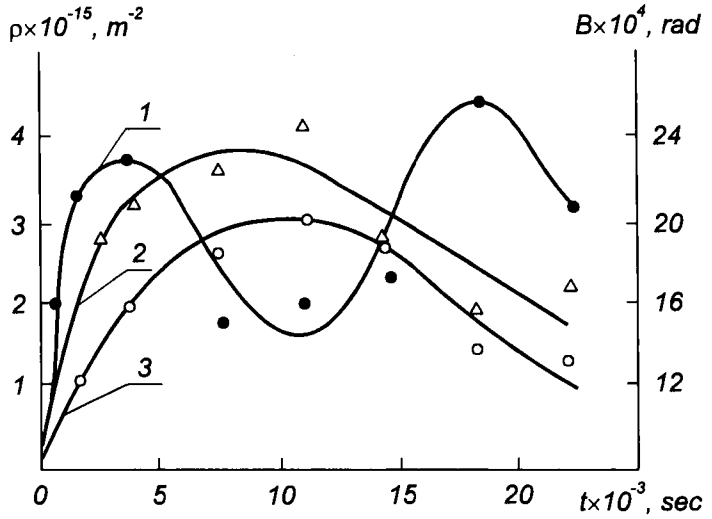

Fig. 4.18. The dislocation density ρ and broadening B of roentgenogram lines as a function of test time t [234]: 1) ρ variation during sliding in TsIATIM-201 lubricant; 2, 3) ρ and Bvariation, respectively, during sliding in TsIATIM-201+3% of fluoroplastic (ftoroplast-3).

In the initial period of friction (see Fig. 4.18, curve 1) the work of dislocation sources induces a sharp growth of the dislocations density in the surface layer which slows down and ceases, i.e. some time after friction start the dislocation density ρ and hardening are maximum. It means that generation of new dislocations and, accordingly, the hardening are accompanied by a competitive reverse process of dislocation relaxation and loss of strength. The latter is the result of annihilation of the opposite sign dislocations and polygonization [235] as well as of the flow of linear defects toward microcracks. Deceleration of the hardening process is caused by a number of factors: suppression of the work of dislocation sources by elastic stress fields created by other dislocations and defect clusters; stress relaxation because of microcrack nucleation in the tip of dislocation pileups; transverse sliding of dislocations in the stage of dynamic rest [234]. All these factors decrease the number of sources of linear defects and reduce elastic interaction between them reducing hardness.

The maximum is followed by the decreasing dislocation density ρ. The competitive loss of hardness becomes dominant. In this case, relaxation of the elastic stresses in the lattice is caused by intensive formation of cracks and polygonal structures in the vicinity of crack tips due to the redistribution of single dislocations and (or) "levelling" of three-dimensional dislocation pileups by sliding dislocations with the formation of small-angle dislocation sub-boundaries. Immediately after or simultaneously with polygonization primary recrystallization

starts in wide shear bands, it substantially decreases the number of crystal defects induced by deformation and, accordingly, the amount of bulk deformation energy.

Intensive development of microcracks, their migration and coalescence, appearance of macro- and fatigue cracks due to cyclic loads in friction, result in the partial (local) failure of the surface layer by the flaking of particular regions of the deformed layer and, eventually, wear, exposure of underlying nondeformed surface areas and their subsequent piling follow. Such conditions of the surface layer (see Fig. 4.18, curve 1) are characterized by the deep minimum ρ which fails to achieve, however, the initial value due to simultaneous presence of hardened and unhardened areas on the surface.

As the test duration increases, the process is repeated (the next ascending portion of ρ in curve 1) and friction spreads to the underlying, unhardened layer.

The wear mechanism is confirmed by electron diffraction [234]. The authors showed that in the thin surface layers with thickness about 0.3 μm the deformable grain orientation first develops periodically and then almost totally disappears. It suggests that integration of the surface cracks which develops in the first period of ρ variations loosens substantially the thin surface layer and causes its flaking, i.e. wear.

In dry sliding the duration of the period of hardness variations is much shorter, therefore the failure process is more intensive since deformation penetrates much deeper (see Figs. 4.13 and 4.18).

The effect of the nature and the composition of the lubricant on plastic deformation in friction can be evaluated from comparison of curves 1 and 2 in Fig. 4.18. During sliding with TsIATIM-201 grease containing a fluoroplastic powder (curve 2) the growth rate of ρ is lower and the period during which the maximum ρ is achieved (the hardening period) is much longer, respectively, the wear is less (this is confirmed by other studies). Data on broadening the roentgenogram lines (see Fig. 4.18, curve 3) agree qualitatively with curve 2 (variations of ρ) and confirm the effect of the fluoroplastic (ftorplast-3) and periodicity of variations of hardness properties of surface layers.

In friction surface layers are mainly deformed. Ultimately deformed (hardened) surface layers block and hinder deformation of the underlying layers leading surface cracking.

Because of lubricant application the additional shear deformation of the surface layer concentrates in the softened layer, the underlying layers of basic metal are deformed uniformly. Decrease of the shear deformation reduces the tangential force as well as the friction coefficient and wear. It can be achieved in particular, by introduction of powder fluoroplastic polymer (ftorplast-3) into TsIATIM-201 grease. In friction, mechanical destruction of the polymer decreases the metal surface free energy since the appearing radicals (see 6.7) interact with dislocations that emerge on the surface and with oxygen preventing the working surface

oxidation. Decrease of the metal surface free energy results in softening of the surfaces and localization of shear deformations within the thin surface layer [4].

Softening can be induced by a relatively small decrease of the surface energy (of an order of several microjoules per square centimeter). The mechanism consists in quicker emergence of dislocations on the surface (displacement of dislocations over the surface), nucleation, and appearance of subsurface dislocation sources due to the reduced surface potential barrier as a result of adsorbtion of surfactant [4].

4.6. A Theoretical Approach to a Description of the Periodicity of Triboparameters

Friction systems and all phenomena associated with them are extremely complex and they seem to be too difficult for successful theoretical description.

Among many theoretical possibilities about how to treat a friction phenomenon, one of them seems to be promising. Namely, since friction systems are open thermodynamical systems, they dissipate energy, and may be nonlinear. Thus, they can be described in terms of dissipative structure theory (DST) [236, 237]. The theory of dynamical systems (DS) [238] with its powerful mathematical machinery can be used in such a case.

The periodicity of physicochemical parameters is a very pronounced proof of the non equilibrium state of such open systems as friction systems. A model applied for its explanation is formulated here [239]. This model shows that two variables, namely the dislocation density of a sliding metal surface and the concentration of monomers (substrates) initially dispersed in a friction interlayer are periodic in time. This model supports some of the experimental data presented in preceding sections (in particular those at Fig. 4.18).

A well-known one-dimensional dynamical system [238, 240] is recalled here. Namely,

$$\frac{d\rho}{dt} = \alpha + \beta\rho - \gamma\rho^{2}, \quad \rho \equiv \rho(t) \tag{4.5}$$

with $\rho(t=t_o)=\rho_o>0$,

where ρ is a surface density of dislocations,

α is an external source of surface dislocations,

β represents a coefficient which reflects the ability of the system to generate dislocations (β and γ are real positive constants) and

ρ_o denotes the initial surface density of dislocations.

Equation (4.5) is often used to describe the time evolution of ρ [237, 235].

Now, assume that the external source of surface dislocations can be in some way assigned to the concentration of monomers c placed between surfaces of two metals during sliding, i.e., we expect that the monomers (via their concentration

function) are the sources of surface dislocations (such a mechanism has already been noticed above (see 4.5)). In other words, we postulate that

$$\alpha = \alpha[c] \tag{4.6}$$

where $c \equiv c(t)$.

On the other hand, it is known that the time evolution of c may be represented by

$$\frac{dc}{dt} = -kc^{\nu} \tag{4.7}$$

(with an initial condition analogous to that associated with eq. (4.5), namely $c(t=t_0)=c_0$),

where k is the chemical reaction rate constant (k may implicitly depend upon temperature T), and

ν stands for reaction degree (in general, ν is a positive real constant).

The sign "–" implies that the concentration of monomers (substrates) decreases with time because of polymer (product) production. The case of $\nu=1$ represents the radical polymerization reaction. The cases $\nu=2$ and $\nu=3$ are assigned to the kinetics of polycondensation with and without a catalyst. Note, that fractional ν-values are possible as well.

In the following we assume that $\alpha[c]$ is linear in c:

$$\alpha[c] = \alpha_0 + \alpha_1 c \ . \tag{4.8}$$

One may consider α_0 as a constant external source of dislocations (influenced by other agents or causes, but not by monomers), and α_1 a nonzero distortion parameter (here, a distortion from a constant α_0 is taken into account). Of course these two positive real coefficients may be interpreted as the two first coefficients taken from the Taylor expansion of $\alpha[c]$.

The next (and the most important) step in our modeling assumes that the system described by eqs. (4.5), (4.7) and (4.8) should be fully coupled, i.e., eq. (4.7) has to be completed by a term which is a function of ρ. We consider again a linear approximation, i.e.

$$\frac{dc}{dt} = -kc^{\nu} + \upsilon(\rho), \tag{4.9}$$

where

$$\upsilon(\rho) = \upsilon_0 + \upsilon_1 \rho \ , \tag{4.10}$$

υ_0 and υ_1 play roles analogous to coefficients α_0 and α_1 (here, however, we assume for simplicity that $\upsilon_0=0$, but υ_1 can be nonpositive). The assumption used

to write down eq. (4.9) is strongly supported by the physics of the friction process (not only may the monomer concentration influence the time evolution of the density of surface dislocations, but also to the contrary, the density of surface dislocations may produce some changes in the time dependence of monomer concentration).

Combining together eqs. (4.5), (4.6), (4.8), (4.9) and (4.10), we get a full two-dimensional dynamical system

$$\begin{aligned} \frac{d\rho}{dt} &= \alpha_0 + \alpha_1 c + \beta\rho - \gamma\rho^2 \\ \frac{dc}{dt} &= -kc^{\nu} + \upsilon_1 \rho \ , \end{aligned} \tag{4.11}$$

which enables the description of a wide range of phenomena occurring in friction systems (e.g., periodicity).

A few remarks on system (4.11) are necessary. First, for $\upsilon_1=0$ (the case with a weak coupling of fields ρ and c), the system is fully solvable analytically. In this case, the solution of the system reads:

$$c(t)=c_o \exp[-k(t-t_o)] \qquad \text{for } \nu\equiv 1$$

$$c(t) = \left[c_0^{1-\nu} + k(\nu-1)(t-t_0)\right]^{1/(1-\nu)} \qquad \text{for } \nu\neq 1 \tag{4.12}$$

$$\rho\,(t) = \beta\,/2\gamma + (2\gamma)^{-1}\lambda(t)\{1+\exp[-\frac{1}{2}\lambda(t)(t-\bar{t})]\cos^{-1/2}(\omega\, t+\phi)\} \tag{4.13}$$

where $\lambda(t)=\{\beta^2+4\gamma[\alpha_0+\alpha_1 c(t)]\}^{1/2}$, $\bar{t}=t_0-\tau_0$ (τ_0 is fully determined by six constants: β, γ, α_0, α_1, c_0, p_0).

Note that eq. (4.13), valid for $\Delta(t)=\beta^2+4\gamma[\alpha_0+\alpha_1 c(t)]>0$, manifests a weak periodicity; the case with $\Delta(t)=0$ was neglected, being not interesting for the physics of the process. Secondly, when $\gamma=0$ and ν=1 we have a system which describes the time behavior for a linear oscillator ([241] and example therein), which can also be solved analytically. Thirdly, when ν=2, we get the so-called prey-predator system (see also [238] for comparison), but with no mixed coupling (i.e., with no terms proportional to c). In this case the system is rather hard to solve analytically, but can successfully be treated numerically (e.g., in [238] or [241]). The most important fact, however, is that such a system already manifests nontrivial periodic behavior [238]. We treat our system (eq. (4.11)) only numerically, using different initial conditions, and varying all possible physical parameters. The numerical simulator PHASER [238] was used, and the Runge-Kutta numerical method [241] was applied.

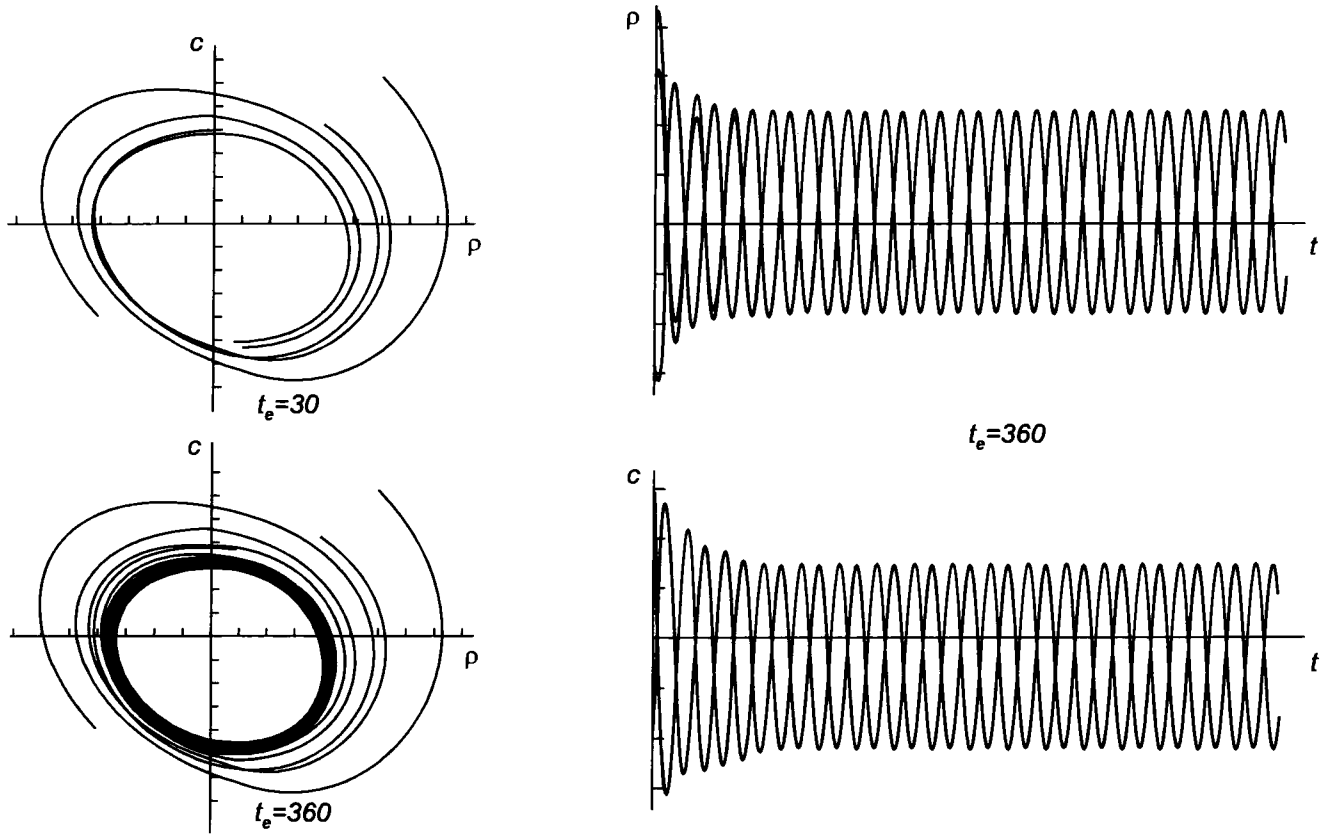

Fig. 4.19. Some demonstration of the system's periodic behavior – a limit cycle is successfully reached.

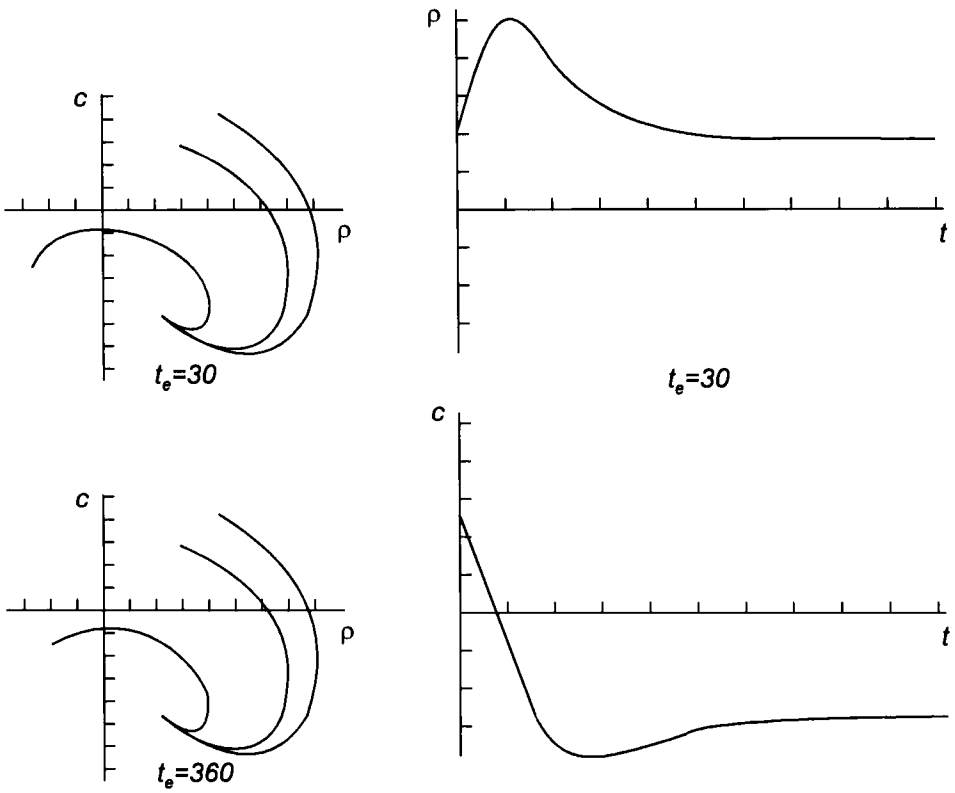

Fig. 4.20. Steady-state limit is reached by the tribochemical system.

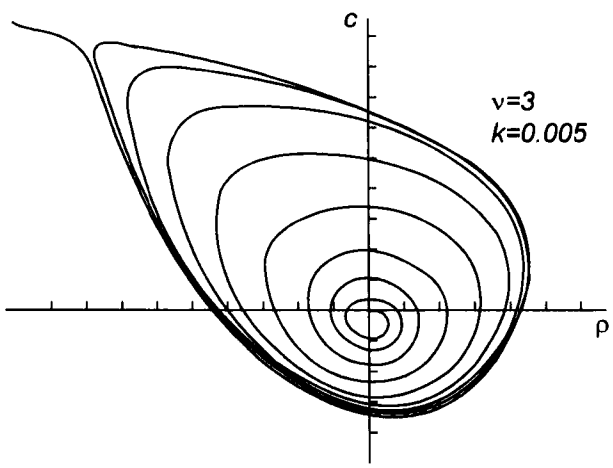

Fig. 4.21. An observation of escape to infinity (a certain instability point is detected).

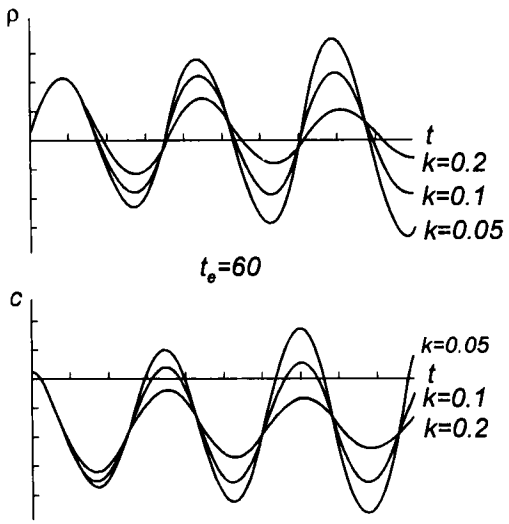

Fig. 4.22. Amplitude regulation in the tribochemical system.

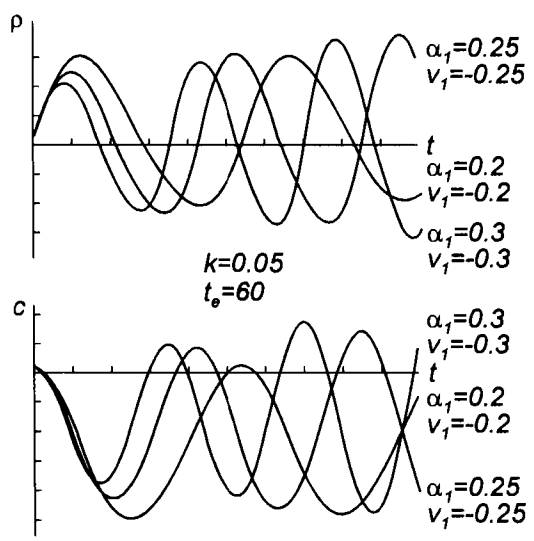

Fig. 4.23. Frequency regulation in the tribochemical system.

The interplay of parameters in our system enables us to control the whole tribopolymerization process. In Fig. 4.19 we observe how the system tends to a limit cycle. This means that a stationary state is reached (parameter k plays here a crucial role). In Fig. 4.20 one can see how it is possible to achieve a steady state in our system (again the role of k is important). It was also stated that the varying k and having a basic set-up of parameters unchanged, we are able to control the escape from a stationary state to infinity (cf. Fig. 4.21). A regulation of the amplitudes of $\rho(t)$ and $c(t)$ is possible, again by varying k (see Fig. 4.22). In turn, the frequency can be changed by the varying of coupling parameters: α_1 and v_1 (as demonstrated in Fig. 4.23).

The changing of parameters allows the stabilization of the system around a limit cycle (or its destabilization). The case of $\nu=2$ should be studied more carefully because it is untypical (look at Fig. 4.24 for details). The role of the remaining parameters, i.e., γ and β seems to be not so pronounced when they are kept on a reasonable level of magnitude. The importance of the different initial conditions chosen has also been demonstrated on almost all figures presented.

Concluding remarks. There exist many experimental data which have been obtained without comparing them to some modeling. Therefore, they may not be suitable for development of a theoretical basis. There is no doubt that some experiments should be redone precisely in connection with an explanatory model. Several important (or typical) examples have been chosen in this work. On the other hand, the model presented here seems to be suitable for elucidating and/or describing periodicity in real friction systems. This model is composed of a two-dimensional system which until now has never been proposed. In fact, e.g., the process of selective transfer and hydrogen wear can clearly be explained by this model. It is also important that the

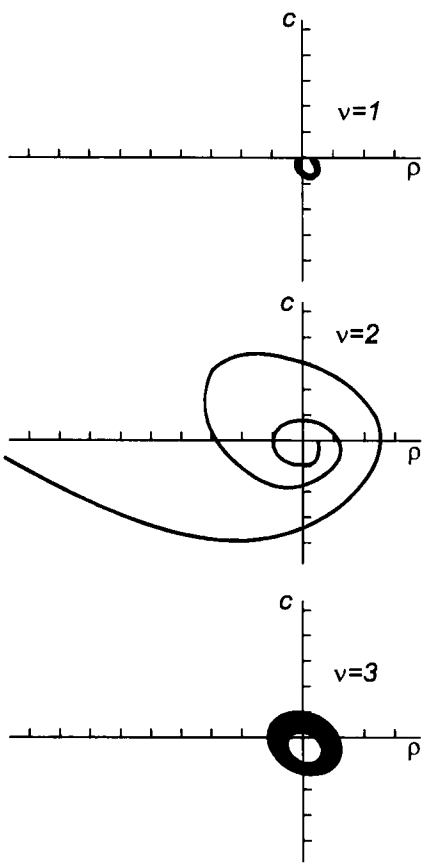

Fig. 4.24. An untypical case with $\nu=2$, which would correspond to, e.g., the case of polycondensation with a catalyst, k=0.05.

theoretical possibilities evidently show how to control at least some of the phenomena occurring during the friction process. Various possibilities for two regulation of some processes emerging in such nonequilibrium open systems are also sketched by means of the theoretical modeling (see Figs. 4.19–4.24 for details). One may believe that the theory of dissipative structures (and also other theoretical tools, e.g. fractals, stochastic processes, etc.) would be of great help for those purposes, and such type of analysis needs to continue.

4.7. Structural Changes of Surface Layers in Friction

G.Beilby [242] using reflection electron diffraction discovered that after polishing metals the diffusive haloes appeared on the electron diffraction pattern like those from amorphous materials. It meant that a very thin surface metal layer, tens or hundreds of nanometers thick, appeared and it was amorphous to a certain extent. By this discovery Beilby initiated systematic research of the structure of surface layers in friction and formed an independent scientific field. Beilby's experiment was repeated by many researchers who used reflection electron diffraction.

The so-called amorphization of metal surfaces could not be found by the transmission electron microscopy because of imperfections of specimen preparation, which resulted in great differences in interpretation of the results. This is due to the following fact. First, an electrolytical treatment makes a hole in varnish coat protecting the surface from the solvent, the latter dissolves it since the ultradispersed quasi-amorphous surface layer has stronger reactivity compared with the basic metal. Second, in the metallic wedge-shaped specimens the dislocation density decreases rapidly toward the foil edge [243]. If the thickness of electrolytically thinned foil is less than 100 nm, dislocation redistribution and "leakage" are observed [244].

An attempt was made to exclude unfavorable effects of the conventional method of one-side electrolytic thinning (actually, it is the method of two-sided thinning of specimens) [70, 245]. In the studies the electrolytic thinning was supplemented with specimen thinning by sliding in the normal mechanochemical wear [246].

Concave specimens of foil made from 15/13 steel, 0.1×10×15 mm, produced with a male die and spherical female die were thinned (worn) by sliding on a disk from carburized and hardened 18KhGT (GOST 4543-71) steel. Petrolatum was used as a lubricant, the sliding speed was v=0.05 m/sec, specific load was up to 10 MPa. Sliding lasted untill complete wear of the central contacting area of the specimen to produce shaped hole with the diameter about 0.2 mm. The specimens were previously subjected to sliding but in routine (plane–plane) contact; some of them were subjected to one-side electrolytic thinning.

Analysis of electron diffraction patterns and photomicrographs showed the following. In one-side electrolytic thinning the structure and phase composition of surface layers were identical to these in the subsurface bulk; a clear dislocation structure, inhomogeneous on the surface and having a dislocation density decreasing towards the edges, was observed. In thinning by sliding no dislocations were found, diffusive haloes with textural maxima were observed that suggested that the sliding surface had a specific ultradisperse structure with a coherent scattering region of 1.5 nm in size. From the results it was concluded that such thinning was better than the electrolytic thinning because it gave information about the real structural surface state [245].

However, the method does not solve the problem since either the authors of [245] or of any other previous relevant studies neglected the basic characteristic of the friction process: periodical variations of the structure and the properties of surface layers (see 4.5).

More than half a century was needed to understand that the experiments to investigate the surface structure with the above methods (visually checked one-side electrolytic thinning; reflection electron diffraction, etc.), separately or in combination, were poorly suitable. Because wear and other friction parameters are cyclic, all the results obtained by different authors cannot be reproduced, they give a random scatter of visual observation results and experimental points which are averaged. The time scale of cyclicity must be known for every friction mode to obtain true relations instead of a random set of points or structural surface states in measuring of particular parameters. This can be confirmed by a brief discussion of some publications [247, 248].

Specimens of pre-electropolished and annealed polycrystalline nickel (thin disks of 5×0.1 mm, 99.99% purity (after sliding in nickel–molybdenum pair in the air with TsIATIM-201 grease, at P=82.3 kPa and linear speed of 0.5 m/sec) were studied with FMR, transmission electron microscopy and microdiffraction. Since the dependence of variations of the FMR line width ΔH combined with variations of the surface dislocation density ρ, on the sliding time t, is cyclic (see 4.5 and Fig. 4.25), electron microscopic studies were carried out of characteristic portions of the curve: in the initial state on the ascending portion of ΔH (or ρ curve) (t=(0.9–1.8)×10^3 sec), at maximum broadening of line ΔH (t=5.4×10^3 sec) on the descending section (t=9×10^3 sec), and at the minimum ΔH (t=10.8×10^3 sec).

A substantial advance [247] was that the one-side electrolytic thinning of specimens for electron microscopic structural studies in [247, 248] was carried out on a jet polishing installation equipped with a sensitive photodiode detector recording thickness of the thinned foil area from the intensity of light passed through it. Holes in the foil and the surface dissolution were eliminated.

Studies [247, 248] showed that within each cycle of ΔH variation there was a

wide spectrum of structural changes in friction. It is noteworthy that the cycle duration for this relatively "mild" mode of friction is short. For more severe modes the frequency of variations within a friction cycle increases.

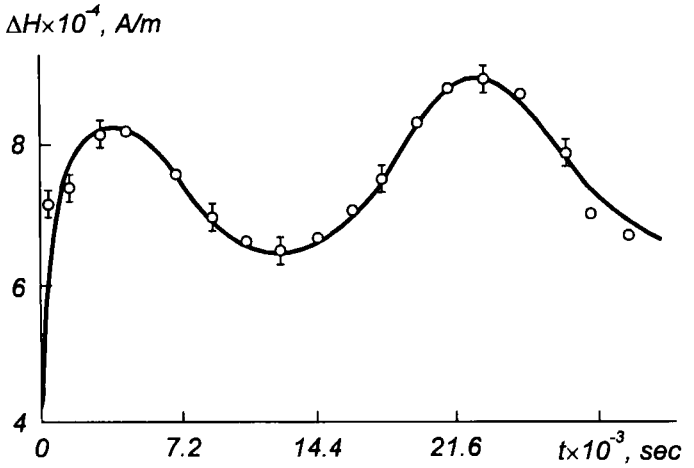

Fig. 4.25. Plot of FMR line broadening ΔH versus sliding time *t* [247].

The dislocation density in the original specimen is 5×10^{12} m^{-2} (found from photomicrographs with the method of mutually perpendicular secants), the grain size is 20 μm. In the initial ascending portion of the ΔH curve (during a relatively short test time up to 9×10^{2} sec) ρ grows to 2×10^{13} m^{-2}, dislocation clusters appear which pile-up mainly near the grain boundary, the grain size being practically invariable. Subsequent growth of ΔH (test duration of 1.8×10^{3} sec) is induced by increasing ρ to 10^{14} m^{-2}. In this case dislocation cells up to 0.1 μm are formed, grains are reduced in size to 0.2–0.5 μm, there are tendencies (found from electrode diffraction patterns) of the development of a highly dispersed phase with the grain size 0.01 μm.

After tests during 5.4×10^{3} sec (the maximum ΔH (see Fig. 4.25)), ρ becomes 10^{16} m^{-2}, the surface layer is even more dispersed: crystallites break into separate elongated subgrains, walls of interlaced dislocations appear and recrystallized grains with a characteristic size 5–10 nm are produced. Dislocations in most of the blocks are so numerous that their resolution is only possible in rare cases. Descent of ΔH is caused by relaxation of elastic stresses, decrease of ρ to 5×10^{13} m^{-2}. The grain size increases from 0.5 to 5.0 μm ($t=9\times10^{3}$ sec) to 10 to 20 μm ($t= 10.8\times10^{3}$ sec). At the minimum ΔH the structure is similar to that of initial (nondeformed) specimens. Then, the cycling of structural variations is repeated in phase with variations of ΔH. Explanation of cyclicity of ΔH, ρ and associated wear rate was discussed in 4.5.

The results suggest that the specific ultradisperse structure observed in [245] probably suits the sliding surface state characterized by maximum ρ of the tribocycle for particular pairs and sliding modes. Besides, a "window" in the foil is most possible just at this surface state (the maximum ρ or ΔH) during sliding; since the wear rate is maximum (see Sect. 4.5) and fully correlates with variation of ρ or ΔH, it must be described by a cycloid.

Periodical dispersion and partial amorphization imply that the metal surface in sliding is periodically transformed into the metastable disordered state inevitable thermodynamically under these conditions. The friction assembly is an open system where contact interaction produces continuous energy and mass transfer between the surface and the environment. Therefore, mechanical interaction is accompanied by heat release, adsorbtion, chemical reactions, diffusion and other processes. Thus, the friction work changes the internal energy of material and dissipates partly as heat. Therefore, the surface layer with fragmentation has an abnormally great stock of free energy compared with the layers in the bulk of material.

The metastable disordered surface state is achieved for different pairs, media, and friction modes (see Figs. 4.15 and 4.18) in different time intervals depending on the specific friction work $A=fPV$, where f is the friction coefficient, P is the specific load; V is the relative sliding speed. Moreover, the phase composition of the surface layer depends on the selected friction mode.

This Page Intentionally Left Blank

Chapter 5

STRUCTURAL AND PHASE CHANGES STUDIED BY MÖSSBAUER SPECTROSCOPY

5.1. Mössbauer Electron Spectroscopy Capability

Wear resistance in friction is increased in most cases by modifying working surfaces. The modification is achieved, in particular, by surface plastic deformation (GOST 18296-72, [249]), diffusion saturation of the surface (chemical and thermal treatment), laser [250], ion implantation, friction [251], etc. The problem of surface treatment influence on the surface properties, structure and phase composition has always been very important for science and technology.

Investigation of modified surfaces especially subjected to friction is complicated because the most significant information lies deep inaccessible to conventional nondestructive testing methods (10–100 nm). The conventional methods are also ineffective for depth-selective nondestructive testing. Therefore, the search of basically new methods to study surface properties of structural metals and alloys and friction-induce changes in them is increasingly carried on. The nuclear gamma resonance spectroscopy based on the Mössbauer effect [252–254] is one helpful technique. The results described in this chapter were obtained by using the equipment provided by the Department of Nuclear Physics of the Byelorussian State University, in cooperation with A.L. Kholmetskii, V.A. Chudakov and others.

The effect of unretrievable emission and absorption of γ-quantum by nuclei bound in the crystal lattice was observed first in 1958 by R. Mössbauer. Since that time the structural resonance analysis based on Mössbauer effect has greatly expanded our knowledge about atomic and magnetic structures, intracrystal fields, hyperfine electronic and nuclear interactions, etc.

The use of Mössbauer effect is especially promising surface studies. The width Γ of a Mössbauer line is very small (of an order of 10^{-5}–10^{-10} eV) compared with that of the energy of nuclear transitions E_0 (10^4–10^5 eV), therefore, the Mössbauer effect is characterized by a high resolution (low relative Γ/E_0 width). So, for ^{57}Fe ($\Gamma=4.67\times10^{-9}$ eV, $E_0=14.39$ keV) the resolution is $\Gamma/E_0=3\times10^{-13}$ against $\Gamma/E_{at}\cong10^{-7}...10^{-8}$ for optical fluorescence (E_{at} is the atomic transition energy). This high resolution allows to measure minutest perturbations at nuclear levels (of the order of 10^{-6}–10^{-10} eV) induced by hyperfine interactions of nuclei with the electron

shell, and with the surrounding nuclei.

The main characteristics of the gamma resonance spectrum to identify the absorption (or scattering) lines and the block diagram of the Mössbauer spectrometer used in this study are explained below.

Probability* f *of the effect. The resonance absorption cross-section without the loss for release has the following form:

$$\sigma'(\omega) = \sigma_0 \frac{\Gamma_\gamma / 2\pi}{(\omega - \omega_0)^2 + \Gamma / 4} e^{-2W(T)},$$

where σ_0 is the so called maximum effective absorption cross-section ;

Γ_γ is the radiation line width;

Γ is the full line width ($\Gamma=\Gamma_\gamma+\Gamma_e$);

Γ_e is the conversion transition line width;

$e^{-2W(T)}=f$ is the Debye-Valler factor, determining the recoil-free process probability.

The exponent degree

$$W(T) = 2\pi^2 < x^2 > /\lambda^2;$$

where $<x^2>$ is the mean root square nuclear shift in time τ from the equilibrium position of γ-quantum direction;

λ is the γ-radiation wave length.

Thus, the lower the crystal temperature (below $<x^2>$) and the smaller the energy (above λ), the more probable is the Mössbauer effect.

Experimentally f is determined from the integrated intensity of spectral lines (the absorption spectrum area).

Isomer (chemical) shift* δ *of the absorption line (the electrical monopole interaction). It is defined by the difference of electron density on the emitter and absorber nuclei. Knowledge of δ provides information on electronic shells of resonance nuclei in the crystal lattice. For solid solutions based on pure metals δ is connected with the conduction electron density and it is determined from the formula

$$\delta = \frac{4}{5}\pi e^2 Z \frac{\Delta R}{R} R^2 \left[\left| \Psi_{e\,absorp}(0) \right|^2 - \left| \Psi_{e\,emit}(0) \right|^2 \right],$$

where e is the electron charge;

Z is the ordinal number of the nucleus;

R is the charge radius of the nucleus;

$\Delta R/R$ is the constant for a particular isotope (the change of nucleus charge radius in the excited-to-grand state transition);

$\left|\Psi_{e\,absorp}(0)\right|^2$ and $\left|\Psi_{e\,emit}(0)\right|^2$ are *s*-electron densities on the absorber and the emitter nuclei.

The shift δ is determined experimentally from the difference in the position of the gravity line center relative to zero velocity.

Absorption (scattering) or emission line width Γ. It is determined from the expression $\Gamma=0.693\hbar/\tau_{1/2}$, where $\tau_{1/2}$ is the average half-life of the excited nucleus; Γ_{exp} is determined in terms of the line maximum half height described by the Lorentz function for a fine absorber as

$$f(\omega)=\frac{\Gamma/(2\pi)}{(\omega-\omega_0)^2+\Gamma^2/4}.$$

For a fine absorber the broadening (distortion) of the experimental absorption (scattering) line over the spectrum depends on the phase composition of the specimen, the nature of impurities, presence of deformations, internal stresses, the angular distribution of γ-quantum bombarding the specimen, the anisotropy of the specimen properties and others.

Quadrupole line splitting ΔE (the electrical quadrupole interaction). It characterizes the interaction of nuclear electrical quadrupole moments with intracrystal electrical fields.

In the inhomogeneous electric field the level with the magnetic quantum number j=3/2 splits into two sublevels with the energy

$$E_{\pm1/2}=-\frac{e^2qQ}{4}\left(1+\frac{\eta^2}{3}\right)^{1/2};$$

$$E_{\pm3/2}=+\frac{e^2qQ}{4}\left(1+\frac{\eta^2}{3}\right)^{1/2};$$

where q is the electrical field gradient on the nucleus;

eQ is the nuclear quadrupole moment;

η is the eQ asymmetry parameter.

The ΔE is found experimentally from the distance between the centers of gravity of the doublet lines (Fig.5.1). It shows the behavior of chemical bonds, atomic distributions just around the resonant nucleus, it yields the mean root square (thermal) deviations of the resonant nucleus from equilibrium and the direction of electrical field gradient, the sign of the quadrupole interaction constant e^2qQ.

Internal effective magnetic field on resonant nuclei H_{eff} (the magnetic dipole interaction). It is determined experimentally from the spectrum of the magnetic (Zeeman) hyperfine splitting of the Mössbauer line as the distance between the centers of gravity of the extreme peaks of splitting (Fig 5.2). The hyperfine Zeeman splitting of the absorption (scattering) line takes place in the nucleus magnetic interaction with the atom electronic shell when the nucleus possesses the nonzero intrinsic magnetic moment μ_j.

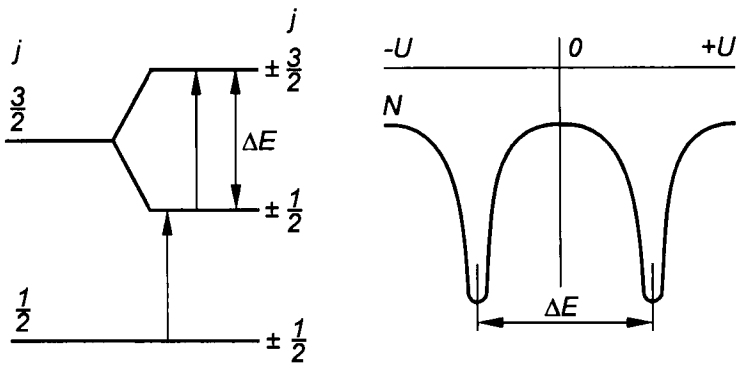

Fig. 5.1 Electrical quadrupole splitting of ^{57}Fe nuclear levels and Mössbauer spectrum shape.

The interaction energy is defined by $W_m=-\mu_j\mathbf{H}(0)$, where $\mathbf{H}(0)$ is the magnetic field formed by electrons at the nucleus site. When the magnetic field direction coincides with that of the nucleus magnetic moment μ_j, the W_m eigenvalues have the form

$$E_m = -(\mu\, Hm_j)/\, j = -g_j\, \mu_n Hm_j\,,$$

where m_j is the magnetic quantum number, $m_j = +j, \ldots, -j$ ($(2j+1)$ values);

$\mu_n=e\hbar/(2m)$ is the Bohr nuclear magneton;

e and m are the proton charge and mass;

j is the nuclear spin;

g_j is the gyromagnetic ratio.

The ground state of ^{57}Fe (j=1/2) splits into two sublevels with the energy interval $g_0=(\mu_0 H_{eff})/j=2\mu_0 H_{eff}$, the excited state ($j$=3/2) splits into four sublevels with the energy interval $g_1=(\mu^* H_{eff})/j=(2\mu^* H_{eff})/3$ (see Fig. 5.2), where $\mu_0=0.09\ \mu_n$ is the nuclear magnetic moment of ^{57}Fe in the ground state; $\mu^*=0.153\mu_n$, the same in the excited state.

The quantity H_{eff} in the Mössbauer spectra recorded within a wide temperature range gives insight into the structural transformations connected with magnetic phase transformation.

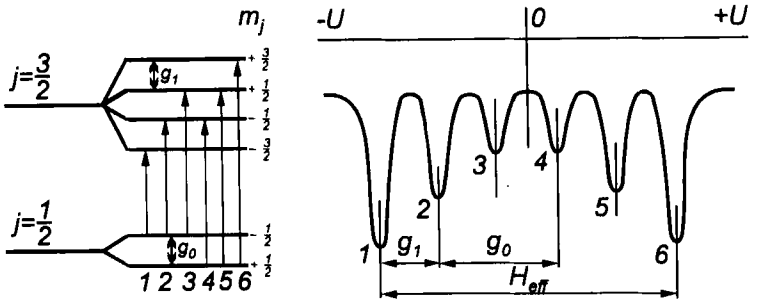

Fig. 5.2 Magnetic hyperfine splitting of ^{57}Fe nuclear levels and Mössbauer spectrum shape.

The magnetic field on the Mössbauer isotope nucleus in alloys depends on the concentration of proximal and distal order components in alloys, therefore, it is possible to study the order degree and the phase composition. It is also possible to determine the magnetization direction and the magnetic texture of specimens because the ratio of line intensities for spectral components in the magnetic dipole splitting depends on the angle θ between the direction of γ-quantum emission and the specimen average atomic magnetic moment directions (the specimen magnetization vector).

The line intensity ratio in the Zeeman sextet ($I_1 : I_2 : I_3 : I_4 : I_5 : I_6$) of the Mössbauer spectrum for monocrystals equals to

$$3:4\sin^2\theta\,/\left(1+\cos^2\theta\right):1:1:4\sin^2\theta\,/\left(1+\cos^2\theta\right):3, \qquad (5.1)$$

and for random arrangement of atomic magnetic moments

$$3:2:1:1:2:3$$

(in the transmission geometry).

Experimental procedure. Measurements of γ-radiation resonant absorption are usually carried out in the transmission and less frequently, in the scattering technique (because it is much more complicated). In the latter case the detecting re-emitted γ-quantum (the registered depth of the order of 10 μm) is most widely used. In our case (the surface layer depths studied are of the order of 100 nm) the detection is made in scattering of electrons emitted by the irradiated specimen as a result of the internal conversion. During resonant absorption of 14.4 keV Mössbauer γ-radiation of ^{57}Fe only 10% of nuclei proceed into the ground state by emitting γ-quantum, the 90% by *K*-capture with emission of 7.3 keV electrons of internal conversion [255]. This gamma-resonance spectroscopy method is more

sensitive than others, especially for small concentrations of n-resonant nuclei and low photoelectric absorption σ_{ph}. The ratio of resonance effects in recording the conversion electrons r_e and γ-quantum r_γ is

$$r_e/r_\gamma=\alpha/[(1+\alpha)\sigma_{ph}n],$$

where α is the internal conversion coefficient.

By recording conversion electrons it is possible to obtain a very high signal-to-noise ratio [255]. For ^{57}Fe the ratio of resonant σ and photoelectric absorption cross-sections is very high: $\sigma/\sigma_{ph}=300$, by using the optimum experimental geometry it is possible to record electrons through a large angle.

Our results have shown that Mössbauer spectroscopy of conversion electrons (MSCE) is really effective and informative in studies of friction surfaces, substantially compensating the shortcomings of the conventional methods and expanding experimental possibilities. MSCE detects low-energy electrons, therefore, it can be used to investigate 100 nm thick surface layers and to carry out depth-selective nondestructive tests of surfaces. According to our results, there are no published reports on Mössbauer spectroscopy of friction surface properties. What is the reason? The use of MSCE for these purposes is constrained by difficulties to register and to measure the spectra of low-energy conversion electrons, as well as, the lack of appropriate equipment and complexity of mathematical processing of the spectra.

In this study we used gamma-resonance spectrometer developed at the Department of Nuclear Physics of the Byelorussian State University [256]. The spectrometry is based on measuring light characteristics of microdischarges caused by conversion electrons escaping from the specimen surface irradiated by γ-quantum in the rarefied air [257]. Thus, the main feature of this Mössbauer spectrometry is the use of a validated, simple and effective method of detecting conversion electrons when they are absorbed by or escaping from the surface. It should be noted that not electrons but light pulses accompanying microdischarges in the rarefied air (pressure ~0.03 MPa) caused by these electrons in the gap between the test surface and the photomultiplier tube photocathode, are recorded. A CPD is applied across them creating electric field 200–300 V/mm in the gap.

No X-ray, gamma-quantum or high-energy Compton electrons are recorded. The detector operation conditions are chosen empirically according to the field intensity, air pressure, presence of appropriate filters at the emitter outlet. The optimal conditions are achieved at high values of the spectrum statistic quality

$$Q=(N_0-N_\infty)/\sqrt{N_0+N_\infty}$$

and resonance effect

$$r=(N_0-N_\infty)/N_\infty,$$

where N_0 and N_∞ are counts within the resonance and away from the resonance, respectively. The measurement time with a 50 mCi ^{57}Co source and a natural isotope ^{57}Fe content in the specimen does not exceed 5 h with the target area at least 3 cm^2.

The measurement is shown in Fig. 5.3. A nearly tangential incidence of the γ-quantum beam on the specimen surface allows to investigate the anisotropy of surface properties, to test flat specimens of any shape and size. Because of the final beam divergence, the angle of tangential incidence was 0 to 10°.

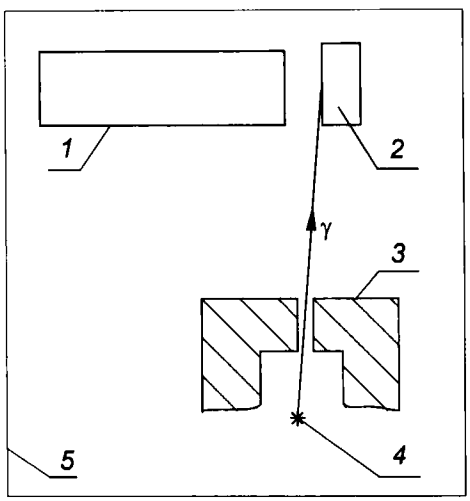

Fig. 5.3 Geometry of light-pulse gas-discharge detector: 1) photoelectron multiplier; 2) test specimen; 3) collimator; 4) radiation source; 5) sealed chamber.

The Mössbauer spectrometry also differs substantially in its other features [256]. Depending on the purpose and the type it is possible to measure Mössbauer absorption of gamma-radiation in both transmission and scattering detecting either re-emitted γ-rays, conversion and Auger electrons or X-rays accompanying the process. The spectrometer ensures high level of computerized data processing. The block diagram is shown in Fig. 5.4. The motion system MS (20 Hz operation frequency of the vibrator) is monitored by the program-controlled registers (PCR) which shape signals of the speed. Pulses from the detector D are applied to the one-level pulse-height analyzer PHA input, the discrimination thresholds are programmed. Pulses from the detector are counted by the pulse-counter PC. When channels are switched over, the PC contents are recorded into the buffer register BR. The accumulator Ac has a direct access to the microcomputer memory. The speed scale stabilization unit (SSSU) controls the address register AR, its commutation signals directly address the memory interface. The speed range is up to 10 cm/sec. The SSSU sets regular speed increments, thus dividing the speed

scale into a required number of channels: 128, 256, 512 or 1024. The channel capacity is 2^{16}. Speed resolution is 0.22 mm/sec for the transmission geometry, and 0.29 mm/sec – for the scattering with the sodium nitroferricyanide reference standard. The integral nonlinearity is below 0.1%., the 24-hour speed drift 0.002 mm/sec.

The experimental nuclear gamma-resonance system is controlled from the desktop terminal DT. Peripherals are the printer Pr, the communication channel CC with the central computer, and the monitor M.

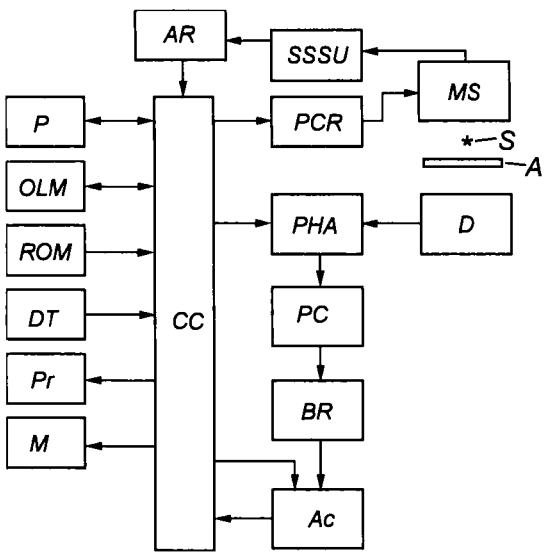

Fig. 5.4. Simplified block diagram of microcomputerized nuclear gamma resonance system: AR is the address register; SSSU is the speed scale stabilization unit; MS is the motion system; P is the processor; PCR is the program-controlled registers; S is the radiation source; A is the absorber (test specimen); OLM is the on-line memory; PHA is the one-level pulse-height analyzer; D is the detector; ROM is the read only memory; DT is the desktop terminal; PC is the pulse-counter; Pr is the printer; BR is the buffer register; M is the monitor; Ac is the accumulator; CC is the communication channel.

5.2. The Mechanism of Polishing

It was noted above that in many cases surfaces of parts in normal boundary friction acquire the shape of typical polished surfaces. Which mechanism forms such surfaces? How does the structure of the surface layer change?

Many studies deal with the theory of polishing, however, there is no general view on the mechanical polishing so far and it is still remains a classical problem of tribology [68].

Surface layer dispersion takes place in polishing. The so-called Beilby layer resulting in the process consists of a great number of randomly arranged very small crystals considered to have the same phase composition as the underlying layer, X-ray diffraction and electron microscopy do not allow to identify crystal sizes. It is assumed that the size does not exceed several elementary cells (on the metal surface of the order of 1 nm) [242 and others]. Diffusion haloes similar to those in amorphous materials can be seen in electron diffraction patterns of polished surfaces. The quasiamorphous partly oxidized Beilby layer has a higher electric resistance and hardness than the underlying layers.

On the one hand, polishing is pure abrasion in which the asperities are just removed. The sizes of the asperities (depending upon the size of abrasives and debris) are commensurable with the light wave length and are of the order of a molecule. On the other hand, it is assumed (this concept is most generally accepted) that during mechanical polishing the surface molecules are set in motion which is so intensive that the surface layer state approaches the molten state (asperities are commensurable with the molecule size). Considering the shape of asperities, a polished surface substantially differs from a worn one disproving the abrasive theory of polishing.

Abrasive polishing without debris occurs in conditions when welding bridges do not have sufficient energy to form abrasive chips after a new surface is exposed. The removal (wear) of asperities in final polishing is connected with the molecular type of wear like in lapping (polishing without abrasives). Therefore, the weaker the chemical bond the higher the polishing speed should be. This conclusion is proved by Samuel experiments [68]. The analogy between polishing and vaporization is noted in the same study.

It is likely that mechanical polishing changes the surface structure more profoundly. Some questions arise, many can be answered in principle by the Mössbauer spectroscopy for selective identification of phases in the multiphase system because the resonance spectrum parameters of the phase components in iron alloys are different. What structures polished surfaces have, what processes are involved in polishing, and what mechanism produces Beilby layers 100 to 200 nm deep? (Note that the depth of electron penetration into the material in reflection photography is 3 to 5 nm, and the scanning X-ray crystallography [259] yields reliable information only to at least 1 μm). Does this type of surface machining produce at all what the term "amorphization" does imply in respect to polished surfaces? Why their hardness increases? Take diamond polishing as a common example.

Standard cylinder specimens from the carbon steel C45e 18 mm in diameter and 16 mm in height were studied. The specimen end faces were ground to

roughness 6 (Ra=1.5 μm) on a surface grinder with a K3 direct profile surface wheel 250 mm in diameter. The rotation speed was 2800 rpm, feed was 10 μm, the feed rate was 5×10^{-3} m/sec. No cooling lubricant was used.

The polished surface was obtained as follows. After machine grinding to roughness 6 one of the end faces was manually made rougher by abrasive cloths of different consecutively decreasing grain sizes from the same abrasive (14A, GOST 6456-75). Then (also by hand) the specimens were lapped with diamond paste with abrasive grains about 0.25 μm in size on a thick lapping cloth to roughness 12c.

Structural changes in the surface layer after polishing were studied using the Mössbauer spectroscopy on ^{57}Fe nuclei to register conversion electrons in the scattering geometry following the procedure described in 5.1 to record gamma-resonance events from the surface layer depth down to 300 nm (90% of information is obtained from a 100 nm thick layer). All measurements were taken at room temperature. Measuring time of each spectrum was 8 h. The obtained statistics were subjected to double smoothing by the weighed average method [260]. A relative error of the numerical values was within 2%. A single line resolution measured with this method was (0.29±0.01) mm/sec.

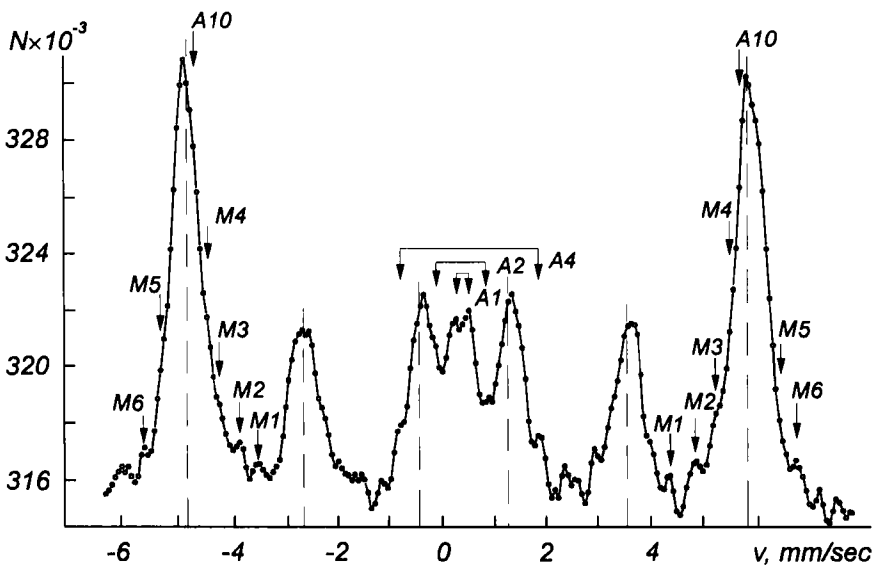

Fig. 5.5. Steel C45e polished surface: Mössbauer spectrum test surface layer is about 0.1 μm; v is the relative velocity; N is the pulse count in the channel; dashed line shows positions of α-Fe HMS lines.

The nuclear gamma-resonance spectrum of the initial polished surface is shown in Fig. 5.5. It mainly consists of a distinct sextet of broadened lines with the center

of gravity corresponding to the pure α-Fe (ferrite) structure. The effective magnetic field strength H_{eff} on iron nuclei is equal to 26.26×10^6 A/m in this phase. The line broadening of the hyperfine magnetic structure (HMS) typical of the steel C45e spectrum is caused by many factors, primarily by different numbers of carbon atoms around iron one appearing in various phases, perfection of the lattice structure, etc.

It is likely that the pure α-Fe spectrum is superimposed (Fig. 5.5) by the substantially less intensive spectrum of the body-centered tetragonal (BCT) martensite phase (a supersaturated carbon solution in α-Fe), the spectrum being a superposition of several (up to six) Zeeman's sextets. It is confirmed by a "comb" typical of the martensite α-phase observed in the spectrum, it is also found in the pattern of the difference spectrum (lines M1–M6 in Figs. 5.5 and 5.6). H_{eff} of NGR line sextets for martensite are both smaller and larger than H_{eff} for the body-centered cubic (BCC) iron at the same measurement temperature, depending on the dampening of Fe resonant nuclei by the interstitial impurity in the BCT structure.

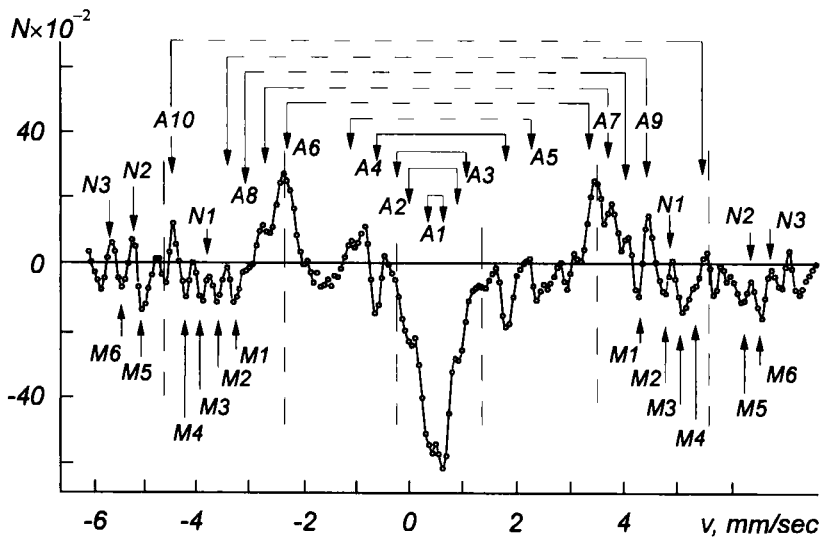

Fig. 5.6. Difference gamma-resonance spectrum between the spectra of polished and ground steel C45e surfaces.

Apart from the sextet of HMS lines there is a split monoline A1 (see Fig. 5.5) of paramagnetic austenite (γ-Fe), residual or resulting from machining. It is known [261], the austenite NGR line that at room temperature is a superposition of the atomic iron monoline (δ=-0.08 mm/sec) without surrounding interstitial atoms and the doublet (δ=-0.04 mm/sec, ΔE=0.63 mm/sec for 1.8%

carbon concentration in austenite) is assigned to iron atoms containing one impurity atom in the first coordination sphere. Austenite concentration based on the spectrum area is about 8.5%. The austenite phase penetrates more than 10 μm deep as the Mössbauer spectra of the specimens with recorded back-scattered gamma-radiation show.

The presence of austenite in the surface layer subjected to grinding is not surprising. Plastic deformation and high temperature in grinding create conditions for almost instant transformation of various steel phases into the austenite [262]. For instance, austenite appears in the hardened layers of 1/XVII and HS18-0-1 steels after grinding [16, 263]. Under the austenite layer the troostite structure and the underlying martensite structure were found. Austenite is usually formed at the grain boundaries, being highly plastic.

The marked splitting of the austenite NGR spectrum monoline (ΔE_1=0.23 mm/sec) (see Fig. 5.5, A1 line) is probably induced by the electric field gradient at the nucleus as a result of deformation (in grinding) of electrons-filled atomic shells or deviation of lattice symmetry from the cubic suggesting distortion of face-centered cubic γ-Fe lattice.

The spectrum indicates both the presence of α-and γ-phases in the steel C45e and its partial anisotropy resulting from grinding and previous treatment. It is known that practically any plastic deformation in rolling, friction, cutting, grinding, etc., except three-dimensional compression, is accompanied by the formation of a crystallographic texture [264]. Three-dimensional compression gives rise to anisotropic magnetic and electric properties which, in their turn, influence the shape of the steel GNR spectrum. The surface magnetic anisotropy (magnetization) changes the ratio of the component intensities in the Mössbauer spectrum as compared with isotropic materials for which the ratio of intensities of the HMS line sextet is 3 : 2 : 1 : 1 : 2 : 3 [253]. For the NGR spectrum shown in Fig. 5.5 the ratio of HMS line intensities in the energy decreasing order is close to 3 : 1 : 1 : 1 : 1 : 3. The prevailing direction of internal fields of the domains along the anisotropy axes probably coinciding with the direction of mechanical action (grinding), produces the effect similar to the external magnetic field. The HMS line intensity ratio shown in Fig. 5.5. corresponds to the angle between the γ-quantum beam direction and the magnetic anisotropy axis close to zero. Thus, such crystallographic anisotropy causes the anisotropy of both electrical properties of the γ-phase and of magnetic properties of the α-phase. The quadrupole electric moment of ^{57}Fe nuclei in the α-phase is zero because the NGR sextet lines are equidistant.

The shape of the surface NGR spectrum considerably changes as a result of structural and phase transformations in polishing (compare Figs. 5.5 and 5.7). First of all, complete disappearance of residual austenite lines along the whole test layer thickness (about 300 nm) is observed. It can be explained as follows.

Polishing is a mechanochemical process. From the mechanical standpoint microabrasion leads to microplastic deformation, shearing and smoothing the microasperities. It is known [261] that plastic deformation resulting from motion of dislocations facilitates decomposition of the austenite. Its transformation in polishing may probably be attributed to the formation of both fine grain martensite and hard highly-dispersed ferrite mixed with cementite (or other carbides), such as sorbite or troostite. Transformation of austenite into pearlite is not likely to occur because the coarse-structured pearlite less hard or as hard as austenite should be formed. Meanwhile, it is known that the metal hardness considerably increases after polishing [16]. Thus accelerated diffusion and/or nondiffusion mechanical and chemical intermediate transformation of austenite takes place during polishing. A mechanical mixture of ferrite and cementite (and other carbides) of various dispersities and hardness is produced corresponding to the hardness and dispersion (in the decreasing order) of sorbite or troostite structures.

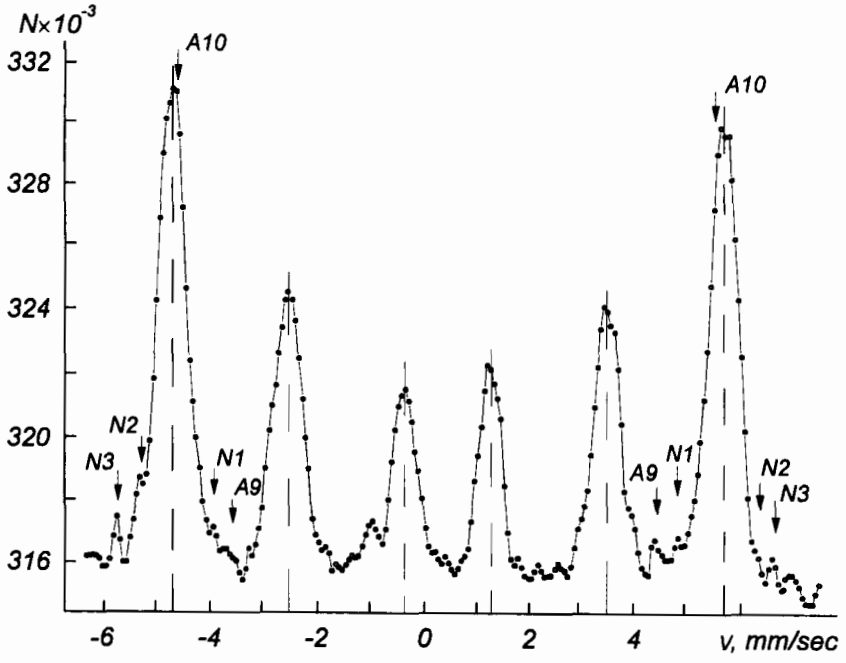

Fig. 5.7. Mössbauer spectrum of polished steel C45e surface.

More detailed information on the character of phase transformations of steel polishing can be obtained by analyzing the spectrum shape (see Fig. 5.6) by substracting the gamma-resonance spectrum of polished steel from ground steel. Fig. 5.6 shows that the processes in polishing are somewhat similar to those in steel tempering [265, 266]. The residual austenite decomposition product

(see Fig. 5.5 and 5.6, lines A1, A2) is a ferrite-carbide mixture, just as at the temperature of steel tempering T≥573 K [261]. Formation of carbide in carbon steel can be expressed as [266]:

$$\alpha \rightarrow \varepsilon \rightarrow \chi \rightarrow \theta\ (Fe_3C),$$

where ε is the Hoffer hexagonal carbide; χ is the Hagg monoclinic carbide (Fe_5C_2); θ is Fe_3C.

In tempering [267], ε→χ transformation does not change the composition in the temperature range 547–615 K. The main carbide phase formed in polishing (see Fig. 5.6) is the monoclinic χ-carbide (its extreme HMS lines are marked A5, A6 and A8), and θ-carbide (cementite) as lines A7. H_{eff} for iron in the cementite structure is 16.55×10^6 A/m (lines A7), in carbide Fe_5C_2 structure, to 18.06×10^6 A/m (Fe^I, lines A8), 14.64×10^6 A/m (Fe^{II}, lines A6), and 8.75×10^6 A/m (Fe^{III}, lines A5) [254].

Increased polished surface hardness and formation of an ultradispersed structure [16] reported by many authors supports the above suggestion. The increased hardness of Beilby layers is attributed to the age hardening caused by intensive development of metal phase surfaces and, accordingly, of interphase interactions of crystallites when their sizes decrease.

Apart higher carbide concentration, the ferrite spectral intensity slightly increases, lines 2 and 5 of the spectrum being partly overlapped by lines 1 and 6 of Fe_5C_2 (Fe^{III}) (see Fig. 5.6, lines A6). It can be attributed to the following. Though austenite transformation is assumed due only to the production of cementite Fe_3C together with carbon, the cementite concentration cannot increase considerably because plastic deformation facilitates cementite decomposition [268]. In this case decomposition results from different energies of carbon binding with dislocations in the cementite lattice.

In the spectra of ground (see Fig. 5.5) and polished (see Fig. 5.7) surfaces, exception the ferrite, cementite and other carbide sextets, one more component A10 (H_{eff} is 25.31×10^6 A/m) is observed, the intensity of which increases after polishing. This line favors the broadening and asymmetry of extreme lines 1 and 6 of the α-Fe NGR spectrum. A similar component is reported in the deformed steel spectrum [269], attributed to iron atoms in dislocation atmospheres during cementite decomposition. Partial decomposition in plastic deformation results from diffusion of carbon atoms from the cementite lattice to dislocation pileups at the phase boundary. It results in the segregation of iron and carbon atoms. A similar situation seems to occur in the present case.

The ratio of MHS lines in the polished surface NGR spectrum is

$$3 : 1.7 : 1 : 1 : 1.7 : 3$$

compared with the ground surface

$$3 : 1 : 1 : 1 : 1 : 3$$

which is close to the ratio of

$$3:2:1:1:2:3$$

for the NGR spectrum of isotropic polycrystalline materials (in the transmission geometry), including annealed steel C45e, its NGR spectrum has also been measured by the present author. The contribution to the increase of intensities lines for 2 and 5 of the polished specimen is partially caused by the increased carbide phase and the reduced surface layer anisotropy upon polishing.

The integrated polished surface area NGR spectrum is approximately 2.5% less than that of the ground. This change may probably be due to different binding energies of iron atoms in the α- and γ-phases influencing the resonance effect magnitude.

Polymorphous transformation of γ-Fe into α-Fe in austenite decomposition occurs at any carbon steel cooling rate, which affects the nature and properties of the decomposition products, its higher rates lower the transformation temperature.

Complete transformation of γ-Fe into α-Fe indicates that the effective polishing temperature reaches the values characteristic of intermediate transformation. The term "effective temperature" implies a dimensionless quantity taking into account the joint action of heat variations and mechanical stresses. According to the kinetic concept of destruction [142], the lifetime of a mechanically stressed single chemical bond τ (Zhurkov's equation) is expressed by

$$\tau = \tau_0 e^{\frac{U-\gamma\sigma_m}{kT}},$$

where τ_0, U, γ, σ_m are the constant, the bond destruction energy, the activation volume, and mechanical stress, respectively. Then, the dimensionless quantity $\gamma\sigma_m/kT$ is the so-called effective temperature.

Fig. 5.6 also show that carbon redistribution in the martensite lattice in polishing results in disappearance of lines M1, M6 and appearance of new lines A9, N1, N2, N3.

As the austenite transformation in polishing is completed, it is possible to find the spectral shape of the austenite phase contained in the surface layer of steel after grinding by substracting the appropriate spectra (see Fig. 5.6). The NGR spectrum of austenite is a superposition of split monoline A1 which can be probably assigned to iron atoms without interstitial atoms in the nearest surrounding (the isomeric shift relative to α-Fe is δ=-0.08 mm/sec, the quadrupole split is ΔE_1=0.23 mm/sec) and doublet A2 assigned to iron atoms with one impurity atom in their first coordination sphere (δ=-0.04 mm/sec, ΔE_2=0.82 mm/sec). One can also see a considerably less intensive doublet A3 (δ=-0.14 mm/sec, ΔE_3=1.35 mm/sec). Doublet A4 (δ=+0.03 mm/sec, ΔE_4=2.52 mm/sec) is very distinctive. It has apparently no relation to the austenite phase, it can probably be assigned to the high spin bivalent iron (Fe^{2+}).

Thus, Mössbauer spectroscopy of steel C45e shows that the diamond paste mechanochemical action does not produce any amorphous phase, the Beilby layer undergoes structural and phase transformations into more stable, steady-state structures. Polishing leads to complete transformation of γ-Fe (austenite) . This is true for any iron alloy having residual (or "burned") austenite, for cast iron Grade 250 in particular (see 5.5).

Since γ-Fe and α-Fe structures have different densities, magnetic and other properties, the γ→α and other transformations naturally result in considerable changes of polished surface properties noticed by many authors [16]. In particular, the increased hardness of the Beilby layers is greatly caused, by carbides produced in carbon steels by polishing. The ultradispersed Beilby layer structure may be considered quasiamorphous because very fine randomly arranged crystals have the size of several elementary cells.

These studies and the reported data allow the following conclusions. Phase and structural transformations, strong diffusion of the surface atoms and dispersion caused by mechanic and chemical action, including microplastic deformation, and accompanied by removal of the material in the molecular scale result from polishing, at least carbon steels. The diamond paste adhesion plays a very important role in polishing. The paste with its high reactivity and oxidation inhibiting properties acts as flux.

5.3. Anisotropy of Surface Properties after Machining

The Mössbauer spectroscopy capabilities to study the anisotropy of surface properties are connected with the fact that hyperfine interaction lines (magnetic dipole or electric quadrupole) are polarized and their intensities depend on the direction of observation relative to fields. These are corollaries of the law of conservation of momentum in the nucleus–γ-quantum system [270] (selection rules). Strong collimation of an incident beam of resonance γ-quantum in the scattering geometry experiments (see Fig. 5.3) yield strong surface anisotropy resolution.

Magnetic anisotropy of ferromagnetic is exhibited in dependence of the sextet HMS lines both on the angle between the magnetization vector and the γ-quantum beam direction and on the specimen magnetization. Consideration of the magnetic dipole interaction within the framework of quantum mechanics shows [270] that lines 2 and 5 (see Fig. 5.2) are always linearly polarized, polarization of other lines changes from circular through elliptic to linear (depending on the radiation direction and the nuclear magnetic field induction vector). Intensities of lines 1 and 6 (see Eq. (5.1)) are equal and always three times larger than the intensities of lines 3 and 4. The ratio of intensities of lines 2 and 5 ($\pm 1/2 \rightarrow \pm 1/2$ transition

with $\Delta m=0$, see Fig. 5.2) those of lines 3 and 4 ($\pm 1/2 \rightarrow \pm 1/2$ transition with $\Delta m=\pm 1$) is

$$I_2/I_3=4\sin^2\theta/(1+\cos^2\theta),$$

where θ is the angle between the ordered electron spin and the γ-radiation directions,

3/2 and 1/2 are spins of the first excitation and the ground levels for the transition E=14.4 keV ^{57}Fe.

Nuclear ^{57}Fe magnetic field induction is antiparallel to the domain magnetization [253]. The average ratio is $I_2/I_3=2$ with disordered orientations of electron spins and without lattice vibration anisotropy in a polycrystalline specimen (absence of the Goldansky-Koryagin effect [254]). Such ratio of the intensities of lines 2 (5) and 3 (4) is always observed for a fine isotropic ferromagnetic specimen in the transmission geometry. It can be shown that the conversion electrons in the geometry of tangentially incident γ-quantum beam (see Fig. 5.3), change this ratio from ratio (5.1) because of different angular distributions of the conversion angle for lines 1 and 6 (3, 4) and lines 2 an 5. In particular, a γ-quantum beam tangentially incident on the magnetic isotropic specimen surface gives the ratio

$$3 : 1.5 : 1 : 1 : 1.5 : 3.$$

If the magnetization vector is perpendicular to the surface, the ratio is

$$\alpha = (S_2+S_5)/(S_1+S_6)>0.5,$$

where S_1, S_2, S_5, S_6 are the areas of lines, 1, 2, 5, and 6 in the HMS sextet. If the magnetization vector lies in the surface plane then this ratio depends on the angle between the beam axis and the magnetization vector.

The Mössbauer effect anisotropy was used largely for monocrystals [253]. Systematic research on the surfaces of polycrystals is in the initial stage. There are few reports on magnetic texture studies [271–273, etc.). For polycrystalline specimens the Goldansky-Koryagin effect manifesting itself in the asymmetry of resonance quadrupole line intensities, has been thoroughly analyzed in [254]. The machining accompanied by plastic deformation is known to produce crystallographic deformation texture of isotropic polycrystalline ferromagnetic specimens making them magnetically anisotropic [264]. So armco-iron has prevailing grain orientation (100) [011], consequently, two directions of fast magnetization lie in the specimen plane.

Section 5.2 notes that the crystallographic texture influences the Mössbauer effect anisotropy in the steel surface layer made completely anisotropic by grinding

and isotropic by polishing. The iron alloy ordering is activated by plastic deformation which leads to numerous detects after grinding. Besides, the resulting stressed surface layer state [73] leads to the magnetoelastic anisotropy as deformation causes additional atomic magnetic interactions and induces lattice distortion. This section presents the results on anisotropy upon directed grinding of steel C45e specimens considered in 5.2 [274]. The grinding direction was fixed within ±3°. Anisotropy effects were measured at various angles θ between the grinding direction and the γ-quantum beam propagation axis. For this the specimen was rotated around its axis normal to its surface.

Fig. 5.8 presents the ground surface Mössbauer spectra measured at θ=0 and π/2, respectively. The spectrum includes the superposed of α-Fe HMS line sextet and a γ-Fe monoline. A great number of low-intensity resonance lines is associated with iron phase states on the surface. The intensities of resonance lines 2 and 5 strongly depend on the observation angle θ, as compared with the intensities of HMS lines 1 and 6. The fact evidences the formation of a grinding-induced magnetic texture on the surface. Figure 5.9 is a plot of $\alpha+(S_2+S_5)/(S_1+S_6)$ versus the angle θ. The shape of the curve suggests that the domain magnetization is oriented mainly along the grinding direction because the extremes of the function α(θ) occur at θ=0 and θ=π/2, respectively, i.e. a certain electron spin ordering relative to the gamma-radiation direction takes place.

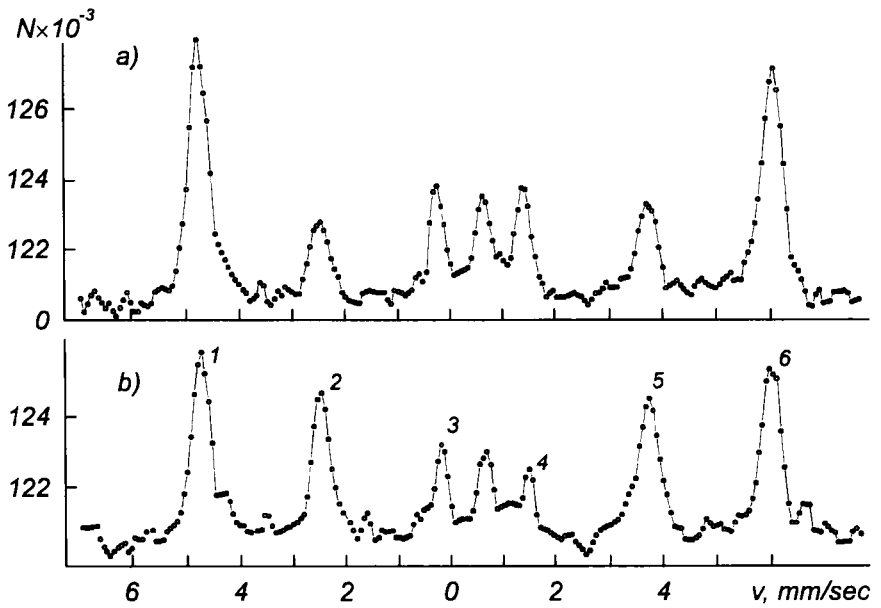

Fig. 5.8. Ground surface Mössbauer spectra measured at θ=0 and θ=π/2: digits are numbers of α-Fe HMS lines.

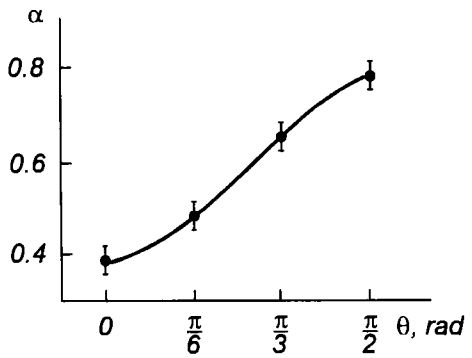

Fig. 5.9. Plot of $\alpha = (S_2+S_5)/(S_1+S_6)$ versus angle θ.

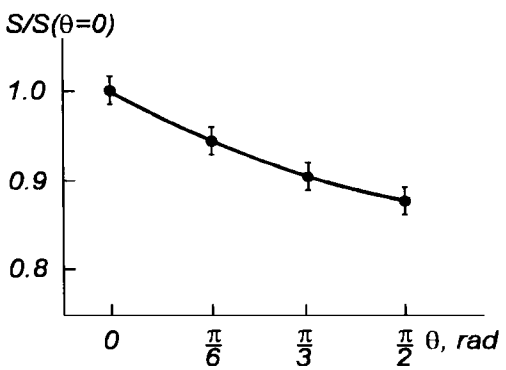

Fig. 5.10. Plot of NGR relative spectrum area versus angle θ.

The dependence of the total area of all resonance lines S on the angle θ is shown in Fig. 5.10. This result cannot be interpreted validly so far.

It is known [272, 273] that the atomic magnetic moment in thin magnetic films is mostly parallel to the surface and they are some kind of magnetic monocrystals. It is possible that a partial orientation of crystal grains in the direction of mechanical action results in the surface structure with some properties similar to the structure of monocrystals with a well-known factor f anisotropy in different directions [253]. Besides, the crystal lattice of polycrystal grains deforms in the direction of the action which can also make the factor f dependent on the observation angle θ because any anisotropy of lattice variations in polycrystalline materials changes the ratio of line intensities.

We consider a simple model of a magnetized surface layer according to [272] (in apply to the experiment as shown in Fig. 5.3). The magnetized surface layer is assumed to be a thin magnetic film having two regions with mutually

perpendicular magnetic moments lying in the planes $A_{\parallel}$ and $B_{\perp}$. The ratio of the areas under (intensity) lines 2 (5) and 3 (4) is zero if the angle between the primary γ-quantum beam direction and the fast magnetization axis is $\theta=0$ the film consists of regions $A_{\parallel}$, the ratio of the areas is 3 at $\theta=\pi/2$ when the film consists of regions $B_{\perp}$. Then the relative area of the regions with magnetic moments parallel to the γ-quantum beam direction is $\alpha=1-\beta/3$, where β is ratio of the areas of lines 2 and 3 (S_2/S_3).

The quantity α characterizes the magnetization vector orientation of a polycrystal. In this case $\alpha\cong0.75$.

Studies of the magnetic ordering of the iron alloy surface layer upon cutting, grinding, rolling, friction, etc., are interesting because the NGR system (Fig. 5.3) for recording conversion electrons can measure the magnetic texture tensor on ferrous surfaces.

Further investigation of Mössbauer effects on polycrystalline textured objects may lead to the development of a method which will provide new information on the solid structure.

5.4. Crystalline Lattice Deformation of Stainless Steel Surface Layer by Grinding

The Mössbauer effect probability is defined in terms of the Debae-Valler factor [253]

$$f = e^{-\langle x^2\rangle/\lambda^2}, \tag{5.2}$$

where $\langle x^2\rangle$ is the atomic root-mean-square oscillation amplitude in the γ-quantum radiation direction;

λ is the Mössbauer radiation wave length λ over 2π.

Eq. (5.2) shows that the Mössbauer effect probability can vary under any actions disturbing atom-lattice bonds. Does grinding change f and, consequently, friction? Grinding does deform grains in the direction of action and causes structural inhomogeneity in the machining plane [275]. Besides, it is found that the resonance quantum fraction varies when the absorber is compressed [276]. Section 5.3 has an assumption that the vector f variations in ferromagnetic steel C45e surface layer are caused by the disturbance of the lattice cubic symmetry by mechanical deformation. This assumption has been verified by studying the Mössbauer effect anisotropy in the stainless steel thin surface layer (the test thickness is 100 nm).

The choice of corrosion–resistant steel 12/13 as the investigation object is purposeful. The absorption spectrum of ^{57}Fe nuclei in stainless steel at room

temperature is relatively simple, consisting of a single broadened line (Γ= 0.40 to 0.50 mm/sec [277]). Stainless steel has a comparatively large f at room temperature (f≅0.684). Moreover, that transformation of austenite into martensite [278] is known to occur in stainless steel at deformation. Meanwhile, there is no generally recognized concept of the structure of the gamma resonance spectrum of single broadened line in the NGR absorption spectrum [277, 279–281] (Γ_0= 0.097 mm/sec). It should also be noted that all the data on the NGR spectroscopy of stainless steel are reported in the γ-quantum transmission geometry.

The measurement method and gamma-resonance spectrum processing procedure are described in 5.1. Steel specimens of 12/13 shaped into of plates 40×40×2 mm^3 were pre-annealed in vacuum at 1373K for 1 h. Then, some were subjected to grinding up to roughness 6–7 on a surface grinder without cooling lubricant. The grinding direction was maintained constant. The conversion electron detection geometry (see Fig. 5.3) was invariable.

An austenite line, 0.45±0.01 mm/sec in width, shifted by δ=-0.137±0.002 mm/sec with respect to α-Fe is observed in the Mössbauer spectrum of annealed steel (Fig. 5.11).

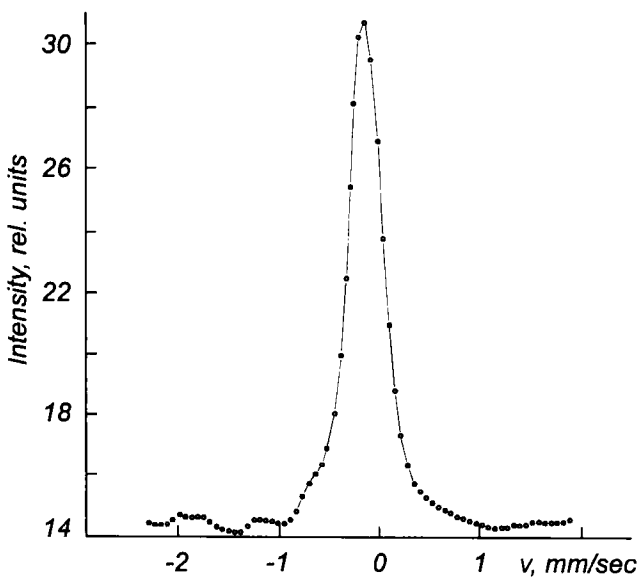

Fig. 5.11. Mössbauer spectrum of annealed 12/13 stainless steel.

To identify the steel surface structure anisotropy, the Mössbauer spectra were measured at two angles θ between the machining direction and the γ-quantum beam propagation axis: θ=0 (Fig. 5.12, curve 1) and θ=π/2 (Fig. 5.12, curve 2) [279].

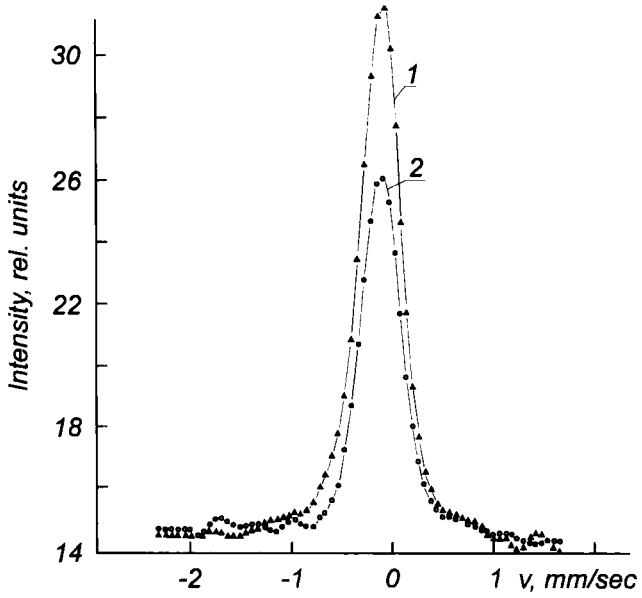

Fig. 5.12. Mössbauer spectrum of 12/13 steel measured at two angles θ between machining direction and γ-quantum beam propagation axis: 1) θ=0; 2) θ=π/2.

High anisotropy of the Debae-Valler factor f is found at different beam orientations. The ratio is

$$f(\theta=0)/f(\theta=\pi/2)=1.50;$$

the total Debae-Valler factor is

$$f=\sqrt{f(\theta=0)\times f(\theta=\pi/2)}=0.662,$$

or 3% less than that of f_0 (f_0 is the Debae-Valler factor of annealed steel) . The inequality $f<f_0$ shows insignificant predominance of tensile strain over compressive strain in the thin ground layer . This fact cannot be explained only by changes in the root-mean-square atomic displacement in the thermal motion of crystal lattice nodes along the grinding line or lattice deformation occurring along it. To evaluate it take Eq. (5.2), the ratio is then

$$1.5=f(\theta=0)/f(\theta=\pi/2)=e^{-(\langle x^2_{\perp}\rangle-\langle x^2_{\parallel}\rangle)/\lambda^2},$$

where $\langle x^2_{\perp}\rangle$, $\langle x^2_{\parallel}\rangle$ are root-mean-square displacements across and along the grinding lines, respectively; $\lambda = 14\ pm$.

Hence, $$\Delta x=\sqrt{\langle x^2_{\parallel}\rangle-\langle x^2_{\perp}\rangle}=\lambda\sqrt{\ln 1.5}=9\,\text{pm}.$$

The γ-Fe lattice characteristic dimension is 0.3 nm. Therefore, the lattice deformation is about 3%.

Since a very thin surface layer (100 nm) is deformed X-rays fail to detect it.

The spectral line width shown in Fig. 5.12 is 0.47 to 0.48 mm/sec. Insignificant broadening of single Mössbauer lines ($\Delta\Gamma$=0.02 to 0.03 mm/sec) after grinding can probably be attributed to the influence of defects on the force constants, electric field gradient, electron and spin densities of resonant nuclei [282].

Mathematical processing of the spectra in Fig. 5.12 indicates that only a negligible quantity (less than 2%) of magnetic phases appear on the vacuum annealed steel surface after grinding giving additional information about the stainless steel spectral structure.

According to some reports [261, 277] a large line width in the stainless steel NGR spectrum can be attributed to fluctuations of the isomeric shift on ^{57}Fe nuclei. According to [280] it is related to a quadrupole splitting unresolved doublet (ΔE=0.11±0.02 mm/sec).

The surface layer crystallographic texture generated by directed machining [264] should result in altered ratios of the line intensities when the hyperfine doublet splits at different angles θ [253]. In particular, the ratio of the line intensities of monocrystals in the quadrupole spectrum is

$$I_\pi / I_\sigma = 3(1+\cos^2\theta)/(5-3\cos^2\theta), \qquad (5.3)$$

where (3/2) → (1/2) nuclear transition is the π-transition;

(1/2) → (1/2) is the σ-transition;

θ is the angle between the γ-quantum escape direction and the axis of the electric field gradient in a monocrystal (for an axi-symmetric field) [253].

The ratio $(I_\pi / I_\sigma)(\theta=0)=3/1$,

$(I_\pi / I_\sigma)(\theta=\pi/2)=3/5$.

In partial grain orientation the line intensity ratios differ from the above values, the difference allows to estimate the grain orientation

$$\varepsilon=(N_{\parallel}-N_{\perp})/(N_{\parallel}+N_{\perp})$$

where $N_{\parallel}$ and $N_{\perp}$ are the numbers of crystal grains oriented parallel and perpendicular to the electric field gradient .

ε is determined by the minimum of function

$$(I_\pi / I_\sigma)(\theta)=(S_1/S_2)(\theta),$$

where S_1, and S_2 are the areas under the respective lines of the quadrupole split doublet.

There are fundamental difficulties in comparing expression (5.3) with the result in Fig. 5.12. because of a very small ΔE. Comparison of expression (5.3) with experimental data is only possible if the components of the quadrupole spectrum are sufficiently spaced ($\Delta E >> 2\Gamma$) [254]; in our case $\Delta E \approx \Gamma$. Nevertheless, the gamma-resonance spectrum shape at $\theta=0$ and $\theta=\pi/2$ is different in the case of doublet splitting.

Indeed (see Table 5.1 and Fig. 5.12) the special center of gravity at $\theta=0$ is shifted to negative (δ=-0.147 mm/sec), and at $\theta=\pi/2$, to positive speeds (δ=-0.115 mm/sec) with respect to the center of gravity of the line for a vacuum annealed specimen (δ=-0.137 mm/sec). The quantity $\Delta\delta$=0.032 mm/sec substantially exceeds the drift of parameters over the velocity scale of the NGR spectrometer (0.002 mm/sec). Therefore, the obtained result can be explained by the presence of an unresolved doublet of the quadrupole splitting in the austenite spectrum. Comparative analysis of the two spectra shown in Fig. 5.12 has also revealed a low-intensity quadrupole splitting doublet A2 (ΔE=0.70 mm/sec; the isomeric shift δ=-0.23 mm/sec) with the intensity 8% of the total spectrum intensity. The presence of doublet A2 can probably be attributed to the electric field gradient on ^{57}Fe nuclei with one atom of dope or impurity in their first coordination sphere.

TABLE 5.1

Mössbauer spectral parameters for the 12/13 steel thin surface layers after machining

Treatment	Mössbauer effect probability f, rel. units	Isomeric shift δ with respect to α-Fe, mm/sec	Half-height line width Γ, mm/sec
Vacuum annealing	0.684	-0.137 ± 0.002	0.45 ± 0.01
Dry grinding ($\theta=0$)	0.810	-0.147 ± 0.002	0.47 ± 0.01
Dry grinding ($\theta=\pi/2$)	0.543	-0.115 ± 0.002	0.48 ± 0.01

Grain deformation anisotropy across and along the grinding direction (crystal lattice deformation) results in the electron redistribution, i.e. in changes of the alloy electric structure. Therefore, changes in f should be accompanied by changes of the isomeric shift in this case.

Thus, δ as function of θ is explained by the changing ratio of the quadrupole splitting line intensities depending on the angle between the axis of the γ-quantum beam propagation and the electric field gradient in the preferable crystal orientation.

In general, the results allow the following conclusions. Grinding causes crystal lattice deformation in a thin surface layer of vacuum-annealed stainless steel (about

100 nm). In the present case deformation amounts to 3%. It should be noted that deformation is unevenly distributed across the layer and increases considerably towards the surface. This results in the crystallographic grain orientation which is estimated in terms of δ as a function of θ. The surface phase composition remains practically unchanged excepting the appearance of negligible iron phase amounts (under 0.2%). The NGR spectral line broadens and a low-intensity quadrupole splitting doublet with ΔE=0.70 mm/sec and δ=-0.23 mm/sec is found in the line. Indirect data indicate existence of an unresolved quadrupole splitting doublet (ΔE=0.11 mm/sec) in the spectrum.

5.5. Influence of Lubricants and Lubricant-Coolants on Surface Layer Structure and Phase Composition

Grinding with abrasive wheels (hones) with various grain sizes and abrasive particle nature, is widely used allowing to achieve the required precision, sizes and shape of surfaces and their specified roughness. Grinding follows hardening because in most cases the latter does not meet working surface quality requirements. A disadvantage of grinding is that in many cases it reduces hardness of parts. Besides, grinding, like other similar methods fails to provide a set of more or less compatible properties required for subsequent treatment, such as hardness, plasticity, wear resistance, etc. Rigidly fixed abrasive grains strongly deteriorate the surface quality without improving fatigue strength because of the process specifics. Numerous surface defects are produced by abrasive particles. A mechanically damaged layer with a high density of dislocations and microcracks is left, with the underlying layer damaged by mechanical stresses. The thickness of mechanically and physically damaged layer depends on the abrasive material quality and other factors. Lubricant-coolants (LC) are used to reduce the negative effects of dry grinding.

This section presents the results on the influence of lubricants, LC, and especially, dispersed particles of plastic materials introduced into the microcut region together with lubricants, on the structure and the phase composition of the surface layer [283].

Cylindrical specimens, 18 mm in diameter and 14 mm in height from Grade 250 grey cast iron were studied. The end faces of the specimens were ground on a silicon carbide abrasive wheel to roughness 7 with a lubricant-coolant. A control specimen was chosen from the group, another one was subjected to dry diamond grinding to roughness 9 in the air, a third was ground and pure BNZ-4 lubricant [284] was applied, a fourth specimen was ground with BNZ-4-based lubricant with added copper (15% w/w) and nickel (3% w/w) powders dispersed to 71 μm.

Mössbauer spectra of specimen surfaces were measured on a NGR constant acceleration spectrometer according to the method described in 5.1, recording both conversion and Auger electrons and characteristic iron X-ray 6.3 keV quanta in the back scattering geometry (see Fig. 5.3). A Mössbauer source of ^{57}Co in a platinum matrix was used in the measurements.

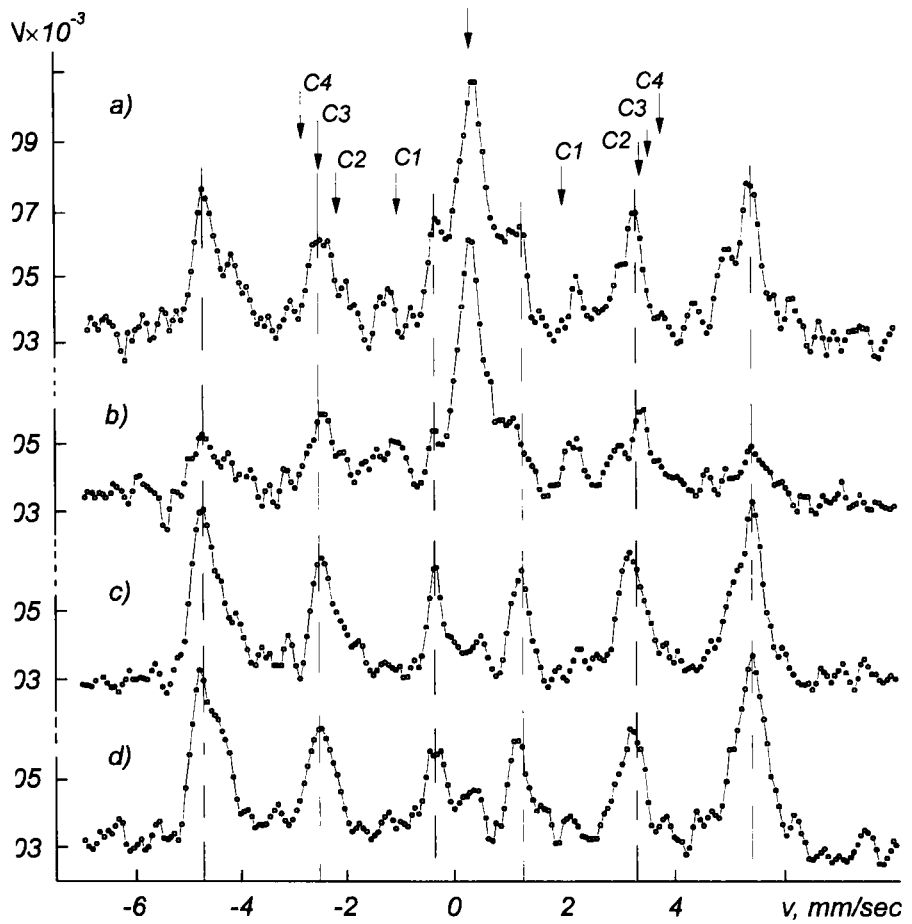

Fig. 5.13. Mössbauer spectra of test Grade 250 cast iron surfaces: penetration is 0.1 μm; a) control specimen; b) after dry grinding; c) after grinding in BNZ-4; d) after grinding in BNZ-4+Cu+Ni.

The results are shown in Figs. 5.13 to 5.15 and Table 5.2. It can be seen from the difference gamma-resonance spectrum (see Fig. 5.14,a) and Table 5.2, that dry grinding of a thin surface layer 0.1 μm increases the carbide concentrations at the following effective magnetic fields on the nucleus ^{57}Fe:

8.12×10^6 A/m ($Fe_5C_2(Fe^{III})$), 14.64×10^6 A/m ($Fe_5C_2(Fe^{II})$),
16.55×10^6 A/m (Fe_3C), 17.51×10^6 A/m ($Fe_5C_2(Fe^{I})$)
(lines C1, to C4, respectively), the austenite concentration slightly increases (lines A1, A2). The Mössbauer spectrum of austenite is a superposition of a monoline

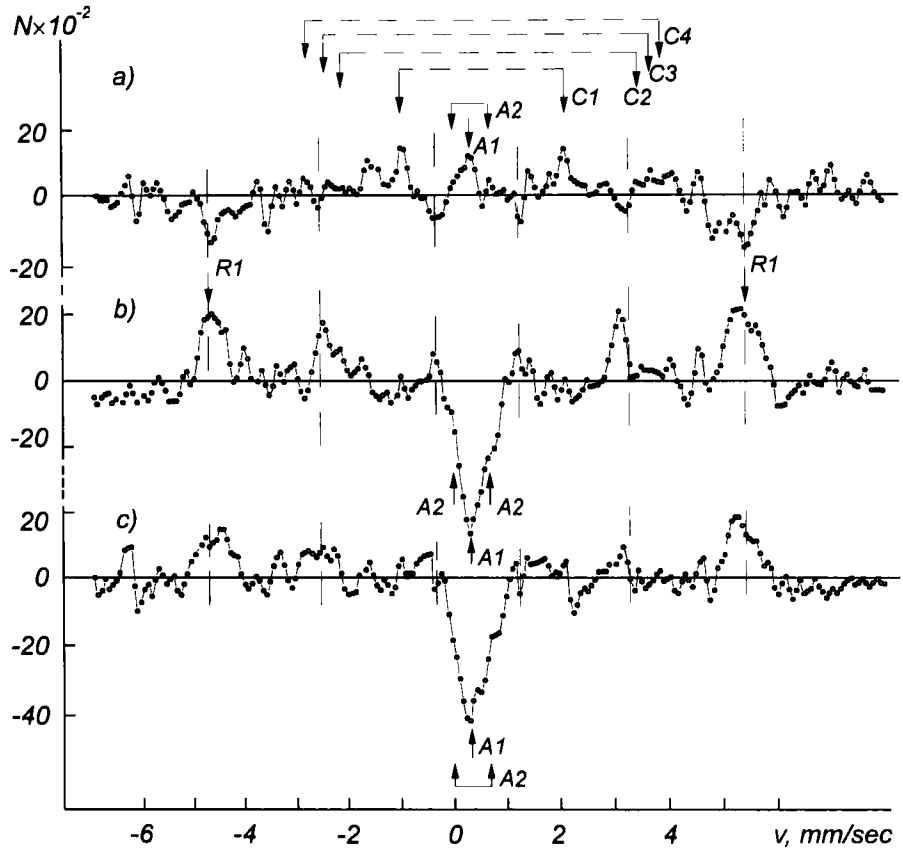

Fig. 5.14. Difference Grade 250 cast iron Mössbauer spectra, control specimen spectrum subtracted; a) dry grinding; b) grinding in BNZ-4; c) grinding in BNZ-4+Cu+Ni.

with the isomeric shift δ=0.39 mm/sec and a doublet with the quadrupole splitting ΔE=0.71 mm/sec and δ=0.43 mm/sec (isomeric shifts relative to sodium nitroferricyanide). At the same time, the intensity of the main broadened HMS line sextet decreases. The lines with effective magnetic fields of 21.65×10^6 A/m, 19.89×10^6 A/m, 18.62×10^6 A/m presumably attributed to carbonaceous martensite [285] produced by heavy heating and quick cooling, are slightly visible, they are not shown in Fig. 5.14,a. Partly, the same tendency but on a much smaller scale

is found in a 10 μm layer. A negligible growth of the austenite phase (see Fig. 5.15,a,b, line A1) is observed. The concentration of α-phases with effective magnetic fields close to the magnetic field intensity for α-Fe decreases.

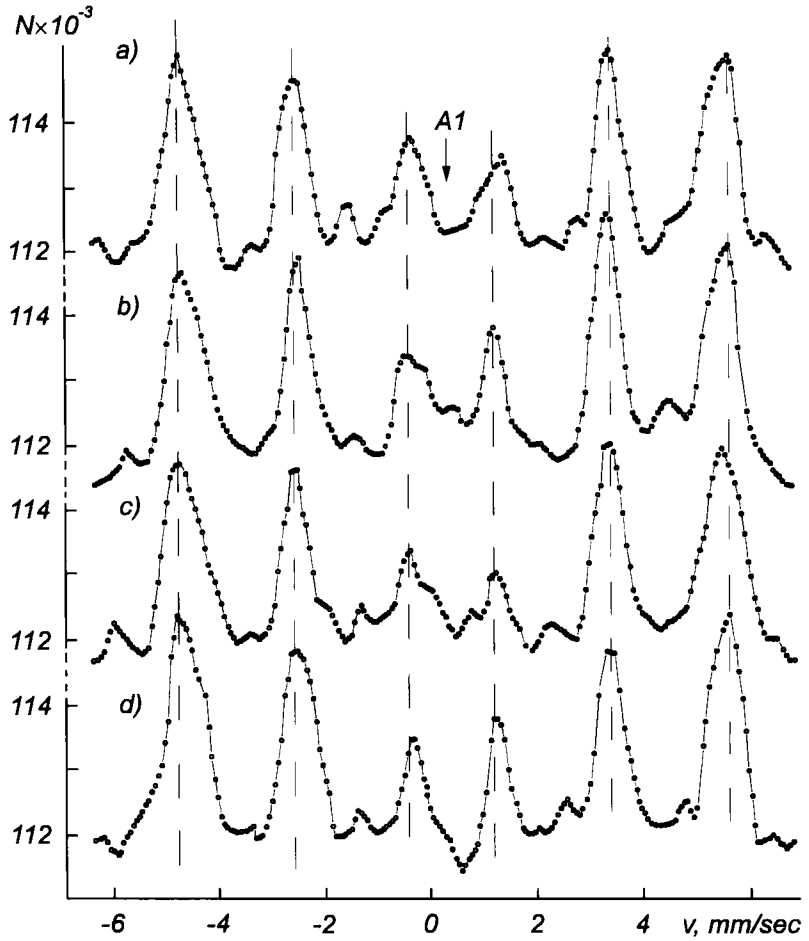

Fig. 5.15. Mössbauer spectra of test Grade 250 cast iron surfaces: penetration depth is about 10 μm; a, b, c, d - same as in Fig. 5.13.

The NGR spectra of Grade 250 cast iron after grinding in BNZ-4 lubricant and in composite BNZ-4+Cu+Ni lubricant are generally the same (see Fig. 5.13,c,d; Fig. 5.15,c,d). First of all, the fact that grinding under such conditions results in practically a complete transformation of the paramagnetic γ-Fe into the ferromagnetic iron and its alloys attracts attention. The difference gamma-resonance spectra (see Fig. 5.14,b,c) show that at the expense of decreased austenite concentration (lines A1, A2), the concentration of α-phases forming the

sextet of broadened HMS lines (extreme lines R1) increases. The intensity of the main broadened HMS sextet also increases in a 10 μm surface layer upon grinding in the lubricant (see Fig. 5.15,c,d).

Grinding of grey cast iron with feritte-pearlite structure induces transformations probably leading to ledeburite which is an evtectic mixture of austenite and cementite. The austenite concentration in the control specimen surface layer about 0.1 mm deep is 20% (see Table 5.2); the estimation is based on the gamma-resonance spectrum area. Dry grinding by diamond wheel with smaller abrasive grains at a higher microcutting speed accelerates ferrite-to-austenite transformation. A high concentration of carbon which is contained in grey cast iron and released as graphite, increases carbon content in the α-Fe lattice and initiates the lattice rearrangement to produce a face-centered γ-phase and carbides.

Table 5.2 shows that the austenite concentration in the 0.1 μm surface layer increases to 23% after dry grinding. The carbide concentration simultaneously increases from 2 to 10% . Meanwhile, the Mössbauer effect probability decreases noticeably. If the probability f on the control specimen is assumed to be 100%, after dry grinding f becomes 85% both in the 0.1 μm and 10 μm thick layers. The decrease of f upon grinding is caused by many reasons. Some of them were discussed here earlier, but in this case another mechanism is possible. The eutectic alloy, which in the solid state is a dispersed mixture of crystals γ-Fe and carbides greatly differing in crystal structure, has a low eutectic formation temperature compared with crystal melting temperature. This is caused by crystal lattice deformations, a large number of defects (vacancies, dislocations, impurities, etc.) in the thin surface layer. Atoms in the interface have a higher energy and a higher thermodynamic potential. These factors are equivalent to a higher surface temperature, thus f reduces.

TABLE 5.2

Influence of grinding conditions on probability of resonance interaction f and surface layer phase composition, %

Parameter	Control specimen	Dry grinding	Grinding in BNZ-4	Grinding in BNZ-4+Cu+Ni
f in 0.1 μm layer	100	85	83	92
f in 10 μm layer	100	85	105	102
Austenite concentration in 0.1 μm layer	20	23	<2	<2
Austenite concentration in 10 μm layer	<1	<1	<0.5	0
Iron carbide concentration in 0.1 μm layer	2	10	<1	<1

BNZ-4 oil functions partly as a lubricant-coolant, thus the effective surface temperature in this case does not reach the temperature for α-Fe to γ-Fe transformation; the inverse transformation typical for alloy tempering [261] takes place instead. The austenite phase (see Fig. 5.13, curves c, d) is almost fully absent. The Mössbauer effect probability slightly increases in the 10 μm layer (Δf=5%) on the contrary, it decreases substantially in 0.1 μm layer (Δf=-17%). It can probably be attributed to the adsorption of lubricant molecules and decomposition products on the surface, in other words, adsorption decreases solid hardness and strength (the Rehbinder effect) leading to almost critical defects in the thin surface layer. The adsorption effect of lubricant makes metals cutting, grinding particularly, easier, hence surfactants are widely used in the lubricant-coolants. Surfactants change the surface layer stress state , decrease the stress gradient normal to the surface directing it into the bulk . All this yields the surface layer change in f we have observed.

Thus, the effect probability f is reduced both by phase transformations, due to grinding, numerous defects and also by surfactants. Therefore, plastic copper and nickel particles in the lubricant quicker curie defects and produce better surface structures. Particles of fusible metals function as an interlayer ("a solder") in the fine-grained surface material. A relative probability of the effect in the 10 μm layer considerably increases and reaches 102%. Also f quickly grows in the 0.1 μm surface layer, however, it does not the probability in the control specimen (see Table 5.2). It can be probably attributed to copper and nickel particles screening of the electron escape into the surface layer. This fact (the growing f) is remarkable because it helps to under stand the positive effect of metal particles in lubricant on grinding [283].

The investigations show that grinding is accompanied by phase and structural transformations in the cast iron surface layer. Dry grinding of Grade 250 cast iron produces austenite, grinding in lubricant transforms the austenite fully into the Fe-C alloy ferromagnetic phases.

Addition of soft plastic metals to lubricant is favorable for the surface layer state. In this case the surface layer is characterized by a higher probability of the Mössbauer effect and a relatively more balanced and stable structure throughout the 10 μm layer. Thus, the layer has a smaller concentration of structural grinding-related defects and a lower effective temperature.

Copper and nickel atoms penetrate into the α-phase cast iron, which is evidenced by the typical broadening of gamma-resonance spectrum lines compared with the cast iron spectral lines after grinding in pure BNZ-4 lubricant (curves c, d in Fig. 5.13). The most essential changes occur in the 0.1 μm surface layer.

A fine structure is seen in the NGR spectra of the austenite formed in the thin cast iron surface layer after grinding. To identify the lines, the NGR spectrum is taken separately in a different measurement scale (the division in the channel is

0.028 mm/sec). The spectrum measured at the tangential γ-quantum incidence in the grinding direction is shown in Fig. 5.16. Apart from monoline AO (the isomeric shift relative to α-iron δ=-0.08±0.02 mm/sec and doublet A1 (δ=-0.09±0.02 mm/sec, quadrupole splitting ΔE=0.70±0.02 mm/sec), corresponding to iron atom nuclei in the lattice nodes with one carbon atom in the first coordination sphere, lines A2 and A2′ are found spaced by 0.35±0.02 mm/sec. These lines are seen most distinctly in the plot of the original spectrum first derivative (Fig. 5.17).

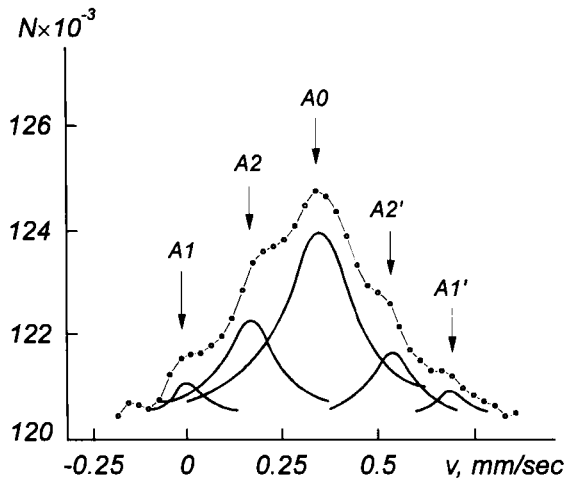

Fig. 5.16. Mössbauer spectrum of austenite measured at tangential γ-quantum incidence in the grinding direction.

Machining is known to create the crystallographic grain orientation [264]. It is mentioned here earlier that the technique of recording conversion electron used in this study is sensitive to the surface layer anisotropy because the γ-quantum beam irradiates the target surface tangentially. It is also known that the intensity of the quadrupole splitting component in monocrystals depends on the angle between the electric field gradient direction and the axis of the incident gamma-radiation beam [253].

Another verification measurement was made to check the assumption that lines A2 and A2′ compose a quadrupole splitting doublet but with the γ-quantum beam incident normal to the grinding direction (Fig. 5.18).

Comparison of Fig. 5.16. with Fig. 5.18 shows that the intensity ratio of both doublet A1 lines and lines A2 and A2′ has changed, similarly. Therefore, lines A2 and A2′ compose a quadrupole splitting doublet (ΔE=0.34±0.01 mm/sec, δ=-0.07±0.01 mm/sec).

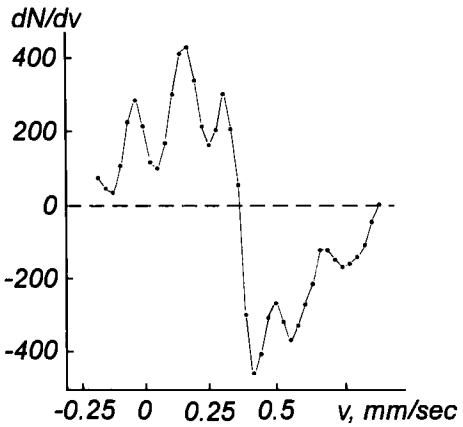

Fig. 5.17. Plot of the first derivative of the spectrum shown in Fig. 5.16.

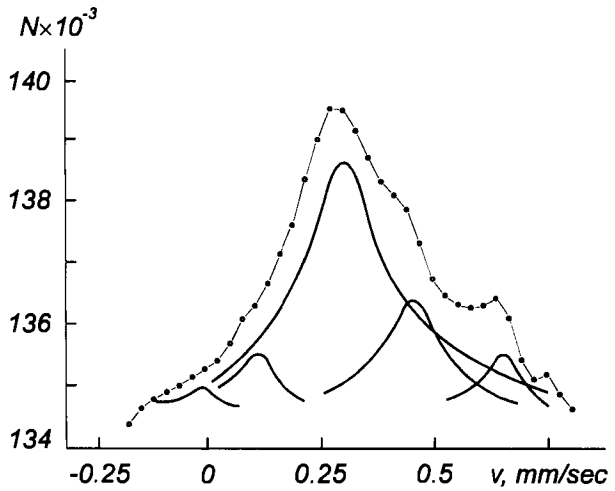

Fig. 5.18. Mössbauer spectrum of austenite measured at γ-quantum beam incidence perpendicular to the grinding direction.

Besides, as it is shown above, the austenite phase together with doublet A2 (see Fig. 5.13,a,c) disappears from the test specimen ground in BNZ-4 lubricant. It is natural assume that doublet A2 may belong to austenite, in our opinion, it corresponds to iron atom nuclei in the nodes of the lattice with carbon in its second coordination sphere [261]. It should be noted that doublet A2 cannot belong to two carbon atoms in the first coordination sphere because its quadrupole splitting is less than that of doublet A1.

A 0.027 mm/sec common shift of the austenite spectrum reproducible in repeated measurements is observed when comparing the spectra in Fig. 5.16 and Fig. 5.18. This result has similar interpretation with that for stainless steel in 5.4.

5.6. Surface Modification by Nonabrasive Antifriction Finishing

One new method of nonabrasive antifriction finishing (NAF) employs a soft polisher as a tool, the active substance contains dispersed soft metal particles [286] instead of abrasive particles. The method serves for controlled tribochemical regeneration of surfaces, increasing the microrelief quality without abrasive shearing of asperities.

It is suggested that NAF partly modifies the surface and makes it better suitable for further modification in machining. Modifications imply new phase compositions and surface layer structures compared with the original.

The conversion electron NGR spectroscopy later validated these assumptions. Structural and phase changes of surfaces were investigated both in NAF and under heavy loads that simulated the existing conditions of operation. The method has been chosen because the NGR spectroscopy is highly sensitive to the Mössbauer atom local environment, its electron structure and oscillation dynamics disturbed by various thermal and mechanical effects.

Steel C45e cylinders, 18 mm in diameter and 16 mm tall, ground to roughess 6–7 were vacuum annealed at 1100–1110 K during 10 hours (the heating rate was 280 K/h, the cooling rate to 823 K was 58 K/h, then the furnace was turned off for further cooling).

The end faces of some annealed specimens were polished by hand with diamond paste on suede, the abrasive grain size for finish lapping was 0.25 μm.

The annealed specimen group (NAF-1) was then subjected to nonabrasive antifriction finishing. Using soft cloth, the active substance was a mixture of TsIATIM-201 grease with 10% weight concentration of electrolytic nickel powder. As pressure grew, the active substance was periodically added on the soft polisher in the contact zone with the workpiece (the specimen surface) [286].

Another group of vacuum-annealed specimens was subjected to NAF by a hard polisher (NAF-2). The same active substance was used, the soft polisher was replaced with a hard steel C45e counterbody lapper. Pressure was periodically varied in the contact zone from 0 (each time a fresh portion of the active substance was added) to 35 MPa.

After NAF-1 and NAF-2 the surfaces had roughness 8–9, after diamond polishing (DP) they had roughness 12.

The procedure for measuring and processing the gamma-resonance spectra is described in 5.1, the controlled thickness was about 100 nm. A Mössbauer source was ^{57}Co in chromium. The resonance effect of the test specimen was ~10%.

The NGR spectrum of specimens subjected to the NAF soft polishing (Fig. 5.19) with nickel (NAF-1) is typical of the rest of specimens subjected to the severe treatment (NAF-2).

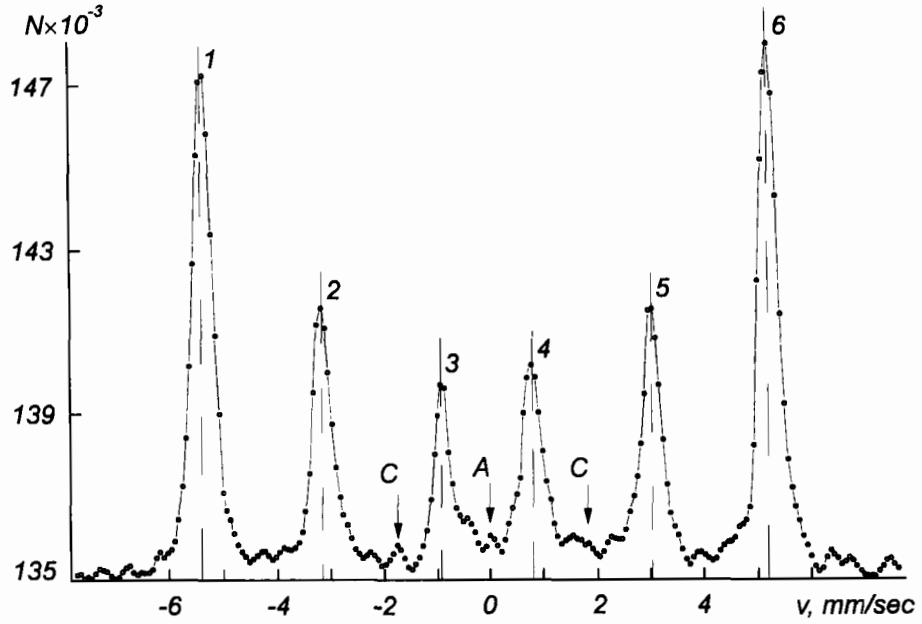

Fig. 5.19. NGR spectrum of steel C45e surfaces after NAF-1.

In order to reveal the differences in the action of these NAF types the difference spectra (obtained by subtraction of the corresponding NGR spectra) of specimens after the soft NAF-1 with nickel and hard NAF-2 (Fig. 5.20,a), and after diamond polishing followed by the soft NAF-1 with nickel (Fig. 5.20,b) were constructed. The results of the spectra processing are presented in Table 5.3.

Diamond polishing of annealed specimens increases the Mössbauer effect probability and narrows lines 1 and 6 of HAS spectra (Table 5.3). These spectra (after diamond polising and vacuum annealing) were measured for comparison and used in the spectra processing of the specimens after NAF.

Soft NAF with nickel (NAF-1). In comparison with the NGR spectrum of specimen No 1 (after VA, see Table 5.3), the NGR spectrum of specimen. No 3 changed considerably. The NAF-1 widths of lines 1 and 6 reduce from 0.42 down to 0.39 mm/sec and lines 2 and 5 broaden.It shows, in particular, the change of the allay phase composition after the treatment and phase component decrease with H_{eff} close to α-Fe.

TABLE 5.3

Mössbauer spectral parameters for a steel C45e surface layer, ~100 nm thick

Treatment	Spectral area S, rel. units	Isomeric shift against α-Fe, mm/sec	$\langle H_{eff} \rangle$ $\times 10^6$ A/m	$\alpha=\frac{S_2+S_5}{S_1+S_6}$	Width of spectral line 1 and 6, mm/sec
Vacuum annealing, VA	1.00±0.01	0.065	26.26	0.50	0.42±0.01
Diamond polishing, DP	1.14±0.01	0.061	26.26	0.51	0.39±0.01
Nonabrasive antifriction finishing, NAF-1 (Ni)	1.17±0.01	0.089	26.28	0.54	0.39±0.01
Nonabrasive antifriction finishing, NAF-2 (Ni)	0.84±0.01	0.025	26.23	0.54	0.41±0.01

Combined processing of the NGR spectra of specimens No 1 and No 3 showed that specimens No 3 acquired lines with $H_{eff}=21.25\times10^6$ A/m presumably due to martensite when in the environment of ^{57}Fe atoms there is one carbon atom. It is reported [287], that the effective magnetic field intensity on ^{57}Fe for this phase is $(21.09 \text{ to } 21.88)\times10^6$ A/m. Besides, Fe_5C_2 (Fe^{III}) carbide with $H_{eff}= 8.75\times10^6$ A/m is formed. Carbide release is known to increase with nickel concentration in Fe–C alloy [288]. Consequently, NAF-1 can diffuse some nickel into the alloy modifying the surface. Phases with H_{eff} of 29.44×10^6 A/m and 32.39×10^6 A/m (lines G and H, respectively, see Fig. 5.20) appear too.

The spectral integral intensity (see Table 5.3) increases approximately by 17%. The quantity $\alpha=(S_2+S_5)/(S_1+S_6)=0.54$ exceeds $\alpha=0.50$ in the magnetoisotropic specimen with the tangential incidence of the γ-quantum beam on the surface. The inequality $\alpha>\alpha_0$ is most likely caused by the components with H_{eff} smaller than 26.26×10^6 A/m (for α-Fe) rather than by magnetic anisotropy that is why the relative intensity of lines 2 and 5 increases. The spectrum center of gravity in Fig. 5.19 shifts to the right by 0.024 mm/sec in comparison with the spectrum of specimens after VA. Indeed, nickel should shift the center of gravity of the spectrum from alloys to the positive velocity region [261], however, the shift here may be due to a difference isomeric shift in the NGR spectra of the phases .

Hard NAF with nickel (NAF-2). Hard polishing with nickel makes the residual paramagnetic phase (line K, see Fig. 5.20), and Fe_5C_2 (Fe^{III}) carbide with $H_{eff}=(8.75\pm0.48)\times10^6$ A/m disappear from the surface layer, instead (line L) Fe_5C_2 (Fe^{II}) carbide with $H_{eff}=(14.64\pm0.32)\times10^6$ A/m (line B) appears, i.e. carbon atoms as the nearest neighbors of ^{57}Fe in nonequivalent sites of Fe^{II} and Fe^{III} in monocline carbide are redistributed. Eleven iron atoms and three carbon are the nearest Fe^{II} neighbors [277].

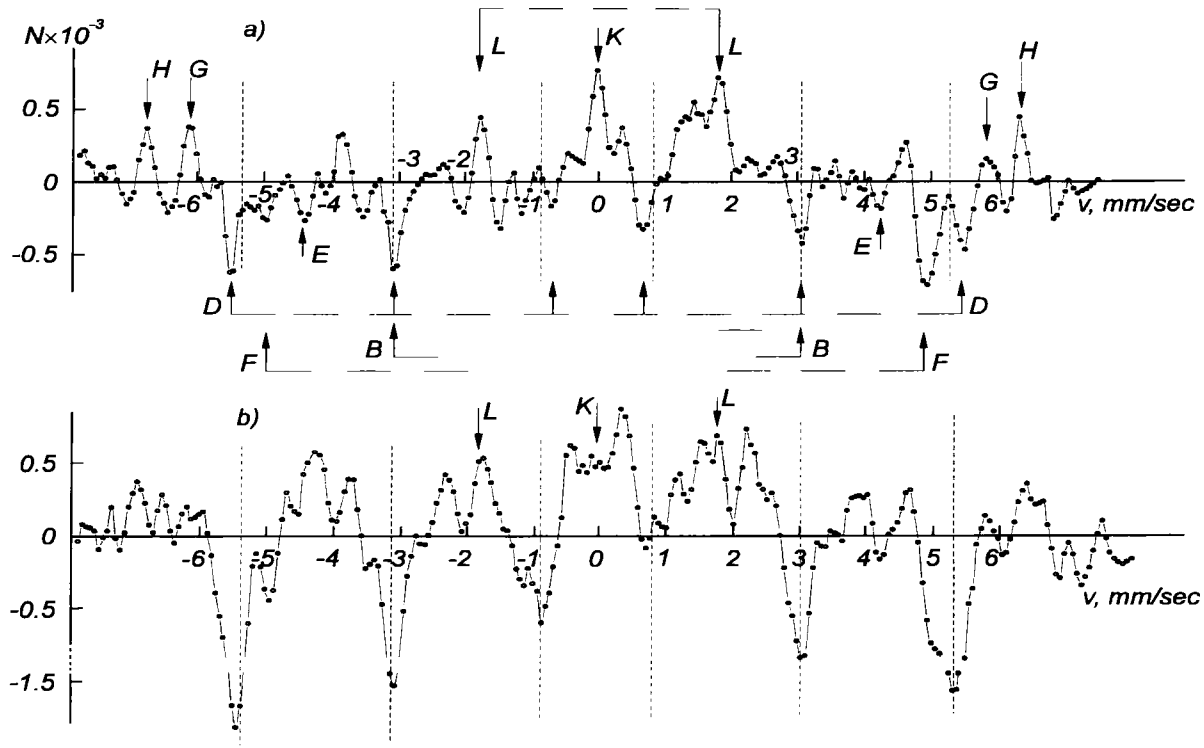

Fig. 5.20. Difference NGR spectra of steel C45e surfaces after NAF-1 and NAF-2 (a) and after NAF-1 and diamond polishing (b).

Considerable result of NAF-2 is the appearance of the HMS line sextet (lines D) with H_{eff}=27.22×10^6 A/m . These lines can presumably be due to the NGR spectrum of Fe–Ni alloy at high contact pressures and shear strains in the hard NAF with nickel. The above H_{eff} coincides with the experimental value 27.18×10^6 A/m reported in other studies for Fe–Ni (1% nickel) alloy.

Compared with NAF-1, the phase concentration with H_{eff}= 21.29×10^6 A/m (line E) corresponding to martensite slightly increases and lines F with H_{eff}=24.39×10^6 A/m appear. The latter may be due to martensite and iron atoms in the nearest neighborhood of carbon atoms because this component (H_{eff}=24.67×10^6 A/m) appears in the spectra of deformed carbon steel and disappears during high-temperature annealing [289].

Concentration of all these phases in the surface layer is negligible in comparison with iron α-phase (H_{eff}=26.26×10^6 A/m), or less than 0.5%.

The extreme lines in the HMS spectrum broaden by 0.021 mm/sec in comparison with the spectral NGR lines of specimens after NAF-1, it is most likely caused by deformations and internal stresses occurring under NAF-2 and by the phase changes mentioned above.

The shift of the center of gravity of the NGR spectrum to the left by -0.040 mm/sec as compared with the control specimen (No 1, VA) cannot be validly explained. The specimen subjected to NAF-2 with nickel shows variations of the isomeric shift which can be due to many factors: such as shifts of atoms from the regular lattice nodes, changes in surface concentrations, phase transitions, conduction electron density changes, etc.

The 27% decrease of the effect probability is most likely due to the screening action of nickel particles penetrating into surface macrodefects, filling asperities, microcracks, and coating separate areas of the surface with a thin film. It is true to assume that the Mössbauer effect probability for steel C45e would not change considerably after NAF-2.

Thus, NAF using plastic metal particles leads to the controlled tribochemical regeneration of the workpiece surface without removing any material even in the molecular scale compared to conventional abrasive polishing when surface modifications occur [286].

5.7. Role of Original Surface State in Structural and Phase Changes at Machining

12/13 stainless steel after VA does not contain ferrite phase (see 5.4). Dry grinding of annealed steel on a surface grinder does not practically change the phase composition providing slight ferrite traces (less than 0.2%) are neglected. Any original material in the form of cold or hot-rolled steel or sheet is plastically deformed and has residual stresses. Indeed, up to 60% of ferrite phase is found

in the NGR spectrum of a thin surface layer (~100 nm) of original commercial 12/13 stainless steel. Subsequent grinding by hand with emery cloth to roughness 7 strictly following grinding rules produces further transformation (Fig. 5.21,b,c). Ferrite phase concentration (α-martensite) in the surface layer increases to 75%. The same results have been obtained when the surface is worked with a file. Comparison of the NGR spectra in Fig. 5.21,b,c with the NGR spectra of annealed stainless steel subjected to various deformations in the γ-quantum transmission geometry [278] indicates that the surface layer resembles to be plastically deformed to 70% .

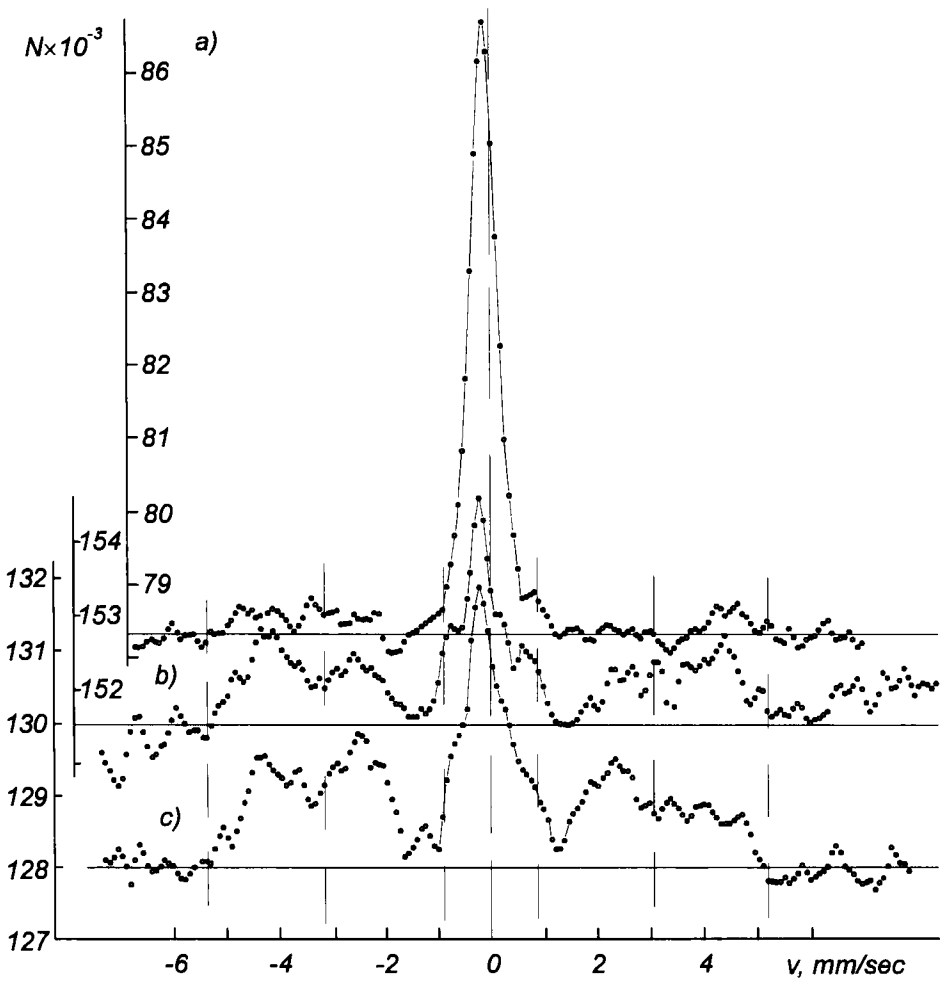

Fig. 5.21. NGR spectra of original 12/13 steel a) after diamond polishing; b) and c) after dry grinding at $\theta=0$ and $\theta=\pi/2$.

The NGR spectrum central line (see Fig. 5.21,b,c) assigned to austenite is asymmetric, its parameters vary within the ranges given in Table 5.1 for a ground specimen after VA.

The NGR spectroscopy sensitivity to structure anisotropy in the sliding gamma-radiation inducing geometry reveals the magnetic grain reorientation on the original surface after grinding. Figure 5.21,b, c shows that the ratio of the sums of lines 2 and 5 intensities with the sums of lines 1 and 6 in the superposed martensite HMS sextet, i.e. $(S_2+S_5)/(S_1+S_6)$ is larger for $\theta=\pi/2$ (see Fig. 5.21,c) which indicates preferential orientation of domain magnetization in the new ferromagnetic phase along the grinding direction.

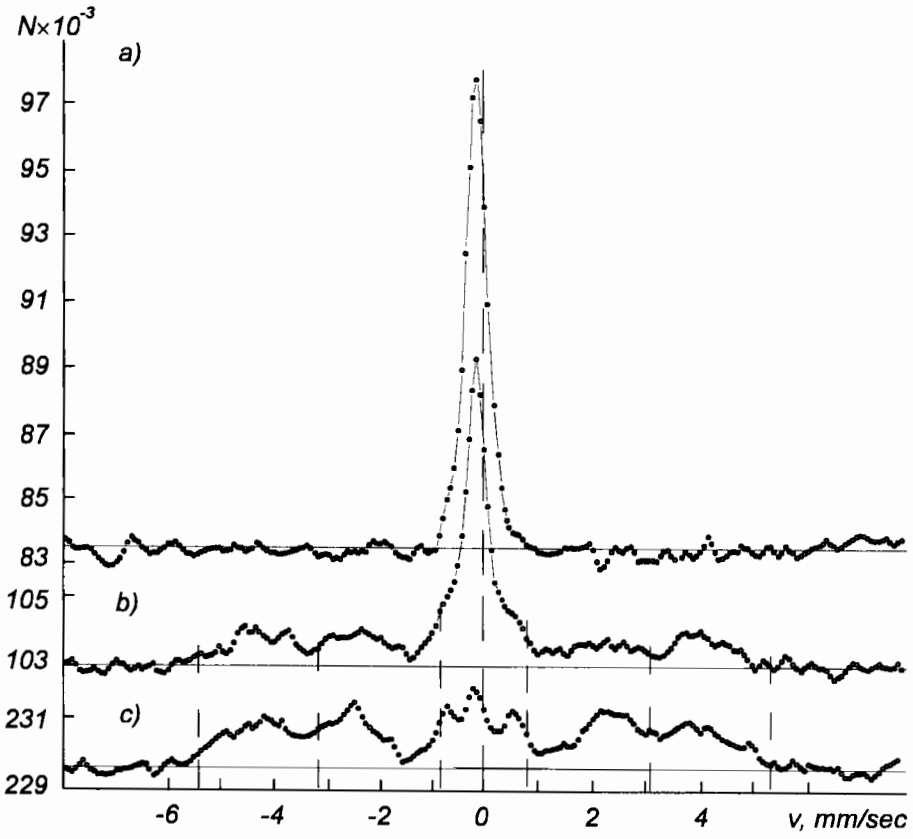

Fig. 5.22. NGR spectra of annealed 12/13 steel: a) after vacuum annealing; b) after diamond polishing; c) after magnetic-abrasive polishing.

Polishing of the original specimen facilitates the inverse $\alpha \rightarrow \gamma$ transformation and the paramagnetic phase concentration increases to 75% (see Fig. 5.21,a). At the same time, polishing of an annealed specimen without any ferrite phase results

in formation of this phase, the paramagnetic phase concentration falls down to 45% (Fig. 5.22,b). The austenite line width (after polishing of the annealed specimen) remains practically unchanged (Γ =(0.462±0.005) mm/sec).

Still more essential structural and phase transformations occur if annealed nonmagnetic metals are polished in the magnetic field. Thus, magnetic abrasive polishing of stainless steel specimens reduces the concentration of the paramagnetic phase in the test surface to 7% (see Fig. 5.22,b). Such strong changes are undoubtedly caused by the magnetic field effect. Explanation of the observed effect is of special interest and is beyond the scope of this book.

In all the cases a substantial change of the Debae-Valler factor f is observed during phase changes. So, the probability of the Mössbauer effect during diamond polishing of annealed stainless steel increases 1.49 times for annealed specimen (see Fig. 5.22 a, b), after magnetic abrasive polishing it is 1.58 times higher (see Fig. 5.22,c). Austenite decomposition is accompanied by changes in the crystal lattice volume causing internal stresses. The α-Fe and γ-Fe structures have different specific gravities, densities, magnetic and other properties (the α-Fe lattice parameter is 0.28 nm, that of γ-Fe is 0.36 nm). The α-Fe lattice in the martensite structure is essentially distorted. The martensite phase is able to induce a nonuniform stress distribution and deformations in the solid solution; resulting in its increased hardness, strength, and brittleness. The maximum deformation is localized before the martensite phase starts growing [290].

The above factors are most likely responsible for substantially higher (about 1.5 times) probability of the Mössbauer effect because they all should reduce the root-mean-square atomic shift $\langle x^2 \rangle$ (see Formula (5.2)).

Thus, the obtained results show that the electron NGR spectroscopy is a unique highly sensitive method of registration of phase transitions, residual stresses and other factors that influence the probability of the phonon-free γ-quantum absorption by the surface. Therefore, to analyze the conversion electron NGR spectra the original state of the specimens should always be taken into consideration.

Chapter 6

INFLUENCE OF EXTERNAL ELECTROMOTIVE FORCES ON CONTACT RESISTANCE AND WEAR

6.1. Electrical Contacts

The state of metal surfaces is modified by various ambient components, electric or magnetic fields, dynamic action by other solid bodies, etc. Mechanical properties of surfaces are governed by the dislocation behavior leading, ultimately, to softening or hardening. At the same time, any action on the surface causes inevitable changes in the surface energy, particularly EWF, which is supported experimentally, by the results described in Chapter 2; it also induces changes in the surface potential barrier which influences the processes of nucleation, motion, and drain of surface dislocations. Hence, ambient actions change the force of atoms bonding to the surface, the work needed to form a new surface, i.e. the surface tension γ. The interaction forces between both atoms inside a body and contacting bodies can be reduced to one fundamental interaction existing in nature, namely, to the electromagnetic interaction. Therefore, an external electric charge changes the energy state of the surface, which inevitably affects its mechanical properties such as plasticity and, hence, wear resistance. Indeed, electric polarization of surfaces in electrolytic solutions accelerates creep in metallic monocrystals and simultaneously inhibits the plastic flow in the presence of thin films, alters dislocation mobility on the surface, hardness, and other mechanical properties of metals [291] .

Electric current through the $metal_1$–lubricant layer–$metal_2$ interface substantially changes the structure and properties of surfaces in steady-state boundary lubrication. To increase the reliability and durability of lubricated sliding electrical contacts (SEC), it is important to know the mechanism of action of the current.

Sliding electrical contacts are characterized by a wear rate of contacting surfaces and high instability of the contact resistance. They are made from noble nonferrous metals and alloys, carbon, graphite, molybdenum disulfide, etc. There exists a wide range of contact materials and lubricants, various designs and operating modes. Each case requires a specific approach to selection of materials to achieve better wear resistance and reliability. In this connection, the effect of external electromotive force (EMF) will be considered in respect to contact resistance and wear of current-collecting devices in which ST in currentless friction cannot be

anticipated. Rotary contact devices (RCD) are designed for continuous supply of electric current from the stationary member to the rotary part. A large variety of RCD of basically different designs are manufactured commercially: brush-type, wire-type, special purpose current-collectors (capacitance-type and coaxial), and comb-type. At the same time relatively compact devices are in constant demand which would contain a large number of circuits, pass both high and low currents, and be reliable in operation within a broad range of temperatures, accelerations, currents, and other parameters. Most of the devices of this class have a comb structure (a "ring–comb" contact). They are fabricated from copper alloys and lubricated with grease once during assembly.

The behavior of a ring–comb pair in operation is affected by many factors: the material of contacting members; alloying and impregnating agents; state of the contacting surfaces; lubricant types; parameters of the ambient medium; pressure upon comb teeth; sliding speed; temperature in the contact; density and frequency of current ; geometry of the contact, etc.

One of the basic shortcomings of commercial comb-type correct collectors is high instability of contact resistance. Grease is uniformly spread over the surface of the ring or the comb teeth, no fresh grease supply is thus possible. In operation, the grease supply is contaminated with wear debris, it changes physical and chemical properties, and eventually begins to function as abrasive powder accelerating wear of the sliding pair.

In order to improve serviceability of ring–comb RCDs, it is necessary to improve their design to utilize new materials and lubricants, to change friction etc., by establishing relations between characteristics of sliding contacts and factors affecting the their operation.

It is difficult to achieve ST in commercial SECs. Selective transfer is observed, as a rule, under continuous renewal of surfactant-containing lubricant, therefore, this operation cannot be realized in principle for each type of sliding contacts. The effect of many parameters on SEC operation has not been studied yet, in particular, the ST possibility without current . With current, the interaction between the macroscopic transfer and ST has still to be found out. It is possible that establishment of the self-restricted macroscopic transfer can become the basic problem of wear control in SEC. Thus, search for methods for developing ST-based lubricated sliding electrical contacts should start with a comprehensive study of the main factors affecting the contact resistance and wear of SEC [292].

Experimental studies of SEC wear mechanism have been carried out, the optimal range of materials and friction parameters has been selected to ensure stable and reliable contact resistance and the minimum wear of contacts. The methods are designed to enhance reliability and durability of ring–comb RCDs. This study has been done together with B.D. Kharkhasov.

6.2. Contact Electrical Resistance

Main requirements for SEC are low and stable contact resistance, reliable transmission of electrical signal, insignificant friction force stable in its value and direction, and low wear.

The stability and reliability of SEC operation can be indirectly estimated by analyzing the contact resistance behavior. It always has higher resistance than the main circuit of the same size because current flows only through the contact spots (see 1.4, Fig. 1.14), i.e. through metallic and quasimetallic contact sites. When closed, interrupting spots, and sliding contacts have to satisfy the requirements set for stationary contacts, therefore the theory of electrical contacts is valid for all kinds of contacts.

Contact resistance represents a "sieve-like" resistance [293] caused by the fact that, current across leads experiences resistance induced by the constriction of current lines, the current constriction density can reach 10^{11} A/m^2. Accurate determination of the relation between the resistance, the contact surface microgeometry and the specific resistance of contacting conductors requires time-consuming mathematical calculations. In the elliptical contact theory, the constriction impedance of two contact electrodes when one contact has radius a [293, 294] is $R_c=\rho/2a$, where ρ is the specific resistance of the contact material.

If the contact is made from different materials with specific resistances ρ_1 an ρ_2, respectively, then $R_c=(\rho_1+\rho_2)/4a$.

For contact with the number of contacting points n, the total true contact area $A=n\pi a^2$, then

$$R_c \approx \rho/(2na)=(\rho/2)\sqrt{\pi/nA}. \tag{6.1}$$

Thus R_c is a function of the number of contacting points n and the total contact area A. The relationship between R_c, material hardness H, and load P_c can be found from the expression $H=P_c/A$; then,

$$R_c=(\rho/2)\sqrt{\pi H/(nP_c)}, \tag{6.2}$$

in other words, the constriction resistance is proportional to the square root of H and inversely proportional to the square root of P_c (this is true for the case of plastic deformation). For plane contacts, n can be assumed proportional to R_c and, consequently, the contact resistance is inversely proportional to the specific load P_c: $R_c=k/P_c$, where k is a constant.

Investigations show that in real conditions the contact resistance is the sum of constriction resistance and the film resistance: $R_c=R_{constr}+R_{film}$.

Insulating or weakly conducting films on contact surfaces may be of various

origin. They are formed both during storage of contact assemblies and in operation with or without current as a result of friction-induced heat release, contact arc heating, dust, lubrication etc. Atmospheric corrosion can result in oxide films. If atmosphere contains sulfides, sulfide films can be formed. Besides, carbonate films, organic films, and others are possible.

Depending on their properties, surface films increase contact resistance, thus reducing the contact reliability. Sometimes, such films are useful since they reduce the friction force, contact weldability, and, in some cases, erosion.

Contact pressure sufficient for plastic deformation results in the cracking of films, the number of real contact spots increases, and, as a result, R_c depends on R_{constr} alone. At low contact pressure the film resistance is important.

High reliability and wear resistance of current collectors can be achieved by introducing a conductive antifriction layer between the contacting surfaces. For this, special greases are applied.

In the presence of grease, the contact crucially depends on the number of metallic and quasimetallic (tunnel effect through the film) contact spots [293]. With the total number of metallic spots m and quasimetallic spots n-m, the contact resistance is

$$R_c = 1 / \left(\sum_{1}^{m} 1 / R_i + \sum_{m+1}^{n} 1 / R_{ni} \right),$$

where R_i is the constriction resistance of an elementary contact; R_{ni} is the resistance of the film on the elementary contact; note that $R_i << R_{ni}$.

The characteristic of the dependence of contact resistance R on voltage across contact U, or the RU characteristic of film-covered contacts, described by the expression

$$R(U) / R(0) = \left(\sum_{i=1}^{m} 1 / R_{io} + \sum_{m+1}^{n} 1 / R_{ni} \right) / \left(\sum_{1}^{m} 1 / R_i + \sum_{m+1}^{n} 1 / R_{ni} \right),$$

where R_{io} is the constriction resistance for $U \rightarrow 0$. Here, R_{ni} depends on the voltage U. Assume U_{ni} independent of U in the domain of small values and comparing it with RU characteristics of clean contacts

$$R(U) / R(0) = \left(\sum_{1}^{n} 1 / R_{io} \right) / \left(\sum_{1}^{n} 1 / R_i \right),$$

it can be seen that the RU characteristic of lubricated contacts must lie below the RU characteristic of clean metallic contacts, the slope of the characteristics of the contacts being determined by the ratio of m to n and by the ratio of constriction

resistance to film resistance. In the case of full crushing of the boundary film by contact asperities, the resistance is equal to the constriction resistance; if solid film persists, the resistance practically equals the film resistance; a partial squeezing of the film is an intermediate case.

The contact resistance value and behavior are determined by a set of many factors [293]. These factors can be divided conventionally into three groups:

1) technological factors (structure, chemical composition, properties of materials);

2) design factors (contact configuration, waviness and roughness of friction surfaces, lubrication method);

3) operation factors (current density, sliding velocity, pressure, temperature, lubricant types and properties).

Thus, the contact resistance is a function of numerous interrelated factors, the limits of their mutual influence cannot be clearly defined, making the development of reliable methods for laboratory tests of SEC difficult. The methods developed [295] allow only to pretest contact pairs in operation and investigate of their applicability range before bench and field tests.

6.3. Contact Resistance of Sliding Electrical Contacts in Experiment

This chapter deals mainly with the analysis of operation factors which influence the performance of ring-comb RCD. However, even this kind of analysis is very complicated, because, on the one hand, contact resistance, even if assessed in relation to operation factors, is a function of many variables:

$$R_c = f(V, t, P, T, j, \ldots),$$

where j is the current density. On the other hand, some of the parameters are interrelated. It is evident, for example, that with velocity V changes, temperature of surface T changes too. This, in turn, changes the specific resistance, and hence, R_c. Finally, in the field of solid phases, the boundary layers considerably change both structure and properties. These changes, impossible to observe directly, are caused by the effects of a complicated stress of surface layers, sign-reversible periodic forces, temperature variations, contact phenomena, and various electrical and mechanochemical processes.

Normally, contact resistance is investigated with the assumption that all parameters, except temperature T, being a function of velocity, are independent. At relative sliding velocity up to 0.3 m/sec (which is true for standard RCD), temperature changes are insignificant and the parameter T can also be assumed an independent. Hence, the relation between R_c and operation parameters can be established by using the following relations:

$R_c=f(t)$ for V, P, j=const;
$R_c=f(P)$ for j, V=const;
$R_c=f(V)$ for j, P=const.

Experimental determination of wear and transient voltage drop on the contact was performed on an AE-5 friction machine and on other laboratory installations having similar friction assembly operation principle. Cylindrical or rectangular mutually insulated parallelepiped-shaped specimens were rubbed with their end faces against disc surface. The contact resistance was estimated by voltage drop across the contact and the current. The contact resistance was investigated as a function of time, initial roughness, load, sliding velocity, contact materials, lubricant type, and current. The effect of lubrication, specimen material, current density and direction on wear was also studied. For this purpose, specimens were washed, dried, and weighed prior to testing.

Standard materials of ring–comb and of ring–brush RCDs were chosen for the studies. Contact pairs from the following materials were tested: beryllium bronze CuBe2 copper Cu-ETP; CuSn6; CuSi3Mn; CuAl10Fe3; CuAl8Fe3; CuSn10P; CuSn5Zn5Pb5. The following lubricants were used: OKB-122-7, TsIATIM-201, TsIATIM-221, both pure and with solid powder admixtures.

The dependence of contact resistance on the run-in time. In most pairs, the contact resistance at lubrication is low in the initial period. It increases with time (Fig. 6.1) up to a certain fixed value, and then stops rising. The run-in time of contacts varies, depending on the operation conditions of pair, from 3 to 8 h. Experiments show that in dry friction R_c etc. decreases as a result of destruction of oxide films and formation direct metallic contact.

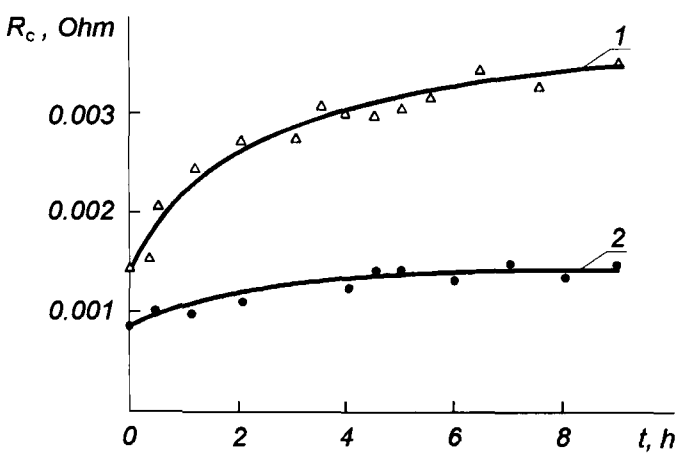

Fig. 6.1. Time dependence of contact resistance for sliding pair CuBe2–CuSn6 with lubricants TsIATIM-201 (1) and OKB-122-7 (2): P=0.08 MPa; v=0.12 m/sec; I=2 A.

In the initial operation period, current passes mainly through metallic contacts on microasperities. As the pair runs in, the real contact area expands, the pressure falls down and a boundary layer appears. All these processes reduce the number of contact spots, hence, increasing the contact resistance. After some time, the electric contacts become mated, the boundary lubricating layer is complete and the contact resistance stabilizes. The run-in end can also be determined from the friction torque which becomes steady simultaneously with R_c (Fig. 6.2).

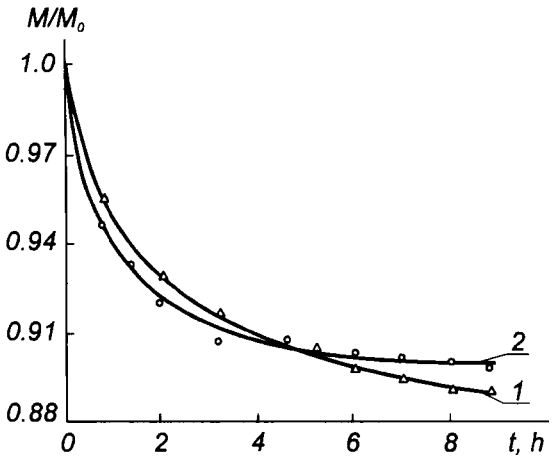

Fig. 6.2. Relative change of friction moment in time for sliding pair CuBe2–CuSn6: conditions are as in Fig. 6.1.

The effect of initial roughness. The running-in rate, wear resistance, and contact resistance of SEC depend, on chemical composition and structure of material; they also depend on friction conditions and treatment of surfaces. Experimental results prove the latter.

In steady-state friction contact resistance has the minimum (Fig. 6.3) for initial roughness 8–10. Similar results are obtained for other contact pairs in various operation modes. Good finish surfaces have asperities comparable with the boundary layer thickness. Metallic contact spots do not appear on flat polished contacts up to pressure corresponding to the metal hardness. Conductance across the boundary layer is effected by the tunnel current. As roughness increases, metallic contact becomes possible at moderate pressure, current passes through metallic and quasimetallic spots, R_c decreases in accordance with the expression (6.1). The shares of the metallic contact and the quasimetallic contact depend on the surface roughness, mechanical properties of contact materials, lubricant type, and the friction mode. At a certain roughness the real contact area is determined by a small number of contact spots, resulting in reduction of the contact resistance. In the present case it is achieved when asperities have R_z about 1.0–1.5 μm.

As roughness increases, (R_z grows) the actual contact area will result from the increasing area of contact spots with simultaneous reduction of their number, which leads to higher contact resistance.

The dependence of contact resistance on the load. For a stationary contact sphere-to-sphere, sphere-to-plane or mutually perpendicular cylinders of equal diameters, the contact resistance (constriction resistance) for small pressure P and elastic deformation is expressed by the following formula [293] :

$$R_c = 0{,}58\,\rho\,\sqrt[3]{E / Pr},$$

where E is the elasticity modulus;

r is the curvature radius of a contact member, i.e. $R_c \sim P^{-1/3}$, and for large P and plastic strain, by formula (6.2), i.e. $R_c \sim P^{-1/2}$. For SEC this dependence is a more complicated, since it is necessary to take into account the sliding velocity, presence of lubricant, configuration of specimens, and current density. Nevertheless, the contact resistance remains inversely proportional to the contact load, which is confirmed by experiment (Fig. 6.4). Thus, decrease of the contact resistance in response to load growth can be explained by the contact area expansion.

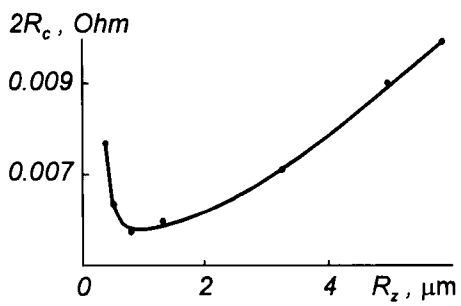

Fig. 6.3. Dependence of contact resistance of CuSi3Mn1–CuBe2–CuSi3Mn1 sliding pairs on initial roughness: I=5 A; V=1.2 m/*sec*; P=0.06 MPa; TsIATIM-201 lubricant.

For high loads, the presence of lubricant does not have any effect on this relation. Such behavior is likely to be caused by degradation of boundary layers and appearance of direct microcontacts between the surfaces in friction. At smaller loads, when current mainly passes across the boundary layer, the dependence of R_c on lubrication is observed. Operation in such conditions is characterized by extreme instability of the contact resistance. For instance, with the CuSi3Mn1–CuBe2 pair, P=0.02 MPa and lubricant OKB-122-7, fluctuations of R_c reach 50% in the average.

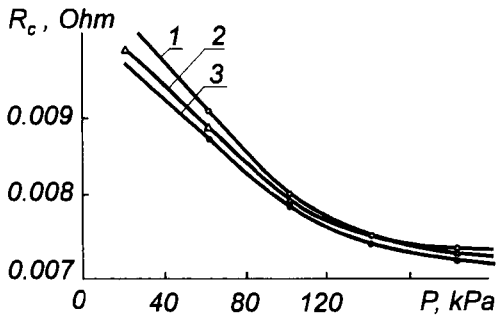

Fig. 6.4. Contact resistance of CuBe2–CuSn6 pair versus specific load:I=5 A; v=0,12 m/sec; 1) TsIATIM-201 lubricant; 2) OKB-122-7 lubricant; 3) no lubricant.

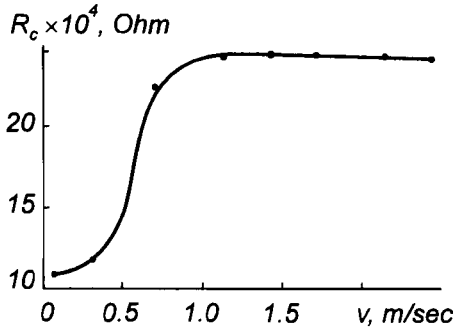

Fig. 6.5. Contact resistance versus sliding velocity: CuSi3Mn1–CuBe2 pairs; P=0.1 MPa; I=5 A; TsIATIM-201 lubricant.

The dependence of contact resistance on sliding velocity. A typical curve of R_c versus sliding velocity is shown in Fig. 6.5. It can be divided into three sections. The first section, corresponding to v<0.4 m/sec, is characterized by a low constant resistance. The conductance in this section is governed mainly by metallic contact spots. Because of a low sliding velocity, asperities are exposed to a deforming force for a long time which destroys the boundary layer and creates direct metallic contact between the friction surfaces. In the second stage, where 0.4<v<1 m/sec, a transition occurs from metallic microcontacts to the contact across the boundary conductance is effected mainly by the tunnel effect. For velocities v>1 m/sec, R_c is constant and independent of the velocity. In view of the screening effect of the lubricant, it can be suggested that the metallic contact is practically absent, and R_c is determined by the resistance created by the lubricant film.

The dependence of contact resistance on the current density. Experiments carried out with various materials and lubricants show that contact resistance falls as current rises. This is true for a wide range of currents, 10^{-4}<I<30 A (Fig. 6.6.).

Such conductance behavior has been observed in thin oil films [16]. At a field intensity exceeding the critical value, breakdown of the boundary layer occurs, and its resistance diminishes.

For small currents ($I<10^{-3}$ A), a marked contribution to the voltage measured across the contact is made by thermo-EMF (tribo-EMF) of sliding pairs. Any nonsymmetric friction is accompanied by triboelectrical effects, even when materials of both members are identical. In the general case, tribo-EMF is induced by different physical properties of materials and heat release in the contact region [296]. It should be noted that even weak currents change the character of oxidation in contact spots.

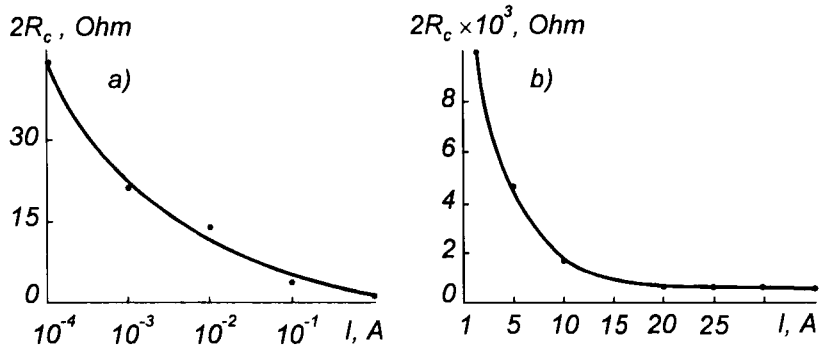

Fig. 6.6. Contact resistance versus commutation current: CuSi3Mn1–CuBe2–CuSi3Mn1 pairs; P=0.1 MPa; v=1.2 m/sec; TsIATIM-201 lubricant; a) $I=10^{-4}$ to 1 A; b) I=1 to 35 A.

The tribo-EMF can be comparable with or even higher than the contact voltage drop. The combined action of the thermocurrent and the external current distorts the transmitted signal, occasionally changing its polarity. Therefore, tribo-EMF plays the main role in commutation of low currents. Investigations have shown that for all materials and lubricants tribo-EMF is not a constant value and changes unpredictably in time (Fig. 6.7).

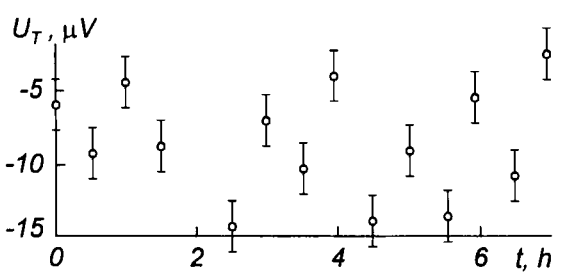

Fig. 6.7. Time variations of tribo-EMF: CuSi3Mn1–CuBe2 pair; P=0.1 MPa; v=1.2 m/sec; TsIATIM-201 lubricant (the ring is grounded).

6.4. Wear of Sliding Electrical Contacts

Wear of SEC results from mechanical and electrical actions. However, mechanical and electrical processes in SEC are closely interrelated, for instance, electric erosion caused by electric current, increases the roughness, thus, spurring mechanical wear; at the same time, mechanical damage of the surface can increase the electric component of wear.

In friction process three periods can be distinguished: run-in, steady wear, and catastrophic wear. In the run-in stage, contact between friction surfaces results rom the displacing of crests of asperities. In the contact spots, high pressure develops. Under the influence of normal and tangential loads asperities are crushed and flattened, the wear debris fill up the hollows. The distance between the bodies in friction decreases, new asperities come into contact, the real contact area expands. During the run-in an intermediate layer is formed which consists of adsorbed moisture, dispersed wear particles and oxides. The best operating conditions for friction pairs are achieved if such layers coat both friction surfaces.

As microasperities level down the real contact area increases, wear decreases and becomes stable. Roughness is directed along the sliding direction. In subsequent operation the wear changes dimensions of parts, removes coatings or basic metal layers, altering friction conditions, and eventually period of catastrophic wear starts. Sometimes, when the run-in period is either short or absent at all, catastrophic wear sets in immediately.

When considering the wear mechanism, it should be taken into account that surface layers have properties different from those of underlying layers. The wear results from mechanical and molecular interaction between friction surfaces under the action of normal pressures and their relative motion. In response to normal and tangential forces the surfaces periodically undergo elastic and plastic deformation. Multiple periodic elastic and plastic strain in the surface layers multiply and pack dislocations and vacancies, which cause generation and development of fatigue cracks, loosening of bonds between crystals, their displacement and spalling.

Mechanical wear Δh, defined by the action of friction forces and elastic strain, can be written as [22]

$$\Delta h = const\, E^{t(1-\beta)-1}\sigma_0^{-t} f^t P^{1-\beta t},$$

where E is the elasticity modulus;

t is the coefficient allowing for antifatigue properties of materials (according to (1.25), Section 1.4.);

β is the coefficient depending on microgeometry of contacts;

σ_0 is the initial strength;

f is the friction coefficient; P is the pressure on friction surfaces.

Wear of contact in current-free operation. The main type of failure (wear) of SEC working surfaces in currentless operation are microcutting, scratching, peeling, spalling, deep tearing, and friction-induced oxidation.

Mechanical wear of the friction pairs is influenced considerably by the choice of materials, particularly, their strength and hardness. There can be three combinations of mechanical properties of brush and counterbody materials [297]:

1) a hard brush against a relatively soft counterbody;

2) a relatively soft brush against a hard counterbody;

3) equal hardness of the brush (H_{br}) and counterbody (H_{cb}).

It is established that the ratio $K=H_{br}/H_{cb}=1.06$ to 1.55 is the optimum. Such K, yields stable and relatively small wear.

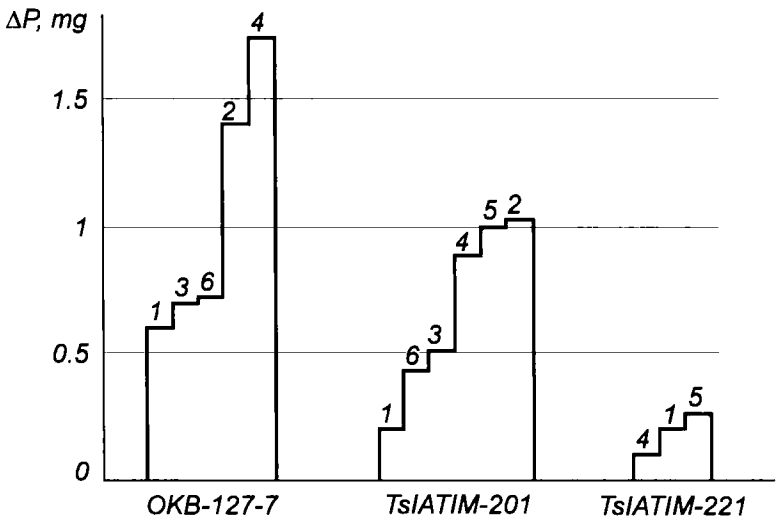

Fig. 6.8. Absolute wear of sliding contacts in current-free friction with lubricants;
1) Cu-ETP–C45e steel,
2) CuSn6–C45e steel,
3) CuAl10Fe3–CuAl10Fe3,
4) CuAl10Fe3–C45e steel,
5) CuSn6–CuAl10Fe3, and
6) CuSn6–CuSn5Zn5Pb5 sliding pairs;
v=2.5 m/sec; P=0.14 MPa; t=14 h.

At K=0.4 to 1.0, wear is even less, though it is more unstable. In that case, however, the brush is not resilient enough to maintain a reliable contact. The less the hardness of the brush material, the longer the service life of the contacting pair.

In order to choose the best pairs of materials and lubricants, it is necessary to know the wear of each pair in current-free friction. A wide range of specific loads

and velocities for various combinations of bronze pairs and lubricants (see Fig. 6.8) have been studied using the procedure described in 6.3. Irrespective of the friction coefficient, TsIATIM-221 grease has demonstrated the lowest wear.

Dependence of wear on current. Figure 6.9 shows the results of experimental studies of wear [298, 299]. Four rings and eight brushes were tested. The wear rate J was calculated by the formula:

$$J=\Delta P/(dSL),$$

where ΔP is the weight wear of the specimen;

d is the specific weight of the specimen material;

S is the contact area;

L is the sliding path during the measurement time.

Analysis of the experimental data has shown that:

1) wear of the brush with the positive potential (relative to the ring) is higher than that of the brush with the negative potential. No trend has been found for the ring;

2) as a rule, the ring wear rate is higher than that of the brush;

3) the optimum current direction for the minimal total wear is determined by the brush material (for example, brushes from CuSn6, CuAl10Fe3 have the minimal wear with the brush-to-ring current direction; brushes from CuSi3Mn1, CuAl8Fe3, Br.SnP10, Cu-ETP have it when the current is reversed;

4) when brushes rub against the ring from of CuAl10Fe3, they wears generally less than ring ;

5) there is no explicit dependence of wear on thermophysical properties of contacts. Apparently, the trends in wear depend on the chemical composition and structural characteristics of metals and alloys rather than on their thermophysical properties. The latter is confirmed by the results for brushes made from CuAl10Fe3 and CuAl8Fe3 with similar thermophysical properties but having the minimum wear at different current directions.

6.5. Electrocapillary and Electroplastic Effects

Softening of solids subjected to electric polarization was discovered by P.A. Rehbinder and studied further by his students and followers. In 1949, the electrocapillary effect inducing deformation was discovered [300].

Electrocapillary effects reflect the dependence of the electrode–solution interface tension on the electrode potential and the solution composition [15]. In the first approximation, a typical electrocapillary curve of liquid metallic electrodes is shaped as an inverted parabola with the maximum located at the zero charge potential (Fig. 6.10). Such a curve was obtained only for liquid metals, their

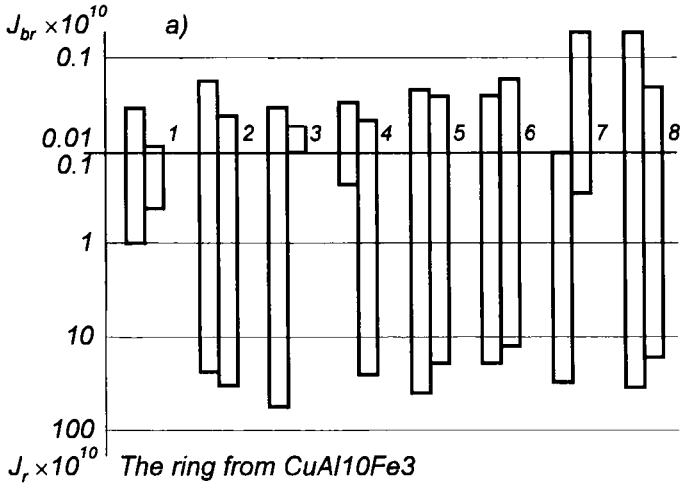
$J_{br} \times 10^{10}$
a)
0.1
0.01
0.1
1
10
100
1
2
3
4
5
6
7
8
$J_r \times 10^{10}$
The ring from CuAl10Fe3

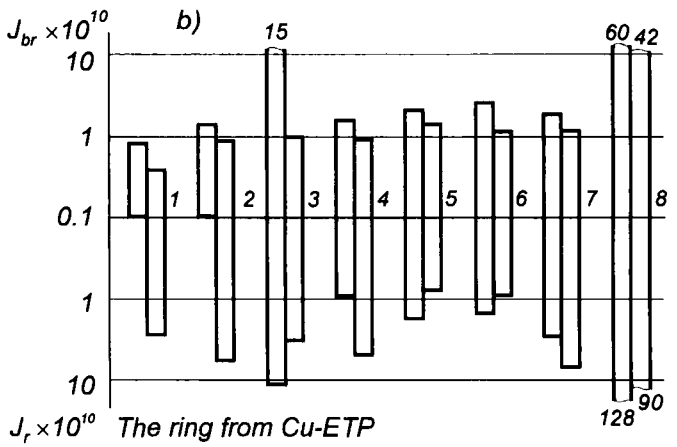
$J_{br} \times 10^{10}$
b)
10
1
0.1
1
10
15
60
42
1
2
3
4
5
6
7
8
128
90
$J_r \times 10^{10}$
The ring from Cu-ETP

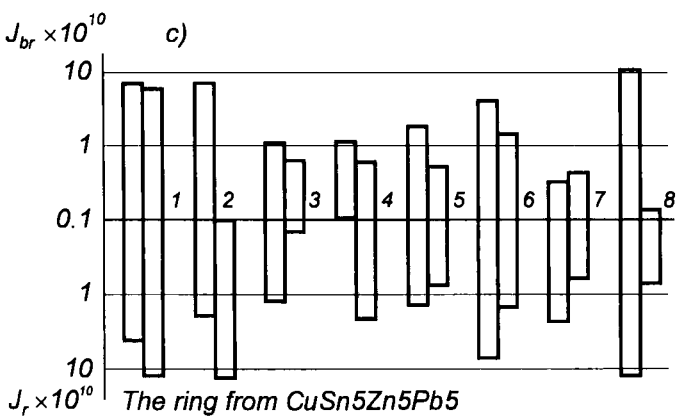
$J_{br} \times 10^{10}$
c)
10
1
0.1
1
10
1
2
3
4
5
6
7
8
$J_r \times 10^{10}$
The ring from CuSn5Zn5Pb5

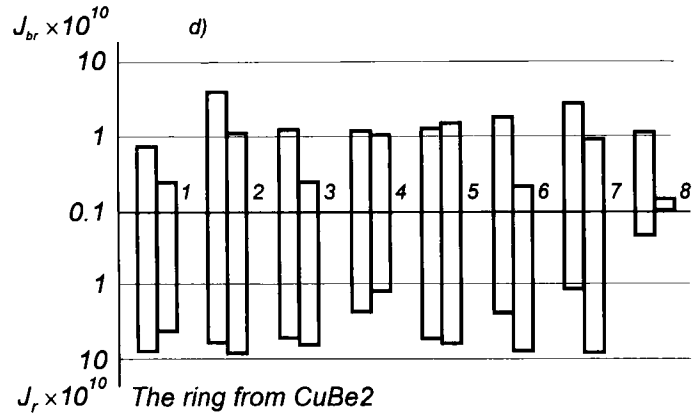

Fig. 6.9. Wear rate of electric contacts (brushes J_{br}; rings J_r) as a function of the contact pair material and current direction;
v=1.2 m/sec, P=0.1 MPa, j=25×10⁴ A/m², TsIATIM-201 grease.
Rings from: a) CuAl10Fe3; b) Cu-ETP; c) CuSn5Zn5Pb5; d) CuBe2.
Brushes from: 1) CuBe2; 2) CuSn6; 3) CuSi3Mn1; 4) CuAl10Fe3; 5) CuAl8Fe3; 6) CuSn10P; 7) CuSn5Zn5Pb5; 8) Cu-ETP.
Left column refers to current direction from brush to ring; right column refers to current direction from ring to brush.

interfacial tension coincides with the reversible surface work σ and can be found experimentally. The shape of the $\gamma=f(\varphi)$ curve is qualitatively explained by the effect of repulsion of like charges q on the surface expansion work the stronger repulsion, the larger the work $|q|$.

As regards solid electrodes, their infinitesimal deformations caused by changes in the potential are obscured by much more intensive side effects, thus preventing direct measurements of not only electrocapillary curves but even γ itself. However, the literature indicates that changes in the surface tension of solids do occur and change the potential; these changes manifest themselves indirectly, being reflected in other measured parameters, and can be described by electrocapillary curves, as in the case of liquid metallic electrodes. One of such parameters is the initial plastic flow rate $\dot{\varepsilon}$.

The plot of $\dot{\varepsilon}$ for lead monocrystals in 0.01 n. H_2SO_4 versus the polarization potential φ [291] (see Fig. 6.11) shows that in deviations from the zero charge potential (φ_0=-0.7 V) to both negative and positive values at 0.10–0.20 V $\dot{\varepsilon}$ substantially increases (approximately two times). The effect is caused by change of the surface potential barrier which hinders emergence of dislocations on the free crystal surface, i.e. prevents formation of a step on the crystal surface. This process is connected with the work of breaking and rearranging interatomic bonds on the surface once the shear is completed.

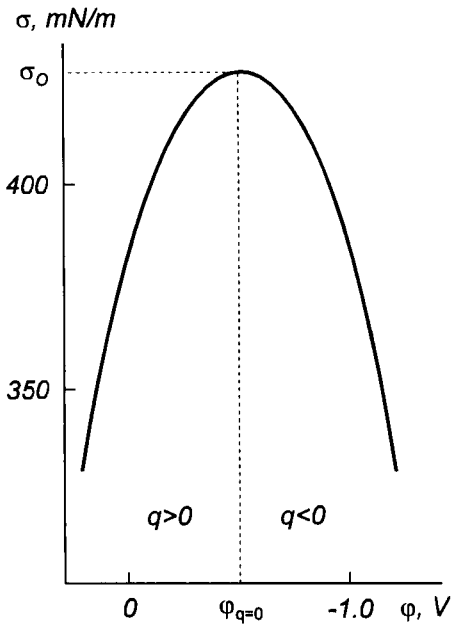

The existence of the surface potential barrier for dislocations, the motion of which results in a new surface, and the possibility of lowering the barrier were proven experimentally by E.D. Shchukin [301], who used microindentation of surfaces in inactive and adsorption-active media and subsequent etching of dislocation emergence points.

Fig. 6.10. Electrocapillary curve for mercury electrode in 1 n. solution of Na_2SO_4 [15].

As it had been expected for polarization, the same microindentation method revealed the same electrocapillary effect which caused softening and reduced strength by lowering the γ of charged surfaces [302, 303]. Let us estimate the free surface energy reduction for the case in Fig. 6.11 [304].

The ratio of $\dot{\varepsilon}$ for a charged surface to the minimum plastic flow rate $\dot{\varepsilon}_0$ corresponding to the zero charge potential, is $\dot{\varepsilon}/\dot{\varepsilon}_0=\exp(\Delta U/(kT))$, where U is the activation energy depending of several factors controlling the behavior of dislocation in the bulk of the crystal and near its surface. In the first approximation, for relatively small changes in the surface energy σ, U is its linear function. In this case ΔU is proportional to the reduction the free surface energy $\Delta\sigma$ and the elementary cell area b^2: $\Delta U \approx b^2\Delta\sigma$. A 2-fold increase of the creep rate (see Fig. 6.11) corresponds $\Delta U \approx kT \approx 4\times10^{-21}$ J. For lead b=0.35 nm and , then, the reduction of the surface potential barrier under polarization by ±0.10–0.20 V will be equal to $\Delta\sigma \approx \Delta U/b^2 \approx 40$ mJ/m^2 which is an order of magnitude higher than the average value obtained from electrochemical measurements.

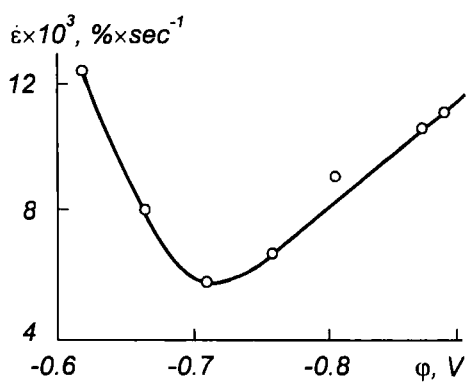

Fig. 6.11. Initial plastic flow rate $\dot{\varepsilon}$ of Pb monocrystals as a function of Pb polarization potential φ in 0.01 n. solution of H_2SO_4 [291].

Disagreement between this estimate and the experimental data is explained [304] by neglecting certain specific factors such as local fluctuations of the charge density at dislocation emergence points where the lattice is extremely distorted and there are "specific" conditions for manifestation of surface effects near the yield limit of specimens, namely, there is a region of the optimum stress where the electrocapillary softening effect upon monocrystals of lead and other metals is most conspicuous.

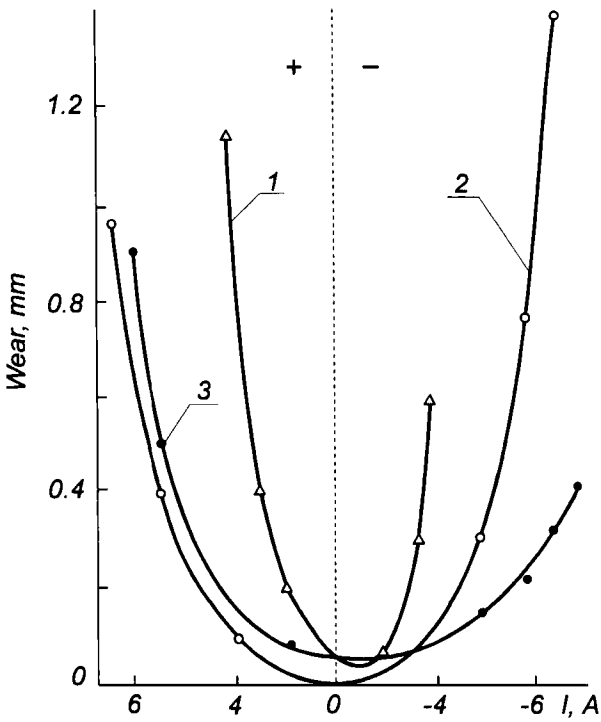

Fig. 6.12. Wear as function of current magnitude and direction [306]: 1) magnesium in DS-11 oil; 2) iron in DS-11 oil; 3) iron in DS-11 oil with 9% Monto-613 additive.

The electrocapillary effect also manifests itself when electric current passes across a metal surface [234, 305]. However, interpretation of the results is not always correct. Thus, the authors of [306] investigate wear of different metals and report that the wear-versus-current curve behaves as classical electrocapillary curves (Fig. 6.12), its behavior is governed by a spatial electric charge induced in the oil film by electric current. The charge affects free electrons in the metal surface layer decreasing the cohesive bonding force, thus, reducing the strength of the surface layer and increasing its wear. However, the authors do not exclude the influence of thermochemical effects in this case [307]. Explanation of the

curves in Fig. 6.12 is debatable, since such currents make erosion dominate which increases wear (this is exactly the situation observed in this case) but not softening which should have resulted in the opposite. Still earlier, the behavior of the wear–potential curve opposite to that shown in Fig. 6.12 (with the maximum near zero charge potential) was found in friction of metal specimens immersed in electrolyte [308–310]. The authors suggested that in such cases the wear was a parameter reflecting changes in γ which could not be validated experimentally so far.

The question is whether the electroplastic effect (EPE), which consists in reduction of plastic strain resistance of metals due to energy transfer from the conduction electrons moving under external electric field to dislocations, can be one of the causes of the electrocapillary effect fostering wear [311]. Let us consider the EPE more thoroughly. This effect is based on interactions between drifting free electrons ("electron gas") and metal ions [312] which attracted serious attention after Hafner's experiments on separation of mercury isotopes by DC current [313].

The necessary condition for manifestation of EPE is excess of the electron drift velocity over the phase velocity of elastic waves of dislocations [314]. This conclusion follows from the expression derived for the force F exerted upon the unit length of a dislocation in the direction of its motion when electrons drift in the same direction:

$$F \sim \frac{b}{4}\left(\frac{v_0}{v}-1\right)\frac{v}{\bar{v}}\frac{\partial n_0}{\partial \mu}\Delta^2, \tag{6.3}$$

where b is the Burgers vector;

v_0 is the electron drift velocity;

v is the dislocation velocity;

$\bar{v}$ is the electron velocity on the Fermi surface;

n_0 is the conduction electrons concentration;

μ is the chemical potential;

Δ is the deformation potential constant.

Normally, free "electron gas" retards the movement of dislocations at low temperatures. This follows from (6.3) for v_0=0. If free "electron gas" drifts over the crystal lattice under the effect of electric field in the direction of dislocations motion, then, at v_0>,v dislocations experience the action of an accelerating force which reduces the plastic deformation resistance of a material.

Depending on the deformation rate, dislocations in a pure crystal, move with the velocity 10^{-3} to 10 m/sec. Consequently, the electron drift velocity should be higher than this velocity (deformation rate). However, even if this condition is not satisfied, i.e. the electron drift velocity is less than the group velocity of

dislocations, this effect still manifests itself to a certain extent, because the friction of electrons for moving dislocations is always less in the presence of electric current (providing that dislocations and "electron wind") move in the same direction.

The experiments with microdeformations show [315], that copper yields at stress levels about 1–10 kPa. For the electron drift velocity $v \leq 1$ m/sec, the "electron wind" exerts about 10 Pa pressure on dislocations (see formula (6.3)). Since in metals dislocations move at pressure more than two orders of magnitude lower than the macroscopic yield limit of specimens, this stress is enough to accelerate the motion.

It is also easy to estimate the current density corresponding to the electron drift velocity v=0.1 m/sec. Consider, for example, a zinc crystal in the form of a wire with cross-section $S=0.8\times10^{-6}$ m^2 and conduction electron density is $n=3.38\times10^{28}$ m^{-3}; then the current density is

$$j=I/S=en\bar{v}=(1.6\times10^{-19})\times(3.38\times10^{28})\times10^{-1}\approx5.4\times10^{8}\ \text{A/m}^2\ [315].$$

In the experiments [311, 315], EPE was observed for the first time on monocrystals of lead, zinc, and indium shaped as wire with diameter $d\cong1$ mm. The method of pulsed current treatment was employed in these experiments, current produced pulse leaps in the deforming source induced by plastic strain and unloading of specimens. The pulsed current amplitude was I=200 A, pulse duration $T\cong10^{-4}$ sec. Under such conditions, the current thermal effect during one pulse is insignificant, amounting to several fractions of a degree. The amount of heat released during a pulse was found from the formula $\Delta Q=I^2RT$, where R is the electric resistance of a specimen. The calculated heat appeared considerably smaller than the heat capacity of specimens.

The electroplastic effect on metal deformation was also observed in the experiments on the dependence of the steady creep rate on the DC magnitude which was much lower than that of the pulsed current amounting to several tens of amperes.

The wear versus the current curve, resembling in shape of the electrocapillary curves and similarly termed, was described by several authors. It is likely that in their studies (see, for example, Fig. 6.12) it is not related to electrocapillary or electroplastic effects. The contact surface is rough, real contact between the surfaces occurs in scarce spots [293]. Current flows only through these conductive spots constituting only 0.01–0.1 % of the nominal area, suffering resistance in these spots due to the constriction of current lines; in these regions the current density can be as high as 10^{11} A/m^2. As will be shown later, at such current densities, the condition of excess of the electron drift velocity over the group velocity of moving dislocations in microcontacts is fulfilled with a great margin. It should be noted here that softening of thin surface layers results, in higher wear resistance (see 1.4) rather than in its fall, similar to that shown in Fig. 6.12.

In the latter case (see Fig. 6.12), as well as in other experiments with high current densities, the main role is played by electric erosion, in particular by its main type or the so-called bridge erosion which is caused by formation of bridges between contacts from a liquid metal. At low current densities, when the bridge transfer is practically impossible, EPE should manifest itself in reduced wear without being obscured by side effects. Indeed, this suggestion has been confirmed experimentally.

6.6. Electroplastic Effect in Sliding Pairs

The dependence of wear of sliding pairs on the density and direction of current across the contact revealed by experiments, appears generally common for all sliding contacting pairs, described here, with different lubricants.

The wear curves for sliding pairs from bronze CuSn6 (brush)–CuBe2 (ring) which operate with greases TsIATIM-201 and OKB-122-7 are a typical example of such relations (Fig. 6.13). The general trends in friction with current can be derived from the analysis of the curves:

1) the wear versus current curve has its minimum; the current at which wear is minimum ranges from 1 to 100 mA for various pairs;

2) wear of the contacting pairs exhibits a clearly pronounced character (i.e. depends substantially on the current direction);

3) the lubricant type influences the wear curve shape only for currents under 10 mA.

The EPE is maximum (reduces the wear considerably) if the current remain below 10 mA. In this case the bridge erosion is insignificant. As the current increases, the bridge erosion builds up gradually bringing to zero the EPE beneficial effect. At currents above 10 A, wear is close or even higher than that measured without current.

Bridge erosion is observed not only with sparks or arcs between contacts but also in the absence of electric discharges. In normal SEC operation (no discharge effects) the main type of electrical erosion is bridge erosion which is caused by formation of liquid metal bridges between contacts. Current passes through the regions covered with a monomolecular layer of a gas, oxide, sulfide, or similar film or through metallic contact spots. When the contacts move apart, pressure decreases, the number and size of contact points become smaller, the contact area becomes so small that the current density reaches the levels sufficient to melt the contact material. The liquid metal forms a bridge connecting two electrodes. Further heating of the liquid metal by current leads to its violent evaporation resembling an explosion, the bridge breaks down, a part of the material is transferred from one electrode to the other.

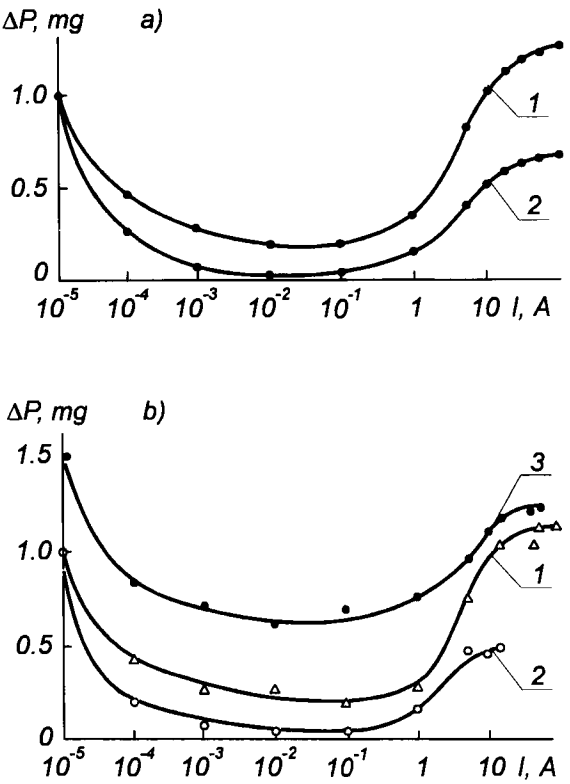

Fig. 6.13. Plot of wear versus current magnitude for brush (1, 2) and ring (3) with TsIATIM-201 (a) and OKB-122-7 (b) lubricants: v=1.2 m/sec; P=0.07 MPa; t=10 h; 1) brush to ring current direction; 2) reverse direction.

Most of the researchers believe that such bridge transfer is caused by several factors, the main factor being the geometrical asymmetry of bridges prior to evaporation which is due to the thermal asymmetry produced by the current across the contact region. This explanation is supported by the experimentally observed thermal asymmetry of contact bridges corresponding to the transfer direction.

For a long time heat redistribution in the bridges due to the Thompson effect has been considered the most probable cause of the thermal asymmetry of contact bridges. Calculations based on this assumption show the best qualitative agreement with experimental data. However, the observed direction of the temperature asymmetry requires that the Thompson coefficient be negative, it is not always the case. For example, gold, silver, and copper have positive Thompson coefficient and the metal transfer is directed towards the cathode; platinum has negative Thompson coefficient and the transfer in nitrogen atmosphere is directed towards the anode. Some authors attribute the temperature asymmetry in the bridge to

the Coler effect. Surface electrons leave the cathode and penetrate via a thin oxide films to the anode, owing to the tunneling effect, energy dissipates in the form of heat, thus inducing the initial thermal asymmetry in the contact. The material bridge transfer calculated with the Coler effect consideration is several times as high as the measured value. Some authors explain the asymmetry along the bridge by the Peltier effect. If a thermo-EMF appears over the "solid metal–liquid bridge", then heat may be absorbed or released as governed by current flow conditions. In this case, the anode temperature should rise, creating asymmetry along the bridge. Qualitatively, the Peltier effect could be the cause of the bridge positive asymmetry in the direction of heat fluxes, but quantitatively, the effect is too weak to induce the bridge transfer. There are also other theories of bridge transfer.

In most cases, the transfer direction is positive, i.e. a crater appears on the anode and a peak appears on the cathode. Because bridge transfer direction can be different, it is possible to create erosion-resistant contacting pairs with the so-called self-restricted bridge transfer. In this case, materials for the anode and the cathode are chosen so that negative transfer exceeds the positive. Then, at the beginning of operation negative transfer prevails and the anode covered with the cathode material. Thereafter, the contacts operate as a homogeneous pair with positive transfer until the anode is free of the cathode material, and the process repeats again. This induces transfer and only a thin layer of the cathode material is involved in it.

The conditions were derived for self-restricted bridge transfer [316] which have been verified experimentally:

$$\rho_c/(\gamma_c c_c)>\rho_a/(\gamma_a c_a),\ \rho_c>\rho_a,\ \lambda_c>>\lambda_a,\ Q_{mc}>Q_{ma},\ Q_{bc}>Q_{ba},$$

where ρ, γ, c, λ, Q_m, Q_b, are the specific resistivity, weight, heat capacity, thermal conductivity, melting temperature, and boiling temperature of the cathode (c) and the anode (a) materials, respectively.

The analysis of the wear versus current curves (see Fig. 6.13) will be continued. The observed reduction of wear under low currents is attributed to the fact that the friction pairs are characterized by loss of strength and softening of the surface. Studies of ferromagnetic resonance (FMR) and microhardness of nickel as a function of current support this suggestion [317]. Since the FMR line width in a plastically deformed ferromagnetic material is mainly determined by the presence of dislocations in the crystal lattice, the state of the surface can be assessed from the line width (see 4.5). A clear minimum of the FMR line width corresponds to $I \approx 10$ mA (Fig. 6.14,a). Reduction of the FMR line width ΔH suggests that the friction surface is softened. The same is confirmed by microhardness measurements (see Fig. 6.14,b).

The ΔH reduction with current across contacting surfaces alters with polarity changes (see Fig. 6.14,a). This is quite natural since current reversals influence

propagation, movement, and mutual interaction of dislocations and other defects in the crystal lattice, thus affecting the wear process (Fig. 6.13) which has been definitely confirmed by experiment. These phenomena affect both wear and other processes as well. For example, the electric current polarity effect was found in the deformation of copper wire pulled through a diamond die [318]; an opposite effect or induction of electric potential in the deformation zone of copper (the so-called electronic deformation effect – EDE) – has also been revealed [319].

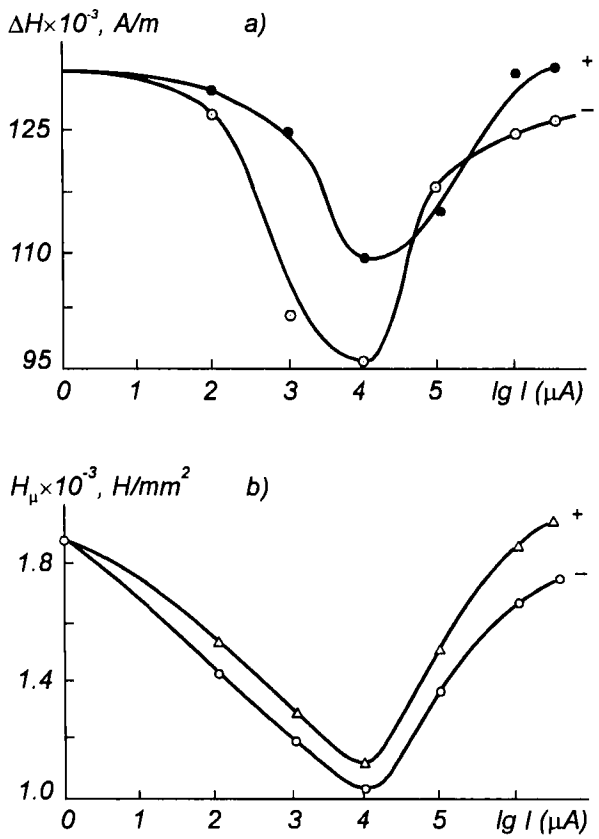

Fig. 6.14. Changes in FMR line width (a) and microhardness (b) of nickel brush as a function of current magnitude and direction: v=0.2 m/sec; P=0.08 MPa; t=2 h; TsIATIM-201 lubricant; frequency ν=9.4 GHz [317].

With forward current direction when the negative terminal of the source is connected to the test specimen, dislocations in the surface layer leave the specimen quite easily since the flow of conduction electrons pushes them out onto the surface.

The free path of movement of dislocations before they exit is short. With the reversed current direction, exit of dislocations from the near-surface layer is

inhibited since electrons tend to drive dislocations into the bulk of a specimen and, as a result, some dislocations can stop in the lattice increasing the local stress concentration stimulating a higher density of dislocation clusters in the underlying layer. In this case, relaxation proceeds dislocations ineffectively. In such phenomena the influence of thermophysical processes is possible. Positive potential on the specimen promotes oxygen adsorption in the friction zone. It is likely that oxide films formed in the process inhibit dislocation emergence, resulting in different hardening levels of Ni surface with forward and reverse current directions [317].

With currents at which the FMR linewidth is minimum (see Fig. 6.14), the conditions favor reduction of the dislocation density; the number of dislocations remains invariable for all current densities, because residual stress levels stay the same within the experimental error. Further rise of the current density seems to bring about domination of the effects associated with thermal processes (including electric erosion). Numerous defects formed thereby "envelop" dislocations and hinder their motion and emergence on the crystal surface. In addition, point defects cluster and produce linear defects. The rise of the ΔH and H_{μ} curves corresponds to increasing density of dislocations and point defects.

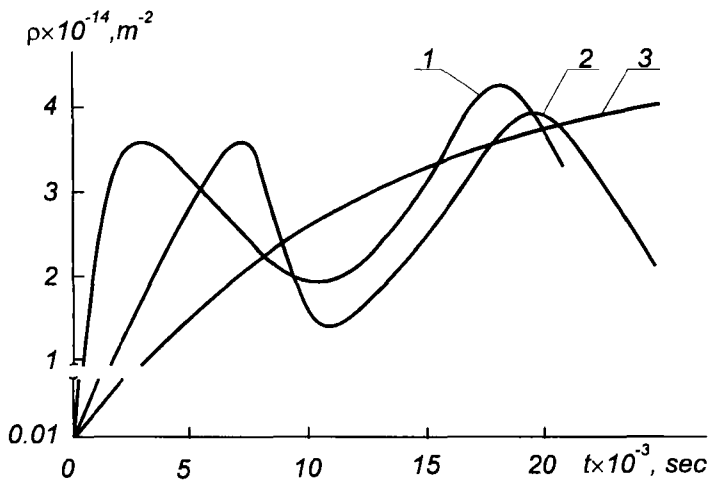

Fig. 6.15. Dislocations density ρ as a function of test duration [305].

The presence of EPE in various friction pairs was confirmed by subsequent FMR results [307]. Studies were also carried out to investigate the changes in the dislocation structure of 99,98% grade nickel as a function of test duration with a current of 10 mA a friction pair [305]. Similarly to the previous case, the dislocations density was determined by formula (4.4) (see 4.5). Figure 6.15 shows

the plot of the dislocations density ρ versus test duration of a nickel specimen without (curve 1) and with (curves 2 and 3) 10 mA current. Two types of lubricants were used: TsIATIM-201 (curves 1 and 2) and TsIATIM-201 mixed with fluoroplastic-3 (curve 3).

As it could be expected, changes in the strength properties in friction exhibited cyclic behavior (see 4.5) due to the two competing processes opposite in their effect, namely, higher strength (owing to new dislocations) and less strength (owing to annihilation of dynamic rest and polygonization processes at the crack tip) [305], which had equal intensities at ρ_{max}.

The electroplastic effect increased the cycle duration when electric current passed across SEC, i.e. strength properties changed more smoothly and the hardening rate decreased. The directed electron drift stimulated emergence of dislocations on the surface causing reduction of the rate of the latent strain energy accumulation.

6.7. Influence of Lubricant on Sliding Electrical Contact Operation

Great importance of lubricant for the SEC operation is confirmed by the experiment discussed in 6.6 (cf. curves 2 and 3 in Fig. 6.15 [305]). We consider this in more detail.

High reliability and wear resistance of SEC can be achieved by creating a conductive antifriction layer between contacting surfaces. Dry contacts are rapidly oxidized and sulfated. Arcing (sparking) between contacts promotes formation of nitrogen oxides. Suitable lubricants eliminate sparking in contacts and reduce the contact resistance. When the contact opens, a conductive lubricating film forms a temporary bridge and the lubricant protects contacts from water, oxygen, ozone, etc.

In SEC lubricants operate under specific conditions. Drying, oxidation, and charring of lubricants cannot be tolerated, since it would disturb normal operation of the contact.

No special greases was produced commercially for SEC early, except the contact grease for lubricating cover plates and joints of rails and KCB lubricant for lubricating contacts of the VAZ motor car turn lights [209].

In the ring-comb type RCD, nonconductive grease OKB-122-7 is used for the instrument panel. Studies were carried out to compare the performance of TsIATIM-201 and TsIATIM-221 lubricants. These lubricants are developed for friction assemblies of various devices and instruments. However, they are not conductive and unable to ensure stable passage of current.

In order to improve the conductive properties of commercial greases, studies were conducted varying their compositions.

Numerous publications report that, addition of powder copper and its alloys, silver, tungsten, cadmium, and other metals, molybdenum disulfides, polymers, etc. to lubricants has a favorable effect on friction processes. Metal-containing greases prepared by adding metal powders improve, in some cases, antiscoring and wear-resistance properties, but they are not effective enough in the friction assemblies through which current is passed because they do not provide stable contact resistance. When these lubricants are used, operation of contacts is accompanied by sparking and noise. Besides, unstable contact resistance results in electrical erosion and, hence, reduced in wear resistance of contacting pairs.

By testing , some efficient compositions have been developed [321].

In order to achieve high electrical conductivity of available greases in a boundary layer, polymer powders can be introduced in addition to coarse copper powder (or other metal). Thus, addition of polymer (e.g. fluoroplastic-3) to a lubricant with copper powder stabilizes the contact resistance which becomes about 10 times lower, while wear resistance of contacts increases five times. Polymers (polytetrafluoroethylene, polyethylene, etc.) are usually employed to improve antifriction properties of lubricants in friction assemblies which do not conduct current.

The effect of simultaneous substantial decrease of contact resistance and increase of wear resistance as a result of polymer addition has been a surprise. In their original form, polymers exhibit high electrical resistance, being excellent insulators ($\sigma \approx 10^{19}$ to 10^{22} Ohm×m), therefore, a rise in the contact resistance could be expected quite naturally.

It is known that free radicals emerging in mechanical destruction of macrochains are extremely sensitive to various kinds of impurities that may be present in polymeric media acting as acceptors. It may be suggested that free radicals interact with oxygen preventing oxidation of working contact surfaces, thus reducing the contact resistance. Consequently, introduction of polymer into the contact zone seems to increase the number of points of metallic and quasimetallic contacts.

Polymers vulnerable to mechanical destruction considerably decrease the surface energy of metals resulting softening of surfaces and localization of shear strain in a thin surface layer.

It follows from [305] (see Fig. 6.15, curves 2 and 3) that addition of even 3% of fine fluoroplastic-3 powder to the grease TsIATIM-201 substantially inhibits growth of dislocations density and results in prolongation of the cycle. Note that whereas in the previous cases (curves 1 and 2) there were two cycles of changes in the strength properties during the experiment, only one stage of ρ-growth (curve 3 shows in the initial section of the 1st cycle) was observed in the latter case during the same period. In this case surface softening is partially induced by the blocking of the Fisher surface sources by surfactants resulting from polymer destruction which reduce the probability of defect clustering near the surface [322].

The rate of mechanical destruction is affected by the polymer-to-metal weight ratio; therefore, normal operation of contacts is ensured by the optimal proportions of components.

The above-mentioned effect (simultaneous reduction of contact resistance and increase of wear resistance) is not characteristic of all polymers. Among the polymers (polyethylene, polytetrafluoroethylene, polytrifluorochloroethylene), the effect was only observed when fluoroplastic-3 was added to the copper-containing lubricant.

The conductive lubricant was prepared by adding metal powders and polymer into greases and subsequent mechanical mixing at room temperature.

For preparing the lubricant several mixtures of ingredients were used, each containing 10 to 30 wt % of copper powder with different concentrations of polytrifluorochloroethylene (flurorplastic-3) powder (0,5; 1; 3; 5 and 10 wt %) and greases (TsIATIM-221, TsIATIM-201 or OKB-122-7) to make up the balance of 100%.

The tests conducted on AE-5 frictional machine followed the scheme: bottom specimen (disk) – top specimen (pin). Contacting pairs were from like and unlike materials: CuBe2; CuSn5Zn5Pb5; CuSn10P; CuAl8Fe3; CuSi3Mn1; CuAl10Fe3; and copper Cu-ETP. Sliding had the following parameters: v=0.02 to 1.20 m/sec; P=0.05 to 0.15 MPa; I=0 to 2.5×10^6 A/m^2.

Table 6.1 gives the data on contact resistance and wear of CuBe2–CuSi3Mn1 sliding pairs.

TABLE 6.1

Disk–pin (CuBe2–CuSi3Mn1) sliding pair: P=0.05 MPa; v=0.02 m/sec; $j=5\times10^4$ A/m^2.

Grease	Average contact resistance $R\times10^2$, Ohm	Wear rate, $J\times10^{10}$
TsIATIM-201	3.85	4.65
TsIATIM-201 + 1% Cu	5.25	5.2
TsIATIM-201 + 10% Cu	3.31	4.5
TsIATIM-201 + 30% Cu	4.78	4.8
TsIATIM-201 + 1% Cu + 0.1% Fl-3	2.11	3.2
TsIATIM-201 + 1% Cu + 10% Fl-3	0.73	2.4
TsIATIM-201 + 10% Cu + 3% Fl-3	0.71	0.6
TsIATIM-201 + 10% Cu + 5% Fl-3	0.34	1.0
TsIATIM-201 + 30% Cu + 0.1% Fl-3	2.54	3.5
TsIATIM-201 + 30% Cu + 10% Fl-3	0.92	2.9

Conductive grease with copper and polytrifluorochloroethylene powders compares well with metal-plating grease (TsIATIM-201 + 10 wt % copper), stabilizing and reducing the contact resistance approximately ten times. The wear

rate decreases also. So, introduction of 5 wt % of fluoroplastic-3 into the metal-plating grease reduces wear rate over four times. The optimum addition of the polymer depends on the grease type, the metal powder content, the type of friction pairs, friction mode, and the current density.

Thus, addition of copper and polytrifluorochloroethylene powder has a favorable effect on SEC performance. The best results are obtained by adding 10 wt % of copper powder with a particle size of up to 15 μm and 3–5 wt % of the polymer to TsIATIM-201. This lubricant also reduces oscillations of the tribo-EMF more than 10 times. An average tribo-EMF is zero, which is very important for commutation of small currents.

The contact resistance and wear in contact pairs of commercial ring–comb current-collectors were also investigated (see Table 6.2). A composite lubricant based on the grease OKB-122-7 was used. In standard ring–comb collectors, the best composition for service life extension was OKB-122-7 +1 wt % of fluoroplastic-3.

TABLE 6.2

Standard ring–comb (CuBe2–CuBe2) sliding pair operated in RCD: P=0.065 MPa; v^*=2.0 m/sec; j=5×10^5 A/m^2.

Grease	Average contact resistance R×10^2, Ohm	Wear rate, J×10^{10}
OKB-122-7	1.70	5.1
OKB-122-7 + 1% Cu	1.85	5.0
OKB-122-7 + 10% Cu	1.53	4.6
OKB-122-7 + 30% Cu	1.67	5.3
OKB-122-7 + 1% Cu + 0.1% Fl-3	0.45	0.75
OKB-122-7 + 1% Cu + 10% Fl-3	1.24	3.5
OKB-122-7+10% Cu+1% Fl-3	0.34	0.6
OKB-122-7+10% Cu+3% Fl-3	0.91	0.7
OKB-122-7+10% Cu+5% Fl-3	1.0	1.1
OKB-122-7+30% Cu+0.1% Fl-3	1.12	3.0
OKB-122-7+30% Cu+10% Fl-3	0.58	2.1

*) Accelerated tests

The EPR-spectroscopy was used for accurate observation of free radicals (unpaired electrons) released by mechanical destruction of polymer-containing lubricants. The tests was carried out for three specimens: fluoroplastic-3 powder; a mixture of fluoroplastic-3 with mineral oil (MVP) as a dense thoroughly mixed mass; a grease containing TsIATIM-201 (85 wt %), fine copper powder (10 wt %), and fluoroplastic-3 (5 wt %) [308].

Mechanical destruction of specimens was conducted in a specially designed brass cup. A brass rod was rubbed with its flat end against the bottom of the cup. The speed of the rod was 350 rpm; the load N varied periodically from 0 to 100 N. Thus doing, real friction conditions were simulated to a certain extent. The duration of mechanical destruction of each specimen was 10 min.

The EPR-signal was measured on a "Varian E-12" spectrometer (sensitivity is 5×10^{10} spin/Gs; frequency stability is 10^6; field resolution is 15 mGs; an H_{102} resonator) at frequency of 9.5 GHz. The specimens were held at 300 K. The duration of scanning each spectrum was 4 minutes; the magnetic field was modulated with a frequency 100 kHz and amplitude of 4 Gs. For measurements 85 mm^3 of the grease were placed into a $30\times8\times0.35$ mm^3 cell fixed by a fluoroplastic holder 3.5 mm in diameter.

After mechanical destruction of the specimens, the EPR-signal appeared in the free electron g-factor region (g=2.0023). The signal intensity was about 10^{13} spin/Gs and the EPR line width was about 25 Gs. The results indicated that there were free radicals in the specimens subjected to mechanical destruction. Since the signal increased in all the specimens and in the same region, fluoroplastic-3 is no doubt the source of free radicals.

A relatively low intensity of the EPR signal can be explained by the fact that measurements were carried out four days after mechanical destruction, only relatively long-living radicals could be detected. The signal intensity can be expected several orders of magnitude higher than the obtained signal if the EPR signal is measured directly during mechanical destruction.

Thus, improved antifriction properties of the metal-plating greases after addition of a polymer [321] seem to result from free radicals appearing during friction.

6.8. Initiation of Selective Transfer by Electric Current

In ST, contact surfaces which ensure the least friction and wear are formed spontaneously. Owing to the recovery properties of lubricants, friction occurs practically without surface oxidation.

Diverse processes which take place on contact surfaces as a result of ST become more complicated under the effect of electric current. Selective transfer has positive effect on SEC performance when the above mentioned characteristics are supplemented with the minimal contact resistance stable in time.

The experiments show that electric current in the initial stage makes surfaces covered with an extremely thin copper layer [323]. The copper film formation rate and its thickness are functions of the current density and direction. A negatively polarized specimen has a smoother softened surface, in addition, it is characterized by the minimum wear. When current direction is brush-to-ring the

surface has a pronounced defective structure, with abundant cavities and microasperities.

Electric current intensifies the ST; the copper film is formed quicker than without current. After a short time (about an hour), however, the film appears oxidized and tarnished, it undoubtedly indicates ST disturbance. The studies of selected materials and lubricants in a wide range of currents and loads show the same trend.

Selective transfer manifests itself to the full extent when surfaces are covered with a fresh lubricant. Operation without refreshing lubricant leads to abnormal ST but, it has been shown experimentally that the friction parameters do not deteriorate. It seems probable that as the lubricant composition and properties change (due to the products of friction surface dispersion and lubricant destruction), an intermediate antifriction layer is formed in the friction zone. Internal friction replaces in this case external friction.

Comb-ring RCD friction assemblies work with grease applied to their surfaces during assembly. This condition also restricts the spontaneous ST maintenance.

In addition to mechanical wear, electrical current gives rise to electric wear, in other words, ST is superimposed by bridge transfer or bridge erosion. Evidently, to achieve conditions for self-restriction of bridge transfer is most essential in order to reduce electrical erosion.

6.9. Practical Recommendations

The experiments discussed in this Chapter allowed several recommendations for improving the reliability and durability of lubricated ring–comb and ring–brush SEC from copper alloys.

Contact resistance:

1) Running-in is necessary for reliable SEC operation. The run-in time varies, depending on the load, from 6 to 10 hrs. After this time, transient contact resistance stabilizes;

2) The minimum contact resistance is observed when the original specimen roughness is related to 8–10 class;

3) As the load increases, the contact resistance diminishes. However, for extremely high loads wear rises. With pure lubricants, it is recommended that the specific load at the contact be about 0.08 to 0.1 MPa; with metal-containing lubricants it should be 0.05 to 0.06 MPa. A specific load below 0.02 MPa induces fluctuations of the contact resistance;

4) Changing the relative sliding velocity in the range 0.02 to 0.20 m/sec does not have any effect on the contact resistance. A further increase in the velocity leads to a rise and subsequent stabilization of R_c. The sliding velocity at which

the contact resistance stabilizes is determined by the load applied at the contact. For P=0.1 MPa, the steady-state is attained at v=1 m/sec;

5) As the current density increases, contact resistance goes down exponentially;

6) The lubricant type has practically no effect on the contact resistance at high loads and low speeds. For other operation modes it is recommended to choose OKB-122-7 among greases, OKB-122-7 +10 wt % Cu +1 wt % Fl-3 and TsIATIM-20 +10 wt % Cu (powder with particle size up to 15 μm or ultradispersed copper) +3 to 5 wt % Fl-3 among composites. The latter gives a zero average tribo-EMF, fluctuations of the tribo-EMF being practically zero. Therefore, it is recommended for use in low-current commutation circuits.

Wear:

1) To increase wear resistance, it is desirable to maintain the current density (calculated for the contact contour area) within 10^2 to 10^3 A/m^2. At such densities, contact wear is minimum and smaller than the wear observed without current. Current densities in excess of 2.5×10^6 A/m^2 can cause welding of contacts;

2) The lubricant type influences wear only at current densities under 10^2 A/m^2. For such conditions, TsIATIM-221 or TsIATIM-201 with copper and polymer additions are recommended;

3) Materials for contacting pairs and current direction should be chosen on the basis of experimental data for wear (see Fig. 6.9);

4) Since the brush (comb) is considered a more important element of current collectors, the ring-to-brush current direction is recommended to save;

5) Longtime operation of current collectors without current should be avoided.

6.10. Problems of Improving Design of Standard Current Collectors

Apart from basic research, attention should be paid to improve design important for wear resistance, operation reliability and durability.

Let us consider, for example, the feasibility of extending trouble-free operation of standard comb-type current collectors consisting of both low-and high-current (500 A and more) circuits [324].

In order to determine the contribution of mechanical and electrical factors to the total wear, the effect of load, resistance and friction force as well as the effect of current on the contact resistance of a standard ring-comb pair have been studied. The ring and comb are made from CuBe2; TsIATIM-201 is used as a lubricant; the number of teeth is 300; and RCD rotation frequency is up to 30 rpm.

Fig. 6.16 illustrates the effect of load on the contact resistance (at current per tooth 2 A, v=0.04 m/sec.). It can be seen from the results that any load over 0.3 N per tooth does not practically reduce the contact resistance (in the high-current pair of standard RCD the load per tooth is twice as high amounting to $P\approx$0.6 N).

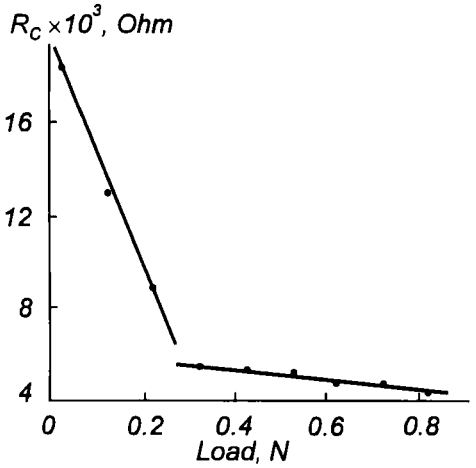

In the experiment (two opposite teeth of the comb are in operation), the friction force is compensated by the elastic force of the spiral spring. One revolution of the ring corresponds to the moment 2×10^{-2} N×m, which is equivalent to the friction force 0.25 N per contacting pair (friction diameter 8 cm; ring rotation velocity 20 rpm. The rotation angle is measured by a liquid potentiometer with ±2° error which corresponds to the force 1.4×10^{-3} N.

Fig. 6.16. Contact resistance versus load on contact.

The results of measurements are shown in Fig. 6.17. As could be expected, the curve is linear. The coefficient of friction is $f=F/P\approx0.16$.

Subsequent investigations showed that the friction force is independent of relative sliding velocity (within the RCD operating rotation velocities), lubricant type, the sort of copper alloy for the ring, and depends on the load. The friction force has been found to depend on the running-in time; the dependence is detectable only during the first 20–30 minutes of operation. Then, the coefficient of friction stabilizes and remains practically constant.

No dependence of the coefficient of friction on the current has been found either, although current across one member the contact comb reaches 12 A. Thus, it can be concluded that the effect of current on the friction torque, if any, does not result in a more than 1.5%. (The latter value is an estimate accuracy for the load 0.6 N).

Because of the low rotation velocity of the ring, the experiment has been conducted so that the influence of the voltage drop and tribo-EMF for a mercury current collector is completely excluded. For the load of 0.7 N, the following results have been obtained:

I, A	0.005	0.01	0.05	0.1	0.5	1	2
R_c, mOhm	5.0	5.0	5.7	5.60	5.64	5.82	5.86

Thus, the contact resistance for a ring–comb pair is practically independent of current.

Power released by one high-current circuit with currents about 600 A is:

$$W_{tot}=I^2R_{tot}=I^2R_1/300=600^2\times5.86\times10^{-3}/300=7 \text{ W},$$

where 300 is the number if teeth in the comb of one RCD high-current circuit.

This power is obviously not enough to heat up the current collector considerably. Experiments show that the current 12 A across one contact tab heats the contact to just 323 K. (There has been no heat-removal copper ring in the measurements). Hence, the comb does not lose its elastic properties at currents under 10 A. It is shown above that the friction moment also remains invariable as the current rises.

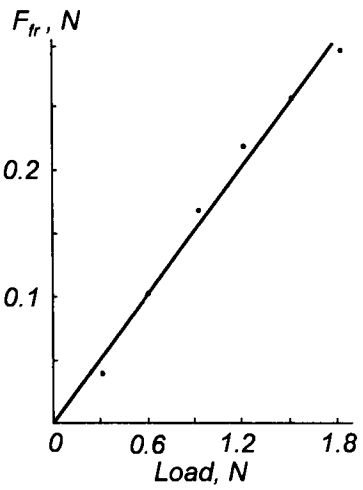

Fig. 6.17. Friction force of the contact pair versus load.

It seems probable that large wear observed in high-current circuits is caused by a high coefficient of friction the comb and inadequate design of the contact pair, i.e., wear of the high-current electrical contacts is mainly caused by the mechanical factor.

Let us consider the wear of high-current and low-current circuits. It is assumed that unit friction work of a contacting pair destroys a certain amount of the comb material and the contact breaks when the contact length of the combs, both in high-current and low-current circuits, is decreased by wear by the same value Δl.

The mass of the worn-out material of the comb is

$$M=\Delta l a b \rho,$$

where a is the comb thickness,

b is its width,

ρ is the comb material density.

The work spent on friction per revolution of the ring is

$$A=F_{fr}\pi D,$$

where D is the friction path diameter.

The amount of comb removed per revolution is

$$m=F_{fr}\pi D k_m,$$

where k_m is the mass of material spent on unit friction work.

Hence it follows that the number of revolutions resulting in the comb wear Δl is

$$n=M/m=\Delta l a b \rho/(F_{fr}\pi D k_m).$$

This formula allows a comparative assessment of wear resistances of high- and low-current circuits:

$$n_1/n_2=a_1b_1F_{fr2}/(a_2b_2F_{fr1}). \quad (6.4)$$

For the high-current comb a=0.3 mm, b=1.6 mm. F_{fr}=0.11 N;
for the low-current comb a=0.1 mm, b=2.5 mm, F_{fr}=0.01 N. After substitution into formula (6.4)

$$n_1/n_2\approx 1/6$$

is obtained.

Thus, the calculations have shown that the service life of low-current circuit is 6 times longer than the high-current circuit (only the mechanical wear component has been taken into account).

The results suggest the following recommendations:

1) As regards increasing the load on the low-current circuit, in order to retain the same friction torque, the number of contacting elements in a comb can be reduced. Such change will reduce the contact resistance, the contact reliability will increase, the service life will be three times longer than for the high-current circuit even if load is doubled.

This conclusion is confirmed by the results of factory tests of RCD which revealed frequent failures of low-current contact circuits and, as a rule, predominant wear of high-current circuits;

2) In order to reduce mechanical wear of the high-current circuit, it is advisable to reduce the load per contact member to 0.3–0.4 N. Then, the contact resistance does not practically change, electrical losses remain the same, mechanical wear becomes almost two times less. It is also useful to rearrange the member so that the load would become independent of the wear. This is impossible for the pair under consideration, and wear leads to decreasing loads and, consequently, to increasing electrical losses owing to higher contact resistance.

3) Laboratory studies have shown that preliminary lapping of the comb is obligatory. Otherwise, the running-in of the contact pair produces coarse abrasive particles on the friction path leading to intensive wear of SEC;

4) Spiral arrangement of contact tabs in a REC is unfavorable for high-current commutation. Because of different length of contact tabs, the load changes from one tab to another, which results in an irregular wear of contact member and, eventually, equalization of the tab lengths (appearance of cutting edges).

Nonaxial arrangement of the ring and comb seems better. This arrangement, makes the friction path width determined by the amount of the misalignment and the load on each contacting member will be constant.

Chapter 7

HYDROGENATION DURING SLIDING AND HYDROGEN WEAR MECHANISM

7.1. Introduction; Hydrogen Embrittlement and Hydrogen Wear of Metals

The concept of hydrogen wear of metals is generally recognized in tribology even though a short time has passed since the first publications by D.N. Garkunov. A.A. Polyakov, G.P. Shpenkov, and V.Ya. Matyushenko appeared [340, 377].

Two concepts should be distinguished: hydrogen embrittlement, and hydrogen wear of metals. The phenomenon of hydrogen embrittlement of steel due to hydrogen absorption has been known for a long time. This process occurs due to contacts in hydrogenous media [325] is promoted by high temperatures, atmospheric pressure, high loads and deformation, and cathodic processes.

Hydrogenation of steel reduces its longterm strength and durability, or induces instantaneous brittle failure of the machine components under load [130].

Hydrogen wear of metals (HW), which is a substantially different phenomenon, occurs only during sliding. A higher-rate of hydrogen absorption occurs during sliding, a different law of hydrogen distribution applies, and creates an unusual pattern of failure. Hydrogen absorption is extremely intensive and an abnormally high hydrogen concentration (impossible under any other conditions) occurs. In addition, hydrogen absorbs mostly below a sliding surface. All this causes quite a different wear of dynamics which can explain the unusual pattern of surface layer failure in some cases. One of them is wear of hard metals operating in contact with soft metals, such as the wear of a hardened steel rubbed against babbitt or bronze. Other examples are, wear of a ruby during sliding on cotton thread, and wear of cast iron (or steel) sliding against plastics, rubber, wood etc.

In some cases, wear of materials is accompanied by material transfer from a hard counterbody to a soft one. This wear was first observed in brakes of railroad using shoes made from plastic operating under severe conditions. HW of metals smearing over plastic in this case reduces the braking efficiency and brake service life. Changes in frictional properties and wear of sliding contacts are mainly caused by physicochemical processes. The hydrogen generated is a result of high-temperature plastic decomposition and is responsible for transfer of cast iron to

plastics [128]. While penetrating into cast iron, hydrogen reduces the wear resistance and strength of sliding surfaces. A mechanism of it would be consider further.

Hydrogen absorption and saturation in metal includes absorption of hydrogen molecules on the metal surface, dissociation of molecules, diffusion of hydrogen atoms (or protons) into metal, and their dissolution there, i.e. formation of a homogeneous system. The concentration of hydrogen from $1–2\times10^{-5}$ m^3/kg and greater impairs plastic properties of metals. At concentrations of $5–10\times10^{-5}$ m^3/kg the plasticity of steel is reduced to its lowest level [129, 130, 325, 326].

A hypothesis outlining the substantial effect of hydrogen absorption for sliding pairs, operating in highly loaded braking devices, was proposed in 1970. The mechanism of hydrogenation during sliding was not fully understood until the mid-1970s. In metals, hydrogen diffuses towards the higher temperature. It is well known. The maximum temperature caused by friction, as it was also known, is located at the surface. Thus, both technological hydrogen, i.e. hydrogen which was generated while the metal was in production, and hydrogen absorbed by a sliding metal surface from hydrogenous media (e.g. a lubricant), has to removed from the metal and desorb from the more heated surface. Therefore, the question of possible hydrogenation of contacting metals during sliding was unexpected.

This chapter deals with mechanisms of hydrogen absorption by metals and wear of metals rubbing against heat resistant high friction (braking) plastics. These were established by the author together with V.Ya. Matyushenko.

7.2. Sources of Hydrogen and Factors Influencing Absorption

Metals absorb hydrogen primarily in melting. Since hydrogen is always present in the furnace atmosphere, the hydrogen absorption rate is very high.

The surrounding medium, especially at high temperatures and pressures, is also a source of solid metal hydrogenation. In this case, hydrogen corrosion occurs. This manifests itself in steel cracking and decarburization ($Fe_3C + 4H \rightarrow Fe + CH_4$); high pressure methane is produced in the micropores and causes swelling and cracking of steel.

Fusion welding is also favorable for hydrogen absorption. Hydrogen, dissolved in metal melt, has no time to diffuse to the external surface of the part after fast cooling [327] and therefore it combines to create molecules in microvoids in the weld region. This results in hydrogen embrittlement.

Metals appear saturated with hydrogen in electrolytic and corrosion processes. In cathode polarization of steel in alkali and acid solutions [129] the steel surface absorbs hydrogen. During hydrogen depolarization, hydrogen is absorbed through

metal areas with a positive electrode potential. Hydrogen absorption by steel parts is intensified by atmospheric corrosion.

The following main factors determine hydrogen absorption intensity:

1. *Composition and state of the medium.* Hydrogen solubility in steel [328], is directly proportional to the square root of the partial molecular hydrogen pressure in gas:

$$(C_H)_{dis} = K\sqrt{(P_{H_2})_{gas}} \quad ,$$

where $(C_H)_{dis}$ is the concentration of hydrogen dissolved in the metal;

$(P_{H_2})_{gas}$ is the partial pressure of molecular hydrogen in the gaseous medium;

K is the hydrogen solubility coefficient.

2. *The treatment* of the metal surface and its condition such as roughness, oxide layer etc.

3. *Chemical composition of metal.* The nickel in steel particularly, increases penetrability of hydrogen, and copper decreases penetrability [328]. Alloying elements which produce chemical compounds with hydrogen (hydrides) retain hydrogen as a solid solution, and hinder its desorption.

4. *Metal structure.* The density of atomic packing, grain boundaries, crystal planes, structural defects in the crystal lattice, and presence of collectors affect hydrogen absorption.

5. *Stresses and deformations.* In particular, deformations of the metal lattice which raises its energy level, has a great effect on the development of dislocation-vacancy structure which will be critical for hydrogen absorption [129].

6. *Hydrogen saturation time.* The amount of hydrogen absorbed by steel rapidly initially increases, then this process slows down. In electrolytic pickling of 1/XVII steel in 5% H_2SO_4 hydrogen concentration increases rapidly during the first two hours.

7. *Conditions of hydrogen desorption from metal.* Under normal conditions gaseous hydrogen is molecular; as temperature increases it dissociates following the scheme $H_2 \leftrightarrow 2H$-104 kcal. In metals, gas diffuses in the atomic state. Hydrogen cannot diffuse in a molecular form because of the atomic structure of metals. Therefore hydrogen dissolution in metals is preceded by dissociation of hydrogen molecules into atoms. Atomic hydrogen is generated by the

interaction of water vapor with metal surfaces at high temperatures: $H_2O+Me \rightarrow MeO+2H^0$. Hydrogen ions interact with metal surfaces as $H^+ + Me \rightarrow Me^+ + H^0$, that also produces H^0. The same result is in electrolysis during hydrogen ions discharge from solution at the negative potential: $H^+ + e \rightarrow H^0$, etc.

7.3. Hydrogen Evolution and Absorption During Sliding of Solids

Hydrogen evolution in vacuum. Following from adsorption isotherms, changes in the ambient gas pressure brings about adsorption or desorption of gas molecules from solid surfaces. Weak bonds in physical adsorption are not favorable for molecular dissociation and penetration of gas into metal, due to a low diffusion rate of diatomic gases. Therefore chemisorption is a first requirement for the penetration of gas into a solid.

The solubility of hydrogen in metals is proportional to the square root of the partial hydrogen pressure in the gas phase and at the thermodynamic equilibrium, gas dissolution in metal stops. Any disturbance of thermodynamic equilibrium is accompanied by gas evolution or absorption, the kinetics of which depends on the diffusion rate. The low pressure conditions of modern vacuum systems, conditions at high altitudes and in space, are greatly different. Gas evolution from metals at low pressures is more intensive. The lower the pressure, the higher the metal temperature.

For metals covered with oxide films, the diffusion rate is substantially decreased or stops. In plastic deformation the hydrogen diffusion rate increases, the rise being especially great in metal deformation in a vacuum. In this case some of the dissolved hydrogen evolves as a result of the motion of dislocations or the formation of new boundaries, from grains and blocks, and slip bands [329].

Friction is accompanied by appreciable heat release, therefore the gas evolution mass spectrum with metal heated in a vacuum without sliding will be discussed first (Fig. 7.1). Physically sorbed gases evolve first. Their composition characterizes the history of a part, that is composition of the medium where the parts were kept after the last chemical or thermal treatment: residues of washing compounds, air and pollutants such as oil vapors, chlorides, sulfurous gases and organic substances (see Fig. 7.1,a) [330].

When parts are heated in a vacuum up to 873 to 1173 K, hydrogen, oxygen, nitrogen, and carbon atoms diffuse from the bulk to the metal surface. They interact with the oxide film or with one another to produce CO_2, H_2O, CO, H_2, N_2, O_2 and hydrocarbon compounds, most often methane CH_4 (see Fig. 7.1,b). Relative amounts of the components of residual gases will change depending on the proportion of the gas components, presence and the thickness of an oxide film.

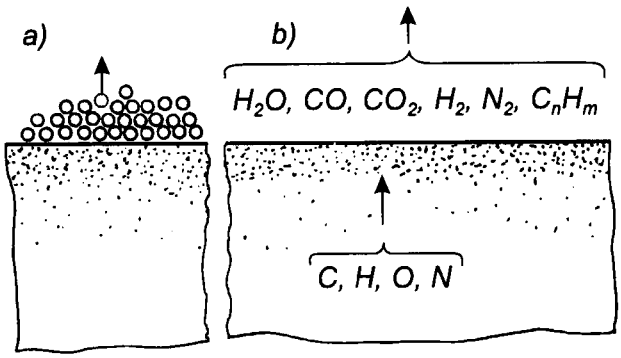

Fig. 7.1. Gas evolution from metal during heating: a) from the surface; b) from the metal volume [330].

Gas diffusion from the bulk to the surface of metal is slow which is seen in the relation [331]:

$$Q_s = \frac{8aN_0}{\pi^2}\left[1-\exp\left(-\frac{D\pi}{4a^2}t\right)\right] \tag{7.1}$$

where Q_s is the amount of diffusing material per unit surface area (1 cm^2);

a is the half thickness of the part;

N_0 is the initial concentration of diffusing material in the volume of the part;

D is the diffusion coefficient;

t is the degasification time.

Complete degasification is only possible, seen in Eq. (7.1), at $t = \infty$, which is unrealistic.

Analysis of the mass spectrum (taken by a MSKh-3A mass spectrometer in conditions of oil-free evacuation) has shown [24] that the main residual gas is hydrogen H_2 (M=2) (Fig. 7.2); in addition, small amounts of H_2O (M=18), CO (M=28), CO_2 (M=44) were found.

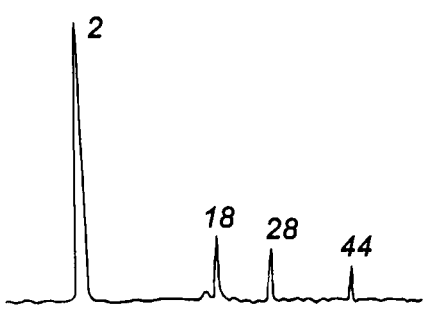

Fig. 7.2. Mass spectrum of residual gases evacuated by a cryogenic pump [24].

Sliding in a vacuum consists of two periods: firstly, destruction and removal of the initial oxide film by sliding and second, interaction of the components in direct contact.

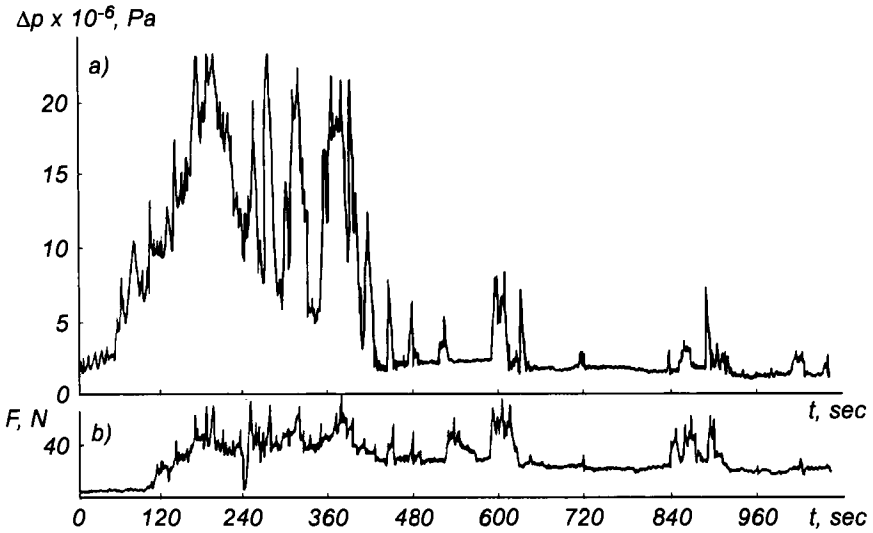

Fig. 7.3. Gas evolution during sliding of carbon steel C45e in a vacuum 1.33×10^{-5} Pa [24]: v=0.24 m/sec; a) height variation of the mass spectrum spike of hydrogen with time in seconds; b) the friction force curve as a function of time.

Gas evolution in a vacuum sliding involves dynamics of the oxide film destruction and formation of surface structures. Studies of hydrogen content in atmosphere of residual gases at various sliding speeds of the ring–indenter friction pair made of steel C45e have clearly revealed three distinct stages (Fig. 7.3,b): the initial stage when the friction force rises smoothly and insignificantly; the transition stage which is characterized by discontinuous changes of the friction force; and the final stage which is more or less stable friction.

During sliding in a vacuum, variations of hydrogen content (Fig. 7.3,a) are noticeably unstable with time. In the 1st stage the hydrogen content in the chamber (gas evolution) is small and varies with a narrow range. Then copious, but discontinuous gas evolution follows with sharp variations of the evolved gas amount (state 2). In the third stage gas evolution is stable with a few relatively sharp gas emissions shown by small groups of spikes against the background of relatively low stable gas evolution. This trend can be explained as follows [24].

During the initial sliding period the surface oxide layers which prevent gas exchange between the metal and the atmosphere, are destroyed. The temperature rises, the surface layers are deformed, both elastically and plastically, and microcutting or surface disturbance by setting occurs. Hydrogen which was previously contained in the bulk of the metal or on its surface, evolves through the produced microcracks into the ambient atmosphere, thus increasing the residual gas pressure. Duration of the first stage depends both on the oxide film thickness and strength, and on the other friction conditions. An increase in the chemical activity of material, and a consequent increase of the gas exchange rate with the atmosphere are induced by some mechanical action on the surface. External mechanical action on metal in a vacuum induces evolution of some of the gas, including hydrogen, adsorbed on the surface or contained in metal. The hydrogen amount evolved in stage 1 is small, and rises as the wear process develops and temperature increases as a result of friction.

Copious gas evolution is observed at the moment of severe plastic deformation. Gas evolution from small volumes occurs almost instantaneously so that the positions of the gas evolution peaks correlates with the surface events which are exhibited by typical jumps of friction force. This is shown in Fig. 7.3.

An experiment [24] was carried out to investigate gas evolution and friction force of steel C45e hardened to HRC 53 and to verify the suggestion that in sliding under a vacuum, hydrogen evolves mainly from a substantially deformed layer (Fig. 7.4). The experiment was based on the fact that hardness of the substrate determines the destruction pattern of the brittle oxide film. Wear of the film with hard substrates is lower than with soft substrates. As was expected, gas evolution changed slightly in the experiment. However, if to anneal the specimen as the trend changed abruptly: intensive gas evolution was observed almost immediately after sliding was started. Subsequently, hardened by friction, the surface layer prevented gas evolution from the underlying layers.

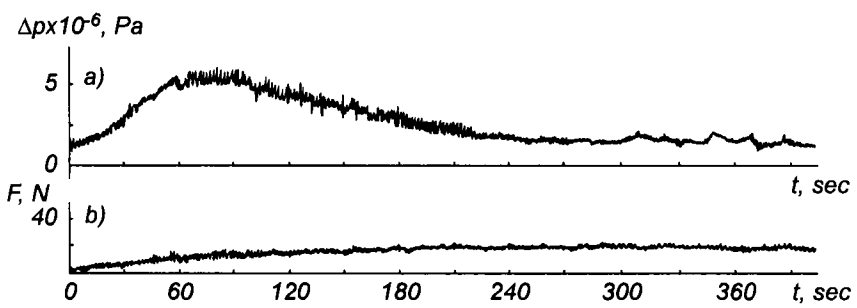

Fig. 7.4. Gas evolution and friction force of hardened steel C45e in a vacuum [24]: the same notations as in Fig. 7.3.

Hydrogen evolution at moderate temperatures can be observed not only in sliding of metal–metal pairs but also in sliding of metals against nonmetallic materials. In the latter case hydrogen evolves from the plastically deformed metal surface and is cleaned of oxide films, due to decomposition of the organic component of the pair.

The results discussed suggest that hydrogen absorption, the inverse of hydrogen evolution, will depend essentially on the extent of plastic deformation, density of defects in the surface.

Hydrogen absorption in rolling. Many of the earlier publications on the reasons of origination and propagation of cracks in rolling contact bearings reported on physical aspects of fatigue life, especially of the interrelation between appearance of cracks and shear stress distributions in steel. Lubrication was often ignored. Later research showed that chemical effects, depending on some additives in lubricants, could be considerably more than an increase of fatigue life which could be achieved by increasing the lubricant viscosity [332–335]. A 35-fold difference in fatigue life was found between the fatigue life of steel balls which were tested in base oil containing 2.5% of zinc dialkyldithiophosphate in one case, and 10% of chlorinated wax in the other. Changes of the viscosity of lubricants of the same class seldom resulted in a more than threefold increase of fatigue life.

In 1963, L. Grunberg and his colleagues [332] investigating the mechanism of fatigue failure of steel balls under the action of water-containing lubricants, suggested for the first time that pitting corrosion of balls was induced by hydrogen embrittlement. The experiments were conducted with a four-ball lubricant tester containing lubricant including 6% of tritium water of high activity. Balls tested in the machine with traces of pitting damages were washed in acetone and immersed in a scincillation liquid, then the radioactivity was measured. The radioactivity in the fatigue place was found to exceed around 50 times the background activity as a result of hydrogen penetration into steel. The experiments with water labeled with tritium isotope proved that the penetration of hydrogen into steel under the rolling contact zone was time- and stress-dependent. In another study carried out to investigate fatigue of rolling element bearings, a lubricant contained deuterium ^2H (in the lubricant was added dusteroparaffin). The mass spectrum showed that the $^2H/H$ ratio was 0.3% in a failed bearing, and 20 times larger than the relative natural content of deuterium in water and air.

Water in lubricant, could be expected to promote a reduction in fatigue life, and should increase the wear rate of rolling bearings. The suggestion was confirmed by subsequent experiments [334]. In wear tests conducted on a four-ball lubricant tester, lubricant was continuously blown with argon, thus reducing the dissolved oxygen content to a minimum. The wear increase observed (with

comparable running-in periods) was caused exclusively by water dissolved in the lubricant.

The mechanism explaining the effect of a small amount of water on fatigue is shown in the following [333–335 and others]. Surface microcracks which were formed under rolling contact conditions, function as fine capillaries. Lubricant is forced into the capillaries, and the water dissolved in it concentrates at the apex of a crack forming a water-rich phase. Then, cyclic stresses concentrated at the crack apex, corrosion by the water, and hydrogen evolution and embrittlement occur together.

Squalane lubricant, a pure paraffin used in the experiments by P.Schatzberg et al. is nonpolar, therefore a question arose immediately about the influence of dissolved water in a lubricant containing polar organic substances. To answer the question, they investigated the effect of the alcohol isopropylaminethanol (IPAE) additive on neutralization of the fatigue inducing effect of water, which together with nonpolar lubricant produces an emulsion. The small amount of IPAE additive eliminated completely the water effect. In [345] a mechanism of hydrogen absorption and IPAE effect in rolling friction was suggested.

Microcracks on the rolling bands of bearing balls tested in a four-ball lubricant tester nucleate from grinding scratches, grooves, and dents, and also generate from subsurface cracks which propagated to the surface. Surface cracks smaller than 1 μm are formed in an early stage of fatigue tests of rolling elements. The propagation rate of these precritical cracks can be increased by chemical substances filling them. The microcracks behave as fine capillaries and water dissolved in lubricant condenses in the cracks exactly in the same way as during capillary condensation in other liquid and gaseous systems. The small size of water molecules and their ability to form a strong hydrogen bond are additional factors favorable for selective adsorption and condensation of water in capillaries. These observation explain the fact that a small amount of water dissolved in a lubricant is capable of significant decreasing the rolling fatigue life [334].

Capillary condensation is also suggested as an explanation for the inhibiting effect of 2-isopropylaminethanol [335]: its molecule has polar characteristics and it therefore dissolves in hydrocarbons and water. IPAE separate from the solution into growing critical microcracks with water. Amyl alcohol is a proton acceptor or a base type compound, i.e. two excess electrons of the nitrogen atom attract and capture protons. Consequently, any hydrogen ions generated in cracks will be captured by IPAE. Hydrogen ions in the cathodic region cannot therefore reduce to hydrogen atoms that could dissolve in steel and cause hydrogen embrittlement. Essentially aqueous IPAE solution in a microcrack forms a solution preventing corrosion. As little as 0.1% of IPAE is apparently sufficient for complete suppression of the harmful effect of 1% of sea water. Observation supports the earlier arguments that only 0.1% of dissolved water (from 1%) condenses in microcracks.

Ordinary corrosion inhibitors cannot in most cases neutralize the water effect because of their inability to dissolve in water and their relative capability of condensing from solution in microcracks. A corrosion inhibitor with a large hydrocarbon component will tend to remain dissolved in the lubricant.

Other organic compounds of nitrogen also effectively eliminate the water effect on rolling fatigue life. Substituting groups of a molecule influence on the electron density of a nitrogen atom. They can block attraction of hydrogen ions, solubility in water, and vapor pressure are factors determining the efficiency of nitrogen compounds as specific inhibitors.

Some authors think that it is not obligatory for a nitrogen atom to act as a proton acceptor because of the excess of electron. The nitrogen may be adsorbed in the anode region of the crack and prevent formation of a corrosion cell. The nitrogen-content additive is most likely to settle on microcrack surfaces together with water and hamper expansion of cracks, preventing generation of atomic hydrogen on the crack tips. Neutralization of corrosion zones at the anode prevents all corrosion reactions, including formation of atomic hydrogen. The mechanism of capturing proton by nitrogen in no way hinders the operation on a corrosion cell in a crack.

Thus, hydrogen enbrittlement was considered by many researchers as the main mechanism reducing fatigue life of rolling bearings. Peeling and fatigue failure of surfaces were thought to be caused by stabilization of microcracks at small stress concentration and could be attributed to hydrogen diffusion in steel.

Hydrogen absorption on sliding. Studies of failure of the metal 15NiCr13 surface of thrust bearings in kerosene pumps sliding against a bronze valve have revealed that with a slight misalignment the valve microscopic steel tabs are smeared over bronze. The following hypothesis is suggested to explain this effect [336]. Misalignment of the thrust bearing-control valve pair results in heating of the surfaces. Further, because kerosene which is the lubricant contains small amounts of corrosion-active impurities (sulfur compounds), components of the copper alloy dissolve selectively, mercaptides are formed and hydrogen evolves and diffuses into the steel. Laboratory tests carried out for the bronze CuAl10Fe3–transformer steel pair in a glycerin lubricant, have confirmed that at 338 K and above in the sliding zone a transformer steel specimen absorbs substantial amounts of hydrogen which results in transfer of the steel to bronze. Transfer can be explained as follows.

During sliding tensile and compression deformations occur which promote diffusion of hydrogen atoms to a depth of 0.02–0.03 mm. After hydrogen molecules are generated and accumulate in intercrystallite cavities, steel fails along the grain boundaries, and adhesion of loose particles with copper alloy occurs. Then sliding of hard particles induces considerable wear of the steel surface.

Sliding in corrosive media promotes tribochemical reactions, and oxidation of lubricant is always accompanied by hydrogen evolution. The rate of hydrogen evolution can be different and in practical operation conditions with sliding parts (for example bronze–steel pairs) can cause different significance: hydrogen absorption by steel surface and its rapid wear due to decrease of plasticity; selective transfer accompanied by formation of a copper film with a high wear resistance at the coupled surfaces.

Hydrogen generated from decomposition of a plastic component at high temperature was also responsible for cast iron transfer to the coupled plastic [128]. Hydrogen embrittles cast iron, eventually causing intensive wear. In the same publication a hypothesis was suggested that at particular conditions premature wear of a more harder material of a sliding couple was a result of its hydrogen embrittlement. This matter will be discussed in more detail.

7.4. Hydrogenation of Metals During Sliding Against High Friction Plastics

Sliding of coupled materials is accompanied by intensive heating which changes properties of the coupled surfaces. Solid, liquid and gaseous wear products of various nature [337] appear in a contact zone if temperature of the surface layer of a sliding plastic exceeds the temperature of its components decomposition. CH_4, C_2H_6, CO, CO_2, mercaptans CH_3CH, large amounts of hydrogen as well as other gases are among the products. Water vapor, metil alcohol, phenol, creosols, xylenol, naphthol, esters, aldehydes, etc. liquid products are evolved for example from FK-24A plastic at about 673 K.

The appearance of gaseous hydrogen, is ascribed to the thermal destruction of the organic binder in the plastic, where hydrogen occurs in a chemically bound state. The hydrogen is then adsorbed by the metal which dissolves hydrogen the more intensively, the higher the temperature. Hydrogen solubility increases by more than an order [339] when the temperature changes from that of room to 1373 K. The evolution of the hydrogen dissolved in metal occurs mainly at small atmospheric pressure [338] (see 7.3).

The behavior of hydrogen in the steel surface layer (steel Fe360A), after sliding against high friction plastic (retinax FK-24A) was investigated. A high friction machine with short-time loading of specimens (P=8 MPa, t=5 min, n=750 rpm) was used. The mutual overlap factor was unity. Loading was applied in several cycles until the temperature in the contact zone reached 1123 K.

The surface layer of 0.1 mm thick was removed from the specimen immediately after the sliding. The amount of hydrogen in the cleaned surface was determined by a local emission spectral analysis [340]. Radiation was excited by a spark

discharge. The hydrogen line H_α intensity ($\lambda=6.562\times10^{-7}$ m, Balmer's series) was measured. Then, using the intensity of H_α line–logarithmic concentration known, the time curve of the concentration logarithm was plotted (Fig. 7.5).

Fig. 7.5. Changes of hydrogen concentration in the steel surface layer after sliding against plastics.

The surface layer contains less hydrogen immediately after friction than before the test. As time passes, hydrogen concentration in the near-surface layer gradually increases and reaches the initial value (the dashed line in Fig. 7.5), then starts to increases again. Such a trend was observed for all the specimens. In this case, the duration of the period of hydrogen concentration increase depends substantially on the linear dimensions of the specimen.

The case seems to be, that as the specimen cools down, diffusion tends to level the hydrogen concentration. Hydrogen diffuses toward the surface from deeper layers, which can be naturally followed by its desorption from the metal. This was checked by cooling the specimens quickly to the room temperature after friction cessation, and subsequently placing them in a closed vessel with an alcohol-glycerine mixture. After 15 or 20 min, gas bubbles nicking rose from the friction surface. Further gas evolution for 30 to 50 hours was less intensive. In some cases gas evolved at high pressure. This was indicated by a sequence of fine bubbles following one another.

Gas, evolved from steel specimens, was collected in a microburette and analyzed by gas chromatography. It consisted of; over 75% of H_2, 4 to 6% of CO, 8–9% of CH_2, 2–3% of N_2.

In the sliding interaction of a steel–plastic pair, the temperature in the contact zone can be very high, 1123 K in our case. Therefore a question arises: is the

hydrogen which is introduced, a result of friction itself, or of friction heating alone? In response to this, the following experiment was carried out. Steel specimens, not subjected to heating by friction, were heated to 1173 K in an electric furnace and the temperature kept constant for 20 min. As in the previous experiment, they were then quickly cooled and immersed in an alcohol–glycerine solution. No noticeable gas evolution from the samples was observed.

The experiment revealed, that after cessation of friction at which the temperature in the contact zone reached high values, the hydrogen amount in the steel surface layer decreased. As time passed, the hydrogen concentration fell to the initial level, and then increased once more when hydrogen was desorbed through the surface. On the one hand, the surface steel layer contains less hydrogen after sliding than before, although the steel surface does evolve a large amount of hydrogen (more than 75% of the total amount of the evolved gas). This hydrogen can be technological or excessive, diffusing into the bulk due to high-temperature hydrogen absorption during sliding. In order to answer this question, the hydrogen content in the specimen volume was determined by vacuum extraction (heating in a high vacuum and measuring the amount of evolved hydrogen) before and after friction.

To prevent fine plastic particles from penetrating the metal surface, a thin layer (0.1 mm) was taken off. Then the specimen was thoroughly washed in alcohol, weighed, and placed into the chamber where vacuum extraction was performed. The experiment allowed constant measuring and the ability to follow the gas evolution kinetics from pressure changes in a differential slop manometer filled with dibuthylphthalate. The chamber was outgassed at 1223 K for 20 min while the specimen was kept in a cold vacuum zone. When the temperature lowered to 923 K, the specimen was placed in the heating zone. After the first 10 min of run, readings of the manometer were then recorded at intervals of 10 min. If the manometer readings remained constant for 1 h, this was indicative of no gas evolution. The gas mixture was evacuated into a gas analyzer. Amounts (m^3/kg) of the evolved gas mixture and of each gas were separately determined from the formula $V=10^{-3}\ Kl/(MT)$, where V is the gas volume at 273 K and 0.1 MPa, m^3; K is the instrument constant; T is the absolute temperature; l is the displacement of the dibutylphthalate level in the manometer; M is the sample weight, kg.

Vacuum extraction therefore reveals, that the sliding created by steel and plastics considerably increases the total hydrogen content in the metal. Table 7.1 indicates hydrogen absorption in the specimens. The time of hydrogen evolution from specimens subjected to sliding, is about twice as high as that for specimens not subjected to sliding (Fig. 7.6). This is connected to changes in the microstructure of the steel and in parameters of hydrogen diffusion in the metal due to intensive heating by friction and subsequent cooling.

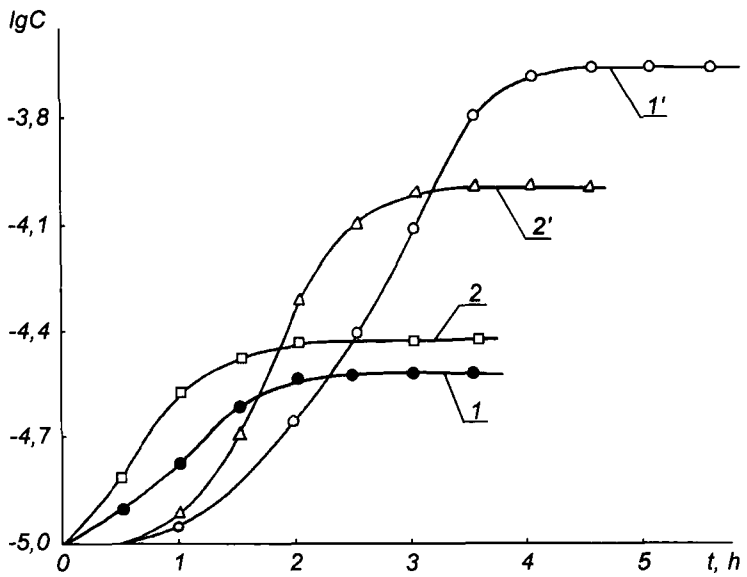

Fig. 7.6. Kinetics of hydrogen evolution from steel C45e (1; 1') and armco-iron (2; 2') during vacuum extraction: 1, 2) before sliding; 1', 2') after sliding.

TABLE 7.1

Hydrogen content in metal specimens, $\times 10^5$, m^3/kg

Specimens	Before sliding	After sliding with plastics			
		FK-24A	1-151M	102-9-68	145-40-69
Steel C45e	3.13	18.65	17.63	14.56	15.47
Steel Fe360A	3.52	17.82	18.08	15.37	13.61
Vacuum melted armco-iron	0.73	10.68	10.73	-	8.68

Hydrogen concentration distribution in metal. In friction of heterogeneous materials, specific high pressures and sliding speeds occur in the contact zone which then give rise to a high temperature. It can reach 1273 K and above, and can change the properties of contacting materials directly during operation.

Temperature and stress gradients along the depth substantially enhance the diffusion processes, both in the surface layers, and in adjacent to them bulks of the interacting bodies. As the temperature increases, hydrogen solubility and diffusion parameters sharply increase. At temperatures corresponding to the points of polymorphous transformation in steels and cast irons, hydrogen solubility increases intermittently and at 1375 K it becomes one order higher [78].

After high temperature hydrogenation during sliding and subsequent quick cooling of metal, the hydrogen state in the metal (when at high temperature) is fixed since hydrogen diffusion slows down. Therefore, a hydrogen concentration gradient induced by temperature and stress gradients, can be found.

The depth distribution of hydrogen concentration after sliding was investigated by spectral tomographic analysis. As the load and test time increased, the amount of dissolved hydrogen increased and its maximum concentration region displaced deeper into the specimen (Fig. 7.7). A further increase in the test time did not advance the hydrogen concentration since hydrogen solubility reaches a maximum in such conditions and solution becomes saturated.

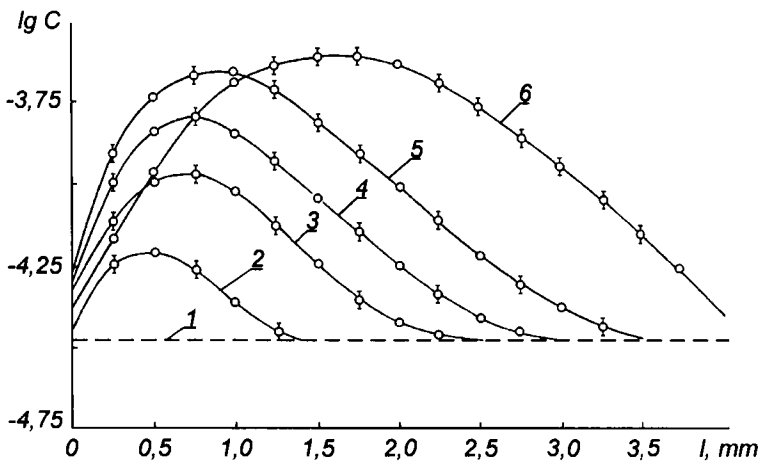

Fig. 7.7. Depth distribution of hydrogen concentration in a steel specimen: 1) before sliding; 2, 4, 6) after sliding (20 min) at a load of 2, 5.8, and 8 MPa, respectively; 3, 4) after sliding at 5.8 MPa for 15 min and 30 min, respectively.

In the process of establishing a thermodynamic equilibrium of hydrogen saturated metal with the ambient atmosphere, desorption of hydrogen from the metal occurs. The maximum hydrogen concentration region become wider (Fig. 7.8), but the total hydrogen concentration remains higher than the technological concentration (before sliding). This can be ascribed to the fact that

during sliding, diffusion-incapable hydrogen is gradually accumulated, creating high pressures. This is because some of the hydrogen combines in molecules, at space defects of the lattice, and does not desorb from the metal.

Multicyclic tests, similar to the practical conditions existing in the operation of braking devices, favor the formation of a stable expanding zone of maximum hydrogen concentration, close to the sliding surface (Fig. 7.9).

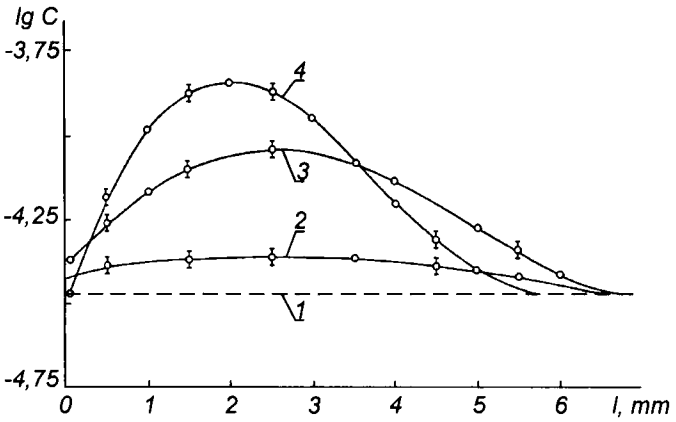

Fig. 7.8. Depth distribution of hydrogen concentration:
1) before sliding; 2, 3, 4) 24, 4, and 2 h after sliding, respectively.

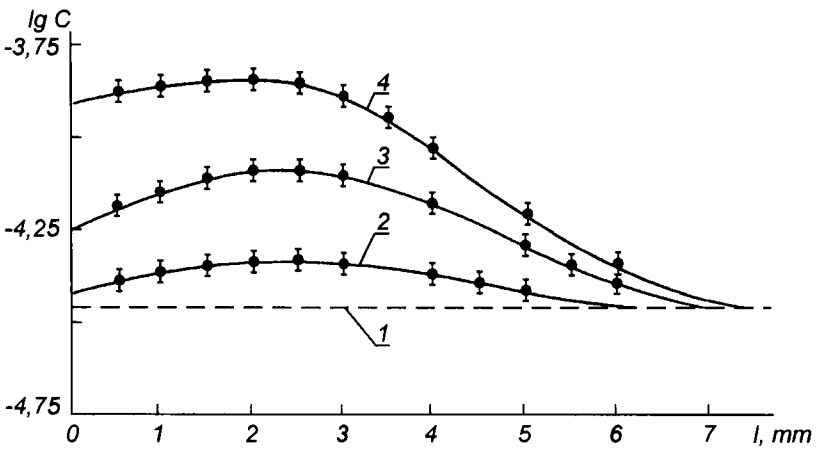

Fig. 7.9. Depth distribution of hydrogen concentration in steel C45e 24 hours after sliding: P=5.8 MPa; v=1.1 m/sec; 1) before sliding; 2, 3, 4) after 1, 10 and 25 test cycles, respectively.

Laboratory and pilot tests have shown that intensive destruction of steel and cast iron sliding surfaces, manifesting itself in the spreading metal over the plastic surface, occurs at hydrogen concentrations in the surface layer of above $(9–10)\times10^{-5}$ m^3/kg. Such a stable, surface, hydrogen concentration is found already after 10 cycles (see Fig. 7.9). Thus, multicyclic friction of a pair results in intensive hydrogen absorption by metal, and eventually substantial wear.

The character of hydrogen absorption by iron alloys in sliding with plastics, is always the same despite differences in the amount of hydrogen absorbed (Fig. 7.10). These differences can be ascribed to the presence of different percentages of chromium, which change the ability of steel to absorb hydrogen, and also hinder its diffusion.

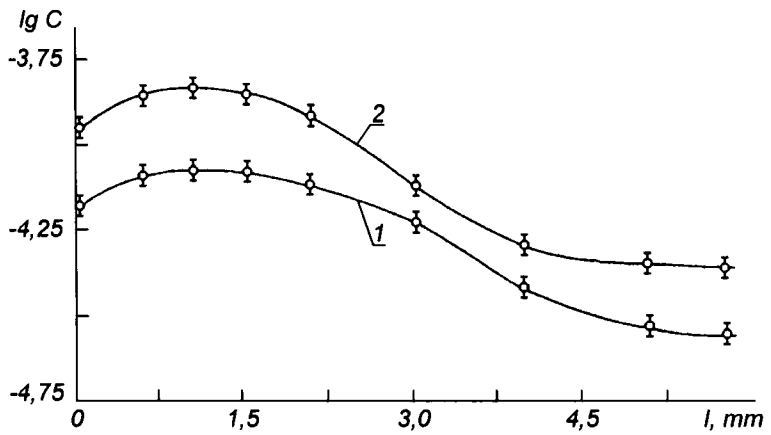

Fig. 7.10. Depth distribution of hydrogen concentration in steel 2/11 (1) and cast iron 200 (2) after 10 cycles of braking with FK-24A and 245-43-71 plastics (brake of a drilling winch and brake lining of a ZIL-130 automobile, respectively).

Studies of metal microhardness at different depths from the sliding surface (by layer-by-layer removal), have shown that the character of microhardness variation is similar to variations of hydrogen by depth (Fig. 7.11). This is confirmed also by studies of metal microstructure at different depths from the surface. Maximum microhardness, and substantially comminuted microstructure, are observed at a maximum hydrogen concentration.

Therefore, during the sliding a large volume of the metal counterbody appears saturated with hydrogen. Heat released during sliding against high friction plastics initiates the destruction of the organic binder in plastics. Gaseous decomposition products contain a sufficient amount of hydrogen capable of active participation

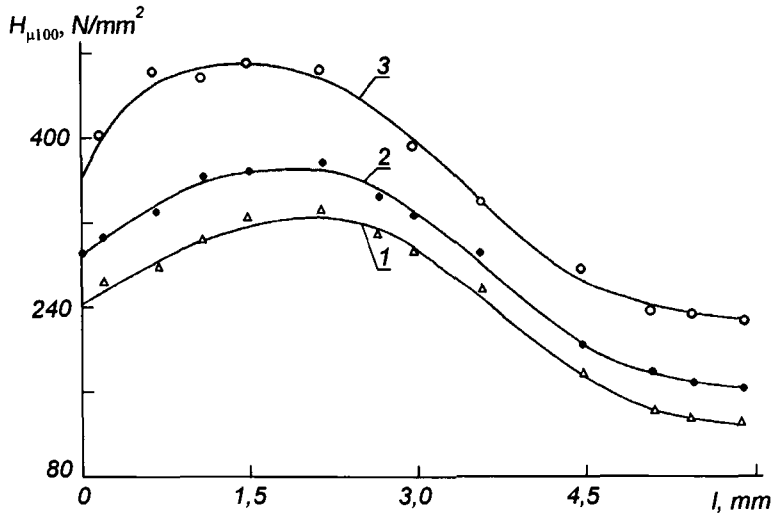

Fig. 7.11. Microhardness variations over the depth of steel C45e (1), cast iron 200 (2) and steel 2/11(3).

in the chemical processes accompany sliding. Friction affects metal surface layers which subsequently undergo irreversible changes in the conditions of hydrogen absorption. The region of metal adjacent to the friction surface, experiences intensive loads which induce plastic deformation and high temperatures (up to 1273 K). At this point technological hydrogen will then be in a saturated solution in a particular region of a steel specimen [327]. The products from destructing the organic binder in plastic probably supply the additional amount of hydrogen which is needed for transforming metal to the state of the saturated solution with hydrogen, at that temperature. Naturally during metal cooling, hydrogen will be in the state of a supersaturated solution, depending on the cooling rate and discontinuous changing at the polymorphism point (because of different solubilities of phases). Therefore, some of it should desorb from the metal (this is experimentally verified).

Friction and rest processes are accompanied by the complicated dynamics of hydrogenation and redistribution of hydrogen concentration, both in the surface layer subjected to friction, and in the nearsurface layers at a depth of 3 or 4 mm (Fig. 7.12). Hydrogen concentration redistribution in the surface layer in various experimental stages, occurs as shown in Fig. 7.13. An explanation of stages 3, 4, and 5 requires knowledge of what the motive force is, of diffusion processes.

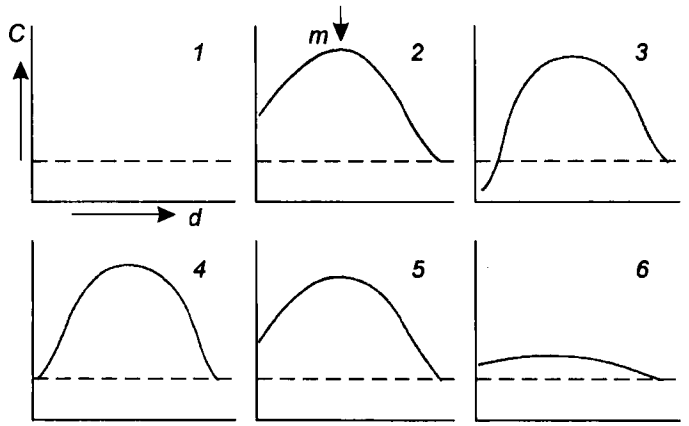

Fig. 7.12. Hydrogen concentration redistribution in the volume of a steel specimen: C, hydrogen concentration; d, distance from the sliding surface; m, a maximum concentration region; 1) initial state; 2) sliding process; 3) final sliding; 4) initial desorption; 5) maximum desorption; 6) final desorption.

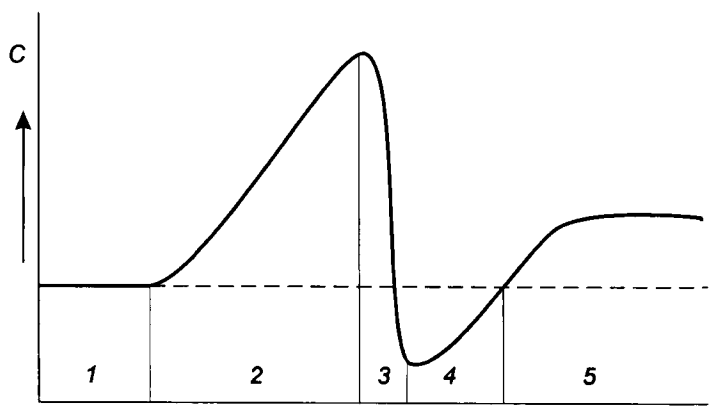

Fig. 7.13. Hydrogen concentration redistribution in the surface layer of a steel specimen: 1) initial state; 2) sliding process; 3) sliding cessation; 4) restoration of initial concentration; 5) start of desorption and gain.

7.5. Mechanism of High Temperature Hydrogenation of Metals During Sliding Against High Friction Plastics

The Motive forces of hydrogen diffusion. The fact that hydrogen shows a great tendency to diffusion, not only in gases but also in solids, stems from the structure of its atom, having one electron, and its small size ($R=0.5\times10^{-10}$ m).

One of the reasons for diffusion lies in the concentration gradient. With a concentration gradient, according to Fick's first law, a phase tends to level its composition: $j_i = -D_i(\partial C_i / \partial x)$, where j_i is the flow of the i-th species of particles through unit surface area for 1 sec; D is the diffusion coefficient; C is the concentration; x is the coordinate.

Sliding is accompanied by elastic or plastic micro- and macrodeformations of contacting surfaces. In this case the diffusion coefficient can increase by several orders. For example, in the plastic deformation of a specimen, a 10^3-fold increase of the coefficient of diffusion, of nickel into copper, was observed. Here, Fick's law takes the form;

$$\frac{\partial C}{\partial t} = D' \frac{\partial^2 C}{\partial x^2} - D'' \frac{\partial^2 \varepsilon}{\partial x^2},$$

where D′ and D″ are diffusion coefficients caused by concentration and stress gradients, respectively, i.e. without concentration diffusion. It can be induced by the stress gradient $\partial\varepsilon / \partial x$. However, concentration and deformation coefficients are not the only reasons for diffusion. In a more general form [341] diffusion in a real body can be expressed by the following: $j_d = -D^*(\partial\varphi / \partial x)$, where D^* is the generalized diffusion coefficient; φ is the chemical potential of the phase which is the interaction energy of particles inside the phase. Since $\varphi=f(C, \varepsilon, T)$, diffusion can be described most completely as follows:

$$j_d = D_C \frac{\partial C}{\partial x} + D_\varepsilon \frac{\partial \varepsilon}{\partial x} - D_T \frac{\partial T}{\partial x},$$

where D_C and $D\varepsilon$ are the diffusion coefficients caused by concentration and stress gradients; D_T is thermal diffusivity.

The third term on the right-hand side of the equation represents thermal diffusion. The diffusion of hydrogen atoms from colder regions to areas with a higher temperature will be the more intensive, the higher the temperature gradient $\partial T/\partial x$.

Studies have revealed that in sliding of steel (or cast iron) and plastic pairs, much more hydrogen is absorbed $(18–20)\times10^{-5}$ m^3/kg. A similar amount of hydrogen is absorbed by steels heated to 1473 K at normal pressure in hydrogen atmosphere. Moreover, contacting surfaces of sliding pairs permanently experience elastic and plastic deformations. The main motive forces of diffusion during sliding of pairs are, therefore, stress and temperature gradients.

Immediately after friction ceases, an effect of the diffusion components, caused by deformation and temperature decreases and diffusion associated with bringing the whole metal volume into thermodynamic equilibrium with the ambient atmosphere, prevails. A little later it predominantly becomes diffusion, brought about by the friction induced, concentration gradient.

Temperature distribution along the normal from the sliding surface. Data concerning the calculation of temperature fields in the deformation zone, are most often obtained from an analysis of steady-state heat processes in a sliding body with heat release at the boundary of contacting bodies. However, this does not give a full physical picture of the processes. Indeed, heat release in friction is associated with the formation and destruction of some structure in the surface layer of sliding bodies, i.e. in its essence, a heat source during sliding is internal and located at a depth varying in a widely range, from a few micrometers to several millimeters.

Meanwhile, studies of the hydrogen behavior during the sliding of high friction materials, show that hydrogen content is closely related with friction heat release. It has been found particularly that, immediately after friction stops, when the metal contact surface has a high temperature as was shown by local spectra analysis, it contains much less hydrogen than before friction. As a metal specimen cools down, the temperature levels off. The hydrogen concentration returns to its initial value and can even increase (see Fig. 7.12).

In an experimental study conducted to investigate temperature distribution along the depth from the sliding surface into a steel Fe360A specimen (l=100 mm, d=18 mm), six thermocouples were installed (chromel-alumel, the junction diameter is 0.3 mm). Each thermocouple was mounted a certain distance from the sliding surface. The junction of one of the thermocouples led directly to the surface. The end face of a steel specimen sliding against a FK-24A friction plastic on a sliding machine at 1180 rpm. There was a specific load of up to 5.8 MPa, with a mutual overlap factor of unity.

Heat release in the contact zone was calculated for a steady-state. It gave temperature distribution curves with a maximum at a particular distance from the contact surface [342, 343]. This finding agrees with our experimental data (Fig. 7.14) and is in opposition with the solution of other researchers, who assumed a surface heat source and a maximum temperature located directly at the boundary.

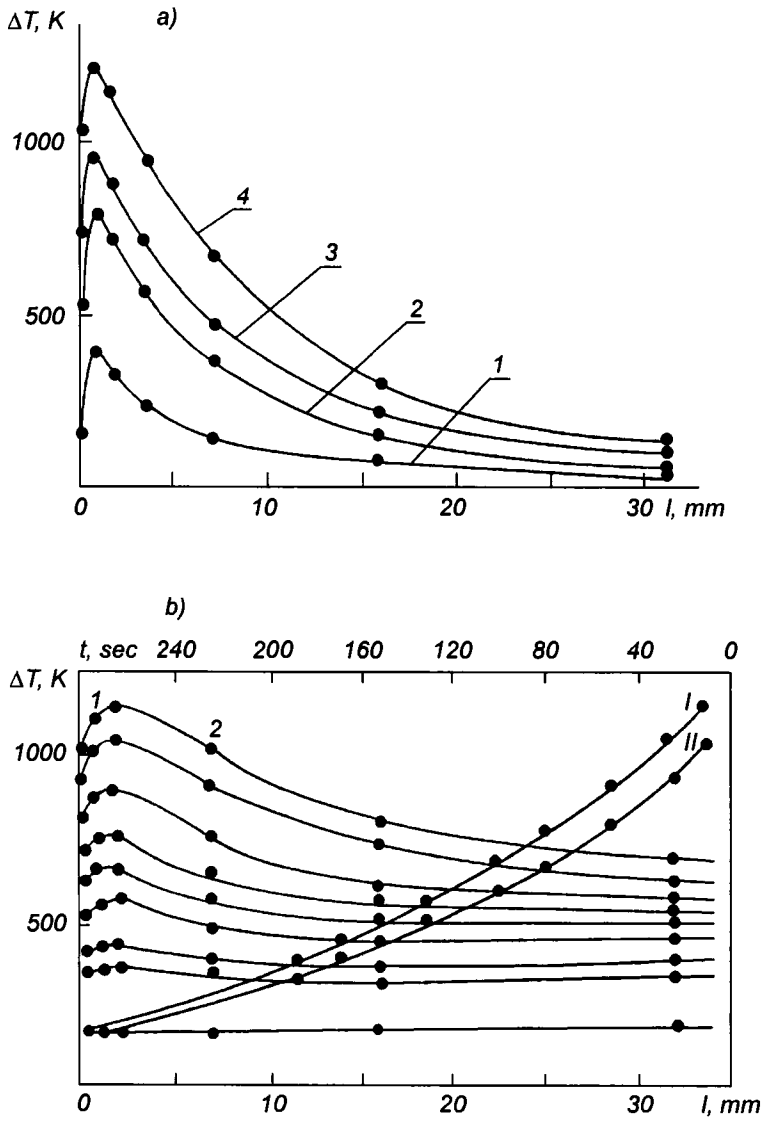

Fig. 7.14. The temperature profile of a steel Fe360A, with friction heating (a) for 5 sec (1), 10 sec (2), 15 sec (3), and 20 sec (4) and the temperature profile nomogram in the specimen being cooled (b): I and II are cooling curves for points 1 and 2, respectively.

Studies [342, 343] restricted to a steady state have a main disadvantage. This is because the heat flux emitted in the contact zone was shared equally between the

bodies in friction. This meant that the difference in heat resistances of heterogeneous materials in the sliding pair, was neglected. Heat removal from the deformable layer was assumed to follow Newton's law, but not the heat conduction law; more importantly, changes in the physical and mechanical properties of the surface layer subjected to deformation, were totally neglected.

In order to find the true nature of the unsteady state of the temperature field in bodies during sliding, consider the heat conduction of a steel rod pressed with a particular level of force to the rotating disk surface [344]. The disk and rod materials are assumed to have essentially different properties; it is also taken into consideration that the properties in the surface layer of the rod differ from those of nondeformed material. Then the solution to the problem on sliding of two bodies reduces to solution of the problem on heat propagation in a system of three bodies with a distributed heat source in the middle body (Fig. 7.15).

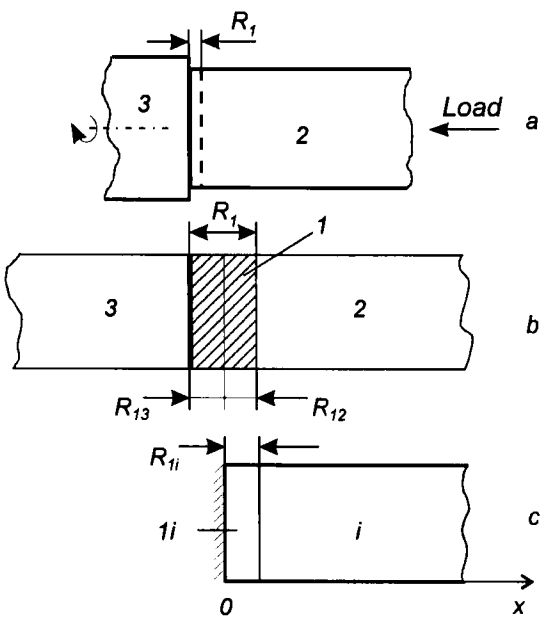

Fig. 7.15. Schematic diagram of the temperature problem.

Putting the coordinate origin (the reference system), in to the cross-section of body 1, where maximum the temperature is, and consequently $\partial T(x,\tau)/\partial x = 0$, will reduce the problem of three bodies and give a solution to the problem of

a pair system, i.e. the equation will be solved:

$$\begin{aligned} &\frac{\partial T_{1i}(x,\tau)}{\partial \tau} = a_1 \frac{\partial^2 T_{1i}(x,\tau)}{\partial x^2} + \frac{\varpi}{\rho C} && (\tau > 0, \quad 0 < x \le R_{1i}), \\ &\frac{\partial T_i(x,\tau)}{\partial \tau} = a_i \frac{\partial^2 T_i(x,\tau)}{\partial x^2} && (_{\tau} > 0, \quad R_{1i} < x < \infty), \end{aligned} \tag{7.2}$$

where i=2, 3 (see Fig. 7.15);

τ is the time;

a is the thermal diffusivity;

ρ is the density;

C is the heat capacity;

ω is the power of volume heat release along the length R1 with the following boundary conditions

$$\begin{aligned} &\frac{\partial T_{1i}(0,\tau)}{\partial x} = 0, && T_{1i}(R_{1i},\tau) = T_i(R_{1i},\tau), \\ & && T_{1i}(x,0) = T_i(x,0) = T_0, \\ &\frac{\partial T_i(\infty,\tau)}{\partial x} = 0, && \lambda_1\left[\frac{\partial T_{1i}(R_{1i},\tau)}{\partial x}\right] = \lambda_i\left[\frac{\partial T_i(R_{1i},\tau)}{\partial x}\right]; \end{aligned} \tag{7.3}$$

where λ is the thermal conductivity.

From analysis of the above equations, it can be seen that bodies 2 and 3 were assumed infinite and that heat exchange with the lateral surface was neglected. These assumptions are reasonable because preliminary studies on the influence of heat transfer and finiteness of the rod were carried out according to [345, 346], by solving the equation;

$$\frac{\partial T(x,\tau)}{\partial \tau} = a \frac{\partial^2 T(x,\tau)}{\partial x^2} - \frac{\alpha P}{C\rho f}[T(x,\tau) - T_0], \tag{7.4}$$

where α is the heat transfer coefficient;

P is the perimeter;

f is the cross-sectional area;

a is the thermal diffusivity with the following boundary and initial conditions for a semi-infinite rod:

$$T(x,0)=T_0, \qquad q=-\lambda\left.\frac{\partial T(x,\tau)}{\partial x}\right|_{x=0}=const,$$
$$T(\infty,\tau)=T_0, \qquad \frac{\partial T(\infty,\tau)}{\partial x}=0 \tag{7.5}$$

and for a finite rod (R in length)

$$T(x,0)=T_0, \qquad q=-\lambda\left.\frac{\partial T(x,\tau)}{\partial x}\right|_{x=0}=const,$$
$$-\lambda\frac{\partial T(R,\tau)}{\partial x}=\alpha\,[T(R,\tau)-T_0] \tag{7.6}$$

Here, and in the following, q is a specific heat flux.

The solution to Eq. (7.4) with the conditions (7.5) has the form

$$T(x,\tau)-T_0=\frac{q\sqrt{a}}{\lambda}\frac{1}{2\sqrt{H}}\left(\exp(-k_0\sqrt{H})\,erfc\left(\frac{k_0}{2\sqrt{\tau}}-\sqrt{H\tau}\right)-\right.$$
$$\left.-\exp(k_0\sqrt{H})\,erfc\left(\frac{k_0}{2\sqrt{\tau}}+\sqrt{H\tau}\right)\right) \tag{7.7}$$

at $H=\alpha/C\rho h$, $h=f/P$, $k_0=x/\sqrt{a}$, which at $\alpha=0$ changes into the conventional solution [345]

$$T(x,\tau)-T_0=\frac{2q\sqrt{a\tau}}{\lambda}\,ierfc\frac{k_0}{2\sqrt{\tau}}. \tag{7.8}$$

The solution to Eq. (7.4) with the conditions (7.6) is of the form

$$T(x,\tau)-T_0=\frac{q\sqrt{a}}{\lambda}\frac{1}{2\sqrt{H}}\left[\sum_{i=0}^{3}\exp(-k_i\sqrt{H})\,erfc\left(\frac{k_i}{2\sqrt{\tau}}-\sqrt{H\tau}\right)-\right.$$
$$\left.-\exp(k_i\sqrt{H})\,erfc\left(\frac{k_i}{2\sqrt{\tau}}+\sqrt{H\tau}\right)\right], \tag{7.9}$$

where $k_1=(2R\text{-}x)/\sqrt{a}$; $k_2=(4R\text{-}x)/\sqrt{a}$; $k_3=(2R+x)/\sqrt{a}$; at $R\to\infty$ Eq. (7.9) changes asymptotically into Eq. (7.7).

The solutions (7.7) and (7.8) are shown in Fig. 7.16 as the dimensionless temperature distribution $\Delta\theta=\Delta T(x, \tau)/\Delta T(0, \tau)$ for the two heating periods: $\tau=10$ sec (curves 1 and 3) and $\tau=20$ sec (curves 2 and 4); in this figure, the exponentially measured temperature distribution in a specimen (curves 5 and 6) is also plotted.

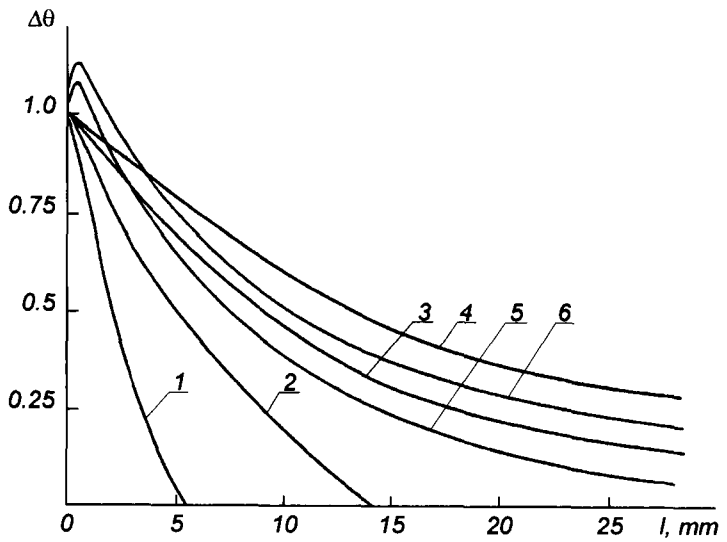

Fig. 7.16. Temperature profile along the rod: 1, 3, 5) t=10 sec; 2, 4, 6) t=20 sec.

From comparison of the curves predicted with (curve 1 and 2), and without, heat transfer (curve 3 and 4) using the experimental data, it follows that, within the conditions of this problem, the effect of heat transfer on the heat propagation in the rod can be neglected (with the accuracy of 5 to 10%) because of relatively short heating periods ($\tau<30$ sec) and a small form-parameter h, less than 4×10^{-3} m. The problem will subsequently be considered without heat exchange with the ambient atmosphere (the heat transfer coefficient α is found from an equation of the form $Nu=0.4\ (Gr)^{1/4}$ [347] for a horizontal tube with free convection, hence $\alpha \approx 30$ W/(m^{2}K) for the present experimental conditions).

Verification of the rod finiteness effect has shown that in the solution to Eq. (7.4) with the conditions (7.6) (without heat transfer)

$$T(x,\tau)-T_0 \cong \frac{2q\sqrt{a\tau}}{\lambda}\left[\sum_{i=0}^{3} iefrc\frac{k_i}{2\sqrt{\tau}}\right], \qquad (7.10)$$

the second and subsequent terms in the sum are practically equal to zero,

i.e. the finiteness effect on the heat conduction can also be ignored.

The study carried out to investigate the influence of heat transfer and finiteness of the rod on heat conduction, [343] confirms that the problems are justifiably noted, and shows that it is possible to find the temperature distribution from the set of Eqs. (7.2) with the conditions (7.3).

A Solution to the steady state heat conduction problem with a distributed heat source in the surface layer. The true behavior of temperature fields in bodies participating in sliding can be described quite accurately by the set of Eqs. (7.2) and concerning the boundary and initial conditions (7.3). With this set, the problem of sliding between two bodies 2 and 3 (see Fig. 7.15) is reduced to the problems of heat conduction for the three bodies. In this case, the power of heat release $\omega=q/R_1$, occurs in the intermediate body. In what follows, the co-ordinate origin is placed at the point where the temperature in body 1 is at maximum, thus the initial problem is solved by a solution of two sets of equations for bodies 2 and 12, and bodies 3 and 13. They are mathematically symmetrical and describe the heat conduction of a system of semi-infinite i and finite $1i$ rods with a volume heat release in finite body $1i$ thermally insulated from the end face (x=0) [348].

A solution for the initial system will be carried out by the Laplace transform. We can express Eqs. (7.2) in the images as

$$\begin{aligned} T''_{\alpha_{1i}}(x,S)-\frac{S}{a_1}\left[T_{\alpha_{1i}}(x,S)-\frac{T_0}{S}-\frac{\omega}{\rho_1 C_1 S^2}\right]=0,\\ T''_{\alpha_i}(x,S)-\frac{S}{a_1}\left[T_{\alpha_i}(x,S)-\frac{T_0}{S}\right]=0, \end{aligned} \tag{7.11}$$

where S is the Laplacian, we obtain solutions in the form;

$$T_{\alpha_{1i}}(x,S)-\frac{T_0}{S}-\frac{\omega}{\rho_1 C_1 S^2}=A_1\exp(x\sqrt{\frac{S}{a_1}})+B_1\exp(-x\sqrt{\frac{S}{a_1}}),$$

$$T_{\alpha_i}(x,S)-\frac{T_0}{S}=A_2\exp(x\sqrt{\frac{S}{a_i}})+B_2\exp(-x\sqrt{\frac{S}{a_i}}).$$

By finding the integration constants A_1, A_2, B_1, B_2 from the initial and boundary conditions (7.3) and inverting the images in the solution by the Laplace inverted transformation, we finally obtain the temperature distribution law in the

finite body 1*i*

$$T_{1i}(x,\tau)-T_0=\frac{\omega\tau}{C_1\rho_1}-\frac{\omega m_i}{C_1\rho_1}\left\{\sum_{j=1}^{2}\sum_{n=1}^{\infty}\left[\frac{2}{d_i}\sqrt{\frac{\tau}{\pi}}\exp(-\frac{k_{nij}^2}{4\tau})-\right.\right.$$
$$\left.\left.-\frac{1+d_ik_{nij}}{d_i^2}erfc\frac{k_{nij}}{2\sqrt{\tau}}+\frac{1}{d_i^2}\exp(d_ik_{nij}+d_i^2\tau)erfc(\frac{k_{nij}}{2\sqrt{\tau}}+d_i\sqrt{\tau})\right]\right\} \quad (7.12)$$

and in the semi-infinite one;

$$T_i(x,\tau)-T_0=\frac{\omega}{C_1\rho_1}\left[\frac{2}{d_i}\sqrt{\frac{\tau}{\pi}}\exp(-\frac{k_i^2}{4\tau})-\frac{1+d_ik_i}{d_i^2}erfc\frac{k_i}{2\sqrt{\tau}}+\right.$$
$$\left.+\frac{1}{d_i^2}\exp(d_ik_i+d_i^2\tau)erfc(\frac{k_i}{2\sqrt{\tau}}+d_i\sqrt{\tau})\right] \quad (7.13)$$

where i=2, 3; j=1, 2; n=1, 3, 5, ...; $k_i=(x-R_{1i})/\sqrt{a_i}$; $k_{ni1}=(nR_{1i}-x)/\sqrt{a_1}$;

$k_{ni2}=(nR_{1i}+x)/\sqrt{a_1}$; $d_i=m_i\sqrt{a_1}/R_{1i}$; $m_i=b_1/b_i$, $b_i=\lambda_i/\sqrt{a_i}$; $\omega=q/R_1$.

The conditions which lead to an agreement of solutions (7.12) and (7.13) are written as $T_{1i}(R_{1i},\tau)=T_i(R_{1i},\tau)$ and of the solutions of two pairs of the sets as $T_{12}(0,\tau)=T_{13}(0,\tau)$. This is because, at the boundary between the bodies i and 1i, there is no heat resistance, and at the point x=0 (body 1) the temperature is at maximum.

In the expressions (7.12) and (7.13) both the properties (C, ρ, a, λ), and extension R_{1i} of the intermediate body, are unknown and should be determined by coordinating the predicted temperature distribution and the experimental data (see Fig. 7.14).

Determining the volumetric heat release power ω necessitates a knowledge of the work done by the deformation resistance forces $\tau\sigma$; per unit time, per unit volume. As in [342], assuming that the resistance $\tau\sigma$ is constant throughout the volume and equal to the friction force F_{fr} divided by the area of the actual contact S_{ac}, we obtain $\omega=\tau\sigma V_{av}/R_1$, where V_{av} is the sliding velocity at the average radius. The most accurate estimates do not give S_{ac} larger than one tenth of the nominal friction area S_{nom}. Assuming $S_{ac}=0.1S_{nom}$, we thereby prescribe the heat source output to be a minimum of the real value.

In analyzing the obtained expression, as applied to the present conditions (body 2: l=100 mm, d=20 mm, material is steel Fe360A; body 3 is FK-24A retinax; n=1180 rpm; pressing force F=1,5 kN; torque M_{fr}=3.8 N×m), we obtain

the specific heat flux $q=1.12\times10^7$ W/m^2; the friction coefficient for steel in sliding with retinax $K=3M_{fr}/(dF)=0.38$ agrees satisfactorily with available literary data [22] where $K=0.37$ to 0.40 is reported for the steel–retinax pair. Allowing for the fact that for steel $C_2=464.5$ J/(kg×K), $\rho_2=7830$ kg/m^3, $a_2=14.72\times10^{-6}$ m^2/sec, $\lambda_2=51.9$ W/(m×K), and for retinax $C_3=963$ J/(kg×K), $\rho_3=1800$ kg/m^3, $a_3=0.349\times10^{-6}$ m^2/sec, $\lambda_3=0.605$ W/(m×K) and the order of, magnitude of R_1 is 10^{-3} m, we obtain $d_2\sqrt{\tau}>5$. Consequently, in the expressions (7.12) and (7.13) the third terms in the right-hand side can be ignored since erfc $A<10^{-4}$ if A is larger than 2.6.

The temperature distribution in the rod will then be found, with sufficient accuracy, from the expressions;

$$T_{12}(x,\tau)-T_0 \cong \frac{\omega\tau}{C_1\rho_1}-\frac{\omega m_2}{C_1\rho_1}\left\{\sum_{j=1}^{2}\sum_{n=1}^{\infty}\left[\frac{2}{d_2}\sqrt{\frac{\tau}{\pi}}\exp\left(-\frac{k_{n2j}^2}{4\tau}\right)-\right.\right.$$
$$\left.\left.-\frac{1+d_2k_{n2j}}{d_2^2}\,erfc\,\frac{k_{n2j}}{2\sqrt{\tau}}\right]\right\}, \tag{7.14}$$

$$T_2(x,\tau)-T_0 \cong \frac{\omega}{C_1\rho_1}\left[\frac{2}{d_2}\sqrt{\frac{\tau}{\pi}}\exp\left(-\frac{k_2^2}{4\tau}\right)-\frac{1+d_2k_2}{d_2^2}\,erfc\,\frac{k_2}{2\sqrt{\tau}}\right] \tag{7.15}$$

(notations are the same). Assuming of $C_1=C_2$, $\rho_1=\rho_2$, $R_{12}=R_{13}$ for the first approximation calculations from Eqs. (7.14) and (7.15), give for $R_1=2.2\times10^{-3}$ m (experimental estimation) the temperature values shown in Fig. 7.17 (curve 2). A comparison of these values with the experimental data (curve 1) shows that the predicted temperatures are much in excess of the experimental values, and that there is a temperature gradient, especially in the contact zone. It should be emphasized that curve 2 is obtained with the assumption of constant thermal properties of the metal rod.

The great differences in the value and shape of the temperature distribution cannot be explained by the suggestion of the heat loss effect. This is because heat losses from the side surface result in a substantial increase of the longitudinal temperature gradient, rather than in a decrease of the absolute temperatures. Meanwhile, the shape of the real temperature distribution is closer to that without any considerable heat losses during the specimen heating time.

Presence of body 3 (a disk of retinax) with very low thermal properties, and consequently, with a high heat resistance at the boundary of the bodies in friction, should also result in a rise of the temperature gradient in the deformed surface layer. This is not the case in the real process (see Fig. 7.17, curve 1).

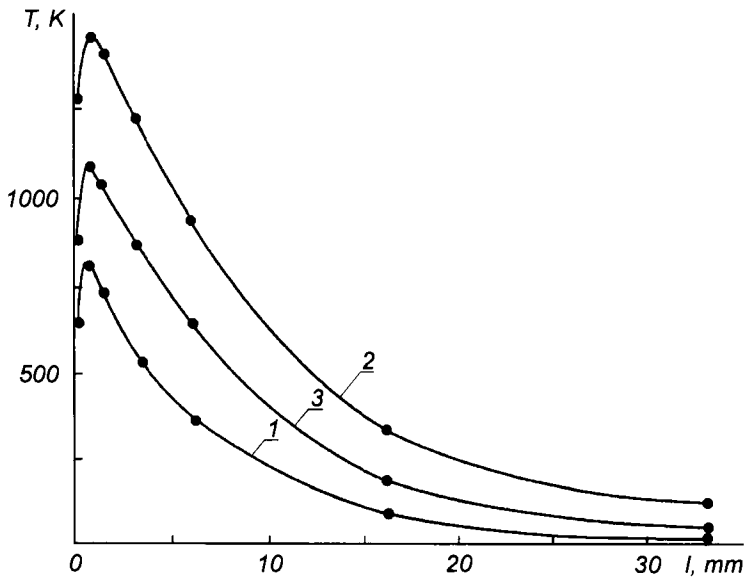

Fig. 7.17. Temperature profile: 1) experimental data; 2) predicted by Eqs. (7.12) and (7.13) with constant thermal properties; 3) predicted with $C_1=C_{liq}$ and $r_1=r_{liq}$.

A considerable smoothing of the temperature peak in the surface layer, may be a result of more intensive heat absorption in the layer, or an increase of its thermal conductivity. Evidently, the heat capacity C_1 of the surface layer heated by friction, to the temperature of polymorphous transformation of steel, must differ from the heat capacity C_2 of the other nondeformed ("cold") volume of the specimen. The heat capacity of metals growing with temperature is well known and, as indicated by some authors, it becomes several times higher at the phase transition point (for iron at the Curie point, heat capacity is as high as 1400–2000 J/(kg×K). Indeed, a similarity is found in the predicted curve 2 and experimental curve 1 ($\Delta T_{cal}=\Delta T_{exp}$), at C_1=820 J/(kg×K) while the earlier value $C_1=C_2$=464.5 J/(kg×K).

If, in view of the effect of spreading steel over the plastic, typical of contact with viscoplastic materials, it is assumed that during sliding, under intensive friction-induced hydrogen absorption by the action of external load at the polymorphous transformation point, the yield strength of metal in the surface layer falls dramatically and so follows, C_1=667 J/(kg×K), ρ_1=7500 kg/m^3 (liquid metal parameters). The temperature distribution (see Fig. 7.17, curve 3) will be more consistent with the real temperature distribution (curve 1) than in the first case (curve 2). The viscous flow effect, with hydrogen supersaturation of metal, was later found in another conditions without friction under gravity force [352, 357]. Processing these results in a similar way, we find that, for predicted curve

3 to agree with the experimental curve it is necessary to assign the thermal conductivity of 93 W/(m×K) to the surface layer.

The calculation of heat release in the contact zone of sliding materials [344, 348], and the experiment, have shown that the temperature maximum generated in friction lies at a certain depth from the metal surface. In this case the hydrogen thermodiffusion flow from the surface, and from the whole volume of the specimen, will be directed to the region with the maximum temperature. This then promotes the production of saturated hydrogen solution in this region and its subsequent hydrogen supersaturation.

As already noted [342], the heat source in sliding is internal in its physical nature. Whilst overcoming the contact interaction forces, the energy of elastic and plastic deformation of the volumes adjacent to the surface, transforms into heat. The depth of the deformation region, which is characterized by the highest dislocation density, can vary over a wide range and depends on the sliding mode, differences in the thermal properties and also coefficients of the mutual overlapping of sliding pairs.

For a metal–plastic sliding pair, these differences are especially pronounced. Because of this, a depth of the temperature maximum is relatively large (of the order of 10^{-3} m). On the sliding surface, friction bonds are broken to produce exposed areas; the metal is intensively redeformed; there are hysteresis losses. The vibration spectrum and amplitude of surface atoms, parameters C, ρ, a, λ, and consequently, the tensor of specific heat fluxes from the actual contact, all differ from the volumetric characteristics. The difference occurring in the thermal physical parameters of the surface, and the adjacent volumes (different thermal diffusivities), is likely to result in the average temperature on the surface, where temperature spikes arise on the actual contact spots, being lower than that in the volume, adjacent to the surface.

Also favorable for the appearance of a temperature maximum is the recombination of hydrogen molecules in defects of the subsurface layer accompanied by large heat releases (105 kcal/mol).

Sliding of frictional pairs is accompanied by irreversible physicochemical changes of the surfaces of contacting metals since during operation they are subjected to high tangential and normal loads, and consequently, to considerable heating. High temperature promotes thermal destruction of the organic binder in frictional plastics. Temperature gradients and inhomogeneous stress fields disturb the thermodynamic state of the whole metal. Concentration currents appear, which change the initial states of components in the metal. All these factors, plus a high chemical activity of the metal surface during sliding, are beneficial for increasing the solubility of the hydrogen. The complicated dynamics of the hydrogen concentration redistribution shown in Figs. 7.12 and 7.13, can be now explained successfully.

Experiments indicated that the temperature difference at a depth, and on the sliding surface, can reach 250 K. When a steel specimen is removed from the friction zone, this difference increases as a result of contact of the surface with the ambient air. The hydrogen thermodiffusion flow in iron-based alloys is directed to the region exhibiting the maximum temperature [327], therefore, hydrogen dissolved by the surface layer flows to these region, forming a saturated solution at high temperature. This is confirmed by a spectral analysis of the surface carried out immediately after the tests.

When passing through the $\gamma \rightarrow \alpha$ phase transition points during cooling (of about 1073 K for steel Fe360A), a supersaturated solid solution of hydrogen is formed because of a lower hydrogen solubility in the α-phase than in the γ-phase. When a specimen is quickly cooled to room temperature, the hydrogen concentration distribution has no time to change considerably, since the heat removal rate is much greater than the rate of hydrogen diffusion to the surface. In this case, the discrepancies between hydrogen concentrations at different distances from the surface will be a motivating force for diffusion. When the hydrogen content at the surface of the test specimen attains its initial value, the excess hydrogen, further accumulates and leaves the specimen. This was discovered during the experiment with a sample dipped in alcohol-glycerine solution described above (see 7.4).

This possible to estimate the hydrogen supersaturation in polymorphous $\gamma \rightarrow \alpha$ transition in iron or steel which takes place under multiple cyclic loading at 1073 to 1123 K.

The curves of the depth distribution of hydrogen concentration in steel specimens shown in Figs. 7.7 to 7.10, were obtained using a spectral method of recording the intensity of the hydrogen emission line at 656.285 nm excited by a spark generator. From the moment of friction loading, removal of the specimen, and subsequent spectral analysis, a certain period clapses during which the hydrogen concentration peak appears substantially smaller and becomes wider because a levelling of the temperature and hydrogen concentration throughout the specimen volume. Therefore, hydrogen concentrations at different depths are underestimated.

This can be seen in Table 7.1, where the total hydrogen concentrations in specimens after sliding against plastics are given. For steel Fe360A–plastic 1-151M pairs the hydrogen content is 18.08×10^{-5} m^3/kg. However, since practically the whole hydrogen is localized in a very narrow, near-surface zone with a maximum temperature, as indicated earlier, the actual hydrogen concentration (based on the volume of the localization area, but not on the whole volume of the specimen) will be an approximately one order of magnitude higher (the volumes of the specimen and the localization region differ by the same order of magnitude). Thus, during the temperature decrease in the cycle (between

successive brakings), accompanied by polymorphous transformation there will be substantial hydrogen supersaturation (of the order of 200×10^{-5} m^3/kg and more).

Under hydrogen supersaturation at the moment of polymorphous transformation, the metastable state of metal is most likely to be characterized by a more substantial decrease in atomic bond energy, compared with the metastable state at the same moment without hydrogen (a higher atomic excitation level). This is because of the additional weakening of bonds of metal atoms by excess protons which are dissolved in the crystal lattice. As a result, at the moment of polymorphic transformation, a viscous flow of the subsurface metal layer occurs.

The transition of metal, saturated with hydrogen, to the state of viscous flow at low (compared with the melting point) temperatures, is likely to manifest itself in the hydrogen atmosphere in many cases, but not only in hydrogen absorption which is induced by sliding. It would therefore be natural to simulate the conditions of hydrogen absorption in a similar way to those described above. Also to verify the results in steady state heating and forced (under pressure in a special chamber) hydrogen saturation of metal, and to substitute temperature variations, due to cyclic braking during sliding, by cyclic decrease and increase temperature near the polymorphous trasformation temperature. In this case the whole metal volume should become a viscous flow. Eight years after publication of the hypothesis [348] such an experiment was conducted, [352]. Its results fully confirmed the viscous flow effect under hydrogen absorption.

The concentration C, of dissolved hydrogen at high gas pressures in particularly constructed steels, is related with the pressure p by the relation $C=K_s\sqrt{p}$, where K_s is the solubility constant. Because, in the dissolution of molecular hydrogen the gas pressure is in direct proportion to its concentration in a solid, the above relation supports the suggestion that hydrogen dissolves in iron, and its alloys, in a dissociated state [353] (see also 7.6). In the temperature range studied, and in a wide gas pressure range, hydrogen forms a solid solution of a corporation type (no hydrogenous phases are produced). Moreover, it is known that hydrogen solubility in austenite steels (γ-Fe) is about 4 times as much as that in carbon steel C20e, and 6 times larger than in martensite and ferrite steels [353]. It is also known that the yield point of iron at the moment of $\alpha\leftrightarrow\gamma$-transition decreases to about 1 MPa, due to the weakening of interatomic bonds in the transient state [354–356].

With this in mind, one of many possible mechanisms of metal transition to the state of a viscous flow was suggested [357]. The viscous flow of iron arises as a result of the formation of a layer substantially supersaturated with hydrogen (an H-layer) at the growing and vanishing phase interface in polymorphous $\gamma\rightarrow\alpha$ transition in the hydrogen atmosphere [357]. Such metal layers are metastable and their viscosity should be several orders lower.

The mechanism has not yet been confirmed by other authors. Therefore, the presence of a transient H-layer at the interface between two phases, still remains hypothetical. An analysis of the study aimed at confirming the hypothesis about forming a transient H-layer between the growing and vanishing crystals, allows for ambiguous interpretation [357]. For example, the suggestion of the existence of a "specific transient layer" (the H-layer) is supported by a photo picture of microareas with portions (the darkened field) of H-martensite, which appears from the two-phase state during hardening. They do not confirm however, the existence of transient H-layers. They only show that the whole γ-phase, supersaturated with hydrogen, was transformed into martensite, but not that any transient regions (H-layers) could be seen at the interface between the growing and vanishing phases.

The interpretation of experimental data used in an analysis of the cooling curves of pure iron and iron in the presence of hydrogen at the temperature of $\gamma \rightarrow \alpha$ transformation, is also doubtful [357].

From the data reported in [357], it follows that in polymorphous transformation the whole γ-phase, decreasing in volume, appears equally supersaturated with hydrogen. An explanation of the viscous metal flow in hydrogen atmosphere, using the H-layer model, [357] seems to be inadequate. This phenomenon can be explained more efficiently with another model, following from the statements and experimental results discussed earlier.

In the normal $\gamma \rightarrow \alpha$ transition, nuclei of the α-phase arise at the grain boundaries or in other defective areas. Because of the differing hydrogen solubilities in α- and γ-phases, as the γ-phase volume decreases, the specific volume of dissolved hydrogen increases, and, at a concentration corresponding to the hydrogen solubility maximum in liquid metal, becomes a viscous flow.

The metastable state of the γ-phase, supersaturated with hydrogen to quasiluidity state (disappearing during polymorphous $\gamma \rightarrow \alpha$ transition), is similar to a kind of "lubricant" which developed, for a short time, between the formed crystal grains of the α-phase. This affects the internal friction forces by decreasing them, and also brings about a laminar metal flow which is exhibited in high temperature hydrogenation during sliding in spreading steel over frictional plastic.

In a polymorphous transformation with particular relations between the interface velocity and the hydrogen diffusion coefficient in austenite, hydrogen has no time to be set off from the metal and sorbs on the newly formed boundaries of polycrystal grains, dislocations, in the regions of tensile stresses, and other defects. When hydrogen fills the macroscopic defects (macropores) it combines to form molecules and can be forced out from the metal through defective areas due to high pressure.

7.6. The Influence of Hydrogen Absorption on the Work Function of Metals and Alloys

The mechanical properties of metals in a hydrogenous medium change as a result of hydrogen diffusion into the bulk of metal with subsequent segregation on dislocations, segregation or evolution in pores, microcracks, in the regions with triaxial stressed state etc.

Hydrogen in metal can be in the following forms: ionized, forming interstitial solid solution; molecular, in pores, cracks, on the boundaries of grains and other defects of polycrystalline solid; and in chemical compounds with impurities or alloying elements.

The interaction of hydrogen with dislocations has been shown to be too small to affect properties, including the yield limit at low temperatures. Hydrogen concentration in the regions with triaxial stressed state exceeds the average hydrogen concentration in the lattice by only three times [5]. Proton diffusion can not induce any significant distortions of the α-Fe lattice and can not thereby affect the parameters of their unit cells. Therefore, the formation of pores and cracks as a result of hydrogen evolution near interstitial, impurities, grain boundaries, in microcracks, and other defects is the governing factor for hydrogen embrittlement.

An experiment was carried out to check the suggestion about the form of hydrogen occurrence in the metal crystal lattice. The experiment consisted of measuring electron work function (EWF) by the contact potential difference (CPD) method with electrolytically hydrogenated metals [33]. The CPD method was suggested by in reference of [32] to determine the hydrogenation level of metals and alloys.

Specimens made of a thin metal rod were ground by abrasive cloth to a roughness 10 class to reduce oxide films, and then washed in toluene to remove the abrasive particles and wear products. Identity of the specimens was controlled by measuring EWF. The measurements showed (the apparatus and procedure were described in Sect. 2.1) that within the measurement error of $\pm$ 5 meV with a 1 meV sensitivity, EWF of all specimens shaped from the same metal were equal.

Electrolytic (cathode) hydrogenation was conducted at room temperature in a 26% water solution of H_2SO_4 with a cathode current density of 5 kA/m^2 and with various hydrogenation times. Platinum was used as the anode.

EWF of the hydrogenated metals was measured several times. Before each measurement their surfaces were ground and washed as above described. Grinding after hydrogenation was necessary to remove the outer most layers. The layers consisted largely of oxides produced by interaction of the metals with the electrolyte during hydrogenation. Outer layers have EWF different from that of the bulk metal. Grinding of the specimens before subsequent measurements was accompanied by removal of some of the surface metal. The amount was determined by weighing. Grinding was done to investigate the EWF variation along the depth of a hydrogenated metals. The time between preparation and

measurements was maintained at 3 min.

The experimental results are given in Fig. 7.18, which shows that for all metals studied electrolytic hydrogenation decreased EWF. The results agree with those in [358], and support the hypothesis of proton state of hydrogen in metals [325, 359]. Hydrogen in the form of protons in the metal lattice and on the metal surface produces a double electric layer (DEL) with its positive side facing outward, thus reducing EWF.

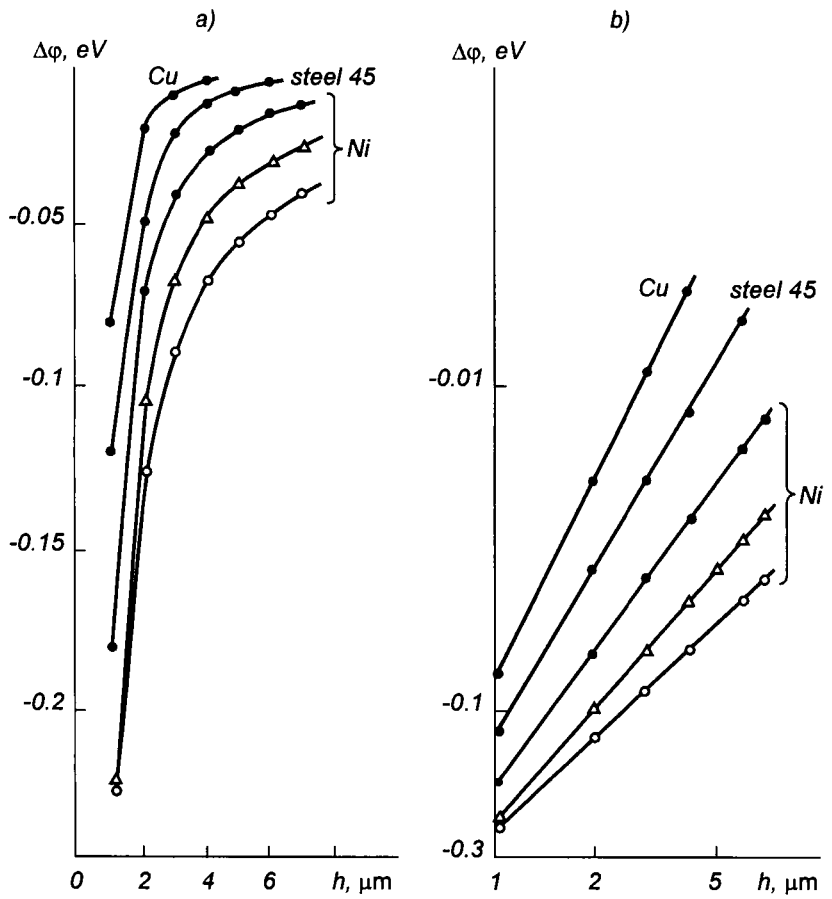

Fig. 7.18. Plot of EWF change $\Delta\varphi$ of copper, steel C45e, and nickel, subjected to electrolytic hydrogenation for 40 min (dark circles), 80 min (triangles), and 120 min (light circles) versus the distance h from the surface layer (as compared with the same untreated materials): a) linear scale; b) double logarithmic scale.

These results elucidate the process of electrolytic hydrogenation, regarding the hydrogen penetration depth into the surface layer, and its distribution. As can be seen from Fig. 7.18, the most essential difference in EWF between hydrogenated and untreated metals was found in the first measurements, i.e. at a small depth from the surface. The work function of hydrogenated metals increases with the distance from the surface, approaching the EWF of untreated metals. Absorbed hydrogen is shown to be distributed nonuniformly in depth. Maximum hydrogen concentration occurred in the thinnest surface layers. At greater depths, the hydrogen concentrations is reduced and the decrease follows the power law, as shown in Fig. 7.18.

Figure 7.18 also contains information about the ability of particular metal to absorb hydrogen. The solubility of hydrogen in copper is known to be lower than in iron (or steel), and much lower that in nickel [325, 326]. This difference is also reflected in changes of EWF of the metals caused by electrolytic hydrogenation. The work function of nickel and copper decreases under the same hydrogenation conditions to the greatest and smallest extents, respectively (Fig. 7.18). Hydrogen permeability in nickel is much higher than in copper [325, 326] which affects the EWF results. The higher the hydrogen permeability in metal, the larger is the distance from the hydrogenated metal surfaces at which differences in their EWF with nonhydrogenated specimens are observed, the hydrogenation conditions being equal.

The amount and depth of hydrogen in metals increases with the hydrogenation time, which is clearly shown by comparison of the curves for nickel after 40-, 80-, and 120 min of hydrogenation.

Thus, the differences for different metals are only manifested in changes of EWF, i.e. in the extent of the effect, in its value but not in its pattern. The character of hydrogen effect on the other properties (mechanical, electrical, magnetic) of various metals remains the same [325]. The reason for this observation is presumably their common physicochemical interaction with hydrogen with all the metals. The present results confirm this hypothesis..

7.7. The Mechanism of Hydrogen Wear

The term "hydrogen wear", as noted in the Preface, is an adopted abbreviation for increased wear as a result of hydrogen absorption induced by sliding.

A scheme of hydrogen wear involves six stages (Fig. 7.19). The first five stages refer to hydrogen absorption induced by sliding. Hydrogen wear is caused by many interrelated processes. The mechanisms of HW are related to worn surface as contrasted with an unworn surface.

Hydrogen absorption in the contact zone is produced in two ways: first, thermal degradation of the organic binder in sliding plastic against steel, second,

mechanical-chemical reactions in sliding surface sites. Molecular hydrogen is not soluble in metal, hydrogen absorption is, therefore, preceded by thermal or adsorption dissociation of hydrogen molecules into atoms. Deformation and high temperature in a sliding surface of steel increase atomic hydrogen solubility and diffusion. Therefore regions of saturated hydrogen are produced in metal.

The failure by HW is manifested in two ways: by dispersing (stage VIa) and "smearing" (stage VIb).

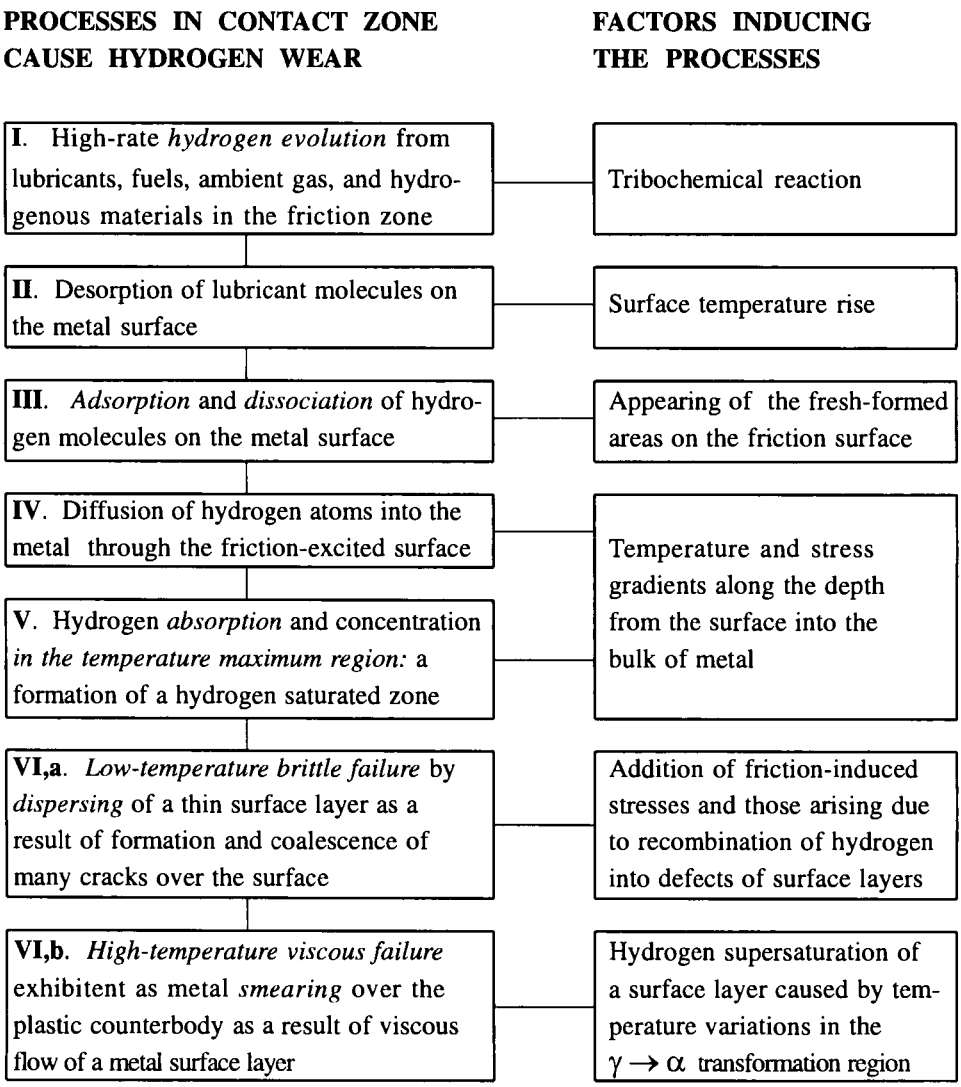

Fig. 7.19. Stages of the hydrogen wear mechanism.

Dispersing hydrogen wear. Let us consider stage VIa (see Fig. 7.19) in more detail. During diffusion, hydrogen infects Griffith's strain cracks and forms molecules. Huge internal pressures appear [360] which can exceed the ultimate strength of metal. Hydrogen which accumulates in microcracks adsorbs in to the fresh formed surface. This facilitates the growth and distribution of cracks. This is caused by an adsorption-induced decrease of the strength of the solid, as a result of the action of surfactant medium.

Estimates [3] show that a decrease in free surface energy induced by possible hydrogen penetration into a cavity at as low pressure as 0.1 MPa can be 0.43 J/m^2, with a true surface energy of 1.0 to 1.6 J/m^2 which is quite essential. More importantly, around this kind of molecular hydrogen collector, strengthened regions with high possible triaxial stresses, can appear [129]. These inhomogeneous stress fields can promote the generation of concentration flows of hydrogen atoms in these regions. The solid crystal lattice in such places will experience additional deformation as a result of incorporated hydrogen atoms. Therefore, sufficient amounts of hydrogen dissolved in the solid will create conditions which forms these superstressed regions. They are most likely to appear in the defective, friction-deformed surface layers of metal. Considerable strengthening of the surface layers during friction, disturbs the positive gradient of the mechanical properties along the depth of the metal specimen [22].

Local stresses, induced by hydrogen concentration in the hydrophilic zone, and the combining of hydrogen into molecules in defects of the crystal lattice, generate areas of crack nuclei. Under the action of cyclic, rather than steady state stresses, and strains in friction, a "pumping effect" is seen which is represented by the development of huge amounts of cracks from nuclei. The cracks appear simultaneously in several places under load and coalescing, and transform the surface steel layer into powder. This wear mechanism continues until the hydrogen saturated subsurface of the steel layer changes to one of a supersaturated state.

One must consider the basic characteristic of HW that distinguishes it from volume hydrogen embrittlement. The latter is an equilibrium or is close to equilibrium phenomenon. Hydrogen wear however, is a result of the cooperative action of an essential nonequilibrium of processes. In general, a friction system is a nonequilibrium system described in terms of nonequilibrium thermodynamics. Hydrogen wear is a result of a synergism of the surface effects during sliding with the nonequilibrium processes which are involved in deformation of the surface metal layer. To exhibit synergism is to behave in a particular way in order that the activity of a simultaneous action of all the factors as a whole would exceed the sum of the activities of their components if taken separately. Hydrogen evolution during sliding therefore, is concurrent with the joint action of factors promoting hydrogen absorption at the friction surface. These produce nonequilibrium concentrations and localization in the subsurface layer. The evolution is also concurrent with the action of factors which promote failure at the surface.

The cyclic volume strength of a specimen depends on the volume of the equilibrium hydrogen concentration and is associated with destruction, as a result of development of a general crack.

Hydrogen wear also depends on a synergism of the action of several effects. Mechanical, chemical, thermal, electrical, magnetic, and others. It also depends on the corresponding fields (of temperature, stresses etc.) which arise during sliding and cause the concentration of hydrogen in the subsurface layer. They can behave in two ways, dispersing or spreading in the surface layer.

Thus, HW essentially differs from the hydrogen embrittlement of steel in the majority of parameters, the most important being hydrogenation sources, hydrogenation rate, hydrogen distribution and destruction patterns.

Spreading Hydrogen Wear. As shown earlier (Sect. 7.5), (as result of hydrogen supersaturation) the surface layer of steel Fe360A during sliding becomes a viscous fluid flow at temperatures (of about 1070 K, see Fig. 7.17) substantially lower than the melting point of the metal (of about 1770 K). These temperatures are close to (in accordance with the state diagram for the iron–carbon alloy) the temperatures of the phase $\gamma \rightarrow \alpha$ transition. Here, the steel surface layer is easily spread over the counterbody (frictional plastic).

The hydrogen, supersaturated, subsurface zone (layer) generated by a viscous fluid flow will be characterized in more detail.

Thermal cycling is develops in the temperatures of the polymorphic $\gamma \rightarrow \alpha$ transformation in the iron-carbon alloy caused by cycling loading in braking. As a process, it determines the effectiveness of the subsurface layer flow (consequently, the spreading effectiveness). Therefore, the zone localized under the surface at the temperature maximum, and supersaturated with hydrogen at the time of polymorphic transformation, is mobile. Temperature and stress gradients, along the perpendicular to the sliding surface, vary cyclically during the sliding and considerably enhance the diffusion processes in the zone. The mobility of the zone is shown in the complicated dynamics of hydrogen absorption and hydrogen concentration in the subsurface layer (see Fig. 7.13). As a consequence of the zone mobility, thermal cycling, activation of diffusion processes, and hydrogen supersaturation, metal properties in the zone change. These changes are exhibited in differences in microhardness and the microstructure of metal. Hydrogenous martensite is produced during hardening from the temperature of the two-phase metal state. Found in the metal, provides additional support for hydrogen supersaturation at the moment of the $\gamma \rightarrow \alpha$ transformation [357].

Hydrogen supersaturation of the vanishing γ-phase, at the point of polymorphous transformation, weakens the atomic bonds so much that the atomic arrangement appears disordered and a viscous metal flow is induced. It

has been found that, even at very small pressures, hydrogen reduces the iron yield limit at the $\gamma \rightarrow \alpha$ moment from 1 to 0.0002 MPa [352].

To recap, the main reasons for hydrogen supersaturation state are, a polymorphous transformation, a decrease in diffusion mobility and in temperature, the rate of temperature changes, and the temperature gradient.

The most distinctive sign of a viscous flow in the metal surface layer in high-temperature sliding hydrogenation conditions is the spreading of metal over the plastic. The layer thickness is limited in a narrow range of metal where the temperature covers the polymorphous transformation region. Being in permanent contact with the plastic friction material, this metal layer will be immediately spread over the counterbody which was observed as instantaneous destruction of the steel surface with a typical structure of nonhardened metal layers which were spread over the plastic surface and solidified (for example, in metal–plastic braking pairs used in rail road vehicles).

Temperatures at which metal changes into a viscous fluid state are relatively high and consequently, steel (cast iron) spreading should behave under heavy loadings occurring in braking devices at an unpredictable time moment. Indeed, the spreading defect behave impetuously when sliding devices operate at very high temperatures. In view of this, it is not a coincidence that the spreading defect in braking devices used in automotive vehicles was discovered for the first time on mountain roads [361]. Spreading failure is typical of vigorous hydrogen absorption [362].

7.8. Preventing Hydrogen Wear in Various Kinds of Sliding Assemblies

During the dynamic, contact interaction of friction plastics with metals, free hydrogen is produced. This is a result of secondary transformations of the products of mechanical, thermal, and thermooxidative destruction. The question, arise as do what specific temperatures initiated by loads at the contact, and as a result of what kind of transformation, hydrogen is produced in operating friction pairs. We will try to answer this using a resin-based friction composite [363],

At low temperatures ($T<500K$) excess water evaporates. Excess phenol, cresol, and other substances evolve from polycondensation of the products obligatorily contained in sliding materials. This process is accompanied by oxidation ($Me+H_2O \rightarrow MeO+H_2$) and hydrogen evolution. In the temperature range of 350 to 400 K, desorption of the products of decomposition of organic compounds with a low molecular mass, takes place. Then, ($T \sim 600–700$ K) when the resins decompose, hydrogen can be produced in the secondary oxidation of the decomposition products (phenol, benzene, toluene, xylene,

and cresol). At 800 to 1000 K the resins become charred and hydrogen H_2 evolves, mixed with other gases (CO, CO_2, and CH_2).

A hydrogen adsorption maximum in iron occurs at 350 K and adsorption ceases after reaching 700 K. This is the reason unbound hydrogen is easily adsorbed by the exited, friction heated coupled metal surface, and subsequently dissociates, and diffuses in to the bulk of the metal counterbody under the action of temperature and stress gradients.

Reacting with cementite, hydrogen decarburizes steel to produce a spongy ferrite with extremely poor mechanical properties. For a stabilization of the carbide-forming component and to prevent the decarburization of steel at high pressures and temperatures, the addition of carbide forming elements (Cr, Mo, V, Nb, and Ti) to steel is recommended [353].

The degree of hydrogen saturation in the steel surface depends on many factors. These are mentioned earlier, in particular, the quality of surface treatment. Strengthened steel absorbs hydrogen more substantially than annealed steel.

Hydrogen diffusion into metal is atomic, because of the atomic structure of the crystal lattice. Therefore, one of the ways to prevent hydrogen absorption during sliding in plastic–metal pairs is to introduce compounds (in particular, CaF_2) into the sliding zone. These would bind the hydrogen and form compounds that would not decompose at 1773 K. (This temperature is used because, in standard braking devices, temperatures beyond this limit can result in the melting of the metal, and catastrophic wear of plastics, loss of braking effectiveness etc.). CaF_2 introduced into the friction zone would interact with free hydrogen to produce hydrogen fluoride ($CaF_2+H_2=Ca+2HF$), which creates thermal dissociation starting at 4273 K.

Hydrogen diffusion can be blocked during sliding by introducing titanium in the composition of brake linings. Dispersing titanium particles with a highly extended surface, actively absorbs hydrogen. This wear control method almost doubled the wear resistance of brake linings and the wear resistance of automotive brake disks rose by 50% (PTZS, TPAT-1 and other titanium powders were used) [364].

At high temperatures, because of chemical changes involving hydrogen which take place on the contact surfaces of friction plastics and components introduced into them, films with a small penetrability for hydrogen can appear spontaneously. Such a film was seen to form on a plastic surface with added Cu_2O (optimal concentration is 5% w/w). The explanation of the process is as follows.

Hydrogen produced in high-temperature sliding reduces copper oxide (I) to copper: $Cu_2O+H_2=2Cu+H_2O$. The pure copper evolves initially on actual contact spots. Copper is a poor hydrogen solvent and adsorber at high temperature [325, 326]. (This also refers to the other elements following hydrogen in the activity series). The developed copper film act as a barrier to hydrogen penetration.

The thermal conductivity of friction plastics is low, and the heat which induces the formation of free hydrogen therefore propagates in it, to a small depth (temperature at 1.5 mm from the surface of FK-24A plastic can be 523 K with a surface temperature of 1373 K). In this case the protective film will inhibit the penetration of hydrogen in to the contact zone, progressively decreasing its amount.

The protective film can be also applied to the surface of a steel or cast iron counterbody during its production by plating steel with metals which have a lower hydrogen penetration (copper, silver, aluminium, 1/13 and 15/13 steels, and others) [363].

And the effective means to suppress hydrogen wear may be the structuring of certain polymers. This is based on the ability of some substances specially added to plastics to bind the macromolecules which are destroyed during sliding, thereby preventing the formation of low molecular products, the secondary transformation of which leads to hydrogen production [365].

So, when choosing materials for friction assemblies, one should take into account the rates of hydrogen absorption and increase of embrittlement of metals, as well as the ability of friction plastics to decay and evolve hydrogen during sliding.

The introduction of brass wire pieces into plastics used for braking materials is also beneficial for their friction characteristics [366]. During intensive braking, hydrogen evolving in the process of thermo-mechanical destruction of plastics reacts with the oxide film of the brass wire. As a result, the hydrogen flow rate to a steel or cast iron counterbody decreases, retarding due to the catastrophic hydrogen failure of coupled surfaces.

For a reduction of hydrogen wear of sliding surfaces it is suggested [366] that the operation modes of sliding assemblies be changed. This can be done by decreasing the temperature, sliding velocity or specific pressure, and shifting the electric potential of the hydrogen absorbing metal. In the last case, we are concerned with idea that hydrogen diffuses in the crystal lattice of metal mainly in the form of a positive ion (proton). Therefore, it is possible to prevent diffusion and consequently, hydrogen absorption, by creating surface conditions on the steel counterbody with a generating potential of the same sign (positive) with respect to friction plastic. This problem was studied by Yu.A. Evdokimov and his associaties using the braking linings of railroad vehicles. A totally electronegative plastic was subsequently developed.

The same principle, of creating a positive electrical potential. is used to prevent hydrogen absorption in rolls used for cold rolling with hydrogenous lubricants.

Another proposed [366] is to remove the so-called hydrogen absorption promoters (substances which facilitate hydrogen penetration such as hydrogen sulfide, phosphorohydrogen, arsenic, selenium, antimony, tellurium compounds)

from the friction zone. For example, hydrogen sulfide, as a promoter, inhibits the recombination reaction of atomic hydrogen.

The hydrogen saturation of metals changes, as well as mechanical, physical properties, especially, electrical and magnetic. The inverse effect seems to occur also, i.e. electric and magnetic fields should affect on hydrogen diffusion in metal in some way. The influence of magnetic induction on mechanical properties of metals (microhardness, internal stresses, wear resistance of cutting tools and others) is also being intensively studied. However, in studies so far, the influence of hydrogen as a rule, is neglected [367]. In only a few publications [368 and one or some others], we found description of experiments dealing with this problem. An increase of wear resistance of cutting tools using a magnetic treatment is explained in relation to the effects of magnetic fields on the hydrogen contained in the tools. An electric field influence on the tools and other sliding parts is explained in the similar way. Since, hydrogen saturation in the technological processes of workpiece machining is rather high, therefore this method of controlling hydrogen absorption and hydrogen wear requires additional verification and further theoretical justification.

According to V.Ya. Matyushenko's data, if the concentration of hydrogen in steel subjected to turning without cutting fluid is 0.4×10^{-5} m^3/kg, with cutting fluid its amount constitutes 5.6×10^{-5} m^3/kg. Hardening, cementation, annealing, tempering, or cold treatment can increase the hydrogen concentration by about 300 percent ($(15–19)\times10^{-5}$ m^3/kg). For technological removal of hydrogen from operating surfaces of parts, the proposal to polish them at the end of the production cycle is put forward. In view of the discussion in this chapter, polishing, whose mechanism is considered in every detail in Sect. 5.2, should promote inverse hydrogen diffusion from the near-surface layer to the surface, as well as hydrogen desorption.

7.9. Examples of the Use of Selective Transfer to Prevent Hydrogen Wear

Water which is present in the friction zone in small amounts, considerably decreases the wear resistance of sliding parts. This is due to its decomposition upon interaction with metal, and of hydrogen absorption by sliding surfaces. (The mechanism of water interaction with friction activated metal surface was used as a basis for the development of an effective high purity hydrogen gas generator at the Institute of Civil Aircraft Engineers, Kiev).

At a stand developed by the Institute of Mechanics of Metal Polymer Systems, in the Academy of Sciences of Belarus, studies were carried out to investigate the friction of journal bearings manufactured as polymerphenol bushings. The studies were carried out in an aqueous oil emulsion at 523 K, load of 2.94 MPa,

and sliding velocity of 5 m/sec [369]. Bushes made from 12/13 steel were used as a counterbody. The roughness of the steel surfaces before tests was of class 8. Specimens were run-in at a load of 1.176 MPa and smoothed by increasing the speed to 1.4 m/sec for 6 h. After running-in, the sliding speed and load were increased to their required values. Examinations and analyses of the coupled surfaces were carried out every 2 h. A hydrogen content spectral analysis was made on a ISP-51 spectrograph.

Investigations after 10-h operation showed that the hydrogen content in the near-surface layer of the steel was double and after 20 h triple as the initial amount. On the surface of a polymer specimen microscopic particles of transferred steel were found. In such conditions hydrogen can be formed both as a result of CH groups contained in the molecular chains of polymerphenol, and by partial water dissociation. Thermooxidative destruction at 523 K results in a splitting of the ethylene chain from phenol groups. This is expressed by a decreased intensity of the absorption band to 1.2×10^{-4} nm in the infrared spectra.

Measurements of the microhardness of the steel revealed that the microhardness curve passed through a maximum, then decreased to a certain level (Fig. 7.20). This variation of microhardness can be explained as follows. Molecular hydrogen performs a double function in metal: firstly, it deforms the crystal lattice adjacent to the microvoid surface thereby increasing microroughness. Then absorbing further, it induces the cracking and loosening of the surface.

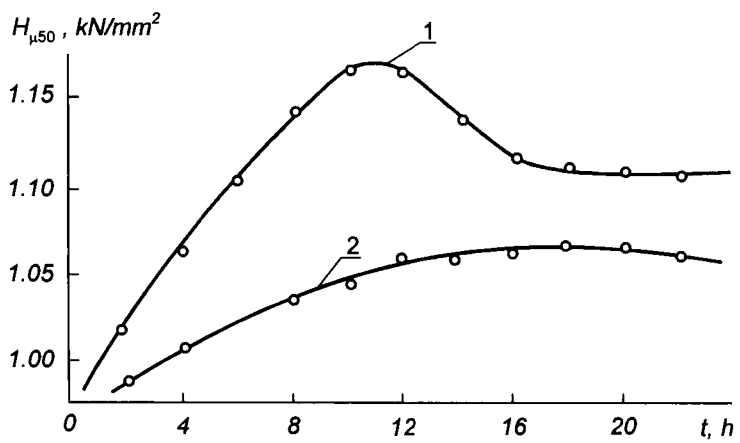

Fig. 7.23. Plot of the microhardness of a steel sliding against polymerphenol-graphite (1), polymerphenol-graphite-copper oxide (II) (2) compositions versus the test duration.

Thus, in extremely severe conditions, the sliding of a heat-resistant composite material–steel pair in aqueous medium, increases the brittleness of the steel surface

and the probability of its destruction by dispersion.

In order to prevent hydrogen absorption by the metal, 45 weight parts of copper oxide were introduced into the composition. The counterbody surface was found to be enriched with copper. The hydrogen which was produced during sliding, interacts with copper oxide, and gives way to the appearance of a copper film on every of the coupled surfaces. Due to the substantial, reducing ability of atomic hydrogen, the copper film does not oxidize and subsequently prevents hydrogen penetration into the steel.

In rolling, small amounts of water contained in the lubricants (up to 1%) substantially decrease the fatigue durability of ball bearings. This is because of water decomposition and hydrogen absorption by friction surfaces [332–335 and others]. The harmful effect of absorbed hydrogen in bearing balls and races, can be eliminated by selecting materials for rolling pairs and cages for which, just as for sliding bearings, selective transfer is realized and a servovite copper layer is produced in particular conditions (lubrication, temperature, load etc.).

Rolling of ball bearings was investigated in extremely severe conditions in aqueous oil emulsion at 523 K [370]. Aqueous spindle oil (10:1) emulsion was used. Races and balls of bearings were made from 1/XVII steel. Cages were manufactured from bronze CuSn5Zn5Pb5. The tests were conducted at a load of 5 MPa and at 1000 rpm. After the 10-h operation, the selective transfer effect was observed in every case. The rolling tracks and surfaces of the balls were covered with very fine copper films of high grade roughness. No noticeable hydrogen absorption by balls and races was found. Therefore, in relatively heavy friction conditions which are favorable for hydrogen absorption, the phenomena was avoided by changing the cage which brought about the selective transfer effect. The copper film on steel surfaces provided a barrier to the hydrogen.

7.10. Magnetic Field Influence on Hydrogen Behavior

The mechanism of influence of hydrogen on metal parts in the different stages of their treatment (product) should to know to develop methods for prevent hydrogenation. Magnetic-abrasive finish treatment is one of the least studied kinds of treatment. The last is characterized by the complexity of actions on the surface, including friction. It is suggested that the magnetic field during the treatment, affect the evolution of hydrogen from treatment parts [378, 379]. It brings about an increase in the durability of cutting tools. Therefore, comprehension of hydrogen behavior in pure magnetic fields is first needed to make known the causes of positive magnetic-abrasive treatment

influence on the treatment tools. It is specified by the fact that pure magnetic action also changes the maintenance properties of parts.

The existing explanations of pure magnetic treatment influence on the increase of the resistance to wear of tools have, as a rule, a hypothetical character. In [368] it is underlined, that steel quenching in relatively low (up to 800 kA/m) constant or alternative magnetic fields does not considerably change the phase composition structure and mechanical properties of steels C45e, 1/XVII, R9 (GOST 19265-73) and others. The author of the work [368] concludes that the increasing of wear resistance of metals observed after magnetic treatment (MT) is connected with the magnetic field influence on hydrogen which is on the surface and in the surface layer. These results was based on Russell effect. It means that only hydrogen formed during condensation and evaporation of moisture from the surface is implied.

In some papers devoted to MT, in particular [380], it was shown, that the remagnetization of samples considerably changes the concentration of chemical elements in a thin surface layer of thickness 10^2 nm. Many other data, generalized in [367], also testify significant structural-phase changes in layers subjected to MT.

To get independent confirmations of the structural-phase changes after MT, the investigations of HS6-5-2 steel was carried out, [378, 379]. The Mössbauer spectroscopy method has been used for this purpose [381]. Based on results obtained and literature data, the behavior of technological hydrogen was analyzed in the process of MT.

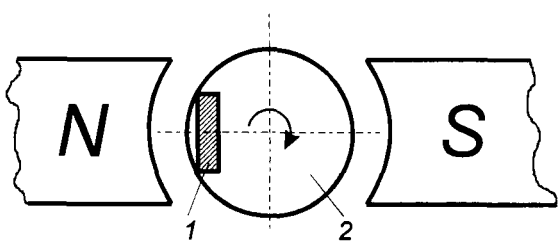

Fig. 7.21. The scheme of the magnetic field treatment: 1 - sample; 2 - mandrel.

The scheme of an experiment is shown in Fig. 7.21. Samples 1 were put into the mandrel 2, rotating in a magnetic field (B=1–1.2 T, n=1250 rpm). Such a treatment results in the effects of repeated remagnetization of the sample, hysteresis effects, and significant eddy current. Samples under MT were heated to 100-300 °C. They were made out from one rod and annealed. Then, all (except the control) were grounded. One, from the last treated samples, was left to be compared, and the others were subjected to MT.

TABLE 7.2
Nuclear gamma-resonance parameters of the HS6-5-2 steel spectra

Treatment	Designation of samples*	*f* effect probability, relative units	Spectrum "center of gravity" relative to α-Fe, mm/s	Isomeric shift of austenite relative to α-Fe, mm/s	Austenite concentration, %
Vacuum annealing	VA	1.00	+0.045	-0.135	30.6
Dry grinding	$DG_{\uparrow\uparrow}$	1.05	+0.135	-0.104	32.7
Magnetic field:					
1 min	$MFT_{\uparrow\uparrow}$-1	1.18	+0.018	-0.078	30.2
	$MFT_{\perp}$-1	1.21	+0.157	-0.126	27.1
3 min	$MFT_{\uparrow\uparrow}$-3	1.03	+0.04	-0.100	33.5
5 min	$MFT_{\uparrow\uparrow}$-5	0.96	+0.145	-0.148	30.0

* $\uparrow\uparrow$- $\theta=0$; $\perp$- $\theta=\pi/2$; θ is the angle between the Mössbauer γ-quantum beam propagation and the grinding direction.

Results are presented in Table 7.2 and in Figs. 7.22 and Fig. 7.23. In the first approximation, nuclear gamma-resonance (NGR) spectra constitute a superposition of Zeeman sextet lines of a magnetic superfine structure (MSFS) α-Fe (lines A1–A5) and paramagnetic γ-Fe (austenite, A_0 line). It means that they have a complex phase composition. The position of A1 lines is similar to the appropriate lines in the structure of pure α-Fe (ferrite). Lines A2–A5 appear due to a martensite phase, available in the investigated alloy. A large number of low intensive lines is specified by the heterogeneity of a phase composition in the analyzed thin surface layer of the sample (~10^2 nm).

The ratio of martensite and α-Fe concentrations influences the mechanical characteristics of the alloy. To identify the lines of NGR spectrum decomposition, data on the value of the effective magnetic field $H_{eff.}$ on Fe^{57} nuclei in substitutional solid solutions in Fe-C, Fe-Cr, Fe-W, Fe-V, Fe-Mo systems has been used.

The austenite concentration in a control sample surface layer (after vacuum annealing VA, Fig. 22,a) amounts to 30.6% (see Table 7.2). The NGR spectra was obtained in the geometry of scattering, beginning at the parallel beam orientation of γ-quanta and mechanical treatment lines, occurring under grinding, that is $\theta=0$ ($\uparrow\uparrow$).

After dry grinding, the intensity of the central line A_0 increased (Fig. 7.22,b), that is the austenite concentration increased by 32.7%. The intensity of the second and fifth MSFS lines decreased. It is connected with an anisotropy of a surface layer caused by grinding. The Mössbauer effect probability *f* increased by 5%.

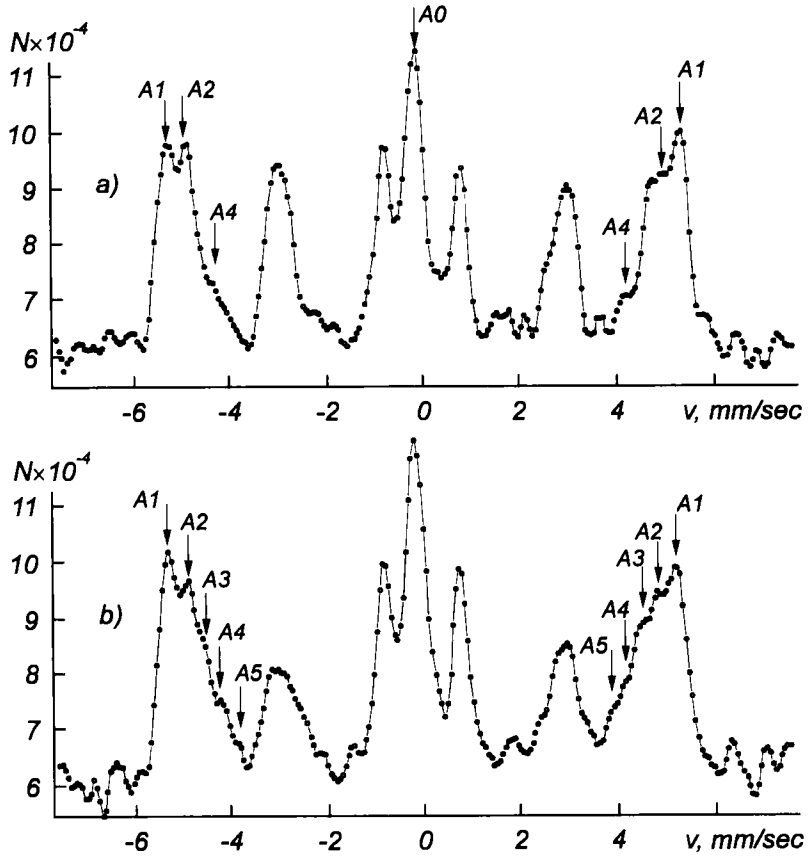

Fig. 7.22. Nuclear gamma-resonance spectra of annealed (a) and ground (b) surfaces of the HS6-5-2 steel with thickness of a controlled surface layer ~10^2 nm: v - relative velocity; N - number of pulses in the channel.

The high sensitivity of NGR to the nuclei dynamics, has a great influence on the f factor. A smaller number of atomic bonds on a solid surface influences the dynamics of their movement at least 4–5 layers deep into the bulk. The Debye-Valler factor f, determined by the energy of the atom and lattice bond, is associated with the atomic oscillation amplitude by the ratio (5.2). At room temperature, for atoms inside the body, f is 60% greater than on the body's surface [382]. The root-mean-square is anisotropic. Displacement of surface atoms in the direction perpendicular to the surface, exceeds twice the appropriate value for atoms inside a solid, but along the surface plane – by 30% [383]. Anisotropy occurs along the surface depending on the direction and mechanical treatment method

(see 5.3). The effect probability was different at different angles of γ-beam drop θ, indicating the significant magnetic and crystallographic anisotropy of the surface and various values of the root-mean-square atomic displacement near the equilibrium position in its crystal lattice. Such a situation appears when a preferred crystal deformation takes place along one selected direction.

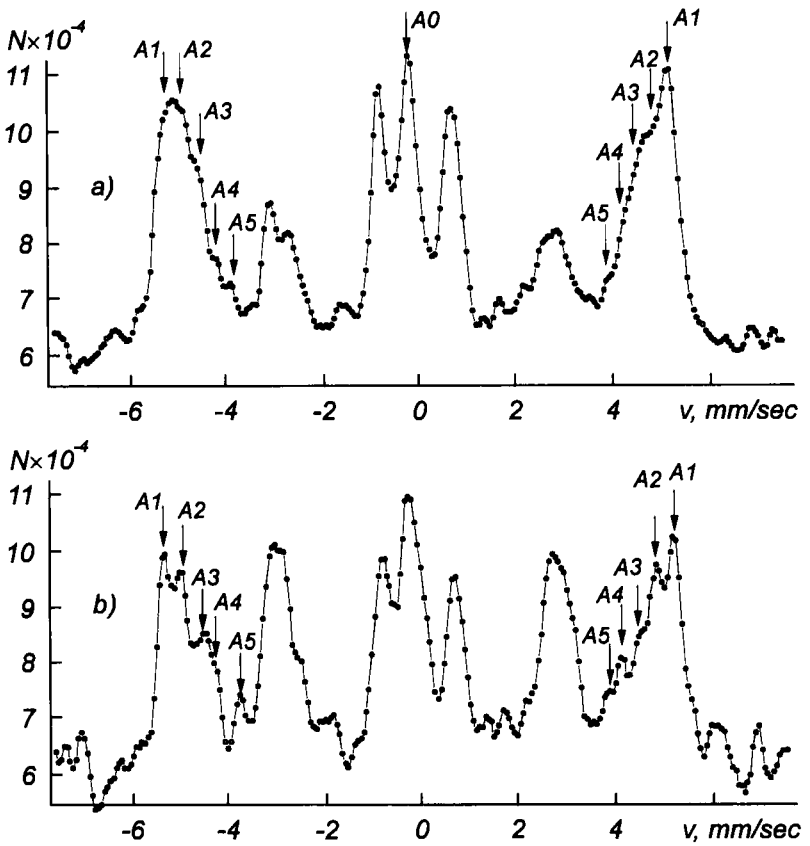

Fig. 7.23. Nuclear γ-resonance spectra of the HS6-5-2 steel after the magnetic field treatment during 1 minute, measured at θ=0 (a) and θ=π/2 (b).

The magnetic field treatment (remagnetization) during one minute ($MFT_{\uparrow\uparrow}$-1) of ground samples according to the scheme in Fig. 7.21, resulted in a decrease in austenite concentration (Fig. 7.23,a) up to 30.2%, that is, practically it became the original value, as under vacuum annealing. Therewith the *f* effect probability significantly increased (by 18%). These facts confirm the experimental data of other

authors, stating that the remagnetization of quenched fast-cutting steels, as well as carbonic steels, is accompanied by a change in the stressed state and structure near the surface layer [367].

The increased resistance of high-alloy HS6-5-2 steel structure, prevents a more considerable austenite decomposition. The austenite decomposition (in our case ~10%), its transition into martensite and carbide phases, is accompanied by the formation of compression stresses, changing f factor. It is difficult to identify carbide phases in such a complicated spectrum, but it may be the case, that finely divided carbide with $H_{eff.} \approx 184$ kOe is formed. Its lines overlaps with the second and fifth lines of the NGR spectrum of the alloy.

The NGR spectrum of the same samples was then registered in the perpendicular ($\perp$) orientation of the gamma-quantum beam to the treatment lines (Fig. 7.23,b; $\theta=\pi/2$). The austenite concentration proved to be still lower (27.1%), but this value should not be compared with former ones. The fact is that the concentration should be estimated, assuming that f is the same for all states of iron, and that it is anisotropic. Thus, with a perpendicular orientation it is determined that the effect probability for the austenite phase decreases and f for ferromagnetic

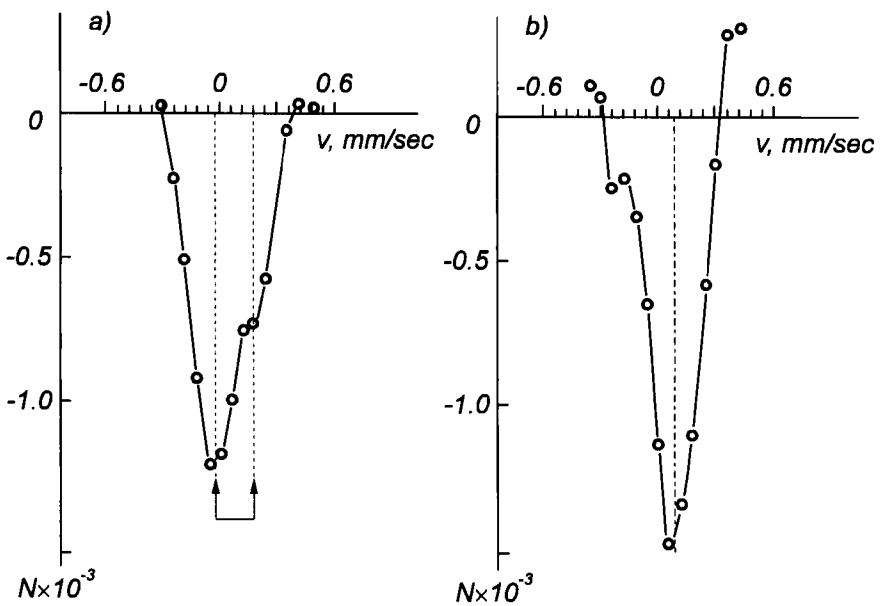

Fig. 7.24. The central part of the difference nuclear gamma-resonance spectra of surfaces of the HS6-5-2 steel: a) – after $MFT_{\uparrow\uparrow}$-1 and VA; b) – after $MFT_{\perp}$-1 and VA.

phases increases, as far as the total f increased, up to 21%. The weight content of carbon in the forming martensite lattice increases, promoting the occurrence of compression stresses, etc. The intensities the 2nd and 5th lines of MSFS in both spectra differ essential for to this reason. All this testifies significant structural changes, as the austenite decomposition is accompanied by parametric changes of a martensite and carbides crystal lattice, and the lattice deformation of HS6-5-2 steel in the surface layer.

The structure anisotropy results in the f anisotropy at different θ. There is a dependence of the austenite line shape on θ, which causes changes seen in the position of the "center of gravity" line (isomeric shift, see Table 7.2). The change of the austenite line shape is found when plotting difference spectra $MFT_{\uparrow\uparrow}$-1 – VA (Fig. 7.24, curve 1) and $MFT_{\perp}$-1 – VA (Fig. 7.24, curve 2).

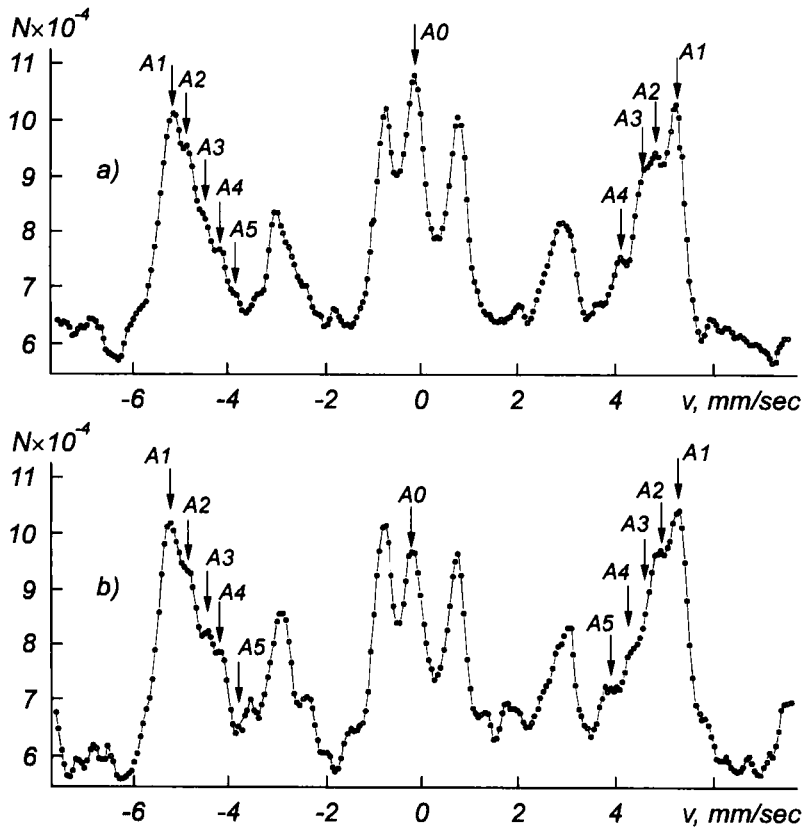

Fig. 7.25. Nuclear γ-resonance spectra of the HS6-5-2 steel after the magnetic field treatment during 3 minutes (a) and 5 minutes (b).

The treatment process, first by grinding, then by magnetic field, is followed by a crystallographic texture formation. Therefore, an existence of the unresolved doublet of quadrupole splitting (ΔE=0.21 mm/s) in the NGR spectrum proves. This is because the ratio of doublet lines depends on the angle between the axis of gamma-quantum beam propagation and the direction of the electrical field gradient.

A more prolonged treatment in a magnetic field (see Fig. 7.25 and Table 7.2) is followed by an intense warming-up of samples (up to 573 K). A relative increase of the austenite content up to 33.5% after 3-minute treatment (Fig. 7.25,a) is noted. Most likely it happens as a result of the grain size reduction of the martencite structure, carbides evolution, and an increase of their number and sizes with the increase of remagnetization cycles, as is underlined in the paper [367]. The increase of remagnetization cycles results in the decrease of the martencite lattice parameter and increase of the Me_6C carbide lattice parameter in HS6-5-2 steel. The carbon weight content in the martencite lattice decreases.

The five-minute treatment (Fig. 7.25,b) practically resulted in the state analogous to deeper vacuum annealing. The *f* probability decreased, characterizing a significant release of pressure in the sample. The austenite concentration dropped to a minimum. However, the magnetic anisotropy, directed under such a treatment, resulted in a low relative intensity of the second and fifth lines of the NGR spectrum of MSFS.

Practice shows, that the most optimal treatment in duration, according to scheme of Fig. 7.21 and at the same regimes, is the magnetic field treatment lasting 1 minute. Indeed, this treatment is characterized by the most significant changes and, in particular, by the maximum value of the *f* effect probability, i.e., the tense state of the surface layer.

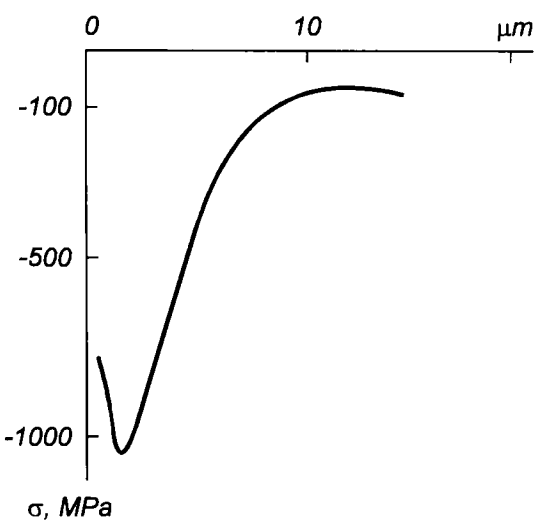

Fig. 7.26. Residual stresses after the magnetic-abrasive polishing.

The most frequent type of epure of near surface stresses after the magnetic-abrasive polishing is shown in Fig. 7.26. Fig. 7.27 shows influence of the remagnetization cycles number N on the value of residual stresses σ (the duration of each cycle τ=0.06 s) of TC-105 steel 0.5 μm deep, having undergone quenching and release [367]. As a rule, in all the cases, regardless of the sign of the original stresses, the remagnetization always results in the formation and increase of compression stresses.

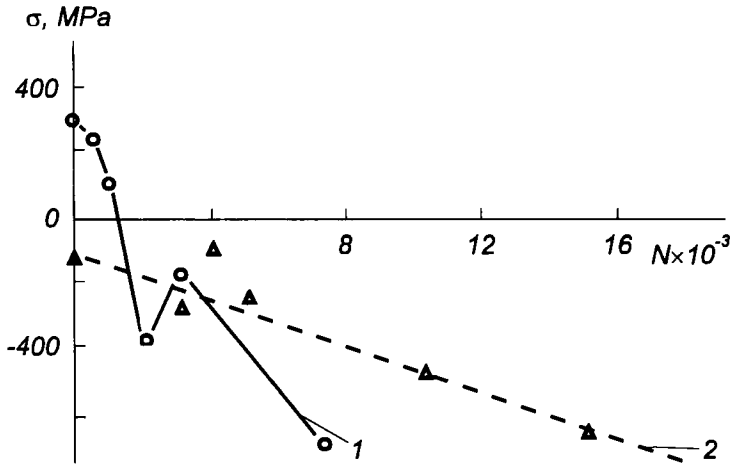

Fig. 7.27. Dependence of residual stresses σ of the TC-105 steel on the cycles number of remagnetization N at magnetic induction B=1.4 T [380]: 1) $\sigma_{orig.}$=200–400 MPa (tension); 2) $\sigma_{orig.}$=100–200 MPa (compression); tangential stresses were determined by the method of N.N. Davidenkov.

The used schema of MT (Fig. 7.21) provides multiple complete remagnetization and gives rise to intensive heating. The magnetic treatment in a less rigid regime, without complete remagnetization and warm-up, also causes a change in the tense state of the controlled surface layer (~10^2 nm). This was found during magnetic field treatment with equipment (Fig. 7.28) used for the magnetic abrasive polishing of planes, with the one-sided closed system described in [384, 385]. The magnetic field induction B is 2 T. The sample, fixed on the table which is the southern pole of the constant electromagnet, reciprocated with the table. Square disks 25×25×8 mm dimensions, manufactured from one rod of 3/VII steel were used as samples. This steel has a greater Debye-Valler factor *f* than HS6-5-2 steel.

The procedure sample preparation consisted of: 1) annealing, carried out in a vacuum under the temperature of 850 °C during a period of 2 hours (cooling rate from 850 to 550 °C was 60 °C/h, followed by subsequent cooling in a non-

operative furnace; 2) grinding; 3) demagnetization after grinding (several times the sample was brought into the demagnetizer coil, fed by a three-phase current).

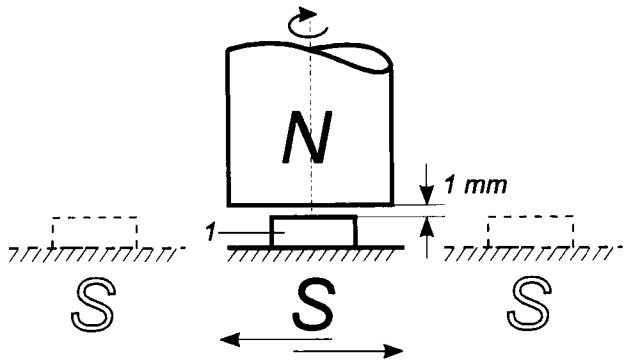

Fig. 7.28. Plan of the magnetic field treatment: 1) sample.

On the NGR spectrum in the regime of conversion electrons registration, the number of noise pulses N_{ph} and the total area under the nuclear gamma-resonance spectrum ΣS was measured. Then the value $f'=\Sigma S/N_{ph}$, proportional to the *f* effect probability, was determined. The error in the relative value estimate of Mössbauer effect is minimized, as $N_{ph}\geq 10^5$ at the resonance effect is $\eta\geq 10\%$.

The obtained dependencies of f' and $\alpha=f(\theta=0)/f(\theta=\pi/2)$ anisotropy (Fig. 7.29,a) testify complex dynamics of pressure redistribution in the controlled surface layer, correlating with the data shown in Fig. 7.29,b.

The homogenous fine-grained structure is formed during the process of vacuum annealing. Chemical and structural inhomogeneity is eliminated. Internal stresses and steel hardness are reduced. The amplitude of the root-mean-square shift of atoms has a maximum, the Mössbauer effect probability is minimal (see formula (5.2). In our case after VA, f' was 2.74 (a dotted right line in Fig. 7.29,a).

Residual compressive or stretch stresses can be obtained by changing the grinding regime, according to the past history of a sample [367]. It influences on the *f* value. With stretch stresses *f* is smaller than with the compressive ones. After dry grinding (DG) f' increased by 0.43, the anisotropy degree $\alpha=1.14$.

During treating all reasons of changing the internal stresses in the surface layer act simultaneously. Therefore, the epure of stresses has a complex character. Compressive stresses in the layer of $\sim 10^2$ nm, prevailing along the treatment lines, as it can be assumed, were formed on the whole after DG.

The magnetic field treatment, as shown in Fig. 7.28, during one minute removes the anisotropy of stresses ($\alpha=1.00$) along the surface and though $f'_{\uparrow\uparrow}$

somewhat decreases, the total $f'=\sqrt{f'_{\uparrow\uparrow} \times f'_{\perp}}$ is increased. The increase of f and, consequently, residual stresses continues, and under magnetic field treatment lusting 5 minutes, the maximum is reached. The anisotropy degree α comes to 1.50, indicating the anisotropy of atoms vibrations along and across the treatment line. The estimation gives for a crystal lattice deformation the value $\Delta x \approx 9$ pm (see sect. 5.4).

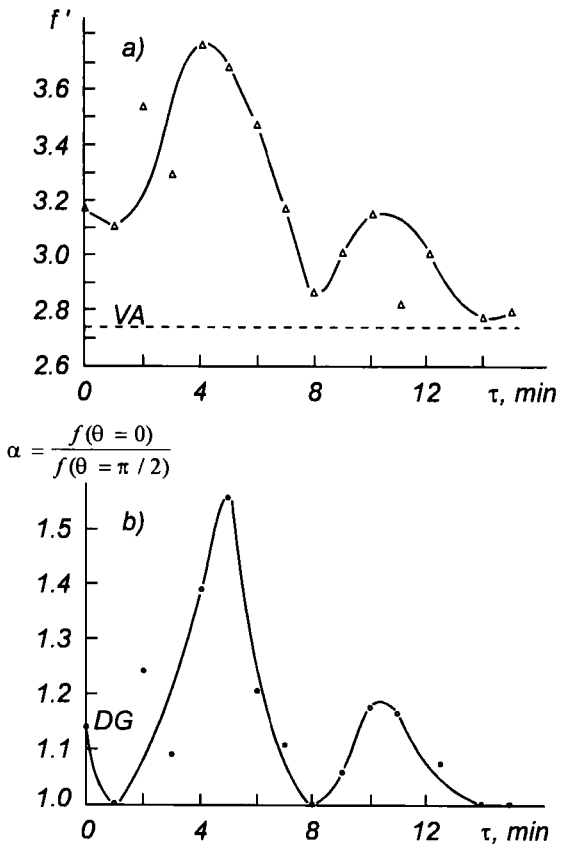

Fig. 7.29. The $f'=\Sigma S/N_{ph}$ value (a), and the $\alpha=f(\theta=0)/f(\theta=\pi/2)$ anisotropy degree (b) of a 3/VII steel layer, ~10^2 nm depth, depending on duration τ of the remagnetization; $\theta=0$.

A polycrystalline solid is practically never free from residual stresses of all the types (3 types are available). This field of stresses does not remain unchanged

[73]. The relaxation of stresses is explained by the instability of the inherent stressed state, specified by the inhomogeneity of the polycrystalline body structure. The elastic-stressed parts are combined with the plastic ones. Their reaction on exterior force actions, including those, caused by MT, will be unlike. A maximum of the f value, and consequently the stressed state and anisotropy maximum, attained by 5-minute treatment in a magnetic field, as shown in Fig. 7.28, is primarily specified by the austenite transformation and the martensite formation. The martensite lattice possesses high strength, hardness and brittleness, and is characterized by a needle and lamellar structure. Thus, the regime of 5-minute MT is the most optimal, as after such a treatment the operating characteristics of parts in many cases (literature data) are improved.

Further magnetic treatment promotes the removal of stresses. Anisotropy after 8-minutes magnetic treatment is disappeared also. The martensite is not stable and is able to spontaneous in decomposition, especially if decomposition is initiated by the MT process. Thus, the decrease of f follows.

The subsequent increase of α after the 10–11 minutes treatment is accompanied by the overall decrease of the effect probability. The redistribution of stresses has here a complicated character. Nevertheless, the general effect of probability is higher than on the annealed samples surface, and approximates those after 14–15 minutes treatment.

The metal grinding brings about strong metastability of a distorted surface layer structure. The metastability is specified by a high density of defects and a nonequilibrium structural-phase composition. Thus, a complicated relationship between the surface stressed state and duration of the magnetic treatment takes place depending on the past history of a sample.

What is the function of hydrogen in the process of magnetic treatment? The alternating magnetic field forms in a sample volume magnetic flowing with different densities and induces currents in it, and growing to the surface. Therefore, the area near the surface layers has undergone the maximum magnetic effect. Besides, the substructure of mechanically treated samples is nonuniform in its cross-section: in surface layers it is more developed than in the bulk. The diffusion coefficients in the layers deformed after grinding, milling, sandblasting and so on are tens and hundreds of times greater than in the electropolished samples [84]. The accelerated diffusion in the deformed surface layer of metal is explained by the dispersion of the structure under deformation, and by the formation of a great number of surface defects. In particular this is proved by a fact that the strengthened steel dissolves 10–20 times more hydrogen in comparison with the unstrengthened one.

The maximum of electromagnetic, thermal and mechanical effects on the ferromagnetic and conducting material under MT is on the surface. Considering all of the above, and the dynamics of hydrogen redistribution in surface layers

(see 7.4), one is led to believe that the technological hydrogen diffuses from the bulk to the surface and is desorbed during MT. Thus, MT promotes the dehydrogenation of steel parts which, as it is known now, improves resistance to wear.

The structure of polished surfaces differs from the bulk structure both in the phases ratio and concentration, and the polycrystal grains dispersity. The structure is similar to that of amorphous alloys. The hydrogen solubility in amorphous alloys is significantly higher than in crystalline alloys. The temperature maximum during polishing is seen at the surface. Technological hydrogen diffuses from the bulk, desorbing gradually.

Hydrogen is localized in steel with the martensite-austenite structure on interfaces. This is indicated by autoradiographic investigations [386]. Hydrogen redistributes in the bulk of samples to the grains boundaries, where deformations and stretch stresses are the highest. Significant stretch stresses on the surface promote hydrogen transition from the depth. The rising diffusion of hydrogen takes place in the stress field. Thus, the mechanical polishing with a thin diamond paste results in a hydrogen content increase by 5–6 times on the surface [386].

Hydrogen absorption to a certain extent can explain the experimental results described in [367]. The samples annealed TC-105 steel, had 200–250 MPa compressive stresses at 0.5 μm depth. These stresses increased up to 280–300 MPa after remagnetization in wet conditions using emulsion with a surfactant. During remagnetization in the air, the stresses decreased by 80–100 MPa. They reach value to zero and even transform into the stretch stresses (0–4 MPa) when the surfaces are covered with an isolating lacquer.

These results correlate with hydrogenation during technological operations. Turning, with a surfactant-contained cutting fluid, increases the hydrogen concentration in a surface layer by more than 10 times in comparison with those after the treatment without surfactant. The partial recombination of atomic hydrogen in surface layer defects, results in an increase in compressive stresses.

The isolation of the surface overlaps the active source of hydrogenation from the medium. Other processes responsible for the drop of compressive stresses prevail in this case. This is never observed in a magnetic field treatment, except for the above case. The compressive stresses and their increase only take place usually after the magnetic treatment in practice.

Thus, the conclusion in [367], that the implantation of atoms from the environment does not specify the stressed state of the remagnetized steel surface layer, is not substantiated enough. The compressive residual stresses are specified by two reasons. The first is the decomposition of residual austenite and the diffusion processes caused by magnetostrictive stresses and microdeformations [367]. The second is the saturation of a surface layer with the environmental atoms, as at beginning was suggested in [367], particularly with easily movable hydrogen.

One more experiment proves the above. Using Auger-spectroscopy [380] the following was found. After the remagnetization of samples the chemical composition of quenched HS6-5-2 steel surface changes. In particular, the mass content of carbide-forming elements: W, Mo, C is increased. The oxygen content is also increased (more light elements, including hydrogen, were not identified by the method). Thereby, the fact of diffusion of elements both from the environment and more deep layers of the metal to the surface during MT is confirmed. Technological hydrogen possessing high diffusibility will diffuse to the surface faster than other elements.

The direction of the body magnetization does not coincide with the direction of the tension vector of a magnetic field and is periodically changed during the above magnetic treatment. Periodically changed force moments, causing the formation of inner circumferential stresses, appear as a result. A magnetic field initiates the formation of the nuclei in the microsites of the alloy with a short-range spin order. These are characterized by a locally higher level of a thermodynamical potential.

The magnetic dispersed hardening of fast-cutting steel take place in the process of MT. Local overstresses increase the probability of a thermofluctuation breakdown of interatomic stressed bonds, and promote the process of dislocations multiplication and movement. The magnetic action initiates diffusion processes, resulting in structural-phase changes. All the crystal structure defects, microdeformation spots and the areas of stretch stresses, etc., are traps for hydrogen [386]. The thermodynamically nonequilibrium state of a surface layer, an availability and a change of deformation gradients and stresses during MT causes an active diffusion of an easily movable hydrogen from the bulk to the surface, as well as its desorption.

This Page Intentionally Left Blank

CONCLUSION

It is generally recognized that control of friction processes is extremely difficult, or even impossible because of the complexity and diversity of phenomena occurring on a standard dynamic contact. This has been highlighted many times in publications and presentations of many leading experts.

As can be seen from the material of this book, any actions exerted on the surface, including slight variations of the friction mode and conditions, substantially change the physical properties of the surface and therefore affect the friction force and wear. The surface layer is easily changeable. In view of this, a question arises as to whether it is possible to control the friction process, and to deliberately change the properties of surfaces in friction by changing the friction mode and conditions. It seems possible because of the interrelation of numerous, seemingly odd facts. These are some of them.

Substance in the contact zone in friction (mainly in running-in) is in a special exited state. This state cannot be attained without friction by simple heating of materials in pairs to the temperatures reached in friction. When the boundary friction is violated, the excitation becomes so high that photo- and electronic emissions, and ionization of the ambient atmosphere around the interacting surfaces, (Sect. 4.1 and 4.2) are observed. That the excitation in friction is unique, is demonstrated by the fact that some material could be synthesized only in friction, whereas their synthesis without friction under the same conditions, temperatures, media etc. is not feasible [147].

Equipotency of temperature and stress, underlying the kinetic concept of failure and contained in the expression for the lifetime of interatomic bond under load, is very important in friction. Because of this fact, and also due to synergism of a simultaneous action of shear deformation and high pressure (obligatory components of friction), solid phase polymerization of organic materials (monomers) (Sect. 4.4) and other phenomena occur. As follows from [358, 359], the peculiar behavior of materials under HP and SD stems form atom-vacancy states arising in heavily distorted crystals. The distorted crystal energy approaches the thermodynamic potential maximum. In such conditions the crystal state is critical and crystal experiences distortion-induce structural

phase transition, which induces a quasiliquid flow of solid similar to a fluid flow.

Antifriction nonabrasive finishing modifies the surface, changing the phase composition and the structure of the surface layer (Sect. 5.6). Coarse grain abrasive with a grain size within 1 mm induces selective transfer, and special metal-plating lubricants have a favorable effect (Sect. 6.7). In particular conditions friction brings about saturation of surfaces with hydrogen that gives rise to anomalous dynamic superplasticity (Sect. 7.5), a viscous flow of the surface. Friction can operate to alloy surface etc.

These and some other factors suggest that by varying ambient conditions, composition, and nature of lubricants, and by changing the mode and level of excitation, chemical activity of the surface, it is possible to control the friction process, to change deliberately the surface properties as required. The importance of the promises offered can hardly be overestimated and, in essence, it is a new stage of tribology.

Understanding of the "wearlessness" mechanism (selective transfer) and its application, have stimulated extensive development and use of specialized lubricants with metallic or metalliferous (containing metal compounds) fillers. Meanwhile, it has become clear how far we have gone beyond the initial interpretation of ST (Sect. 3.1 and 3.13) and that, as a matter of fact, we deal with a more general phenomenon, classical ST being a particular case. This conclusion can be made from generalization and analysis of the presented results, and publications reporting implementation of metal-plating lubricants. These ideas were partly expressed by the author in [273, 360]. Antifriction nonabrasive finishing with metalplating lubricants is a controlled tribochemical building-up of the workpiece surface, which improves the treatment quality.

Thus, the favorable effect achieved by applying many metal-plating lubricants in production processes and in friction assemblies, seems to be a consequence of a more general phenomenon, the essence of which can be formulated as follows.

Regeneration of friction surfaces of metals and alloys consists in the fact that, in friction in the medium stimulating selective dissolution of alloys and/or containing disperse particles of plastic metals or their chemical compounds, the friction surfaces are modified by building-up a passivating layer. The modification is caused by the difference in chemical potentials of metallic components of friction pairs, medium, tribochemical processes, and mechanical influences exceeding the yield limit of the disperse particles of materials, and adhesion. All these reduce the friction coefficient and wear. This definition includes ST as a particular case [99] and does not exclude other factors that may be involved. Taken together, they give a technological effect of improving the surface quality and "wearlessness" of the friction assembly. This definition is also convenient as it does not arouse question about what effect is being really studied.

Directed development of metal-plating lubricants consisting of the oil base, additives, and a metalliferous filler specialized for particular applications, are promising for controlling friction processes [361]. The use of such lubricants solves many problems. For example, it increases the efficiency of some technological processes (running-in mechanisms, pressure treatment of metals, plastic deformation hardening of surfaces, restoration of worn surfaces of mated parts, modification and strengthening of surfaces, provides friction alloying of surfaces and antifriction nonabrasive finishing, and gives a new approach to choosing the lubricant composition for friction units in machines and mechanisms etc.

It appears that results of studies on hydrogen adsorption in friction carried out to find method for controlling hydrogen wear, have a basic importance for solid state physics. They were developed further and are used now in metal industry. Among them is transition of iron, or its carbon alloys, saturated with hydrogen to a viscous flow, which makes it possible to change the pattern of phase and structural transformation in metals with the aid of hydrogen [339, 344]. The trends in friction-induced hydrogen absorption also allowed the hydrogen wear effect to be used as a favorable factor for improving machinability of steel [362], for facilitating compression deformation etc.

It is possible that formation of a hydrogen saturated zone in the subsurface metal layer in friction, may be used to investigate the reactions in cold nuclear synthesis if it were necessary to choose the most effective pumping of hydrogen isotopes into metal up to concentrations corresponding to excessive partial pressure of gaseous hydrogen [363].

There is no doubt that further, deeper investigation into friction processes, to discover the trends in variation of physical and chemical properties of friction surfaces, will promote perfection of wear control processes and the development of tribology. Overall these are certainly the most important conclusions of the book.

This Page Intentionally Left Blank

REFERENCES

1 D.N. Skorov, A.I. Dashkovskii, V.N. Maskalets, and V.K. Khizhnyi, in: Surface Energy of Solid-State Metallic Phases, Moscow, Atomizdat, 1973.
2 M.B. Partenskii, Uspekhi Fiz. Nauk, Vol. 128, Issue 1 (1979), 69–106.
3 Ya.E. Geguzin and N.M. Ovcharenko, Uspekhi Fiz. Nauk, Vol. 76, Issue 2 (1962), 283–328.
4 V.I. Likhtman, E.D. Shchukin, and P.A. Rehbinder, Physicochemical Mechanics of Materials, Moscow, Izd. Akad. Nauk SSSR, 1962.
5 A.R.C. Westwood and N.S. Stoloff (eds.), Environment-Sensitive Mechanical Behavior, Gordon and Breach Science Publishers, N.Y.–London–Paris, 1966.
6 B.B. Damaskin, O.A. Petrii, and V.V. Batrakov, Adsorption of Organic Compounds on Electrodes, Moscow, Nauka, 1968.
7 A.Ya. Gokhshtein, Surface Tension of Solids and Adsorption, Moscow, Nauka, 1976.
8 T.R. Beck, J. Phys. Chem., Vol. 73 (1969), 466–468.
9 A. Soffer and M. Folman, Electroanal. Chem., Vol. 38 (1972), 25–43.
10 M. Green (ed.), Solid State Surface Science, Vol. 1, N.Y., Narcel Dekker, 1969.
11 N.M. Aleinikov and S.P. Gribkov, Poverkhnost (Fizika, Khim., Mekhanika), Vol. 12 (1985), 70–76.
12 V.V. Mitrofanov and V.A. Fogel, Physics and Chemistry of Semiconductors, Leningrad, Sudostr., 1965.
13 A. Rose, Fundamentals of the Photoconduction Theory (Russian translation), Moscow, Mir, 1966.
14 L.I. Antropov, Theoretical Electrochemistry, Moscow, Vyzsh. Shkola, 1969.
15 B.B. Damaskin and O.A. Petrii, Fundamentals of Theoretical Electrochemistry, Moscow, Vyssh. Shkola, 1978.
16 A.S. Akhmatov, Molecular Physics of Boundary Friction, Moscow, Fizmatgiz, 1963.
17 A.I. Levin, Theoretical Fundamental Principles of Electrochemistry, Moscow, Metallurgiya, 1972.
18 S.P. Galetskii and G.P. Shpenkov, Application of Selective Transfer in

Friction Units of Machines, Proc. of Sci. Conf., Part 2, 125–129, Moscow, Gosstandart SSSR, VISM, 1976.
19 G.P. Shpenkov, V.S. Urbanovich, and S.P. Galetskii, A Double Layer and Adsorption on Solid Electrodes, in: Proceedings of the Vth Symposium, Tartu, 294–297, 1978.
20 E.M. Makushok, Mechanics of Friction, Minsk, Nauka i Tekhnika, 1974.
21 B.V. Deryagin, Zh. Fiz. Khim., Vol. 5, Issue 9 (1934), 1165–1176.
22 I.V. Kragelskii, Friction and Wear, Moscow, Mashinostroenie, 1968.
23 I.V. Kragelskii, N.M. Mikhin, and K.S. Lyapin, Mashinovedenie, 3 (1970), 92–97.
24 I.V. Kragelskii, I.M. Lyubarskii, A.A. Guslyakov, et al, in: Friction and Wear under Vacuum, Moscow, Mashinostr., 1973.
25 D.N. Garkunov, I.V. Kragelskii, and A.A. Polyakov, Selective Transfer in Friction Units, Moscow, Transport, 1969.
26 G.S. Khodakov, Physics of Comminution, Moscow, Nauka, 1972.
27 G.P. Cherepanov, Mechanics of Brittle Destruction, Moscow, Nauka, 1974.
28 Yu.V. Goryunov, N.V. Pertsov, and B.D. Summ, The Rehbinder Effect, Moscow, Nauka, 1966.
29 Yu.N. Shekhter and S.E. Krein, Crude Oil Surfactants, Moscow, Khimiya, 1971.
30 R.M. Matveevsky, A.B. Vipper, A.A. Markov, et al, Wear, Vol. 45, No. 2 (1977), 143–150.
31 A.A. Markov, V.V. Sashevskii, B.F. Korobov, and B.A. Englin, The Method Based on Jet Fuel Adsorption Properties, USSR Inventor's Certificate 356546, MKI G 01n 27/60. Otkryt. Izobret. No. 32 (1972).
32 A.A. Markov, A.I. Lipin, and K.N. Pikovets, The Method to Determine a Degree of Hydrogenation of Metals and Alloys, USSR Inventor's Certificate 212695, MKI C 23v 5/48, G 01n 3/00. Otkryt. Izobret. No. 9 (1968).
33 V.G. Kuznetsov and G.P. Shpenkov, Fiz. Khim. Obrab. Mater., No. 5 (1981), 130–131.
34 L.F. Kolesnichenko and V.V. Kovbasenko, Fiz. Khim. Mekh. Mater., Vol.7, No. 2 (1971), 86–89.
35 D.N. Garkunov, A.A. Markov, and G.A. Golikov, The Technique to Determine Antifriction Properties of Materials. USSR Inventor's Certificate 179975, MKI G 011 3/00, Otkryt. Izobret. No. 6 (1966).
36 V.D. Evdokimov and Yu.I. Semov, Exoelectron Emission on Friction, Moscow, Nauka, 1973.
37 S.N. Postnikov, Electric Phenomena on Friction and Cutting, Gor'kii, Volgo-Vyatsk. Izd., 1975.
38 F. Chehab, H. Erhart, W. Kirstein and F. Thieme, J. Catalysis, Vol. 73, No. 2 (1982), 288–293.

39 D.V. Morgan, A.E. Guile and Y. Bektore, J. Phys. D: Appl. Phys., Vol. 13, No. 2 (1980), 307–312.
40 A.M. Ilyukovich, Elektrometry Equipment, Moscow, Energiya, 1976.
41 A.L. Zharin and G.P. Shpenkov, Pribory i Tekhnika Eksperimenta, No. 2 (1978), p. 267.
42 A.L. Zharin, Development of the Non-Destructive Testing of a Friction Surface and Its Application to Friction Kinetics Investigation of Some Materials, Candidate's Dissertation of Technical Sciences, Minsk, 1981.
43 V.S. Kortov, A.I. Slesarev, and V.V. Rogov, Exoemission Testing of Workpieces Surfaces after Treatment, Kiev, Nauk. Dumka, 1986.
44 V.G. Kuznetsov and G.P. Shpenkov, in: New Methods to Improve Wear Resistance of Friction Units Using Selective Transfer, Proc. of the Ukr. NIINTI, 11–12, 13–14, 27–28, 1978.
45 A.L. Zharin and G.P. Shpenkov, in: New Methods to Improve Wear Resistance of Friction Units Using Selective Transfer, Proc. of the Ukr. NIINTI, 12–13, 1978.
46 V.G. Kuznetsov and G.P. Shpenkov, in: The Ways to Improve Quality and Reliability of Electric Contacts, Proc. of the Leningrad PEO VNIIPEM, 59–60, Leningrad, 1978.
47 A.L. Zharin and G.P. Shpenkov, in: The Ways to Improve Quality and Reliability of Electric Contacts, Book of Abstracts of the Leningrad PEO VNIIPEM, 61–62, Leningrad, 1978.
48 A.L. Zharin, V.G. Kuznetsov, and G.P. Shpenkov, in: New Physical Methods and Means of Testing of Commercial Items, Book of Abstracts of the OFNK Akad. Nauk BSSR, p. 230, Minsk, 1978.
49 V.G. Kuznetsov and G.P. Shpenkov, Fiz. Khim. Obrab. Mater. No. 3 (1980), 125–127.
50 A.L. Zharin and G.P. Shpenkov, Proc. of the 5th All-Union Symposium on Mechanoemission and Mechanochemistry of Solids, p. 206, Est. NIINTI, Tallinn, 1975.
51 A.L. Zharin and G.P. Shpenkov, Application of Selective Transfer in Friction Units of Machines, Collected Papers of Scient. Conf. (two-book edition), Gosstandart SSSR, Inst. of Standartization and Metrology, Vol. 1, 46–49, Moscow, 1976.
52 A.L. Zharin and G.P. Shpenkov, Wear, Vol. 56 (1979), 309–313.
53 R.B. Tagirov and A.L. Stolov, in: Collected Papers of the Annual Scient. Conf. of the Kazan State Univ. for 1963, Precise Sciences. Kazan Univ. Press, 26–30, 1964.
54 V.S. Kortov and R.I. Mints, Fiz. Khim Obrab. Mater., No. 1 (1968), 48–53.
55 V.D. Evdokimov and V.I. Ryaboshapchenko, Izv. Vuzov, Fizika, Vol. 16 (1973), 112–115.

56 I.L. Roikh and I.P. Bolotich, Dokl. Akad. Nauk SSSR, Vol. 137, No. 1 (1961), 126–129.
57 I.L. Roikh, V.V. Ordynskaya, and I.P. Bolotich, Dokl. Akad. Nauk SSSR, Vol. 146, No. 6 (1962), 1316–1317.
58 V.S. Ivanova and V.F. Terentiev, The Nature of Fatigue of Metals, Moscow, Metallurgy., 1975.
59 V.S. Ivanova, S.E. Gurevich, I.M. Kopiev et al, in: Fatigue and Brittleness of Metallic Materials, Moscow, Nauka, 1968.
60 L.M. Rybakova, R.F. Merenkova, and B.M. Rozinskii, Mechanism of Plastic Deformation of Metals, Kiev, Nauk. Dumka, 1965.
61 L.M. Rybakova and R.F. Merenkova, Fizika Metallov i Metallovedenie, Vol. 21, No. 6 (1966), 915–919.
62 R.I. Mints, V.S. Kortov, V.L. Aleksandrov, and V.I. Kryuk, Fizika Metallov i Metallovedenie, Vol. 26, No. 4 (1968), 681–687.
63 V.D. Evdokimov, Friction Reversal and Quality of Machines, Kiev, Tekhnika, 1977.
64 V.I. Mints and V.S. Kortov, Izv. Akad. Nauk SSSR. Metally, 2 (1967), 165–171.
65 V.I. Kryuk and V.V. Pavlov, Investigation of the Surface of Structural Materials by the Electron Emission Method, Collected Papers of the Ural Polytechnik Institute, Sverdlovsk, Ural Polytech. Inst. Press, 116–122, 1969.
66 D. Mak-Lin, Mechanical Properties of Metals, Moscow, Metallurg., 1965.
67 E.M. Gutman, Mechanochemistry of Metals and Protection Against Corrosion, Moscow, Metallurg., 1981.
68 E. Rabinovich, Contact Interaction of Solids and Calculation of Friction Forces and Wear, Moscow, Nauka, 15–22, 1971.
69 V.P. Pukh, Glass Strength and Fracture, Moscow, Nauka, 1973.
70 V.P. Severdenko and L.I. Gurskii, High-Reduction Rolling, Minsk, Nauka i Tekhnika, 1968.
71 G. Buchheim, B. Junghans, and H. Lippmann, Phys. Status. Solidi, Vol. 44, No. 2 (1977), 585–591.
72 Suwa Yoshiki, Kikuchi Tadashi, and Furuya Keiichi, Mag. Spectrosc., Vol. 25, No. 4 (1977), 371–378.
73 A.D. Manasevich, Physical Principles of Stresses State and Strength of Metals, Moscow, Mashgiz, 1962.
74 V.S. Fomenko and I.A. Podchernyaeva, Emission and Adsorption Properties of a Substance and Materials, Handbook, Moscow, Atomizdat, 1975.
75 Zh. Benar, Oxidation of Metals (two-volume edition), Vol. 1, 499, Moscow, Metallurg., 1968.
76 I.M. Vasinyuk and L.A. Khamaza, Problemy Prochnosti, Vol. 5, No. 4 (1973), 75–77.

77 L.M. Rybakova and L.I. Kuksenova, Fiz. Metal. i Metalloved., Vol. 39, No. 2 (1975), 362–366.
78 L.M. Rybakova and L.I. Kuksenova, Metal Structure and Wear Resistance, Moscow, Mashinostr., 1982.
79 V.S. Kortov, A.I. Slesarev, and V.V. Rogov, Exoemission Testing of Workpiece Surfaces after Working, Kiev, Nauk. Dumka, 1986.
80 V.G. Kuranov and B.M. Kuzmichenko, in: Selective Transfer in Friction and Its Economic Effectiveness, Collected Papers of the Meeting, 215–223, MDNTP, Moscow, 1972.
81 L.I. Rabinovich, N.N. Kazakova, and T.P. Bregman, in: Selective Transfer in Friction and Its Economic Effectiveness, Collected Papers of the Meeting, 229–232, MDNTP, Moscow, 1972.
82 S.A. Shchukarev, Inorganic Chemistry (two-volume edition), Vol. 2, 384, Moscow, Vyssh. Shkola, 1974.
83 Ya.D. Vishnyakov, Packing Defects in a Crystalline Structure, Moscow, Metallurg., 1970.
84 S.Z. Bokshtein, Diffusion and Structure of Metals, Moscow, Metallurg., 1973.
85 Diffusion Processes, Structure and Properties of Metals, Collected Papers, Moscow, Mashinostr., 1964.
86 M. Roberts and Ch. Mackey, Chemistry of the Metal–Gas Interface (Russian translation), Moscow, Mir, 1981.
87 I.K. Kikoin (ed.), Tables of Physical Quantities, Handbook, Moscow, Atomizdat, 1976.
88 R. Hirschberg and E. Lange, Naturwiss, Vol. 39 (1952), 131.
89 M. Sienko, R. Plain, and R. Hester, Structural Inorganic Chemistry, Moscow, Mir, 1968.
90 D.N. Garkunov (ed.), Selective Transfer – Based Improvement of Wear Resistance, Moscow, Mashinostr., 1977.
91 D.N. Garkunov and A.A. Markov, New Aspects in the Friction Theory, Moscow, Nauka, 1966.
92 V.S. Kortov, A.I. Slesarev, N.I. Kordyukov, and E.A. Plekhanovba, Mikroelektronika, Vol. 5, Issue 6 (1976), 549–552.
93 V.S. Kortov, V.P. Shifrin, and A.I. Gaprindashvili, Mikroelektronika: Moscow, Sov. Radio, 8 (1975), 28–49.
94 V.S. Kortov, V.I. Kryuk, R.I. Mints et al, Fiz. Khim. Obrab. Mater., No. 5 (1970), 91–96.
95 Yu.S. Zharkikh and A.D. Evdokimov, Mikroelektronika, Vol. 9, Issue 1 (1980), 82–85.
96 P.I. Sanin, Trenie i Iznos, Vol. 1, No. 1 (1980), 45–57.
97 Yu.N. Shekhter and S.E. Krein, Crude-Oil Surfactants, Moscow, Khim., 1971.
98 A.L. Zharin and G.P. Shpenkov, The Device for Testing of Friction Units,

USSR Inventor's Certificate 615379, MKI G 01 M 13/04. Otkryt. Izobret. No. 26 (1978).
99 D.N. Garkunov and I.V. Kragelskii, Selective Atomic Transfer, Scientific Discovery Diploma No. 41, in: USSR Discoveries for 1957–1967, Moscow, TsNIIPI, (1968) 52–53.
100 Lin, Transactions of ASME: Friction and Lubrication Problems, No. 3 (1974), 164–170.
101 A.P. Semenov, in: The Friction and Wear Theory, 164–170, Moscow, Nauka, 1965.
102 S.B. Ainbinder, E.F. Dubrovskii, and E.F. Rastrigina, Dokl. Akad. Nauk SSSR, Vol. 179, No. 5 (1968), 1076–1078.
103 S.B. Ainbinder, in: Increase of Wear Resistance and Service Life of Machines, 7–12, Kiev, Tekhnika, 1970.
104 V.I. Likhtman, in: On the Nature of Seizuring of Solids, 30–32, Moscow, Nauka, 1967.
105 G.V. Samsonov, A.Ya. Artamonov, and M.F. Idzon, Fiz. Khim. Mekh. Mater., Vol. 4, No. 4 (1968), 424–431.
106 N.N. Rykalin, M.Kh. Shorshorov, and Yu.L. Krasulin, Izv. Akad. Nauk SSSR, Ser. Neorgan. Mater., Vol. 1, No. 1 (1965), 29–36.
107 L.G. Gindin, Dokl. Akad. Nauk SSSR, Vol. 73, No. 3 (1950), 515–518.
108 G.P. Shpenkov and A.N. Podalov, in: Selective Transfer in Friction Units, Moscow, MDNTP, 44–55, 1971.
109 B.D. Voronkov and B.I. Lebedev, in: Electrochemical Processes on Friction and Their Application for Combatting Wear, Odessa, VSNTO, 136–137, 1973.
110 Ya.E. Geguzin, Yu.S. Kaganovskii, V.V. Kalinin, and V.V. Slezov, Fiz. Tverd. Tela, Vol. 12, Issue 7 (1970), 1953–1962.
111 B.I. Boltax, Diffusion in Semiconductors, Moscow, Fizmatgiz, 1961.
112 G.P. Shpenkov, A.N. Podalov, and A.P. Chelyshev, Vesti Akad. Nauk BSSR, Ser. Fiz-Tekh. Nauk, No. 3 (1973), 59–62.
113 G.P. Shpenkov, D.N. Garkunov, V.Ya. Matyushenko, and B.D. Kharkhasov, Izv. Vuzov, Fizika, No. 5 (1973), 41–45.
114 G.P. Shpenkov and A.P. Chelyshev, Vesti Akad. Nauk BSSR, Ser. Fiz-Tekh. Nauk, No. 2 (1973), 125–128.
115 Yu.R. Evans, Corrosion and Oxidation of Metals, Moscow, Mashgiz, 1962.
116 G.V. Akimov, Theory and Method of Investigation of Metal Corrosion, Moscow–Leningrad, USSR Akad. Sci. Press, 1945.
117 I.M. Melnichenko and G.P. Shpenkov, in: Selective Transfer on Friction and Its Economic Effectiveness, 40–44, Moscow, MDNTP, 1972.
118 V.B. Fix, Ionic Conduction in Metals and Semiconductors, Moscow, Nauka, 1969.
119 R.A. Machevskaya and A.V. Turkovskaya, in: Protective Metal and Oxide

Coatings, Metal Corrosion, and Electrochemistry Investigations, 403–409, Moscow–Leningrad, Nauka, 1965.
120 I.V. Vasiliev, Khim Mashinostr., No. 3 (1965), 30–33.
121 M.J. Allen, Electrode Processes in Organic Chemistry, Leningrad, Goskhimizdat, 1961.
122 Ya.M. Kolotyrkin (ed.), Electrochemistry of Metals in Nonaqueous Solutions, Moscow, Mir, 1974.
123 D.S. Yas', V.B. Podmokov, and I.S. Dyadenko, Friction and Wear Tests, Kiev, Tekhnika, 1971.
124 V.D. Kuznetsov, Surface Energy of Solids, Moscow, GITTL, 1954.
125 E. Rabinovich, J. Appl. Phys., Vol. 32, No. 8 (1961), 1440–1444.
126 D.N. Garkunov, A.A. Markov, and G.A. Golikov, in: The Lubrication Effect Theory and Noval Materials, 12–15, Moscow, Nauka, 1965.
127 V.G. Kuznetsov and G.P. Shpenkov, in: Friction and Wear in Machines, Proc. of the All-Union Scientific Conference in Chelyabinsk, 64, 1979.
128 A.A. Polyakov, I.V. Kragelskii, and D.N. Garkunov, Dokl. Akad. Nauk SSSR, Vol. 195, No. 3 (1970), 666–668.
129 G.V. Karpenko and R.I. Kripyakevich, The Hydrogen Effect on Steel Properties, Moscow, Metallurg., 1962.
130 A.N. Morozov, Hydrogen and Nitrogen in Steel, Moscow, Metallurg., 1968.
131 P.A. Thiesses, K. Meyer, and G. Heinicke, Grundlagen der Tribochemie, Berlin, Akademie Verlag, 1967.
132 J.R. Lowry, Glycerine and Glycols, Leningrad, Goskhimtekhizdat, 1933.
133 Yu.S. Simakov, in: Proc. of the IVth All-Union Symposium on Mechanoemission and Mechanochemistry of Solids (Irkutsk), 157–159, Moscow, USSR Acad. Sci. Press, 1973.
134 M.M. Khrushchev and M.A. Babichev, Abrasive Wear, Moscow, Nauka, 1970.
135 G.I. Bortnik and G.P. Shpenkov, in: Proc. of the All-Union Conference on Wear Investigation to Reveal the Ways of Inereasing the Service Life and Quality of Produced Machines, 10–11, Moscow, N.E. Bauman MVTU Press, 1971.
136 S.V. Ventsel and N.M. Starchenko, Problemy Treniya i Iznashiv., Kiev, Tekhnika, Issue 1 (1971), 66–69.
137 M.L. Barabash, M.V. Korogodskii, A.S. Krayushkin, and F.A. Fedotov, in: Improvement of Wear Resistance and Service Life of Machines (two-volume edition), Vol. 2, 249–261, Kiev, Ukr.SSR Acad. Sci. Press, 1960.
138 M.L. Barabash, G.I. Valchuk, and E.M. Natanson, in: Collected Papers of the Institute for Superstrength Materials, Ukr. Academy of Sciences, Kiev, Ukr.SSR Acad. Sci. Press, No. 22 (1956), 17–21.
139 G.I. Bortnik, in: Selective Transfer on Friction and Its Economic

Effectiveness, 151–156, Moscow, MDNTP, 1972.
140 N.D. Tomashov and G.P. Chernova, Corrosion and Corrosion-Resistant Alloys, Moscow, Metallurg., 1973.
141 H.W. Pickering, C.J. Wagner, and P.J. Byrne, Electrochem. Soc., Vol. 114, No. 7 (1967), 698–706; Vol. 116, No. 11 (1969), 1492–1496.
142 V.R. Regel, A.I. Slutsker, and E.E. Tomashevskii, Kinetic Nature of the Strength of Solids, Moscow, Nauka, 1974.
143 Ya.I. Gerasimov (ed.), The Course of Physical Chemistry, Moscow, Khim., 1973.
144 G.P. Shpenkov, in: Physicochemical Principles of Lubricating, Proc. of the All-Union Conf., 49–50, Kishinev, 1979.
145 D.N. Garkunov (ed.), Selective Transfer in Heavy-Loaded Friction Units, Moscow, Mashinostr., 1982.
146 A.S. Kuzharov, G.P. Barchan, and V.V. Chuvaev, Zh. Fiz. Khim., Vol. 51, No. 11 (1977), 2949–2951.
147 A.S. Kuzharov and V.V. Suchkov, Zh. Fiz. Khim., Vol. 54, No. 12 (1980), 3114–3118.
148 A.S. Kuzharov, V.V. Suchkov, L.A. Vlasenko, et al., Zh. Fiz. Khim., Vol. 55, No. 10 (1981), 2588–2592.
149 A.S. Kuzharov, S.A. Zhuravleva, and I.K. Shakurova, Zh. Fiz. Khim., Vol. 55, No. 11 (1981), 2872–2875.
150 G.K. Dvoryadkina, A.S. Ivanov, and S.A. Borisov, Fiz. Metal. i Metalloved., Vol. 50, Issue 3 (1980), 633–634.
151 A.S. Ivanov, V.Ya. Ganelin, Yu. M. Shulga, et al., Poverkhnost'. Fiz., Khim., Mekh.. 8 (1982), 144–148.
152 J.P. Stark, Diffusion in Solids (Russian translation), Moscow, Energiya (1980).
153 E.A. Markovskii and B.A. Kirievskii, Problemy Treniya i Iznashiv., Kiev, Tekhnika, Issue 6 (1974), 105–112.
154 K. Nakajima, A Isogai, and Y. Taga, Japan J. Appl. Phys., Vol. 2, No. 1 (1974), 309–312.
155 G.P. Shpenkov, S. Sagatovski, A Method for the Manufacture of an Additive for Lubricants, Cooling Liquids and Fuels, and Additive for Lubricants, Cooling Liquids and Fuels. Summery of the Patent Application, Reg. Nr 293400, Bulletin of the Patent Department, Warsaw, Poland, Nr 15 (485) 1992, p. 26.
156 G.P. Shpenkov, Energy and Resources Saving by New Multifunctional Addition Agent, Proceeding of 9th International Colloquium "Ecological and Economical Aspects of Tribology", January 11–13 (1994), Ostfildern, FRG, 2, 11.4–1 – 11.4–3.
157 N.N. Kurchik, V.V. Vainshtok, Yu.N. Shehter, "Lubricant materials for cutting treatment of metals", Himiya, Moscow, 1972.

158 Cutting fluids, Reference book (edited by S.G.Entelis and E.M. Berlinger), Mashinostroenye, Moscow, 1986.
159 Patent GB 1561082, Improvements relating to the lubrication of bearings.
160 V.E. Fertman, Magnetic fluids, Reference book, Vysheishaya Shkola, Minsk,1988.
161 Patent JP 56064204, Fuel combustion by burning with colloidal dispersion of fine particles of divalent metal-iron oxide cpd.
162 P.A. Thiesses, Zeitschrift Chemie, Vol. 5 (1965), 162–171.
163 F. Bowden and A.D. Ioffe, Explosion Initiation and Excitation in Liquids and Solids, Moscow, Izd. Inostr. Lit., 1955.
164 A. Knappwost, A. Aranson, J. Sohn, Schmiertechnick und Tribologie, Nr. 2 (1978), 53–55.
165 F. Bowden and D. Taybor, Friction and Lubrication of Solids, Moscow, Mashgiz, 1960.
166 R. Weichert, Untersuchungen zur Temperatur an der Bruchspitze, Karlsruhe, Inst. Verfahrtechnik, 1976.
167 H.K. Kassik, Intern. J. Fract. Mechanics, Vol. 5, No. 3 (1968), 167–169.
168 R. Rice and W. Lewy, in: Physics of Strength and Plasticity, 225–230, Ed. by A.S. Argon, Cambridge USA, MTI, 1969.
169 R. Weichert and K. Schopert, J. Mech. Phys. Solids, Vol. 22 (1974), 127–133.
170 S.M. Belyaev, Yu.N. Martyshev, and Yu.E. Yushin, in: The Active Surface of Solids, Moscow, USSR Acad. Sci. Press, 245–248, 1976.
171 V.V. Boldyrev, Experimental Methods in Mechanochemistry of Solid Inorganic Substances, Novosibirsk, Nauka, 1983.
172 B.V. Deryagin and N.A. Krotova, Adhesion, Moscow–Leningrad, USSR Acad. Sci. Press, 1949.
173 B.V. Deryagin, N.A. Krotova, and V.P. Smilga, Adhesion of Solids, Moscow, Nauka, 1973.
174 Engineering and Methods of Measuring Exoelectronic and Acoustic Emission, Sverdlovsk, Ural Polytechnic Institute Press, No. 215, 1973.
175 V.S. Kortov, R.I. Mints, I.E. Myasnikov, and A.I. Gaprindoshvily, Phys. Stat. Sol. (a), Vol. 3, No. 1 (1970), K13–K14.
176 V.N. Marochkin, in: Electrochemical Processes on Friction and Their Use for Combatting Wear, Odessa, VSNTO (1973), 134–135.
177 B.M. Tsarev, Contact Potential Difference and Its Effect on Operation of Electrovacuum Devices, Moscow, GITTL, 1955.
178 V.I. Kozus' and G.P. Shpenkov, The Integrating Picoampermeter, USSR Inventor's Certificate 524133, MKI G 01 R 19/26, Otkryt. Izobret., No. 29 (1976).
179 V.I. Kozus' and G.P. Shpenkov, The Solid-State X-Ray Vidicon, USSR Inventor's Certificate 663128, MKI H 04 N 5/30, Otkryt. Izobret., No. 18

(1979).
180 V. Kment and A. Kun, Measuring Technique of Radioactive Radiation, Moscow, Nauka, 1964.
181 V.B. Brodskii, S.E. Zagik, and V.A. Lyutomskii, Zh. Tekh. Fiz., Vol. 36, Issue 4 (1966), 640–642.
182 V.D. Evdokimov, in: The Friction, Wear, and Lubrication Theory, Proc. of the All-Union Scient. Conf. (three-part edition), Part 2, 83–84, Tashkent, 1975.
183 A.A. Petrosyants and V.A. Avanesov, in: Electrochemical Processes on Friction and Their Use for Combatting Wear, Odessa, VSNTO (1973), 174–178.
184 A.A. Petrosyants, V.A. Fedotov, D.N. Olifirov, et al., in: Application of Selective Transfer in Friction Workpieces, Proc. of the Standard. and Metrol. Inst. (two-part edition), Part 1, 139–141, Moscow, VISM, 1976.
185 B.D. Voronkov and V.G. Shadrin, in: Application of Selective Transfer in Friction Workpieces, Proc. of the Standard. and Metrol. Inst. (two-part edition), Part 1, 112–115, Moscow, VISM, 1976.
186 K. Simionescu and K. Oprea, Mechanochemistry of High-Molecular Compounds (Russian translation), Moscow, Mir, 1970.
187 N.K. Baramboim, Mechanochemistry of High-Molecular Compounds, Moscow, Khim., 1978.
188 V.V. Boldyrev and E.G. Avvakumov, Uspekhi Khim, Vol. 40, Issue 10 (1971), 1835–1856.
189 P.Yu. Butyagin, Uspekhi Khim, Vol. 40, Issue 11 (1971), 1935–1959.
190 N.S. Enikolopov, A.A. Zharov, and V.M. Kapustyan, The Regularity of Solid-Phase Polimerization of Organic Substances of Monomers under Shear Strain and High Pressure Conditions, Scientific Discovery , Diploma No. 288. Otkryt. Izobret., No. 40 (1984).
191 M.G. Matveev, A.A. Zharov, and V.M. Zhulin, Izv. Akad. Nauk SSSR, Ser. Khim., No. 3 (1982), 719–720.
192 M.G. Matveev, A.A. Zharov, V.M. Zhulin, and E.B. Zhuravleva, Dokl. Akad. Nauk SSSR, Vol. 270, No. 5 (1983), 1156–1159.
193 N.P. Chistotina, A.A. Zharov, M.G. Matveev, and V.M. Zhulin, Dokl. Akad. Nauk SSSR, Vol. 269, No. 3 (1983), 648–651.
194 E.V. Zubova and G.L. Aparnikov, Dokl. Akad. Nauk SSSR, Vol. 215, No. 5 (1974), 1150–1152.
195 V.A. Zhorin, G.A. Nikiforov, A.L. Khristyuk, and N.S. Enikolopyan, Dokl. Akad. Nauk SSSR, Vol. 271, No. 3 (1983), 650–652.
196 V.A. Zhorin, A.Yu. Shaulov, and N.S. Enikolopyan, Vysokomolekul. Soedinen., Vol. 195, No. 1 (1977), 841–843.
197 V.A. Zhorin, A.A. Zharov, Yu.V. Kissin, and N.S. Enikolopyan, Dokl. Akad.

Nauk SSSR, Vol. 219, No. 3 (1974), 647–649.
198 V.A. Zhorin, I.F. Makarova, M.Ya. Gen, and N.S. Enikolopyan, Dokl. Akad. Nauk SSSR, Vol. 261, No. 2 (1981), 405–408.
199 V.A. Zhorin, V.A. Makarov, O.S. Kozlov, et al., Dokl. Akad. Nauk SSSR, Vol. 265, No. 3 (1982), 646–649
200 V.V. Neverov, V.N. Burov, and A.I. Korotkov, Fiz. Metal. i Metalloved., Vol. 46, Issue 5 (1978), 978–983.
201 Yu.S. Zaslavskii and R.N. Zaslavskii, The Mechanism of Antiwear Dopes for Oils, Moscow, Khim., 1973.
202 Yu.A. Berlin, S.I. Beshenko, V.A. Zhorin, and N.S. Enikolopyan, Dokl. Akad. Nauk SSSR, Vol. 262, No. 2 (1982), 364–367
203 Yu.A. Berlin, S.I. Beshenko, V.A. Zhorin, at al., Dokl. Akad. Nauk SSSR, Vol. 264, No. 6 (1982), 1402–1404.
204 H.W. Hermance and T.F. Egan, Bell Systems Technical Journal, Vol. 37 (1958), 739–776.
205 A.A. Zharov, Z.G. Makarova, G.P. Shakhovskii, and V.M. Zhulin, Pribory i Tekhnika Eksper., No. 1 (1979), 248–249.
206 A.B. Solovieva, V.A. Zhorin, L.A. Krinitskaya, et al., Izv. Akad. Nauk SSSR, Ser. Khim., No. 5 (1977), 1161–1164.
207 V.D. Berezin, Coordination Compounds of Porphyrins and Phthalocianin, Moscow, Nauka, 1978.
208 A.S. Kuzharov and N.Yu. Onishchuk, in: Friction and Lubrication in Machines (two-part edition), Proc. of the All-Union Scientific Conf., Part 2, 289–290, Chelyabinsk, 1983.
209 V.V. Sinitsyn, Choice and Application of Plastic Lubricants, Moscow, Khim., 1974.
210 V.A. Zhorin, A.V. Nefediev, V.A. Linskii, et al., Dokl. Akad. Nauk SSSR, Vol. 256, No. 3 (1981), 598–600.
211 R.H. Dickerson, R.C. Lowell, and C.T. Tomizuka, Phys. Rev., Vol. 137, No. 2A (1965), A612–A619.
212 Ya.E. Geguzin, Macroscopic Defects in Metals, Moscow, Metallurg., 1962.
213 Van Büren, Defects in Crystals, Moscow, Izd. Inostr. Lit., 1962.
214 Superplasticity of Metal Materials, Moscow, Nauka, 1973.
215 E.A. Marchenko, E.F. Nepomnyashchii, and G.M. Kharach, Dokl. Akad. Nauk SSSR, Vol. 181, No. 5 (1968), 1103–1104.
216 K. Endo and J. Pukyda, Bull. of JSMS, Vol. 12, No. 15 (1969), 280–286.
217 L.I. Pogodaev, A.P. Nekoz, and A.I. Slyn'ko, Problemy Treniya i Iznashiv., Kiev, Issue 2 (1972), 44–46.
218 Z.V. Ignatieva, in: Investigation of a Structure of Friction Materials, Moscow, Nauka (1972), 56–61.
219 B.I. Kostetskii, I.A. Kravets, and I.I. Krivenko, Tekhnol. i Organiz.

Proizvodstva, No. 7 (1973), 69–71.
220 V.M. Sinaiskii and E.A. Marchenko, in: Heat Dynamics and External Friction Simulation, Moscow, Nauka (1975), 60–64.
221 E.A. Marchenko, Yu.V. Romanchuk, and A.O. Sheivekhman, in: Calculation-Experimental Methods of Evaluating Friction and Wear, Moscow, Nauka (1980), 92–95.
222 E.A. Marchenko, B.M. Rovinskii, and G.M. Kharach, in: Calculation and Simulation of Operating Conditions of Braking and Friction Facilities, Moscow, Nauka (1974), 35–45.
223 N.P. Suh, Wear, Vol. 25 (1973), 111–124.
224 N.P. Suh, Wear, Vol. 44 (1977), 1–16.
225 I.V. Kragelskii, in: Some Aspects of Mechanical Fatigue, Moscow, Nauka (1964), 355–369.
226 V.S. Ivanova, in: The Fatigue of Metals and Alloys, Moscow, Nauka (1971), 3–14.
227 L.F. Koffin, in: The Fatigue and Durability of Metals, Moscow, Izd. Inostr. Lit. (1963), 257–273.
228 S. Jahanmir and N.P. Suh, Wear, Vol. 44 (1977), 17–38.
229 J.R. Fleming and N.P. Suh, Wear, Vol. 44 (1977), 39–56.
230 V.G. Bar'yakhtar, M.A. Savchenko, and V.V. Tarasenko, Zh. Eksp. Teor. Fiz., Vol. 54, Issue 5 (1968), 1603–1612.
231 J. Morkowski, Acta Phys. Polon., Vol. 35 (1969), 565–583.
232 A.N. Pogorelyi, in: Metallofiz., Fiz. Metal. Plenok, Kiev, Nauk. Dumka, Issue 26 (1969), 33–43.
233 A.S. Bulatov, V.G. Pinchuk, and M.B. Lazareva, Fiz. Metal. i Metalloved., Vol. 34, Issue 5 (1972), 1066–1069.
234 V.G. Pinchuk, B.D. Kharkhasov, V.V. Torop, and Yu. Gerberger, Trenie i Iznos, Vol. 2, No. 3 (1981), 389–392.
235 P.I. Polukhin, S.S. Gorelik, and V.K. Vorontsov, Physical Principles of Plastic Deformation, Moscow, Metallurg., 1982.
236 G. Polzer and W. Ebeling, in: Longevity of Friction Parts of Machines, Collected Papers, Ed. D.N. Garkunov, Issue 3, 89–95, Moscow, Mashinostr., 1988.
237 G. Nicolis and I. Prigogine, Self-Organization in Nonequilibrium Systems, N.Y., A Wiley–Interscience Publ., 1977.
238 H. Kocak, Differential and Difference Equations through Computer Experiments, N.Y., Springer–Verlag, 1986.
239 G.P. Shpenkov and A. Gadomski, in: Selective Transfer, Coatings and Self-Organization: Practice and Development, Proc. of the International Conference in Sofia, Bulgaria, 23–37, 1994.
240 B.I. Smirnov, Dislocation Structure and Strengthening of Crystals, Leningrad,

Nauka, 1981.
241 Z.J. Grzywna and A. Gadomski, in: Process Technology Proceedings "Gas Separation Technology", E.F. Vansant and R. Dewolfs (eds), Amsterdam, Elsevier, 1990, 49–56, and references therein.
242 G. Beilby, Aggregation and Flow of Solids, London, Mc Millan, 1921.
243 V.P. Severdenko and E.I. Tochitskii, Structure of Thin Metal Films, Minsk, Nauka i Tekhnika, 1968.
244 I.L. Lebedeva, Nizkotemperat. i Vakuum. Materialoved., No. 4 (1974), 27–34, Khar'kov, Ukr.SSR Acad. Sci. Press.
245 A.K. Karaulov and V.S. Romanov, Trenie i Iznos, Vol. 1, No. 4 (1980), 610–614.
246 B.I. Kostetskii, A.K. Karaulov, N.B. Kostetskaya, et al., Zavod. Lab., No. 10 (1977), 1364–1367.
247 V.G. Pinchuk, B.A. Savitskii, and A.S. Bulatov, Poverkhnost'. Fizika, Khimiya, Mekhanika, No. 9 (1983), 72–75.
248 V.G. Pinchuk and V.I. Sverdlikov, Trenie i Iznos, Vol. 4, No. 5 (1983), 908–914.
249 V.A. Gorokhov, Pressure Shaping of Workpieces, Kiev, Tekhnika, 1978.
250 V.M. Andriyakhin, N.V. Edneral, Kh.A. Mazorra, and Yu.A. Skakov, Poverkhnost'. Fizika, Khimiya, Mekhanika, No. 10 (1982), 134–139
251 I.E. Brainin and N.N. Seleznev, The Method of Surface Layer Doping, USSR Inventor's Certificate 137946, MKI C 21d 3/00, Otkryt. Izobret., No. 9 (1961).
252 S.M. Irkaev, R.N. Kuz'min, and A.A. Opalenko, Nuclear Gamma-Resonance, Moscow, Moscow State Univ. Press, 1970.
253 V.S. Shpinel, Resonance of Gamma-Rays in Crystals, Moscow, Nauka, 1969.
254 V.I. Gol'danskii and E.F. Makarov, in: The Mössbauer Spectroscopy as Applied in Chemistry, Edited by V.I. Gol'danskii, L.M. Krizhanskii, V.V. Khrapov, Moscow, Mir, 1970.
255 U. Gonser (ed.), Mössbauer Spectroscopy II, The Exotic Side of the Method, Berlin–Heidelberg–N.Y., Springer–Verlag, 1981.
256 E.V. Bildyukevich, V.L. Gurachevskii, Yu.M. Litvinovich, et al., The Gamma-Resonance Complex in The Line with a Microcomputer, Deposited in VINITI 19.11.85, No. 4112–85, Moscow, 1985.
257 V.L. Gurachevskii, M. Mashlan, O.V. Misevich, et al., Dokl. Akad. Nauk BSSR, Vol. 29, No. 4 (1985), 329–332.
258 L.I. Podolskii, The GUASIC System for Computer Programing, Pushchino, 1982.
259 L.M. Rybakova, L.I. Kuksenova, and S.V. Bosov, Zavod. Labor., Vol. 39, No. 3 (1973), 293–296.
260 D. Pollard, Handbook on Computational Methods of Statistics, Moscow, Mir,

1982.
261 V.S. Litvinov, S.D. Karakishev, and V.V. Ovchinnikov, Nuclear Gamma-Resonance Spectroscopy of Alloys, Moscow, Metallurg., 1982.
262 A.D. Kuritsina, in: Friction and Wear in Machines, Moscow, USSR Acad. Sci. Press, 1956, 182–203.
263 L.V. Altshuller and M.P. Speranskaya, Vestnik Metallopromysh., No. 1 (1940), 15–21.
264 V.P. Severdenko and L.I. Gurskii, Structure in the Bulk and on the Surface of Rolled Materials, Minsk, Nauka i Tekhnika, 1972.
265 N. Cristofaro and R. Kaplow, Metal. Trans, Vol. 8A, No. 1 (1977), 35–43.
266 H. Ino, T. Moriya, F.E. Fujita et al., J. Phys. Soc. Japan, Vol. 25, No. 1 (1968), 88–93.
267 R.A. Arents, Yu.V. Maksimov, I.P. Suzdalev, et al., Fiz. Metallov i Metalloved., Vol. 36, Issue 2 (1973), 277–285.
268 V.G. Gavrilyuk, Fiz. Metallov i Metalloved., Vol. 45, Issue 5 (1978), 968–980.
269 O.S. Kozlova and V.A. Makarov, Fiz. Metallov i Metalloved., Vol. 48, Issue 5 (1979), 974–978.
270 U. Gonser and G. Fisher, in: Mössbauer Spectroscopy II, The Exotic Side of the Method, Edited by U. Gonser, Berlin–Heidelberg–N.Y., Springer–Verlag, 1981, 125–172.
271 N.S. Kolpakov, V.A. Kondratenko, V.P. Melnichuk, et al., Izv. Akad. Nauk SSSR, Ser. Fiz., Vol. 49, No. 8 (1985), 1656–1657.
272 L. Takacs, Solid State Comm., Vol. 21 (1977), 611–613.
273 J.M. Greneche, M. Henry, and F. Varret, J. of Mag. and Magnetic Materials, Vol. 26 (1982), 153–156.
274 V.L. Gurachevskii, M. Mashlan, G.P. Shpenkov, et al., Dokl. Akad. Nauk BSSR, Vol. 29, No. 10 (1985), 917–919.
275 D.M. Turley and L.E. Samuels, Metallography, Vol. 14 (1981), 275–278.
276 R.V. Pound, G.B. Benedek, and R. Drever, Phys. Rev. Lett., Vol. 7, No. 11 (1981), 405–408.
277 V.V. Chekin, Mössbauer Spectroscopy of the Iron, Gold and Tin Alloys, Moscow, Energoizdat, 1981.
278 V.A. Lagunov, V.I. Polozenko, and V.A. Stepanov, Fiz. Tverdogo Tela, Vol. 11, Issue 1 (1969), 238–239.
279 O.V. Misevich, A.L. Kholmetskii, V.A. Chudakov, and G.P. Shpenkov, in: Proc. of the 2nd Meeting on Nuclear-Spectroscopic Studies of Superfine Interactions, Groznyi (1987), 213–214.
280 T. Dosmaganbetov and A.K. Zhetbaev, in: Applied Nuclear Spectroscopy, Leningrad, Energoatomizdat, 171–177, 1984.
281 V.S. Kortov, R.I. Mints, and Yu.N. Sekisov, Fiz. Tverdogo Tela, Vol. 9, Issue

9 (1967), 2755–2756.
282 L.B. Kvashnina and M.A. Krivoglaz, Fiz Metallov i Metalloved., Vol. 23, Issue 1 (1967), 3–14.
283 P.I. Yashcheritsin, N.N. Makarov, V.V. Smolyak, et al., The Method of Abrasive Treatment, USSR Inventor's Certificate 975336, MKI B 24 B 1/00. Otkryt. Izobret., No. 4 (1982).
284 R.S. Ralokovich, S.L. Stepanyants, A.A. Mishuk, et al., Grease, USSR Inventor's Certificate 476308, MKI C 10m 5/26, C 10n 7/50. Otkryt. Izobret., No. 25 (1975).
285 V.N. Gridnev, V.G. Gavrilyuk, V.V. Nemoshkalenko, et al., Fiz. Metallov i Metalloved., Vol. 43, Issue 3 (1977), 582–590.
286 G.I. Bortnik and G.P. Shpenkov, The Method of Finish Treatment, USSR Inventor's Certificate 1093504, MKI B 24 B 29/00. Otkryt. Izobret., No. 19 (1984).
287 J.M. Genin and P.A. Flinn, Trans. TMS. AIME, Vol. 242, No. 7 (1968), 1419–1430.
288 A.E. Leikin and B.I. Rodin, Material Science, Moscow, Vyssh. Shkola, 1971.
289 V.G. Gavrilyuk, Fiz. Metallov i Metalloved., Vol. 45, Issue 5 (1978), 968–980.
290 V.S. Kortov, V.S. Novikova, and A.I. Slesarev, Izv. Vuzov. Chernaya Metallurgiya, No. 11 (1978), 177–179.
291 V.I. Likhtman, L.A. Kochanova, D.I. Leikis, and E.D. Shchukin, Elektrokhim., Vol. 5 (1969), 729–733.
292 B.D. Kharkhasov and G.P. Shpenkov, in: Selective Transfer in Friction Units, Moscow, MDNTP, 96–99, 1971.
293 R. Holm, Electric Contacts (Russian translation), Edited by D.E. Bruskin, A.A. Rudnitskii, Moscow, Izd. Inostr. Lit., 1961.
294 I.S. Taev, Elevtric Apparatuses, Moscow, Energiya, 1977.
295 P.S. Livshits, The Sliding Contact of Electric Machines, Moscow, Energiya, 1974.
296 V.A. Bobrovskii, Electrodiffusion Wear of Tools, Moscow, Mashinostr., 1970.
297 V.V. Usov, Metal Science of Electric Contacts, Moscow, Gosenergoizdat, 1963.
298 B.D. Kharkhasov, G.P. Shpenkov, and G.V. Ivanov, in: Selective Transfer in Friction and Its Economic Effectiveness, Moscow, MDNTP, 224–228, 1972.
299 B.D. Kharkhasov, S.P. Galetskii, G.V. Ivanov, and G.P. Shpenkov, in: Application of Selective Transfer in Friction Units of Machines (two-book edition), Proc. of Sci. Conf., Part 2, 71–76, Moscow, Gosstandart SSSR, VISM, 1976.
300 E.K. Venstrem and P.A. Rehbinder, Dokl. Alad. Nauk SSSR, Vol. 68 (1949), 329–332; Zh. Fiz. Khim., Vol. 26, No. 12 (1952), 1847–1853.
301 E.D. Shchukin, L.A. Kochanova, and V.I. Savenko, in: Advances in the

Mechanics and Physics of Surfaces, Eds. Latanision R.M. and Courtel R.J., London–N.Y., Acad. Publ., Vol. 1, 111–152, 1981.
302 N.H. Macmillan, R.D. Huntington, and A.R.C. Westwood, J. Material Sci., Vol. 9 (1974), 697–706.
303 E.D. Shchukin, Fiz. Khim. Mekhanika Mater., Vol. 1 (1976), 3–20.
304 E.D. Shchukin, L.A. Kochanova, and V.I. Savenko, Poverkhnost. Fizika, Khimiya, Mekhanika, Vol. 2 (1982), 25–41.
305 V.G. Pinchuk, B.D. Kharkhasov, and V.V. Torop, Problemy Treniya i Iznashiv., Issue 19 (1981), 31–33, Kiev, Tekhnika.
306 G.I. Shor and E.V. Evstigneev, Fiz. Khim. Mekhanika Materialov, Vol. 5, No. 5 (1969), 565–568.
307 K.K. Namitokov, Electroerosion Phenomena, Moscow, Energiya, 1978.
308 J.P. Bowden and L. Young, Research, Vol. 3 (1950), 235–237.
309 J. O'M. Bockris and R. Parry-Jones, Nature, Vol. 171 (1953), 930–931.
310 D.N. Staicopolus, J. Electrochem. Soc., Vol. 108, No. 9 (1961), 900–904.
311 O.A. Troitskii and A.G. Rozno, Fiz. Tverdogo Tela, Vol. 12, Issue 1 (1970), 203–210.
312 V.B. Fix, Ionic Conduction in Metals and Semiconductors, Moscow, Nauka, 1969.
313 E. Hoeffner, Nature, Vol. 172 (1953), 774–776.
314 V.Ya. Kravchenko, Zh. Eks. Teor Fiziki, Vol. 51, Issue 6 (12) (1966), 1676–1688.
315 V.I. Spitsyn and O.A. Troitskii, Electroplastic Deformation of Metals, Moscow, Nauka, 1985.
316 V.T. Omelchenko, in: Vestn. Kharkov. Politekh. Inst., Problems of Automatic Contact Devices, Kharkov, KhPI, Issue 2 (1967), 8–9.
317 V.G. Pinchuk, V.V. Torop, and B.D. Kharkhasov, in: The Friction, Wear and Lubrication Theory, Proc. of the All-Union Sci. Conf. (two-book edition), Part 2, 133–134, Tashkent Polytech. Inst. Press, Tashkent, 1975.
318 V.I. Spitsyn, O.A. Troitskii, V.G. Ryzhkov, and A.S. Kozyrev, Dokl. Akad. Nauk SSSR, Vol. 231, No. 2 (1976), 402–404.
319 O.A. Troitskii and V.G. Ryshkov, Pis'ma v Zh. Tekh. Fiz., Vol. 3, Issue 14 (1977), 680–684.
320 V.G. Pinchuk, V.V. Torop, and B.D. Kharkhasov, Problemy Treniya i Iznashivaniya, Issue 13 (1978), 115–118, Kiev, Tekhnika.
321 D.N. Garkunov, B.D. Kharkhasov, and G.P. Shpenkov, An Antifriction Lubricant, USSR Inventor's Certificate 690063, MKI C 10 M 5/02. Otkryt. Izobret., No. 37 (1979).
322 A. Westwood, Phil. Mag., Vol. 7, No. 76 (1962), 633–649.
323 B.D. Kharkhasov and G.P. Shpenkov, in: High-Current Electric Contacts and Electrodes, Proc. of the All-Union Sci. Conf., UkrSSR Sci. Acad., Inst. of

Applied Mathematics, 173–178, Kiev, 1972.
324 G.V. Ivanov, V.G. Kuznetsov, N.N. Sauk, and G.P. Shpenkov, in: The Ways to Improve the Quality qnd Reliability of Electric Contacts, Proc. of the All-Union Meeting, 60–61, Leningrad, 1978.
325 N.A. Galaktionova, Hydrogen in Metals, Moscow, Metallurgiya, 1967.
326 L.S. Moroz and B.B. Chechulin, Hydrogen Brittleness of Metals, Moscow, Metallurgiya, 1967.
327 V.V. Frolov, A Behavior of Hydrogen on Fusion Welding, Moscow, Mashinostr., 1966.
328 K. Smittell, Gases and Metals, Introduction to the Theory of Equilibrium of Gases with Metals, Moscow–Leningrad, Metallurgizdat, 1940.
329 L.P. Rekova, Ya.M. Fogel, and L.V. Nesterov, Fiz. Tverdogo Tela, Vol. 11 (1969), 1891–1894.
330 N.V. Cherepnin, Sorption Phenomena in Vacuum Technology, Moscow, Sov. Radio, 1973.
331 V. Heintse, Introduction to Vacuum Technology (two-book edition), Vol. 1, Moscow–Leningrad, Gosenergoizdat, 1960.
332 L. Grunberg, D.T. Jamieson, and D. Scott, Phil. Mag., Vol. 8 (1963), 1553–1568.
333 P. Schatsberg and I.M. Felsen, Wear, Vol. 12 (1968), 331–342.
334 P. Shatsberg and I.M. Felsen, Transaction of the ASME, Ser. F. Friction and Lubrication Problems (Russian translation), Vol. 91, No. 2 (1969), 101–113.
335 P. Shatsberg, Transaction of the ASME, Ser. F. Friction and Lubrication Problems (Russian translation), Vol. 93, No. 2 (1971), 19–23.
336 A.A. Polyakov and D.N. Garkunov, Fiz. Khim. Mekhanika Mater., Vol. 5, No. 2 (1969), 197–200.
337 G.A. Georgievskii, M.Ya. Olina, and N.N. Maltseva, in: The Lubrication Effect Theory and New Materials, Moscow, Nauka, 202–208, 1965.
338 A.A. Guslyakov, A.V. Ashukin, V.I. Kuleba, and I.M. Lyubarskii, Fiz. Khim. Mekhanika Mater., Vol. 6, No. 1 (1970), 106–107.
339 P.V. Sklyuev, Hydrogen and Flakes in Large Forgings, Moscow, Mashgiz, 1963.
340 V.Ya. Matyushenko and G.P. Shpenkov, in: Physicochemical Mechanics of Friction Interaction, Proc. of the All-Union Sci.-Engin. Meeting, Inst. Mashinoved. USSR Sci. Acad., 62–64, Moscow, 1971.
341 S.D. Gertsriken and I.Ya. Dekhtyar, Diffision in Metals and Alloys in a Solid Phase, Moscow, Fizmatgiz, 1960.
342 V.A. Kudinov, in: Proc. of the 2nd All-Union Conf. on Friction and Wear in Machines, Vol. 2, 57–61, USSR Acad. Sci. Press, 1960.
343 E.V. Kutser, Investigation of the Heating of Components of Metallopolymeric Friction Units with Local Force Contact, Candidate's Dissertation

(Engineering), Tbilisi, 1969.
344 D.N. Garkunov, V.Ya. Matyushenko, V.V. Kharitonov, and G.P. Shpenkov, in: Electrochemical Processes on Friction and Their Application Against Wear, Odessa, VSNTO, 88–95, 1973.
345 A.V. Lykov, The Heat Conduction Theory, Moscow, Vyssh. Shkola, 1967.
346 S.I. Mantulenko and V.V. Kharitonov, Teplofiz. Vys. Temper., Vol. 9, No. 2 (1971), 373–377.
347 M.A. Mikheev, Fundamentals of Heat Transfer, Moscow–Leningrad, Gosenergoizdat, 1956.
348 V.V. Kharitonov, G.P. Shpenkov, and V.Ya. Matyushenko, in: Electrochemical Processes on Friction and Their Application Against Wear, Odessa, VSNTO, 208–212, 1973.
349 G.T. Timoshchenko and M.S. Metsik, in: Heat and Mass Transfer, Vol. 7: Physical Parameters of Heat and Mass Transfer, Minsk, Nauka i Tekhnika, 573–580, 1968.
350 V.V. Kharitonov, Inzh.–Fiz. Zh., Vol. 16, No. 2 (1969), 240–245.
351 A.A. Gukhman, The Similarity Theory as Applied to Heat and Mass Transfer Process Investigations, Moscow, Vyssh. Shkola, 1967.
352 V.I. Shapovalov and V.Yu. Karpov, Dokl. Akad. Nauk UkrSSR, No. 7 (1981), 90–94.
353 Yu.I. Archakov, Hydrogen Resistance of Steel, Moscow, Metallurg., 1978.
354 A.A. Baranov, Phase Transformation and Thermocycling of Metals, Kiev, Nauk. Dumka, 1974.
355 M.L. Bernshtein, Structure of Deformed Metals, Moscow, Metallurg., 1977.
356 M.V. Grabskii, Structural Ductility of Metals, Moscow, Metallurg., 1975.
357 V.I. Shapovalov and V.Yu. Karpov, Fiz. Metal. i Metalloved., Vol. 55, Issue 4 (1983), 805–811.
358 M.M. Shved and G.V. Karpenko, in: An Effect of Working Media on Properties of Materials, Kiev, UkrSSR Acad. Sci. Press, Issue 2, 159–164, 1963.
359 A.I. Krasnikov, Izv. Akad. Nauk SSSR, Otd. Tekh. Nauk, No. 1 (1946), 133–135.
360 V. Rachinski and M. Smyalovski, Zashchita Metallov, Vol. 5, No. 5 (1969), 482–490.
361 A.A. Polyakov and Yu.S. Simakov (eds.), Investigation of Hydrogen Wear, Moscow, Nauka, 1977.
362 A.A. Polyakov (ed.), Protection Against Hydrogen Wear in Friction Units, Moscow, Mashinostr., 1980.
363 S.F. Scieszka, Wear, Vol. 64, No. 2 (1981), 367–378.
364 I.V. Vasiliev, N.M. Zhuravlev, R.A. Melamud, and V.A. Fedotova, in: Longevity of Friction Parts of Machines, Collected Papers, Ed. D.N.

Garkunov, Issue 1, 159–165, Moscow, Mashinostr., 1986.
365 Yu.S. Simakov, in: Investigation of Hydrogen Wear, Moscow, Nauka, 39–43, 1977.
366 D.N. Garkunov and A.A. Polyakov, in: Investigation of Hydrogen Wear, Moscow, Nauka, 3–12, 1977.
367 Yu.M. Baron, Magnetic-Abrasive and Magnetic Treatment of Workpieces and Cutting Tools, Leningrad, Mashinostr., 1986.
368 G.I. Suranov, in: Longevity of Friction Parts of Machines, Moscow, Mashinostr., 129–136, 1986.
369 P.V. Sysoev, G.P. Shpenkov, A.I. Korshunov, and V.Ya. Matyushenko, in: Friction and Wear Problems, Kiev, Tekhnika, Issue 4, 151–155, 1973.
370 B.V. Balashov and V.Ya. Matyushenko, in: Selective Transfer on Friction and Its Economic Effectiveness, Moscow, MDNTP, 139–140, 1972.
371 V.E. Panin, V.A. Likhachev, and Yu.V. Grinyaev, Structural Levels of Deformation of Solids, Novosibirsk, Nauka, 1985.
372 V.E. Panin, A New Field of the Physics of Solids, Izv. Vuzov, Fizika, No. 1 (1987), 3–8.
373 G.P. Shpenkov and G.I. Bortnik, in: Friction and Lubrication in Mashines, Proc. of the All-Union Conf., Chelyabinsk, 284–285, 1983.
374 A.S. Kuzarov and N.Yu. Onishchuk, Properties and Application of Metal-Plating Lubricants: Survey, Moscow, Izd. TsNIITEneftekhim, 1985.
375 E.A. Stanchuk and A.P. Shumilov, in: Longevity of Friction Parts of Machines, Collected Papers, Ed. D.N. Garkunov, Isuue 1, 153–159, Moscow, Mashinostr., 1986.
376 A.A. Polyakov, D.N. Garkunov, G.P. Shpenkov, and V.Ya. Matyushenko, The Phenomenon of Formation of the Hydrogen-Saturated Zone in the Near-Surface Layer of Metals Under Friction (the Phenomenon of "Hydrogen Wear of Metals"), Scientific Discovery Diploma No. 378, Otkryt. Izobret., No. 30, 1990.
377 D.N. Garkunov, V.Ya. Matyushenko, A.A. Polyakov, and G.P. Shpenkov, Fiz. Khim. Mekh. Mater., Vol. 8, No. 3 (1972), 104–105.
378 G.P. Shpenkov, in: Non-Wear Effect and Tribotechnology, Moscow, Issue 3–4, 56–67, 1992.
379 G.P. Shpenkov, in: Theory and Practice of Tribology, Proc. of the 6th International Congress on Tribology EUROTRIB'93, Budapest, Vol. 3, 100–105, 1993.
380 Yu.M. Baron, I.A. Senchilo, in: Precision and Productivity of Mechanical Treatment, Leningrad, LPI, No. 368, 88–90, 1980.
381 G.P. Shpenkov, A.L. Kholmetskii, V.A. Chudakov, and O.V. Misevich, in: Longevity of Friction Parts of Machines, Collected Papers, Ed. D.N. Garkunov, Isuue 4, 80–96, Moscow, Mashinostr., 1989.

382 M. Rich, Phys. Letters, Vol. 4, No. 3 (1963), 153–155.
383 A.A. Maradudin, I. Meingailis, Phys. Rev., Vol. 133A, No. 4 (1964), 1188–1193.
384 F.Yu. Sakulevich, L.K. Minin, L.A. Olender, Magnetic-Abrasive Treatment of Precise Parts, Minsk, Tekhnika, 1977.
385 F.Yu. Sakulevich, Fundamentals of Magnetic-Abrasive Treatment, Minsk, Tekhnika, 1981.
386 S.Z. Bokshtein, S.S. Ginzburg, S.T. Kishkin, et al, Autoradiography of Interfaces and Structural Stability of Alloys, Moscow, Metallurgiya, 1987.

SUBJECT INDEX

This Page Intentionally Left Blank